Reports File

Book 4 of 8

GEORGIA INSTITUTE OF TECHNOLOGY

OFFICE OF RESEARCH ADMINISTRATION

RESEARCH PROJECT INITIATION

Date: March 19, 1971

Project Title: Investigations of Lubricant Rheology as Applied to Elastohydrodynamic Lubrication

Project No: B-1149 (E-2356-00)

Principal Investigator: Dr. W. O. Winer

Sponsor: National Aeronautics and Space Administration

Agreement Period: From March 3, 1971 Until March 2, 1972

Type Agreement: Grant No. NGR 11-002-133

Amount: $34,100 NASA Funds (B-1149)
3,500 Ga. Tech Contribution
$37,600 Total Budget

Reports Required: Semi-annual Status - due Sept. 3, 1971
Final Technical - due March 2, 1972

Sponsor Contact Person (s):

Administrative Officer
Herman Barnett
NASA Grants Specialist
National Aeronautics & Space Administration
Lewis Research Center
21000 Brookpark Road
Cleveland, Ohio 44135
Mail Stop No. 500-309
Telephone: 216-433-4000 ext. 238

Technical Officer
William R. Jones, Jr.
Fluid Systems Components Division
National Aeronautics & Space Administration
Lewis Research Center
21000 Brookpark Road
Cleveland, Ohio 44135
Telephone: 216-433-4000 ext. 6895

Assigned to: M.E.

COPIES TO:

- Principal Investigator
- School Director
- Dean of the College
- Director, Research Administration
- Deputy Controller (2)
- Security-Reports-Property Office
- Patent Coordinator
- Library
- Rich Electronic Computer Center
- Photographic Laboratory
- Project File
- Other

RA-3 (2-71)

GEORGIA INSTITUTE OF TECHNOLOGY
OFFICE OF CONTRACT ADMINISTRATION

SPONSORED PROJECT TERMINATION

Date: January 24, 1977

Project Title: Investigations of Lubricant Rheology as Applied to Elastohydrodynamic Lubrication

Project No: E-25-620

Project Director: Dr. Ward O. Winer

Sponsor: National Aeronautics and Space Administration

Effective Termination Date: April 4, 1976

Clearance of Accounting Charges: April 4, 1976

Grant/Contract Closeout Actions Remaining:

_ Final Invoice and Closing Documents
_ Final Fiscal Report
_ Final Report of Inventions
_ Govt. Property Inventory & Related Certificate
_ Classified Material Certificate
_ Other _____

Assigned to: Mechanical Engineering (School/Laboratory)

COPIES TO:

Project Director
Division Chief (EES)
School/Laboratory Director
Dean/Director—EES
Accounting Office
Procurement Office
Security Coordinator (OCA)
Reports Coordinator (OCA)
Library, Technical Reports Section
Office of Computing Services
Director, Physical Plant
EES Information Office
Project File (OCA)
Project Code (GTRI)
Other _____

CA—4 (3/76)

E-25-620

GEORGIA INSTITUTE OF TECHNOLOGY
ATLANTA, GEORGIA 30332

SCHOOL OF
MECHANICAL ENGINEERING

September 8, 1971

National Aeronautics and Space Administration
Lewis Research Center
21000 Brookpark Road
Cleveland, Ohio 44135

Attention: Mr. Robert L. Johnson
Mr. William R. Jones, Jr.

Subject: NASA Grant NGR 11-002-133 Semi-Annual # 1
Six months Progress Report

Our activities on this grant during the last six months fall naturally into the following four catagories:

INFRARED RADIATION DETECTION IN ELASTOHYDRODYNAMIC SIMULATOR

Initial studies in EHD film temperature measurement were undertaken using a Barnes Model RM-2A infrared microscope. The system being studied is primarily the same as that used in previous EHD experiments in this laboratory, i.e. sliding contacts with steel and sapphire surfaces and peak Hertzian pressures of about 150,000 lbf/in^2. A calibration curve for the steel-thin oil film system was determined, thus incorporating the emissivity of thin oil films. Under constant sliding speed and load condition, and after about five minutes running time, IR microscope traverses both parallel and perpendicular to the sliding velocity were made through the contact. In addition, the radiant energy at the contact center was recorded as a function of time starting with load application and ending at 10^3 seconds.

It has been found that unlike visual microscopes, the focal plane in the IR system is simply the plane where the size of the spot seen by the detector is a minimum. All other sources within a certain solid angle, typical of the objective being used, can emit energy which will fall on the detector. The current effort in our investigations is to determine the energy contribution of the sapphire and steel bounding the EHD contact and either correct our measurements to account for it, or to modify our system so that these contributions are insignificant. Once this has been accomplished, the EHD peak film temperature and/or temperature profile can be determined under a variety of operating conditions. Even if a temperature profile cannot be ascertained with high accuracy, the fact that all the radiation collected by the detector is a result of viscous shearing in the contact and not background radiation should be of value in studying EHD films and their failure modes.

PRESSURE VISCOSITY PROGRAM

As mentioned in the proposal for this project, we have observed a significant (up to 1 sec) time delay for the pressure difference signal across the capillary compared to the signal indicating flow through the capillary. The phenomena was observable at high pressure and seemed to increase with increasing pressure. It was important to determine whether this observation was the result of a fluid property or an artifact of the apparatus. If it is a property of the fluid it may have important consequences in elastohydrodynamic lubrication and if it is an artifact of the apparatus care must be taken to avoid its influence on the data reported. Three separate methods of examining this question were investigated and the conclusion is that the phenomena is an artifact of the system related to the viscous pressure drop associated with the flow required to actuate the pressure transducers.

The first method of examining this point was to take high speed recordings of the data at several pressure levels from 10,000 psi up to 70,000 psi. It was found that the time delay existed at all pressure levels, was very small (0.02 sec) at low pressures and increased monatonically with increasing pressure. This suggested that it was not a transition phenomena in the fluid. The second technique used was to connect two pressure transducers in series separated by about 30 inches of high pressure tubing. At a high pressure level (25, 50, and 75 kpsi) the pressure at one end of the tubing was increased at a constant rate (i.e 15 psi/sec) and the signals of the two transducers were compared. The signal of the transducer farthest from the pressure source, as expected, lagged that of the other. The lag time was comparable to the delay time previously observed and mentioned above. An elementary calculation based on the viscous pressure drop associated with the flow in the tubing which is the result of fluid compressibility and tubing elastic expansion predicted the response delay within 30%. It is therefore reasonably clear that the delay observed when taking high pressure viscosity data is a result of the apparatus response and not a fluid property. This must be taken into account when taking data while the system variables are changing.

The third experiment was performed in the elastohydrodynamic simulator and tends to confirm the above conclusion. Both film thickness and traction measurements were made with the mean Hertzian pressure both above and below the pressure at which the pronounced delay behavior was observed in the high pressure viscometer. The fluids used in these experiments were those which exhibited the greatest delay time in the viscometer. No significant difference in either the traction or the film thickness was found between the data taken at the two load conditions. These data also confirm the above conclusions regarding the origin of the observed time delay.

During this reporting period a significant improvement in the high pressure viscometer system has been made. The system has been modified by the utilization of an analog-to-digital converter which accepts the transducer analog signals and converts them to digital signals. These are recorded on magnetic tape. The tape is then used directly as input to the computer which in turn completes the data reduction. This method of data recording and reduction eliminates one of the most time consuming steps in taking high pressure viscosity data, namely the transcription of the continuous galvanometer recordings to computer input. It also eliminates the

possibility of transcriber error, increases the number of data sets taken for a given high pressure experiment, and should expand the range of variables over which data can be taken. Experiments have been performed with temporary wiring and have shown that the data is consistant with that obtained by the former method on the same fluid. The permanent wiring is now being completed and the system is expected to operate in the automatic data reduction mode for all future experiments.

The above modification has been made possible through cooperation with Dr. Samuel Shelton in this department. Dr. Shelton has an AFOSR contract (AFOSR-70-1934) entitled "Direct Measurement of Solid Propellent Response Functions" which paid for part of the recording system ($6400). The remaining $3500 was paid by departmental matching funds. The system was designed by Datum Inc. and contains Datum analog-to-digital converters and 20 channel multiplier. The data amplifiers are by Honeywell and the recorder by PEC, Inc. It is a portable unit and therefore readily available to us.

ELASTOHYDRODYNAMIC LUBRICATION CORRELATIONAL STUDIES

The film thickness results of EHD sliding point contact studies conducted in this laboratory during the past two and a half years are being studied in light of the dimensionless groups proposed by Dowson and Higginson, Blok, Moes, and Greenwood. The groups proposed by the last three investigators are relatively new and are based on physical arguments. The film thickness data being considered is taken from experiments in this laboratory on 29 different fluids. Viscosity data at high pressure and high shear rates has also been generated in this laboratory. Good correlation was not found when the low shear viscosity value was used for the contact inlet viscosity in any of the four sets of dimensionless parameters mentioned above. Attempts are now being made to determine a viscosity for each fluid whichwill improve correlation using the above techniques. This viscosity will then be compared with the high-shear, capillary viscometer data at shear rates typical of the EHD contact inlet. It is hoped that such a study will enable the designer to select the pertinent fluid properties in trying to predict EHD film thicknesses in point contacts.

NON-NEWTONIAN ELASTOHYDRODYNAMIC LUBRICATION ANALYSIS

The lubrication of elastic machine elements with non-Newtonian fluids is considered in an attempt to develop a model of this system applicable to the design of heavily loaded contacts. Only the Eulerian steady state is analyzed. The undeformed geometry is assumed to be that of a cylinder and plane. The fluid properties are described by an apparent viscosity and apparent elasticity. The apparent viscosity is considered as dependent on the shear strain rate, as well as temperature and pressure, and may be obtained from viscometric measurements. The appropriate method of measurement of the apparent elasticity is still under consideration and the apparent elasticity is treated as an adjustable parameter in the intermediate analysis. Heat transfer is also considered. The problem is formulated in terms of the conservation principles of mass, momentum and energy with the appropriate

boundary conditions. This system will be solved iteratively by methods similar to those used to obtain solutions for Newtonian fluids. This work is significant in extending the theory to include non-Newtonian fluids exhibiting time dependent and shear strain rate dependent effects.

The initial problem in the solution method, referred to above, is to find an adequate replacement for the closed form analytic representations used in the Newtonian case. Such a representation can only be determined numerically for the non-Newtonian case. At present investigations are being made to determine the most appropriate representations for fluids showing both upper and lower asymptotes in their apparent viscosities. The preliminary results are optimistic and should allow continuation and completion of the proposed solution method.

If there are any questions regarding the above described activities please contact me.

Sincerely,

Ward O. Winer
Professor

WOW:lb

CC: S. P. Kezios

GEORGIA INSTITUTE OF TECHNOLOGY
ATLANTA, GEORGIA 30332

SCHOOL OF
ECHANICAL ENGINEERING

November 9, 1972

National Aeronautics and Space Administration
Lewis Research Center
21000 Brookpark Road
Cleveland, Ohio 44135

Attention: Mr. Robert L. Johnson
Mr. Wm. R. Jones, Jr.

Subject: NASA Grant NGR-11-002-133, Supplement No. 1
Six Month Progress Report 3-9/72 Semi-Annual #2

Because of the delay in completing last year's annual report (submitted 6/72), much of the activity completed during the first half of this six month period has already been covered in that report. Those portions will be briefly reviewed here in addition to progress since June.

Infrared Radiation Measurement

The infrared radiation measurement to determine temperature distributions in elastohydrodynamic contacts continues to be a major activity. A technique has been developed for determining the lubricant layer emissivity as a function of film thickness for the very thin film range encountered in ehd contacts. This is accomplished by putting a layer of the sample lubricant between two sapphire plates the separation of which is maintained by spacers made of shim stock. By varying the shim stock the oil layer thickness can be varied. The transmission of infrared radiation by this layer is measured by placing the test cell between a black body calibration source and the IR microscope. With the measured transmission and known reflectivities of the surfaces the absorptively, and hence emmissivity, of the film can be determined. Measurements of the IR spectra of the oil in the cell were also made in an IR spectrometer (Perkin-Elmer, Model 457, Grating Infrared Spectraphotometer). Qualitative agreement between the two methods was obtained. Quantitative differences were related to the differences in IR response characteristics of the two instruments. The emissivities used will be those determined with the IR microscope.

Two techniques have been developed to seperate the total IR radiation received by the microscope detector into those portions which come from the oil and the ball surface respectively. This separation is necessary so that oil and surface temperatures can be determined as opposed to some average temperature for the oil-surface combination. Each technique appears to be able to give the oil and surface temperatures. The first technique involves the use of two spheres which are identical except for the surface appearance. One has the original shiny surface and the other surface has been darkened by slight heating. The emissivity of the first is about one half that of the second. The ehd film thickness and traction behavior of the two are identical within our limits of observation. By measuring the IR radiation distribution in each case and assuming the temperature distributions are the same, the radiation from the oil can be separated from that of the surface and then, with knowledge of the respective emissivities, the temperature distribution can be obtained.

The second technique involves the use of an IR filter made in the same fashion as the cell described above for fluid emissivity determinations. The IR radiation distribution in an ehd contact is then measured with and without the filter between the contact and the microscope. When the filter is in place it selectively absorbs the IR radiation from the fluid and passes the radiation from the surface (except for that in the same narrow band as the fluid spectra absorption). Again the two measurements allow the separation of the fluid and surface radiation and hence temperature.

Both methods have given preliminary data to indicate they are workable. It is believed that the second method will be more successful at elevated temperatures of the ehd system than it is for normal room temperature experiments. The first method is probably the better method for experiments where the normal temperature of the ehd experiment is near room temperature. Further exploration and comparison of the two techniques were delayed for six weeks when the IR microscope dewar lost its vacuum and was unable to cool the detector. The detector and dewar had to be replaced at the factory. The instrument was realligned and recalibrated at the same time and has just recently been returned to our laboratory.

Elastohydrodynamic (ehd) Simulation

In addition to the above IR research we have investigated the effect of high Hertz pressure on film thickness. This work was mentioned in the annual report and the paper submitted to ASME has since been rewritten. Copies of the revised manuscript have been submitted to the NASA personnel listed in the heading of this letter. The result of this work is to confirm the pronounced increase of film thickness dependency on Hertz pressure at high pressures which was earlier reported by the NASA-Battelle program.

With the support of an NSF grant, two related projects are well underway which should have direct bearing on the research under this NASA grant. These are the measurement of the pressure distribution in the ehd contact and the collection and detailed analysis of a sample of fluid from the high pressure region of the ehd contact. Although neither of these efforts are to the point of quoting results, the equipment development in both cases is far enough along to warrant being optimistic about their success.

Pressure-Viscosity Measurements

As mentioned in the annual report, considerable effort during the first part of this year was put into the extensive recalibration of the pressure viscometer and the development of an automated data collection and reduction program. In addition, the program to extend the upper shear stress and shear rate limits of the instrument have been continuing. The objective of this effort is to a) simulate the shear rate and shear stress conditions in the ehd contact and b) to distinquish between shear thinning and viscous heating effects in fluids at high shear stresses. This requires the utilization of smaller diameter and smaller length capillaries than before. Thus far we have reached shear stresses of over 10^7 dynes/cm^2 which are within a factor of five of the average found in ehd contacts. This development work has been done primarily with two-ethylhexyl sebacate and to a lesser extent with DN 600 (Fluid E from annual report) and it indicates that these fluids are Newtonian up to 10^7 dyne/cm^2.

Elastohydrodynamic Analysis

In this phase of our efforts we now have a computer program which converges to a solution in a reasonable amount of time. This program appears to be unique in that the entire domain is treated at once as opposed to the Cheng, and Dowson and Higginson approaches of dividing the domain into three regions (inlet, center, and exit) which are solved separately and then matched at their boundaries. The approach is also unique in applying a finite difference technique to the ehd problem and solving the resulting non-linear equations by the Newton-Raphson method. Unlike other solutions in this area the program is capable of solving the full range of load conditions from the light load Martin type to the heavily loaded full ehd conditions with its resulting pressure spike. Improvements are still expected in the rate of convergence and the effect of grid spacing on convergence.

The program thus far has dealt with linear fluids and isothermal conditions, but has been designed to readily incorporate fluid compressibility, non-linear viscosities and temperature effects.

Dimensional Analysis Correlations

As mentioned in the annual report there has been an attempt to correlate our ehd data by the several dimensional analysis schemes existing in the literature. Little further progress has been made in this effort. None of the schemes from the literature lead to correlation of ehd data between different fluids. We have not been able to determine the reason for this lack of correlation. Much speculation is possible but no clear ideas seem to immerge. We are now beginning to believe that the jump from material properties and kinematics to such global quantities as average film thickness and traction may be too great a gap to bridge at this time. Since we are developing the ability to measure pressure and temperature distributions in the ehd contact we may be able to learn more about fluid rheological behavior in the ehd contact by examining the pressure and temperature distributions which might be thought of as an intermediate step between the two extremes mentioned above.

If you have any questions regarding our efforts, we would appreciate discussing them with you.

Sincerely,

Ward O. W'ner
Professor

WOW:hdr

FTR

SCHOOL OF MECHANICAL ENGINEERING

GEORGIA INSTITUTE OF TECHNOLOGY

ATLANTA, GEORGIA

Investigations of Lubricant Rheology as Applied to Elastohydrodynamic Lubrication

NASA GRANT No.
11-002-133

By:

M. Bohn

S. Carlson

D. Lee

J. Jakobsen

Graduate Students

D. M. Sanborn
Assistant Professor

W. O. Winer
Professor &
Principal Investigator

For:

NASA-Lewis Research Center
21000 Brookpark Road
Cleveland, Ohio 44135

June 1972

SCHOOL OF MECHANICAL ENGINEERING

GEORGIA INSTITUTE OF TECHNOLOGY

ATLANTA, GEORGIA

Investigations of Lubricant Rheology as Applied to Elastohydrodynamic Lubrication

NASA GRANT No.
11-002-133

By:

M. Bohn

S. Carlson

D. Lee

J. Jakobsen

Graduate Students

D. M. Sanborn
Assistant Professor

W. O. Winer
Professor &
Principal Investigator

For:

NASA-Lewis Research Center
21000 Brookpark Road
Cleveland, Ohio 44135

June 1972

Abstract

This is the final technical report for NASA Grant No. NGR 11-002-133. The research under this grant consisted of elastohydrodynamic lubrication (ehd) studies and pressure-viscosity studies. Existing equipment was modified to more closely simulate practical ehd conditions. Analyses of ehd and pressure-viscosity data on eleven fluids previously investigated for NASA were also conducted. Near the end of the grant period it was found that the pressure-viscometers needed recalibration. A complete recalibration was conducted. Corrected viscosity-pressure data on all fluids measured for NASA (under purchase orders numbered NAS 3-14546 and NAS 3-15383) are presented in this report, and supersede previously reported data. This recalibration and analysis of the pressure-viscosity data was the cause of the lateness of this report. Data taken on NASA purchase order number C-57357-B was not corrected but is reported here for completeness.

I. INTRODUCTION

This report is the final technical report for NASA Grant No. NGR 11-002-133 entitled "Investigations of Lubricant Rheology as Applied to Elastohydrodynamic Lubrication." Investigations conducted fall into the two broad categories of the elastohydrodynamic lubrication (ehd) simulation and analyses program and the pressure-viscosity program.

In the ehd program the simulator was modified in several respects permitting higher sliding speed, higher Hertz pressure and higher bulk temperature experiments as well as the measurement of infrared radiation distribution from the ehd contact. Correlational studies have also been undertaken employing ehd dimensional analyses from the literature along with ehd and pressure viscosity data taken under both this grant and earlier measurements for NASA purchase orders (C-57357-B, NAS 3-14546 and NAS 3-15383). An analytical investigation has also been undertaken in an attempt to understand the behavior of non-linear fluids in ehd contacts.

In the pressure viscosity program the equipment was modified to permit viscosity-pressure measurements at much higher shear stresses (2×10^7 dynes/cm^2), which better simulate conditions in the ehd contact. An analog-to-digital data recorder/converter has also been adapted to the equipment to facilitate taking data. The pressure-viscometer was also completely recalibrated and it was found that certain transducer characteristics had changed since it was first calibrated by J. D. Novak (1,2). By spot checking data it was found that transducer characteristic changes had occurred during the Summer of 1969 when the equipment was

moved to Georgia Tech. As a result of the recalibration all the pressure-viscosity data taken for NASA under purchase orders NAS 3-14546 and NAS 3-15383 have been re-analyzed and the corrected data is reported in this document. These data supersede all pressure-viscosity data previously reported under purchase orders numbered NAS 3-14546 and NAS 3-15383.* The data is reported in both tabular form and in semi-log viscosity pressure plots and plots following Roeland's correlational method (3). Several viscosity-pressure parameters as functions of temperature are also reported for each fluid.

For completeness the data taken in 1969 under NASA purchase order number C-57357-B is also included in the same format as other data reported here. We have no reason to believe that the recalibration should be applied to that data. That data however does give values of α_{oT} at 210 and 300°F which are suspect in appearance.

*
The ehd data reported previously for purchase orders numbered NAS 3-14546 and NAS 3-15383 is correct as originally reported.

II. ELASTOHYDRODYNAMIC LUBRICATION INVESTIGATIONS

a. EHD Equipment Modifications

One of the major modifications made to the point contact simulator, described in (4,5,6) during the past year has been the addition of equipment needed in the infrared temperature measurements. A model RM2A Barnes infrared microscope was added in place of the visual microscope used for film thickness measurements. With the standard 15X objective the system can detect the IR radiance (watts steradian^{-1} cm^{-2}) in the wavelength band 1.8 - 5.5 microns with a resolution of 0.0014 inch in the EHD contact. The addition of this equipment allows one to scan the EHD contact with the IR microscope and obtain an oscilloscope trace of radiance as a function of position in the contact and/or time. The objective of this measurement is to ultimately deduce the temperature profile in the EHD film (see a later section of this report).

In order to reduce IR emission from the upper sapphire bearing surface, a sapphire disk of 0.010" thickness has been used. Unlike in the film thickness experiments, an uncoated surface is desirable in IR temperature measurements.

The drive mechanism in the EHD simulator has been extensively modified to allow an increase in possible sliding velocities of up to 1000 inches per second. This has been accomplished by replacing the synchronous motor/gear box assembly (5) with a speed controlled DC motor driving the shaft of the spherical bearing element through a flat belt. This technique has two additional advantages in addition to the increase in sliding velocity, The first is to allow one to continuously vary the sliding velocity, thus aiding in film thickness interference fringe order determination. The second is to isolate the vibration in the drive mechanism from the load

and traction transducers. This is a necessity at higher speeds and could not have been accomplished with the previous gear-driven system. In the new system the instantaneous shaft speed, and therefore the sliding velocity, are determined by optically sensing the number of shaft revolutions per unit time.

A new sphere support mechanism has been designed and constructed which will allow EHD experiments to be conducted at lubricant inlet temperatures of up to 400°F. In addition, the new sphere support mechanism should introduce less vibration into the system than the previous system using three radial ball bearings. The modified design consists of an enclosed heated container surrounding the sphere and having the sapphire bearing disk as its upper surface. The driven sphere (1.25 inch diameter) is supported by three identical spheres in the bottom of the high temperature enclosure. The enclosure will be completly filled with the test lubricant, heated to the desired temperature and, after the temperature of both bearing surfaces have stabilized, the elevated temperature EHD experiment can be performed. This system is expected to have the additional benefit of increasing the probability of having sufficient lubricant in the contact inlet to avoid starvation. In the previous system, the lubricant was introduced on the ball surface well ahead of the contact inlet. The high temperature enclosure will require that the sphere be completely submerged in the test lubricant.

The load capacity of the EHD simulator has been increased from 15 lbs. (150,000 psi. Hertz) to 52 lbs. (225,000 psi. Hertz). In addition, equipment modifications have nearly been completed which will raise this capacity to 125 lbs. (300,000 psi. Hertz). The design changes

necessary to allow the 125 lbs. load include a new load cell and modifications to the air bearing system used in traction measurements (4,6).

Finally, the optical system used in film thickness measurements has been improved. A new camera allowing 4" x 5" graphic or polaroid prints of film thickness interference patterns has been installed. This will aid in rapid film thickness determination in steady-state experiments while the 16mm reflex motion picture camera can still be used in transient studies. A 1000 watt illumination system has been constructed which will eventually aid in the study of transient EHD phenomena through the use of a very short exposure still camera or a high speed rotating prism camera.

b. Infrared Measurements

As mentioned in the previous section, we are now able to detect the IR radiance with a resolution as small as 0.0014 inches in the EHD contact. Since the IR microscope responds to all radiation collected by the objective within a specified solid angle, care must be taken to maximize the radiance contribution of the EHD film and to minimize those of the sapphire disk and the steel sphere, portions of which lie within the solid angle defined by the objective. By using a sapphire disk of 0.010 inch thickness, the fraction of the total IR radiance emitted by the sapphire has been reduced to less than 5%. The chromium steel sphere without an oil film has an emissivity of 0.275. Based on experiments performed thus far, a substantial portion of the radiance detected in the EHD contact is believed to originate at the sphere surface. An investigation is currently underway to accurately access the relative roles of the EHD film and sphere surface in the observed radiance.

Figure 1 shows the transient radiance response from the IR microscope positioned at the EHD contact center. The 15 lb load (P_H = 150,000 psi) is applied in approximately 80 milliseconds. The increase in IR radiance at the contact center above background radiation reaches a steady-state value as rapidly as the load. The apparent lead of the radiance curve may be due to the fact that the EHD film is established sometime prior to 0.020 seconds and during the remaining time, the film thickness is changing relatively little (4,5).

Figure 2 shows a set of steady-state radiance data taken on a naphthenic fluid at three different sliding velocities. The EHD contact was scanned along two different axes as shown in Figure 2. It can be noted that the radiance rises sharply at one Hertz radius from the contact center; that the peak is reached just beyond the contact center; and that the radiance at the contact exit is significantly lower than at the peak, but also higher than at the contact inlet.

The current emphasis in the IR investigations is to deduce the temperature in the EHD film from the IR radiance data obtained. This requires the determination of emissivity data for the fluid and bearing materials and an analytical investigation to determine the relative contributions of the steel sphere, the fluid film and the sapphire disk to the total radiance observed.

c. EHD Correlations

Using the four dimensionless parameter systems proposed by Dowson and Higginson (7), Blok (8), Moes (9), and Greenwood (10), a correlation study is being undertaken involving the ehd film thickness and traction

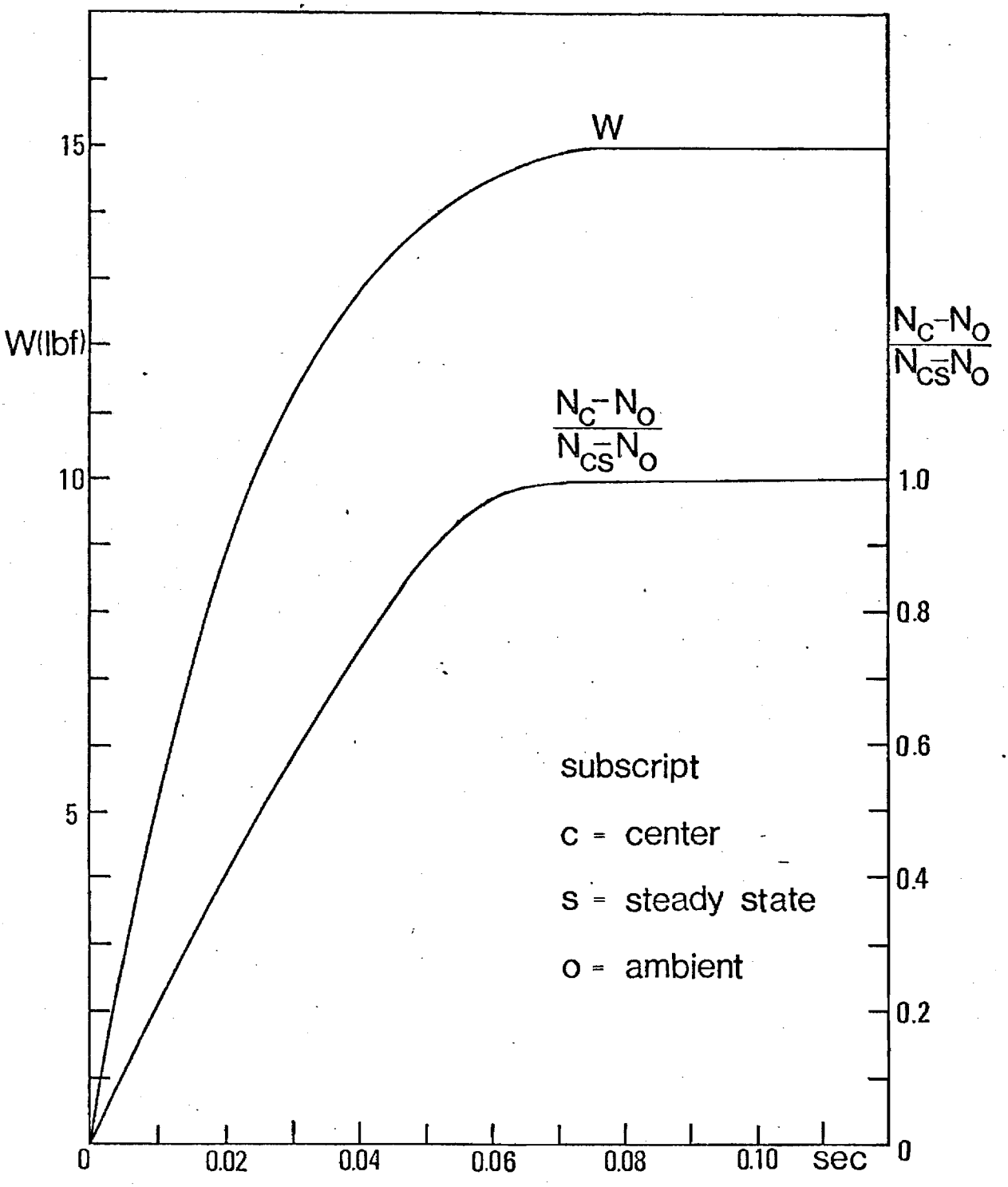

Figure 1. Infrared Radiance Emitted at the EHD Contact Center as a Function of Time

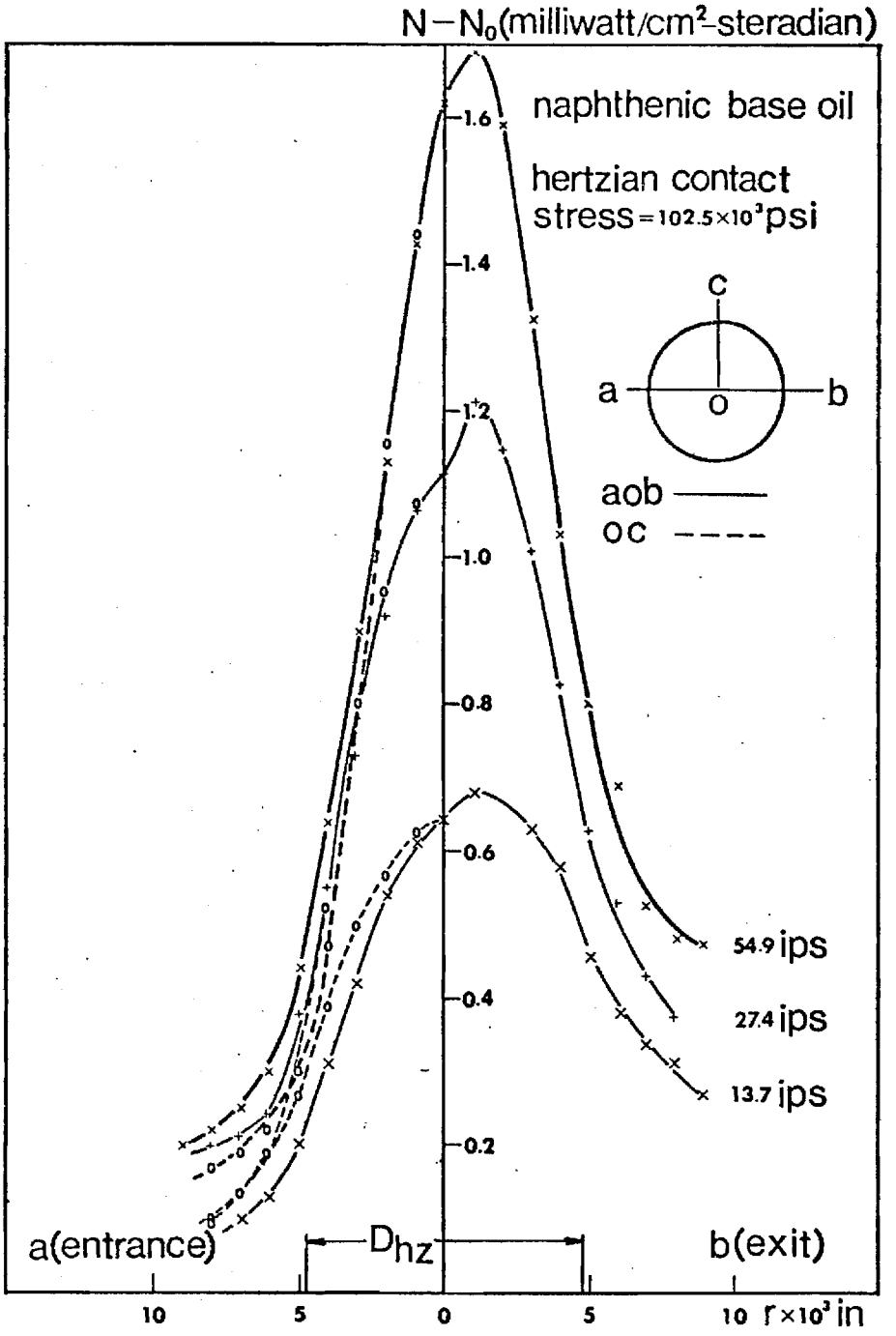

Figure 2. Infrared Radiance Profiles

data and the pressure, temperature, shear stress-viscosity data obtained for NASA purchase orders C-57357-B, NAS 3-14546 and NAS 3-15383. At the present time, the lubricant rheology is characterized in the above dimensionless parameter systems by the low shear rate viscosity evaluated at atmospheric pressure and contact inlet temperature, and the pressure-viscosity parameter α^* (defined in section IIIc.). With this description of the fluid there is a significant amount of scatter when the film thickness data is plotted in terms of the dimensionless parameters proposed in the above systems. The remaining step is to show that the dimensionless parameter correlation is improved, meaning a single functional relation exists between the independent and dependent dimensionless parameters, if an atmospheric pressure, but high shear rate (indicative of the contact inlet region) viscosity is used. Also, using the fluids believed to be Newtonian in the pertinent shear stress range, it is hoped that one of the above groups of dimensionless parameters will be shown to be more applicable to sliding point contacts. Once a system for correlating and predicting both centerline and minimum film thickness has been clearly established, the techniques will be extended to traction data.

d. EHD Film Thickness at High Hertz Pressure

The dependence of film thickness on Hertz pressure at pressure levels typical of design applications has been investigated. The data presented by investigators at Battelle using an x-ray transmission technique showing a dependence much greater than that indicated by commonly accepted theories has been substantiated by an independent study using the optical interference film thickness measurement technique. It has

also been shown that the minimum film thickness is influenced to a much greater extent by the Hertz pressure than the centerline film thickness. The manuscript of a paper discussing this finding has been included as Appendix B of this report.

e. EHD Non-linear Fluid Analysis

Previous investigations into the lubrication of contacts occurring in heavily loaded machine elements such as gears, cams and roller bearings have dealt largely with fluids which are described by constitutive equations which are linear with respect to both the stress and rate of deformation tensors. This was a reasonable approach in terms of the general applicability of the results to a large class of fluids exactly and to an even larger class approximately. This was further necessitated by the complexity of the system under consideration involving, as it does, the deformation of the solids, pressure dependent fluid properties, and heat transfer as well as nonlinear constitutive equations. However, there are important classes of fluids such as the bulk polymers and polymeric solutions which are not described by such linear equations and are of increasing technical importance. It is possible with the techniques developed here to extend the previous investigations of linear constitutive equations and to treat the more general situation described by nonlinear constitutive equations. A full predictive capacity for the lubrication of contacts by such fluids is being developed.

The model of the contact assumes the two dimensional geometry of an initially undeformed cylinder and plane in steady state operation (Fig. 3a). Other assumptions are laminar flow, an incompressible fluid and isothermal

operation. These are acceptable assumptions in the case of linear constitutive equations and are a reasonable beginning for the study of the more general case of nonlinear constitutive equations. Some of these assumptions can be relaxed in future studies and their importance examined.

The model is formulated in terms of the independent variables x and y which are the coordinates in the flow and cross flow directions respectively. The corresponding local velocities are u and v. The remaining dependent variables are the pressure p, the shear stress τ, deviatoric normal stresses σ_x and σ_y and the film thickness h. The rupture coordinate of the film $\bar{x}$ must also be determined. The parameters of the model are the surface velocities u_1 and u_2, the average velocity U, the equivalent elasticity E, the equivalent radius R, a reference film thickness (say $\bar{h} = h(\bar{x})$), the normal load W, the base viscosity η_o, the pressure viscosity coefficient β and any other parameters occurring in the constitutive equation (Fig. 3).

Assuming that the constitutive equation involves only the parameters η_o and β, ie., the linear isothermal case, the system can be non-dimensionalized and W and p expressed as

$$W/E\bar{h} = \phi\ (U\eta_o R/E\bar{h}^2\ ,\ \beta\ WE/R) \tag{1}$$

$$p^2R/WE = \psi\ (x/R,\ U\eta_o R/E\bar{h}^2\ ,\ \beta^2 WE/R) \tag{2}$$

Similar expressions with additional dimensionless groups arise when other parameters are included in the constitutive equations.

Applying the conservation principles of mass and momentum to the fluid and using the Hertzian equation for the deformation of the solids and the Reynolds condition to determine the rupture coordinate results

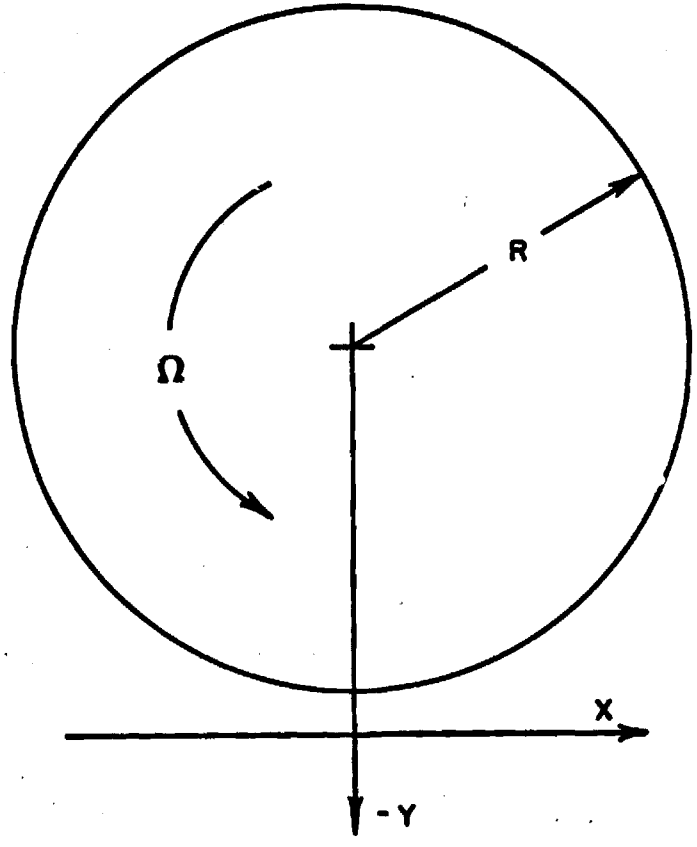

MODEL GEOMETRY

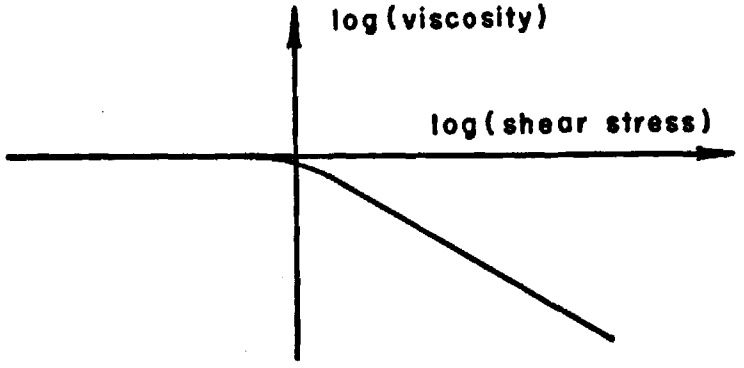

BULK POLYMERS

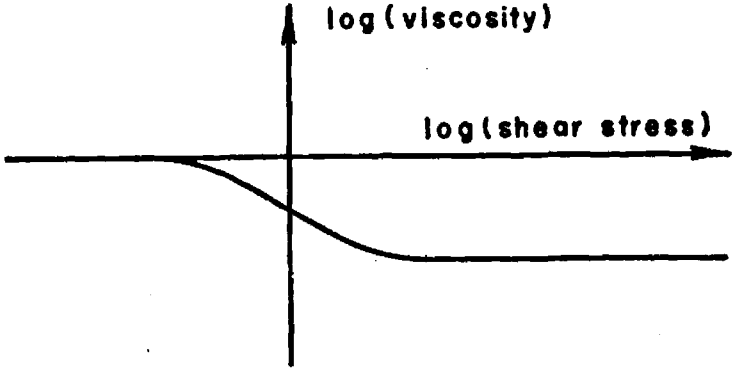

POLYMERIC SOLUTIONS

VISCOSITY FUNCTIONS

Figure 3. a) Model Geometry and b) Viscosity Functions Used in Non-linear EHD Fluid Analysis Studies

in the following first order system

$$\int_o^h u\,dy = U\bar{h} \tag{3}$$

$$\partial p/\partial x = \partial \sigma_x/\partial x + \partial \tau/\partial y \tag{4}$$

$$\partial p/\partial y = \partial \tau/\partial x + \partial \sigma_y/\partial y \tag{5}$$

$$u = u_1 \text{ at } y = 0,\ u = u_2 \text{ at } y = h \tag{6}$$

$$h = \bar{h} + (x^2 - \bar{x}^2)/2R + 1/E \int_{-\infty}^{\infty} p(\xi) \ln \left|(\xi - x)/(\xi - \bar{x})\right| d\xi \tag{7}$$

$$p = 0 \text{ at } x = -\infty,\ p = 0 \text{ at } x = \bar{x} \tag{8}$$

Further reduction of the system requires the specification of the constitutive equations relating the stress $\tilde{T}$ and the deformation rate $\tilde{D} = 1/2\ (\nabla\bar{u} + (\nabla\bar{u})^T)$. To this end several classes of fluids are considered.

The simplest nonlinear class is that of the purely viscous fluids defined by

$$\tilde{T} = \tilde{f}^*(p, \text{tr } \tilde{T}^2)\ \tilde{D} \tag{9}$$

Such fluids exhibit no first order normal stresses and the tensor equation can be reduced to the first order scalar equation

$$\tau = 2\eta(p, \tau^2)\ \gamma \text{ where } \gamma = 1/2\ \partial u/\partial y \tag{10}$$

The special case

$$\eta\ (p, \tau^2) = \eta_o \exp(\beta p) \tag{11}$$

is the linear viscous fluid. However, this class includes the majority of present knowledge of the bulk polymers, polymeric solutions and other nonlinear

fluids since viscosity data are the most convenient and important measurements that have been made (Fig. 3b). Thus, bulk polymers can be modeled by

$$\eta(p, \tau^2) = \eta_o \exp(\beta p) \quad (\tau_c^{2\sigma} (\tau_c^{2\sigma} + \tau^{2\sigma})^{-1}) \tag{12a}$$

$$\text{or} = \eta_o \exp(\beta p) \quad (\tau^2 (\sinh ((\tau/\tau_c)^2))^{-1}) \tag{12b}$$

and the polymeric solutions can be modeled by

$$\eta(p, \tau^2) = \eta_o \exp(\beta p) \quad ((\tau_c^{2\sigma} + \lambda^2\tau^{2\sigma})(\tau_c^{2\sigma} + \tau^{2\sigma})^{-1}) \tag{13a}$$

$$\text{or} = \eta_o \exp(\beta p) \ (\lambda^2 + (1 - \lambda^2) \tau^2 (\sinh ((\tau/\tau_c)^2))^{-1}) \tag{13b}$$

The first model of each type is obtained, a posteriori, from the fitting of viscosity measurements and the second is obtained, a priori, from the considerations of the Ree-Eyring theory.

More general classes of fluids can be considered in which first order normal stresses arise. The simplest such fluids are the algebraic fluids defined by

$$\tilde{T} = \tilde{f}(p, \tilde{D}) = \alpha_1(\text{tr } \tilde{D}^2)\tilde{I} + \alpha_2(\text{tr } \tilde{D}^2)\ \tilde{D} + \alpha_3(\text{tr } \tilde{D}^2)\ \tilde{D}^2 \tag{14}$$

This class contains all continuous algebraic fluids as special cases but the accurate determination of the functions α_1, α_2 and α_3 limits its application.

Still more general classes of fluids exist which exhibit rate effects to the first or higher orders. The general first order rate fluids are defined by

$$\overset{\nabla}{\tilde{T}} + \tilde{T}\tilde{W} - \tilde{W}\tilde{T} = \tilde{F}(p,\tilde{T},\tilde{D}) \text{ where } \tilde{W} = 1/2(\nabla\bar{u} - (\nabla\bar{u})^T) \tag{15}$$

The functional dependence is difficult to determine and use. However, this class is reducible with the assumption of linearity, ie., $\tilde{F}(p,\tilde{T},\tilde{D}) = -G/\eta_o \tilde{T} + 2G\tilde{D}$, to the class of linear viscoelastic fluids for which the

parameters may be determined. Here η_o is the base viscosity and G is the apparent fluid elasticity. With the additional assumption of almost parallel flow, these linear viscoelastic fluids are equivalent to purely viscous fluids with an equivalent viscosity given by

$$\eta(p,\tau^2) = 2\eta_o \exp(\beta p)\,(1/4(2\tau/G)^2\,(1 - (2\tau/G)^2)^{-1/2}) \tag{16}$$

Using any one of the above constitutive equations, the set of equations 3,4,5,6 can be reduced to a set of two equations which determine the local shear stress on the plane τ_1 and the local pressure gradient dp/dx for a given value of the local film thickness h. This is a generalization of the Reynolds equation derived for the linear viscous fluid. For the class of the purely viscous fluids, these equations are

$$U \int_{\tau_1}^{\tau_1 + h(dp/dx)} \tau\,(\eta(p,\tau^2))^{-1}\,d\tau = 2(u_2 - u_1)\,h(dp/dx) \tag{17}$$

and

$$U \int_{\tau_1}^{\tau_1 + h(dp/dx)} \tau^2\,(\eta(p,\tau^2))^{-1}\,d\tau = 2(u_2 - u_1)h^2\tau_1(dp/dx) + (u_2 - \bar{h}/h\,u_1)\,h^2(dp/dx)^2 \tag{18}$$

which are called the first and second Reynolds equations.

The model is now complete and the problem consists of solving numerically the first and second Reynolds equations, 17 and 18, together with the Hertzian equation, 7, subject to the Reynolds condition, 8, for a prescribed viscosity function. This yields p, h, τ_1 and $\bar{x}$ for given values of E, $\bar{h}$, R, u_1 and u_2. The problem is a nonlinear free boundary value problem.

The most promising method of solution appears to be a combination of finite difference techniques with the Newton-Raphson technique. First a value of $\bar{h}$ is assumed. Then a value of the rupture coordinate $\bar{x}$ is assumed and a mesh is established. The dependent variables and their derivatives are approximated at the mesh points and the resulting system of nonlinear algebraic equations solved by the Newton-Raphson technique. The Newton-Raphson technique is then used to update $\bar{x}$ and the process is repeated until $p = 0$ at $x = \bar{x}$. The method should give sufficiently accurate results with a properly chosen mesh. Techniques of automatically chosing and improving the mesh enhance the convergence.

Some effort was spent on solution methods using the classical shooting techniques and iteration. One approach used the discontinuous viscosity function given by

$$\eta(p,\tau^2) = \eta_o \exp(Bp)\,(1 - (1 - \lambda^2)u^*(\tau^2 - \tau_c^2))$$

$$\text{where} \quad u^*(\tau^2 - \tau_c^2) = 0 \quad \text{if} \quad \tau^2 \leq \tau_c^2 \qquad (19)$$

$$= 1 \quad \text{if} \quad \tau^2 > \tau_c^2$$

This allows the integration in the first and second Reynolds equations to be performed and these are reduced respectively to a quadratic and cubic in τ_1 and $\partial p/\partial x$. These equations may be degenerate depending on the order relationships of τ_1 and $\partial p/\partial x$ with τ_c. However, in all cases, the system can be reduced to a quartic in $\partial p/\partial x$ which can be solved in closed form. Difficulty often arises in chosing the proper root, but once this is chosen, the problem can be approached by the shooting technique and the pressure distribution and rupture coordinate determined for a given film thickness distribution. The new film thickness distribution is obtained by an integration of Hertzian equation and the calculations repeated to convergence.

Another approach used continuous viscosity functions which are integrable in terms of the elementary functions (for example, $\sigma = 1$ in 13a). This reduced the first and second Reynolds equations to higher order algebraic or transendental equations which were solved for τ_1 and $\partial p/\partial x$ by the Newton-Raphson technique. Once $\partial p/\partial x$ was obtained the solution procedure was the same as in the discontinuous case above.

The present approach is based on the combination of the finite difference technique and the Newton-Raphson technique described above and seems to be preferable to other methods in ease of programming, efficiency of operation and accuracy. Efforts are being made to develop this method and results should be forthcoming in the next few months. These would provide design information on film thicknesses, pressure distributions and shear stresses and their dependence on fluid viscosities.

Some mention should also be made of possible extensions of this model to clarify the importance of the assumptions made. Thus, the requirement of integrability of the viscosity function in elementary functions could be relaxed and empirical viscosity functions which are given as data points rather than analytical expressions could be used. Incompressibility could be relaxed. The isothermal assumption could be dropped and the problem could be treated by iteration much as it has been for the case of linear viscous fluids. Extension to point contacts should also be possible. Finally, some additional assumptions might be made in order to develop simplified design criteria.

The development of a predictive capacity for the lubrication of contacts by nonlinear fluids seems feasible for certain classes of such fluids that are also of technical importance. A general formulation is given here that unifies the previous work in the general solutions of contacts.

Further, a solution method is being developed based on finite differences and the Newton-Raphson technique which is new to this field and offers significant advantages over the previous methods based on shooting techniques and iteration. The existence of a predictive capacity and the development of design charts for the classes of bulk polymer and polymeric solution fluids will facilitate design with these fluids.

III. PRESSURE VISCOSITY MEASUREMENTS

Several phases of the pressure-viscosity research were conducted. These consisted of recalibration of the equipment, modification of the equipment, high shear stress investigations, and analysis of previously taken data.

a. Equipment Recalibration

Late in the grant period it was discovered that the pressure-viscometer calibration had apparently changed from when it was originally done. A complete recalibration was conducted which included; a) calibration of all pressure transducers and their recording circuits from 0 - 40,000 psi and 0-100,000 psi employing 16" diameter Heise bourdon gages in each range. They had to be calibrated to within 0.1% full scale reading each, b) calibration of both displacement transducers and their recording circuits employing calibrated dial indicators, c) pressure vessel geometry, d) capillary geometry employing viscosity standard fluids, e) recorder timing circuits and paper driver, and f) thermometer checks with more recently calibrated thermometers.

The recalibration revealed that the pressure level transducer and the displacement transducer characteristics had changed. A spot check of previous data indicated that the change had occurred during the fall of 1969 and all data taken after that time has been re-analyzed employing the new calibration information.

As a check on the recalibration, measurements were made on two-ethylhexyl sebacate, a diester, which had been measured and reported

by Novak (1,2) and in the ASME 1953 Pressure-Viscosity Report (11). Figure 4 shows these data.

b. Revised Pressure-Viscosity Data

As a result of the instrument recalibration the data for all fluids for which pressure-viscosity measurements have been made for NASA have been reanalyzed and are reported here. The data for the nine fluids measured under purchase orders NAS 3-14546 and NAS 3-15383 have changed from what was earlier reported, but the data for the two fluids measured under purchase order C-57357-B was essentially unchanged. Data on all eleven fluids are reported in a uniform fashion here in both tabular form and figures of semi-log viscosity-pressure isotherms and Roeland pressure-viscosity isotherm plots (appendix A).

Appendix A contains all these data including fluid descriptions, data supplied by NASA, and data measured in this laboratory. This includes density-temperature measurements at atmospheric pressure made in calibrated pyncnometers fabricated and calibrated in this laboratory. Accurate density measurements as a function of temperature are necessary to convert the atmospheric glass capillary kinematic viscosity to dynamic viscosity (centipoise) for the pressure viscosity plots.

c. Pressure-Viscosity Parameters

In ehd studies several parameters describing fluid pressure-viscosity characteristics have been proposed and used. If the isothermal pressure-viscosity behavior of a fluid were exponential most of these parameters would be identical. Since few fluids exhibit a truly

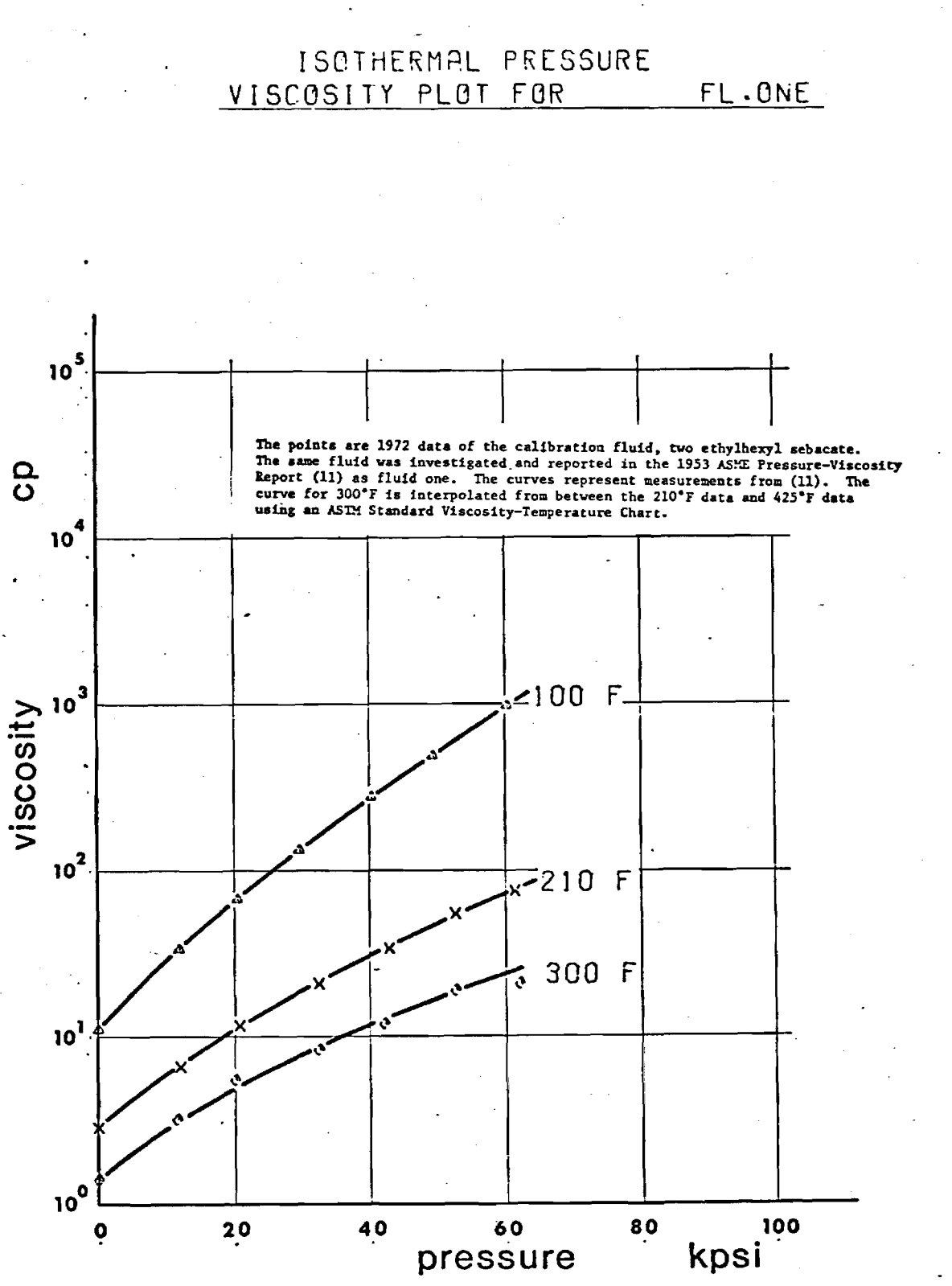

Figure 4a. Calibration Check: Pressure-Viscosity Isotherm

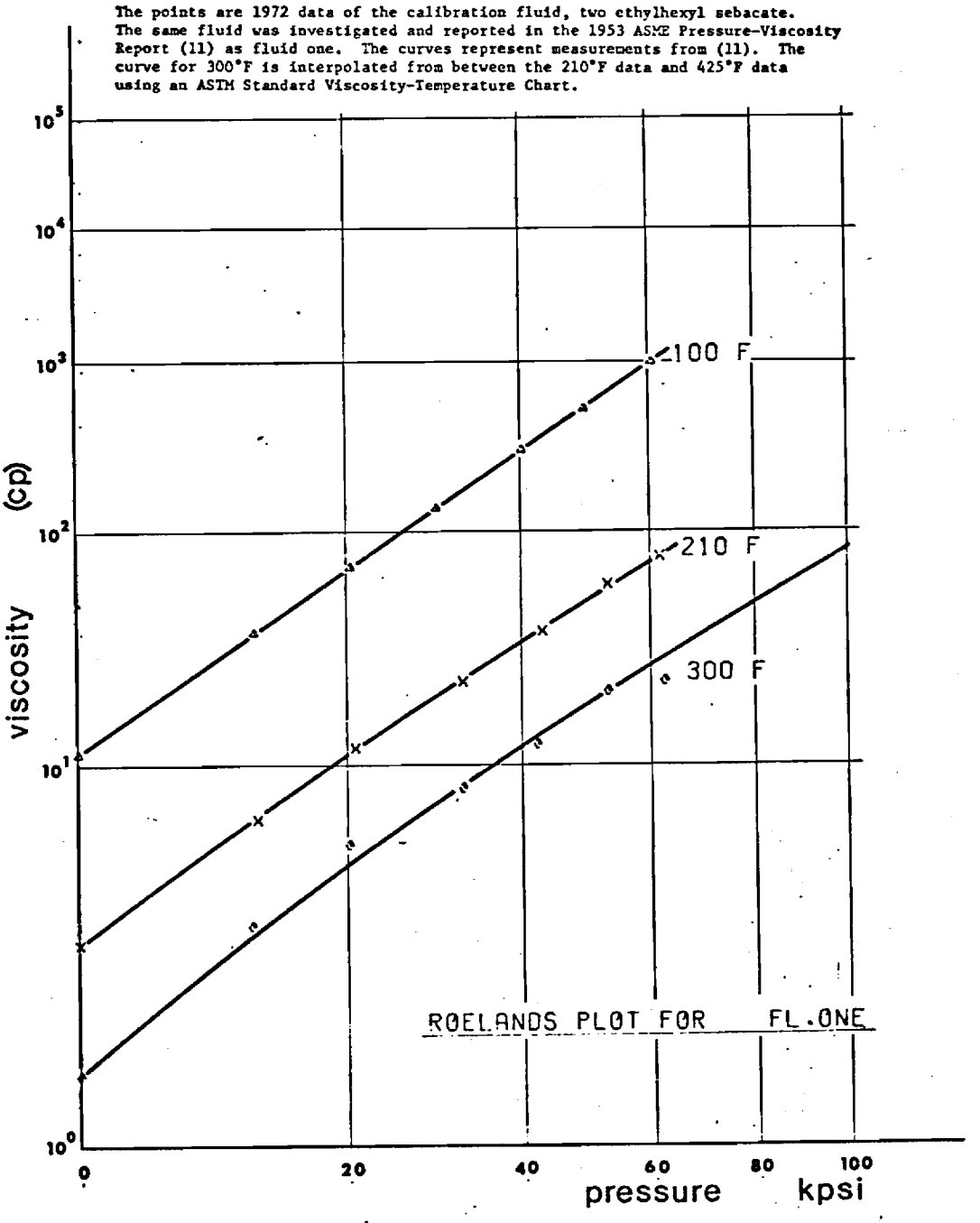

Figure 4b. Calibration Check: Roeland's Plot

exponential viscosity-pressure isotherm there is some question as to the most meaningful method of describing this characteristic for ehd proposes.

Several of the proposed parameters are related to the slope of the pressure-viscosity isotherm and are shown in Figure (5a). In addition to these, α^* which is obtained from the Weibull transformation and shown in Figure (5b) has been proposed by Blok (12). Lastly the slope Z, of the isotherm on a Roelands viscosity-pressure plot is useful in viscosity correlation studies.

All of these viscosity-pressure parameters have been calculated for each of the eleven fluids at each temperature at which measurements were made (100,210,300F). These are shown in Tables 1-3. Temperature dependence plots of the three most common parameters, α_{ot}, α^*, Z are shown in Figures 6-8. All three of these were calculated in the data reduction program. The Z was obtained by a least squares fit of a straight line to points calculated and used in the plotting routine for the Roeland's charts. The α^* was obtained by a numerical integration of a curve fit through the data on a reciprocal viscosity versus pressure isotherm. The $\alpha_{\dot{o}t}$ was the initial slope of a curve fit through the lowest three pressures on a viscosity-pressure isotherm.

It appears from the temperature plots of the data that $\alpha^*$and Z are the most well behaved parameters. The α^*'s were used in the ehd correlations mentioned earlier in this report.

d. <u>High Shear Stress Investigations of Lubricants</u>

Preparatory work has been carried out with the purpose of gaining an overall insight into the shear stress generating mechanism in highly

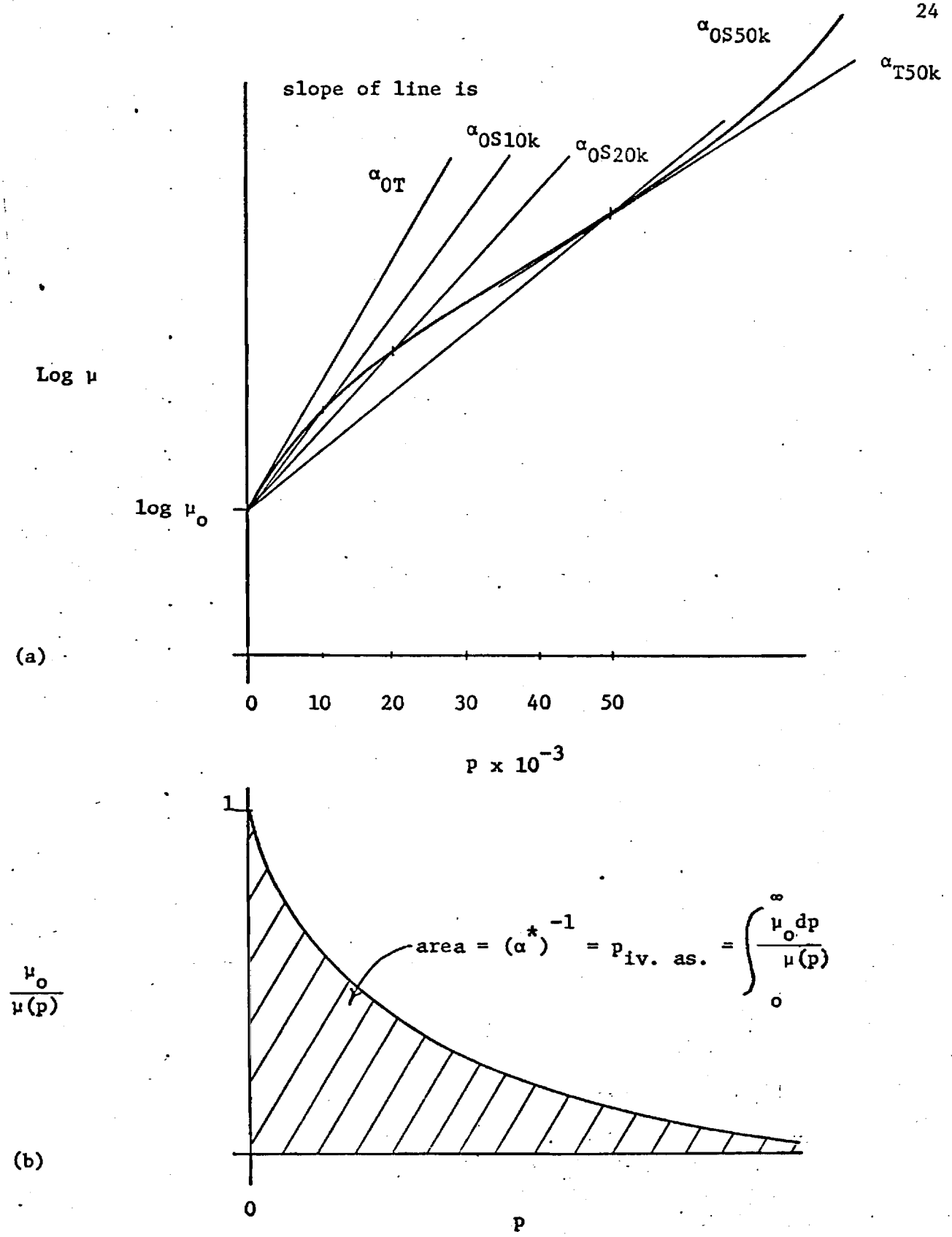

Figure 5. Schematic Relationship Between Different Viscosity-Pressure Characteristics and a Typical Viscosity-Pressure Isotherm (Curvature exaggerated for illustration).

Table 1. PRESSURE VISCOSITY CHARACTERISTICS - α_{oT}

$\alpha_{oT} \times 10^4$ $(psi)^{-1}$

Fluids	100°F	210°F	300°F	75°F*
Advanced Ester	1.05	1.07	1.45	1.08
Formulated Advanced Ester	1.27	1.46	1.87	1.25
Naphthenic Mineral Oil Plus Additive	2.27	1.76	1.62	2.32
Synthetic Paraffinic Oil Plus Additive	1.61	1.34	1.17	1.66
DN-600 Plus Additive	1.42	1.39	1.10	1.43
DN-600	1.47	1.27	1.05	1.43
FN-2961	2.12	1.25	1.29	2.53
MCS-418	1.17	0.81	0.42	1.27
MCS-460	2.17	0.94	1.03	3.00
Krytox	4.51	3.02	2.08	4.80
XRM-109	1.67	1.88	0.97	1.25

* Extrapolated data from Figure 6.

TABLE 2. PRESSURE VISCOSITY CHARACTERISTICS - α^*

Fluids	$\alpha^* \times 10^4$ (psi)$^{-1}$ 100°F	210°F	300°F	75°F*
Advanced Ester	0.885	0.680	0.586	0.94
Formulated Advanced Ester	0.942	0.691	0.602	1.03
Naphthenic Mineral Oil Plus Additive	1.726	1.196	0.941	1.85
Synthetic Paraffinic Oil Plus Additive	1.248	0.941	0.782	1.33
DN-600 Plus Additive	1.168	0.885	0.729	1.24
DN-600	1.091	0.862	0.697	1.15
FN-2961	1.728	1.065	0.873	1.98
MCS-418	1.235	0.675	0.548	1.43
MCS-460	2.146	1.175	0.647	2.43
Krytox	2.869	2.234	2.083	3.00
XRM-109	1.216	1.044	0.750	1.23

* Extrapolated data from Figure 7.

TABLE 3. PRESSURE VISCOSITY CHARACTERISTICS - Z

Fluids	Z 100°F	210°F	300°F	75°F*
Advanced Ester	.481	.478	.485	.482
Formulated Advanced Ester	.489	.474	.485	.495
Naphthenic Mineral Oil Plus Additive	.675	.653	.655	.681
Synthetic Paraffinic Oil Plus Additive	.434	.441	.453	.432
DN-600 Plus Additive	.545	.548	.555	.542
DN-600	.554	.541	.548	.558
FN-2961	.670	.669	.640	.664
MCS-418	.717	.497	.504	.765
MCS-460	1.06	.848	.691	1.025
Krytox	.773	.794	.802	.762
XRM-109	.426	.435	.394	.418

* Extrapolated data from Figure 8.

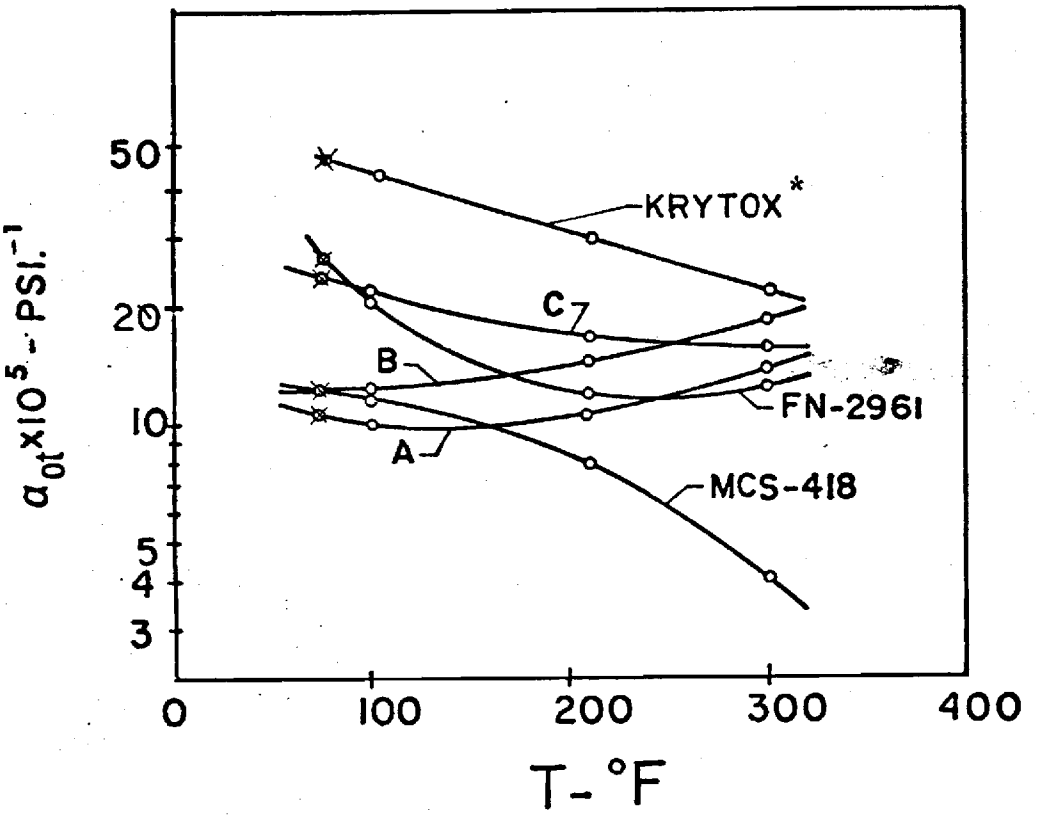

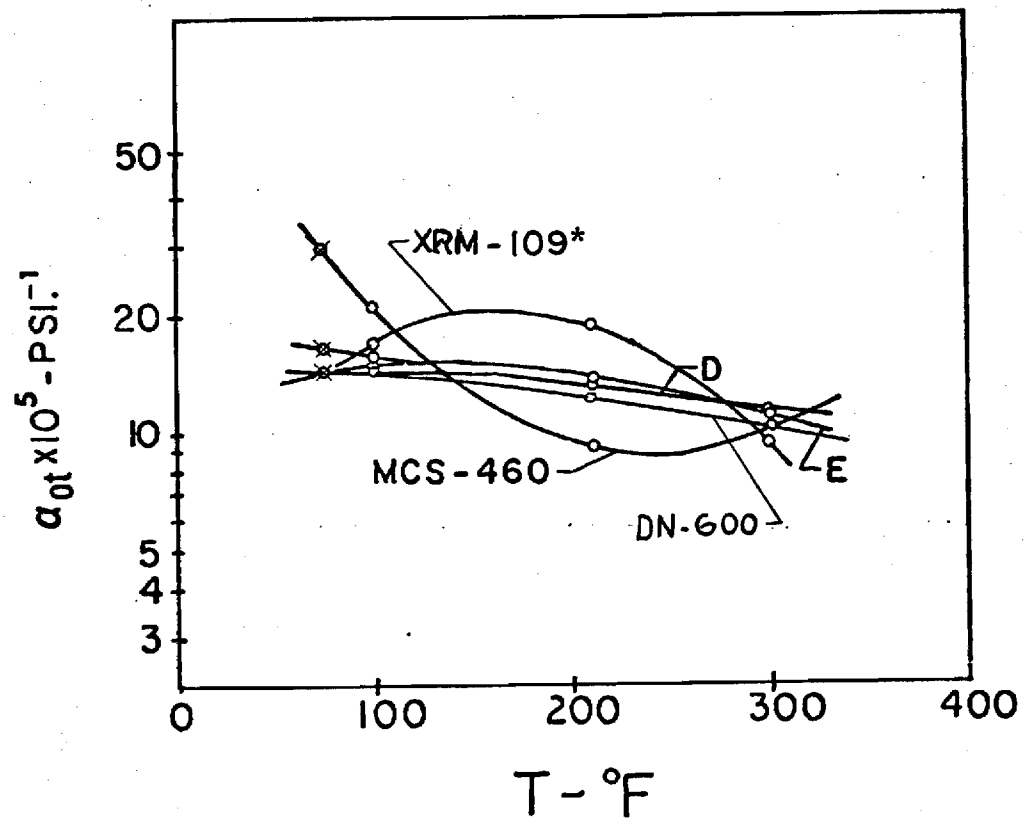

* @ 210F & 300F values are questionable

Figure 6. Viscosity-Pressure Characteristic α_{0T} as a Function of Temperature (o measured, ⊠ extrapolated).

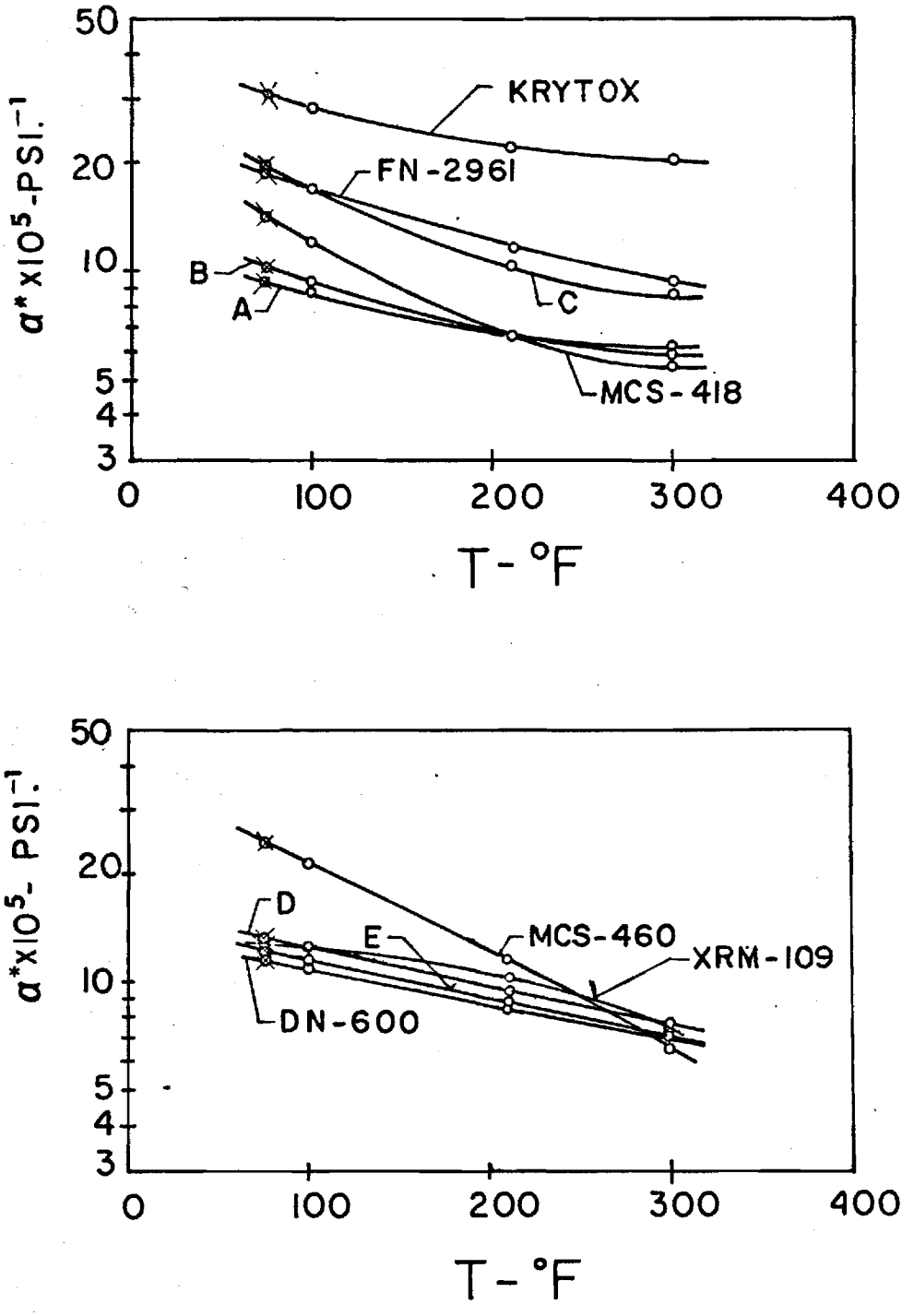

Figure 7. Viscosity-Pressure Characteristic α* as a Function of Temperature (o measured, ⊠ extrapolated).

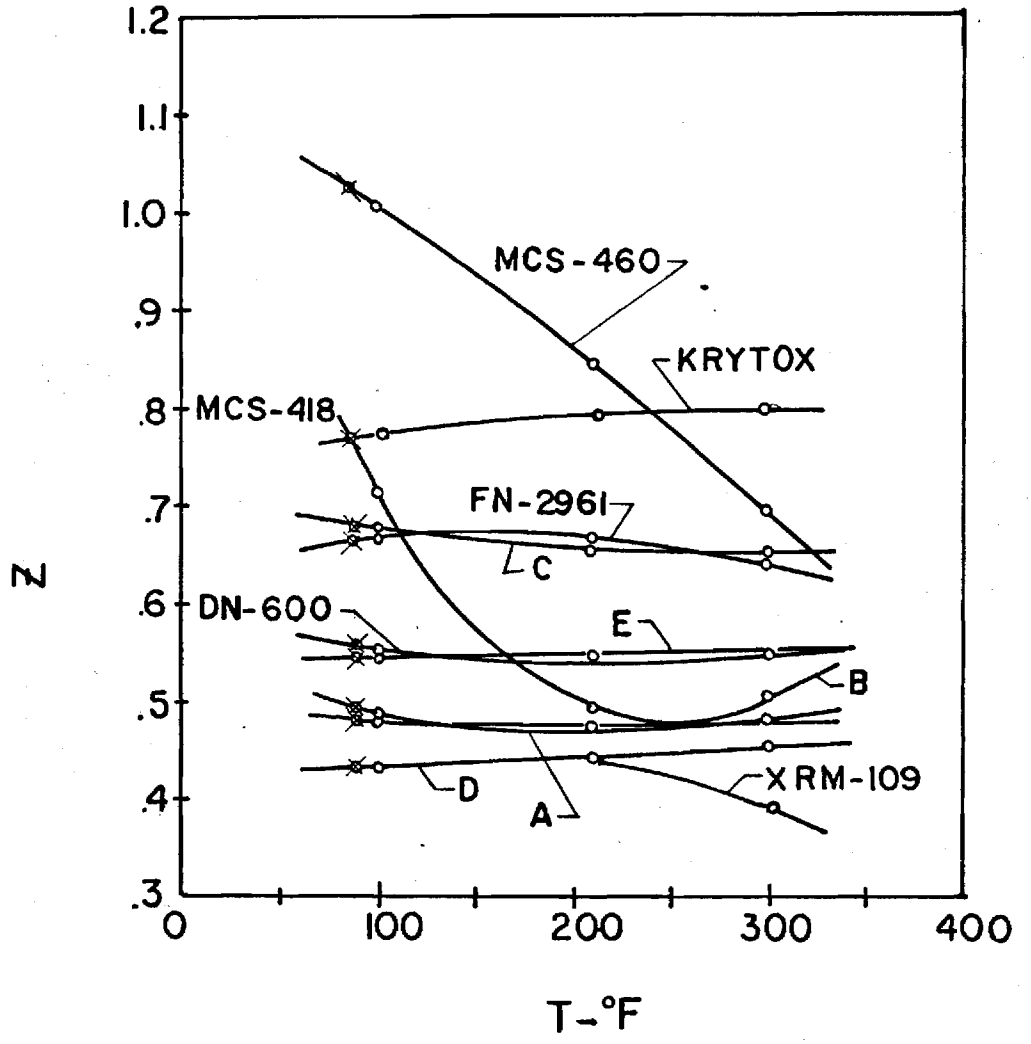

Figure 8. Viscosity-Pressure Characteristic Z as a Function of Temperature (o measured, ⊠ extrapolated).

loaded bearing surfaces, particularly with respect to elastohydrodynamic lubrication situations. The intention is to develop a general approach to the prediction of shear stresses and film temperatures in ehd bearing contacts.

The work consists of two phases: an experimental investigation of rheological behavior of lubricants subjected to high shear stress and an analytic investigation into distributions of temperatures and viscosities, stresses and lubricant velocities in the elastohydrodynamic fluid film. The experimental determination of lubricant properties from phase one is a necessary basis for the usefulness of results from phase two. A preliminary rheological investigation has been carried out in the high pressure viscometer. The main goal has been to extend the measuring range of shear stress from the present upper limit of about 1.4×10^6 dyn/cm^2 (20 psi) to stresses encountered in ehd contacts.

Extension of the measuring range is achieved by modification of the capillaries. The modifications consist of decreasing the capillary diameter and decreasing the ratio of capillary length-to-diameter.

A preliminary series of measurements with capillary diameter and length as small as .00348 inch has been performed. Previous minimum values have been d = .00822 and l = .117 (capl). Figure 9 shows the results and gives a comparison with measurements performed with the standard high stress capillary (cap 1). It is seen that the fluid behaves as a Newtonian fluid even at high shear stresses (maximum shear stress of 0.9×10^7 $dynes/cm^2$ or 125 psi) when measured with the modified capillary. This observation is interesting as the test fluid (fluid E =

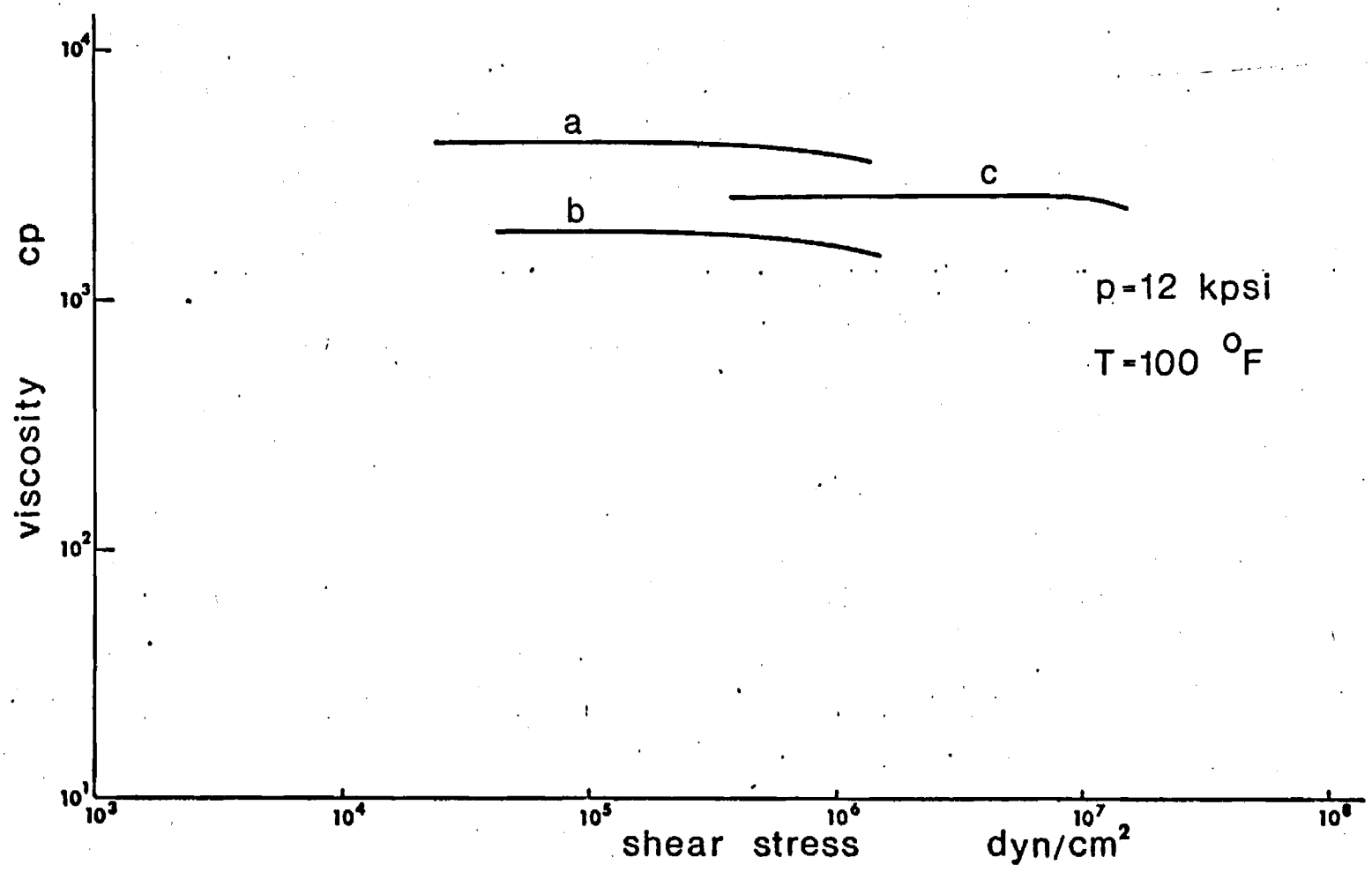

Viscosity-Shear Stress Relation for Fluid E

Figure 9. Comparison of high shear stress measurements.
a.) capillary 1 (d = .00822 in., l = .117 in.) at 100°F, 51 ksi,
b.) capillary 1 at 100°F, 41 ksi,
c.) modified capillary (d = .00348 in., l = .00348 in.) at 77°F, 32 ksi

DN600 + add.) previously was believed to have non-Newtonian behavior when subjected to stresses higher than 2 x 10^5 dyn/cm^2 (3 psi). From the Figure it is seen that the limit of the modified capillary is approximately 1.4 x 10^7 dyn/cm^2 (200 psi). The modified capillary configuration corresponds therefore to an increase of the upper shear stress limit by a factor of about 10, but yields Newtonian characteristics for shear stresses up to about 40 times higher stresses than obtained with the standard capillary (cap 1).

It is expected that the above mentioned limits for shear stress can be further extended by applying even smaller diameters and shorter lengths. Materials and technology are available to obtain l = d = .0015 inch, but the intention is to reach d = .0005 inch and l/d less than unity.

The decrease in viscosity previously observed is believed to be at least partly caused by viscous heating in capillary. Temperature increase due to viscous heating in the capillary is a limitation of the use of capillary viscometry for high shear stress ranges. The heating will give the same trend in the reduced data as a shear thinning effect of the fluid. (see Figure 9) The temperature profile in a capillary will show a maximum near the wall (r = 0.9R) and minimum for r = 0 and r = R (13). The temperature increase will be approximately a line or function of the axial coordinate for short lengths of the capillary and for low lubricant heat conductivity. The temperature distribution of the test fluid during passage through the modified capillary was determined analytically by two basically different approximate methods; by collocation with an eight term polynominal and by direct calculation

under certain simplifying assumptions. The maximum temperature increase was found at the exit of the capillary at a radius of about .88 times R and was approximately 10°F for a corresponding pressure drop of 500 psi. A pressure drop of 500 psi or less was found to correspond to the constant-viscosity Newtonian part of the fluid characteristic measured with the modified capillary (see Fig. 9). It can be shown that the viscosity measurement is not influenced significantly for temperature maximum less than 10°F and pressure drops of less than 500 psi. A lowering of measured viscosity can, however, be expected for a capillary pressure drop greater than 500 psi due to an increased temperature of the test fluid.

The second phase of this work is directed toward the investigation of the behavior of a fluid being sheared between two surfaces as in an ehd contact. An analytical approach to determine shear stress distributions in the contact area is under development. The method aims at giving traction coefficient, temperatures and velocity distributions. The approach is believed to be new. The incorporating of non-Newtonian fluid properties, the more complete thermal and kinematic boundary conditions for the bearing surfaces and the obtained information about fluid behavior at high shear stress from the extended range capillary viscometer should aid in our investigating of ehd traction phenomena.

e. Equipment Modification

In addition to the recalibration and high shear stress modifications discussed above, an analog-to-digital data recorder has been adapted to the high pressure viscometer. This equipment greatly facilitates data collection

and reduction in the viscometer by coverting the analog signals from the viscometer to digital signals which are then recorded on magnetic tape. This tape is then used as input for the data reduction program. This addition will be particulary useful in the continued high shear stress studies during the coming year.

REFERENCES

1. Novak, J. D., "An Experimental Investigation of the Combined Effects of Pressure, Temperature, and Shear Stress Upon Viscosity," Doctoral Thesis, Univ. Mich., 1968.

2. Winer, W. O., and Novak, J. D., "Some Measurements of High Pressure Lubricant Rheology," Journal of Lubricant Technology, Trans. ASME, Series F, Vol. 90, No. 3, July 1968, pp. 580-591.

3. Roelands, C.J.A., Correlational Aspects of the Viscosity - Temperature - Pressure Relationship of Lubricating Oils, 1966, O. P. Books Program, University Microfilm, Ann Arbor, Michigan.

4. Sanborn, D. M., "An Experimental Investigation of the Elastohydrodynamic Lubrication of Point Contacts in Pure Sliding," Doctoral Thesis, Univ. Mich., 1969.

5. Sanborn, D. M., and Winer, W. O., "Fluid Rheological Effects in Sliding Elastohydrodynamic Contacts with Transient Loading: II-Traction." Trans. ASME, Journal of Lubrication Technology, Vol. 93, pp. 262-271, 1971.

6. Sanborn, D. M., and Winer, W. O., "Fluid Rheological Effects in Sliding Elastohydrodynamic Contacts with Transient Loading: I-Film Thickness," Trans. ASME, Journal of Lubrication Technology, Vol. 93, pp. 342-348, 1971.

7. Dowson, D. and Higginson, G. R., Elastohydrodynamic Lubrication, 1966, Pergamon Press, Oxford.

8. Blok, H, Review of Data on Elastohydrodynamic Lubrication, 1959, Technische Hogeschol, Laboratorium voor Werkluigonderdelen, Delft.

9. Moes, H., Discussion, Proceedings of the Institution of Mechanical Engineers, Vol. 180, Pt. 3B., pp. 244-5, 1965-66.

10. Greenwood, J. A., "Presentation of Elastohydrodynamic Film-Thickness Results," Journal of Mechanical Engineering Science, Vol. 11, pp. 128-32, 1969.

11. ASME Pressure-Viscosity Report, I, II. A report prepared by the ASME Research Committee on Lubrication, N. Y., ASME, 1953.

12. Blok, H., "Inverse Hydrodynamics," Proceedings of the International Symposium on Lubrication and Wear, Muster, D. and Sternlicht, B., ed., McCutchan Publishing Corp., Berkeley, Calif., 1964, pp. 1-151.

13. Gerrard, J. E., Stiedler, F. E., and Appeldoorn, J. K., "Viscous Heating in Capillaries: The Isothermal-Wall Case," ACS Petroleum Division Meeting, Atlantic City, N. J., Sept., 1965, pp. 73-81.

APPENDIX A

Pressure Viscosity Data

Table 1A - Fluid Definitions

Table 2A - Data supplied by NASA

Table 3A - Data Measured on fluid samples including: atmospheric pressure viscosity, density, and refractives index

These tables are followed by

a. Roeland's Viscosity Pressure Plots for each of the eleven fluids

b. Semilog viscosity pressure isotherms for each of the eleven fluids

c. Viscosity shear stress curves at $100^{\circ}F$ and one pressure for each of the eleven fluids

d. Tables of data for each of the eleven fluids consisting of; 1) low shear stress viscosity-pressure data at 100, 210, and $300^{\circ}F$ respectively, 2) summary of the averaged data used for the plots and α^* and $\alpha_{\delta T}$ at each of the three temperatures and, 3) the high shear stress data at $100^{\circ}F$ and a single pressure used for the high shear stress plots. In these tables the following symbol definitions were used:

RUN ---------- Measurement indentification number.

P3, P(PSI) ------ Pressure level of measurement in psi.

VISCP ---------- Viscosity in Poise.

NSRATE ---------- Shear rate in sec^{-1}.

KEC ---------- Kinetic energy correction applied to pressure drop in psi.

DELTAP ---------- Pressure drop across the capillary in PSI.

TAUDYN ---------- Shear stress in $dyne/cm^2$.

REYN ---------- Reynolds Number of flow.

V(CP) ---------- Viscosity in centipoise.

TABLE 1A

Fluid Descriptions

Designation	Description
A	Advanced ester
B	Formulated advanced ester (fluid A + additive)
C	Naphthenic Mineral Oil Plus Additive (FN-2961 Plus additive)
D	Synthetic Paraffinic Oil plus additive (base oil similar to XRM-109 but different lot than XRM-109 listed below)
E	DN 600 - polyalkyl aromatic plus additive
DN-600	Polyalkyl aromatic
FN-2961	Superrefined Naphthenic Mineral Oil
MCS-418	Modified Polyphenyl Ether
MCS-460	Synthetic Hydrocarbon
Krytox	Dupont Krytox 143-AB (lot 10) perfluorinated polymer
XRM-109	Mobil XRM-109F-3 Synthetic Paraffinic Hydrocarbon

The following pairs of fluids are related by virtue of having common base components.

A and B

C and FN2961

D and XRM-109

E and DN600

TABLE 2A

Description and Properties of Experimental Fluids Received from NASA-Lewis

Fluid	A	B	C	D	E
Designation and Chemical Type	Advanced Ester	Formulated Advanced Ester	Naphthenic Mineral Oil plus Additives	Synthetic Paraffinic Oil plus Additives	DN600 (polyalkyl) Aromatic plus Additives
Kinematic Viscosity, cs					
@ 400F	1.38	1.38	6	5.8	
@ 210F	5.35	5.35	9.5[a]	40.0	6.1
@ 100F	29.3	29.3	94.0[a]	440.0	37.6
Density, g/cc					
@ 100F	b	b	0.875[a]	0.84[a]	
@ 210F	b	b	0.835[a]		
@ 300F	b	b	0.805[a]	0.78[a]	
Specific gravity @ 60F	0.9937	0.9937	b	b	

a Estimated

b Not Available

TABLE 2A

DESCRIPTION AND PROPERTIES OF EXPERIMENTAL FLUIDS

Fluid	DN-600	FN-2961	MCS-418	MCS-460
Chemical Type	Polyalkyl Aromatic	Superrefined Naphthenic Mineral Oil	Modified Polyphenyl Ether	Synthetic Hydrocarbon
Viscosity, cs				
-40°F	9,700	---	---	---
0°F	---	10,300	13,040	26,075
100°F	30	78	25	37.2
210°F	5.0	8.2	4.1	4.0
300°F	2.3	3.3	2.0	1.9
Pour Point, °F	- 75	-30	-20	-20 to -25
Density, g/ml				
0°F	.884	.908	---	0.9595
77°F	---	---	1.195	0.9327
100°F	.851	.873	1.184	0.9219
300°F	.783	.803	1.101	0.8504

TABLE 2A

Physical Properties of Test Fluids

Purchase Order C-57357-B

Fluid	Mobil XRM-109F-3	DuPont Krytox 143-AB (Lot 10)
Chemical Type	Synthetic Paraffinic Hydrocarbon	Perfluorinated Polymer
Kinematic Viscosity, CS		
@ 400°F	6.05	1.928
@ 210°F	42.63	11.45
@ 100°F	493.2	96.6
@ 0°F	45,829	7,494
@ -25°F	-	52,642
@ -40°F	>99,000	-
Flash Point, °F	565	*
Fine Point, °F	620	*
Pour Point, °F	<-40	-40
Density, gm/ml.		
@ 75°F	-	1.89
@ 100°F	0.8389	-
@ 200°F	0.8082	-
@ 210°F	-	1.76
@ 300°F	0.7777	-
@ 400°F	0.7428	1.57
Surface Tension, dynes/cm @ 78°F	30.9	18.5

* Does not flash or burn in hot manifold test up to 1200°F.

TABLE 3A

Fluid Properties Measured at Georgia Tech

Fluid	A	B	C	D	E
Viscosity (cs)					
100°F	25.78	28.16	91.9	442	37.76
210°F	5.05	5.30	9.43	40	6.10
300°F	2.33	2.40	3.52	12.92	2.64
Density (gm/cc)					
100°F	.979	.980	.876	.836	.853
210°F	.932	.935	.838	.799	.814
300°F	.895	.897	.805	.770	.781
Viscosity (cp)					
100°F	25.25	27.60	80.50	369.5	32.21
210°F	4.71	4.96	7.90	31.96	4.97
300°F	2.09	2.15	2.83	9.95	2.06

Refractive Index (atm. pressure, 77°F, tungsten light)

A - 1.4517	DN-600 - 1.4824
B - 1.4570	FN-2961 - 1.4787
C - 1.4815	MCS-418 - 1.6735
D - 1.4690	MCS-460 - 1.5044
E - 1.4838	KRYTOX - 1.2989
	XRM-109 - 1.4698

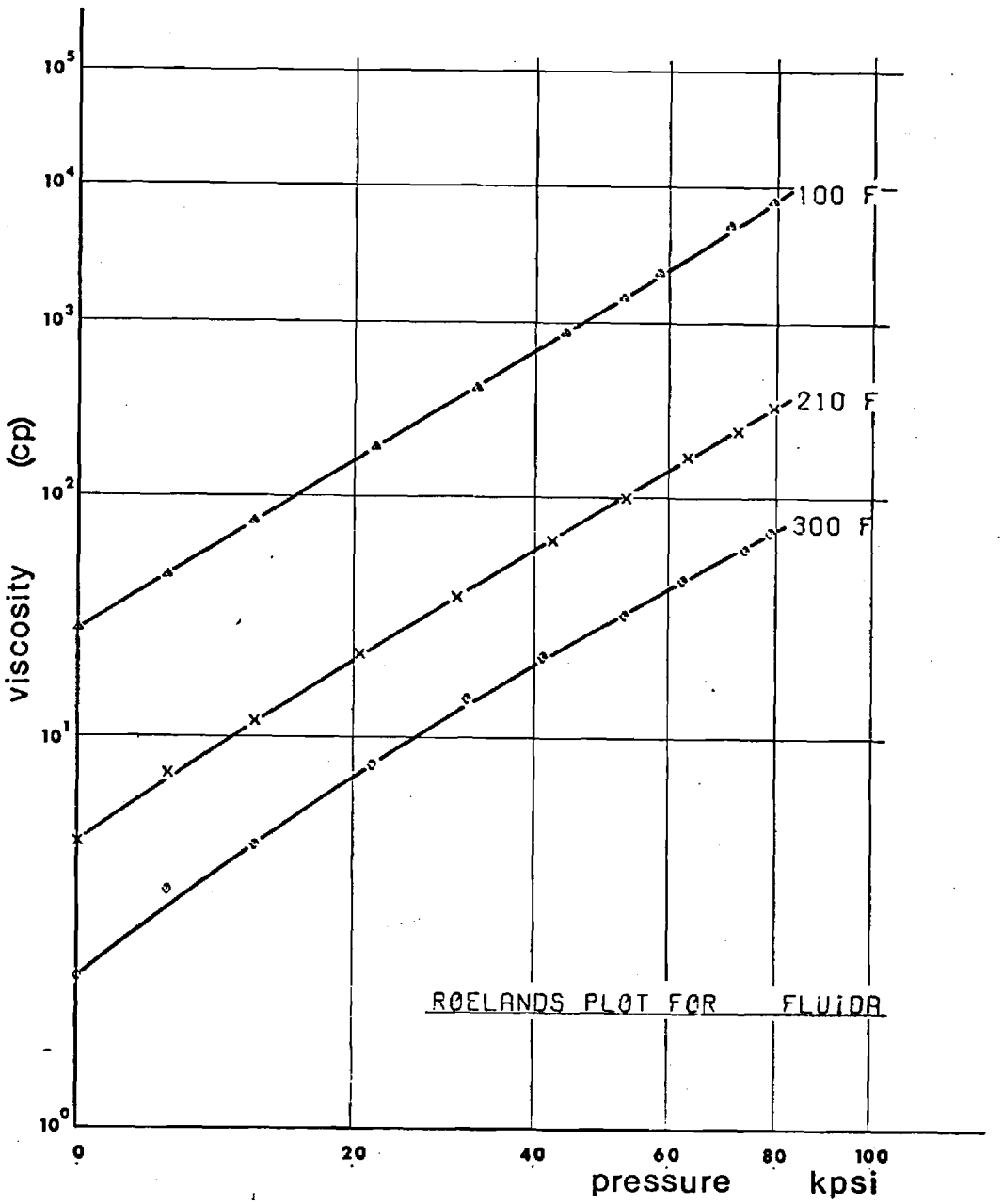
viscosity (cp)
10^5
10^4
10^3
10^2
10^1
10^0
100 F
210 F
300 F
0
20
40
60
80
100
pressure kpsi
ROELANDS PLOT FOR FLUID A

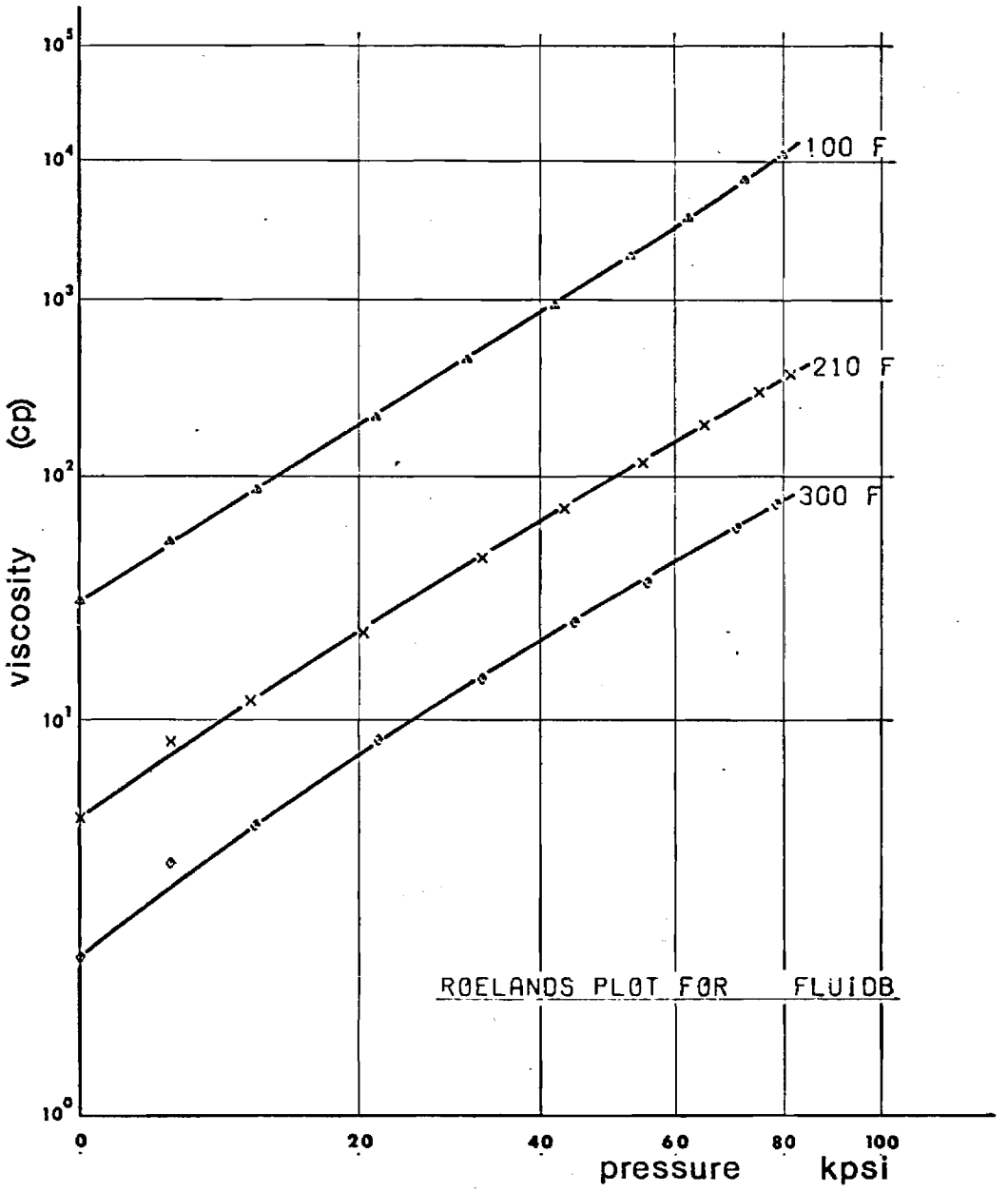
viscosity (cp)
10^5
10^4
10^3
10^2
10^1
10^0
100 F
210 F
300 F
ROELANDS PLOT FOR FLUID B
0
20
40
60
80
100
pressure kpsi

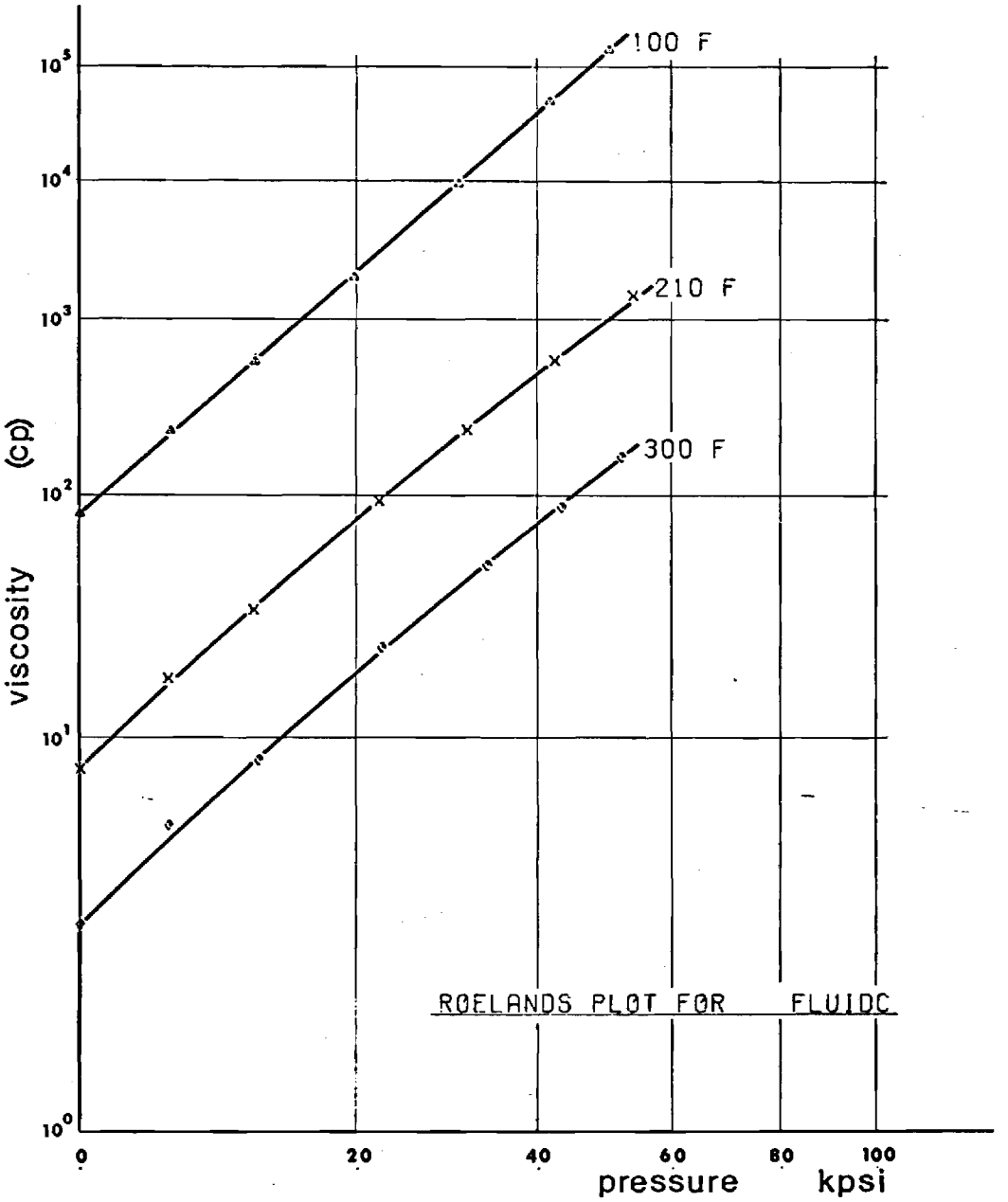
100 F
210 F
300 F
viscosity (cp)
10^5
10^4
10^3
10^2
10^1
10^0
0
20
40
60
80
100
pressure kpsi
ROELANDS PLOT FOR FLUIDC

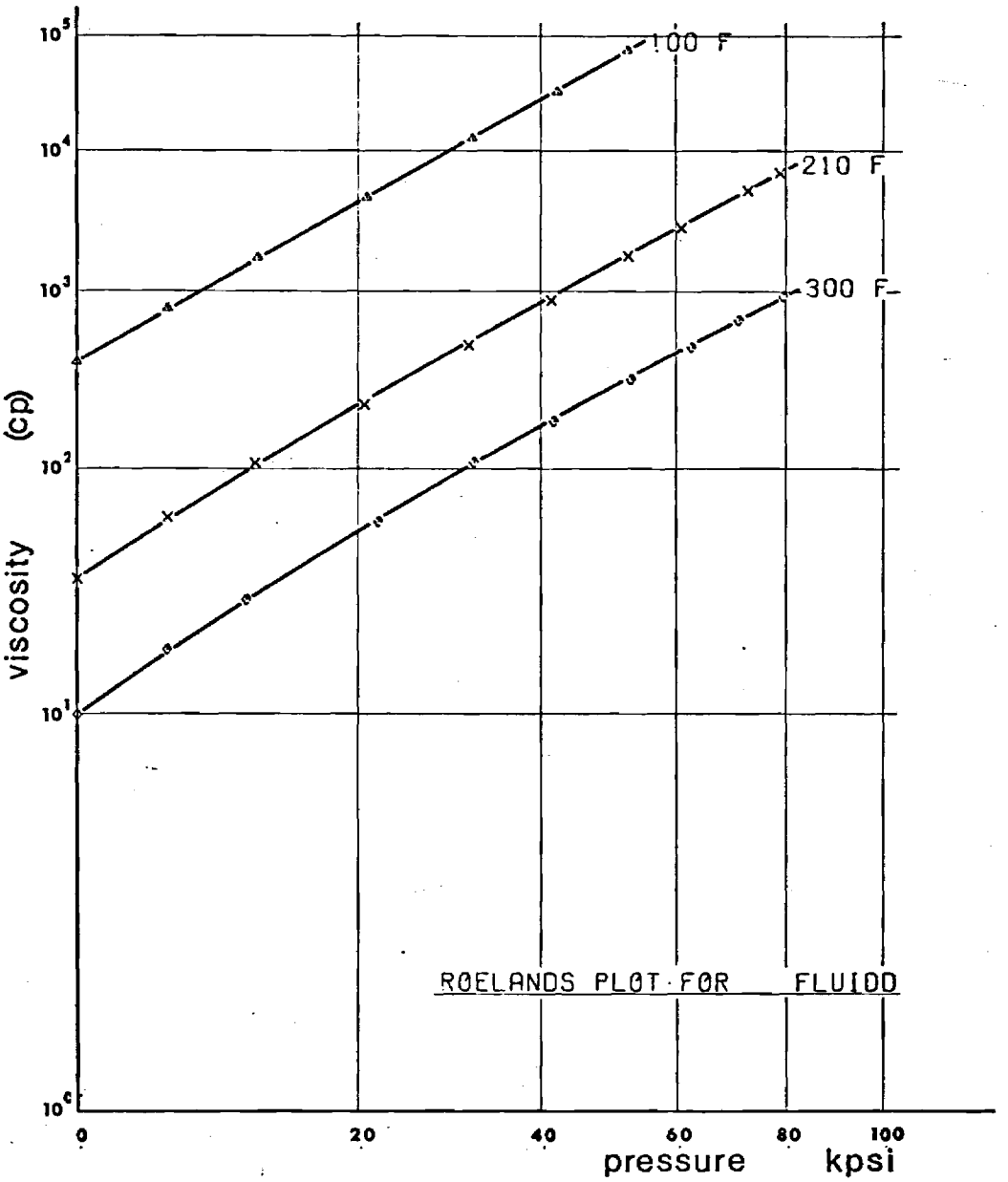
100 F
210 F
300 F
viscosity (cp)
10^5
10^4
10^3
10^2
10^1
10^0
0
20
40
60
80
100
pressure kpsi
ROELANDS PLOT FOR FLUID0

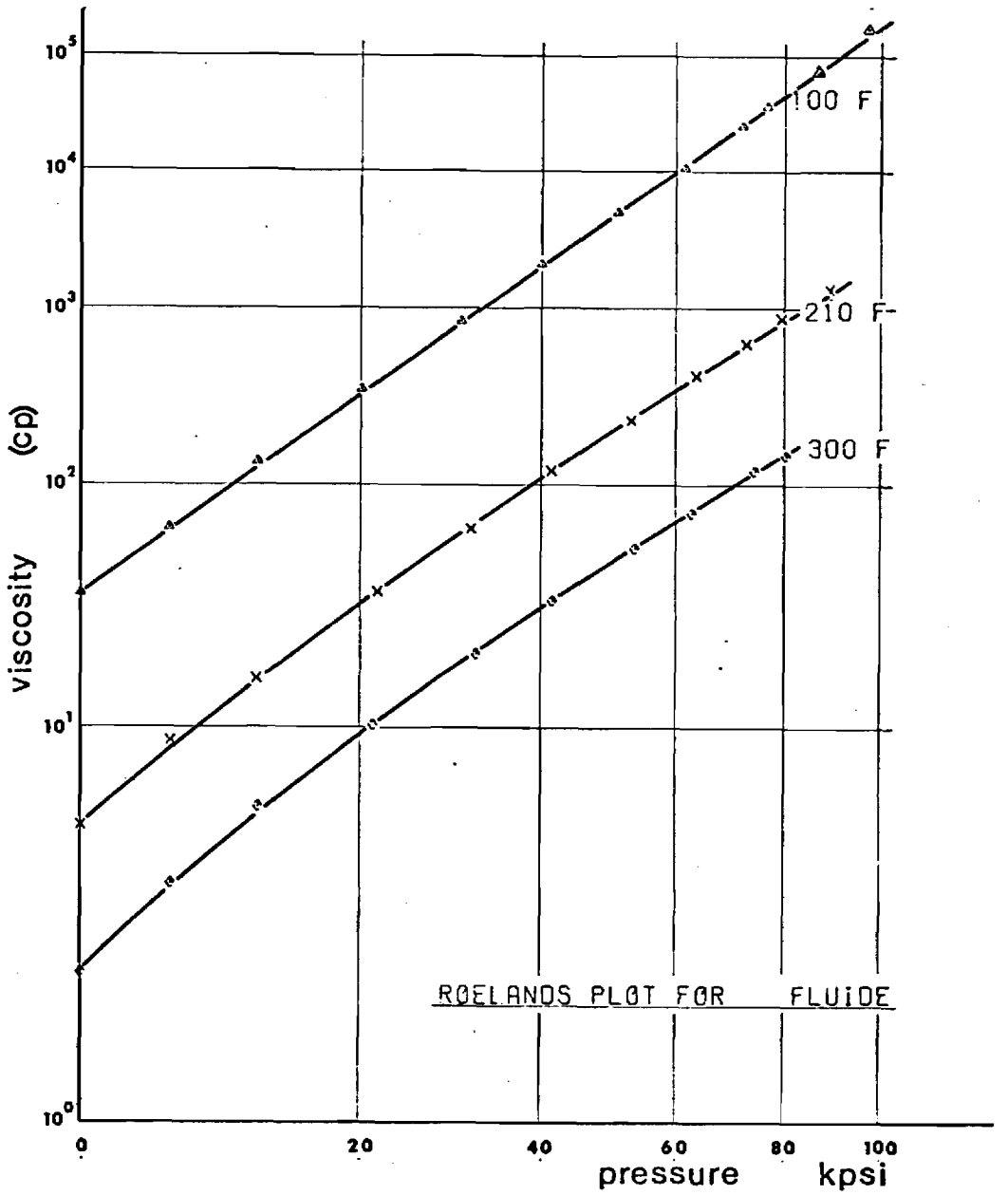
viscosity (cp)
10^5
10^4
10^3
10^2
10^1
10^0
100 F
210 F
300 F
0
20
40
60
80
100
pressure kpsi
ROELANDS PLOT FOR FLUIDE

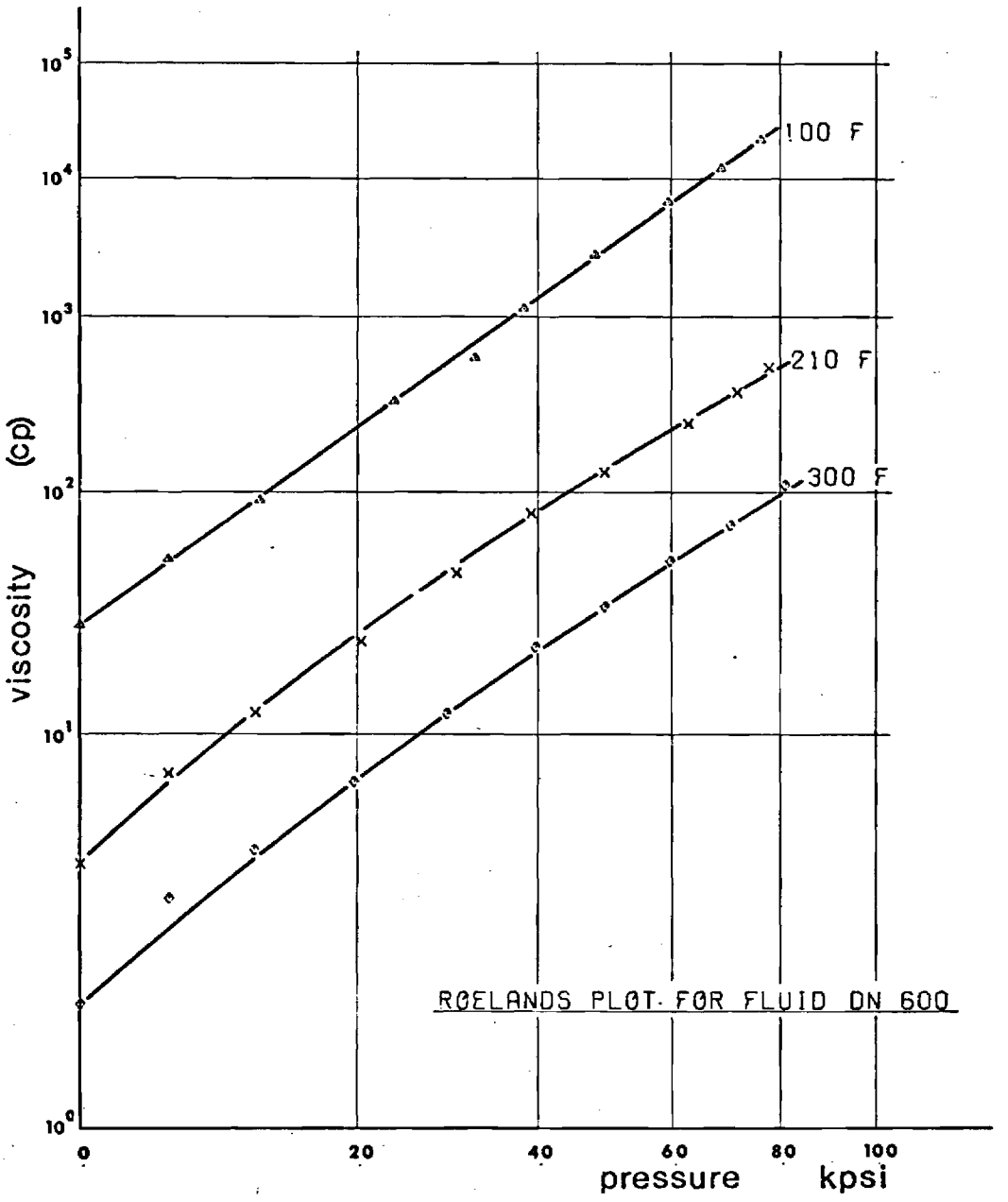
viscosity (cp)
10^5
10^4
10^3
10^2
10^1
10^0
100 F
210 F
300 F
0
20
40
60
80
100
pressure kpsi
ROELANDS PLOT FOR FLUID DN 600

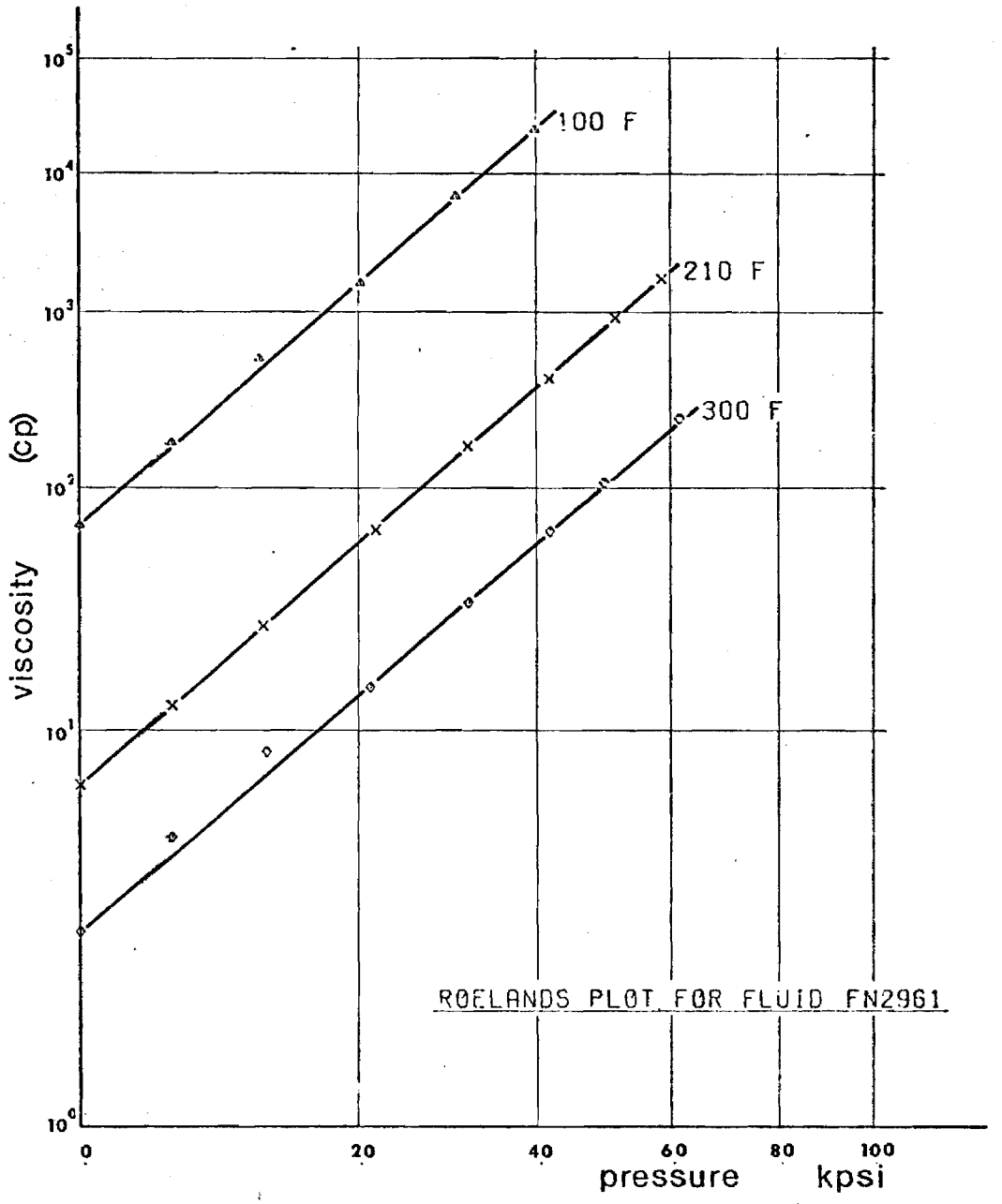
100 F
210 F
300 F
viscosity (cp)
10^5
10^4
10^3
10^2
10^1
10^0
0
20
40
60
80
100
pressure kpsi
ROELANDS PLOT FOR FLUID FN2961

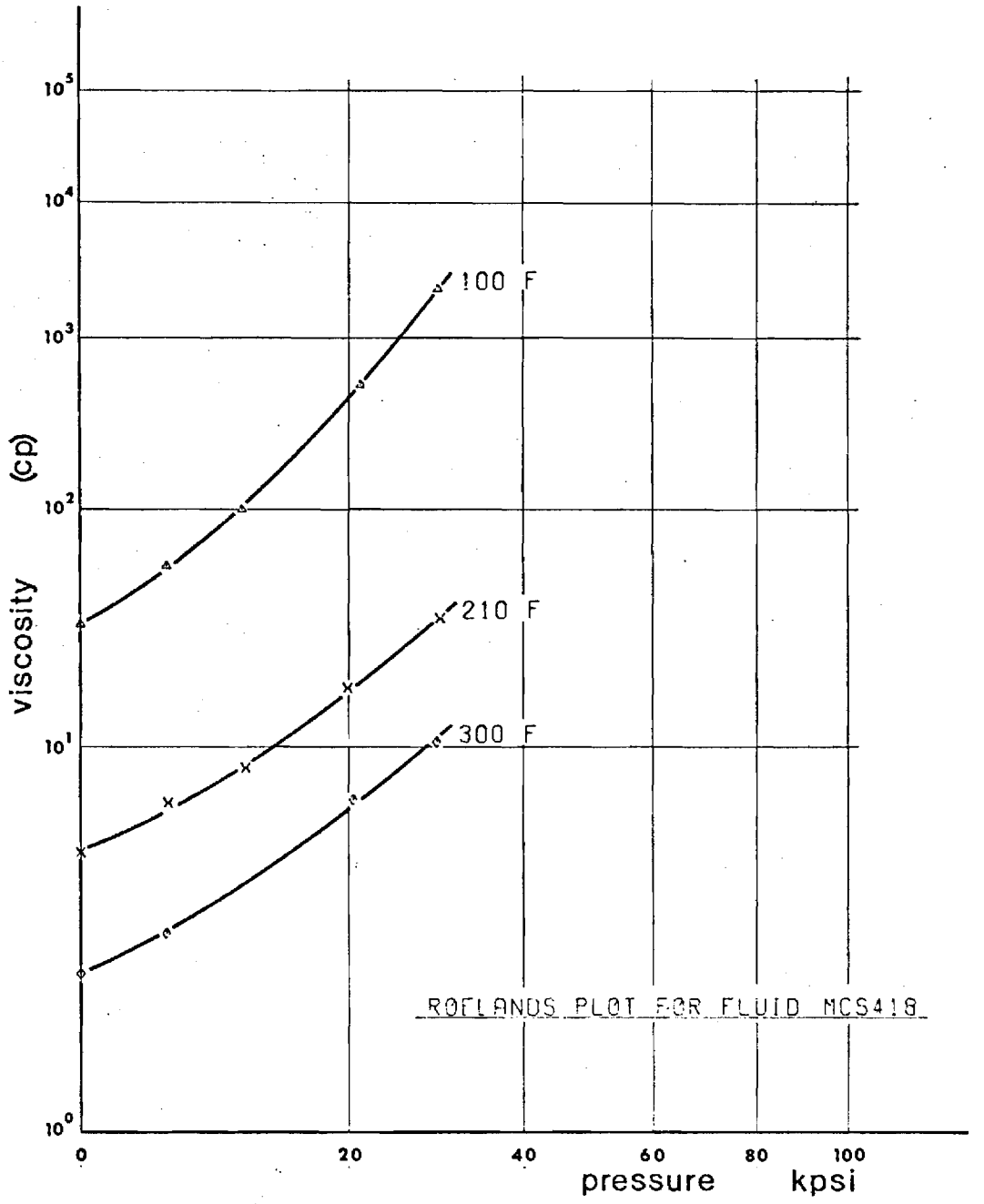

ROFLANDS PLOT FOR FLUID MCS418

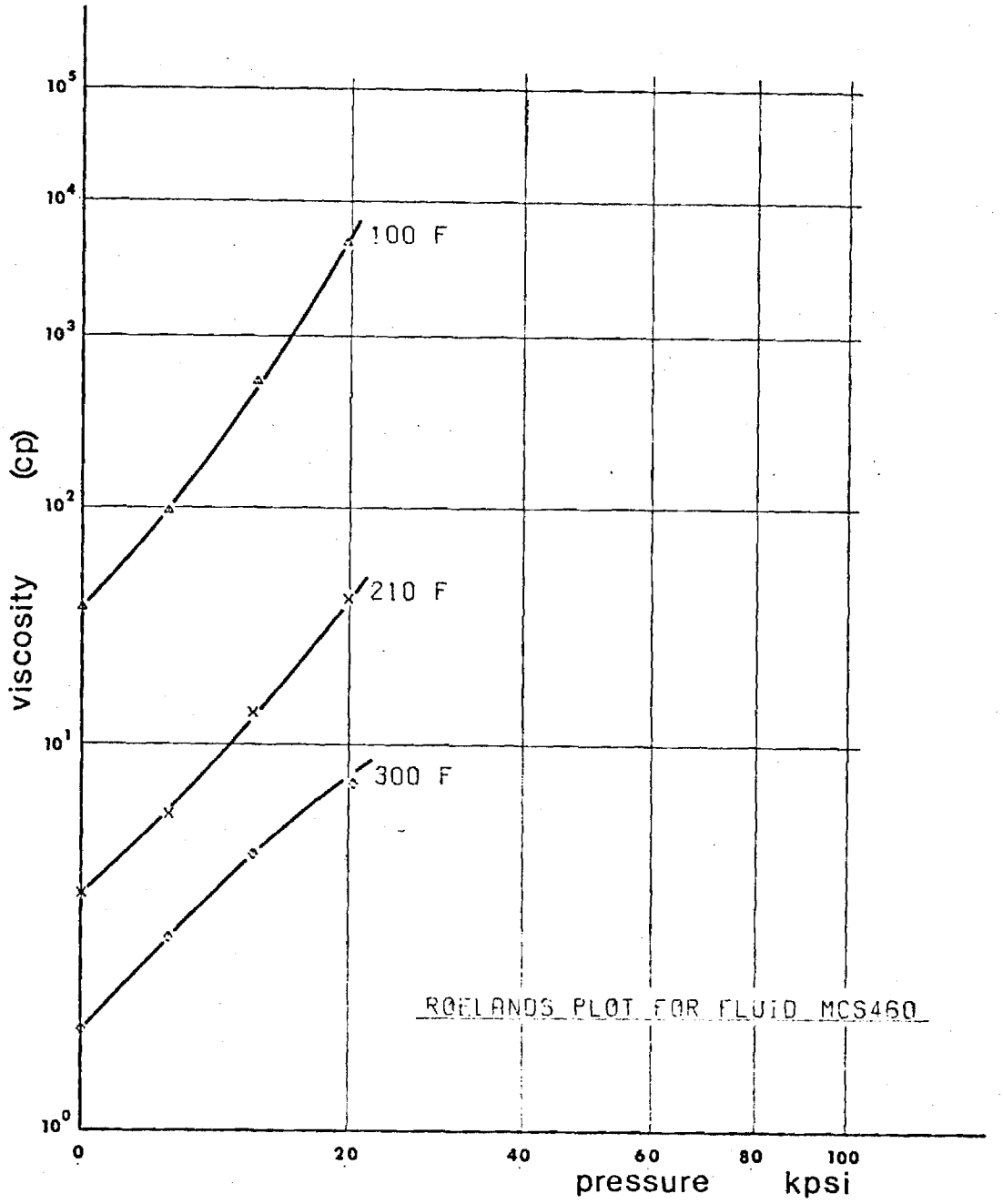

ROELANDS PLOT FOR FLUID MCS460

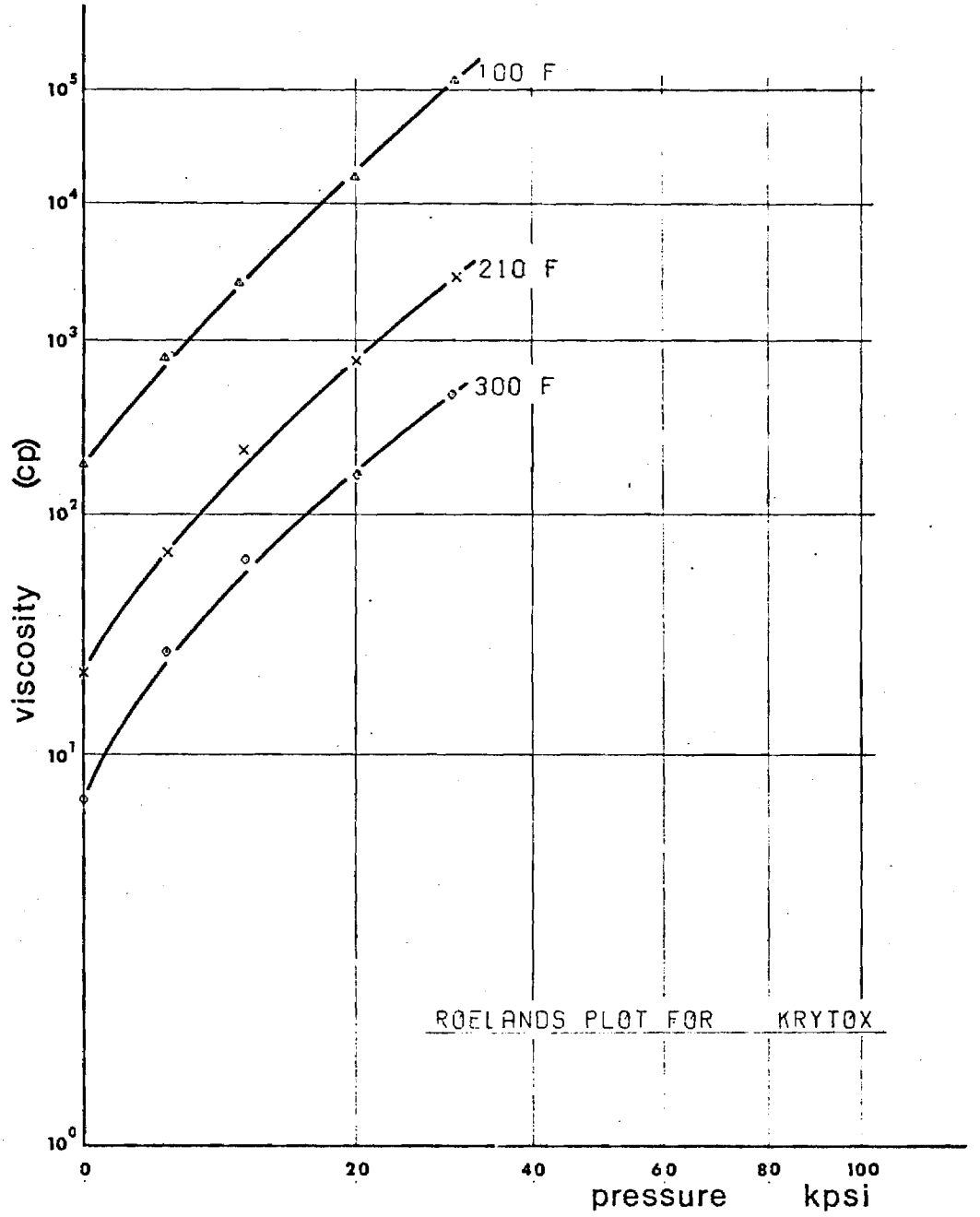
100 F
210 F
300 F
viscosity (cp)
10^5
10^4
10^3
10^2
10^1
10^0
0
20
40
60
80
100
pressure kpsi
ROELANDS PLOT FOR KRYTOX

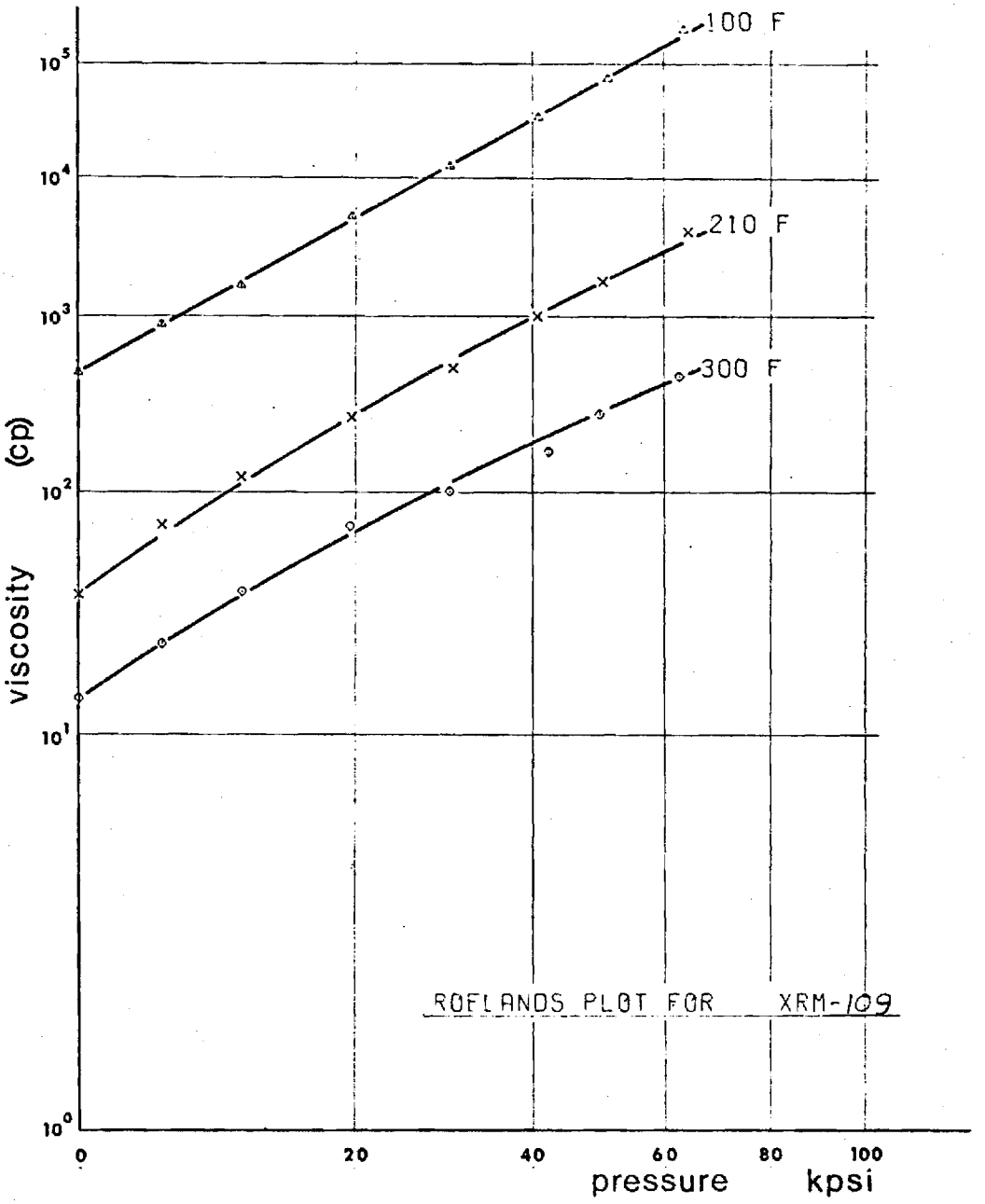
100 F
210 F
300 F
viscosity (cp)
10^5
10^4
10^3
10^2
10^1
10^0
0
20
40
60
80
100
pressure kpsi
ROFLANDS PLOT FOR XRM-109

ISOTHERMAL PRESSURE
VISCOSITY PLOT FOR FLUIDA

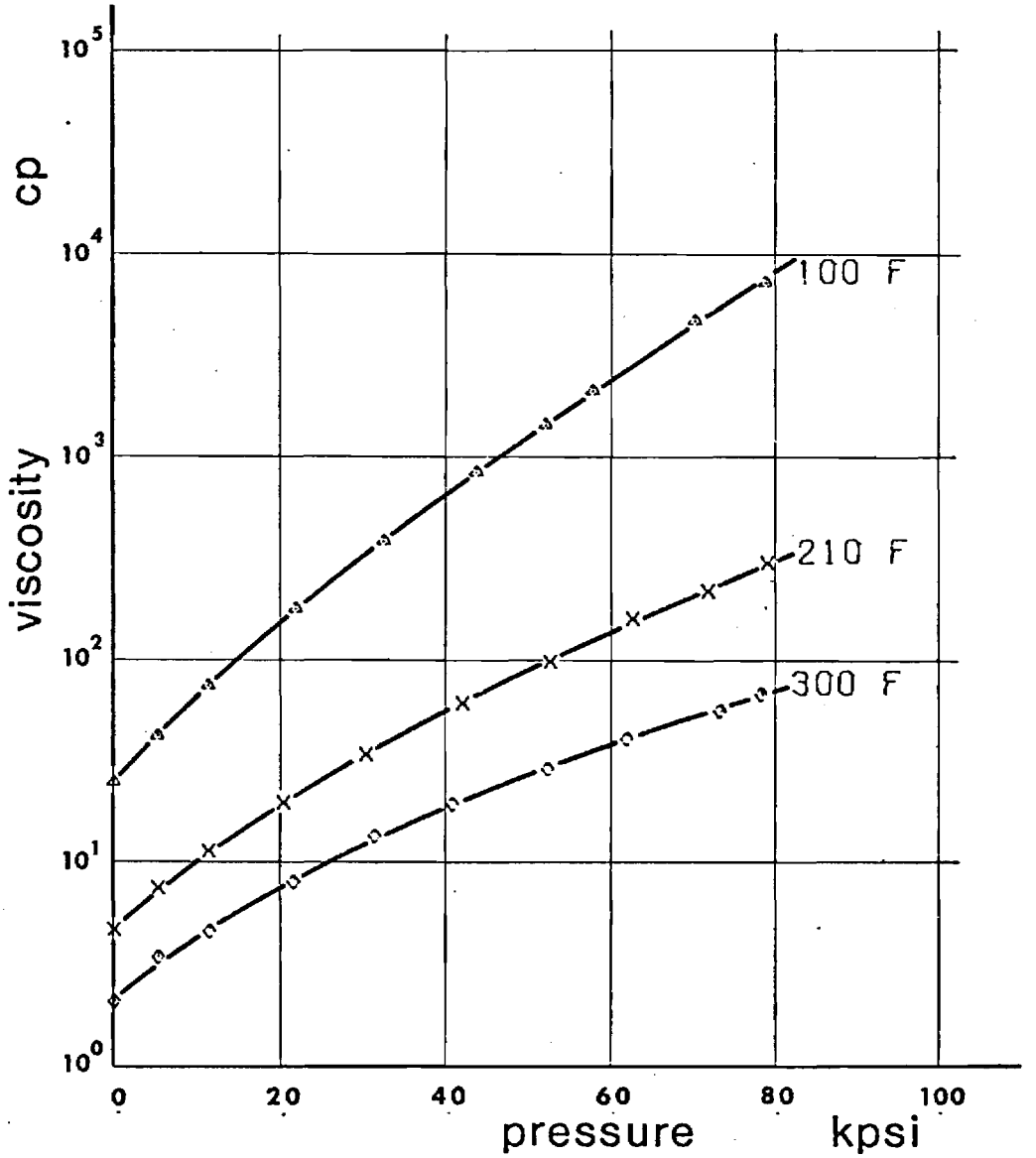

ISOTHERMAL PRESSURE
VISCOSITY PLOT FOR FLUIDB

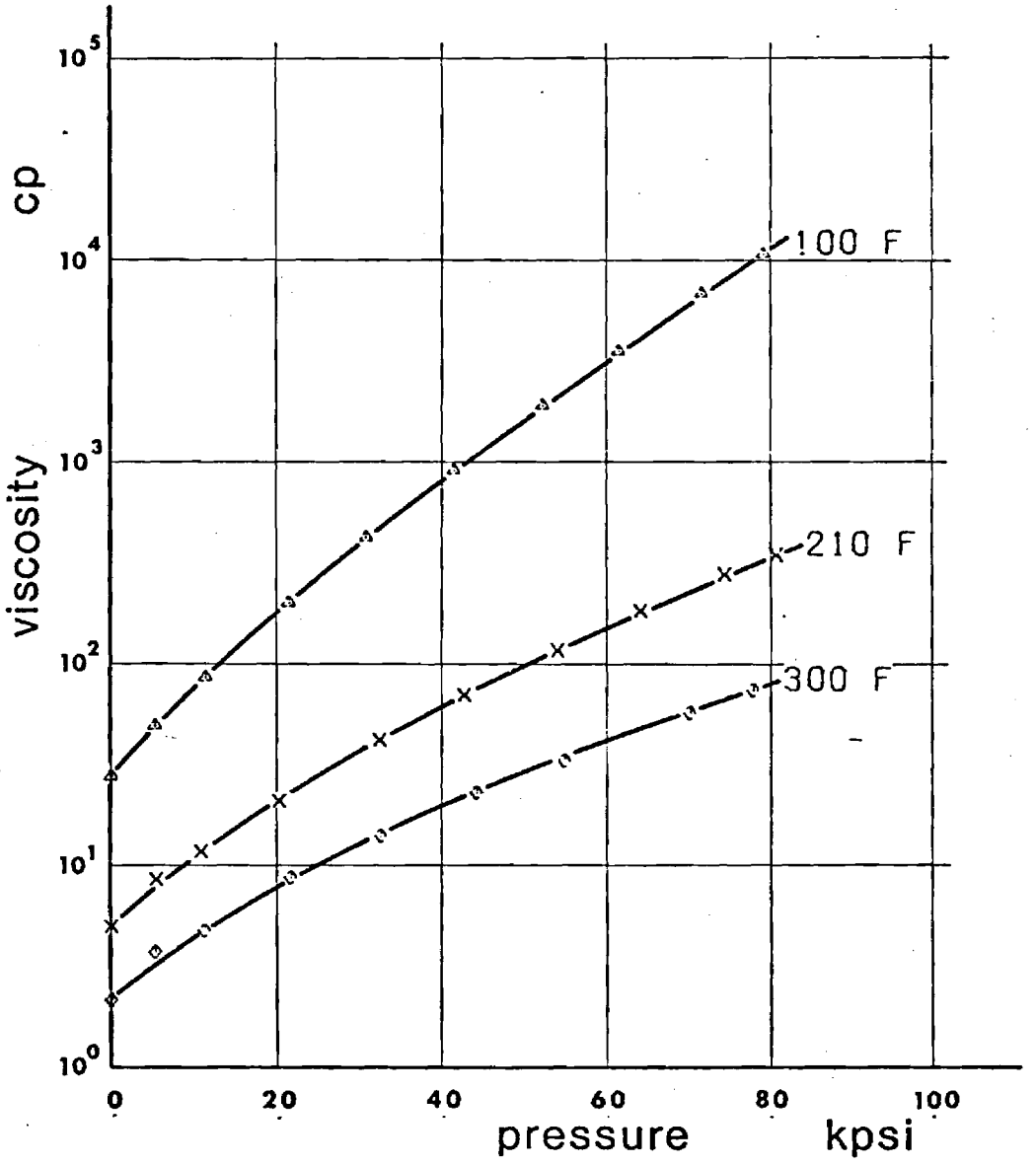

ISOTHERMAL PRESSURE
VISCOSITY PLOT FOR FLUIDC

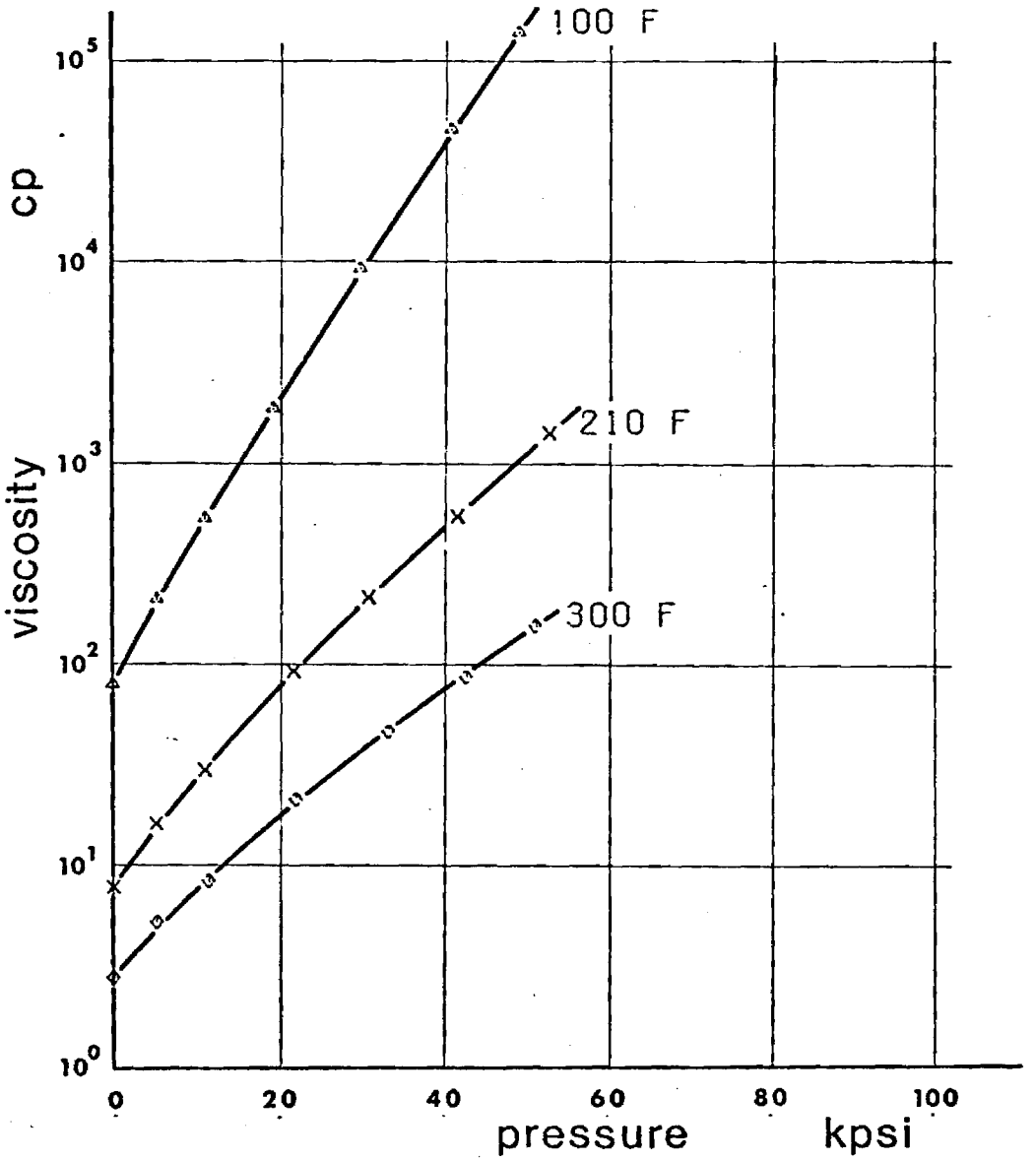

ISOTHERMAL PRESSURE
VISCOSITY PLOT FOR FLUIDD

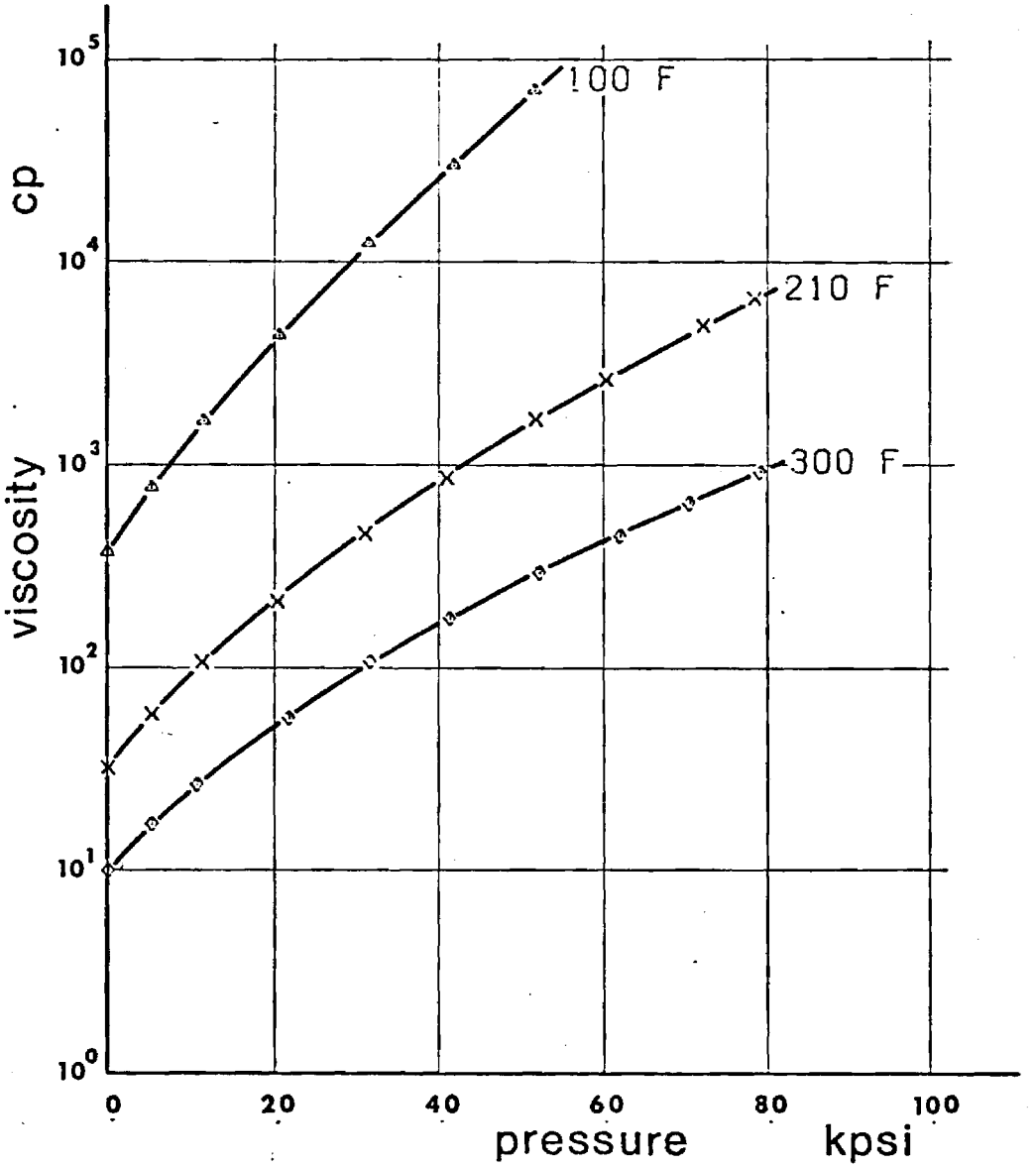

ISOTHERMAL PRESSURE
VISCOSITY PLOT FOR _____ FLUIDE

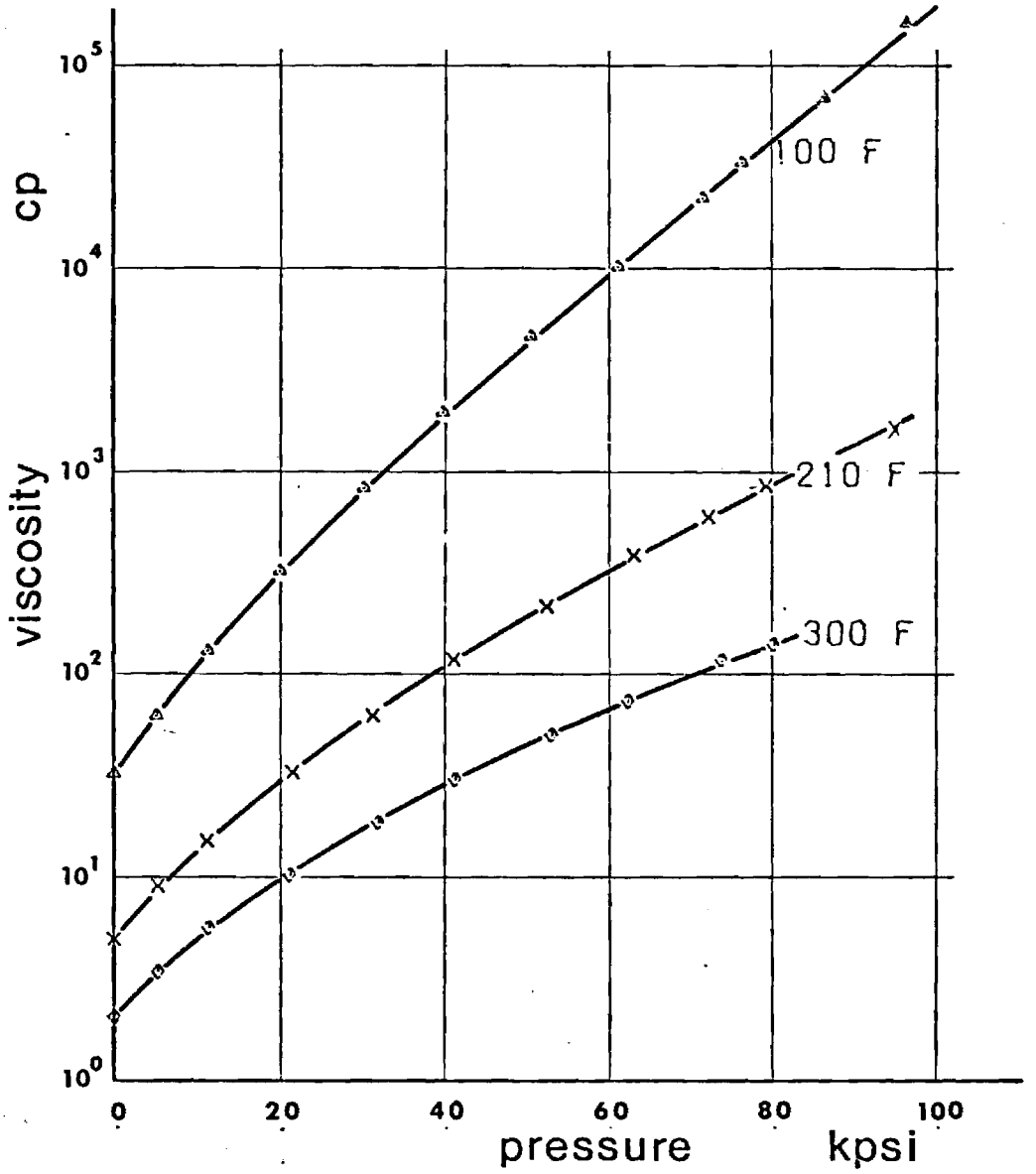

ISOTHERMAL PRESSURE
VISCOSITY PLOT FOR FLUID DN 600

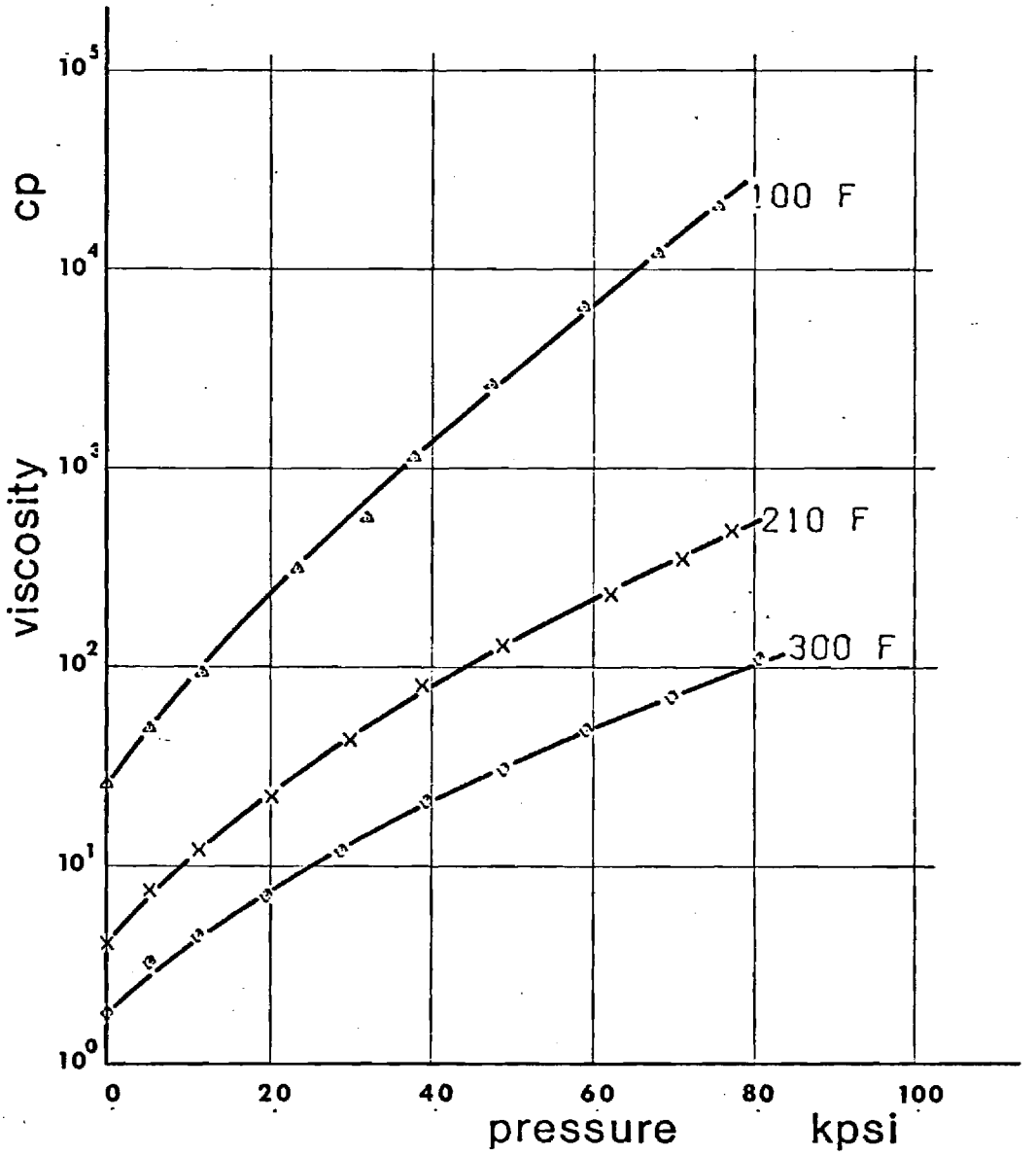

ISOTHERMAL PRESSURE
VISCOSITY PLOT FOR FLUID FN2961

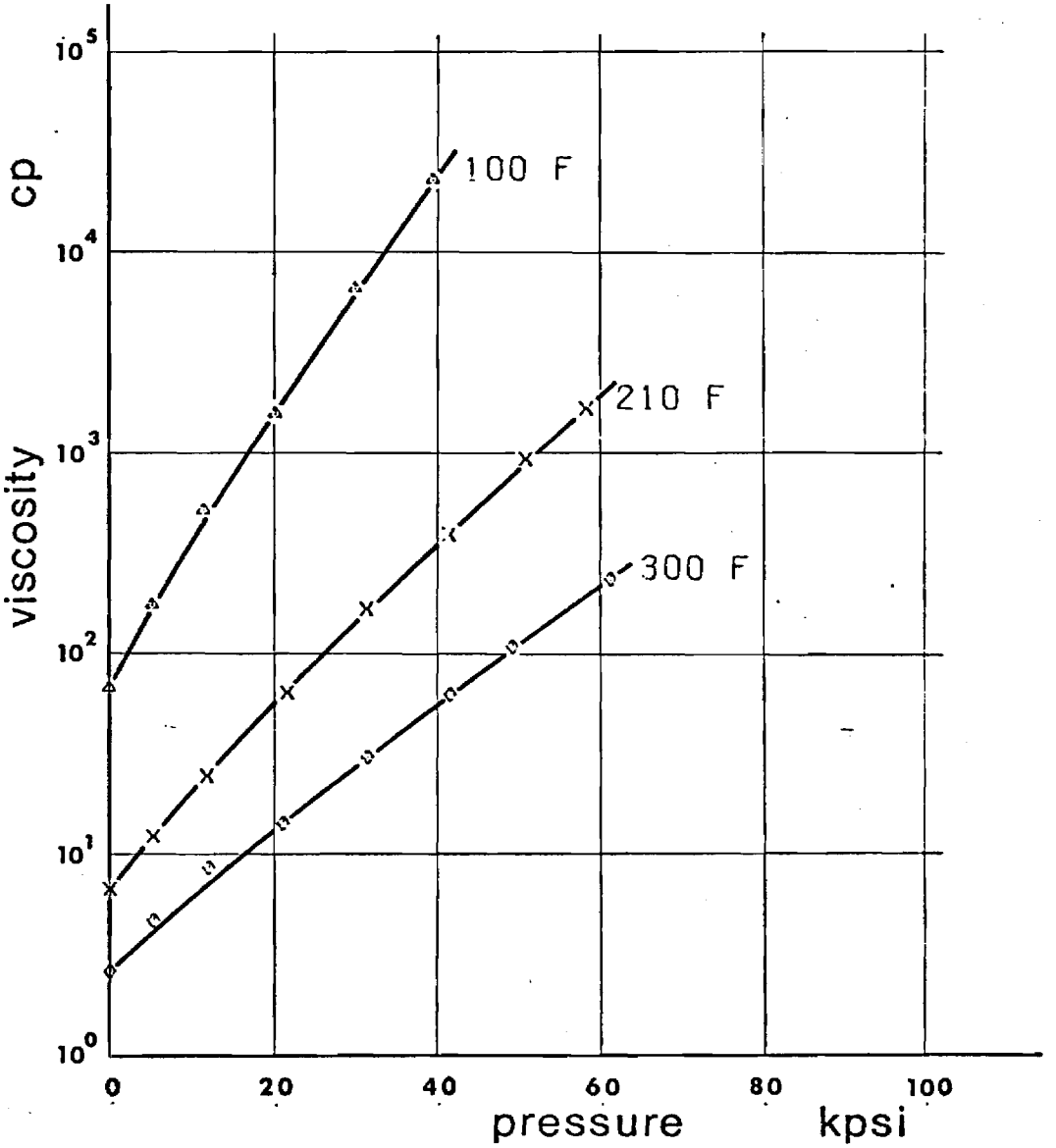

ISOTHERMAL PRESSURE
VISCOSITY PLOT FOR FLUID MCS418

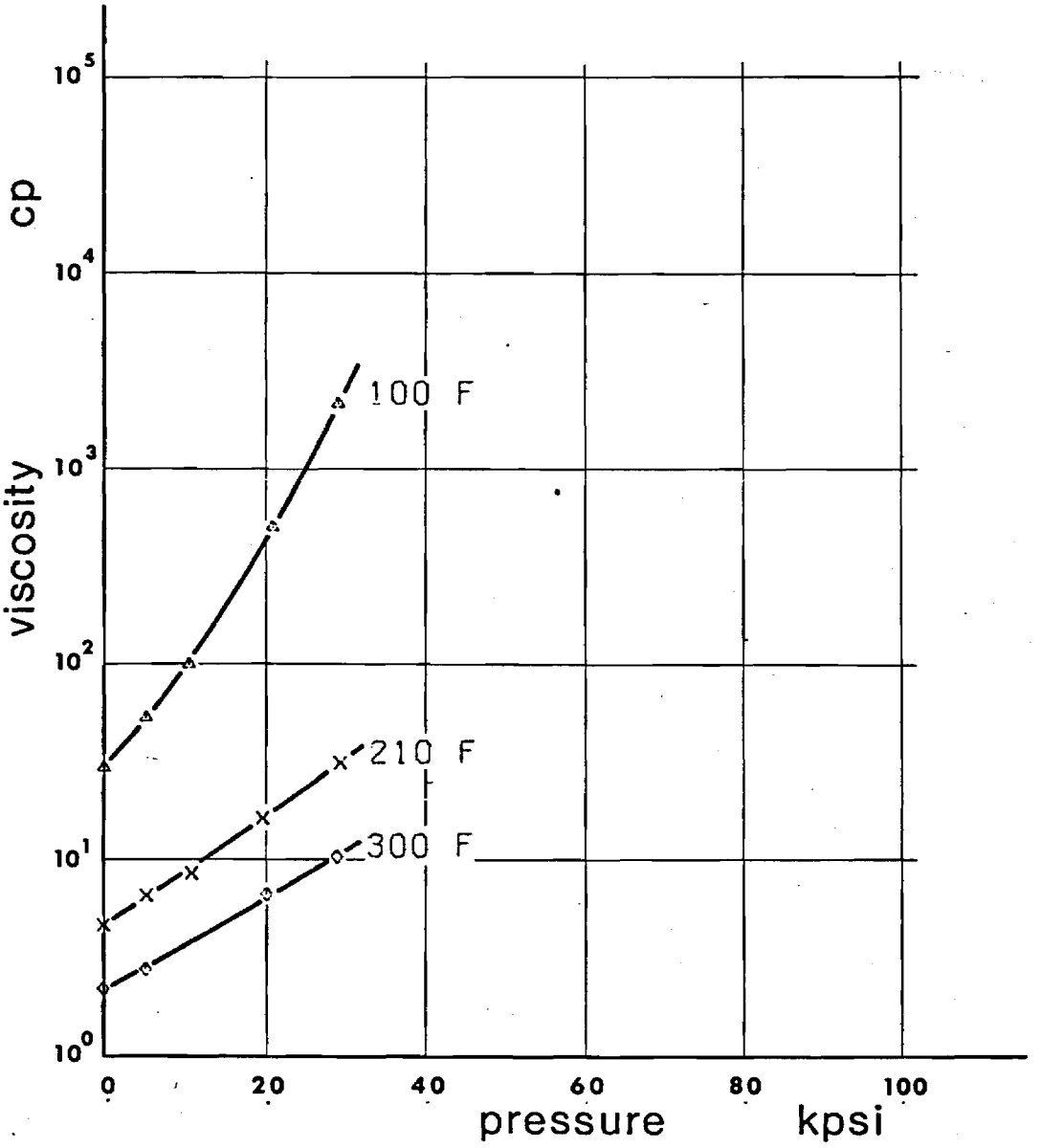

ISOTHERMAL PRESSURE
VISCOSITY PLOT FOR FLUID MCS460

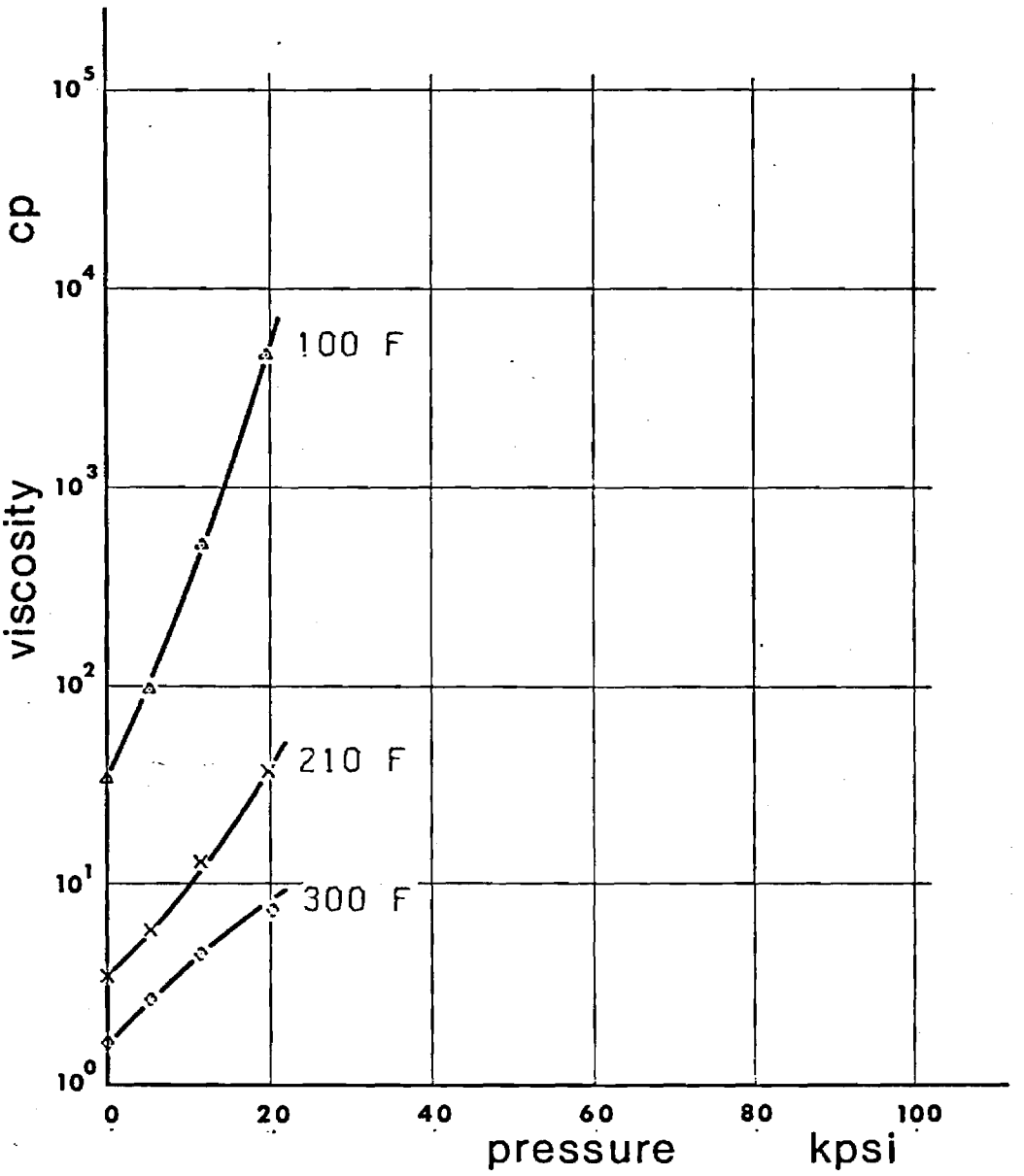

ISOTHERMAL PRESSURE
VISCOSITY PLOT FOR KRYTOX

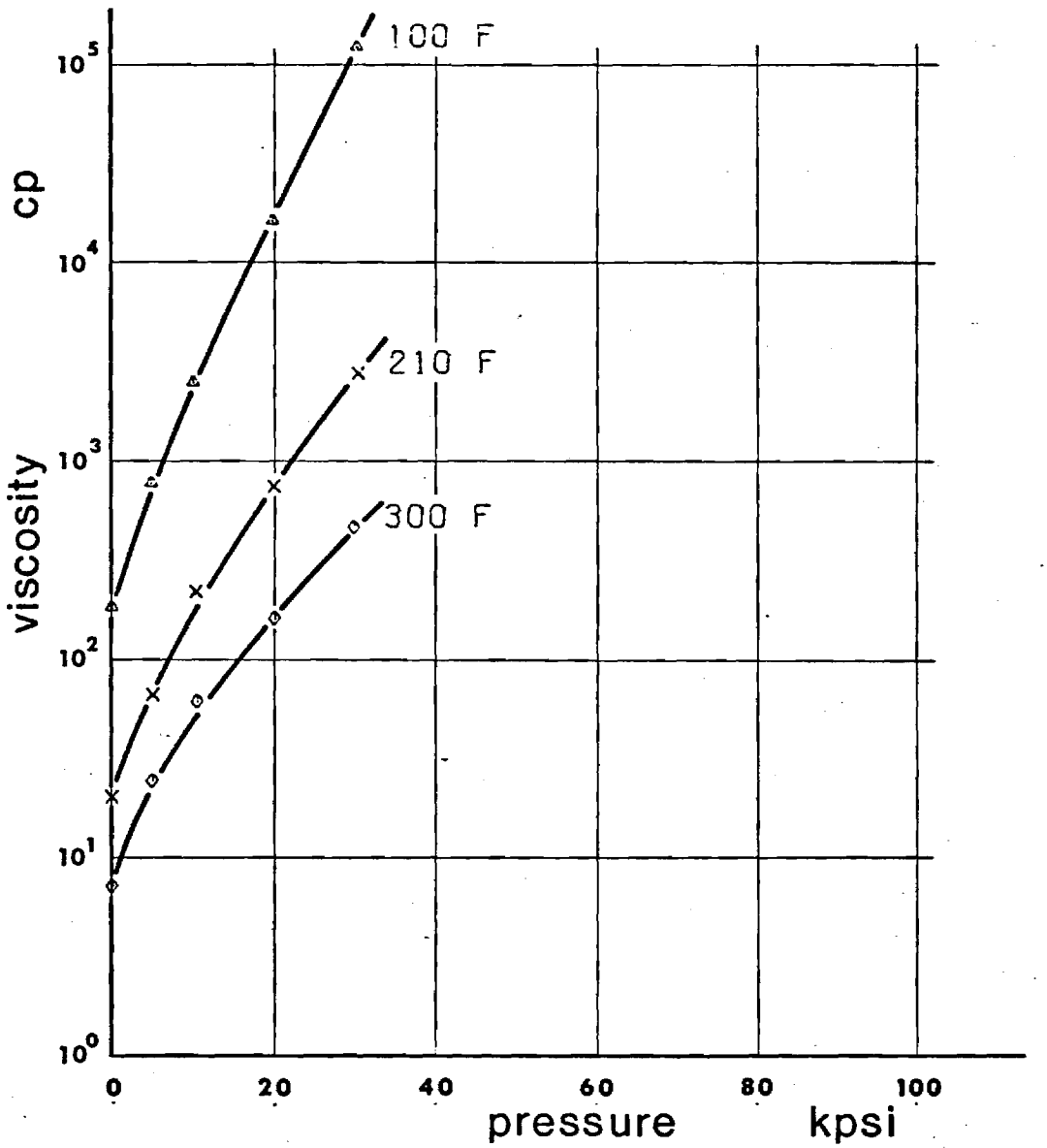

ISOTHERMAL PRESSURE
VISCOSITY PLOT FOR XRM-109

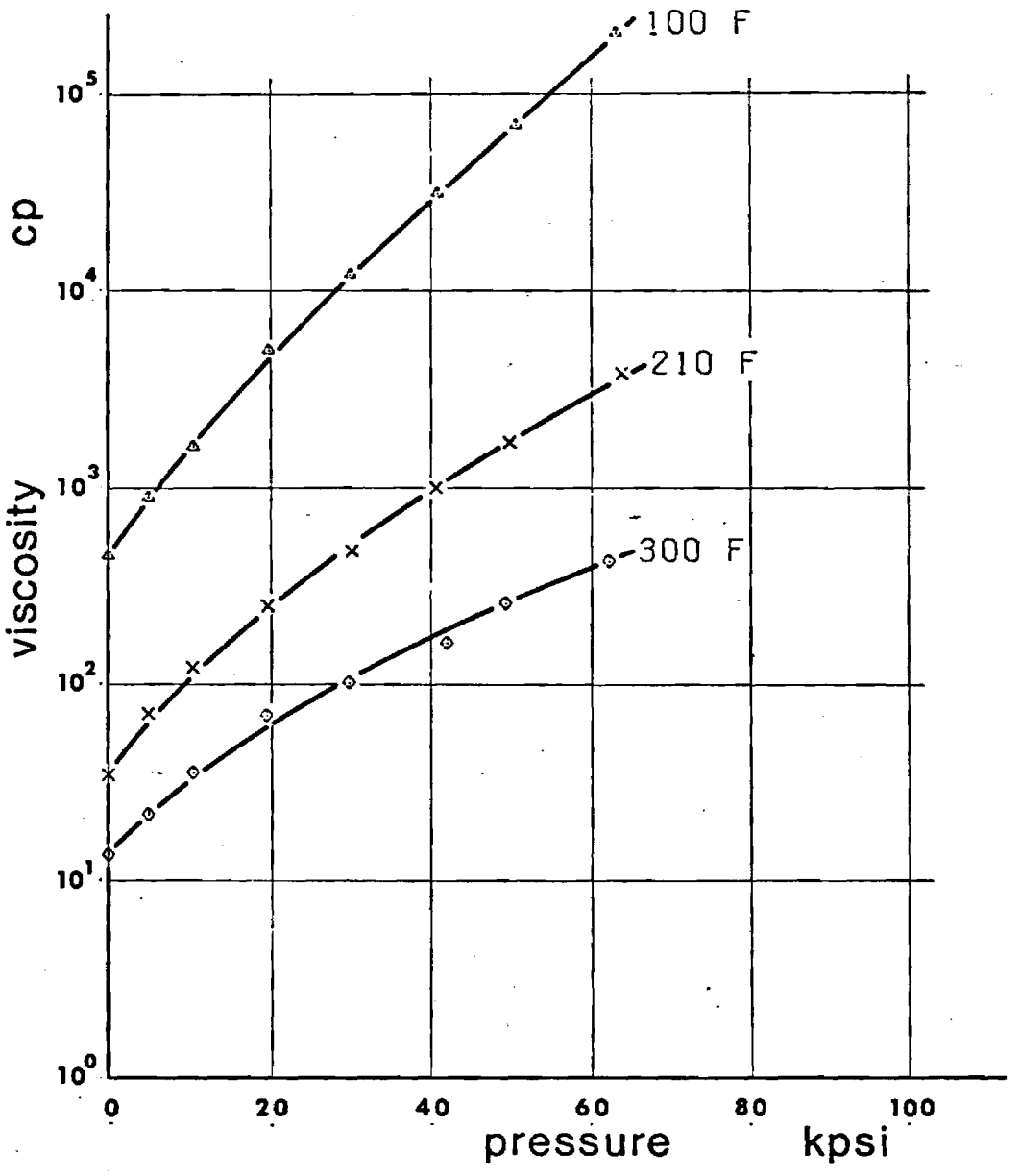

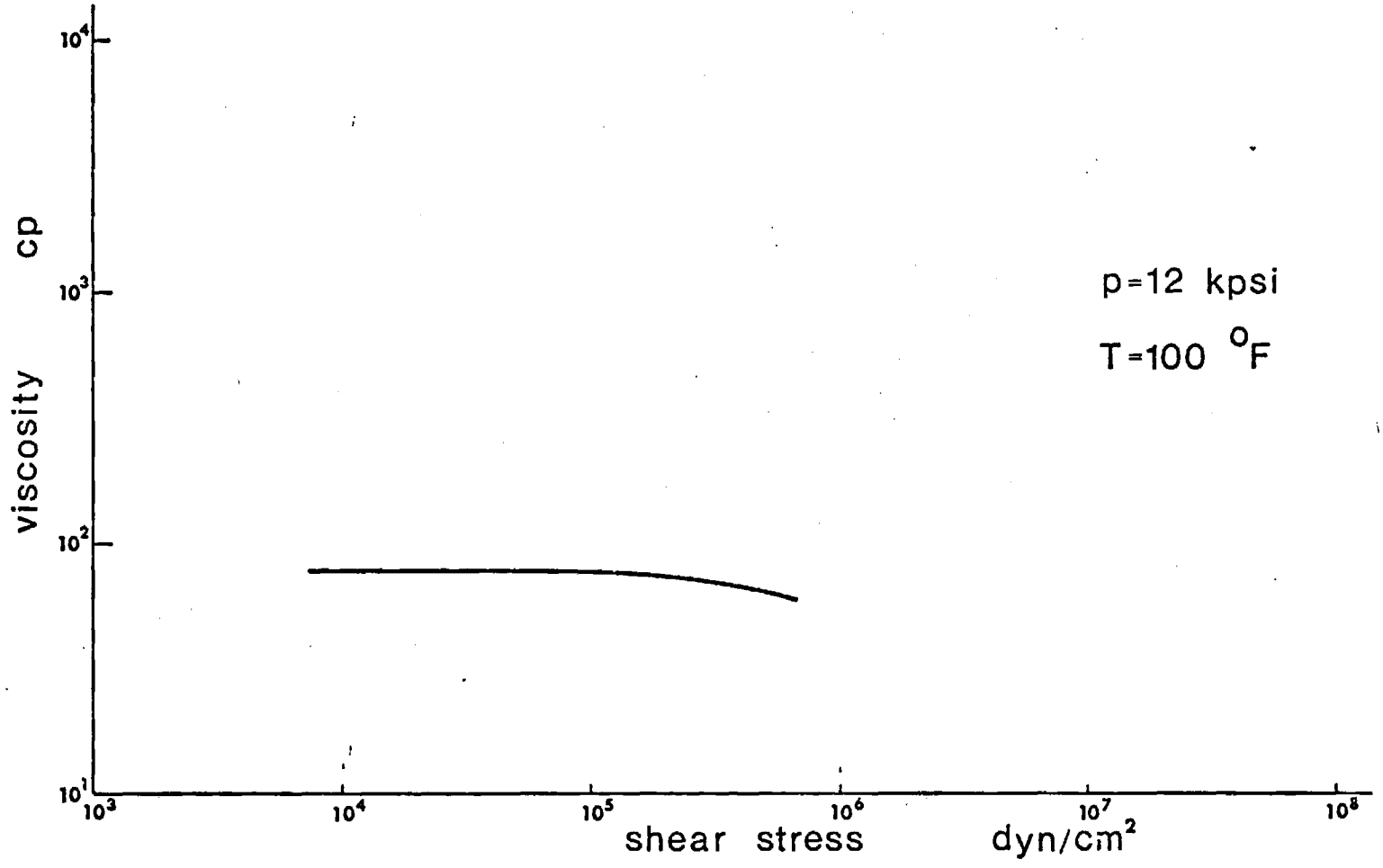

Viscosity-Shear Stress Relation for Fluid A

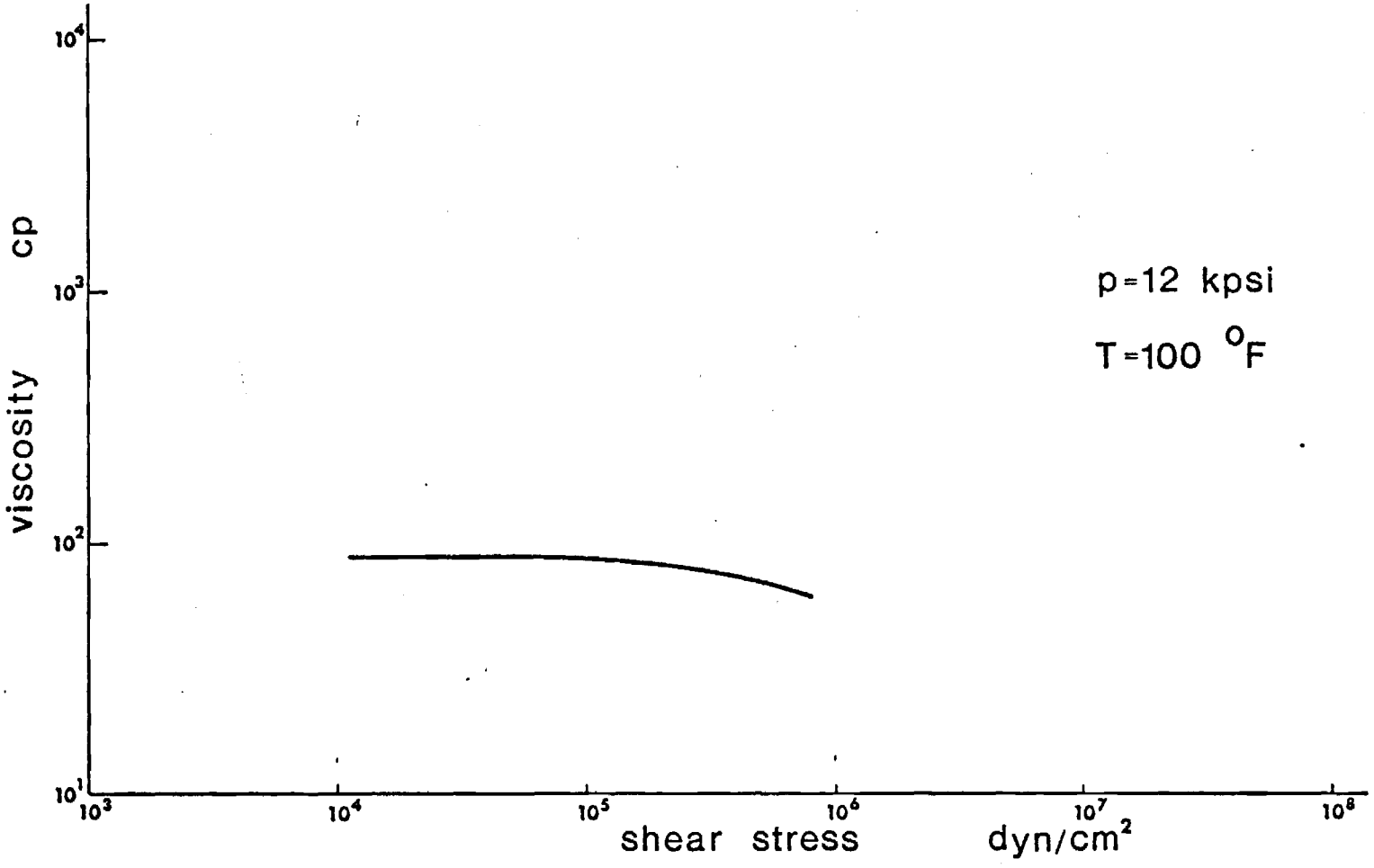

Viscosity-Shear Stress Relation for Fluid B

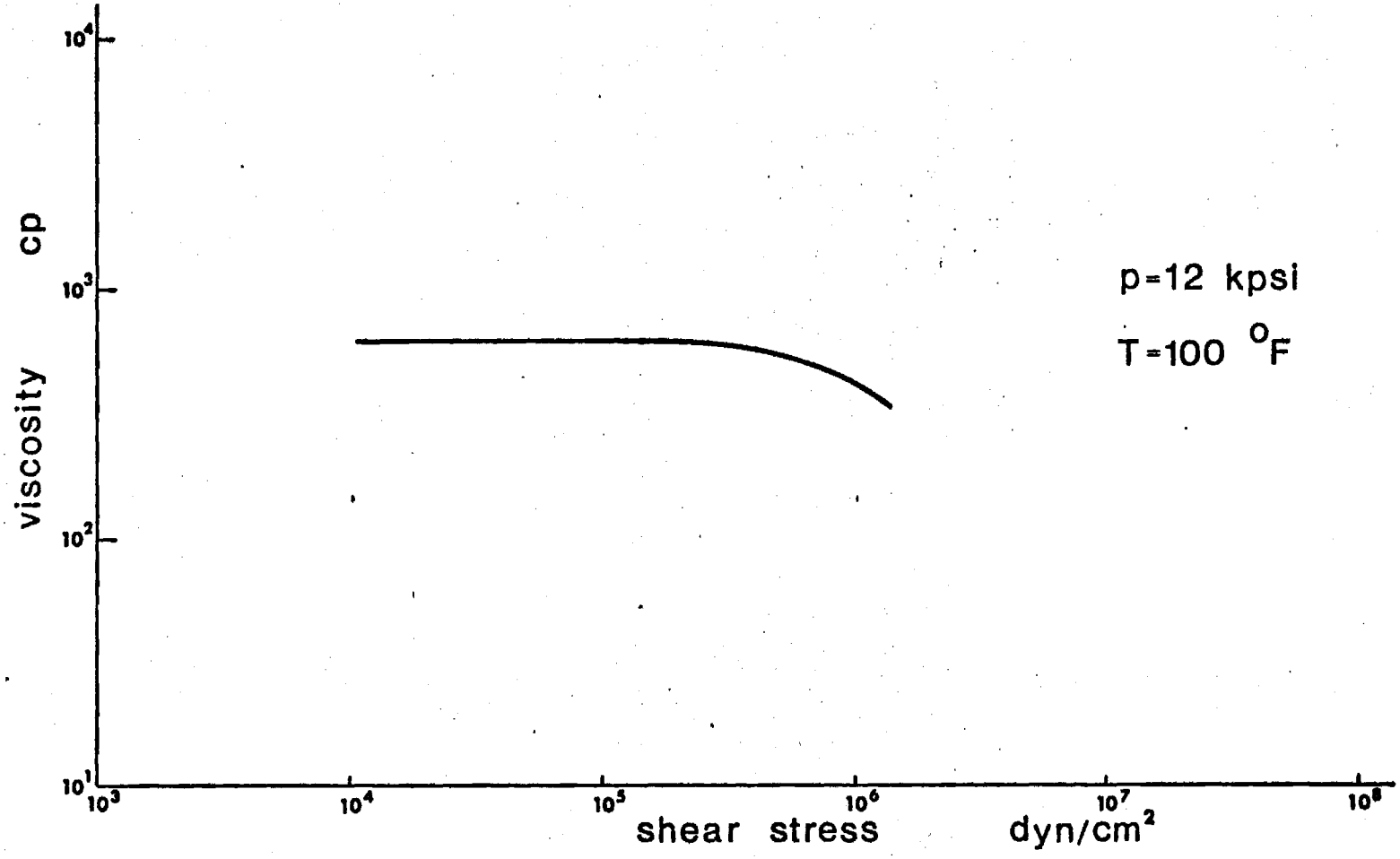

Viscosity-Shear Stress Relation for Fluid C

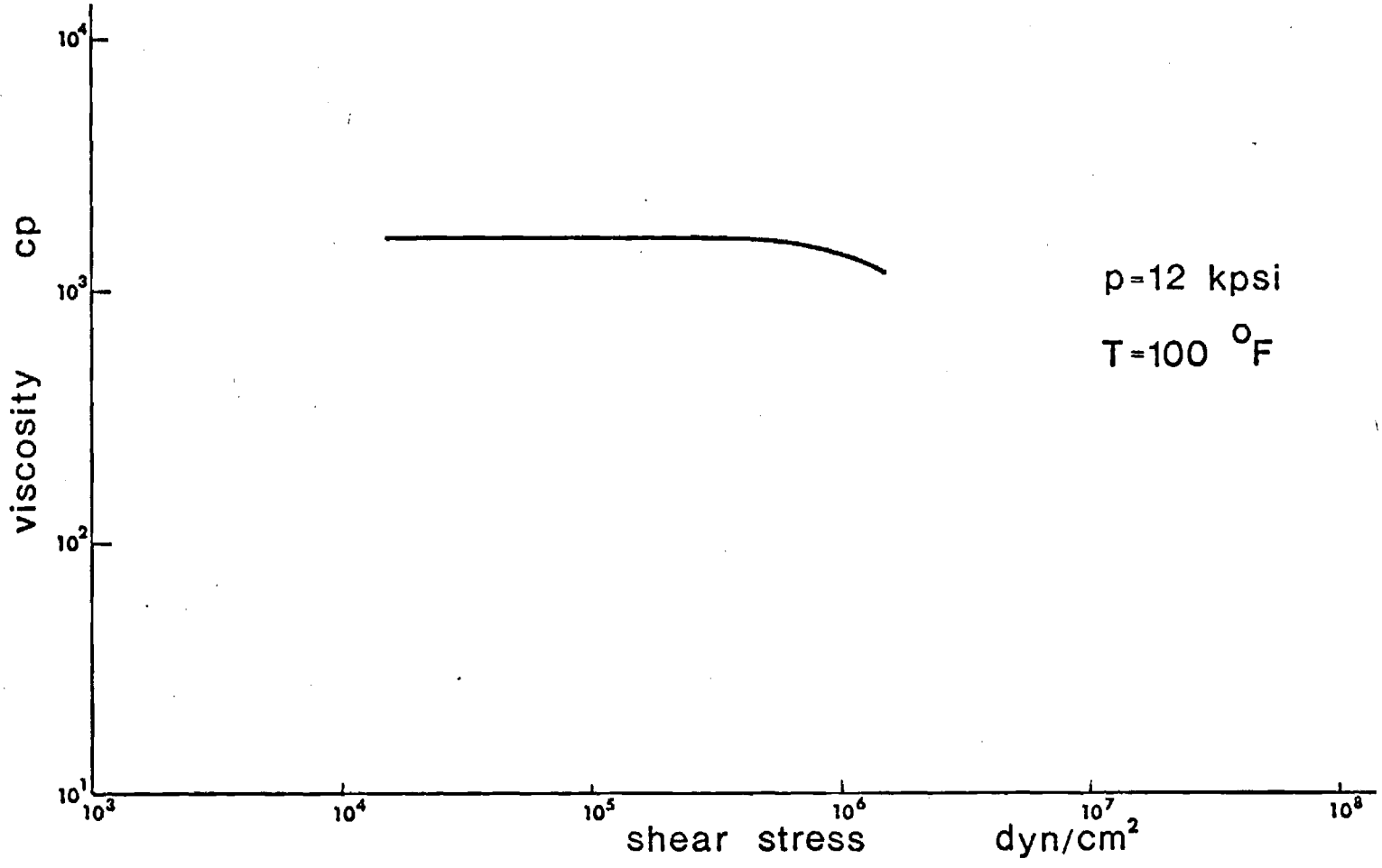

Viscosity-Shear Stress Relation for Fluid D

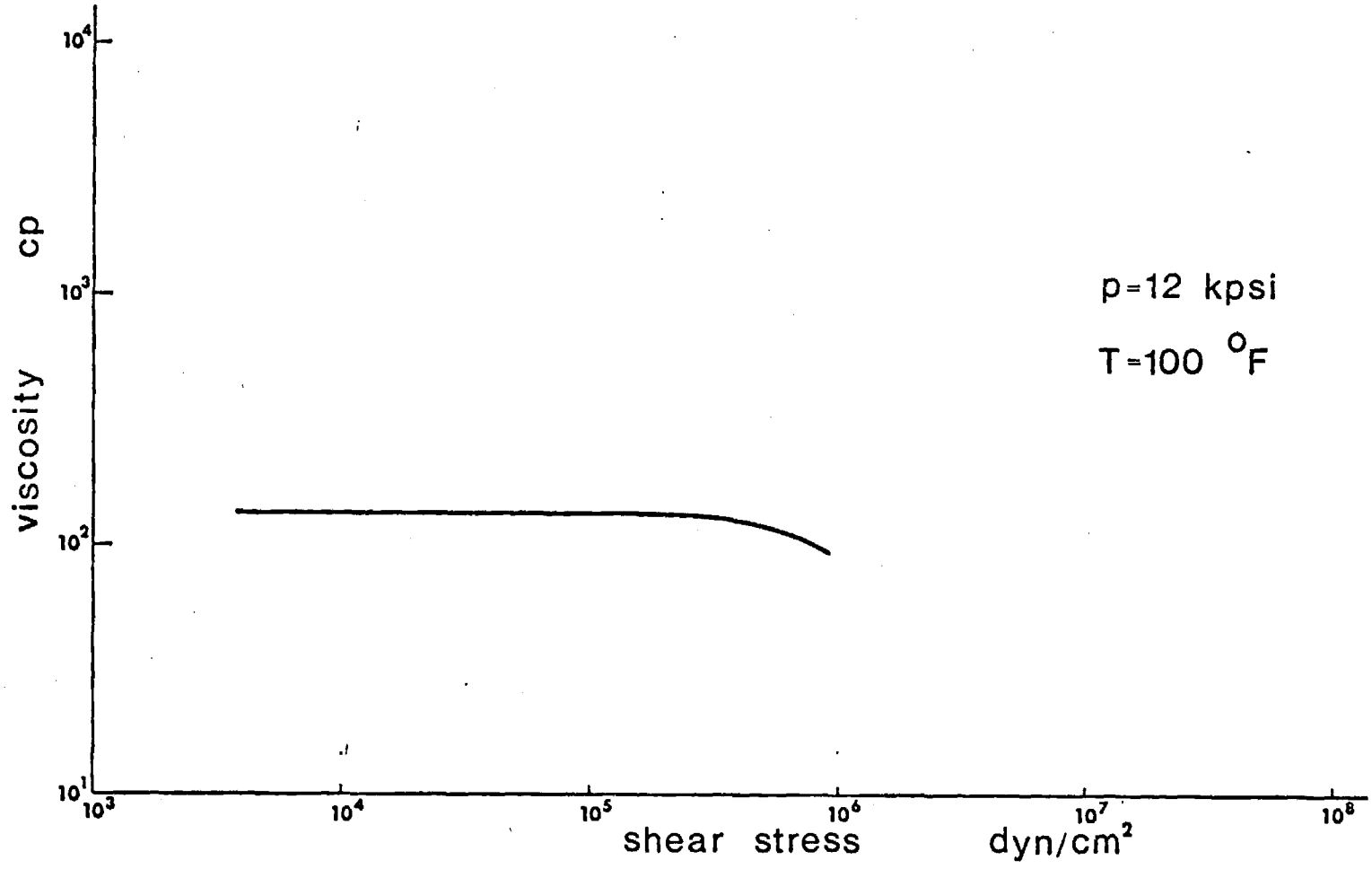

Viscosity-Shear Stress Relation for Fluid E

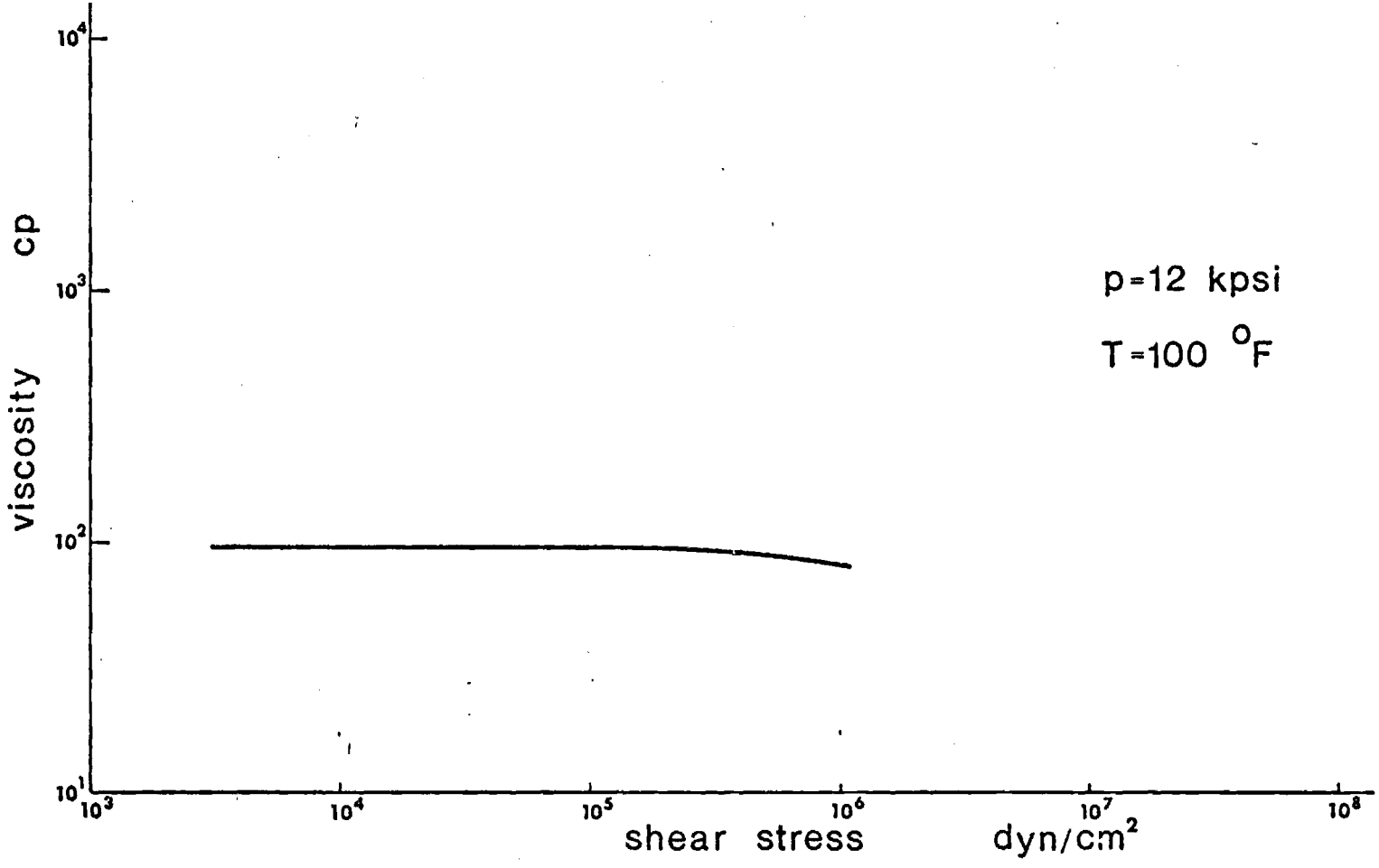

Viscosity-Shear Stress Relation for Fluid DN600

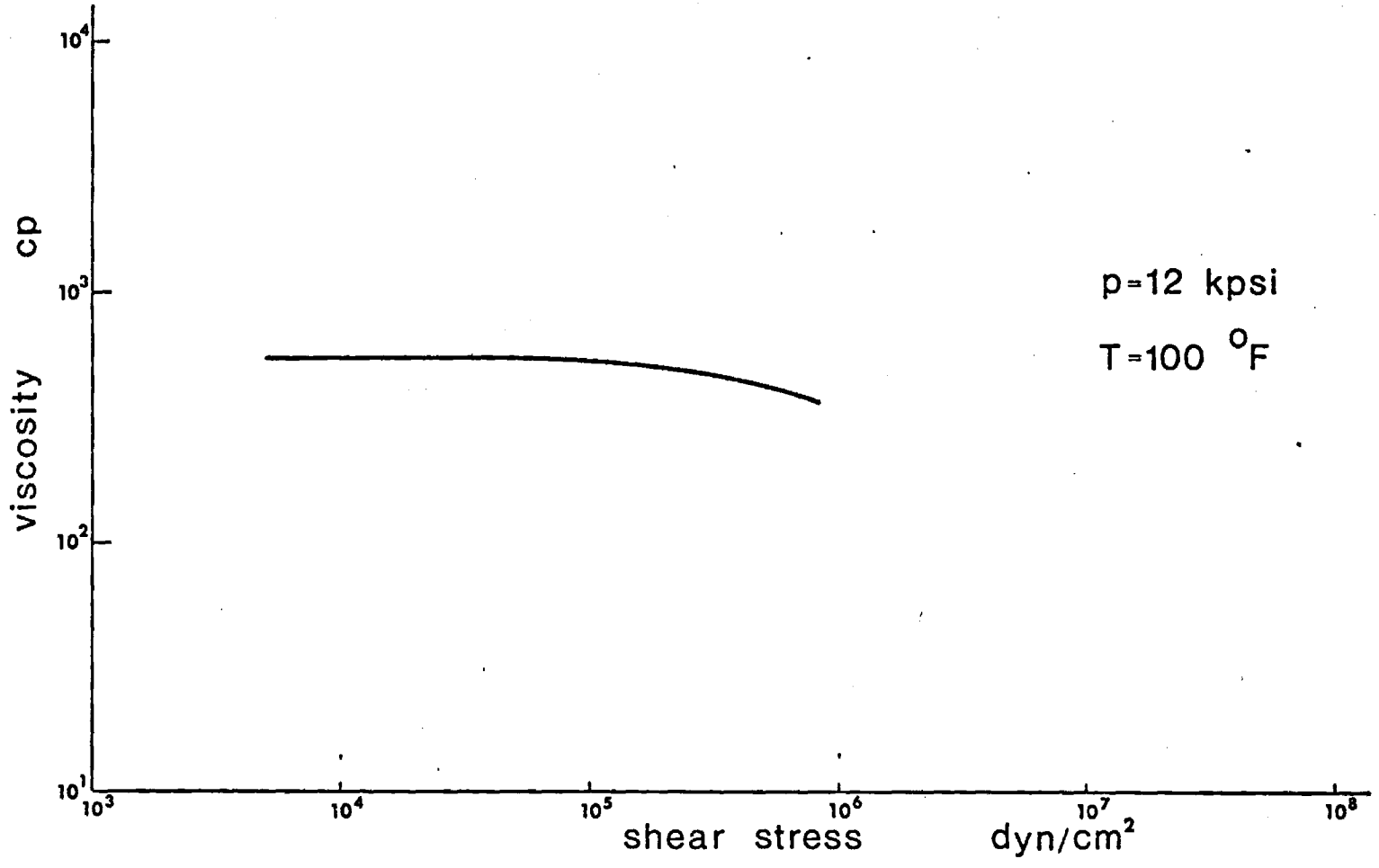

Viscosity-Shear Stress Relation for Fluid FN2961

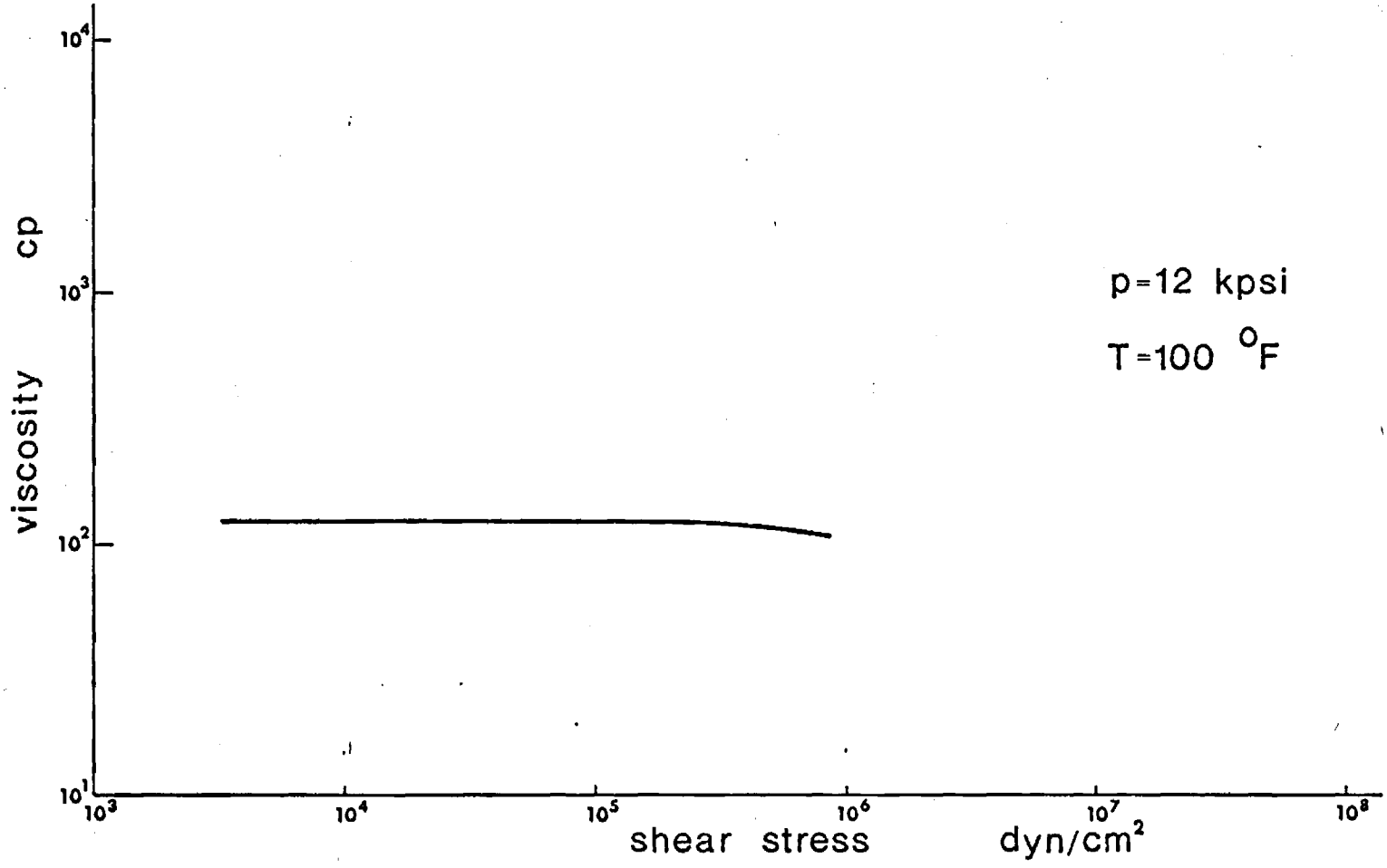

Viscosity-Shear Stress Relation for Fluid MCS418

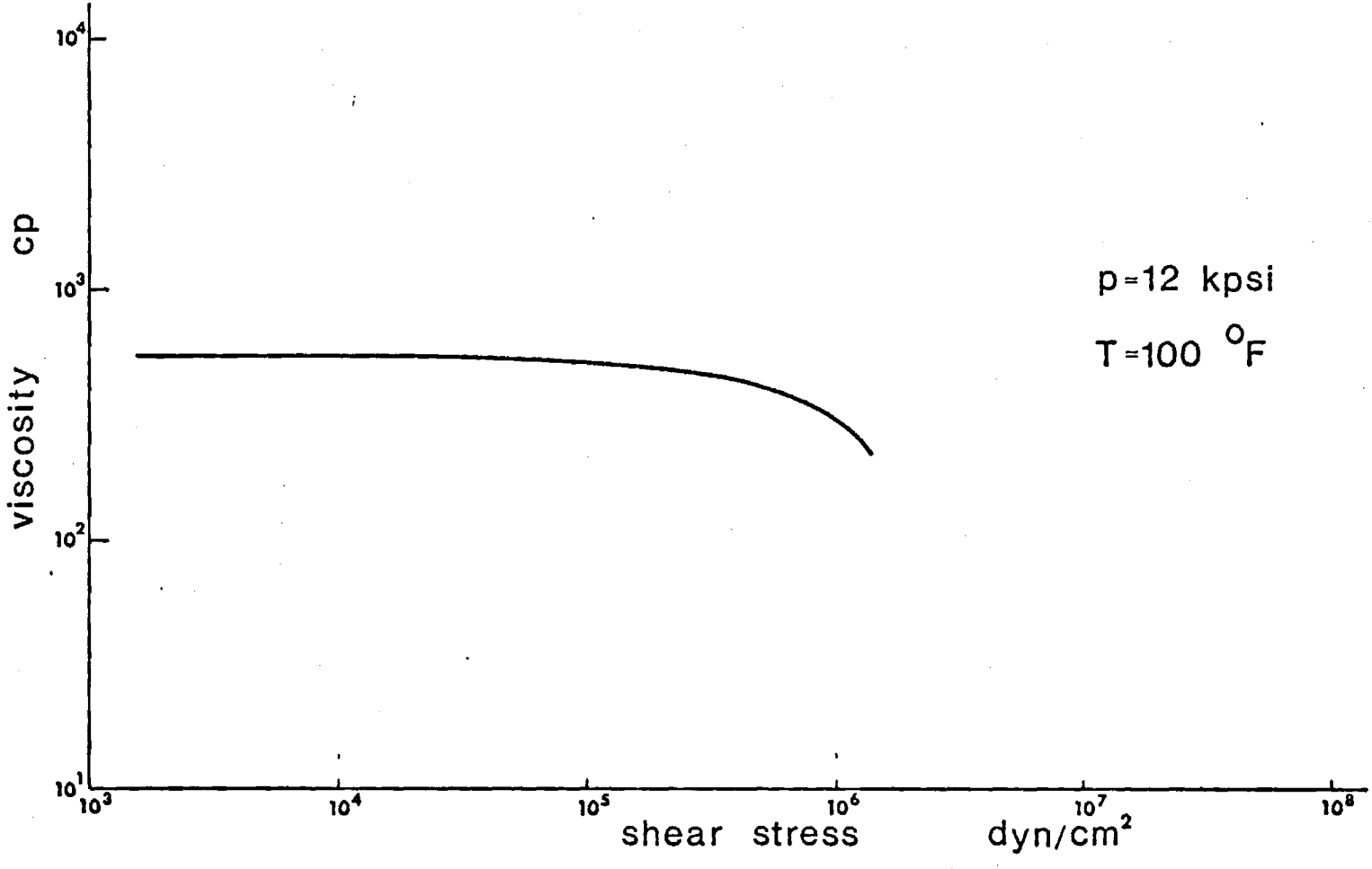

Viscosity-Shear Stress Relation for Fluid MCS460

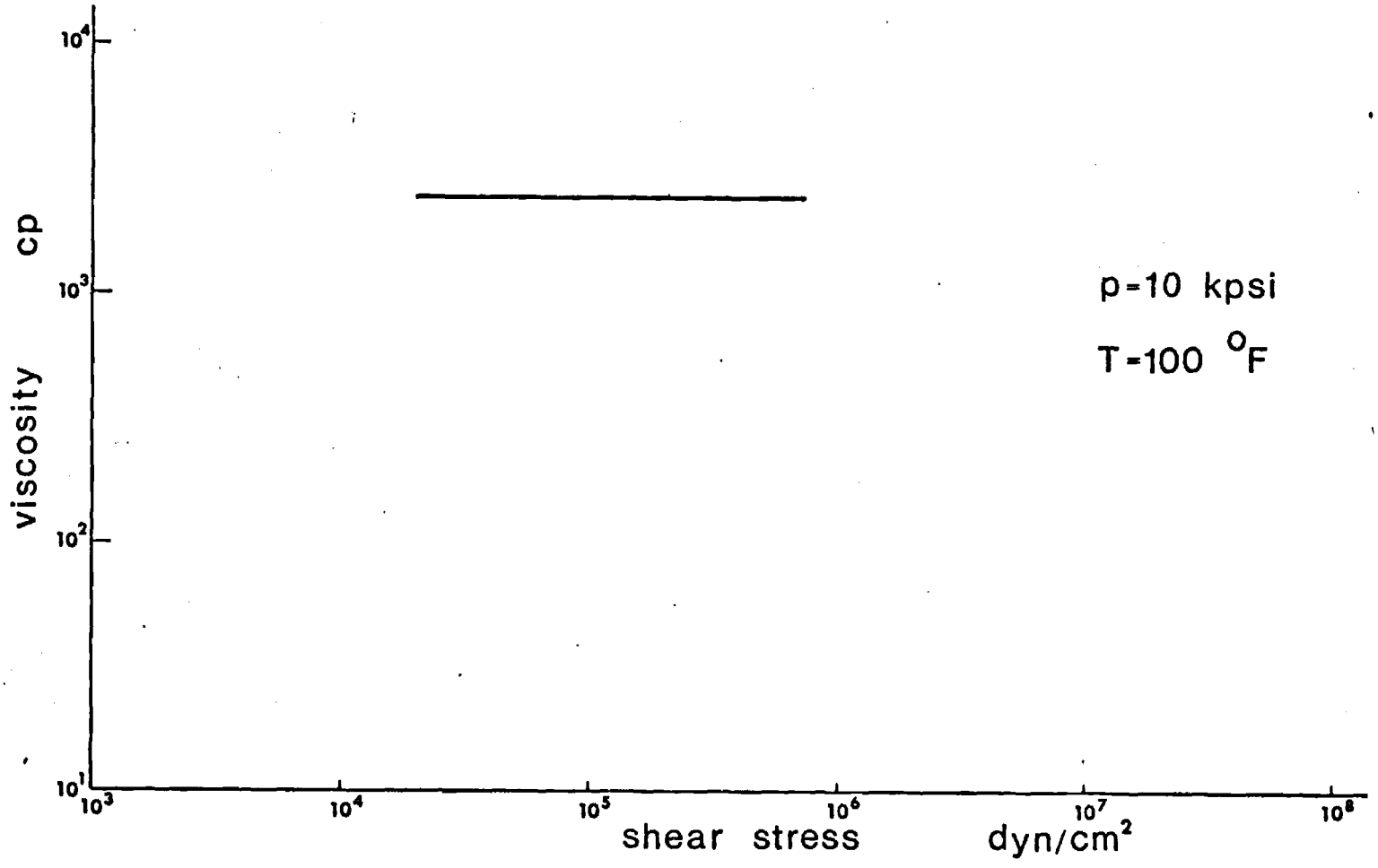

Viscosity-Shear Stress Relation for Fluid KRYTOX

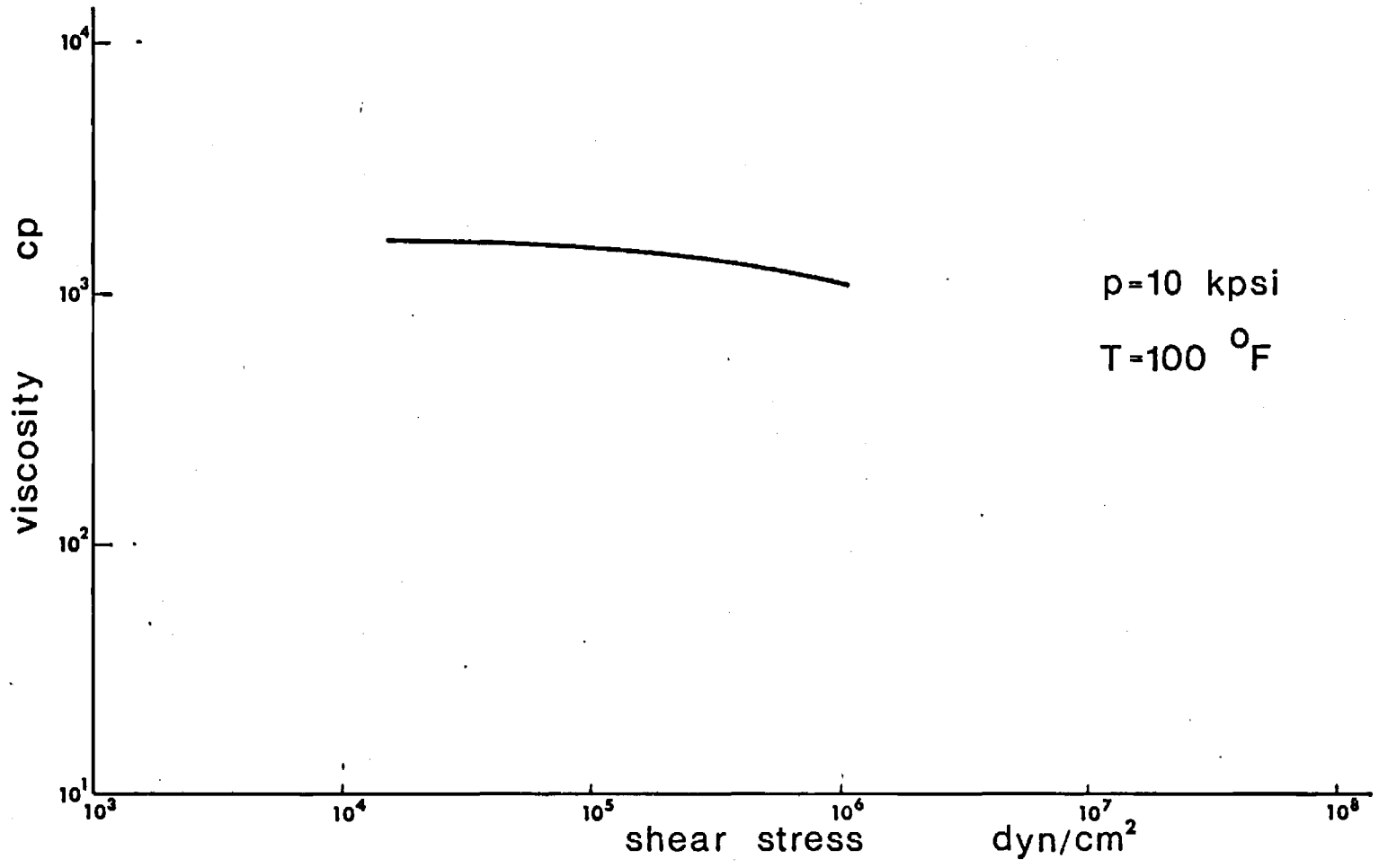

Viscosity-Shear Stress Relation for Fluid XRM-109

FLUID A, ADVANCED ESTER CAP 4, 100 F

RUN	P3	VISCP	NSRATE	KEC	DELTAP	TAUDYN	REYN
100-1	5306.	.4259+00	.3652+05	.1949+00	.2651+03	.1556+05	.6910+01
100-2	5306.	.4158+00	.3238+05	.1531+00	.2294+03	.1346+05	.6275+01
100-3	5325.	.4141+00	.2734+05	.1092+00	.1929+03	.1132+05	.5320+01
100-4	5325.	.4260+00	.3100+05	.1404+00	.2250+03	.1320+05	.5863+01
100-5	5325.	.4372+00	.3021+05	.1333+00	.2250+03	.1321+05	.5567+01
100-7	11548.	.7420+00	.2376+05	.8245-01	.3003+03	.1763+05	.2580+01
100-8	11548.	.7739+00	.2606+05	.9921-01	.3436+03	.2017+05	.2713+01
100-9	11548.	.7514+00	.7147+05	.7462+00	.9150+03	.5370+05	.7664+01
100-10	11548.	.7249+00	.7265+05	.7711+00	.8973+03	.5267+05	.8076+01
100-11	11548.	.7514+00	.6989+05	.7136+00	.8947+03	.5252+05	.7495+01
100-12	11432.	.7324+00	.6199+05	.5614+00	.7735+03	.4540+05	.6821+01
100-13	11432.	.7706+00	.6120+05	.5472+00	.8035+03	.4716+05	.6400+01
100-14	11432.	.7332+00	.7029+05	.7216+00	.8780+03	.5153+05	.7724+01
100-15	11356.	.7420+00	.6041+05	.5332+00	.7637+03	.4483+05	.6561+01
100-16	11356.	.7854+00	.1520+05	.3376-01	.2034+03	.1194+05	.1560+01
100-17	11356.	.7294+00	.2264+05	.7487-01	.2813+03	.1651+05	.2501+01
100-20	11356.	.7443+00	.1106+05	.1786-01	.1402+03	.8229+04	.1197+01
100-21	21994.	.1753+01	.9430+04	.1299-01	.2816+03	.1653+05	.4335+00
100-23	21994.	.1814+01	.1342+05	.2632-01	.4149+03	.2435+05	.5963+00
100-24	21994.	.1762+01	.1670+05	.4073-01	.5012+03	.2942+05	.7637+00
100-25	21994.	.1818+01	.1467+05	.3143-01	.4542+03	.2666+05	.6503+00
100-26	32872.	.3944+01	.6760+04	.6676-02	.4543+03	.2666+05	.1381+00
100-27	32872.	.3776+01	.1044+05	.1591-01	.6715+03	.3941+05	.2227+00
100-28	32872.	.3937+01	.5577+04	.4544-02	.3741+03	.2196+05	.1142+00
100-29	32425.	.3766+01	.9042+04	.1194-01	.5802+03	.3406+05	.1934+00
100-30	32425.	.3725+01	.6380+04	.5946-02	.4049+03	.2376+05	.1380+00
100-31	44049.	.8436+01	.4209+04	.2588-02	.6049+03	.3551+05	.4021-01
100-32	43975.	.8454+01	.4972+04	.3611-02	.7161+03	.4203+05	.4739-01
100-33	43945.	.8368+01	.3446+04	.1735-02	.4913+03	.2884+05	.3318-01
100-34	43945.	.8200+01	.3446+04	.1735-02	.4814+03	.2826+05	.3387-01
100-35	43945.	.8535+01	.4788+04	.3349-02	.6962+03	.4086+05	.4520-01
100 41	52469.	.1420+02	.1037+04	.1570-03	.2507+03	.1471+05	.5884-02
100 42	52395.	.1457+02	.1012+04	.1495-03	.2511+03	.1474+05	.5596-02
100-36	56195.	.1824+02	.7043+03	.7245-04	.2188+03	.1284+05	.3112-02
100-37	56120.	.1839+02	.1002+04	.1466-03	.3139+03	.1842+05	.4390-02
100-39	56120.	.1610+02	.1525+04	.3398-03	.4183+03	.2455+05	.7633-02
100-40	56120.	.1896+02	.1138+04	.1893-03	.3677+03	.2158+05	.4836-02
100 43	60218.	.2427+02	.4330+03	.2738-04	.1790+03	.1051+05	.1438-02
100 44	59920.	.2335+02	.6333+03	.5859-04	.2519+03	.1479+05	.2186-02
100 45	59846.	.2359+02	.6993+03	.7144-04	.2810+03	.1649+05	.2389-02
100 46	59697.	.2345+02	.9126+03	.1216-03	.3645+03	.2140+05	.3136-02
100 47	59250.	.2206+02	.7935+03	.9198-04	.2952+03	.1750+05	.2899-02
100 48	69681.	.4603+02	.3118+03	.1421-04	.2446+03	.1435+05	.5459-03
100 49	71172.	.4869+02	.3979+03	.2313-04	.3301+03	.1938+05	.6586-03
100 50	70874.	.4583+02	.4451+03	.2894-04	.3475+03	.2040+05	.7825-03
100 51	70725.	.4698+02	.2915+03	.1241-04	.2333+03	.1369+05	.4999-03
100 56	78772.	.6981+02	.2676+03	.1046-04	.3183+03	.1868+05	.3089-03
100 55	78921.	.6734+02	.2455+03	.8805-05	.2817+03	.1653+05	.2938-03
100 54	79070.	.6960+02	.1815+03	.4813-05	.2153+03	.1263+05	.2101-03
100 53	79294.	.7385+02	.1757+03	.4510-05	.2211+03	.1298+05	.1917-03
100 52	79592.	.8025+02	.1059+03	.1638-05	.1446+03	.8487+04	.1063-03

FLUID A, ADVANCED ESTER CAP 4, 210 F

RUN	P3	VISCP	NSRATE	KEC	DELTAP	TAUDYN	REYN
210-1	5372.	.7673-01	.3287+05	.1578+00	.4297+02	.2522+04	.3451+02
210-2	5372.	.7241-01	.2205+05	.7100-01	.2720+02	.1596+04	.2453+02
210-3	5372.	.7959-01	.4569+05	.3077+00	.6223+02	.3653+04	.4646+02
210-4	5372.	.7550-01	.4569+05	.3050+00	.5878+02	.3450+04	.4877+02
210-5	11494.	.1152+00	.3086+05	.1392+00	.6059+02	.3557+04	.2158+02
210-6	11494.	.1220+00	.2225+05	.7229-01	.4624+02	.2714+04	.1469+02
210-7	11494.	.1117+00	.3247+05	.1540+00	.6179+02	.3627+04	.2342+02
210-8	11494.	.1098+00	.3126+05	.1428+00	.5848+02	.3432+04	.2295+02
210-9	11494.	.1123+00	.2265+05	.7492-01	.4331+02	.2542+04	.1626+02
210-10	20503.	.1994+00	.2868+05	.1218+00	.9813+02	.5760+04	.1167+02
210-11	20503.	.2071+00	.2194+05	.7032-01	.7740+02	.4543+04	.8538+01
210-12	20503.	.1931+00	.1571+05	.3603-01	.5166+02	.3032+04	.6555+01
210-13	20503.	.1984+00	.1636+05	.3918-01	.5537+02	.3250+04	.6649+01
210-14	20503.	.2058+00	.1381+05	.2786-01	.4841+02	.2842+04	.5409+01
210-15	30488.	.3336+00	.1061+05	.1646-01	.6033+02	.3541+04	.2564+01
210-16	30488.	.3347+00	.8287+04	.1003-01	.4725+02	.2773+04	.1995+01
210-17	30488.	.3206+00	.1022+05	.1526-01	.5583+02	.3277+04	.2569+01
210-18	30488.	.3580+00	.9865+04	.1422-01	.6016+02	.3531+04	.2221+01
210-19	30488.	.3732+00	.1626+05	.3861-01	.1034+03	.6068+04	.3510+01
210-20	42261.	.6184+00	.4814+04	.3386-02	.5072+02	.2977+04	.6273+00
210-21	42261.	.6141+00	.6432+04	.6044-02	.6729+02	.3950+04	.8440+00
210-22	42261.	.6063+00	.6116+04	.5465-02	.6318+02	.3708+04	.8129+00
210-23	42261.	.6017+00	.8366+04	.1022-01	.8576+02	.5034+04	.1120+01
210-24	42261.	.6158+00	.8168+04	.9747-02	.8570+02	.5030+04	.1069+01
210-25	42261.	.6186+00	.8563+04	.1071-01	.9025+02	.5297+04	.1115+01
210-26	52931.	.9641+00	.6077+04	.5395-02	.9982+02	.5859+04	.5079+00
210-27	52931.	.1000+01	.6353+04	.5896-02	.1083+03	.6354+04	.5118+00
210-28	52931.	.9850+00	.5919+04	.5118-02	.9933+02	.5830+04	.4842+00
210-29	52931.	.9921+00	.7261+04	.7701-02	.1227+03	.7204+04	.5897+00
210-30	52931.	.9737+00	.7024+04	.7207-02	.1165+03	.6839+04	.5812+00
210-31	63124.	.1600+01	.3630+04	.1925-02	.9895+02	.5808+04	.1829+00
210-32	62975.	.1556+01	.4143+04	.2508-02	.1099+03	.6448+04	.2145+00
210-33	62975.	.1669+01	.4972+04	.3611-02	.1414+03	.8299+04	.2400+00
210-34	62975.	.1586+01	.4025+04	.2367-02	.1088+03	.6383+04	.2045+00
210-35	62975.	.1551+01	.3131+04	.1432-02	.8271+02	.4855+04	.1627+00
210-36	72215.	.2185+01	.4262+04	.2653-02	.1586+03	.9310+04	.1572+00
210-37	72215.	.2219+01	.4051+04	.2398-02	.1532+03	.8991+04	.1471+00
210-38	72215.	.2031+01	.4630+04	.3132-02	.1602+03	.9403+04	.1837+00
210-39	72215.	.2229+01	.3736+04	.2039-02	.1419+03	.8326+04	.1350+00
210-40	72215.	.2220+01	.4262+04	.2653-02	.1612+03	.9459+04	.1547+00
210-41	79368.	.3030+01	.2708+04	.1071-02	.1398+03	.8204+04	.7202-01
210-42	79368.	.3019+01	.1711+04	.4277-03	.8801+02	.5166+04	.4567-01
210-43	79368.	.2949+01	.1934+04	.5465-03	.9719+02	.5705+04	.5284-01
210-44	79368.	.3036+01	.2842+04	.1180-02	.1470+03	.8627+04	.7543-01
210-45	79368.	.2934+01	.2202+04	.7083-03	.1101+03	.6461+04	.6048-01

FLUID A, ADVANCED ESTER CAP 4, 300 F

RUN	P3	VISCP	NSRATE	KEC	DELTAP	TAUDYN	REYN
300-1	5355.	.3487-01	.5135+05	.3531+00	.3051+02	.1791+04	.1088+03
300-2	5355.	.3646-01	.8872+05	.1054+01	.5510+02	.3234+04	.1797+03
300-3	5355.	.3655-01	.7912+05	.8384+00	.4927+02	.2892+04	.1599+03
300-4	5355.	.3177-01	.7952+05	.8468+00	.4304+02	.2526+04	.1549+03
300-5	5355.	.3354-01	.8352+05	.9341+00	.4772+02	.2801+04	.1639+03
300-6	11575.	.5030-01	.4036+05	.2181+00	.3459+02	.2030+04	.5927+02
300-7	11575.	.4705-01	.5675+05	.4312+00	.4548+02	.2670+04	.8909+02
300-8	11575.	.4415-01	.6474+05	.5612+00	.4869+02	.2858+04	.1083+03
300-9	11575.	.4522-01	.6514+05	.5682+00	.5018+02	.2945+04	.1064+03
300-10	11575.	.4553-01	.6913+05	.6400+00	.5363+02	.3148+04	.1122+03
300-11	11575.	.4434-01	.7873+05	.8299+00	.5947+02	.3491+04	.1311+03
300-12	21696.	.8256-01	.5402+05	.3908+00	.7598+02	.4460+04	.4834+02
300-13	21696.	.7721-01	.5893+05	.4651+00	.7752+02	.4550+04	.5638+02
300-14	21696.	.7919-01	.5933+05	.4713+00	.8004+02	.4698+04	.5534+02
300-15	21696.	.8624-01	.6169+05	.5095+00	.9063+02	.5319+04	.5283+02
300-16	21696.	.7981-01	.5854+05	.4589+00	.7960+02	.4672+04	.5418+02
300-17	31680.	.1453+00	.3575+05	.1712+00	.8848+02	.5194+04	.1818+02
300-18	31680.	.1337+00	.2750+05	.1013+00	.6266+02	.3678+04	.1519+02
300-19	31382.	.1366+00	.3418+05	.1565+00	.7953+02	.4668+04	.1849+02
300-20	31680.	.1323+00	.3055+05	.1250+00	.6884+02	.4041+04	.1706+02
300-21	31680.	.1374+00	.3310+05	.1467+00	.7747+02	.4547+04	.1780+02
300-22	41069.	.2363+00	.2200+05	.6482-01	.8858+02	.5199+04	.6877+01
300-23	41069.	.2007+00	.2436+05	.7946-01	.8328+02	.4888+04	.8966+01
300-24	41069.	.2015+00	.2534+05	.8600-01	.8699+02	.5106+04	.9290+01
300-25	41069.	.1980+00	.2966+05	.1178+00	.1001+03	.5874+04	.1106+02
300-26	40920.	.1840+00	.3870+05	.2006+00	.1215+03	.7120+04	.1554+02
300-27	52693.	.3013+00	.2053+05	.5647-01	.1054+03	.6187+04	.5034+01
300-28	52693.	.2637+00	.1901+05	.4841-01	.8542+02	.5014+04	.5326+01
300-29	52693.	.2819+00	.2111+05	.5965-01	.1014+03	.5951+04	.5529+01
300-30	52544.	.2950+00	.3625+05	.1760+00	.1822+03	.1069+05	.9079+01
300-31	52693.	.3089+00	.1420+05	.2699-01	.7472+02	.4386+04	.3394+01
300-32	52693.	.2925+00	.3993+05	.2135+00	.1990+03	.1168+05	.1008+02
300-33	62230.	.4108+00	.8155+04	.8905-02	.5707+02	.3350+04	.1466+01
300-34	62230.	.4178+00	.9000+04	.1085-01	.6407+02	.3760+04	.1591+01
300-35	62230.	.4266+00	.1006+05	.1354-01	.7309+02	.4290+04	.1741+01
300-36	62230.	.4138+00	.1944+05	.5059-01	.1387+03	.8140+04	.3428+01
300-37	62230.	.3718+00	.1944+05	.5059-01	.1231+03	.7227+04	.3861+01
300-38	73705.	.5676+00	.1310+05	.2298-01	.1267+03	.7436+04	.1705+01
300-39	73556.	.5594+00	.1184+05	.1877-01	.1128+03	.6623+04	.1563+01
300-40	73556.	.5885+00	.1302+05	.2271-01	.1306+03	.7663+04	.1635+01
300-41	73556.	.5538+00	.1563+05	.3270-01	.1474+03	.8654+04	.2084+01
300-42	73556.	.5309+00	.9076+04	.1103-01	.8209+02	.4818+04	.1263+01
300-43	78623.	.6966+00	.8721+04	.1018-01	.1035+03	.6075+04	.9247+00
300-44	78623.	.6630+00	.7695+04	.7929-02	.9692+02	.5102+04	.8573+00
300-45	78623.	.6711+00	.8721+04	.1018-01	.9971+02	.5853+04	.9598+00
300-46	78623.	.6724+00	.8366+04	.9371-02	.9584+02	.5625+04	.9189+00
300-47	78623.	.6744+00	.8405+04	.9460-02	.9657+02	.5668+04	.9206+00

©2 **********AVERAGED DATA POINTS********

FLUID A, ADVANCED ESTER CAP 4, 100 F

P (PSI)	V (CP)
.00000	.25240+02
.53175+04	.42382+02
.11455+05	.74841+02
.21994+05	.17865+03
.32694+05	.38297+03
.43972+05	.83984+03
.52432+05	.14382+04
.58164+05	.21145+04
.70613+05	.46862+04
.79130+05	.72171+04

ALPHA STAR= .88539-04
ALPHA OT= .45408-04 ×2.3o3

FLUID A, ADVANCED ESTER CAP 4, 210 F

P (PSI)	V (CP)
.00000	.47100+01
.53719+04	.76058+01
.11494+05	.11420+02
.20503+05	.20076+02
.30488+05	.34402+02
.42261+05	.61249+02
.52931+05	.98303+02
.63005+05	.15924+03
.72215+05	.21766+03
.79366+05	.29936+03

ALPHA STAR= .67979-04
ALPHA OT= .46568-04 ×2.3o3

FLUID A, ADVANCED ESTER CAP 4, 300 F

P (PSI)	V (CP)
.00000	.20900+01
.53546+04	.34636+01
.11575+05	.46097+01
.21696+05	.80999+01
.31621+05	.13704+02
.41032+05	.19604+02
.52668+05	.29056+02
.62230+05	.40916+02
.73586+05	.56063+02
.78623+05	.67550+02

ALPHA STAR AND ALPHA OT MUST BE CALCULATED BY HAND

02 **********RAW DATA POINTS**

FLUID A. ADVANCED ESTER

RUN	P3	VISCP	NSRATE	KEC	DELTAP	TURDYN	REYN
100-1	11522.	.5183-01	.1122+07	.1194+03	.4800+02	.5813+05	.1133+04
100-2	11522.	.6982+00	.3602+06	.1231+02	.2077+03	.2515+06	.2700+02
100-3	11522.	.6681+00	.6498+06	.4005+02	.3584+03	.4341+06	.5090+02
100-4	11522.	.6483+00	.6338+06	.3811+02	.3393+03	.4119+06	.5116+02
100-5	11522.	.6718+00	.6178+06	.3622+02	.3428+03	.4151+06	.4813+02
100-6	11522.	.6079+00	.9598+06	.8740+02	.4818+03	.5835+06	.8262+02
100-8	11503.	.6243+00	.7569+06	.5435+02	.3902+03	.4726+06	.6344+02
100-9	11503.	.6658+00	.8800+06	.7347+02	.4839+03	.5860+06	.6917+02
100-13	11464.	.7646+00	.1352+06	.1733+01	.8534+02	.1034+06	.9251+01
100-14	11464.	.7861+00	.1878+06	.3348+01	.1219+03	.1477+06	.1251+02
100-15	11464.	.7172+00	.2107+06	.4212+01	.1248+03	.1511+06	.1537+02
100-16	11464.	.7439+00	.4301+05	.1755+00	.2642+02	.3199+05	.3025+01
100-17	11464.	.7480+00	.8012+05	.6090+00	.4949+02	.5993+05	.5605+01
100-18	11464.	.7829+00	.5463+05	.2831+00	.3531+02	.4276+05	.3651+01
100-19	11464.	.8385+00	.5515+05	.2885+00	.3818+02	.4624+05	.3442+01

FLUID B FORMULATED ADVANCED ESTER CAP 4, 100 F

RUN	P3	VISCP	NSRATE	KEC	DELTAP	TAUDYN	REYN
100-1	5258.	.4907+00	.2888+05	.1265+00	.2414+03	.1417+05	.4924+01
100-2	5258.	.5298+00	.2741+05	.1140+00	.2474+03	.1452+05	.4329+01
100-3	5258.	.4696+00	.2575+05	. 006+00	.2061+03	.1209+05	.4588+01
100-4	5258.	.4756+00	.3024+05	.1387+00	.2451+03	.1438+05	.5320+01
100-5	5258.	.4909+00	.2478+05	. 313-01	.2072+03	.1216+05	.4223+01
100-6	11294.	.8168+00	.1727+05	.4522-01	.2405+03	.1410+05	.1769+01
100-7	11294.	.8677+00	.1625+05	.4007-01	.2405+03	.1410+05	.1567+01
100-8	11408.	.8854+00	.1694+05	.4350-01	.2555+03	.1500+05	.1600+01
100-9	11370.	.8489+00	.1682+05	.4290-01	.2433+03	.1428+05	.1658+01
100-10	11370.	.8433+00	.3414+05	.1768+00	.4906+03	.2880+05	.3387+01
100-11	21547.	.1999+01	.7596+04	.6752-02	.2587+03	.1518+05	.3179+00
100-12	21547.	.1996+01	.1231+05	.2299-01	.4186+03	.2457+05	.5161+00
100-13	21442.	.2022+01	.7465+04	.8453-02	.2572+03	.1510+05	.3088+00
100-14	21442.	.1995+01	.1153+05	.2015-01	.3917+03	.2299+05	.4833+00
100-15	21472.	.1933+01	.1096+05	.1823-01	.3609+03	.2119+05	.4745+00
100-16	30935.	.4144+01	.5493+04	.4576-02	.3876+03	.2276+05	.1109+00
100-17	30935.	.4106+01	.8417+04	.1075-01	.5988+03	.3456+05	.1715+00
100-18	30935.	.4233+01	.7775+04	.9168-02	.5607+03	.3291+05	.1537+00
100-19	30935.	.4196+01	.5408+04	.4437-02	.3866+03	.2269+05	.1078+00
100-20	30935.	.4289+01	.7352+04	.8199-02	.5373+03	.3154+05	.1434+00
100-21	41695.	.9140+01	.2665+04	.1077-02	.4150+03	.2436+05	.2440-01
100-22	41695.	.8818+01	.3157+04	.1512-02	.4745+03	.2784+05	.2995-01
100-25	41695.	.9036+01	.2920+04	.1293-02	.4495+03	.2638+05	.2704-01
100-26	52544.	.1926+02	.1265+04	.2426-03	.4149+03	.2435+05	.5495-02
100-27	52544.	.1907+02	.1525+04	.3528-03	.4954+03	.2908+05	.6692-02
100-28	52544.	.1927+02	.1246+04	.2355-03	.4092+03	.2402+05	.5409-02
100-29	52544.	.1846+02	.8927+03	.1209-03	.2806+03	.1648+05	.4046-02
100-30	52544.	.1873+02	.1213+04	.2230-03	.3870+03	.2272+05	.5416-02
100-31	61932.	.3615+02	.5728+03	.4977-04	.3528+03	.2071+05	.1326-02
100-32	61873.	.3459+02	.5951+03	.5372-04	.3507+03	.2059+05	.1440-02
100-34	61783.	.3526+02	.7886+03	.9432-04	.4737+03	.2780+05	.1871-02
100-35	61515.	.3481+02	.7439+03	.8394-04	.4412+03	.2589+05	.1788-02
100-36	72394.	.6728+02	.4052+03	.2490-04	.4645+03	.2726+05	.5039-03
100-37	72334.	.7006+02	.3521+03	.1881-04	.4203+03	.2467+05	.4205-03
100-38	71917.	.6938+02	.4637+03	.3262-04	.5481+03	.3217+05	.5592-03
100-39	71917.	.6630+02	.4712+03	.3367-04	.5522+03	.3124+05	.5945-03
100-40	71544.	.6728+02	.4067+03	.2509-04	.4662+03	.2736+05	.5057-03
100-41	80381.	.1075+03	.1422+03	.3069-05	.2606+03	.1529+05	.1107-03
100-42	79890.	.9074+02	.3918+03	.2328-04	.6057+03	.3555+05	.3613-03
100-43	79592.	.1233+03	.2430+03	.8958-05	.5104+03	.2996+05	.1649-03
100-44	79070.	.1067+03	.2932+03	.1304-04	.5331+03	.3129+05	.2299-03
100-45	79070.	.1058+03	.2321+03	.8174-05	.4183+03	.2455+05	.1836-03

FLUID B, FORMULATED ADVANCED ESTER CAP 4, 210 F

RUN	P3	VISCP	NSRATE	KEC	DELTAP	TAUDYN	REYN
210-1	5330.	.8555-01	.5338+05	.4080+00	.7780+02	.4567+04	.4928+02
210-2	5330.	.8402-01	.4279+05	.2621+00	.6125+02	.3595+04	.4021+02
210-3	5330.	.8777-01	.4357+05	.2718+00	.6515+02	.3824+04	.3920+02
210-4	5330.	.8613-01	.4318+05	.2669+00	.6336+02	.3719+04	.3959+02
210-5	5330.	.8288-01	.4396+05	.2767+00	.6208+02	.3644+04	.4189+02
210-6	10943.	.1158+00	.2473+05	.8755-01	.4877+02	.2863+04	.1687+02
210-7	10904.	.1163+00	.3631+05	.1887+00	.7196+02	.4223+04	.2465+02
210-8	10904.	.1203+00	.3631+05	.1887+00	.7440+02	.4367+04	.2384+02
210-9	10637.	.1146+00	.1511+05	.3269-01	.2950+02	.1732+04	.1041+02
210-10	10904.	.1157+00	.4357+05	.2718+00	.8586+02	.5039+04	.2975+02
210-11	10904.	.1188+00	.2748+05	.1081+00	.5564+02	.3266+04	.1826+02
210-12	20355.	.2021+00	.1063+05	.1617-01	.3660+02	.2148+04	.4152+01
210-13	20174.	.2151+00	.1103+05	.1741-01	.4041+02	.2372+04	.4048+01
210-14	20174.	.2091+00	.1136+05	.1847-01	.4047+02	.2375+04	.4289+01
210-15	20355.	.2098+00	.3002+05	.1291+00	.1073+03	.6299+04	.1130+02
210-16	20355.	.2035+00	.2630+05	.9906-01	.9116+02	.5352+04	.1021+02
210-17	32740.	.3975+00	.1755+05	.4409-01	.1186+03	.6975+04	.3486+01
210-18	32643.	.4061+00	.1120+05	.1797-01	.7751+02	.4550+04	.2179+01
210-19	32450.	.4145+00	.8623+04	.1064-01	.6090+02	.3575+04	.1643+01
210-20	32547.	.4473+00	.4515+04	.2918-02	.3441+02	.2020+04	.7970+00
210-21	42872.	.7103+00	.6752+04	.6526-02	.8171+02	.4796+04	.7506+00
210-22	42872.	.6663+00	.8948+04	.1146-01	.1016+03	.5962+04	.1061+01
210-23	43065.	.7328+00	.2847+04	.1160-02	.3555+02	.2087+04	.3068+00
210-24	43065.	.7189+00	.5044+04	.3642-02	.6177+02	.3626+04	.5540+00
210-25	43058.	.7216+00	.8782+04	.1104-01	.1080+03	.6337+04	.9611+00
210-26	43058.	.6684+00	.9162+04	.1202-01	.1043+03	.6124+04	.1082+01
210-27	43058.	.7020+00	.8383+04	.1006-01	.1003+03	.5885+04	.9429+00
210-28	43058.	.6728+00	.1058+05	.1602-01	.1213+03	.7118+04	.1242+01
210-29	43058.	.6622+00	.6627+04	.6286-02	.7476+02	.4388+04	.7903+00
210-30	54365.	.1160+01	.4112+04	.2420-02	.8125+02	.4769+04	.2799+00
210-31	54365.	.1141+01	.5389+04	.4158-02	.1048+03	.6150+04	.3729+00
210-32	54365.	.1150+01	.5309+04	.4035-02	.1040+03	.6103+04	.3647+00
210-33	54365.	.1150+01	.3633+04	.1889-02	.7119+02	.4179+04	.2494+00
210-34	54365.	.1188+01	.6447+04	.5950-02	.1305+03	.7661+04	.4284+00
210-36	64466.	.1883+01	.6347+04	.5767-02	.2036+03	.1195+05	.2662+00
210-37	64466.	.1823+01	.4591+04	.3017-02	.1426+03	.8371+04	.1988+00
210-38	64466.	.1794+01	.4711+04	.3177-02	.1439+03	.8449+04	.2074+00
210-39	64466.	.1721+01	.5070+04	.3680-02	.1486+03	.8724+04	.2327+00
210-40	74717.	.2664+01	.3022+04	.1307-02	.1372+03	.8051+04	.8957-01
210-41	74717.	.2736+01	.2603+04	.9698-03	.1213+03	.7121+04	.7513-01
210-42	74868.	.2734+01	.2315+04	.7674-03	.1076+03	.6329+04	.6688-01
210-43	74868.	.2715+01	.2116+04	.6408-03	.9786+02	.5745+04	.6153-01
210-44	74868.	.2854+01	.1844+04	.4869-03	.8968+02	.5264+04	.5102-01
210-45	81049.	.3396+01	.4511+04	.2913-02	.2610+03	.1532+05	.1049+00
210-46	81049.	.3348+01	.3233+04	.1497-02	.1845+03	.1083+05	.7626-01
210-47	81049.	.3373+01	.4391+04	.2760-02	.2523+03	.1481+05	.1028+00
210-48	81049.	.3553+01	.2435+04	.8489-03	.1474+03	.8651+04	.5413-01
210-49	81049.	.3436+01	.2595+04	.9639-03	.1519+03	.8914+04	.5964-01

FLUID B FORMULATED ADVANCED ESTER CAP 4, 300 F

RUN	P3	VISCP	NSRATE	KEC	DELTAP	TAUDYN	REYN
300-1	5296.	.3530-01	.6653+05	.6046+00	.4001+02	.2348+04	.1420+03
300-2	5296.	.3027-01	.1116+06	.1701+01	.5755+02	.3378+04	.2778+03
300-3	5296.	.4086-01	.5580+05	.4253+00	.3885+02	.2280+04	.1029+03
300-4	5296.	.3631-01	.4761+05	.3096+00	.2945+02	.1729+04	.9878+02
300-5	5296.	.3705-01	.4722+05	.3045+00	.2980+02	.1749+04	.9602+02
300-6	5296.	.3637-01	.3766+05	.1937+00	.2335+02	.1369+04	.7801+02
300-7	11275.	.4300-01	.3044+05	.1265+00	.2230+02	.1309+04	.5333+02
300-8	11275.	.4573-01	.4878+05	.3250+00	.3800+02	.2230+04	.8037+02
300-9	11256.	.5679-01	.3649+05	.1818+00	.3530+02	.2072+04	.4840+02
300-10	11218.	.5087-01	.3414+05	.1592+00	.2959+02	.1737+04	.5056+02
300-11	11218.	.4927-01	.4819+05	.3172+00	.4046+02	.2375+04	.7369+02
300-12	21866.	.8780-01	.2539+05	.8807-01	.3796+02	.2230+04	.2179+02
300-13	21792.	.7462-01	.1820+05	.4526-01	.2314+02	.1358+04	.1838+02
300-14	21644.	.8798-01	.4766+05	.3102+00	.7144+02	.4193+04	.4081+02
300-15	21644.	.9482-01	.3110+05	.1321+00	.5023+02	.2949+04	.2471+02
300-16	21644.	.8584-01	.3516+05	.1688+00	.5142+02	.3018+04	.3086+02
300-17	32979.	.1515+00	.1406+05	.2701-01	.3630+02	.2131+04	.6993+01
300-18	32831.	.1445+00	.2051+05	.5745-01	.5047+02	.2963+04	.1070+02
300-19	32534.	.1428+00	.2578+05	.9080-01	.6274+02	.3683+04	.1360+02
300-20	32534.	.1302+00	.2656+05	.9638-01	.5894+02	.3459+04	.1537+02
300-21	32534.	.1304+00	.3145+05	.1351+00	.6984+02	.4099+04	.1818+02
300-23	44536.	.2238+00	.2012+05	.5528-01	.7672+02	.4503+04	.6771+01
300-24	44462.	.2398+00	.1768+05	.4268-01	.7222+02	.4239+04	.5553+01
300-25	44388.	.2318+00	.1973+05	.5316-01	.7790+02	.4572+04	.6413+01
300-26	44388.	.2189+00	.1377+05	.2590-01	.5136+02	.3014+04	.4740+01
300-27	55205.	.3448+00	.8710+04	.1036-01	.5117+02	.3004+04	.1903+01
300-28	55205.	.3145+00	.9299+04	.1181-01	.4983+02	.2925+04	.2227+01
300-29	55205.	.3211+00	.8632+04	.1018-01	.4722+02	.2772+04	.2025+01
300-30	55205.	.3334+00	.9220+04	.1161-01	.5237+02	.3074+04	.2083+01
300-31	55205.	.3352+00	.9318+04	.1186-01	.5322+02	.3124+04	.2094+01
300-32	65132.	.4797+00	.1678+05	.3844-01	.1371+03	.8048+04	.2635+01
300-33	65132.	.4696+00	.2213+05	.6688-01	.1771+03	.1039+05	.3550+01
300-34	65132.	.4622+00	.9809+04	.1314-01	.7725+02	.4534+04	.1599+01
300-35	65132.	.4785+00	.1624+05	.3604-01	.1324+03	.7773+04	.2557+01
300-36	65132.	.4636+00	.2880+05	.1133+00	.2275+03	.1335+05	.4680+01
300-37	74097.	.6752+00	.1016+05	.1410-01	.1169+03	.6862+04	.1134+01
300-38	74097.	.6244+00	.1130+05	.1744-01	.1202+03	.7056+04	.1363+01
300-39	74097.	.6437+00	.7651+04	.7995-02	.8391+02	.4925+04	.8955+00
300-40	74097.	.6204+00	.1860+05	.4724-01	.1960+03	.1154+05	.2258+01
300-41	74097.	.6343+00	.1569+05	.3364-01	.1690+03	.9954+04	.1864+01
300-42	78172.	.7051+00	.1954+05	.4214-01	.2347+03	.1378+05	.2088+01
300-43	77727.	.7325+00	.1185+05	.1918-01	.1479+03	.8680+04	.1219+01
300-44	78616.	.7231+00	.1361+05	.2532-01	.1677+03	.9845+04	.1419+01
300-45	78468.	.7328+00	.5768+04	.4543-02	.7201+02	.4227+04	.5930+00
300-46	78320.	.7651+00	.6081+04	.5051-02	.7927+02	.4653+04	.5989+00

@2 ********************** **********AVERAGED DATA POINTS*********

FLUID B, FORMULATED ADVANCED ESTER CAP 4, 100 F

P (PSI)	V (CP)
.00000	.27600+02
.52581+04	.49133+02
.11347+05	.85246+02
.21490+05	.19890+03
.30935+05	.41938+03
.41695+05	.89978+03
.52544+05	.18958+04
.61776+05	.35202+04
.72021+05	.68062+04
.79507+05	.10667+05

ALPHA STAR= .94181-04
ALPHA OT= .55186-04 x2.303

FLUID B, FORMULATED ADVANCED ESTER CAP 4, 210 F

P (PSI)	V (CP)
.00000	.49600+01
.53295+04	.85269+01
.10866+05	.11691+02
.20282+05	.20793+02
.32595+05	.41635+02
.43018+05	.69504+02
.54365+05	.11578+03
.64466+05	.18052+03
.74808+05	.27407+03
.81049+05	.34210+03

ALPHA STAR= .69099-04
ALPHA OT= .63512-04 x2.303

FLUID B, FORMULATED ADVANCED ESTER CAP 4, 300 F

P (PSI)	V (CP)
.00000	.21500+01
.52960+04	.37176+01
.11246+05	.47219+01
.21718+05	.86213+01
.32683+05	.13986+02
.44444+05	.22856+02
.55205+05	.32982+02
.70511+05	.56747+02
.78261+05	.73172+02

ALPHA STAR= .60198-04
ALPHA OT= .81004-04 x2.303

**********RAW DATA POINTS*******

02

FLUID B. FORMULATED ADVANCED ESTER

RUN	P3	VISCP	NSRATE	KEC	DELTAP	TAUDYN	REYN
100-1	11390.	.7863+00	.1761+06	.3054+01	.1143+03	.1384+06	.1217+02
100-2	11390.	.7108+00	.5502+06	.2982+02	.3229+03	.3911+06	.4206+02
100-3	11390.	.7566+00	.3851+06	.1461+02	.2406+03	.2914+06	.2766+02
100-4	11390.	.7145+00	.5062+06	.2524+02	.2987+03	.3617+06	.3849+02
100-5	11390.	.6866+00	.6602+06	.4294+02	.3743+03	.4533+06	.5225+02
100-6	11390.	.7230+00	.5986+06	.3530+02	.3574+03	.4328+06	.4499+02
100-7	11390.	.7516+00	.7087+06	.4947+02	.4396+03	.5326+06	.5123+02
100-8	11390.	.7317+00	.6999+06	.4825+02	.4229+03	.5121+06	.5197+02
100-9	11390.	.6369+00	.9772+06	.9406+02	.5139+03	.6223+06	.8337+02
100-10	11390.	.6196+00	.1048+07	.1081+03	.5360+03	.6491+06	.9186+02
100-11	11390.	.6012+00	.1250+07	.1539+03	.6205+03	.7515+06	.1130+03
100-12	11390.	.8220+00	.3785+06	.1412+02	.2569+03	.3112+06	.2502+02
100-13	11353.	.7700+00	.1555+06	.2383+01	.9889+02	.1198+06	.1097+02
100-14	11353.	.8171+00	.2296+06	.5194+01	.1549+03	.1876+06	.1527+02
100-15	11390.	.8522+00	.1209+06	.1440+01	.8507+02	.1030+06	.7708+01
100-16	11390.	.8254+00	.9978+05	.9807+00	.6801+02	.8236+05	.6569+01
100-17	11390.	.9110+00	.6476+05	.4131+00	.4872+02	.5900+05	.3863+01

FLUID C, NAPHTHENIC MINERAL OIL + ADDITIVE CAP 4, 100 F

RUN	P3	VISCP	NSRATE	KEC	DELTAP	TAUDYN	REYN
100-1	5376.	.2243+01	.9573+04	.1218-01	.3658+03	.2147+05	.3130+00
100-2	5376.	.2072+01	.1817+05	.4389-01	.6415+03	.3765+05	.6430+00
100-3	5376.	.2129+01	.7977+04	.8460-02	.2894+03	.1699+05	.2747+00
100-4	5376.	.2119+01	.1702+05	.3850-01	.6144+03	.3606+05	.5889+00
100-5	5376.	.2204+01	.1081+05	.1555-01	.4061+03	.2384+05	.3597+00
100-6	5376.	.2001+01	.1985+05	.5240-01	.6769+03	.3973+05	.7276+00
100-7	11188.	.5332+01	.1216+04	.1966-03	.1105+03	.6484+04	.1672-01
100-8	11188.	.5476+01	.3529+04	.1656-02	.3292+03	.1933+05	.4726-01
100-9	11188.	.5358+01	.5344+04	.3796-02	.4878+03	.2863+05	.7314-01
100-10	11490.	.5182+01	.2319+04	.7149-03	.2047+03	.1202+05	.3282-01
100-11	11490.	.4950+01	.4235+04	.2384-02	.3572+03	.2096+05	.6273-01
100-12	11339.	.5090+01	.9276+03	.1144-03	.8044+02	.4722+04	.1336-01
100-13	11339.	.5566+01	.2057+04	.5624-03	.1951+03	.1145+05	.2710-01
100-14	11301.	.5558+01	.1785+04	.4234-03	.1690+03	.9919+04	.2355-01
100-15	11301.	.5588+01	.3983+04	.2109-02	.3792+03	.2226+05	.5226-01
100-16	11301.	.5066+01	.5848+04	.4546-02	.5045+03	.2963+05	.8465-01
100-17	19758.	.1852+02	.9670+03	.1243-03	.3050+03	.1790+05	.3829-02
100-18	19758.	.1907+02	.1391+04	.2572-03	.4520+03	.2653+05	.5348-02
100-20	19609.	.1797+02	.3308+03	.1455-04	.1013+03	.5943+04	.1350-02
100-21	19609.	.1863+02	.5717+03	.4345-04	.1815+03	.1065+05	.2250-02
100-22	19609.	.1950+02	.7917+03	.8331-04	.2630+03	.1544+05	.2977-02
100-23	29892.	.8866+02	.1994+03	.5284-05	.3012+03	.1768+05	.1649-03
100-24	29892.	.8741+02	.2470+03	.8109-05	.3678+03	.2159+05	.2072-03
100-25	29892.	.9269+02	.1196+03	.1902-05	.1889+03	.1109+05	.9463-04
100-26	29892.	.8988+02	.1964+03	.5127-05	.3008+03	.1765+05	.1602-03
100-27	29892.	.7937+02	.3035+03	.1225-04	.4104+03	.2409+05	.2804-03
100-36	32127.	.1029+03	.2217+03	.6532-05	.3886+03	.2282+05	.1579-03
100-37	32127.	.1153+03	.1943+03	.5019-05	.3816+03	.2240+05	.1236-03
100-38	32127.	.1131+03	.2444+03	.7937-05	.4708+03	.2763+05	.1584-03
100-28	39579.	.3614+03	.3630+02	.1752-06	.2236+03	.1312+05	.7365-05
100-31	39549.	.3859+03	.5609+02	.4183-06	.3688+03	.2164+05	.1066-04
100-32	39549.	.3090+03	.1042+03	.1442-05	.5483+03	.3218+05	.2471-04
100-39	42261.	.4923+03	.4771+02	.3025-06	.4002+03	.2349+05	.7105-05
100-40	42410.	.5190+03	.6342+02	.5346-06	.5608+03	.3291+05	.8959-05
100-41	42708.	.5380+03	.8611+02	.9856-06	.7892+03	.4633+05	.1174-04
100-42	42708.	.4783+03	.7912+02	.8322-06	.6448+03	.3785+05	.1213-04
100-43	50010.	.1436+04	.2199+02	.6429-07	.5379+03	.3157+05	.1123-05
100-44	49712.	.1325+04	.3002+02	.1198-06	.6775+03	.3977+05	.1662-05
100-45	49712.	.1360+04	.3281+02	.1431-06	.7604+03	.4463+05	.1769-05

FLUID C, NAPHTHENIC MINERAL OIL + ADDITIVE CAP 4, 210 F

RUN	P3	VISCP	NSRATE	KEC	DELTAP	TAUDYN	REYN
210-1	5204.	.1580+00	.2635+05	.9229-01	.7091+02	.4162+04	.1223+02
210-2	5204.	.1556+00	.5700+05	.4319+00	.1511+03	.8867+04	.2607+02
210-3	5204.	.1816+00	.2224+05	.6578-01	.6882+02	.4040+04	.8982+01
210-4	5204.	.1596+00	.4131+05	.2269+00	.1123+03	.6593+04	.1998+02
210-5	5204.	.1621+00	.3257+05	.1410+00	.9998+02	.5281+04	.1473+02
210-6	5204.	.1631+00	.3337+05	.1480+00	.9272+02	.5442+04	.1500+02
210-7	11194.	.3122+00	.2999+05	.1196+00	.1595+03	.9364+04	.7043+01
210-8	11194.	.2887+00	.4032+05	.2161+00	.1983+03	.1164+05	.1024+02
210-9	11194.	.2919+00	.3764+05	.1883+00	.1872+03	.1099+05	.9455+01
210-10	11194.	.2947+00	.3198+05	.1359+00	.1605+03	.9423+04	.7956+01
210-11	11194.	.3245+00	.2304+05	.7056-01	.1274+03	.7476+04	.5206+01
210-12	21994.	.8942+00	.1297+05	.2235-01	.1975+03	.1159+05	.1063+01
210-13	21994.	.8936+00	.1087+05	.1571-01	.1655+03	.9713+04	.8920+00
210-14	21994.	.9709+00	.9561+04	.1215-01	.1581+03	.9282+04	.7221+00
210-15	21994.	.9609+00	.9508+04	.1202-01	.1557+03	.9137+04	.7255+00
210-16	21994.	.9283+00	.8906+04	.1054-01	.1408+03	.8267+04	.7035+00
210-17	31233.	.2144+01	.4873+04	.3157-02	.1780+03	.1045+05	.1667+00
210-18	31233.	.2184+01	.5801+04	.4473-02	.2158+03	.1267+05	.1948+00
210-19	31233.	.2166+01	.8879+04	.1048-01	.3277+03	.1924+05	.3005+00
210-20	31233.	.2157+01	.9549+04	.1212-01	.3510+03	.2060+05	.3246+00
210-21	31233.	.2132+01	.1006+05	.1346-01	.3656+03	.2146+05	.3460+00
210-22	42112.	.5367+01	.2875+04	.1099-02	.2629+03	.1543+05	.3928-01
210-23	42112.	.5650+01	.3052+04	.1238-02	.2937+03	.1724+05	.3960-01
210-24	42112.	.5191+01	.2616+04	.9108-03	.2315+03	.1359+05	.3697-01
210-25	42112.	.5598+01	.3052+04	.1238-02	.2911+03	.1708+05	.3997-01
210-26	42112.	.5283+01	.3591+04	.1714-02	.3232+03	.1897+05	.4984-01
210-27	53587.	.1410+02	.8630+03	.9899-04	.2074+03	.1217+05	.4487-02
210-28	53438.	.1381+02	.1086+04	.1568-03	.2555+03	.1500+05	.5767-02
210-29	53289.	.1373+02	.1324+04	.2331-03	.3097+03	.1818+05	.7073-02
210-30	53289.	.1440+02	.1213+04	.1955-03	.2975+03	.1746+05	.6174-02

92

FLUID C, NAPHTHENIC MINERAL OIL + ADDITIVE CAP 4, 300 F

RUN	P3	VISCP	NSRATE	KEC	DELTAP	TAUDYN	REYN
300-1	5325.	.5812-01	.6198+05	.5107+00	.6138+02	.3603+04	.7819+02
300-2	5325.	.5714-01	.9094+05	.1099+01	.8853+02	.5196+04	.1167+03
300-3	5325.	.5227-01	.9015+05	.1080+01	.8028+02	.4712+04	.1265+03
300-4	5248.	.5468-01	.1518+06	.3064+01	.1414+03	.8301+04	.2036+03
300-5	5248.	.4908-01	.1589+06	.3358+01	.1329+03	.7800+04	.2375+03
300-6	5248.	.4750-01	.1672+06	.3718+01	.1353+03	.7944+04	.2582+03
300-7	11644.	.9093-01	.8540+05	.9695+00	.1323+03	.7766+04	.6886+02
300-8	11644.	.7993-01	.6702+05	.5970+00	.9125+02	.5356+04	.6148+02
300-9	11644.	.8367-01	.7354+05	.7189+00	.1048+03	.6153+04	.6445+02
300-10	11644.	.8206-01	.7235+05	.6959+00	.1012+03	.5938+04	.6465+02
300-11	11644.	.8721-01	.9608+05	.1227+01	.1427+03	.8378+04	.8078+02
300-12	22292.	.2256+00	.5901+05	.4629+00	.2269+03	.1332+05	.1918+02
300-13	22292.	.2218+00	.5350+05	.3805+00	.2022+03	.1187+05	.1769+02
300-14	22292.	.2153+00	.5036+05	.3371+00	.1847+03	.1084+05	.1715+02
300-15	22292.	.2078+00	.5704+05	.4326+00	.2020+03	.1186+05	.2012+02
300-16	22292.	.2030+00	.5130+05	.3498+00	.1775+03	.1042+05	.1853+02
300-17	33618.	.4816+00	.2134+05	.6053-01	.1751+03	.1028+05	.3249+01
300-18	33618.	.5009+00	.2547+05	.8622-01	.2174+03	.1276+05	.3728+01
300-19	33618.	.4518+00	.3653+05	.1774+00	.2812+03	.1651+05	.5928+01
300-20	33618.	.4812+00	.3704+05	.1824+00	.3037+03	.1783+05	.5645+01
300-21	33618.	.4599+00	.2933+05	.1143+00	.2298+03	.1349+05	.4676+01
300-22	33618.	.4354+00	.4358+05	.2525+00	.3233+03	.1898+05	.7339+01
300-23	43304.	.8836+00	.1506+05	.3024-01	.2271+03	.1333+05	.1251+01
300-24	43304.	.8664+00	.1831+05	.4458-01	.2703+03	.1587+05	.1550+01
300-25	42857.	.8860+00	.9336+04	.1159-01	.1409+03	.8272+04	.7726+00
300-26	42857.	.8322+00	.1706+05	.3867-01	.2413+03	.1419+05	.1503+01
300-28	51650.	.1451+01	.7710+04	.7902-02	.1906+03	.1119+05	.3897+00
300-30	51650.	.1607+01	.6076+04	.4908-02	.1664+03	.9767+04	.2772+00
300-31	51650.	.1595+01	.7148+04	.6793-02	.1943+03	.1140+05	.3286+00
300-32	51650.	.1542+01	.5668+04	.4270-02	.1489+03	.8737+04	.2696+00

**********AVERAGED DATA POINTS**********

FLUID C, NAPHTHENIC MINERAL OIL + ADDITIVE CAP 4, 100 F

P (PSI)	V (CP)
.00000	.30500+02
.53762+04	.21281+03
.11312+05	.53166+03
.19669+05	.18738+04
.30339+05	.92318+04
.41506+05	.45217+05
.49812+05	.13735+06

ALPHA STAR= .17263-03
ALPHA OT= .98563-04 x 2.3o3

FLUID C, NAPHTHENIC MINERAL OIL + ADDITIVE CAP 4, 210 F

P (PSI)	V (CP)
.00000	.79000+01
.52044+04	.16332+02
.11194+05	.30240+02
.21994+05	.92957+02
.31233+05	.21567+03
.42112+05	.54179+03
.53401+05	.14011+04

ALPHA STAR= .11958-03
ALPHA OT= .76540-04 x 2.3o3

FLUID C, NAPHTHENIC MINERAL OIL + ADDITIVE CAP 4, 300 F

P (PSI)	V (CP)
.00000	.28300+01
.52866+04	.53131+01
.11644+05	.84759+01
.22292+05	.21473+02
.33618+05	.46849+02
.43081+05	.86708+02
.51650+05	.15488+03

ALPHA STAR= .94080-04
ALPHA OT= .70238-04 x 2.3o3

**********RAW DATA POINTS**********

2

FLUID C. NAPHTHENIC MINERAL OIL + ADDITIVE

RUN	P3	VISCP	NSRATE	KEC	DELTAP	TAUDYN	REYN
100-1-1	11909.	.5947+01	.3158+05	.8611-01	.1551+03	.1878+06	.2529+0(
100-1-2	11909.	.6216+01	.3635+05	.1141+00	.1866+03	.2260+06	.2785+0(
100-1-3	11909.	.6186+01	.3891+05	.1307+00	.1988+03	.2407+06	.2995+0(
100-1-4	11458.	.5151+01	.1393+06	.1675+01	.5924+03	.7175+06	.1286+01
100-1-5	11346.	.6490+01	.1263+05	.1378-01	.6770+02	.8199+05	.9269-01
100-1-6	11346.	.5657+01	.2260+05	.4409-01	.1056+03	.1278+06	.1902+0(
100-1-9	11233.	.5932+01	.2316+05	.4631-01	.1134+03	.1374+06	.1859+0(
100-1-10	11233.	.5955+01	.6714+04	.3892-02	.3302+02	.3998+05	.5369-01
100-1-11	11233.	.6155+01	.4913+04	.2084-02	.2497+02	.3024+05	.3801-01
100-1-12	11233.	.5878+01	.1228+05	.1302-01	.5961+02	.7219+05	.9950-01
100-1-13	11233.	.5546+01	.1548+05	.2067-01	.7087+02	.8583+05	.1329+0(
100-1-15	11196.	.6539+01	.1597+05	.2201-01	.8621+02	.1044+06	.1163+0(
100-1-16	11196.	.5958+01	.2653+05	.6076-01	.1305+03	.1581+06	.2120+00
100-1-18	11233.	.4916+01	.3463+05	.1036+00	.1406+03	.1702+06	.3355+00
100-1-19	11233.	.5141+01	.7074+05	.4321+00	.3003+03	.3637+06	.6552+00
100-1-20	11233.	.6022+01	.4680+05	.1891+00	.2327+03	.2818+06	.3701+00
100-1-21	11233.	.5606+01	.7379+05	.4700+00	.3415+03	.4136+06	.6266+00
100-1-22	11233.	.4717+01	.1712+06	.2530+01	.6668+03	.8075+06	.1728+01
100-1-23	11233.	.3757+01	.3276+06	.9266+01	.1016+04	.1231+07	.4153+01
100-1-23	11233.	.3375+01	.3527+06	.1074+02	.9930+03	.1190+07	.4976+01
100-1-24	11233.	.4621+01	.1815+06	.2844+01	.6925+03	.8387+06	.1871+01
100-1-25	11233.	.4098+01	.2597+06	.5824+01	.8786+03	.1064+07	.3016+01
100-1-26	11233.	.4811+01	.1290+06	.1437+01	.5126+03	.6207+06	.1277+01
100-1-27	11233.	.4331+01	.1796+06	.2785+01	.6424+03	.7780+06	.1975+01

FLUID D, SYNTHETIC PARAFFINIC OIL + ADDITIVE CAP 4:

RUN	P3	VISCP	NSRATE	KEC	DELTAP	TAUDYN	REYN
100-1	5330.	.7677+01	.3548+04	.1606-02	.4641+03	.2724+05	.3253-01
100-2	5330.	.7594+01	.5024+04	.2221-02	.6501+03	.3816+05	.4656-01
100-3	5330.	.7848+01	.2996+04	.1145-02	.4006+03	.2351+05	.2687-01
100-4	5330.	.7505+01	.4547+04	.2637-02	.5814+03	.3412+05	.4263-01
100-5	5330.	.7896+01	.2773+04	.9808-03	.3730+03	.2189+05	.2471-01
100-6	11580.	.1673+02	.1041+04	.1382-03	.2967+03	.1741+05	.4377-02
100-7	11592.	.1605+02	.2970+04	.1125-02	.8121+03	.4766+05	.1302-01
100-8	11592.	.1649+02	.3890+04	.1930-02	.1092+04	.6412+05	.1660-01
100-9	11592.	.1644+02	.3785+04	.1827-02	.1060+04	.6223+05	.1620-01
100-10	11592.	.1602+02	.4231+04	.2284-02	.1155+04	.6778+05	.1859-01
100-11	11668.	.1633+02	.1735+04	.3839-03	.4826+03	.2833+05	.7475-02
100-12	20801.	.4426+02	.3670+03	.1718-04	.2768+03	.1625+05	.5835-03
100-13	20801.	.4295+02	.5505+03	.3866-04	.4028+03	.2364+05	.9020-03
100-14	20742.	.4511+02	.6051+03	.4671-04	.4650+03	.2729+05	.9439-03
100-15	20742.	.4099+02	.5059+03	.3265-04	.3533+03	.2074+05	.8684-03
100-16	20742.	.4360+02	.6100+03	.4747-04	.4531+03	.2660+05	.9846-03
100-17	20742.	.4212+02	.6646+03	.5635-04	.4769+03	.2799+05	.1110-02
100-18	31636.	.1221+03	.1984+03	.5021-05	.4127+03	.2422+05	.1143-03
100-19	31636.	.1330+03	.2529+03	.8162-05	.5733+03	.3365+05	.1338-03
100-20	31636.	.1151+03	.3125+03	.1245-04	.6128+03	.3597+05	.1910-03
100-21	31636.	.1234+03	.4067+03	.2110-04	.8549+03	.5018+05	.2319-03
100-22	31636.	.1234+03	.3720+03	.1765-04	.7820+03	.4590+05	.2121-03
100-23	42037.	.3080+03	.1012+03	.1307-05	.5312+03	.3118+05	.2313-04
100-24	42037.	.3122+03	.1373+03	.2405-05	.7305+03	.4287+05	.3095-04
100-25	42037.	.2892+03	.2176+03	.6040-05	.1072+04	.6293+05	.5294-04
100-27	42037.	.2945+03	.2211+03	.6236-05	.1109+04	.6511+05	.5283-04
100-28	52246.	.7274+03	.4119+02	.2165-06	.5105+03	.2996+05	.3985-05
100-29	52171.	.6658+03	.5027+02	.3224-06	.5702+03	.3347+05	.5313-05
100-30	51873.	.7094+03	.6493+02	.5378-06	.7847+03	.4606+05	.6441-05
100-31	51873.	.7745+03	.7296+02	.6790-06	.9627+03	.5651+05	.6629-05
100-32	51799.	.6402+03	.1012+03	.1307-05	.1104+04	.6481+05	.1113-04

FLUID D SYNTHETIC PARAFFINIC OIL + ADDITIVE CAP 4,

RUN	P3	VISCP	NSRATE	KEC	DELTAP	TAUDYN	REYN
210-2	5311.	.5668+00	.2620+05	.2454-01	.2530+03	.1485+05	.3140+01
210-3	5311.	.5912+00	.3920+05	.1893+00	.3046+03	.2317+05	.4505+01
210-4	5311.	.5778+00	.3073+05	.1163+00	.3025+03	.1775+05	.3614+01
210-5	5311.	.6250+00	.2915+05	.1047+00	.3104+03	.1822+05	.3169+01
210-6	11481.	.1295+01	.9192+04	.1041-01	.2026+03	.1190+05	.4824+00
210-7	11385.	.1022+01	.2275+05	.6376-01	.3961+03	.2325+05	.1513+01
210-8	11404.	.1172+01	.1615+05	.3214-01	.3226+03	.1893+05	.9362+00
210-9	11404.	.9942+00	.2462+05	.7468-01	.4170+03	.2448+05	.1683+01
210-10	11328.	.1008+01	.1326+05	.2167-01	.2277+03	.1337+05	.8942+00
210-11	11328.	.1116+01	.1641+05	.3319-01	.3120+03	.1831+05	.9998+00
210-12	20503.	.2095+01	.9168+04	.1035-01	.3272+03	.1921+05	.2973+00
210-13	20503.	.2156+01	.1008+05	.1253-01	.3705+03	.2175+05	.3178+00
210-14	20503.	.2105+01	.1467+05	.2651-01	.5260+03	.3087+05	.4736+00
210-15	20503.	.2522+01	.7989+04	.7863-02	.3432+03	.2014+05	.2153+00
210-16	20503.	.2082+01	.1441+05	.2557-01	.5110+03	.2998+05	.4702+00
210-17	31233.	.4639+01	.4732+04	.2759-02	.3740+03	.2195+05	.6932-01
210-18	31233.	.4445+01	.7775+04	.7446-02	.5888+03	.3456+05	.1189+00
210-19	31233.	.4522+01	.5256+04	.3404-02	.4049+03	.2377+05	.7899-01
210-20	31233.	.4603+01	.7944+04	.7774-02	.6229+03	.3656+05	.1173+00
210-21	31159.	.4550+01	.8282+04	.8449-02	.6420+03	.3768+05	.1237+00
210-22	41218.	.8819+01	.3749+04	.1731-02	.5633+03	.3306+05	.2889-01
210-23	41218.	.8518+01	.3473+04	.1486-02	.5040+03	.2958+05	.2770-01
210-24	41218.	.8405+01	.4091+04	.2062-02	.5856+03	.3438+05	.3307-01
210-25	41218.	.8445+01	.2447+04	.7374-03	.3520+03	.2066+05	.1969-01
210-26	41218.	.8616+01	.3591+04	.1589-02	.5271+03	.3094+05	.2832-01
210-27	52097.	.1646+02	.1622+04	.3240-03	.4547+03	.2669+05	.6697-02
210-28	52097.	.1717+02	.1510+04	.2810-03	.4417+03	.2593+05	.5977-02
210-29	52097.	.1656+02	.9299+03	.1065-03	.2624+03	.1540+05	.3816-02
210-30	52097.	.1631+02	.1303+04	.2093-03	.3623+03	.2126+05	.5429-02
210-31	52097.	.1683+02	.1413+04	.2461-03	.4052+03	.2378+05	.5708-02
210-32	60591.	.2606+02	.7925+03	.7738-04	.3518+03	.2065+05	.2067-02
210-33	60591.	.2497+02	.5257+03	.3405-04	.2336+03	.1313+05	.1431-02
210-35	60591.	.2638+02	.7514+03	.6955-04	.3377+03	.1982+05	.1935-02
210-36	60591.	.2671+02	.9820+03	.1188-03	.4469+03	.2623+05	.2498-02
210-37	72438.	.4965+02	.5059+03	.3153-04	.4279+03	.2512+05	.6923-03
210-38	72438.	.4746+02	.4826+03	.2869-04	.3902+03	.2290+05	.6910-03
210-39	72438.	.4961+02	.6844+03	.5771-04	.5785+03	.3396+05	.9374-03
210-40	72438.	.4710+02	.6423+03	.5082-04	.5153+03	.3025+05	.9267-03
210-41	72438.	.4790+02	.4811+03	.2851-04	.3926+03	.2304+05	.6825-03
210-42	78772.	.5896+02	.4957+03	.3027-04	.4979+03	.2923+05	.5713-03
210-43	78772.	.6335+02	.3316+03	.1355-04	.3579+03	.2101+05	.3557-03
210-44	78623.	.6831+02	.3805+03	.1784-04	.4428+03	.2599+05	.3785-03
210-45	78623.	.6953+02	.3840+03	.1816-04	.4549+03	.2670+05	.3753-03
210-46	78623.	.6914+02	.2880+03	.1022-04	.3393+03	.1991+05	.2830-03

FLUID D, SYNTHETIC PARAFFINIC OIL + ADDITIVE CAP 4, 300 F

RUN	P3	VISCP	NSRATE	KEC	DELTAP	TAUDYN	REYN
300-1	5291.	.1560+00	.2787+05	.9209-01	.7405+02	.4346+04	.1169+02
300-2	5291.	.1760+00	.2748+05	.8952-01	.8241+02	.4837+04	.1021+02
300-3	5291.	.1694+00	.5299+05	.3329+00	.1529+03	.8975+04	.2046+02
300-4	5291.	.1749+00	.5044+05	.3017+00	.1503+03	.8820+04	.1887+02
300-5	5291.	.1698+00	.3297+05	.1289+00	.9541+02	.5600+04	.1270+02
300-6	10752.	.2542+00	.1191+05	.1681-01	.5157+02	.3027+04	.3063+01
300-7	10752.	.2561+00	.1361+05	.2195-01	.5938+02	.3486+04	.3474+01
300-8	10714.	.2604+00	.2316+05	.6359-01	.1027+03	.6030+04	.5817+01
300-9	10714.	.2783+00	.2054+05	.5003-01	.9740+02	.5717+04	.4827+01
300-10	10714.	.2692+00	.2351+05	.6555-01	.1079+03	.6330+04	.5712+01
300-11	21836.	.5687+00	.1862+05	.4111-01	.1804+03	.1059+05	.2141+01
300-12	21836.	.5661+00	.1224+05	.1776-01	.1181+03	.6929+04	.1414+01
300-13	21836.	.5607+00	.1341+05	.2133-01	.1281+03	.7520+04	.1565+01
300-14	21836.	.5592+00	.1387+05	.2280-01	.1321+03	.7755+04	.1622+01
300-15	21836.	.5589+00	.1393+05	.2302-01	.1327+03	.7787+04	.1631+01
300-16	31794.	.1089+01	.5630+04	.3758-02	.1045+03	.6131+04	.3381+00
300-17	31794.	.1042+01	.8402+04	.8371-02	.1491+03	.8752+04	.5276+00
300-18	31794.	.1078+01	.2884+04	.9860-03	.5296+02	.3109+04	.1749+00
300-19	31794.	.1095+01	.5419+04	.3482-02	.1011+03	.5932+04	.3238+00
300-20	31794.	.1034+01	.9495+04	.1069-01	.1672+03	.9813+04	.6008+00
300-21	41573.	.1800+01	.3139+04	.1168-02	.9625+02	.5650+04	.1141+00
300-22	41573.	.1677+01	.5127+04	.2116-02	.1564+03	.8596+04	.2000+00
300-23	41573.	.1755+01	.3165+04	.1188-02	.9464+02	.5555+04	.1179+00
300-24	41573.	.1654+01	.5532+04	.3629-02	.1558+03	.9147+04	.2188+00
300-25	41573.	.1754+01	.3400+04	.1371-02	.1016+03	.5963+04	.1268+00
300-26	52538.	.2906+01	.1760+04	.3675-03	.8714+02	.5115+04	.3963-01
300-27	52538.	.2838+01	.2271+04	.6114-03	.1098+03	.6445+04	.5233-01
300-28	52538.	.2906+01	.1546+04	.2834-03	.7654+02	.4493+04	.3479-01
300-29	52538.	.2973+01	.1465+04	.2543-03	.7417+02	.4354+04	.3222-01
300-30	52538.	.2970+01	.1975+04	.4625-03	.9992+02	.5865+04	.4350-01
300-31	62317.	.4578+01	.1328+04	.2090-03	.1036+03	.6079+04	.1897-01
300-32	62317.	.4272+01	.1933+04	.4430-03	.1407+03	.8258+04	.2959-01
300-33	62317.	.4482+01	.1220+04	.1766-03	.9319+02	.5470+04	.1781-01
300-34	62317.	.4446+01	.1516+04	.2726-03	.1149+03	.6741+04	.2231-01
300-35	62317.	.4464+01	.1901+04	.4285-03	.1446+03	.8486+04	.2785-01
300-36	70763.	.6455+01	.9357+03	.1038-03	.1029+03	.6040+04	.9480-02
300-37	70763.	.6442+01	.8617+03	.8805-04	.9458+02	.5551+04	.8749-02
300-38	70763.	.6601+01	.5622+03	.3747-04	.6325+02	.3711+04	.5569-02
300-39	70763.	.6275+01	.8876+03	.9342-04	.9890+02	.5570+04	.9251-02
300-40	70763.	.6554+01	.8358+03	.8283-04	.9335+02	.5478+04	.8341-02
300-41	79357.	.9204+01	.5326+03	.3363-04	.8351+02	.4902+04	.3785-02
300-42	79357.	.9456+01	.6065+03	.4362-04	.9772+02	.5735+04	.4195-02
300-43	79357.	.8896+01	.6879+03	.5611-04	.1043+03	.6120+04	.5057-02
300-44	79357.	.9151+01	.8063+03	.7707-04	.1257+03	.7378+04	.5762-02
300-45	79357.	.8893+01	.9394+03	.1046-03	.1423+03	.8354+04	.6909-02

2 **********AVERAGED DATA POINTS**********

FLUID D, SYNTHETIC PARAFFINIC OIL + ADDITIVE CAP 4, 100 F

P (PSI)	V (CP)
.00000	.36950+03
.53295+04	.77041+03
.11603+05	.16343+04
.20762+05	.43172+04
.31636+05	.12340+05
.42037+05	.30099+05
.51992+05	.70346+05

ALPHA STAR= .12480-03
ALPHA OT= .69975-04 x2.3e3

FLUID D, SYNTHETIC PARAFFINIC OIL + ADDITIVE CAP 4, 210 F

P (PSI)	V (CP)
.00000	.31960+02
.53115+04	.59021+02
.11370+05	.10624+03
.20503+05	.21095+03
.31218+05	.45518+03
.41218+05	.85608+03
.52097+05	.16665+04
.60591+05	.26031+04
.72438+05	.48343+04
.78683+05	.65859+04

ALPHA STAR= .94092-04
ALPHA OT= .58023-04 x2.3e3

FLUID D, SYNTHETIC PARAFFINIC OIL + ADDITIVE CAP 4, 300 F

P (PSI)	V (CP)
.00000	.99500+01
.52913+04	.16921+02
.10729+05	.26366+02
.21836+05	.56271+02
.31794+05	.10674+03
.41573+05	.17277+03
.52538+05	.29184+03
.62317+05	.44484+03
.70763+05	.64655+03
.79357+05	.91200+03

ALPHA STAR= .78194-04
ALPHA OT= .50644-04 x2.3e3

**********RAW DATA POINTS**********

FLUID D. SYNTHETIC PARAFFINIC OIL + ADDITIVE

RUN	P3	VISCP	NSRATE	KEC	DELTAP	TAUDYN	REYN
100-1	11586.	.1617+02	.2249+05	.4192-01	.3003+03	.3637+06	.6358-01
100-2	11586.	.1332+02	.1027+06	.8747+00	.1130+04	.1368+07	.3526+00
100-3	11586.	.1337+02	.9010+05	.6726+00	.9950+03	.1205+07	.3079+00
100-4	11586.	.1222+02	.1208+06	.1208+01	.1219+04	.1476+07	.4516+00
100-5	11586.	.1361+02	.8780+05	.6386+00	.9869+03	.1195+07	.2948+00
100-6	11586.	.1396+02	.7027+05	.4092+00	.8101+03	.9811+06	.2301+00
100-7	11586.	.1327+02	.9086+05	.6840+00	.9957+03	.1206+07	.3129+00
100-8	11547.	.1347+02	.8818+05	.6442+00	.9811+03	.1188+07	.2991+00
100-9	11695.	.1374+02	.8818+05	.6442+00	.1000+04	.1211+07	.2933+00
100-10	11695.	.1395+02	.7591+05	.4774+00	.8745+03	.1059+07	.2487+00
100-11	11625.	.1345+02	.9086+05	.6840+00	.1009+04	.1222+07	.3088+00
100-12	11625.	.1429+02	.7246+05	.4350+00	.8546+03	.1035+07	.2318+00
100-14	11625.	.1535+02	.4409+05	.1611+00	.5589+03	.6768+06	.1313+00
100-15	11664.	.1634+02	.1285+05	.1368-01	.1734+03	.2100+06	.3594-01
100-16	11625.	.1627+02	.1319+05	.1442-01	.1773+03	.2147+06	.3705-01
100-17	11625.	.1696+02	.8807+04	.6426-02	.1235+03	.1494+06	.2373-01
100-18	11664.	.1656+02	.9400+04	.7322-02	.1285+03	.1556+06	.2595-01
100-19	11664.	.1686+02	.1319+05	.1442-01	.1837+03	.2225+06	.3576-01
100-20	11703.	.1702+02	.3748+04	.1164-02	.5268+02	.6379+05	.1006-01
100-21	11703.	.1637+02	.3183+04	.8395-03	.4303+02	.5211+05	.8887-02
100-22	11703.	.1678+02	.5365+04	.2385-02	.7433+02	.9002+05	.1461-01
100-23	11703.	.1649+02	.7598+04	.4784-02	.1035+03	.1253+06	.2106-01

FLUID E DN 600 + ADDITIVE CAP 4, 100 F

RUN	P3	VISCP	NSRATE	KEC	DELTAP	TAUDYN	REYN
100-2	5177.	.6224+00	.7360+04	.6990-02	.7805+02	.4581+04	.8416+00
100-3	5177.	.6273+00	.1550+05	.3102-01	.1657+03	.9726+04	.1759+01
100-4	5177.	.6152+00	.9224+04	.1098-01	.9669+02	.5675+04	.1067+01
100-5	11401.	.1345+01	.3219+04	.1337-02	.7381+02	.4332+04	.1702+00
100-6	11401.	.1310+01	.7458+04	.7177-02	.1665+03	.9772+04	.4052+00
100-7	11420.	.1256+01	.5103+04	.3360-02	.1092+03	.6407+04	.2893+00
100-8	11420.	.1232+01	.1001+05	.1293-01	.2103+03	.1234+05	.5777+00
100-10	11439.	.1326+01	.6280+04	.5090-02	.1419+03	.8326+04	.3372+00
100-11	11439.	.1336+01	.6477+04	.5413-02	.1474+03	.8653+04	.3451+00
100-12	20142.	.3210+01	.2272+04	.6660-03	.1242+03	.7293+04	.5036-01
100-13	20142.	.3252+01	.3070+04	.1216-02	.1701+03	.9984+04	.6720-01
100-14	20142.	.3207+01	.3746+04	.1810-02	.2047+03	.1201+05	.8313-01
100-15	20142.	.3255+01	.4482+04	.2593-02	.2486+03	.1459+05	.9803-01
100-16	20142.	.3044+01	.5403+04	.3763-02	.2303+03	.1645+05	.1263+00
100-17	20142.	.3178+01	.6816+04	.5994-02	.3690+03	.2166+05	.1527+00
100-18	30392.	.8422+01	.1644+04	.3487-03	.2359+03	.1384+05	.1389-01
100-19	30392.	.8459+01	.2084+04	.5602-03	.3003+03	.1763+05	.1753-01
100-20	30392.	.8079+01	.2739+04	.9682-03	.3770+03	.2213+05	.2413-01
100-21	30392.	.8363+01	.2141+04	.5914-03	.3050+03	.1790+05	.1822-01
100-22	30392.	.7617+01	.2561+04	.8466-03	.3324+03	.1951+05	.2393-01
100-23	40066.	.1916+02	.8105+03	.8476-04	.2646+03	.1553+05	.3011-02
100-24	40066.	.2065+02	.1132+04	.1652-03	.3867+03	.2270+05	.4016-02
100-25	40066.	.1926+02	.1338+04	.2310-03	.4392+03	.2578+05	.4944-02
100-26	40066.	.1923+02	.1545+04	.3078-03	.5060+03	.2970+05	.5717-02
100-27	40066.	.1950+02	.7952+03	.8159-04	.2641+03	.1550+05	.2903-02
100-28	50894.	.4603+02	.8120+03	.8509-04	.6368+03	.3738+05	.1256-02
100-29	50894.	.4423+02	.4853+03	.3039-04	.3357+03	.2146+05	.7810-03
100-30	50894.	.4741+02	.7303+03	.6383-04	.5899+03	.3463+05	.1096-02
100-31	50605.	.4554+02	.1086+04	.1522-03	.6426+03	.4946+05	.1697-02
100-32	50605.	.4648+02	.6631+03	.5673-04	.5251+03	.3082+05	.1015-02
100-33	61506.	.9961+02	.4084+03	.2152-04	.6931+03	.4068+05	.2918-03
100-34	61506.	.1043+03	.4469+03	.2577-04	.7938+03	.4659+05	.3050-03
100-35	61434.	.1025+03	.2835+03	.1037-04	.4952+03	.2907+05	.1968-03
100-36	61434.	.1019+03	.3544+03	.1907-04	.6575+03	.3918+05	.2684-03
100-37	61434.	.1008+03	.3219+03	.1337-04	.5527+03	.3244+05	.2274-03
100-38	71829.	.2163+03	.1550+03	.3100-05	.5712+03	.3353+05	.5100-04
100-39	71829.	.2410+03	.1849+03	.4410-05	.7590+03	.4455+05	.5461-04
100-40	71829.	.2221+03	.2390+03	.7370-05	.9042+03	.5307+05	.7660-04
100-41	71829.	.2157+03	.2379+03	.7301-05	.8740+03	.5130+05	.7850-04
100-42	71829.	.2206+03	.2582+03	.8599-05	.9700+03	.5694+05	.8331-04
100-43	76593.	.3257+03	.1330+03	.2283-05	.7382+03	.4333+05	.2907-04
100-44	76593.	.3327+03	.1533+03	.3033-05	.8691+03	.5101+05	.3280-04
100-45	76593.	.3330+03	.1420+03	.2603-05	.8059+03	.4730+05	.3036-04
100-46	76593.	.3316+03	.1150+03	.1706-05	.6495+03	.3813+05	.2468-04
100-47	76593.	.3373+03	.1161+03	.1740-05	.6673+03	.3917+05	.2450-04
100-48	87277.	.6382+03	.7327+02	.6928-06	.7967+03	.4676+05	.8173-05
100-49	86700.	.6691+03	.9469+02	.1157-05	.1079+04	.6336+05	.1007-04
100-50	86700.	.6516+03	.7215+02	.6717-06	.8009+03	.4701+05	.7881-05
100-51	86555.	.7111+03	.7440+02	.7143-06	.9014+03	.5291+05	.7447-05
100-52	86267.	.7944+03	.6313+02	.5142-06	.8544+03	.5015+05	.5656-05
100-53	96518.	.1352+04	.2300+02	.6824-07	.7258+03	.4260+05	.8836-06
100-54	96513.	.1399+04	.3247+02	.1360-06	.7737+03	.4541+05	.1652-05

FLUID E DN 600 + ADDITIVE CAP 4, 210 F

RUN	P3	VISCP	NSRATE	KEC	DELTAP	TAUDYN	REYN
210-1	5325.	.9531-01	.3179+05	.1252+00	.5162+02	.3030+04	.2280+02
210-2	5317.	.8982-01	.3613+05	.1618+00	.5529+02	.3245+04	.2750+02
210-3	5306.	.9040-01	.4482+05	.2489+00	.6903+02	.4052+04	.3389+02
210-4	5306.	.6797-01	.3870+05	.1856+00	.5800+02	.3404+04	.3607+02
210-5	5306.	.8912-01	.4363+05	.2359+00	.6625+02	.3888+04	.3347+02
210-6	5306.	.9073-01	.3514+05	.1530+00	.5432+02	.3188+04	.2648+02
210-7	11317.	.1439+00	.1514+05	.2839-01	.3711+02	.2178+04	.7190+01
210-8	11317.	.1492+00	.2725+05	.9199-01	.5924+02	.4064+04	.1249+02
210-9	11317.	.1477+00	.2619+05	.8502-01	.6591+02	.3869+04	.1212+02
210-10	11317.	.1479+00	.2909+05	.1049+00	.7330+02	.4302+04	.1344+02
210-11	11317.	.1596+00	.1158+05	.1663-01	.3149+02	.1849+04	.4961+01
210-12	21666.	.3063+00	.1062+05	.1397-01	.5577+02	.3273+04	.2354+01
210-13	21666.	.3302+00	.9970+04	.1232-01	.5608+02	.3292+04	.2064+01
210-14	21666.	.3325+00	.2162+05	.5794-01	.1225+03	.7190+04	.4445+01
210-15	21666.	.3423+00	.1864+05	.4308-01	.1087+03	.6382+04	.3723+01
210-16	21666.	.3173+00	.3766+05	.1759+00	.2040+03	.1198+05	.8104+01
210-17	21666.	.3249+00	.3515+05	.1531+00	.1946+03	.1142+05	.7396+01
210-18	31463.	.6068+00	.2033+05	.5121-01	.2101+03	.1233+05	.2290+01
210-19	31463.	.5940+00	.1308+05	.2119-01	.1323+03	.7768+04	.1505+01
210-20	31463.	.6157+00	.3166+05	.1242+00	.3321+03	.1949+05	.3515+01
210-21	31463.	.6572+00	.1806+05	.4043-01	.2023+03	.1187+05	.1879+01
210-22	31463.	.6172+00	.2447+05	.7421-01	.2573+03	.1510+05	.2710+01
210-23	41482.	.1266+01	.4894+04	.2968-02	.1056+03	.6197+04	.2642+00
210-24	41432.	.1095+01	.9970+04	.1232-01	.1859+03	.1091+05	.6225+00
210-25	41187.	.1143+01	.1450+05	.2606-01	.2825+03	.1658+05	.8671+00
210-26	41335.	.1210+01	.1185+05	.1739-01	.2443+03	.1434+05	.6692+00
210-27	41335.	.1161+01	.1489+05	.2748-01	.2945+03	.1729+05	.8767+00
210-28	52826.	.2155+01	.4096+04	.2079-02	.1564+03	.8827+04	.1299+00
210-29	52753.	.2192+01	.3862+04	.1849-02	.1442+03	.8464+04	.1205+00
210-30	52753.	.2136+01	.3784+04	.1775-02	.1377+03	.8083+04	.1211+00
210-31	52753.	.2108+01	.5033+04	.3139-02	.1807+03	.1061+05	.1632+00
210-32	52753.	.2133+01	.7002+04	.7544-02	.2836+03	.1665+05	.2500+00
210-33	63950.	.3878+01	.1691+04	.3542-03	.1117+03	.6555+04	.2980-01
210-34	63434.	.3885+01	.4083+04	.2066-02	.2703+03	.1586+05	.7185-01
210-35	63287.	.3820+01	.3433+04	.1461-02	.2117+03	.1243+05	.6483-01
210-36	63287.	.3849+01	.3251+04	.1310-02	.2132+03	.1251+05	.5773-01
210-37	63287.	.3910+01	.3589+04	.1596-02	.2391+03	.1403+05	.6276-01
210-38	72569.	.5987+01	.1574+04	.3070-03	.1605+03	.9423+04	.1797-01
210-39	72569.	.5835+01	.1515+04	.2845-03	.1506+03	.8841+04	.1775-01
210-40	72569.	.5953+01	.1552+04	.2984-03	.1574+03	.9238+04	.1782-01
210-41	72569.	.6042+01	.1589+04	.3128-03	.1635+03	.9598+04	.1797-01
210-42	72569.	.5941+01	.1537+04	.2924-03	.1556+03	.9133+04	.1768-01
210-43	79567.	.8386+01	.1324+04	.2172-03	.1891+03	.1110+05	.1079-01
210-44	79567.	.8419+01	.1397+04	.2420-03	.2002+03	.1175+05	.1136-01
210-45	79567.	.8477+01	.1214+04	.1825-03	.1753+03	.1029+05	.9786-02
210-46	79567.	.8342+01	.1095+04	.1488-03	.1651+03	.9690+04	.8472-02
210-47	79567.	.8344+01	.7575+03	.7112-04	.1077+03	.6321+04	.6206-02
210-48	91501.	.1568+02	.7943+03	.7819-04	.2123+03	.1246+05	.3462-02
210-49	91501.	.1668+02	.6399+03	.5074-04	.1818+03	.1067+05	.2622-02
210-50	91501.	.1633+02	.6766+03	.5674-04	.1882+03	.1105+05	.2833-02

FLUID E DN 600 + ADDITIVE CAP 4, 300 F

RUN	P3	VISCP	NSRATE	KEC	DELTAP	TAUDYN	REYN
300-1	5282.	.3210-01	.4310+05	.2207+00	.2357+02	.1383+04	.8799+02
300-2	5282.	.3593-01	.4489+05	.2394+00	.2748+02	.1613+04	.8188+02
300-3	5282.	.3217-01	.3595+05	.1535+00	.1970+02	.1156+04	.7325+02
300-4	5282.	.3555-01	.4806+05	.2745+00	.2911+02	.1708+04	.9862+02
300-5	5282.	.3592-01	.5025+05	.3000+00	.3075+02	.1805+04	.9168+02
300-6	11426.	.5406-01	.2522+05	.7559-01	.2323+02	.1364+04	.3058+02
300-7	11426.	.5496-01	.2443+05	.7091-01	.2288+02	.1343+04	.2913+02
300-8	11426.	.5450-01	.2364+05	.6307-01	.2139+02	.1256+04	.2771+02
300-9	11426.	.5925-01	.1827+05	.3967-01	.1845+02	.1083+04	.2021+02
300-10	11426.	.5963-01	.2000+05	.9990-01	.2946+02	.1729+04	.3107+02
300-11	21249.	.9847-01	.1395+05	.2311-01	.2340+02	.1374+04	.9283+01
300-12	21249.	.1101+00	.2515+05	.7512-01	.4719+02	.2770+04	.1496+02
300-13	21249.	.9986-01	.3222+05	.1233+00	.5481+02	.3217+04	.2114+02
300-14	21249.	.1020+00	.2259+05	.6064-01	.3927+02	.2305+04	.1451+02
300-15	21249.	.1007+00	.4440+05	.2342+00	.7619+02	.4472+04	.2889+02
300-16	31978.	.1477+00	.2829+05	.9508-01	.9048+02	.5311+04	.9875+01
300-17	32127.	.1820+00	.1532+05	.2790-01	.4750+02	.2788+04	.5519+01
300-18	32127.	.1891+00	.2947+05	.1032+00	.9493+02	.5572+04	.1021+02
300-19	31978.	.1335+00	.1532+05	.2790-01	.4791+02	.2812+04	.5471+01
300-20	31978.	.1338+00	.1473+05	.2579-01	.4613+02	.2707+04	.5255+01
300-21	41516.	.2924+00	.1218+05	.1763-01	.6067+02	.3561+04	.2730+01
300-22	41516.	.3455+00	.1945+05	.4494-01	.1012+03	.5941+04	.4173+01
300-23	41516.	.2957+00	.1866+05	.4138-01	.9402+02	.5518+04	.4136+01
300-24	41516.	.3058+00	.9626+04	.1101-01	.5015+02	.2944+04	.2063+01
300-25	41516.	.3007+00	.2043+05	.4959-01	.1047+03	.6144+04	.4453+01
300-26	53289.	.5929+00	.9444+04	.1060-01	.8092+02	.4750+04	.1231+01
300-27	53289.	.5124+00	.1420+05	.2395-01	.1239+03	.7275+04	.1816+01
300-28	53289.	.4693+00	.1268+05	.1909-01	.1058+03	.6209+04	.1696+01
300-29	53289.	.5070+00	.1103+05	.1445-01	.9525+02	.5591+04	.1426+01
300-30	53289.	.4984+00	.6716+04	.5363-02	.5704+02	.3348+04	.8834+00
300-31	62677.	.7285+00	.4380+04	.2279-02	.5437+02	.3191+04	.3940+00
300-32	62677.	.7503+00	.3551+04	.1499-02	.4540+02	.2665+04	.3102+00
300-33	62677.	.7426+00	.3275+04	.1275-02	.4144+02	.2432+04	.2891+00
300-34	62677.	.7154+00	.6866+04	.5601-02	.8423+02	.4932+04	.6264+00
300-35	62528.	.7245+00	.5327+04	.3372-02	.6576+02	.3860+04	.4819+00
300-36	74152.	.1159+01	.4025+04	.1925-02	.7948+02	.4665+04	.2276+00
300-37	74152.	.1204+01	.3749+04	.1670-02	.7693+02	.4515+04	.2040+00
300-38	74152.	.1239+01	.2644+04	.8305-03	.5579+02	.3275+04	.1399+00
300-39	74152.	.1140+01	.4854+04	.2799-02	.9423+02	.5531+04	.2791+00
300-40	74152.	.1118+01	.4814+04	.2754-02	.9172+02	.5383+04	.2822+00
300-41	80411.	.1478+01	.4025+04	.1925-02	.1013+03	.5948+04	.1785+00
300-42	80411.	.1445+01	.3473+04	.1433-02	.8547+02	.5017+04	.1575+00
300-43	80411.	.1236+01	.3214+04	.1227-02	.6769+02	.3973+04	.1704+00
300-44	80411.	.1413+01	.3125+04	.1160-02	.7524+02	.4416+04	.1449+00
300-45	80411.	.1437+01	.2916+04	.1010-02	.7138+02	.4189+04	.1330+00

@2

**********AVERAGED DATA POINTS**********

FLUID E 3N 600 + ADDITIVE CAP 4, 100 F

P (PSI)	V (CP)
.00000	.32210+02
.51768+04	.62165+02
.11420+05	.13011+03
.20142+05	.31909+03
.30392+05	.81881+03
.40065+05	.19441+04
.50779+05	.45938+04
.61463+05	.10182+05
.71829+05	.22311+05
.76593+05	.33208+05

ALPHA STAR= .11680-03
ALPHA OT= .61445-04 x2.3o3

FLUID E 3N 600 + ADDITIVE CAP 4, 210 F

P (PSI)	V (CP)
.00000	.49700+01
.53109+04	.90560+01
.11317+05	.14965+02
.21666+05	.32601+02
.31463+05	.61818+02
.41364+05	.11751+03
.52768+05	.21447+03
.63449+05	.38283+03
.72569+05	.59517+03
.79567+05	.84917+03

ALPHA STAR= .88481-04
ALPHA OT= .60340-04 x2.3o3

FLUID E 3N 600 + ADDITIVE CAP 4, 300 F

P (PSI)	V (CP)
.00000	.20600+01
.52817+04	.34332+01
.11426+05	.56481+01
.21249+05	.10225+02
.32030+05	.18522+02
.41516+05	.30001+02
.53289+05	.50211+02
.62648+05	.73295+02
.74152+05	.11720+03
.80411+05	.14018+03

ALPHA STAR AND ALPHA OT MUST BE CALCULATED BY HAND

**********RAW DATA POINTS**********

p 2

FLUID E. DN 600 + ADDITIVE

RUN	P3	VISCP	NSRATE	KEC	DELTAP	TAUDYN	REYN
100-1	11186.	.1370+01	.8728+05	.6384+00	.9876+02	.1196+06	.2944+01
100-2	11186.	.1285+01	.9753+05	.7971+00	.1035+03	.1253+06	.3508+01
100-3	11186.	.1316+01	.9803+05	.8054+00	.1066+03	.1290+06	.3443+01
100-4	11186.	.1138+01	.2113+06	.3740+01	.1985+03	.2404+06	.8583+01
100-5	11039.	.1181+01	.2265+06	.4298+01	.2206+03	.2674+06	.8867+01
100-6	11039.	.1164+01	.2888+06	.6989+01	.2776+03	.3362+06	.1147+02
100-7	11117.	.1160+01	.1315+06	.1449+01	.1260+03	.1525+06	.5238+01
100-8	11117.	.1090+01	.3937+06	.1299+02	.3542+03	.4290+06	.1670+02
100-9	11117.	.1124+01	.4674+06	.1831+02	.4336+03	.5252+06	.1923+02
100-10	11155.	.1064+01	.6475+06	.3513+02	.5687+03	.6888+06	.2814+02
100-11	11155.	.1033+01	.7113+06	.4240+02	.6066+03	.7346+06	.3184+02
100-12	11233.	.1187+01	.3666+06	.1126+02	.3593+03	.4351+06	.1428+02
100-13	11233.	.1051+01	.6338+06	.3366+02	.5500+03	.6661+06	.2788+02
100-14	11233.	.9221+00	.9211+06	.7110+02	.7013+03	.8493+06	.4617+02
100-15	11233.	.9327+00	.8116+06	.5521+02	.6251+03	.7570+06	.4023+02
100-16	11233.	.8353+00	.1067+07	.9540+02	.7359+03	.8912+06	.5905+02
100-17	11271.	.1291+01	.6711+05	.3774+00	.7152+02	.8662+05	.2404+01
100-18	11271.	.1294+01	.5411+05	.2453+00	.5780+02	.6999+05	.1933+01
100-19	11271.	.1268+01	.8386+05	.5894+00	.8779+02	.1063+06	.3058+01
100-20	11194.	.1253+01	.1238+06	.1285+01	.1281+03	.1552+06	.4567+01
100-21	11194.	.1289+01	.7946+05	.5291+00	.8459+02	.1024+06	.2849+01
100-22	11194.	.1251+01	.9512+05	.7582+00	.9829+02	.1190+06	.3513+01
100-23	11194.	.1259+01	.4864+05	.1983+00	.5056+02	.6123+05	.1786+01
100-24	11194.	.1184+01	.3319+05	.9232-01	.3245+02	.3929+05	.1296+01
100-25	11194.	.1280+01	.5046+05	.2134+00	.5334+02	.6459+05	.1822+01

FLUID DN-600 CAP 4, 100 F

RUN	P3	VISCP	NSRATE	KEC	DELTAP	T UDYN	REYN
1DN01	5226.	.4807+00	.8568+04	.9419-02	.7017+02	.4119+04	.1261+01
1DN02	5226.	.5049+00	.5489+04	.3866-02	.4722+02	.2771+04	.7694+00
1DN03	5226.	.5048+00	.1767+05	.4007-01	.1520+03	.8921+04	.2477+01
1DN05	5226.	.4547+00	.2254+05	.6521-01	.1745+03	.1025+05	.3509+01
1DN06	11697.	.1094+01	.2509+04	.8076-03	.4674+02	.2744+04	.1624+00
1DN07	11697.	.8899+00	.7636+04	.7460-02	.1153+03	.6795+04	.6073+00
1DN08	11697.	.8259+00	.4636+04	.2757-02	.6523+02	.3829+04	.3972+00
1DN09	11697.	.8915+00	.1276+05	.2090-01	.1938+03	.1138+05	.1013+01
1DN10	11697.	.1029+01	.4254+04	.2322-02	.7456+02	.4376+04	.2927+00
1DN11	11697.	.9567+00	.1363+05	.2365-01	.2222+03	.1304+05	.1009+01
1DN12	23492.	.3022+01	.1464+04	.2749-03	.7536+02	.4423+04	.3429-01
1DN13	23492.	.2908+01	.2442+04	.7653-03	.1210+03	.7103+04	.5943-01
1DN14	23492.	.3145+01	.9785+03	.1228-03	.5242+02	.3077+04	.2202-01
1DN15	23492.	.3078+01	.3413+04	.1495-02	.1790+03	.1050+05	.7849-01
1DN16	23492.	.3148+01	.2714+04	.9448-03	.1455+03	.8542+04	.6101-01
1DN17	32151.	.5639+01	.1722+04	.3805-03	.1654+03	.9710+04	.2162-01
1DN18	32151.	.5504+01	.1037+04	.1380-03	.9725+02	.5708+04	.1334-01
1DN19	32133.	.5391+01	.2114+04	.5731-03	.1941+03	.1139+05	.2775-01
1DN20	32133.	.5609+01	.1221+04	.1913-03	.1167+03	.6850+04	.1541-01
1DN21	32133.	.5403+01	.2119+04	.5760-03	.1950+03	.1145+05	.2775-01
1DN22	38055.	.1193+02	.9067+03	.1055-03	.1844+03	.1082+05	.5377-02
1DN23	38055.	.1032+02	.1484+04	.2827-03	.2610+03	.1532+05	.1018-01
1DN24	38055.	.1100+02	.1141+04	.1670-03	.2139+03	.1255+05	.7337-02
1DN25	38055.	.1129+02	.1365+04	.2391-03	.2625+03	.1541+05	.8558-02
1DN26	38055.	.1128+02	.5432+03	.3786-04	.1044+03	.6129+04	.3407-02
1DN27	47659.	.2579+02	.3793+03	.1846-04	.1667+03	.9782+04	.1041-02
1DN28	47659.	.2327+02	.4049+03	.2104-04	.1605+03	.9420+04	.1232-02
1DN29	47659.	.2741+02	.8220+03	.8669-04	.3838+03	.2253+05	.2123-02
1DN30	47659.	.2619+02	.8098+03	.8415-04	.3613+03	.2121+05	.2189-02
1DN31	47659.	.2698+02	.3030+03	.1178-04	.1393+03	.8176+04	.7950-03
1DN32	59076.	.4702+02	.3636+03	.1696-04	.2913+03	.1710+05	.5473-03
1DN33	59076.	.6511+02	.4693+03	.2826-04	.5205+03	.3056+05	.5101-03
1DN34	59076.	.7220+02	.5818+03	.4343-04	.7156+03	.4201+05	.5703-03
1DN35	59076.	.6315+02	.5454+03	.3817-04	.5868+03	.3444+05	.6113-03
1DN36	59076.	.6361+02	.4872+03	.3046-04	.5280+03	.3099+05	.5421-03
1DN37	68399.	.1225+03	.1365+03	.2390-05	.2848+03	.1671+05	.7889-04
1DN38	68399.	.1148+03	.1226+03	.1936-05	.2403+03	.1410+05	.7572-04
1DN39	68399.	.1213+03	.2559+03	.8404-05	.5289+03	.3104+05	.1493-03
1DN40	68399.	.1176+03	.2078+03	.5541-05	.4164+03	.2444+05	.1250-03
1DN41	68399.	.1432+03	.2095+03	.5632-05	.5112+03	.3000+05	.1035-03
1DN42	75974.	.1920+03	.1092+03	.1530-05	.3573+03	.2097+05	.4024-04
1DN43	75974.	.1971+03	.1225+03	.1925-05	.4113+03	.2414+05	.4400-04
1DN44	75974.	.2643+03	.1066+03	.1457-05	.4798+03	.2816+05	.2854-04
1DN45	75974.	.2254+03	.1228+03	.1936-05	.4716+03	.2768+05	.3858-04

@2

FLUID DN-600 CAP 4, 210 F

RUN	P3	VISCP	NSRATE	REC	DELTAP	TAUDYN	REYN
2DN01	5212.	.6834-01	.2527+05	.7586-01	.2942+02	.1727+04	.2423+02
2DN02	5212.	.7532-01	.4117+05	.2014+00	.5285+02	.3171+04	.3582+02
2DN03	5212.	.7208-01	.2511+05	.7489-01	.3085+02	.1810+04	.2283+02
2DN04	5212.	.7997-01	.5021+05	.2996+00	.6841+02	.4015+04	.4115+02
2DN05	5212.	.8002-01	.4302+05	.2199+00	.5865+02	.3442+04	.3523+02
2DN06	11342.	.1312+00	.1554+05	.2869-01	.3472+02	.2038+04	.7764+01
2DN07	11308.	.1182+00	.4064+05	.1963+00	.8185+02	.4806+04	.2253+02
2DN08	11308.	.1118+00	.4064+05	.1963+00	.7741+02	.4544+04	.2383+02
2DN09	11308.	.1198+00	.2449+05	.7128-01	.4999+02	.2934+04	.1340+02
2DN10	11308.	.1187+00	.4031+05	.1931+00	.8152+02	.4785+04	.2226+02
2DN11	20318.	.2125+00	.1987+05	.4691-01	.7195+02	.4223+04	.6127+01
2DN12	20318.	.3043+00	.9797+04	.1140-01	.5080+02	.2982+04	.2110+01
2DN13	20318.	.2340+00	.8634+04	.8857-02	.3442+02	.2020+04	.2418+01
2DN14	20318.	.2212+00	.1319+05	.2066-01	.4969+02	.2916+04	.3907+01
2DN15	20318.	.2140+00	.2590+05	.7972-01	.9444+02	.5543+04	.7932+01
2DN17	30033.	.4687+00	.5163+04	.3167-02	.4123+02	.2420+04	.7218+00
2DN18	30033.	.4027+00	.1327+05	.2092-01	.9103+02	.5343+04	.2160+01
2DN19	30033.	.4137+00	.1328+05	.2094-01	.9357+02	.5492+04	.2103+01
2DN20	30033.	.4096+00	.8854+04	.9314-02	.6179+02	.3627+04	.1416+01
2DN21	39015.	.7484+00	.1058+05	.1329-01	.1349+03	.7916+04	.9262+00
2DN23	39015.	.7995+00	.6319+04	.4744-02	.8603+02	.5052+04	.5180+00
2DN24	39015.	.7863+00	.4815+04	.2754-02	.6456+02	.3786+04	.4013+00
2DN25	39015.	.8410+00	.5073+04	.3053-02	.7270+02	.4267+04	.3953+00
2DN26	49042.	.1276+01	.6319+04	.4744-02	.1374+03	.8065+04	.3245+00
2DN27	49042.	.1245+01	.5015+04	.2988-02	.1064+03	.6246+04	.2639+00
2DN28	49042.	.1239+01	.6575+04	.5136-02	.1387+03	.8143+04	.3479+00
2DN30	49042.	.1294+01	.5868+04	.4091-02	.1294+03	.7595+04	.2971+00
2DN31	62788.	.2224+01	.3606+04	.1545-02	.1365+03	.8019+04	.1063+00
2DN32	62788.	.2410+01	.5879+04	.4107-02	.2414+03	.1417+05	.1599+00
2DN33	62788.	.2233+01	.6365+04	.4814-02	.2421+03	.1421+05	.1868+00
2DN34	61873.	.2255+01	.6100+04	.4422-02	.2343+03	.1375+05	.1773+00
2DN35	62173.	.2283+01	.6984+04	.5795-02	.2716+03	.1594+05	.2005+00
2DN36	71482.	.3419+01	.4845+04	.2789-02	.2822+03	.1657+05	.9285-01
2DN37	71482.	.3388+01	.3324+04	.1313-02	.1919+03	.1126+05	.6430-01
2DN38	71330.	.3516+01	.3464+04	.1442-02	.2087+03	.1225+05	.6495-01
2DN39	71330.	.3450+01	.5156+04	.3159-02	.3030+03	.1779+05	.9797-01
2DN40	71330.	.3410+01	.3987+04	.1888-02	.2316+03	.1359+05	.7663-01
2DN41	78804.	.4779+01	.4390+04	.2290-02	.3574+03	.2098+05	.6020-01
2DN42A	76516.	.4301+01	.4312+04	.2209-02	.3160+03	.1855+05	.6569-01
2DN43	77431.	.4971+01	.1672+04	.3323-03	.1416+03	.8314+04	.2205-01
2DN44	77431.	.5072+01	.1769+04	.3718-03	.1529+03	.8973+04	.2286-01

@2

FLUID DN-600 CAP 4, 300 F

RUN	PJ	VISCP	WSRATE	KEC	DELTAP	TUDYN	REYN
3DN01	5258.	.3639-01	.8925+05	.8697+00	.5532+02	.3247+04	.1478+03
3DN02	5258.	.3390-01	.5143+05	.2888+00	.2970+02	.1743+04	.9138+02
3DN03	5258.	.2941-01	.2319+05	.5674-01	.1162+02	.6820+03	.4751+02
3DN04	5221.	.3136-01	.3449+05	.1299+00	.1872+02	.1089+04	.6519+02
3DN05	5258.	.3139-01	.4622+05	.2333+00	.2472+02	.1451+04	.8868+02
3DN06	11176.	.4143-01	.3445+05	.1296+00	.2432+02	.1427+04	.5010+02
3DN07	11176.	.4319-01	.3563+05	.1386+00	.2622+02	.1539+04	.4969+02
3DN08	11176.	.4211-01	.1844+05	.3711-01	.1323+02	.7764+03	.2637+02
3DN09	11251.	.4537-01	.2271+05	.5634-01	.1756+02	.1031+04	.3015+02
3DN10	11326.	.4953-01	.3493+05	.1332+00	.2947+02	.1730+04	.4248+02
3DN11	19716.	.7159-01	.1583+05	.2737-01	.1931+02	.1133+04	.1332+02
3DN13	19657.	.7040-01	.1567+05	.2652-01	.1880+02	.1103+04	.1341+02
3DN14	19598.	.6775-01	.1525+05	.2539-01	.1760+02	.1033+04	.1356+02
3DN15	19539.	.7302-01	.1993+05	.4338-01	.2480+02	.1455+04	.1644+02
3DN16	28955.	.1210+00	.8160+04	.7272-02	.1682+02	.9876+03	.4062+01
3DN17	28955.	.1144+00	.9041+04	.8926-02	.1762+02	.1034+04	.4760+01
3DN18	28955.	.1134+00	.9616+04	.1010-01	.1858+02	.1091+04	.5107+01
3DN19	28955.	.1249+00	.1341+05	.1963-01	.2854+02	.1675+04	.6464+01
3DN20	28955.	.1201+00	.8634+04	.8141-02	.1767+02	.1037+04	.4330+01
3DN21	39640.	.2092+00	.7946+04	.6894-02	.2832+02	.1662+04	.2288+01
3DN22	39490.	.1890+00	.1126+05	.1384-01	.3624+02	.2127+04	.3589+01
3DN23	39640.	.2122+00	.1059+05	.1226-01	.3831+02	.2249+04	.3007+01
3DN24	39640.	.2095+00	.1064+05	.1236-01	.3798+02	.2229+04	.3059+01
3DN25	39340.	.2255+00	.9491+04	.9837-02	.3646+02	.2140+04	.2535+01
3DN26	49227.	.3311+00	.9547+04	.9953-02	.5385+02	.3161+04	.1737+01
3DN27	49078.	.2919+00	.6947+04	.5269-02	.3455+02	.2028+04	.1433+01
3DN28	49078.	.3052+00	.5068+04	.2804-02	.2635+02	.1547+04	.1000+01
3DN29	49078.	.1949+00	.6194+04	.4189-02	.2057+02	.1207+04	.1914+01
3DN30	49227.	.3154+00	.6692+04	.4869-02	.3596+02	.2111+04	.1278+01
3DN31	59415.	.4530+00	.6272+04	.4295-02	.4840+02	.2841+04	.8339+00
3DN32	59415.	.4737+00	.3593+04	.1410-02	.2900+02	.1702+04	.4569+00
3DN33	59415.	.4646+00	.4290+04	.2009-02	.3395+02	.1993+04	.5562+00
3DN34	59415.	.4886+00	.2561+04	.7162-03	.2132+02	.1251+04	.3157+00
3DN35	59415.	.5060+00	.1491+04	.2427-03	.1285+02	.7543+03	.1775+00
3DN36	70051.	.6589+00	.4851+04	.2569-02	.5445+02	.3196+04	.4434+00
3DN37	70051.	.7365+00	.4027+04	.1771-02	.5053+02	.2966+04	.3294+00
3DN38	70051.	.7284+00	.3542+04	.1370-02	.4395+02	.2580+04	.2929+00
3DN39	70201.	.6654+00	.4789+04	.2504-02	.5429+02	.3186+04	.4335+00
3DN40	81137.	.1036+01	.4254+04	.1976-02	.7510+02	.4408+04	.2473+00
3DN41	81137.	.1071+01	.5282+04	.3046-02	.9642+02	.5659+04	.2969+00
3DN42	80688.	.1115+01	.4430+04	.2143-02	.8417+02	.4940+04	.2393+00
3DN43	80688.	.1040+01	.4284+04	.2004-02	.7589+02	.4454+04	.2481+00
3DN44	80688.	.1066+01	.3416+04	.1274-02	.6201+02	.3639+04	.1931+00
3DN45	81137.	.1209+01	.4383+04	.2097-02	.9027+02	.5299+04	.2184+00

**********AVERAGED DATA POINTS**********

FLUID DN-600 CAP 4, 100 F

P (PSI)	V (CP)
.00000	.25530+02
.52258+04	.48628+02
.11697+05	.91855+02
.23492+05	.30600+03
.32140+05	.55091+03
.38055+05	.11167+04
.47659+05	.25925+04
.59076+05	.63957+04
.68399+05	.11905+05
.75974+05	.20482+05

ALPHA STAR= .10911-03
ALPHA OT= .63813-04 x2.3o3

FLUID DN-600 CAP 4, 210 F

P (PSI)	V (CP)
.00000	.40500+01
.52124+04	.75148+01
.11315+05	.11994+02
.20318+05	.22042+02
.30033+05	.42368+02
.39015+05	.79381+02
.49042+05	.12636+03
.62483+05	.22808+03
.71391+05	.34365+03
.77545+05	.47809+03

ALPHA STAR= .86186-04
ALPHA OT= Hand Calculated

FLUID DN-600 CAP 4, 300 F

P (PSI)	V (CP)
.00000	.18060+01
.52509+04	.32568+01
.11221+05	.44324+01
.19627+05	.70669+01
.28955+05	.11878+02
.39550+05	.20907+02
.49128+05	.30416+02
.59415+05	.47717+02
.70089+05	.69728+02
.80912+05	.10895+03

ALPHA STAR= .69710-04
ALPHA OT= Hand Calculated

2 **********RAW DATA POINTS**********

FLUID DN-600

RUN	P3	VISCP	NSRATE	REC	DELTAP	TAUDYN	REYN
DN201	12031.	.8987+00	.6606+06	.3636+02	.4848+03	.5871+06	.3417+02
DN202	12031.	.8137+00	.8949+06	.6673+02	.6013+03	.7282+06	.5055+02
DN203	11919.	.7631+00	.1244+07	.1290+03	.7839+03	.9494+06	.7494+02
DN204	11882.	.7563+00	.1174+07	.1148+03	.7446+03	.9018+06	.7022+02
DN205	11861.	.8082+00	.1049+07	.9173+02	.7002+03	.8480+06	.5967+02
DN206	11882.	.1067+01	.1588+06	.2101+01	.1399+03	.1694+06	.6839+01
DN207	12203.	.1187+01	.6957+06	.4033+02	.6818+03	.8257+06	.2694+02
DN208	11071.	.9963+00	.1004+06	.8403+00	.8261+02	.1000+06	.4633+01
DN209	10958.	.9061+00	.3305+06	.9101+01	.2472+03	.2994+06	.1676+02
DN210	11071.	.7352+00	.1491+07	.1853+03	.9053+03	.1096+07	.9324+02
DN211	11222.	.8631+00	.1119+07	.1043+03	.7974+03	.9656+06	.5958+02
DN212	12127.	.8269+00	.1088+07	.9871+02	.7432+03	.9001+06	.6050+02
1DN46	91212.	.5294+03	.5246+03	.2293-04	.2294+03	.2778+06	.4555-04
1DN47	91212.	.5453+03	.5515+03	.2535-04	.2485+03	.3009+06	.4646-04
1DN48	91212.	.5766+03	.6117+03	.3118-04	.2923+03	.3540+06	.4860-04
1DN49	91514.	.5142+03	.7162+03	.4274-04	.3041+03	.3682+06	.6403-04
1DN50	91665.	.5716+03	.4181+03	.1456-04	.1973+03	.2390+06	.3362-04
1DN51	91061.	.6283+03	.3712+03	.1148-04	.1926+03	.2332+06	.2716-04
10DN6.9	96275.	.7220+03	.4635+03	.1790-04	.2764+03	.3347+06	.2951-04
10DN6.10	96275.	.8704+03	.6693+03	.3733-04	.4811+03	.5826+06	.3534-04
10DN6.11	96275.	.9195+03	.6039+03	.3039-04	.4585+03	.5553+06	.3019-04
10DN6.12	96275.	.9376+03	.6646+03	.3681-04	.5146+03	.6231+06	.3258-04
10DN6.13	96275.	.9019+03	.1024+04	.8734-04	.7624+03	.9233+06	.5218-04
10DN6.14	95371.	.8552+03	.1519+04	.1924-03	.1073+04	.1299+07	.8166-04
10DN6.15	95371.	.8347+03	.1627+04	.2206-03	.1122+04	.1358+07	.8960-04
10DN6.16	95522.	.9418+03	.1020+04	.8663-04	.7929+03	.9603+06	.4976-04
10DN6.17	95371.	.7388+03	.2417+03	.4867-05	.1474+03	.1785+06	.1504-04
10DN6.18	95371.	.9473+03	.2109+03	.3705-05	.1649+03	.1997+06	.1023-04
10DN6.19	96577.	.9457+03	.1030+04	.8842-04	.8044+03	.9742+06	.5006-04

FLUID FN-2961 CAP 4, 100 F

RUN	P3	VISCP	NSRATE	KEC	DELTAP	TAUDYN	REYN
FN01	5274.	.1683+01	.2835+04	.1059-02	.8130+02	.4772+04	.1224+00
FN02	5274.	.1758+01	.3829+04	.1931-02	.1147+03	.6730+04	.1583+00
FN03	5274.	.1848+01	.4058+04	.2169-02	.1278+03	.7500+04	.1596+00
FN04	5274.	.1723+01	.2675+04	.6428-03	.7853+02	.4609+04	.1128+00
FN06	5274.	.1741+01	.4737+04	.2956-02	.1405+03	.8247+04	.1977+00
FN07	11552.	.5544+01	.1620+04	.3457-03	.1530+03	.8982+04	.2123-01
FN08	11552.	.4972+01	.1482+04	.2891-03	.1255+03	.7366+04	.2165-01
FN09	11552.	.5234+01	.2862+04	.1079-02	.2552+03	.1498+05	.3973-01
FN10	11552.	.5103+01	.1354+04	.2413-03	.1177+03	.6907+04	.1927-01
FN11	11552.	.5145+01	.1238+04	.2184-03	.1129+03	.6625+04	.1818-01
FN12	11552.	.5150+01	.3739+04	.1841-02	.3280+03	.1925+05	.5275-01
FN14	20284.	.1622+02	.5468+03	.3938-04	.1511+03	.8870+04	.2449-02
FN15	20284.	.1545+02	.6608+03	.5752-04	.1739+03	.1021+05	.3106-02
FN16	20284.	.1540+02	.1069+04	.1506-03	.2805+03	.1646+05	.5045-02
FN17	20284.	.1597+02	.4302+03	.2438-04	.1170+03	.6869+04	.1958-02
FN18	30128.	.6703+02	.3767+03	.1869-04	.4302+03	.2525+05	.4083-03
FN19	30128.	.7127+02	.4894+03	.3155-04	.5943+03	.3488+05	.4990-03
FN20	30128.	.6328+02	.2351+03	.7279-05	.2535+03	.1488+05	.2699-03
FN21	30128.	.6657+02	.3176+03	.1328-04	.3602+03	.2114+05	.3466-03
FN22	30128.	.6416+02	.5884+03	.4561-04	.6432+03	.3775+05	.6664-03
FN23	39728.	.2203+03	.1602+03	.3378-05	.6010+03	.3527+05	.5283-04
FN25	39728.	.2273+03	.1201+03	.1900-05	.4651+03	.2730+05	.3840-04
FN27	39728.	.2449+03	.1178+03	.1829-05	.4917+03	.2886+05	.3496-04

1349017

FLUID FN-2961 CAP 4, 210 F

RUN	P3	VISCP	NSRATE	KEC	DELTAP	TAUDYN	REYN
FN.01	5293.	.1198+00	.1010+05	.1244-01	.2061+02	.1209+04	.5672+01
FN.02	5312.	.1321+00	.6551+04	.5235-02	.1474+02	.8652+03	.3338+01
FN.03	5334.	.1155+00	.1262+05	.2006-01	.2525+02	.1481+04	.7470+01
FN.04	5330.	.1278+00	.1092+05	.1454-01	.2377+02	.1395+04	.5750+01
FN.05	5330.	.1281+00	.1146+05	.1602-01	.2501+02	.1468+04	.6020+01
FN06	11807.	.2350+00	.8611+04	.9044-02	.3447+02	.2023+04	.2466+01
FN07	11807.	.2435+00	.2130+05	.5532-01	.8836+02	.5186+04	.5883+01
FN08	11869.	.2510+00	.1933+05	.4558-01	.8265+02	.4851+04	.5182+01
FN09	11869.	.2495+00	.6973+04	.5930-02	.2964+02	.1740+04	.1880+01
FN10	11869.	.2592+00	.1859+05	.4217-01	.8211+02	.4819+04	.4827+01
FN11	21739.	.6314+00	.8143+04	.8087-02	.8759+02	.5141+04	.8677+00
FN13	21739.	.6277+00	.7452+04	.6773-02	.7969+02	.4677+04	.7988+00
FN14	21739.	.6519+00	.4641+04	.2627-02	.5154+02	.3025+04	.4790+00
FN15	21739.	.6394+00	.5618+04	.3850-02	.6120+02	.3592+04	.5912+00
FN16	21624.	.6602+00	.7084+04	.6122-02	.7968+02	.4677+04	.7220+00
FN17	31593.	.1758+01	.3910+04	.1864-02	.1171+03	.6873+04	.1496+00
FN18	31450.	.1709+01	.2682+04	.8774-03	.7810+02	.4584+04	.1056+00
FN19	31450.	.1552+01	.2565+04	.8024-03	.6785+02	.3982+04	.1112+00
FN21	31383.	.1640+01	.2197+04	.5889-03	.6138+02	.3603+04	.9016-01
FN22	41601.	.3738+01	.2265+04	.6255-03	.1442+03	.8465+04	.4076-01
FN23	41601.	.3917+01	.3562+04	.1548-02	.2377+03	.1395+05	.6119-01
FN24	41601.	.3864+01	.5502+04	.3692-02	.3622+03	.2126+05	.9580-01
FN25	41601.	.4047+01	.4012+04	.1964-02	.2766+03	.1624+05	.6671-01
FN26	41601.	.4083+01	.8794+04	.9433-02	.6116+03	.3591+05	.1449+00
FN27	51048.	.8758+01	.2749+04	.9218-03	.4102+03	.2408+05	.2112-01
FN28	51048.	.9010+01	.2345+04	.6709-03	.3600+03	.2113+05	.1751-01
FN29	51048.	.9754+01	.2683+04	.8782-03	.4459+03	.2617+05	.1851-01
FN30	51048.	.9145+01	.2012+04	.4940-03	.3135+03	.1840+05	.1481-01
FN31	51048.	.9895+01	.2594+04	.8210-03	.4374+03	.2567+05	.1764-01
FN32	58504.	.1808+02	.1368+04	.2282-03	.4215+03	.2473+05	.5089-02
FN33	58504.	.1684+02	.1251+04	.1910-03	.3590+03	.2107+05	.5000-02
FN34	58353.	.1555+02	.9385+03	.1074-03	.2487+03	.1460+05	.4060-02
FN35	58353.	.1667+02	.8591+03	.9002-04	.2440+03	.1432+05	.3467-02

FLUID FN-2961 CAP 4, 300 F

RUN	P3	VISCP	NSRATE	KEC	DELTAP	TAUDYN	REYN
FN29.500	5328.	.4615-01	.2995+05	.1004+00	.2355+02	.1382+04	.4008+02
FN 29.50	5328.	.4719-01	.3442+05	.1327+00	.2767+02	.1624+04	.4505+02
FN 29.50	5328.	.5073-01	.3584+05	.1438+00	.3098+02	.1818+04	.4364+02
FN 29.50	5328.	.4634-01	.3401+05	.1295+00	.2685+02	.1576+04	.4533+02
FN01	12109.	.8211-01	.2984+05	.9974-01	.4175+02	.2450+04	.2245+02
FN02	12109.	.8120-01	.2303+05	.5938-01	.3185+02	.1870+04	.1752+02
FN03	12109.	.9085-01	.2048+05	.4696-01	.3170+02	.1860+04	.1392+02
FN04	12109.	.8960-01	.1021+05	.1168-01	.1559+02	.9149+03	.7040+01
FN05	12109.	.9101-01	.1065+05	.1270-01	.1651+02	.9691+03	.7228+01
FN06	21184.	.1628+00	.7033+04	.5540-02	.1951+02	.1145+04	.2668+01
FN07	21184.	.1405+00	.6583+04	.4853-02	.1576+02	.9251+03	.2894+01
FN08	21184.	.1359+00	.8777+04	.8628-02	.2032+02	.1192+04	.3991+01
FN09	21184.	.1395+00	.1010+05	.1142-01	.2400+02	.1409+04	.4472+01
FN10	31570.	.2991+00	.8000+04	.7168-02	.4077+02	.2393+04	.1652+01
FN12	31570.	.3107+00	.4624+04	.2395-02	.2448+02	.1437+04	.9194+00
FN13	31570.	.3325+00	.3163+04	.1120-02	.1792+02	.1052+04	.5876+00
FN14	31570.	.2915+00	.4166+04	.1943-02	.2069+02	.1214+04	.8828+00
FN15	41653.	.5527+00	.2073+04	.4814-03	.1952+02	.1146+04	.2318+00
FN16	41653.	.5680+00	.3389+04	.1286-02	.3279+02	.1925+04	.3686+00
FN18	41653.	.5871+00	.4152+04	.1931-02	.4153+02	.2438+04	.4370+00
FN19	41653.	.6153+00	.5329+04	.3181-02	.5587+02	.3279+04	.5350+00
FN20	41841.	.7035+00	.5434+04	.3307-02	.6512+02	.3823+04	.4772+00
FN21	41841.	.6952+00	.6374+04	.4551-02	.7550+02	.4431+04	.5664+00
FN22	41841.	.6549+00	.5030+04	.2833-02	.5612+02	.3294+04	.4745+00
FN24	41841.	.6764+00	.5636+04	.3557-02	.6494+02	.3812+04	.5147+00
FN25	49387.	.1072+01	.2749+04	.8464-03	.5022+02	.2948+04	.1584+00
FN26	49387.	.1064+01	.3222+04	.1162-02	.5840+02	.3428+04	.1870+00
FN27	49387.	.1062+01	.3419+04	.1309-02	.6189+02	.3633+04	.1988+00
FN28	49387.	.1090+01	.5567+04	.3471-02	.1034+03	.6069+04	.3154+00
FN29	49387.	.1146+01	.3405+04	.1298-02	.6649+02	.3903+04	.1835+00
FN30	61417.	.2337+01	.1808+04	.3662-03	.7201+02	.4227+04	.4779-01
FN32	61417.	.2362+01	.2079+04	.4841-03	.8368+02	.4911+04	.5436-01

**********AVERAGED DATA POINTS**********

FLUID FN-2961 CAP 4, 100 F

P (PSI)	V (CP)
.00000	.68090+02
.52743+04	.17505+03
.11552+05	.51913+03
.20284+05	.15759+04
.30128+05	.66461+04
.39728+05	.23081+05

ALPHA STAR= .17288-03
ALPHA OT= .92126-04 x 2.3e3

FLUID FN-2961 CAP 4, 210 F

P (PSI)	V (CP)
.00000	.68100+01
.53197+04	.12464+02
.11844+05	.24763+02
.21716+05	.64210+02
.31469+05	.16648+03
.41601+05	.39297+03
.51048+05	.93122+03
.58428+05	.16787+04

ALPHA STAR= .10648-03
ALPHA OT= .54490-04 x 2.3e3

FLUID FN-2961 CAP 4, 300 F

P (PSI)	V (CP)
.00000	.26500+01
.53281+04	.47606+01
.12109+05	.86955+01
.21184+05	.14468+02
.31570+05	.30847+02
.41747+05	.63162+02
.49387+05	.10871+03
.61417+05	.23499+03

ALPHA STAR= .87259-04
ALPHA OT= .55842-04 x 2.3e3

********************RAW DATA POINTS**********

FLUID FN-2961

RUN	P3	VISCP	NSRATE	KEC	DELTAP	TAUDYN	REYN
FN 29.1	11980.	.4944+01	.1627+05	.2263-01	.6640+02	.8042+05	.1552+00
FN29.2	11712.	.4219+01	.1439+06	.1772+01	.5015+03	.6071+06	.1610+01
FN29.3	12363.	.3846+01	.2114+06	.3824+01	.6715+03	.8133+06	.2594+01
FN 29.4	10620.	.3612+01	.2558+06	.5596+01	.7629+03	.9239+06	.3341+01
FN 29.5	11415.	.3897+01	.1519+06	.1974+01	.4088+03	.5919+06	.1839+01
FN 29.6	12059.	.3893+01	.1921+06	.3157+01	.6175+03	.7478+06	.2329+01
FN29.7	12437.	.2889+01	.5200+06	.2313+02	.1240+04	.1502+07	.8495+01
FN 29.20	11980.	.4486+01	.6781+05	.3933+00	.2512+03	.3042+06	.7133+00
FN 29.20	11980.	.4627+01	.6781+05	.3933+00	.2591+03	.3138+06	.6915+00
FN 29.21	11865.	.4782+01	.5696+05	.2775+00	.2249+03	.2724+06	.5621+00
FN 29.23	11827.	.4543+01	.5471+05	.2560+00	.2052+03	.2485+06	.5681+00
FN 29.15	47304.	.3307+03	.1342+03	.1540-05	.3665+02	.4436+05	.1914-04
FN 29.14	47304.	.2533+03	.4523+03	.1750-04	.9462+02	.1146+06	.8425-04
FN 29.13	47603.	.2076+03	.7892+03	.5327-04	.1353+03	.1639+06	.1793-03
FN 29.12	47603.	.1949+03	.1144+04	.1119-03	.1840+03	.2229+06	.2769-03
FN 29.8	50373.	.3568+03	.2861+04	.6999-03	.8427+03	.1021+07	.3783-03
FN 29.9	50373.	.5443+03	.2489+04	.5299-03	.1119+04	.1355+07	.2158-03
FN 29.10	49916.	.5403+03	.1856+04	.2945-03	.8276+03	.1003+07	.1620-03
FN 29.11	49916.	.5495+03	.2559+04	.5602-03	.1161+04	.1406+07	.2197-03
FN 29.30	54577.	.2253+04	.2924+03	.7312-05	.5436+03	.6586+06	.6124-05
FN 29.31	55760.	.1153+04	.6342+03	.3440-04	.6037+03	.7311+06	.2596-04
FN 29.31	55760.	.1218+04	.5101+03	.2226-04	.5126+03	.6210+06	.1977-04
FN 29.32	54577.	.1784+04	.3832+03	.1256-04	.5645+03	.6837+06	.1013-04
FN 29.33	55253.	.1159+04	.6600+03	.3726-04	.6314+03	.7647+06	.2688-04
FN 29.34	54577.	.1350+04	.7046+03	.4742-04	.8299+03	.1005+07	.2603-04
FN 29.35	54577.	.1404+04	.6234+03	.3325-04	.7229+03	.8755+06	.2095-04
FN 29.36	53901.	.1434+04	.5705+03	.2784-04	.6756+03	.8182+06	.1877-04
FN 29.37	55422.	.1221+04	.1018+04	.8857-04	.1026+04	.1242+07	.3934-04

@2

FLUID MCS-418 CAP 4, 100 F

RUN	P3	VISCP	NSRATE	KEC	DELTAP	TURBYN	REYN
M18.02	5328.	.6099+00	.7035+04	.8856-02	.7310+02	.4291+04	.1138+01
M18.03	5328.	.5177+00	.7299+04	.9553-02	.6438+02	.3779+04	.1391+01
M18.04	5328.	.4824+00	.8487+04	.1239-01	.6975+02	.4094+04	.1737+01
M18.05	5270.	.4933+00	.8815+04	.1391-01	.7409+02	.4349+04	.1764+01
M18.06	5270.	.5748+00	.8246+04	.1217-01	.8075+02	.4740+04	.1416+01
M18.07	10718.	.1006+01	.3715+04	.2469-02	.5365+02	.3736+04	.3646+00
M18.08	10718.	.9918+00	.4386+04	.3442-02	.7411+02	.4350+04	.4365+00
M18.10	10718.	.1017+01	.5035+04	.4536-02	.8725+02	.5121+04	.4586+00
M18.11	10718.	.9879+00	.7185+04	.9237-02	.1209+03	.7098+04	.7178+00
M18.12	21162.	.4650+01	.2366+04	.1002-02	.1874+03	.1100+05	.5022-01
M18.13	21162.	.5249+01	.1759+04	.5538-03	.1573+03	.9234+04	.3308-01
M18.14	21162.	.4792+01	.1787+04	.5714-03	.1459+03	.8562+04	.3681-01
M18.15	21162.	.5149+01	.1354+04	.3281-03	.1188+03	.6972+04	.2596-01
M18.16	21162.	.5078+01	.1794+04	.5759-03	.1552+03	.9110+04	.3487-01
M18.17	29388.	.2217+02	.4510+03	.3639-04	.1703+03	.9998+04	.2008-02
M18.18	29388.	.2090+02	.9501+03	.1615-03	.3383+03	.1986+05	.4487-02
M18.19	29388.	.2220+02	.8551+03	.1308-03	.3233+03	.1898+05	.3803-02
M18.21	29531.	.2022+02	.1572+04	.4424-03	.5417+03	.3179+05	.7676-02

FLUID MCS-419 CAP 4, 210 F

RUN	P3	VISCP	NSRATE	KEC	DELTAP	TAUDYN	REYN
M1801	5336.	.6095-01	.2533+05	.1064+00	.2630+02	.1544+04	.3801+02
M1802	5336.	.6516-01	.8604+04	.1227-01	.9552+01	.5606+03	.1207+02
M1803	5336.	.6616-01	.1607+05	.4279-01	.1811+02	.1063+04	.2221+02
M1804	5375.	.6785-01	.2356+05	.9219-01	.2725+02	.1600+04	.3178+02
M1805	5375.	.7000-01	.1215+05	.2447-01	.1449+02	.8504+03	.1537+02
M1806	10993.	.8302-01	.1952+05	.6380-01	.2775+02	.1629+04	.2161+02
M1807	10993.	.8579-01	.2270+05	.8546-01	.3319+02	.1948+04	.2420+02
MC1808	10993.	.8791-01	.2177+05	.7861-01	.3261+02	.1914+04	.2265+02
MC1809	10993.	.8367-01	.1195+05	.2367-01	.1703+02	.9999+03	.1306+02
MC1810	10993.	.8717-01	.2722+05	.1223+00	.4042+02	.2373+04	.2856+02
MC1811	19901.	.1632+00	.1205+05	.2419-01	.3359+02	.1972+04	.6767+01
MC12	19901.	.1547+00	.1251+05	.2722-01	.3596+02	.2111+04	.7114+01
M1813	19901.	.1613+00	.9345+04	.1448-01	.2568+02	.1507+04	.5300+01
MC14	19901.	.1755+00	.1460+05	.3532-01	.4364+02	.2562+04	.7605+01
M1815	19712.	.1578+00	.1521+05	.3837-01	.4090+02	.2401+04	.8816+01
M1816	29473.	.3115+00	.4310+04	.3080-02	.2287+02	.1343+04	.1265+01
M1817	29700.	.3190+00	.6736+04	.7523-02	.3661+02	.2149+04	.1931+01
M1818	29511.	.3105+00	.6043+04	.6054-02	.3197+02	.1876+04	.1780+01
M1819	29700.	.3179+00	.4769+04	.3770-02	.2583+02	.1516+04	.1372+01
M1820	29700.	.3153+00	.7853+04	.1023-01	.4219+02	.2476+04	.2278+01

FLUID MCS-418 CAP 4, 300 F

RUN	P3	VISCP	SRATE	KEC	DELTAP	TAUDYN	REYN
M1801	5270.	.2751-01	.3236+05	.1612+00	.1517+02	.8902+03	.9986+02
M1802	5270.	.2865-01	.1960+05	.5909-01	.9565+01	.5614+03	.5806+02
M1804	5270.	.2712-01	.2800+05	.1206+00	.1294+02	.7594+03	.8763+02
M1811	20370.	.7408-01	.1540+05	.3656-01	.1944+02	.1141+04	.1765+02
M1812	20370.	.6743-01	.1356+05	.2831-01	.1558+02	.9145+03	.1708+02
M1813	20370.	.6062-01	.1356+05	.2831-01	.1401+02	.8223+03	.1899+02
M1815	29187.	.1074+00	.7168+04	.7774-02	.1301+02	.7636+03	.5616+01
M1817	29187.	.1051+00	.9872+04	.1500-01	.1768+02	.1038+04	.7973+01
M1818	29187.	.1052+00	.1817+05	.5077-01	.3256+02	.1911+04	.1465+02
M1819	29187.	.1006+00	.2344+05	.3452-01	.4016+02	.2357+04	.1978+02

160841

02

**********AVERAGED DATA POINTS**********

FLUID MCS-418 CAP 4, 100 F

P (PSI)	V (CP)
.00000	.29600+02
.53049+04	.53562+02
.10710+05	.10007+03
.21162+05	.49936+03
.29424+05	.21372+04

ALPHA STAR= .12353-03
ALPHA OT= .11678-03

FLUID MCS-418 CAP 4, 210 F

P (PSI)	V (CP)
.00000	.46550+01
.53514+04	.66024+01
.10993+05	.85513+01
.19865+05	.16451+02
.29617+05	.31456+02

ALPHA STAR AND ALPHA OT MUST BE CALCULATED BY HAND

FLUID MCS-418 CAP 4, 300 F

P (PSI)	V (CP)
.00000	.22000+01
.52700+04	.27759+01
.20370+05	.67372+01
.29187+05	.10458+02

ALPHA STAR= .54761-04
ALPHA OT= .42177-04

**********RAW DATA POINTS**********

FLUID MCS-418

RUN	P3	VISCP	NSRATE	KEC	DELTAP	TAUDYN	REYN
418.1	11592.	.1312+01	.8961+05	.9333+00	.9709+02	.1176+06	.4578+01
418.2	10747.	.1085+01	.7382+05	.6334+00	.6617+02	.8014+05	.4360+01
418.3	10747.	.1078+01	.1069+06	.1328+01	.9516+02	.1153+06	.6355+01
418.4	10705.	.1040+01	.1141+06	.1512+01	.9795+02	.1186+06	.7030+01
418.5	11676.	.1296+01	.9049+05	.7529+00	.8615+02	.1043+06	.3981+01
418.6	11549.	.1248+01	.2075+06	.5002+01	.2138+03	.2589+06	.1066+02
418.7	11423.	.1019+01	.7202+06	.6028+02	.6060+03	.7339+06	.4530+02
418.8	11254.	.1009+01	.8733+06	.8864+02	.7280+03	.8816+06	.5546+02
418.9	11169.	.9653+00	.8244+06	.7899+02	.6572+03	.7959+06	.5475+02
418.10	11381.	.1141+01	.4220+06	.2070+02	.3975+03	.4814+06	.2372+02
418.11	42745.	.3724+03	.1155+04	.1551-03	.3553+03	.4303+06	.1989-03
418.16	42913.	.4193+03	.7652+03	.7164-04	.2719+03	.3292+06	.1200-03
418.15	42745.	.4111+03	.1610+04	.3013-03	.5466+03	.6619+06	.2511-03
418.12	42745.	.3560+03	.2123+04	.5239-03	.6941+03	.7558+06	.3823-03
418.14	42913.	.5816+03	.1046+04	.1271-03	.5021+03	.6081+06	.1152-03
418.13	42576.	.4040+03	.2010+04	.4697-03	.6707+03	.8122+06	.3190-03

FLUID MCS-460 CAP 4, 100 F

RUN	P3	VISCP	NSRATE	KEC	DELTAP	TAUDYN	REYN
M6.04	5341.	.9444+00	.5018+04	.3501-02	.8075+02	.4740+04	.4075+00
M6.05	5284.	.9973+00	.3821+04	.2030-02	.6492+02	.3811+04	.2938+00
M6.06	5322.	.9587+00	.4222+04	.2478-02	.6896+02	.4048+04	.3377+00
M6.07	5322.	.1194+01	.3906+04	.2121-02	.7946+02	.4665+04	.2508+00
M6.09	11653.	.5101+01	.1456+04	.2955-03	.1267+03	.7437+04	.2192-01
M6.10	11691.	.5135+01	.1339+04	.2493-03	.1176+03	.6903+04	.1992-01
M6.11	11996.	.5277+01	.2677+04	.9966-03	.2407+03	.1413+05	.3691-01
M6.12	11996.	.5386+01	.3455+04	.1660-02	.3171+03	.1861+05	.4919-01
M6.13	11768.	.4551+01	.3497+03	.1700-04	.2711+02	.1591+04	.5893-02
M6.14	19610.	.5464+02	.2501+03	.8698-05	.2329+03	.1367+05	.3510-03
M6.16	19330.	.4851+02	.1514+03	.3165-05	.1251+03	.7342+04	.2392-03
M6.15	19330.	.4995+02	.1871+03	.4856-05	.1592+03	.9345+04	.2872-03
M5.01	20509.	.3836+02	.3539+03	.1741-04	.2313+03	.1358+05	.7074-03
M6.02	20411.	.4026+02	.4921+03	.3366-04	.3375+03	.1981+05	.9372-03

FLUID MCS-460 CAP 4, 210 F

RUN	P3	VISCP	NSRATE	KEC	DELTAP	TSUDYN	REYN
M6.02	5371.	.6449-01	.2232+05	.6477-01	.2453+02	.1440+04	.2482+02
M6.03	5371.	.6302-01	.2177+05	.6164-01	.2336+02	.1372+04	.2478+02
M6.04	5371.	.5849-01	.2101+05	.5738-01	.2093+02	.1229+04	.2576+02
M6.05	5371.	.5391-01	.1930+05	.4845-01	.1773+02	.1041+04	.2568+02
M6.06	11551.	.1279+00	.1036+05	.1401-01	.2262+02	.1328+04	.5821+01
M6.07	11551.	.1368+00	.8314+04	.8936-02	.1936+02	.1137+04	.4359+01
M6.08	11551.	.1263+00	.7956+04	.8230-02	.1712+02	.1005+04	.4518+01
M6.09	11551.	.1281+00	.7506+04	.7324-02	.1636+02	.9612+03	.4203+01
M6.10	11588.	.1396+00	.1205+05	.1688-01	.2867+02	.1683+04	.6190+01
M6.011	19897.	.3822+00	.6963+04	.6303-02	.4534+02	.2661+04	.1306+01
M6.12	19850.	.3846+00	.3295+04	.1411-02	.2159+02	.1267+04	.6143+00
M6.13	19850.	.3973+00	.4076+04	.2160-02	.2759+02	.1620+04	.7356+00
M6.14	19897.	.3661+00	.6051+04	.4760-02	.3774+02	.2215+04	.1185+01
M6.15	19897.	.3621+00	.4403+04	.2520-02	.2716+02	.1594+04	.8720+00
M6.16	19897.	.3671+00	.8170+04	.8679-02	.5110+02	.2999+04	.1596+01

FLUID MCS-460 CAP 4, 300 F

RUN	P3	VISCP	NSRATE	KEC	DELTAP	TAUDYN	REYN
M6.01	5371.	.2576-01	.7450+05	.6580+00	.3269+02	.1919+04	.1692+03
M6.02	5371.	.2630-01	.3202+05	.1215+00	.1435+02	.8420+03	.7962+02
M6.03	5371.	.2656-01	.8017+05	.7621+00	.3626+02	.2130+04	.1974+03
M6.04	5371.	.2679-01	.7563+05	.6782+00	.3452+02	.2026+04	.1846+03
M6.05	5371.	.2887-01	.7583+05	.6782+00	.3720+02	.2183+04	.1713+03
M6.06	11514.	.4533-01	.3630+05	.1583+00	.2803+02	.1645+04	.5238+02
M6.07	11532.	.4835-01	.1629+05	.3145-01	.1342+02	.7874+03	.2203+02
M6.09	11626.	.4068-01	.2916+05	.1008+00	.2031+02	.1192+04	.4666+02
M6.10	11626.	.4693-01	.2491+05	.7360-01	.1992+02	.1169+04	.3472+02
M6.12	20411.	.7687-01	.2080+05	.5131-01	.2724+02	.1599+04	.1770+02
M6.13	20411.	.7650-01	.2824+05	.9455-01	.3690+02	.2160+04	.2414+02
M6.14	20411.	.7211-01	.1767+05	.3703-01	.2171+02	.1274+04	.1603+02
M6.15	20411.	.7509-01	.2390+05	.6773-01	.3058+02	.1795+04	.2082+02

©2 **********AVERAGED DATA POINTS**********

FLUID MCS-460 CAP 4, 100 F

P (PSI)	V (CP)
.00000	.34290+02
.53160+04	.96681+02
.11821+05	.50941+03
.19691+05	.46241+04

ALPHA STAR= .21457-03
ALPHA OT= .94145-04 ×2.3o3

FLUID MCS-460 CAP 4, 210 F

P (PSI)	V (CP)
.00000	.35200+01
.53707+04	.59976+01
.11558+05	.13173+02
.19882+05	.37659+02

ALPHA STAR= .11750-03
ALPHA OT= .40983-04 ×2.3o3

FLUID MCS-460 CAP 4, 300 F

P (PSI)	V (CP)
.00000	.16200+01
.53707+04	.26855+01
.11574+05	.45371+01
.20411+05	.75142+01

ALPHA STAR= .64744-04
ALPHA OT= .44901-04 ×2.3o3

**********RAW DATA POINTS**********

FLUID MCS-460

RUN	P3	VISCP	NSRATE	KEC	DELTAP	TAUDYN	REYN
460.01	11700.	.4309+01	.5622+05	.2854+00	.2000+03	.2423+06	.6498+00
460.02	11628.	.4164+01	.7787+05	.5474+00	.2678+03	.3243+06	.9312+00
460.03	11700.	.4274+01	.8578+05	.6644+00	.3028+03	.3667+06	.9995+00
460.04	11592.	.4043+01	.1057+06	.1006+01	.3527+03	.4271+06	.1302+01
460.05	12132.	.5204+01	.3447+05	.1073+00	.1481+03	.1794+06	.3299+00
460.06	12132.	.5003+01	.2700+05	.6583-01	.1116+03	.1351+06	.2688+00
460.07	12348.	.2630+01	.5241+06	.2480+02	.1138+04	.1379+07	.9922+01
460.08	11736.	.4161+01	.5896+05	.3138+00	.2026+03	.2453+06	.7056+00
460.09	12060.	.2209+01	.5667+06	.2899+02	.1034+04	.1252+07	.1277+02
460.11	12636.	.1395+01	.1117+07	.1127+03	.1287+04	.1558+07	.3989+02
460.12	11988.	.1869+01	.7213+06	.4697+02	.1113+04	.1347+07	.1923+02
460.13	12456.	.2040+01	.7859+06	.5576+02	.1324+04	.1603+07	.1918+02
460.20.1	20180.	.2627+02	.1735+05	.2718-01	.3764+03	.4558+06	.3289-01
460.20.0	19992.	.2607+02	.2218+05	.4442-01	.4774+03	.5782+06	.4238-01
460.20.0	19992.	.2822+02	.3052+05	.8408-01	.7111+03	.8612+06	.5385-01
460.20.0	20651.	.2879+02	.2818+05	.7168-01	.6699+03	.8113+06	.4873-01
460.20.0	20651.	.2159+02	.4309+05	.1677+00	.7789+03	.9433+06	.9805-01
460.20.0	20180.	.3274+02	.1579+05	.2252-01	.4270+03	.5171+06	.2402-01
460.20.0	20180.	.3517+02	.7284+04	.4791-02	.2115+03	.2562+06	.1032-01
460.30.0	30827.	.7741+03	.8392+03	.6359-04	.5364+03	.6496+06	.5399-04
60.30.02	30827.	.7954+03	.5774+03	.3010-04	.3792+03	.4592+06	.3615-04
60.30.03	31204.	.4603+03	.7343+03	.4868-04	.2791+03	.3380+06	.7946-04
60.30.04	31015.	.8593+03	.9537+03	.8211-04	.6767+03	.8195+06	.5527-04
60.30.05	31204.	.7367+03	.7386+03	.4926-04	.4494+03	.5442+06	.4993-04

013566 DECK

FLUID: DUPONT KRYTOX 143-AB (LOT 16)

TEMP. (DEG.F)	PRESS. (PSIG)	DENSITY (GM/CC)	VISCOSITY (POISE)	SHEAR STRESS (DYNE/SQ.CM.)	SHEAR RATE (1/SEC.)	CAP.
100	ATM	1.87	1.795	0	0	300
100	ATM	1.87	1.622	36130	22280	1
100	ATM	1.87	1.707	40970	24000	1
100	ATM	1.87	1.845	48080	26060	1
100	ATM	1.87	1.776	53640	30200	1
100	ATM	1.87	1.865	99890	53560	1
100	ATM	1.87	1.900	144400	76000	1
100	ATM	1.87	1.885	298700	158500	1
100	ATM	1.87	1.853	317900	171600	1
100	ATM	1.87	1.979	398300	201200	1
100	4918		7.888	24910	3150	1
100	4918		7.728	35430	4585	1
100	4918		7.874	35660	4229	1
100	4918		7.498	42400	5656	1
100	4918		7.737	57740	7592	1
100	4918		7.961	60610	7613	1
100	4918		7.368	63230	8582	1
100	4918		7.634	67750	8874	1
100	4918		7.413	83870	11310	1
100	4953		7.769	301300	38780	1
100	4953		7.594	438600	57750	1
100	4918		7.852	699000	89030	1
100	10190		25.04	21320	851.5	1
100	10190		24.58	33720	1372	1
100	10190		25.27	41680	1650	1
100	10190		24.68	45200	1832	1
100	10230		23.92	47650	1992	1
100	10190		24.45	54270	2219	1
100	10190		24.52	65000	2650	1
100	10190		24.98	94190	3771	1
100	10060		24.56	106600	4340	1
100	10190		24.09	133000	5521	1
100	10060		25.02	143300	5729	1
100	10020		25.10	181600	7233	1
100	10190		25.36	193000	7612	1
100	10060		25.10	196100	7812	1
100	10190		24.18	226700	9375	1
100	10060		24.18	233800	9672	1
100	10020		24.87	244200	9815	1
100	9915		25.23	407300	16150	1
100	10100		24.67	456400	18500	1
100	10060		25.16	567800	22570	1
100	10060		25.02	598900	23940	1
100	10060		24.54	615000	25060	1
100	10150		24.85	666300	26810	1
100	20170		169.0	71340	422.1	1
100	19840		167.6	91310	544.7	1
100	20170		160.0	102500	640.8	1
100	19720		151.7	119000	784.7	1
100	19840		170.5	126600	742.4	1

TEMP. (DEG.F)	PRESS. (PSIG)	DENSITY (GM/CC)	VISCOSITY (POISE)	SHEAR STRESS (DYNE/SQ.CM.)	SHEAR RATE (1/SEC.)	CAP. NO.
00	20170		162.2	159600	983.5	1
00	19840		161.4	176500	1094	1
00	20170		158.0	230200	1286	1
00	19840		164.9	227500	1379	1
00	19720		167.4	243100	1453	1
00	19840		157.2	249700	1588	1
100	30430		1341	194100	144.8	1
100	30430		1057	219400	207.6	1
100	30430		1082	488500	451.6	1
100	30430		1367	605500	442.9	1
100	30430		1280	738200	576.8	1
210	ATM	1.76	0.2020	0	0	150
210	ATM	1.76	0.2121	18370	86610	1
210	ATM	1.76	0.2041	21960	107600	1
210	ATM	1.76	0.1910	24740	129500	1
210	5096		0.6844	19710	28810	1
210	5062		0.6403	25810	40310	1
210	5062		0.6686	26380	39460	1
210	5062		0.6477	27480	42430	1
210	5096		0.6978	28960	41500	1
210	5096		0.6544	30420	46480	1
210	5062		0.6737	33050	49050	1
210	5062		0.6703	36450	54390	1
210	5062		0.6245	166700	266900	1
210	4958		0.6656	187400	281500	1
210	10310		2.269	16780	7396	1
210	10470		2.316	20380	8800	1
210	10310		2.233	22040	9868	1
210	10510		2.227	25950	11660	1
210	10470		2.158	28410	13160	1
210	10310		2.186	29140	13330	1
210	10470		2.286	31000	13560	1
210	10510		2.181	31050	14240	1
210	10510		2.262	34360	15190	1
210	10310		2.164	34560	15970	1
210	10470		2.128	35320	16160	1
210	10510		2.271	36140	15910	1
210	10470		2.100	38560	18370	1
210	10510		2.084	39860	19130	1
210	10470		2.098	49880	23710	1
210	10470		2.206	53140	24090	1
210	10470		2.112	77350	36620	1
210	10510		2.107	78130	37080	1
210	10470		2.223	94560	42540	1
210	10510		2.226	97300	43720	1
210	20080		7.481	34100	4558	1
210	20080		7.420	37090	4998	1
210	20080		7.365	47330	6426	1
210	20080		7.616	54040	7096	1
210	20080		7.275	86820	11930	1
210	20080		7.297	105600	14470	1

TEMP. (DEG.F)	PRESS. (PSIG)	DENSITY (GM/CC)	VISCOSITY (POISE)	SHEAR STRESS (DYNE/SQ.CM.)	SHEAR RATE (1/SEC.)	CAP.
210	30750		27.82	28500	1024	1
210	30590		27.84	33250	1194	1
210	30750		28.26	33700	1193	1
210	30750		27.85	33980	1220	1
210	30590		27.00	39650	1468	1
210	30590		27.44	44910	1637	1
210	30590		26.56	68950	2596	1
210	30590		27.58	76090	2759	1
210	30590		27.09	78150	2885	1
210	30590		26.12	90420	3462	1
210	30590		28.98	106700	3683	1
300	ATM	1.67	0.06900	0	0	150
300	ATM	1.67	0.07678	17610	229300	1
300	ATM	1.67	0.07067	18410	260600	1
300	5000		0.2594	14940	57580	1
300	5000		0.2403	17480	72740	1
300	5000		0.2352	17790	75620	1
300	5000		0.2345	18430	78610	1
300	5000		0.2383	19510	81900	1
300	5000		0.2382	19600	82260	1
300	5000		0.2597	22270	85740	1
300	5000		0.2491	23910	95970	1
300	10630		0.5839	18190	31140	1
300	10630		0.5873	18570	31610	1
300	10590		0.6329	21100	31760	1
300	10590		0.6519	26720	40980	1
300	10630		0.6071	28610	47130	1
300	10550		0.5923	31300	52820	1
300	10590		0.6037	43080	71350	1
300	10550		0.6515	77420	118800	1
300	20170		1.658	13250	7993	1
300	20170		1.565	14210	9081	1
300	20230		1.529	16190	10590	1
300	20170		1.687	18140	10750	1
300	20170		1.521	19510	12830	1
300	20170		1.675	23470	14010	1
300	20170		1.588	23990	15100	1
300	20170		1.588	27340	17220	1
300	20170		1.675	31280	18680	1
300	30120		4.619	13430	2908	1
300	30120		4.740	15750	3323	1
00	30120		4.740	15750	3323	
00	30120		4.639	17920	3863	
00	30120		4.490	19810	4412	
00	30120		4.445	21950	4938	

JXQT FNOV.X

**********AVERAGED DATA POI

FLUID: DUPONT KRYTOX 103 F

P (PSI)	V (CP)
.00000	.18230+03
.49238+04	.75930+03
.10120+05	.24755+04
.19938+05	.15272+05
.30430+05	.12254+06

ALPHA STAR= .2869+-03
ALPHA OT= .45129-03

FLUID: DUPONT KRYTOX 210 F

P (PSI)	V (CP)
.00000	.2 230+02
.50618+04	.66273+02
.10452+05	.21918+03
.20080+05	.74090+03
.30634+05	.27504+04

ALPHA STAR= .22344-03
ALPHA OT= .30170-03

FLUID: DUPONT KRYTOX 300 F

P (PSI)	V (CP)
.00000	.72150+01
.50000+04	.24434+02
.10595+05	.61390+02
.20177+05	.16098+03
.30120+05	.46122+03

ALPHA STAR= .20832-03
ALPHA OT= .36949-03

FLUID: MOBIL XRF-109E-3

MP. G.E)	PRESS. (PSIG)	DENSITY (GM/CC)	VISCOSITY (POISE)	SHEAR STRESS (DYNE/SQ.CM.)	SHEAR RATE (1/SEC.)	CAP. NO.
00	ATM	.8389	4.490	0	0	400
00	10720		17.79	19340	1087	1
100	10800		18.96	26100	1376	1
100	10760		18.26	28830	1579	1
100	10720		17.36	31090	1791	1
100	10800		17.80	31340	1761	1
100	10800		18.41	43090	2340	1
100	10800		18.04	47710	2645	1
100	10760		18.35	53470	2915	1
100	10920		16.77	54230	3235	1
100	10800		18.32	62280	3400	1
100	10840		17.44	75940	4354	1
100	10760		16.83	85170	5062	1
100	10350		17.48	85630	4898	1
100	10920		17.01	103700	6096	1
100	10840		17.01	107900	6345	1
100	10920		17.27	151800	8787	1
100	10430		14.79	166900	11290	1
100	10760		17.18	169200	98470	1
100	10310		14.20	204000	14370	1
100	10350		14.81	214300	14460	1
100	10430		13.75	219100	15940	1
100	10350		15.97	253900	15900	1
100	10350		14.95	269700	18040	1
100	10350		14.59	294100	20160	1
100	10350		14.21	338100	23790	1
100	10350		14.24	383800	26940	1
100	10350		13.87	387200	27920	1
100	10350		14.39	419400	29150	1
100	10350		13.37	427700	31990	1
100	10310		15.08	434700	28830	1
100	10310		13.93	474700	34070	1
100	10350		13.46	523100	38860	1
100	10350		11.69	1003000	85840	1
100	30300		128.2	41840	326.3	1
100	30200		126.1	60750	481.7	1
100	30300		129.7	60760	488.4	1
100	30100		123.1	66720	541.9	1
100	30100		118.4	83150	702.5	1
100	30300		129.8	87150	671.5	1
100	30100		126.4	93100	736.8	1
100	30100		117.1	100100	854.7	1
100	30200		121.0	111000	917.6	1
100	30200		119.9	188700	1574	1
100	30200		109.9	233000	2120	1
100	41060		312.5	138300	442.5	1
100	41230		321.3	168000	523.0	1
100	51050		671.5	111800	166.5	1
100	51050		696.0	144000	206.9	1
100	51050		683.7	150700	220.4	1

TEMP. (DEG.F)	PRESS. (PSIG)	DENSITY (GM/CC)	VISCOSITY (POISE)	SHEAR STRESS (DYNE/SQ.CM.)	SHEAR RATE (1/SEC.)	CAP. NO.
100	51050		721.2	256800	356.1	1
100	51050		716.8	353900	493.7	1
100	51050		732.0	421600	575.9	1
100	63860		21270	268500	126.3	1
100	63530		21010	453400	215.8	1
100	63360		19990	478100	239.2	1
210	ATM	.8052	.3480	0	0	150
210	10550		1.225	18390	15010	1
210	10550		1.211	22520	18600	1
210	10550		1.213	33680	27780	1
210	19820		2.546	13270	5213	1
210	19880		2.546	20680	8121	1
210	19820		2.587	26080	10080	1
210	19940		2.539	26610	10480	1
210	19940		2.402	31800	13240	1
210	19880		2.456	36750	14960	1
210	19940		2.481	39390	15880	1
210	19940		2.460	39500	16060	1
210	19880		2.533	41010	16190	1
210	19940		2.526	54070	21410	1
210	30600		4.744	24280	5118	1
210	30400		5.143	29980	5829	1
210	30500		4.524	31030	6858	1
210	30500		4.610	34340	7449	1
210	30600		4.593	39440	8582	1
210	30400		5.073	40110	7905	1
210	30400		4.625	44380	9596	1
210	30400		4.662	47960	10290	1
210	30400		4.924	51820	10530	1
210	41110		10.05	25270	2514	1
210	40940		10.38	27010	2603	1
210	40940		9.652	31370	3250	1
210	40940		9.636	34110	3540	1
210	40780		10.56	34360	3254	1
210	40940		9.742	35110	3604	1
210	40940		9.961	37850	3800	1
210	41110		9.551	41440	4339	1
210	40780		10.13	49170	4852	1
210	40940		10.01	55400	5532	1
210	50410		17.00	35170	2068	1
210	50080		17.45	33800	2175	1
210	50410		16.86	39890	2367	1
210	50570		17.21	43480	2527	1
210	50080		16.86	41710	2711	1
210	50080		16.40	48150	2937	1
210	64350		41.46	23880	573.7	1
210	64350		36.44	59420	1631	1
210	64350		40.11	61630	1536	1
210	64350		36.02	69740	1936	1

MP. (D.F)	PRESS. (PSIG)	DENSITY (GM/CC)	VISCOSITY (POISE)	SHEAR STRESS (DYNE/SQ.CM.)	SHEAR RATE (1/SEC.)	CAP. NO.
10	64350		36.52	70720	1936	1
10	64350		38.62	76470	1980	1
00	ATM	.7777	.1370	0	0	150
00	10390		.3649	19590	53680	1
00	10680		.3707	20430	55120	1
00	10680		.3495	20690	59180	1
00	10680		.3493	22350	63980	1
00	10680		.3597	22550	62700	1
00	19760		.6733	4457	6620	1
00	19690		.7033	9906	14090	1
00	19820		.7199	11880	16500	1
00	19690		.7010	12010	17130	1
00	19820		.7006	13010	18570	1
00	30060		1.040	10340	9934	1
00	29960		.9633	13770	14290	1
00	30060		1.047	17270	16480	1
00	30060		1.091	18860	17290	1
00	30160		.9882	19090	19310	1
00	42430		1.511	19470		1
00	42430		1.624	10590	6521	1
00	42430		1.677	12400	7379	1
00	42430		1.738	15580	8967	1
00	42160		1.706	18960	11110	1
00	42430		1.511	19470	12890	1
00	49550		2.613	4999	1913	1
00	49870		2.570	11770	4580	1
00	49710		2.681	12420	4631	1
00	49710		2.456	13210	5378	1
00	49870		2.620	15120	5773	1
00	49870		2.657	20760	7813	1
00	62740		4.159	10260	2466	1
00	62740		4.091	12260	2997	1
00	62740		4.477	15660	3498	1

343 LINES PRINT

```
@XQT FNOV.X

**********AVERAGED D

                    FLUID= MOBIL XRM 100 F

 P (PSI)                    V (CP)
    .00000              .44900+03
    .50000+04           .89000+03
    .10581+05           .16132+04
    .20000+05           .50000+04
    .30191+05           .12269+05
    .41145+05           .31690+05
    .51050+05           .76353+05
    .63563+05           .20757+07

 ALPHA STAR=    .12188-03
 ALPHA OT=      .16679-03

                    FLUID= MOBIL XPM 210 F

 P (PSI)                    V (CP)
    .00000              .34800+02
    .50000+04           .71000+02
    .10550+05           .12163+03
    .19693+05           .25076+03
    .30467+05           .47664+03
    .40942+05           .99672+03
    .50272+05           .16963+04
    .64350+05           .38195+04

 ALPHA STAR=    .10435-03
 ALPHA OT=      .18769-03

                    FLUID= MOBIL XRM 300 F

 P (PSI)                    V (CP)
    .00000              .13700+02
    .50000+04           .22000+02
    .10622+05           .35882+02
    .19756+05           .69962+02
    .30060+05           .10259+03
    .42375+05           .16278+03
    .49763+05           .25995+03
    .32740+05           .42423+03

 ALPHA STAR AND ALPHA OT MUST BE CALCULATED BY HAND
```

APPENDIX B

School of Mechanical Engineering
Georgia Institute of Technology
Atlanta, Georgia
April, 1972

SOME OBSERVATIONS OF THE RELATIONSHIP BETWEEN FILM THICKNESS AND LOAD IN HIGH HERTZ PRESSURE ELASTOHYDRODYNAMIC CONTACTS

Submitted by

D. Lee
Graduate Student

D. M. Sanborn
Assistant Professor

W. O. Winer
Professor

Submitted to

American Society of Mechanical Engineers

INTRODUCTION

Laboratory simulation of elastohydrodynamic lubrication has received a great deal of attention in the last decade because of its importance in engineering design. It is now common to read in the literature that good agreement exists between observed film thickness behavior and theoretical predictions. It also appears that the only discrepancies between theory and experimental observation are associated with the traction in the contact. However, most experimental observations have been made at peak Hertz contact pressures ($\leq$ 100,000 psi) considerably less than the 200,000 psi or more pressures employed in the design of devices in which ehd contacts are to be expected. Exceptions to the 100,000 psi experimental limit are the findings of Battelle and NASA-Lewis (1,2,3) and those of the authors (4,5). The NASA-Battelle work suggests that the relationship between ehd film thickness and peak Hertz pressure (or load) is quite unlike that predicted by the commonly accepted theories.

The Battelle film thickness data are obtained by measuring x-ray transmission through the ehd film. Their data indicate that the film thickness dependence on peak Hertz pressure (or load) is greater than that predicted by the generally accepted theories over the Hertz pressure range of 80,000 to 225,000 psi (1) and up to 350,000 psi (2,3). By the nature of their experimental technique, they measure the minimum film thickness along the path of the x-ray beam. Their technique and data have come under criticism because; a) it is a novel technique unfamiliar to most other researchers, b) it is difficult to duplicate or verify, and c) the data trends are radically different from the generally accepted theories, while other experimental data in lower pressure ranges do show

reasonable agreement with theoretical predictions.

The Battelle researchers themselves have taken a skeptical view of their data. They have devoted one paper (1) to critically examining the experimental technique and have concluded that the data is valid. The true skeptic can, of course, point out that they have only eliminated those criticisms which they have thought of, which does not mean that the results are valid. Confirmation or rebuttal of the results in the form of film thickness data in similar peak Hertz pressure ranges, but employing a different measurement technique would be very helpful in settling the controversy. This paper presents the results of such a study. The data presented tend to confirm the trends reported in the Battelle publications over a portion of their Hertz pressure range.

The authors were also skeptical of the Battelle data (1,2,3) because we had previously published data (4,5) in the 72 to 176 kpsi range which overlapped Battelle's 80 to 225 kspi range (1) without observing the radical behavior they had reported. There are some differences between our ehd film thickness work and that done at Battelle, however. We have investigated sliding point contacts by the optical interference technique, whereas Battelle's film thickness data is taken for rolling modified line contacts using the x-ray transmission technique. In addition, Battelle's data are for higher temperatures and higher entrainment velocities. However, their results indicate that film thickness trends with the dimensionless speed parameter ($\mu u/E'R$) are about what would be expected from the commonly accepted theories. The discrepancy seems to be uniquely related to peak Hertz pressure or load and, therefore, should be observable using other measurement techniques at similar loads.

This report describes measurements of film thickness versus peak Hertz pressure from 70 kpsi to 225 kpsi on three different fluids. The

high pressure results tend to agree with Battelle's findings. The rate of decrease of film thickness (center, trailing edge, or minimum)* with increasing peak Hertz pressure is considerably greater than predicted by currently accepted theories. Since the methods used are quite different, the agreement between the Battelle work and our own suggests that these effects at high Hertz pressure are real. These findings should then have serious implications in engineering design.

EXPERIMENTAL TECHNIQUE

The experimental apparatus used consists of a 1¼ in. diameter steel sphere rotated and loaded against a sapphire plate. Optical interferometry was employed to measure the film thickness profile. This apparatus has been previously described in detail elsewhere (4,5). The fluids examined are described in Table I. All tests were conducted at approximately 75°F.

It is believed that neither surface heating nor change of refractive index with pressure can account for the trends in the data observed. The film thickness determination was made within one minute after the time the load was applied. The data for a series of loads at a given speed were performed in about twenty minutes by incrementally increasing the load. This sequence was later repeated after several hours at zero load and no rotation, but by starting at the maximum load and incrementally decreasing the load. Surface heating effects should be more pronounced in the later measurements regardless of the sequence followed, but the data were repeatable in the two loading sequences. At several speed and load conditions the film thickness was observed not to change for the first two or three minutes of operation which also suggests that surface heating

*Depending on the film thickness profile the minimum film thickness can occur at the side lobes, trailing edge or contact center.

was not an influence on film thickness. Changes in refractive index with pressure for the types of fluids being examined will result in changes in the deduced film thickness of less than 10 to 15 percent. These are small compared to the overall effects being observed.

DISCUSSION OF EXPERIMENTAL RESULTS

The film thickness-peak Hertz pressure relationships are shown in Figures 1-3. In Figure 1, a typical curve from the Battelle work (1) for a polyphenyl ether fluid (6800 fpm, 178°F) and our previous data (4,5) for a polybutene fluid at 27.4 ips sliding velocity are shown. Unfortunately, the manner in which our data was presented in (4,5) does not make evident either the change of slope at high pressure nor the obvious importance of the minimum film thickness trend which are both shown in the Battelle publication. Also shown in Figure 1 are lines with slopes corresponding to those predicted by typical theoretical analyses as recently summarized by Cheng (6). The differences between point and line contact reported by Cheng are small compared to those between theory and experiment as shown.

In Figure 1, the centerline film thickness data for the polybutene fluid shows a trend with Hertz pressure which is not radically different from that predicted by the theories of Archard and Cheng (6). The agreement is reasonably good up to 170 kpsi and is better at 90 ips than at 27.4 ips. It was for this reason that the Battelle data was suspect to us. However, the trailing edge and minimum film thicknesses clearly show the same behavior as the Battelle data. These data indicate an increasing film thickness dependence on peak Hertz pressure with both increasing pressure and decreasing film thickness.

The constant ratio between center and trailing edge film thicknesses suggested by theory seems to be valid for the lower pressure part of the range, but clearly is not true for the high pressure portion of the data. The minimum film thickness decreases more rapidly with increasing pressure than the center film thickness.

Figure 2 shows similar film thickness data as a function of Hertz pressure for a modified polyphenyl ether at two sliding speeds. The same comments made above regarding the polybutene fluid can also be made for this fluid. Figure 3 shows the same type data for a super-refined napthenic mineral oil. This fluid also exhibits the same film thickness-Hertz pressure trends.

Table 2 contains film thickness data on a synthetic paraffinic hydrocarbon similar to that employed by Battelle (2). The limited amount of data does not allow a meaningful plot to be drawn, but clearly does show that the minimum and center film thicknesses can be very sensitive to Hertz pressure and that the effect of pressure is greater at thinner film conditions.

Based on viscosity pressure measurements made on these fluids in our laboratory, the synthetic paraffinic fluid does clearly exhibit a shear thinning viscosity with increasing shear stress, while the others do not up to shear stresses of about 10^6 dynes/cm^2. It is not obvious from the data that this shear thinning behavior has an important influence on film thickness-load relations.

CONCLUSIONS

1. The strong dependence of film thickness on peak Hertz pressure at higher pressures as reported by Battelle from x-ray data has been confirmed using an independent measurement technique.
2. The centerline and minimum film thicknesses both show a stronger dependence on Hertz pressure than currently accepted theories indicate.
3. The minimum film thickness variation with Hertz pressure is greater than the centerline film thickness variation.
4. The ratio of the centerline to minimum film thickness, whether at the side lobes or trailing edge, is not constant as is commonly accepted.
5. The deviation from theoretical predictions increases as the film thickness decreases.

ACKNOWLEDGEMENT

This work was supported in part by a grant from NASA Lewis Research Center. We appreciate the support and encouragement of Mr. R. L. Johnson of NASA in connection with this grant.

BIBLIOGRAPHY

1. Kannel, J. W., and Bell, J. C., "Interpretations of the Thickness of Lubricant Films in Rolling Contact. 1. Examination of Measurements Obtained by X-Rays," Transactions of ASME, Journal of Lubrication Technology, Vol. 93, No. 4, October 1971, pp. 478-484.

2. Parker, R. J., and Kannel, J. W., "Elastohydrodynamic Film Thickness Between Rolling Disks with a Synthetic Paraffinic Oil," NASA TN D-6411, July 1971.

3. Parker, R. J., and Kannel, J. W., "Elastohydrodynamic Film Thickness Measurements with Advanced Ester, Fluorocarbon, and Polyphenyl Ether Lubricants to 589 K (600°F), NASA TN D-6608, December 1971.

4. Sanborn, D. M., and Winer, W. O., "Fluid Rheological Effects in Sliding Elastohydrodynamic Point Contacts with Transient Loading: I - Film Thickness," Trans. ASME, Journal Lubrication Technology, Vol. 93, pp. 262-271, 1971.

5. Sanborn, D. M., and Winer, W. O., "Fluid Rheological Effects in Sliding Elastohydrodynamic Point Contacts with Transient Loading: II - Traction," Trans. ASME, Journal of Lubrication Technology, Vol. 93, pp. 342-348, 1971.

6. Cheng, H. S., "Isothermal Elastohydrodynamic Theory for the Full Range of Pressure-Viscosity Coefficient," Trans. ASME, Journal of Lubrication Technology, Vol. 94, pp. 35-43, 1972.

LIST OF TABLES

TABLE 1

Experimental Fluids

Name	μ_0[cp] @75F	$\alpha_{ot}^{(1)}$[psi]$^{-1}$ @100F	$\alpha^{*(1)}$[psi]$^{-1}$ @75F
1. Modified polyphenyl ether	58	1.167×10^{-4}	1.43×10^{-4}
2. Super-refined napthenic mineral oil	168	2.121×10^{-4}	1.98×10^{-4}
3. Polybutene polmer	190	2.30×10^{-4}	2.85×10^{-4}
4. Synthetic paraffinic hydrocarbon	1200	1.667×10^{-4}	1.23×10^{-4}

(1) Pressure-viscosity coefficients are defined as follows:

$$\alpha_{o\tau} \equiv \left.\frac{d\ln u}{dp}\right|_{p = \text{atmospheric}}$$

$$\alpha^* \equiv \left[\int_0^\infty \frac{\mu_0}{\mu(p)}\, dp\right]^{-1}$$

TABLE II

Film Thickness Behavior of a
Synthetic Paraffinic Fluid (XRM-109F)
(Similar to That Used by Battelle (2)).

Sliding Speed [ips]	Hertz Pressure [kpsi]	$h_c/R \times 10^6$ [in]	$h_m/R \times 10^6$ [in]
13.7	77	30	30*
13.7	150	22	7.4
27.4	77	40	40*
27.4	150	35	17
54.7	77	48	48*
54.7	150	48	30

*At the lower Hertz pressure (77 ksi) the surfaces appear to be essentially undeformed causing the minimum film thickness to occur at the contact center.

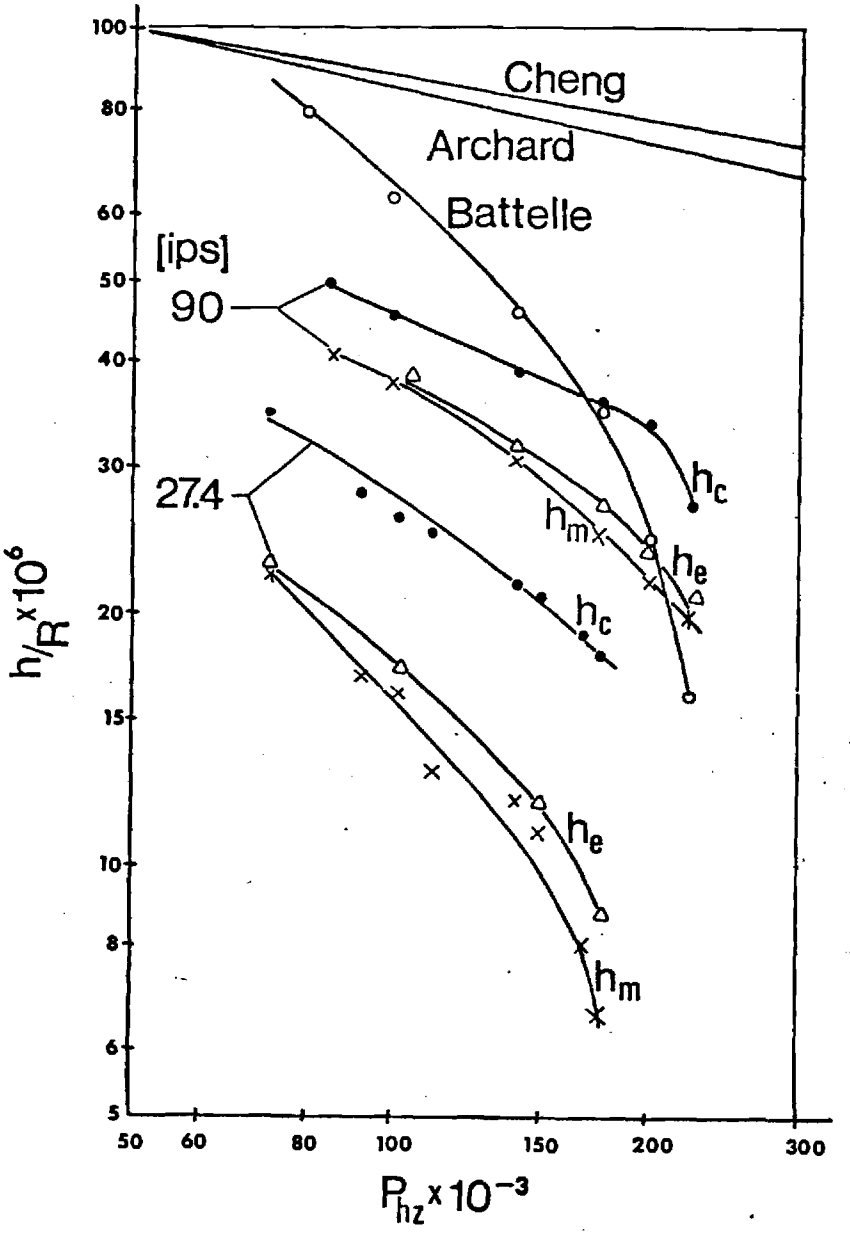

Fig. 1. Center (h_c -•-), minimum (h_m -x-), and trailing edge (h_e -Δ-) film thickness versus pressure for a polybutene fluid compared with data from Battelle (—o-) and slopes from theory (6).

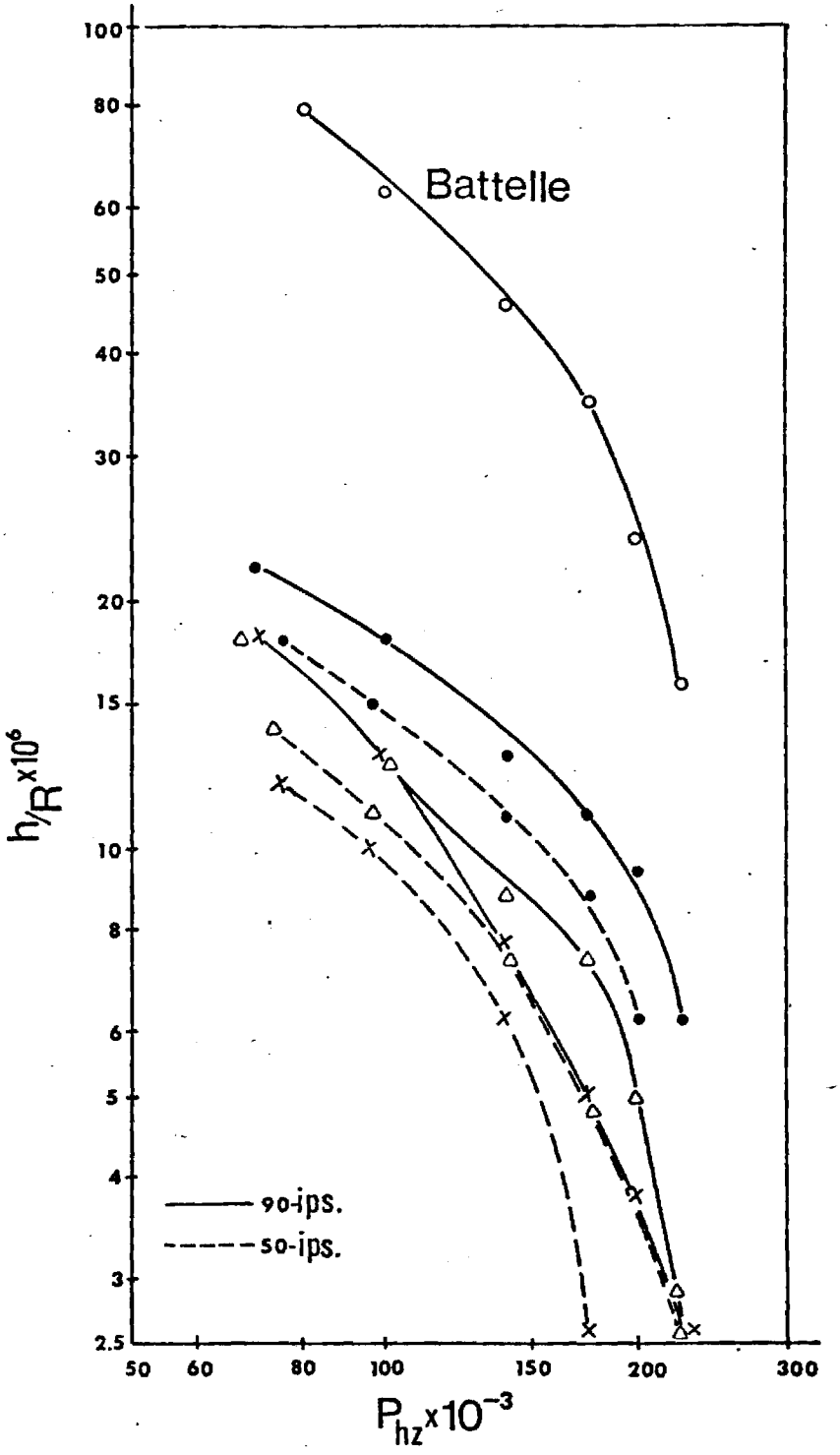

Fig. 2. Center (h_c -●-), minimum (h_m -x-), and trailing edge (h_e -Δ-), film thickness versus pressure for a modified polyphenyl ether.

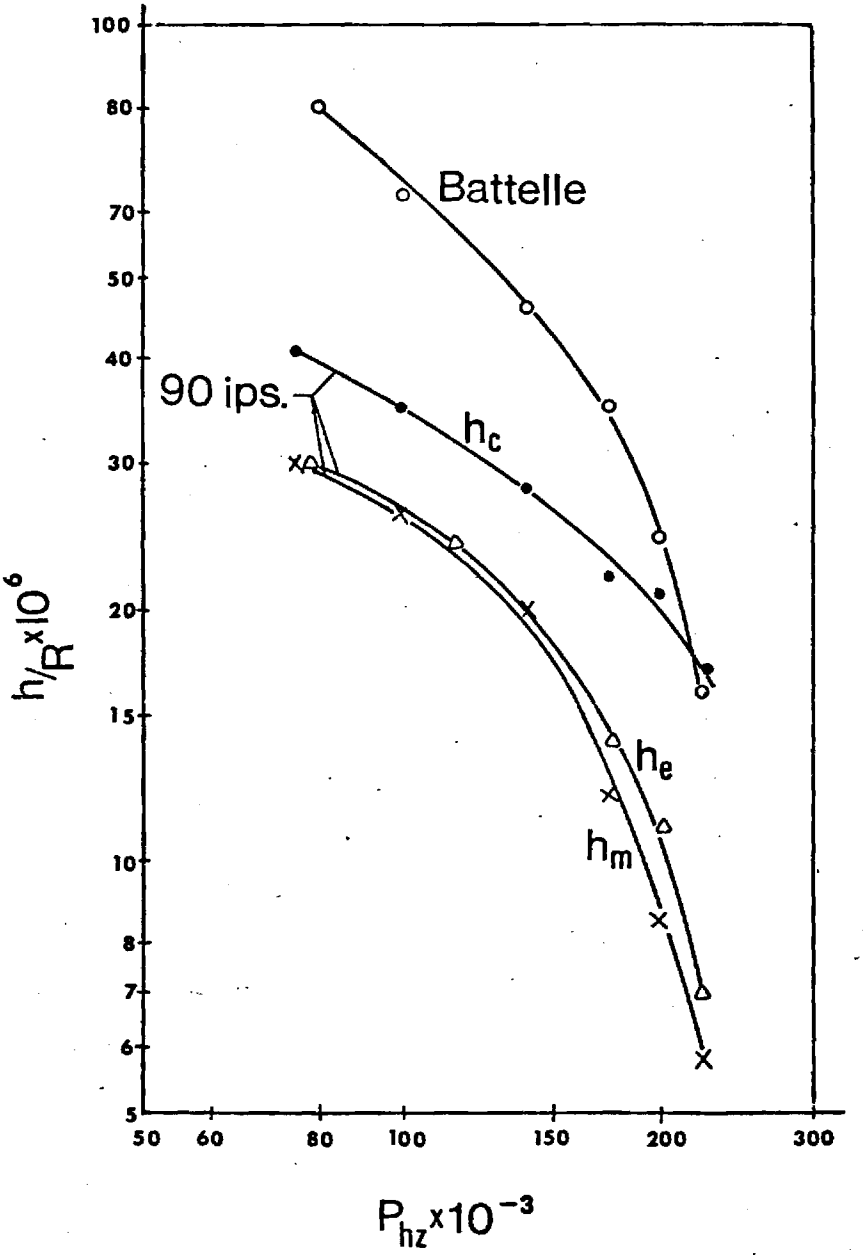

Fig. 3. Center (h_c -•-), minimum (h_m -x-), and trailing edge (h_e -Δ-), film thickness versus pressure for a super-refined napthenic mineral oil.

E-25-620

FTR

SCHOOL OF MECHANICAL ENGINEERING

GEORGIA INSTITUTE OF TECHNOLOGY

Atlanta, Georgia

Investigations of Lubricant Rheology as Applied to Elastohydrodynamic Lubrication

NASA GRANT No.
11–002–133

By:
S. Carlson
V. Turchina
J. Jakobsen
Graduate Students
D. M. Sanborn, Assistant Professor
W. O. Winer, Professor & Principal Investigator

For:
NASA–LEWIS RESEARCH CENTER
21000 BROOKPARK ROAD
CLEVELAND, OHIO 44135

OCTOBER 1973

1. Report No.	2. Government Accession No.	3. Recipient's Catalog No.
CR - 134539		

4. Title and Subtitle	5. Report Date
INVESTIGATIONS OF LUBRICANT RHEOLOGY AS APPLIED TO ELASTOHYDRODYNAMIC LUBRICATION	October, 1973
	6. Performing Organization Code

7. Author(s)	8. Performing Organization Report No.
S. Carlson, V. Turchina, J. Jakobsen, D. M. Sanborn, and W. O. Winer	
	10. Work Unit No.

9. Performing Organization Name and Address	11. Contract or Grant No.
School of Mechanical Engineering Georgia Institute of Technology Atlanta, Georgia 30332	NGR 11-002-133
	13. Type of Report and Period Covered
12. Sponsoring Agency Name and Address	Contractor Report
National Aeronautics and Space Administration Washington, D.C. 20546	14. Sponsoring Agency Code

15. Supplementary Notes

Project Manager, William R. Jones, Jr., Fluid System Components Division, NASA Lewis Research Center, Cleveland, Ohio

16. Abstract

This is the final technical report for NASA Grant No. NGR 11-002-133. The research under this grant consisted of pressure-viscosity and of elastohydrodynamic lubrication (ehd) studies. The pressure viscometer has been modified to permit the measurement of viscosity at elevated pressures and shear stresses up to 5×10^6 N/m^2 (720 psi). This shear stress is within a factor of three of the shear stress occurring in a sliding ehd point contact such as occurs in the ehd simulator in this laboratory. Viscosity data were taken on five lubricant samples and it was found that viscous heating effects on the viscosity were predominant and not non-Newtonian behavior at the high shear stresses. The development of the infrared temperature measuring technique for the ehd simulator was completed and temperature data for a set of operating conditions and one lubricant are reported. The numerical analysis of the behavior of non-linear lubricants in the lubrication of rollers has progressed and the results are reported.

17. Key Words (Suggested by Author(s))	18. Distribution Statement
Elastohydrodynamic Lubrication Pressure Viscosity Measurements Liquid Lubricants Lubricant Rheology	Unclassified - unlimited

19. Security Classif. (of this report)	20. Security Classif. (of this page)	21. No. of Pages	22. Price*
Unclassified	Unclassified	140	$3.00

* For sale by the National Technical Information Service, Springfield, Virginia 22151

I. INTRODUCTION

The research efforts over the past contract year have resulted in significant progress in several areas. These include:

1. The extension of pressure-viscosity data on lubricants to shear stresses of 5×10^7 d/cm^2 (N/m^2) which is within a factor of 3 to 5 of the average shear stress occurring in the sliding ehd simulator used in this laboratory. For all lubricants examined except a high polymer blend and a dimethyl siloxane polymer the data appears to be explainable on the basis of viscous heating up to at least 5×10^6 d/cm^2. Analysis of the capillary flow which is in progress but not reported here is expected to verify this interpretation. It appears that for the other lubricants examined no non-Newtonian behavior was observed in the range of parameters very near those occurring in a sliding ehd contact.
2. The development of the technique for the infrared temperature measurement in an ehd film was completed and data at a set of operating conditions for a single lubricant were obtained. It is expected during the present contract year to utilize the technique to explore the thermal behavior of ehd films as a function of operating conditions and lubricant composition.
3. The computer analysis of the behavior of non-linear fluids in the lubrication of rollers has progressed to the stage where results are presented for the case of rigid cylinders with non-linear pressure dependent fluid properties. During the present contract year we expect to complete the program including elastic

cylinder behavior under the ehd conditions and possibly to begin to introduce thermal effects.

Other related research conducted in the laboratory but under the sponsorship of an NSF Grant deserves mention. A program to explore the extent of lubricant molecular degradation in a sliding ehd contact has been undertaken. Modification of the ehd simulator mentioned in this report permitted the acquisition of a 10-15 μl lubricant sample from the ehd contact just outside the high pressure region near the film exit. Samples were also taken from the inlet zone and the supply reservior, which served as a control sample. Eight fluids were examined and varying amounts of molecular degradation were observed. In general the degradation increases with increasing energy dissipation per grammole of lubricant. Typically the degradation increased as molecular weight increased but measurable degradation occurred even for relatively low molecular weight lubricants such as 2-ethyl hexyl sebacate. This research is being prepared for publication in the near future.

II. LUBRICANT RHEOLOGY STUDIES

a. High Shear Stress Behavior of Some Lubricants

Introduction

Investigations have been carried out in the high pressure viscometer to determine lubricant behavior at high shear stress. The operating temperatures, pressures and shear stresses for a lubricant in an EHD-contact can be approached in the viscometer. Furthermore, all these operational parameters can be varied independently of each other.

Five lubricants were investigated: a diester, a polyalkyl aromatic plus additive (DN 600 plus Additive), a synthetic paraffinic oil (XRM 177 F4), a silicone oil (Dimethyl Siloxane DC-200-50) and a mixture (B3J) of paraffinic, mineral oil with 11.5% polyalkylmethacrylate (PL 4523) with an average molecular weight of $.2 \times 10^7$. A detailed description is found in Appendix A.

Apparent Newtonian behavior has been found for all fluids except B3J up to a shear stress of approximately 700 psi ($\sim 4.8 \times 10^7$ dyn/cm^2), which is the present upper limit of shear stress for the high pressure viscometer. Viscous dissipation heating alone seems to dominate up to the maximum stress in causing an apparent shear thinning effect. The data for the mixture (B3J) of paraffinic mineral oil and 11.5% polymer (PL 4523) shows a significant amount of scatter when the apparent viscosity is plotted against calculated capillary wall shear stress. The scatter of the data is pronounced at shear stresses above 1 - 2 psi ($\sim 10^5$ dyn/cm^2) making interpretation difficult in terms of liquid behavior alone.

Distinct non-liquid behavior was observed at extreme pressures

and temperatures for the lubricant DN 600 plus Additive. Similar behavior was observed for the siloxane but at high shear stresses, 150-600 psi ($1 - 4 \times 10^6 dyn/cm^2$)

Modifications of the High Pressure Viscometer

The measurements were carried out in a high pressure viscometer. The design and operation of the viscometer is described in [1] and [2]. The equipment has since then been modified in some respects and the operational procedure has been changed. Figure 1 shows a schematic of the viscometer including the most recent modifications.

The displacement transducer, which is used for flow rate measurement, has been replaced with a velocity transducer, Hewlett-Packard L6V1, and a high gain amplifier. The change was motivated by the addition of the analog-to-digital data recorder, which made a direct signal preferable to a differentiated signal. Interest in the possibility of measurements of transient phenomena also motivated the change. The addition of the recorder has been mentioned in a previous report.

Two high precision pressure gauges (Heise Bourdon Tube Co., 40 kpsi and 100 kpsi) have been added to facilitate and improve calibration and operations.

An infinitely variable drive has been provided for displacing the translating piston (see Figure 1) with constant velocity. The piston is moved hydraulically as before by charging volume III or IV with a low pressure fluid. The flow rate of this fluid is, however, kept constant by direct coupling of the drive unit to the piston of the charging pump. The drive unit gives good reproducibility of the measurements. The displacement of the pump piston is, however, not big enough to obtain a satisfactory

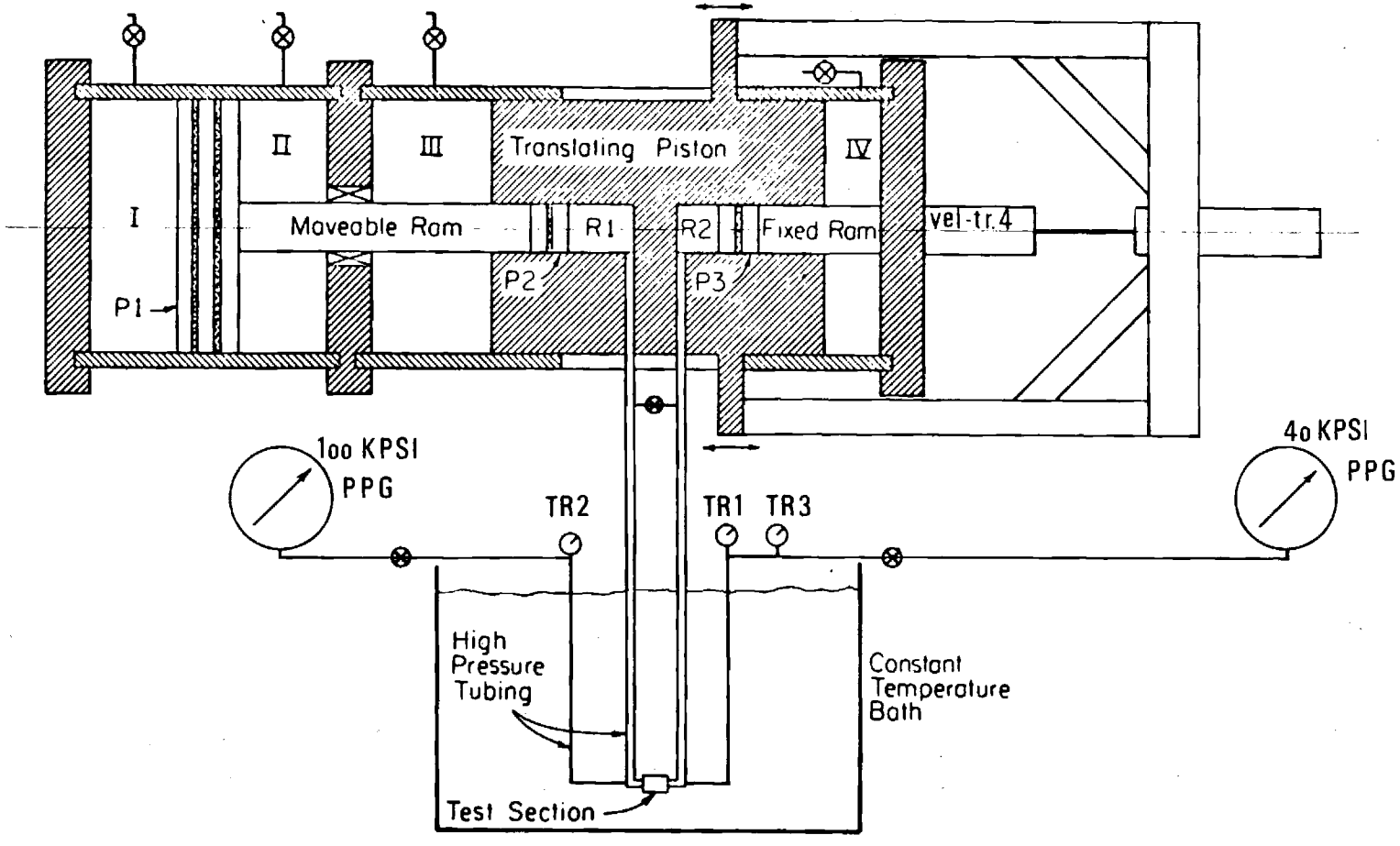

Schematic Drawing of Viscometer.

Figure 1. The Modified Viscometer.

flow rate for measurements at the highest attainable shear stresses. Manual drive (hand pull) is therefore used for these measurements. Satisfactory reproducibility can be obtained for these higher speed displacements of the translating piston of the viscometer.

Capillaries with a low L/D ratio have been used. The smallest ratio applied has been L/D = .1 (L = 0.001 inch and D = .01 inch) this ratio, however, was used only for exploratory purposes. The entrance correction was found to be excessive for the L/D ratio of .1. Measurements were therefore not carried out with this capillary. The lowest ratio used so far is L/D = 1.35 and the smallest diameter used is .0035 inch.

The measurements were carried out with capillaries of L/D = 297, L/D = 14.9 and L/D = 1.35.

Table I

Capillary Dimensions and Materials

	L/D	D Inch	L Inch
Stainless Steel Capillary No. 4	297	.01009	2.996
Stainless Steel Capillary No. 1	14.9	.00785	.117
Sapphire Capillary No. 0	1.35	.0035	.0047

Calibration Procedures

The viscosity measurements are carried out essentially as measurements of pressure drop and flow rate in the capillary. Shear stress is derived from the pressure drop measured with the differential pressure transducers TR1 and TR2 (Figure 1). Shear rate is determined from measurements of flow rate indicated by the velocity transducer TR4. Pressure transducer TR3 measures the pressure level.

The differential pressure transducers have been calibrated with an approach involving summation of small increments of pressure in the test section of the viscometer. Pressure readings from the Heise precision gauges are recorded simultaneously with the amplifier outputs from TR1 and TR2. Only one transducer is calibrated at a time. The pressure increments are applied with the small piston diameters pressurizing hand pump of the viscometer and controlled through measurements of the transducer-amplifier output. The output is measured with a DC-Differential Voltmeter (Hewlett-Packard 3420B) which has a precision of 10 μvolts. The voltmeter is used as a null meter. The steps are accurately monitored and measured to 6.0 volts, from an output of -3.0 volts to +3.0 volts from the symmetric transducer amplifier. The estimated accuracy of the setting of a pressure increment is equivalent to .02 volt. The precision range (10 μV) of the differential voltmeter is, therefore, completely sufficient.

The amplifier output is changed from +3.0 volts to -3.0 volts after each pressure measurement by balancing the input potentiometers of the amplifier. This change is a preparation for the next pressure increase. The accuracy of the change in potentiometer setting is estimated to be .01 volt. Total estimated accuracy of a measurement of a pressure increment is therefore .03 volt, on a deflection of 6.0 volts, which is equivalent to .5%. This error estimate is also valid for the voltage sum of the steps. Each increment of 6.0 volts is equivalent to approximately 440 psi for 6 volts excitation of the transducers. The accuracy of the high pressure gauges is better than .1% of full scale deflection (40 psi or 100 psi). This is about 10% to 25% of a single pressure increment. This high inaccuracy will, however, diminish rapidly with

increasing numbers of steps. The gauge accuracy of .1% is constant. A typical calibration of a transducer-amplifier involves nearly 100 pressure increments. The pressure gauge error will, therefore, typically be of the order of .1% - .2%. The estimated accuracy of .5% for the voltage sum and the pressure gauge accuracy of .1% - .2% may safely imply that the calibration procedure is correct within considerably less than 1% of the full range of calibration.

It is essential for the accuracy of the calibration procedure that the system pressure remain constant during the change of potentiometer setting of amplifier output from +3.0 volts to -3.0 volts. The constancy of system pressure has been assured by steady state conditions. These are obtained when temperature transients, possible relaxation of seals, etc., have faded away from each pressure increment. The change of potentiometer setting can be carried out in about 10 seconds. The constancy of system pressure during this period can be verified and measured with the transducer-amplifier, which is not undergoing calibration. Changes as small as 30 millivolts (~ 2.0 psi) can be detected with this channel when it is used as null indicator. System pressure constancy is assumed to be achieved when no pressure variation is detected for a period of about 100 seconds.

The exitation voltage for the transducers was measured continuously during the calibration procedure. Changes in the voltage were, however, insignificant and about .1 millivolts. The average value was applied in calculations. Standard excitation voltage level is 6 volts. Some high shear stress measurements, however, were carried out with 1.5 volt excitation. The transducer sensitivity is directly proportional to the excitation

voltage. Measurement accuracy is, therefore, not impaired by changes in excitation voltage. A series of control measurements confirmed this assumption.

The pressure level transducer (TR3, Figure 1) was calibrated by recording transducer output and pressure readings from the high precision gauges. An interval of 5 kpsi was used. The transducer characteristic was linear above 5 kpsi within calibration accuracy.

The velocity transducer measures linear, straight line velocity. It consists of a shielded coil and an axially located, cylindrical core. The core is a high coercitive force permanent magnet. Motion of the core generates a voltage in the coil proportional to linear velocity with an output of 545 millivolts/ips. The working range is 1.0 inch. Manufacturer's specifications show a linearity of better than 1% and output variations between 95% and 100% of nominal output over the total working range.

Considerations of the function of the transducer suggest considerably increased accuracy above the mentioned magnitude of ±2.5%, however, for a reduced working range. A working range of about 0.5 inch was, therefore, maintained during the experiment.

The transducer and amplifier calibration were carried out as measurements of displacement and corresponding time duration. The velocity of the traversing piston was maintained constant with the above mentioned drive unit during the calibration. The amplifier output was sampled by the appropriate channel on the analog-to-digital recorder. A typical calibration speed was 0.001 in/sec.

These switches were connected electrically over the inputs of two dummy channels on the analog-to-digital converter. The opening times can, therefore, easily be assessed from a computer printout.

The travelled distance between activation of the switches was measured with a precision dial indicator and was typically 0.01 - 0.02 inch. The accuracy of the indicator is guaranteed to be better than 0.0001 inch. This was confirmed in a series of measurements performed with parallel gauge blocks (Grade L).

The amplifier gain was approximately 890. The transfer function for the transducer and amplifier was therefore 485 V/in/sec. The input to the analog-to-digital recorder will be 485 millivolts for a calibrating speed of 0.001 in/sec. This output level of about 500 mv is appropriate for accurate recording by the analog-to-digital converter, which has a threshold of destinction of 4.85 millivolts. This 1% ratio between threshold and signal magnitude is however lowered considerably by the great amount of sampled data and the following averaging process in the computer treatment.

Two calibration fluids were used, a viscosity standard, S-60 from Cannon Instrument Company, and diester (bis 2-ethylhexylsebacate) from Rohm and Haas Company. Table 2 summarizes the viscosities of the fluids.

Table 2

Viscosities (cp) of Calibration Fluids
at Atmospheric Pressure

	100 °F	210 °F	300 °F
S-60	51.06 cp	5.899 cp	--
Diester	11.41 cp	2.86 cp	1.46 cp

Viscosities for S-60 are from the manufacturer's specifications.

The fluid S-60 was used only at low shear stress calibrations. The diester was used over the total range of shear stress. Both fluids are assumed to be Newtonian liquids in the sense that the ratio between measured shear stress and shear rate is constant.

The viscosity of the diester was determined at 100 °F, 210 °F and 300 °F with a Cannon-Fenske Routine Glass viscometer 150-E707. This viscometer was calibrated with the S-60 fluid. Capillary 4 (see Table I) was used as the standard capillary for high pressure measurements. Calibration of capillary 4 was carried out at atmospheric pressure with diester and checked with the S-60 fluid. The diameter of capillary 4 was found to be 0.01009 inch. Later calibrations confirmed this measurement within 5 μinch.

These statements about the diameter of capillary 4 assume the physical length of the capillary tube to be 2.996 ± .001 inch as measured with a micrometer screw. The diameter 0.01009 inch contains, therefore, all possible corrections originating outside the capillary cavity, however, only for Newtonian liquids.

Calibration of the capillary 1 was carried out as a comparison of low shear stress measurements with capillary 4 measurements. The diester was used as calibration fluid. The pressure range applied was 10 - 40 kpsi. Calibration temperature was 31.9 °F ± 0.1 °F. This temperature was selected because the viscosity of the calibrating fluid for the applied pressures is then about 10^3 cp, well within the expected viscosity range in the elastohydrodynamic lubrication film. The selected calibration temperature is also appropriate for comparison with previous work, notably ASME 1953 [3].

The diameter of capillary 1 was found to be 0.00785 inch for a measured physical length of 0.117 inch. This diameter statement includes all possible corrections originating outside the capillary cavity, however, only for Newtonian liquids.

The capillary with L/D = 1.35, capillary 0, is a sapphire ring (see Figure 2) embedded in stainless steel high pressure seals of a similar type as employed by AMINCO (AMINCO is the manufacturer of the utilized standard high pressure tubes and fittings). The seals are of local design and manufacture.

Calibration of capillary 0 was carried out as a comparison of low shear stress measurements with capillary 1 and capillary 4 measurements. The calibration fluid was the diester. The applied pressure range was 10 - 40 kpsi. The calibration was carried out at 31.9 ± 0.1 °F. The diameter of the sapphire capillary was determined with a high power microscope (200X and 500X) to be 0.0035 inch with an estimated accuracy of 3%. The magnitude 0.00348 inch was actually used in the computer program because this number was believed to be the most nearly accurate.

The comparison with capillary 1 and capillary 4 measurements showed the effective capillary length to be 0.0047 inch. This calibration also takes into account all possible corrections originating outside the cylindrical part of the capillary cavity. It will, therefore, also give a correct shear stress determination, according to the expression $\tau = \Delta pD/4L$.

One known correction originating outside the capillary is the pressure drop in the conical part of the sapphire (see Figure 2). An estimate of this correction can be given in terms of equivalent length for the capillary diameter D_o. The equivalent length is $D_o/6\ tg\psi$, where 2ψ is

Figure 2

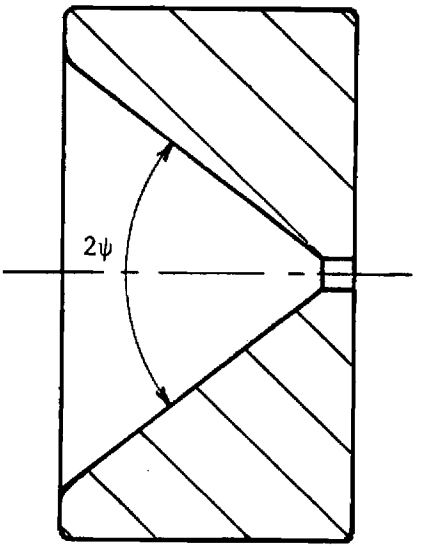

Capillary 0. Sapphire. Outside diameter .055 inch. Thickness .030 inch. Cone angle ≃ 80°. Capillary diameter .0035 inch. Capillary length ≃ .0047 inch.

the cone angle, see Appendix B.

The cone angle of capillary 0 is approximately 80°, which gives an equivalent length of about 0.0008 inch and, therefore, a physical length of the capillary of about 0.0039 inch. This is somewhat greater than the manufacturer's specified length of 0.0035 inch. The difference may be associated with a further correction due to flow contraction and dispersion outside the capillary cavity or possibly to a small inaccuracy in the manufacture.

No directional effect was found for the capillaries during the calibration measurements. Reversal of flow direction for all capillaries gave consistantly identical results within the measuring accuracy.

The distance in the capillary from the entrance to the point of

nearly fully developed flow (95%) is called the entrance length [1]. The calibration of capillary 0 was carried out for entrance length from 1% down to 0.03%. The corresponding Reynolds numbers for the low shear stress measurements were 0.2 to 0.006. Entrance lengths as great as 4% did not, however, produce significant deviations in apparent viscosity. It should be added that calibration for capillary 1 was carried out for equally small Reynolds numbers.

The calibration measurements are found in Table 5 - Diester, 32 °F. The measurements with the standard high pressure capillary, capillary 4, are plotted in Figures 3 and 4 . Table 3 gives a comparison of the averaged data of a diester with data for a diester reported as sample A1 in the ASME Pressure Viscosity Report of 1953 [3].

The data summarized in Table 3 are taken from two different charges. The dates of the measurements are about 20 years apart. The viscosity values in columns 1973 and 1953 are interpolated graphically. This process also incorporates inaccuracies in the data of corresponding pressure levels (5 - 40 kpsi) aside from graphically generated inaccuracies in the viscosity values. It must furthermore be delineated that the viscosity values are obtained in two basically different ways of calibration and measurement approaches.

Table 3 shows that the 1973 data deviate less than ± 2% from the 1953 data. This small magnitude of deviation can be interpreted as a verification and a support of the previous stated measurement inaccuracy of ± 1%, when all prepositioned conditions for the data of Table 3 are taken into consideration.

The data of Table 3 indicate also that a search for further

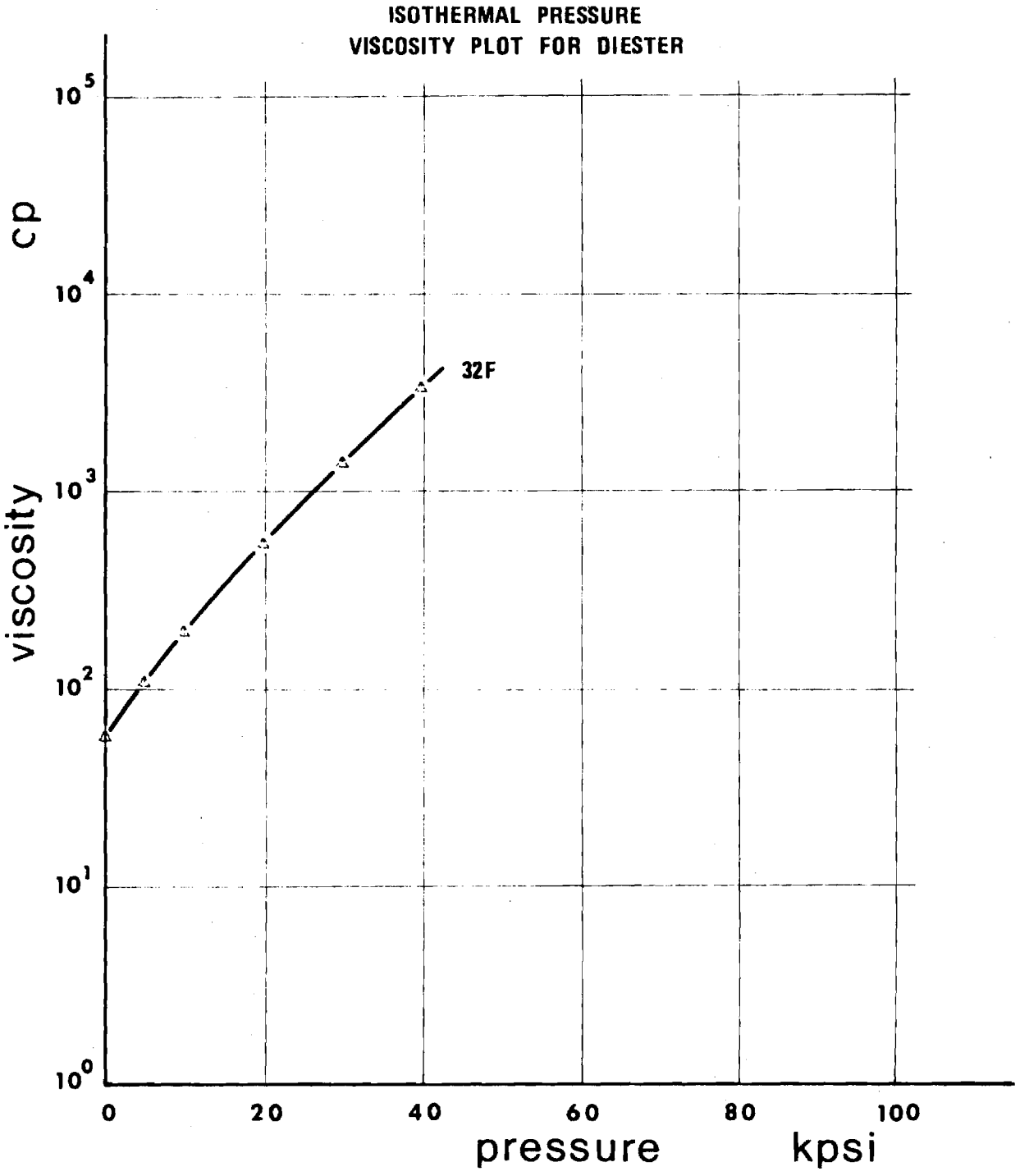

Figure 3. Isothermal Pressure Viscosity Plot for Diester. (Semilog Presentation.)

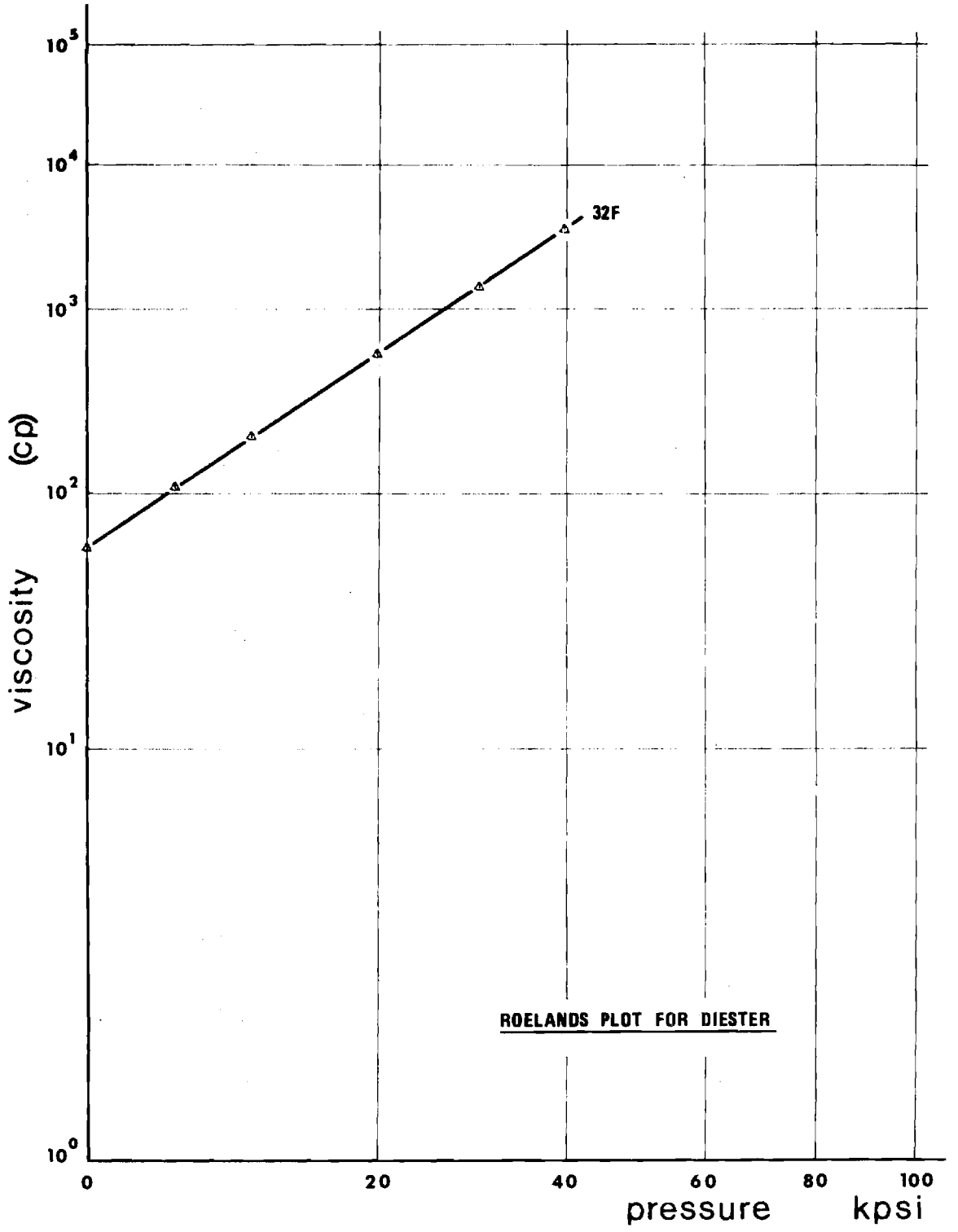

Figure 4. Roelands Plot for Diester.

Table 3

Pressure Viscosity Relation (Diesters)

32 °F at:	Data 1973 - Capillary 4	ASME 1953 - A1	Deviation of 1973 Data from ASME 1953 Data
0 kpsi	57.5 cp	56.8 cp	+1.2%
5	109.5 cp	108 cp	+1.4%
10	196. cp	194 cp	+1.0%
20	546. cp	547. cp	- .2%
30	1400. cp	1420. cp	-1.4%
40	3365. cp	3310. cp	+1.7%

All viscosities are interpolated graphically on expanded semilog diagrams.

For the column: DATA 1973 - capillary 4:

Measurements at pressure levels 5 kpsi to 40 kpsi are performed in the high pressure viscometer. Measurements at atmospheric pressure are extrapolated from straight line pressure viscosity characteristics mapped on a rectifying diagram ($\ln\ln\eta T$) of type ASTM D 341-43.

increase of measuring accuracy will probably not be of particularly great value. An accuracy of ± 1% seems to be satisfactory for general investigations of high pressure properties of lubricants as long as the lubricants are no more well defined. The conclusions of the work are not at all impaired by a ± 1% accuracy of the measurements. A greater accuracy would only have contributed insignificantly, it is believed, to refinements of the results.

Figure 5 shows the viscosity measurements plotted as function of shear stress. The figure illustrates the high degree of correspondence of the low shear stress measurements for capillary 0 and capillary 1 with those of capillary 4. The high shear stress measurements of Figure 5 (μ vs τ) show for both capillary 0 and capillary 1 an apparent shear thinning behavior of the diester. This calibration liquid, which is assumed to have completely Newtonian properties, is presumably then subject to dissipation heating in the capillary cavity. A series of measurements with only one capillary cannot easily discern shear thinning effects from dissipation. Comparison between measurements with different L/D ratios will allow a differentiation of these effects.

The measurements plotted in Figure 5 for capillary 0 (L/D = 1.35) and capillary 1 (L/D = 14.9) show for the same fluid at each pressure level consistently lower measured viscosity values for capillary 1 in the overlap zone of the shear stress ranges of the capillaries. This holds true whatever shear stress or shear rate is used as a basis of comparison.

The general form of the characteristics of Figure 5 at 20 - 30 - 40 kpsi and particularly the comparison between capillary 0 and capillary 1 measurements at the overlap zone ($\sim 5 \times 10^5$ dyn/cm^2) where capillary 1

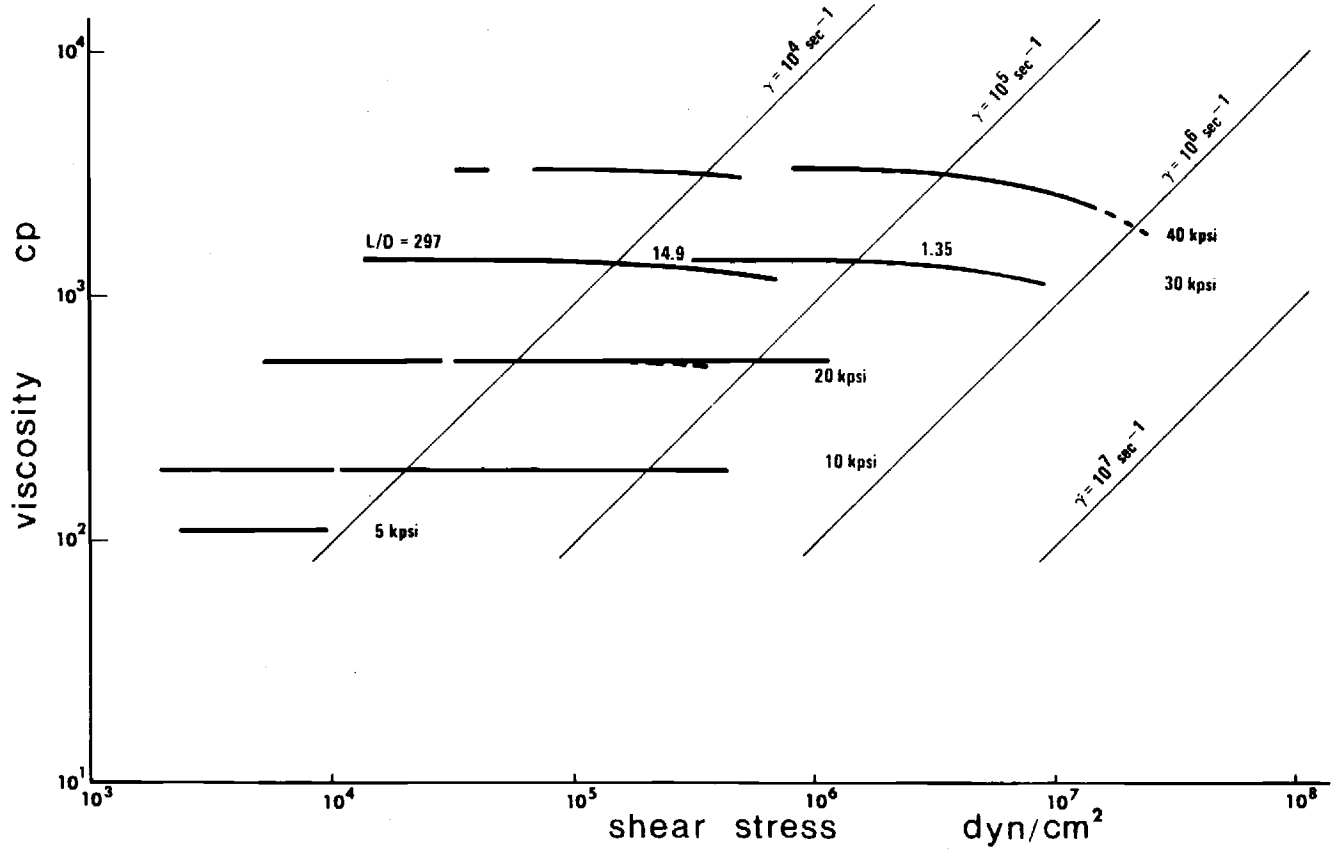

Figure 5. Flow Curves for Diester, Calibration, T = 32°F.

results deviate from the Newtonian characteristic, indicates strongly that shear thinning effects cannot explain the high shear stress behavior of the diester as it is measured with capillary 1.

The diester behaves, therefore, as a Newtonian liquid up to about 10^6 dyn/cm^2 which is the upper limit for capillary 1 measurements in this series of experiements. The common form of the characteristic leads furthermore to the supposition that the diester behaves as a Newtonian fluid up to about 2×10^7 dyn/cm^2 (about 300 psi) shear stress.

Attempts were undertaken to use capillaries with L/D as small as 0.1 in order to increase the upper limit for the shear stress at the capillary wall. The corrections, which necessarily had to be applied, made interpretation of the measurements questionable. The approach was therefore abandoned.

Fluid Measurements

Diester. The high shear stress behavior of diester was investigated at somewhat greater viscosity levels than the calibration measurements. Higher viscosities were achieved by applying a low temperature of 10° F and maintaining the pressure levels 10 - 20 - 30 - 40 kpsi. Figure 6 shows the results of the measurements as a graphical presentation. Measurements with capillary 4 were not performed because the low shear stress viscosities measured with capillary 0 and capillary 1 showed consistency with previously obtained data for the diester when interpreted through mapping on a ASTM Standard Viscosity-Temperature Chart. The mapping is illustrated in Figure 7.

The presentation of Figure 6 shows the same values of limiting low shear stress viscosity for capillary 0 and for capillary 1 at every pressure

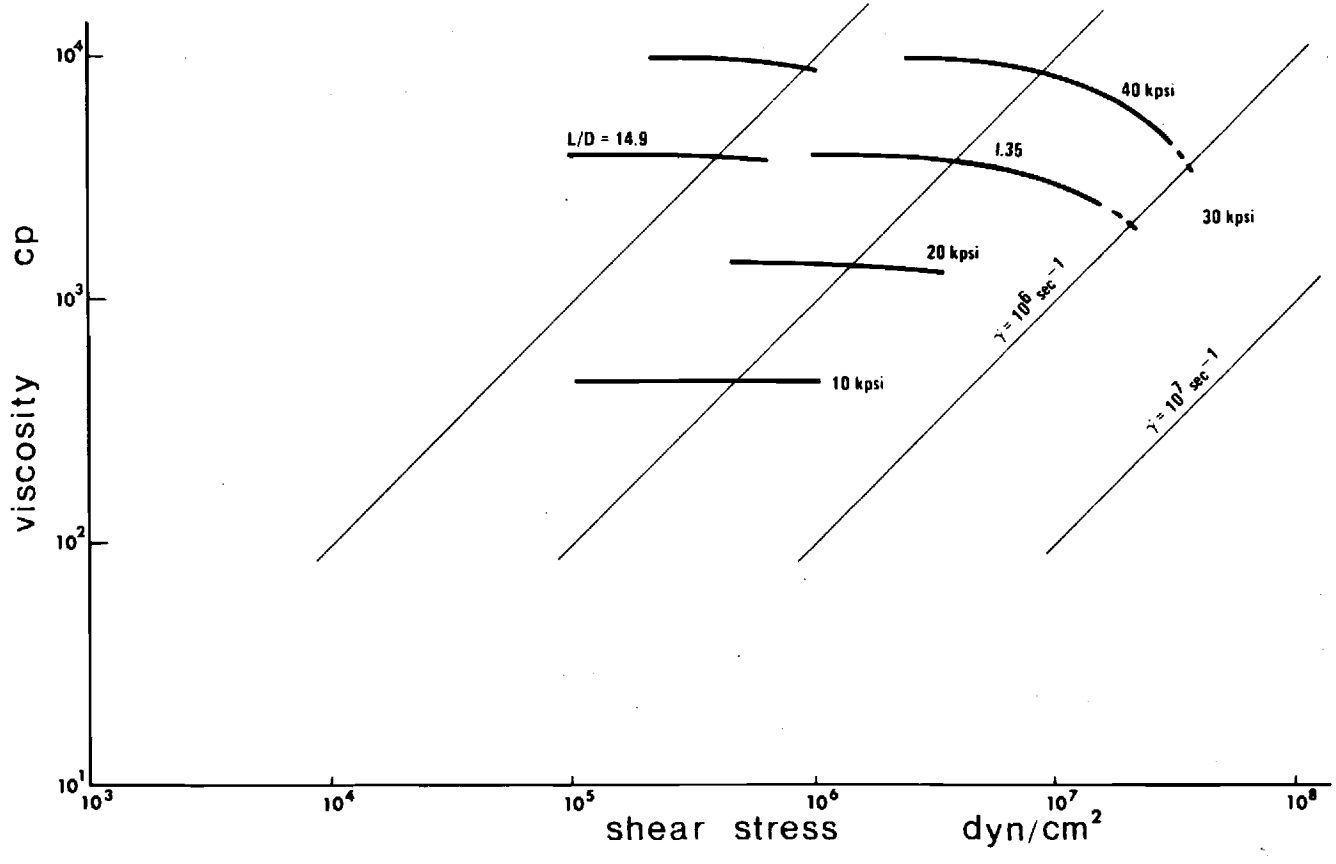

Figure 6 . Flow Curves for Diester, High Shear Stress, T = 10°F.

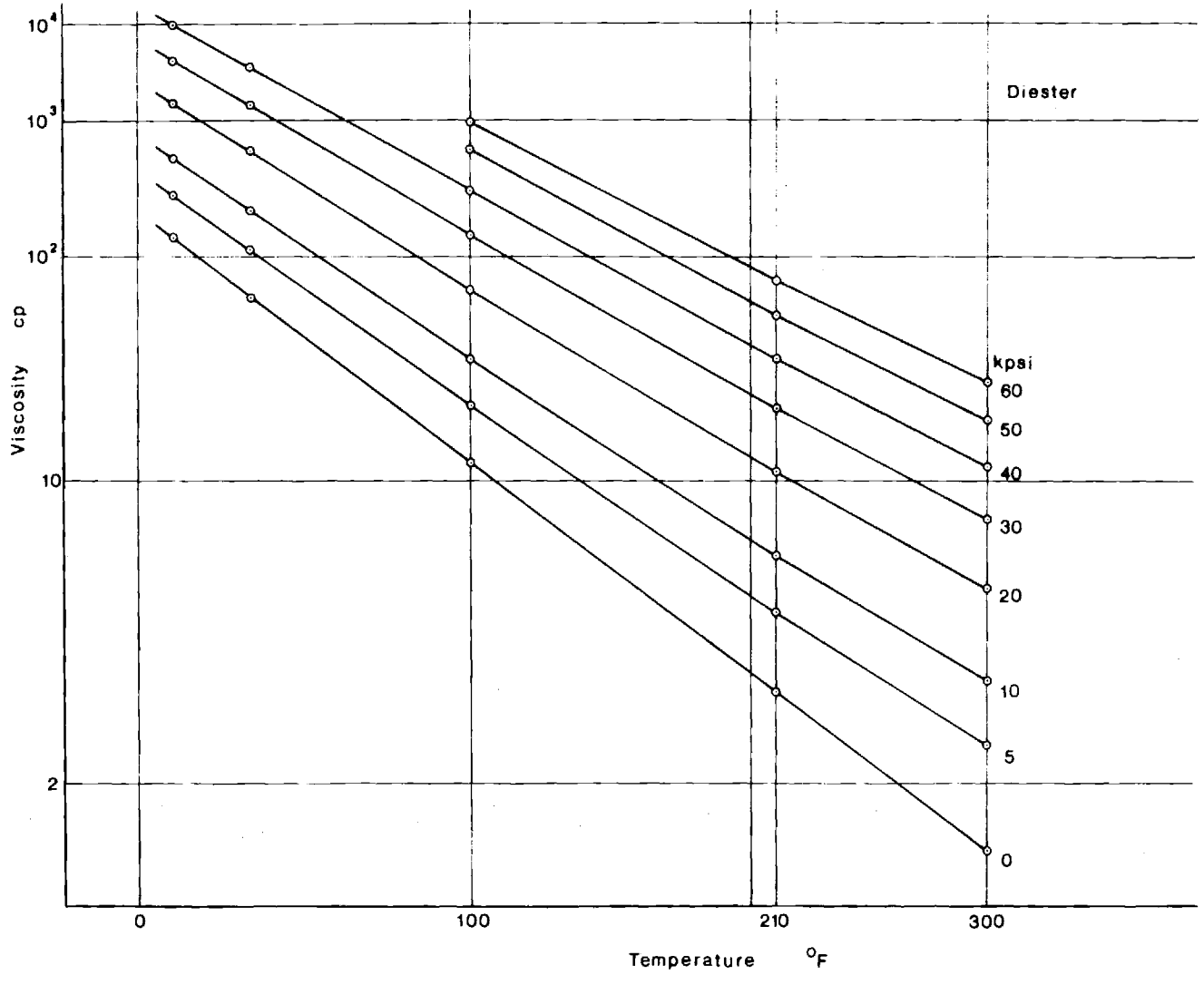

Figure 7. Temperature Pressure Viscosity Presentation for Diester. (ASTM D-341-43).

level. These viscosities are within procedural accuracy of the viscosities predicted by straight line characteristics as applied in Figure 8.

Comparison with Figure 3 shows that the high shear stress characteristics have the same general form of constant shear stress. The measurements with capillary 1 also show deviation at the same shear stress or the same shear rate downward from the Newtonian characteristic measured with capillary 0 in the same way as found in Figure 5. This confirms the statement that the deviation of capillary 1 measurements at high shear cannot be explained by a shear thinning effect.

The flow curves of Figure 5 (Diester, 10°F) are similar to the flow curves for the diester at 32°F (Figure 5). A translation along the viscosity axis (shear stress constant) will allow one flow curve to be superimposed on another flow curve. This holds also for flow curves measured at the same temperature. These observations suggest that the mechanism responsible for the flow curve deviation from constant viscosity is dependent on the pressure drop over the capillary, capillary geometry (L and D), and possibly some fluid properties; but it is not dependent on viscosity level nor on shear rate. It can be shown that dissipation heating satisfies these requirements.

The highest shear stress shown in Figure 6 is about 3×10^7 dyn/cm^2 ($\sim$435 psi). Slightly higher stresses were applied. However, amplifier saturation of the velocity signal prevented proper measurements from being taken. Similar conditions had also arisen for the diester, 32°F, 40 kpsi (Figure 5). These measurements are not incorporated in Table 5. An extrapolated flow curve signature has been used in Figure 5 and 6 to show an estimated behavior of the fluid.

Figure 7 shows the low shear stress behavior of diester over the temperature range covered. Table 4 gives the numerical values of the pressure temperature viscosity characteristics of the diester plotted in Figure 7.

The rectifying diagramatic presentation of Figure 7 is essentially that of the ASTM Standard Viscosity-Temperature Charts (D 341 - 43). The generating formula for the chart is $\ln\ln(\nu + c_o) = \ln A - Q \ln T$, for example, see reference [4], where ν is the kinematic viscosity in centistokes at the absolute temperature T (°R) and c_o, A , Q are constants (c_o = .6 cs for ν < 2cs). A and Q are material constants. The usefulness of these rectifying charts is based on the observation that mineral oils plot as straight lines presumably, however, only at atmospheric pressure. Hersey [4] states that fair results can be obtained by plotting the values of dynamic viscosity directly using the scale of kinematic viscosities. Figure 7 is generated with such a simplified plotting method.

The error that arises from the simplified use of the rectifying charts is, however, not significant for use in traction investigations of elastohydrodynamic lubrication. The density of the lubricant varies at most from about 0.9 g/cm^3 to 1.1 g/cm^3 [3] in the pressure and temperature ranges of interest. This is a change in density of ± 10%. The equivalent plotted error is totally about ± 0.7% at 1000 cp, ± 1.4% at 100 cp and ± 5% at 10 cp. The relative error between consecutive points is certainly smaller. A somewhat greater error may be expected because the characteristics for many fluids tend to show a slight curvature above atmospheric pressure and for large temperature ranges. The lower bound for the viscosity range of interest in traction investigations is 100 cp to

Table 4

Pressure Temperature Viscosity Relationship for Diester

kpsi	Temperature 10	32	100	210	300 °F
			units centipoise		
0	[130.]	[57.5]	11.41	2.86	1.46
5	250.	109.5	18.6	4.3	2.28
10	472.	196.0	28.95	6.0	3.05
20	1420.	546	64.2	10.7	4.92
30	3900.	1400.	134.5	18.0	7.52
40	9900.	3365.	268.	79.1	11.1
50	-	-	510.	46.7	16.2
60	-	-	940.	72.0	23.2
70	-	-	-	-	

The table values above kpsi are interpolated graphically on expanded semilog diagrams.

[4] : Extrapolated from straight line pressure viscosity characteristics mapped on a rectifying diagram $\ln\ln\eta$-$\ln T$ of type ASTM D 341-43.

1000 cp. The maximum error due to simplifications of the generating formula is then about 1%. It will in most cases be considerably smaller. The simplified plotting method may, therefore, safely be applied without any appreciable loss of accuracy.

The constant c_o (0.6cs) can also be discarded for traction investigations. The magnitude of this change is about 0.1% at 100 cp and diminishes rapidly for higher viscosities. The generating formula can therefore be regarded as having the form: $\ln\ln\eta = \ln A - Q\ln T$ which conveniently is a formula with two constants. The constant A stands for some defined base viscosity. The constant Q expresses the change of viscosity with temperature such that a large Q represents great changes in viscosity for a given temperature change.

Figure 7 shows that diester has straight line characteristics in the lnln - ln rectifying diagram for viscosities above 100 cp. It is also seen that the characteristics are straight lines for the ranges 0 - 40 kpsi and 10°F to 100°F as well as for atmospheric pressure and 10°F to 300°F. There is a minor curvature at all the reported pressure levels above atmospheric pressure and above 100°F, when the viscosity is less than 100 cp. The curvature is, however, equivalent to deviations less than about 5% of predicted viscosities. These deviations are furthermore found at viscosity levels, less than 100 cp, which is outside the range of interest for the high pressure range in elastohydrodynamic lubrication.

The high shear stress measurements of the calibration liquid, diester, show that dissipation heating most likely is the cause of the well observed deviation of flow curves of many lubricants from the Newtonian characteristics toward smaller apparent viscosities for high

shear stress conditions. It was further shown that the diester has a constant viscosity in the shear stress range up to about 14 psi ($\sim 10^6 dyn/cm^2$) measured with capillary 1. This indicates that the diester is a Newtonian liquid up to 14 psi. Non-Newtonian effects thus do not participate in the generation of the deviationg flow curves for diester measured with capillary 1.

Heat generation per unit volume and unit time is equal to the product of shear stress and shear rate. The measurements of the diester showed that the flow curves, Figures 5 and 6, for both capillary 1 and 0 were influenced by changes in shear stress, but hardly influenced by changes in viscosity, or changes in shear rate. Decreasing shear rates, or lower flow velocities, give equally longer resident times for the liquid in the same capillary. The heat generation per unit volume in a capillary is, therefore, independent of the shear rate and depends alone on the shear stress, or on the pressure drop experienced by the fluid. The temperature changes depend on the amount of heat generated, on capillary geometry (location in the capillary cavity) and on fluid properties. Possible important fluid parameters are specific heat and density.

The specific heat per unit mass, and the density are both very nearly constant for many lubricants. The values are in the range c_v: 0.3 to 0.5 Btu/lbm°F (0.3 to 0.5 cal/g°C) and ρ:0.03 to 0.036 lbm/in^3 (0.83 to 1.0 g/cm^3) giving a specific heat c per unit volume of 85 - 170 lbf/in^2°F. The thermal conductivity and the previously mentioned material constant Q are other possible important parameters.

The thermal conductivity does not vary drastically for mineral oil lubricants and for many of the synthetic lubricants. The operational values are in the range 0.015 - 0.017 lbf/sec°F (.7 - 0.8 Btu/hr°F ft)

with lower and upper extremes at 0.013 and 0.020 lbf/sec°F. The conductivity decreases about 3% per 100°F temperature increase and decreases about 1% per percent increase in density [4]. Deviations from these levels of thermal conductivities are few. Table 5 gives some examples of deviations.

Dimethyl Siloxane DC-200-50. One outstanding property of silicone oils is the relatively small decrease of viscosity with increasing temperature. The Q-exponent is a factor of 2 to 4 less than the Q-exponent of the diester. The flow curves for siloxane will therefore expectedly show considerably less deviation from the Newtonian characteristic than the diester flow curve for the same shear stress. Typical flow curves for the siloxane and for the diester is plotted in Figure 8 . The figure shows the much smaller loss of apparent viscosity for the siloxane, thus supporting the hypothesis of heat dissipation as an important mechanism in generating the deviating flow curves for the capillary 0 measurements.

Figures 9, 10 and 11 show the low shear behavior of the siloxane as a function of pressure at 100°F, 210°F and 300°F. The characteristics of Figure 9a are S-shaped and have inflection points at 20 - 60 kpsi. This is similar to the shape of the characteristic of a 550 silicone oil reported in [3] as sample 53 - H.

Figure 11 shows the considerably smaller slope of the characteristics as compared to the curves of Figure 7 - Diester. Table 10 gives the results of the measurements plotted in Figures 9, 10, 11. These measurements were carried out before the modifications to the high pressure viscometer were made. A second series of measurements of the siloxane were

Table 5

The Coefficient of Heat Conduction for Some Liquids

	k_t (lb_f/ ^oFsec)
Clorofluorcarbon	.0087
Fluorinated polyether	.0117
Most hydrocarbon and methyl siloxane lubricants	.0150 to .0170
Methylalcohol	.024
Fluorsilicones	.034
Glycerin	.036
Water-Glycol mixtures	.05 to .06
Water 32 ^oF	.073
Water 140 ^oF	.082

Values from references [5] and [6]

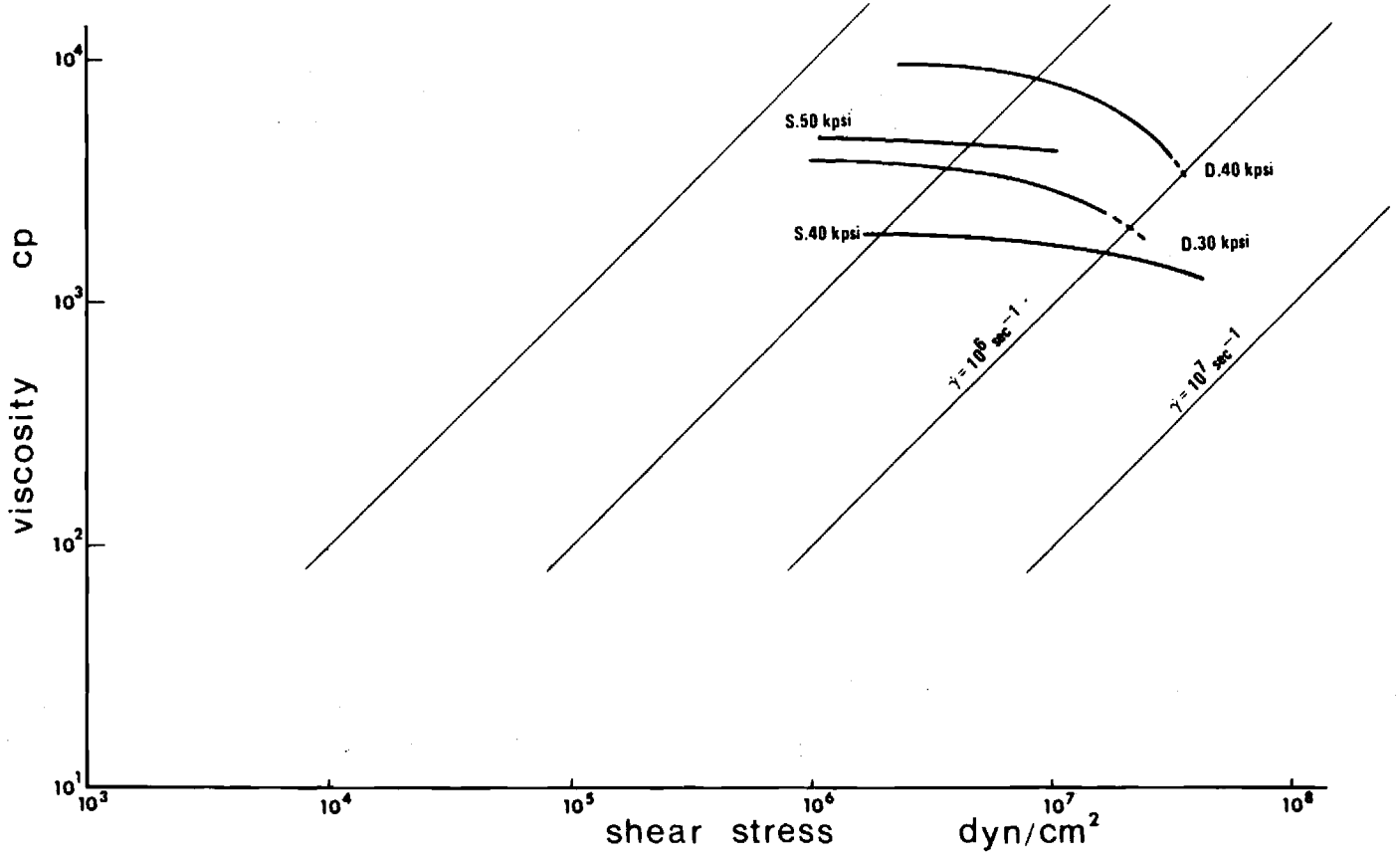

Figure 8 . Typical Flow Curves for Siloxane (S) and Diester (D). (Deviation from Newtonian behavior is more pronounced for the diester, which has a greater Q-exponent, than for the Siloxane.

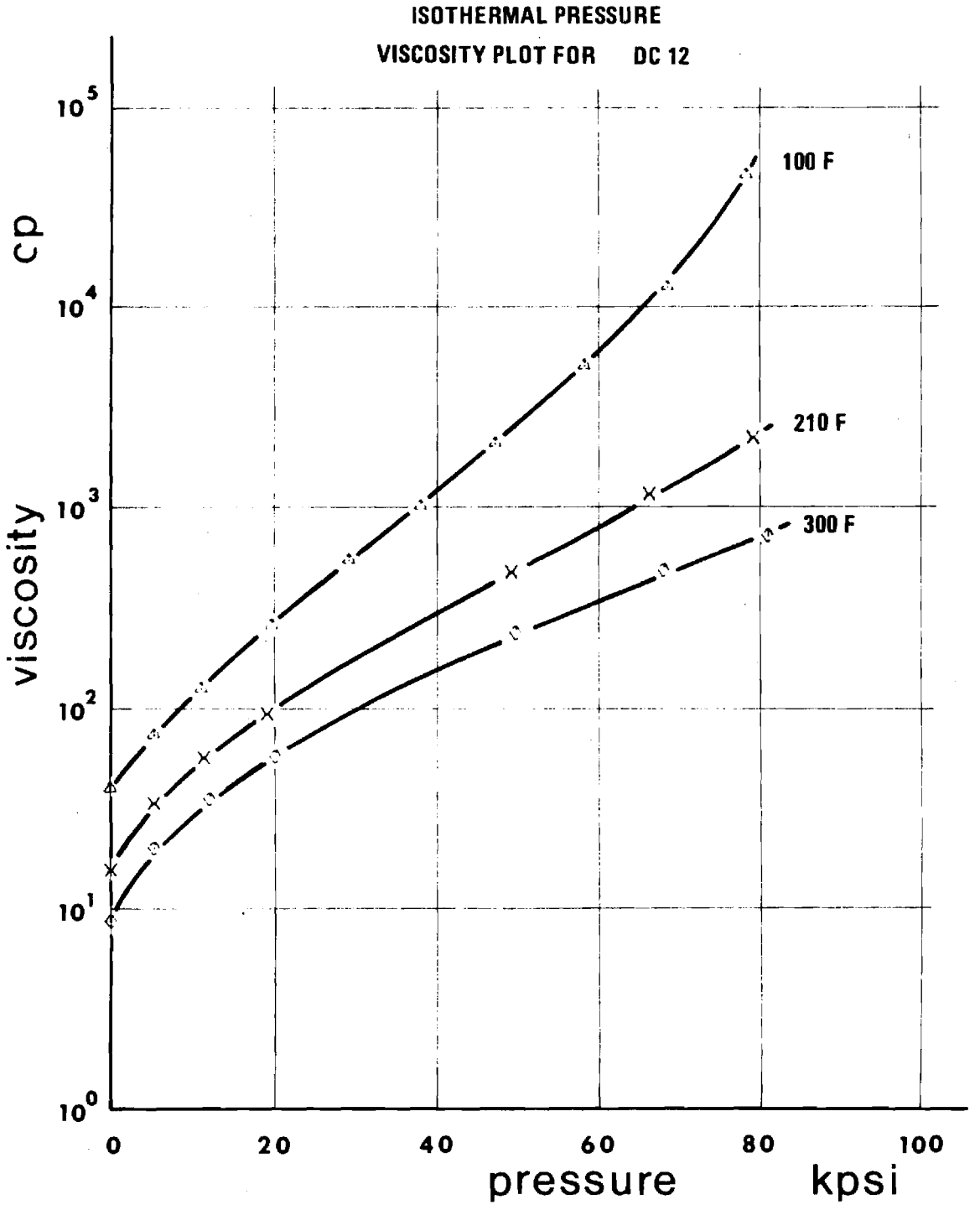

Figure 9. Low Shear Pressure Temperature Viscosity Characteristics for Dimethyl Siloxane DC-200-50 (DC-12). (Semilog representation.)

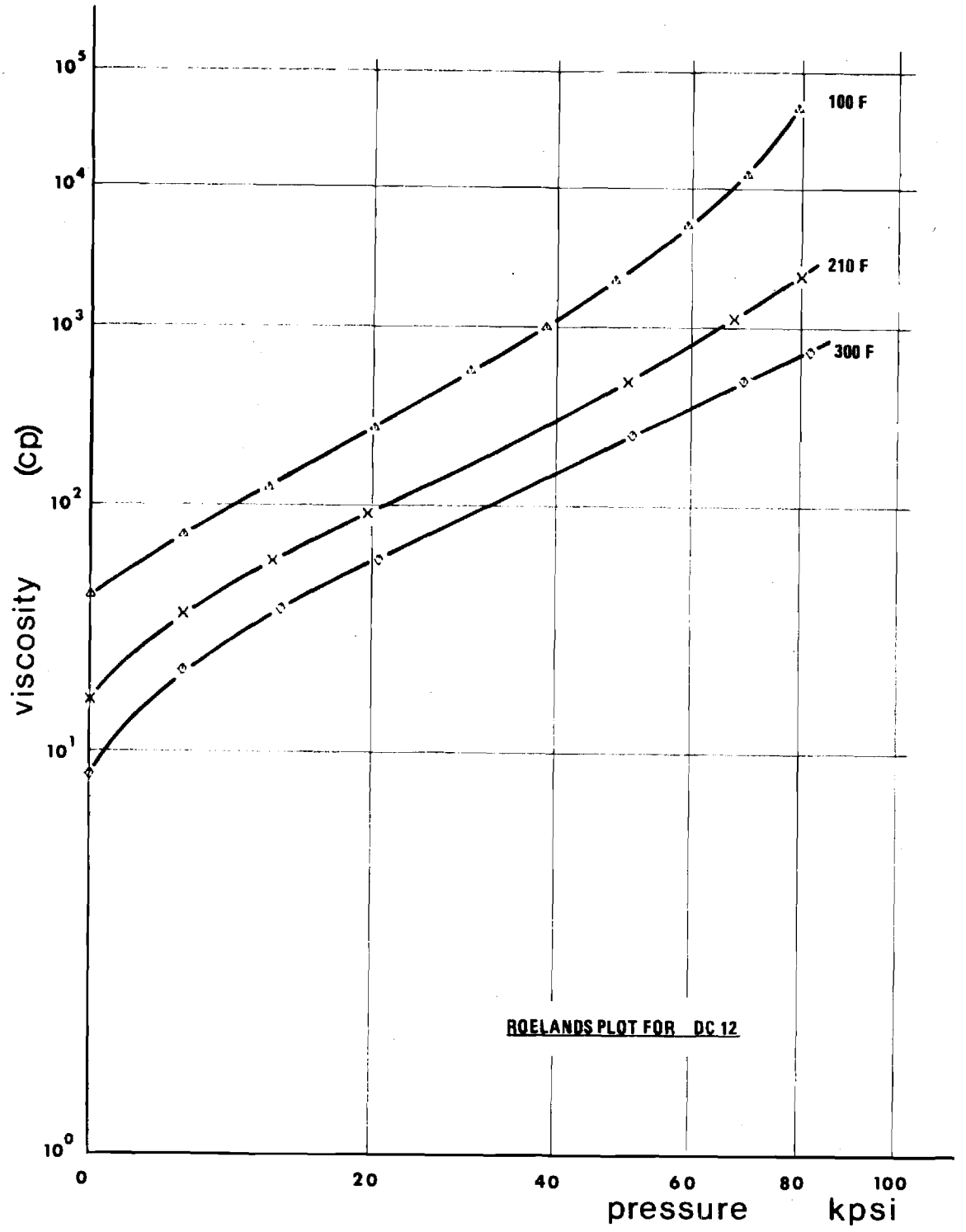

Figure 10. Low Shear Pressure Temperature Viscosity Characteristics for Dimethyl Siloxane DC-200-50. (DC-12.)

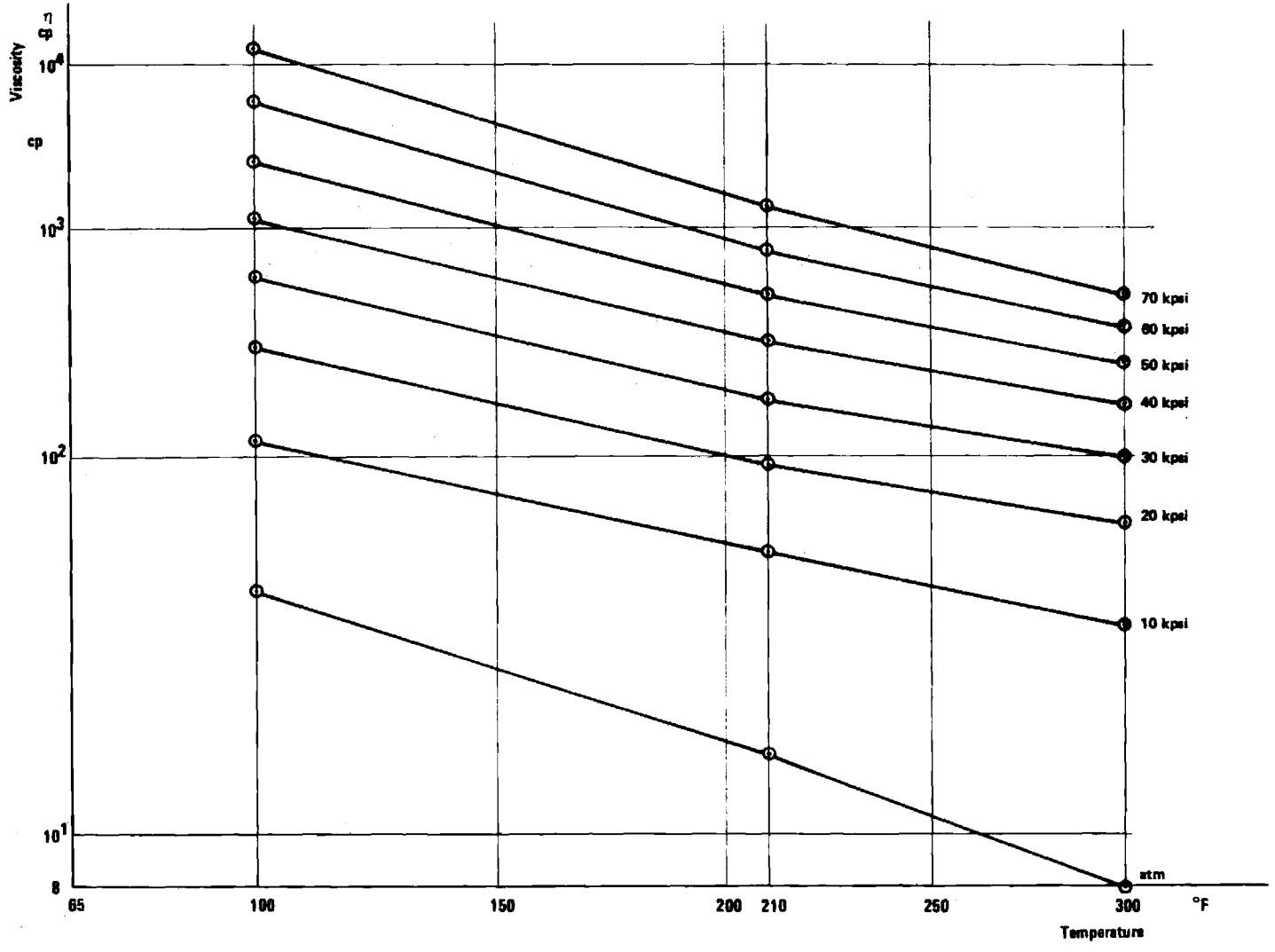

Figure 11. Low Shear Temperature Pressure Viscosity Characteristics for Dimethyl Siloxane DC-200-50. (DC-12).

Table 6. Dimethyl Siloxane DC - 200 - 50

L/D = 297 Averaged Data Points

DC200-20CS,CAP4,100F,3-23-71

P (PSI)	V (CP)
.00000	.39100+02
.53657+04	.72110+02
.11194+05	.12259+03
.19878+05	.25050+03
.29445+05	.52787+03
.38386+05	.97799+03
.47685+05	.20003+04
.58765+05	.48742+04
.69115+05	.12161+05
.78921+05	.44270+05

ALPHA STAR= .96336-04
ALPHA OT= .13550-03

DC200-20CS,210F,CAP4,3 24-71

P (PSI)	V (CP)
.00000	.15200+02
.53667+04	.32812+02
.11503+05	.55443+02
.19311+05	.91511+02
.49638+05	.45749+03
.66850+05	.11242+04
.79730+05	.21371+04

ALPHA STAR= .95620-04
ALPHA OT= .20481-03

DC200-20CS,300F,CAP4,3 25-71

P (PSI)	V (CP)
.00000	.84600+01
.53631+04	.19630+02
.12202+05	.34464+02
.20354+05	.56270+02
.50249+05	.23016+03
.68638+05	.46701+03
.81603+05	.69932+03

ALPHA STAR= .95546-04
ALPHA OT= .24187-03

carried out at low temperatures 32°F, 75°F and 100°F. Figures 12 and 13 summarize these measurements. The same general characteristics of the siloxane were found in the low temperature range. The pressure viscosity curve at 32°F, Figure 12, is S-shaped, however, the inflection point is located as low as 15 kpsi. The temperature viscosity characteristics, Figure 13, at low temperatures are straight lines with slopes of the same magnitude as the slopes in the temperature range 100-210°F, Figure 11 .

High shear stress measurements of the siloxane fluid were carried out at 75°F. The results are shown in Table 11 and Figure 14 . The flow curves, Figure 12, for capillary 1 measurements also deviate downward from the curves of capillary 0 at the same shear stress or the same shear rate in the shear stress range covered by both capillaries. Shear thinning is therefore not present for dimethyl siloxane for stresses up to at least $4 \times 10^6 dyn/cm^2$ (57 psi). This is particularly well illustrated with the flow curves at 30 kpsi where the overlap zone is more than a decade wide, $10^5 - 10^6 dyn/cm^2$, Figure 14. The flow curves for the siloxane fluid for both capillaries are seen to be similar in form. A translation along the viscosity axis will allow one flow to be superimposed on another curve. This indicates that dissipation heating is the cause of the observed deviation from Newtonian behavior for both capillary 1 and capillary 0 as was the case for the diester, and suggests further that the range where shear thinning effects are absent can be extended to the highest stress reported in Figure 12, which is $4 \times 10^7 dyn/cm^2$ (570psi).

Partial blockage of the capillary was occasionally experienced during the high shear experiment with capillary 0. Figure 15 shows the results from measurements at 30 and 40 kpsi with such partially blocked

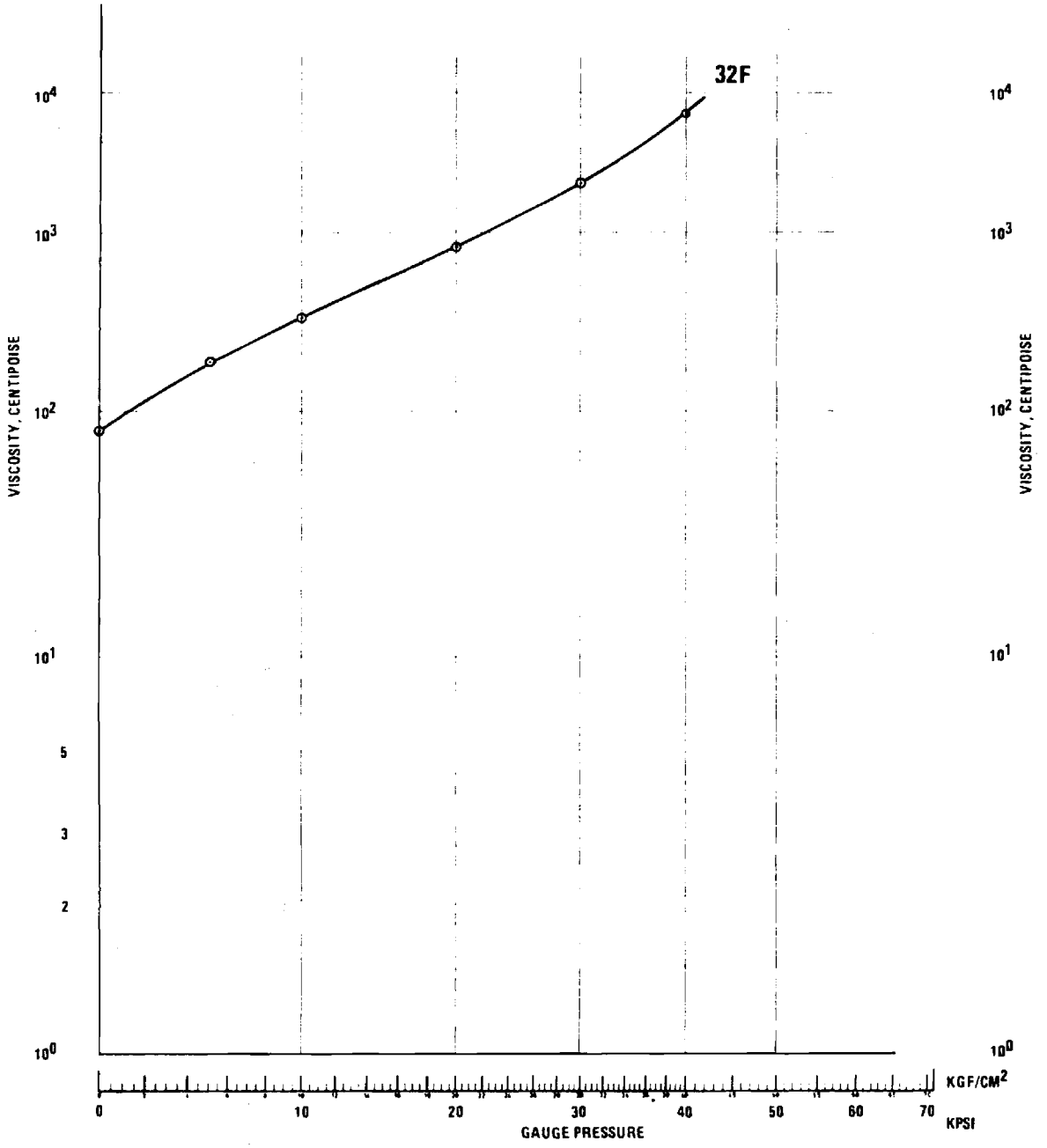

Figure 12 . Low Shear Pressure Viscosity Characteristic of Dimethyl Siloxane DC-200-50, 32°F.

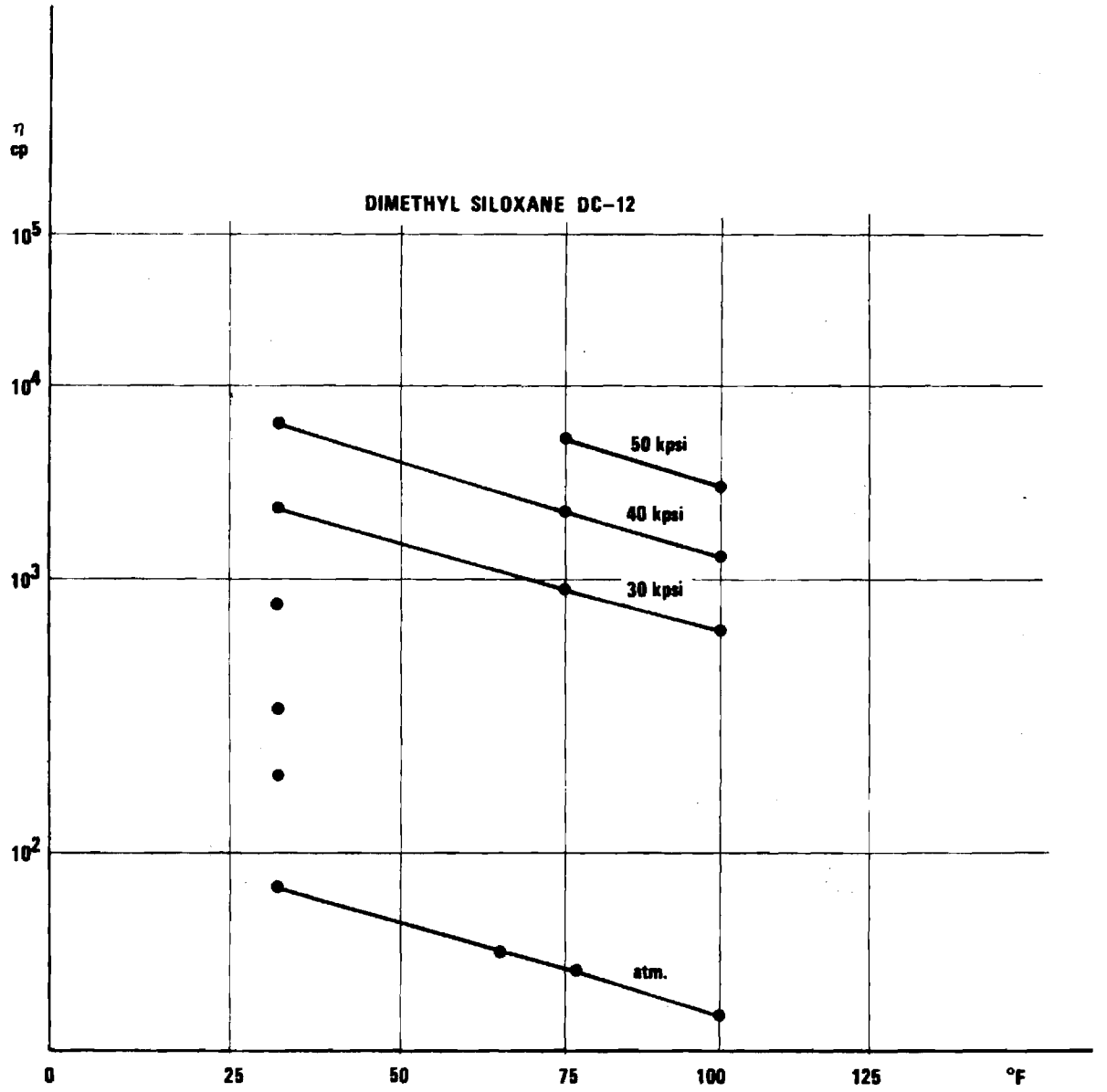

Figure 13. Low Shear Temperature Pressure Viscosity Characteristics of Dimethyl Siloxane DC-200-50 in the Range 32 - 100°F, (ASTM D 341-43).

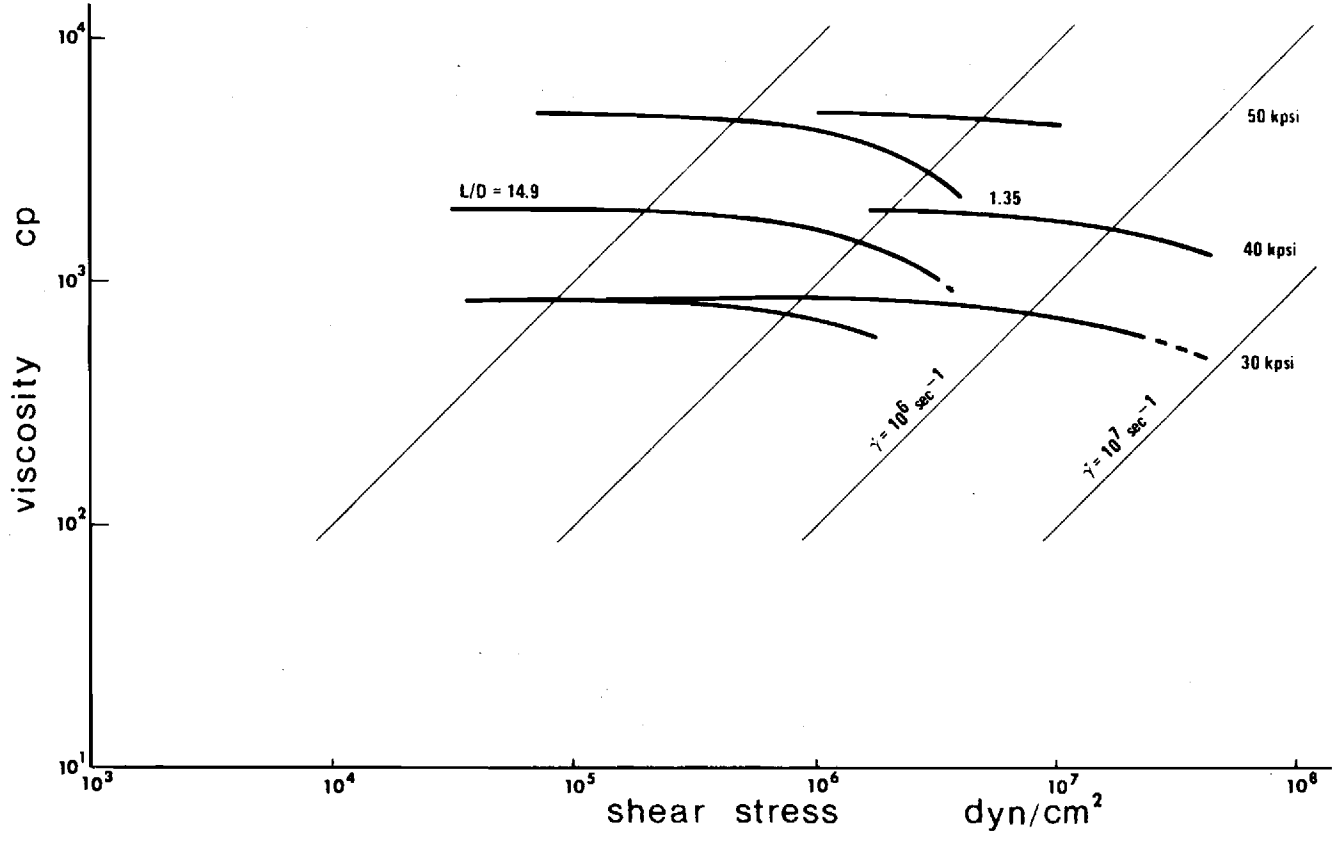

Figure 14. High Shear Measurements of Dimethyl Siloxane DC-200-50, T = 75°F.

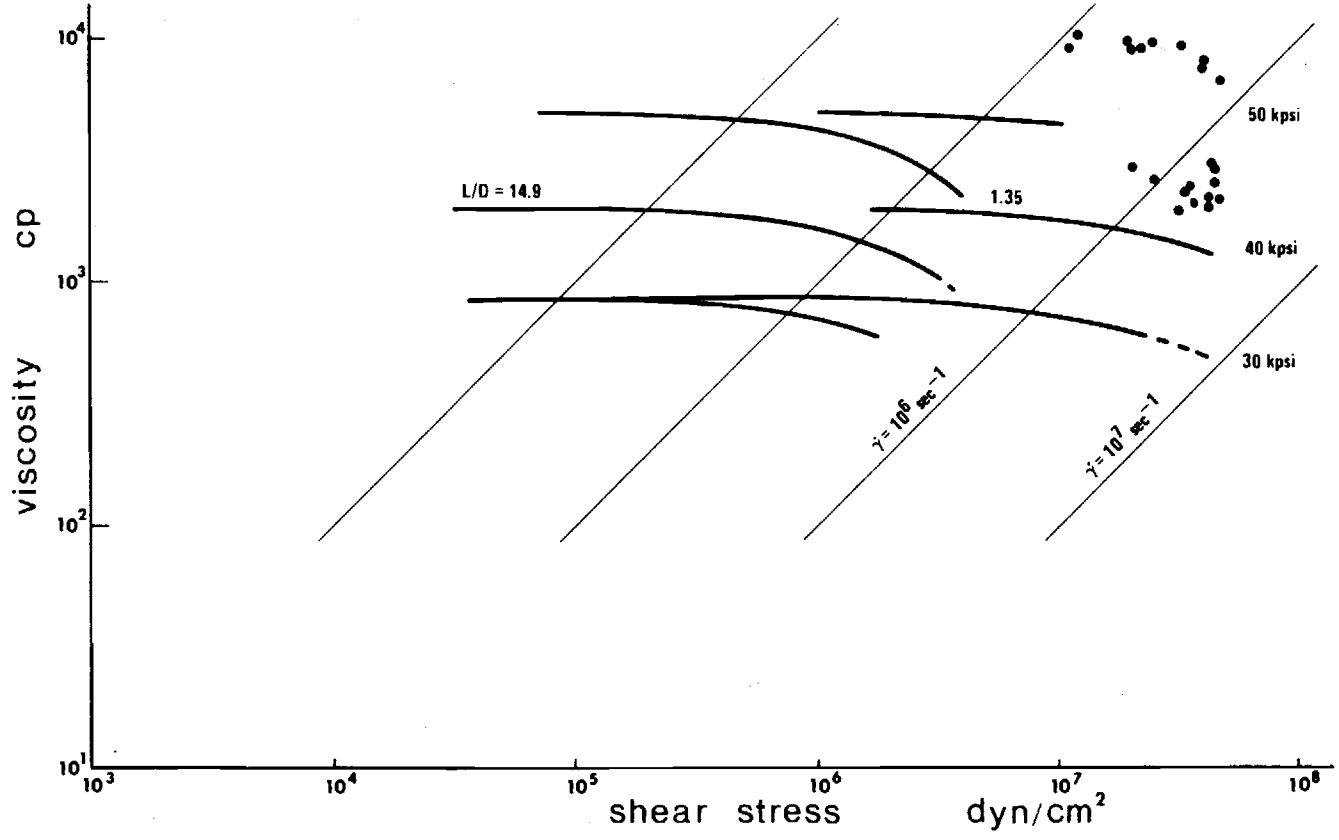

Figure 15. High Shear Measurements with Partially Blocked Capillary. (Dimethyl Siloxane DC-200-50. T = 75°F. The results are plotted with Figure 14 as the background.)

capillary and tubing. The results are plotted with Figure 14 as the background. It is apparent from Figure 15 that the plotted results are grouped in a meaningless pattern in terms of liquid behavior. All apparent viscosities are higher than what would be expected for liquid behavior. These higher values of apparent viscosities possibly indicate partial solidification of the siloxane.

The results of the first measurements taken follow the previously measured flow curve for 40 kpsi - 75°F conditions. The applied shear stress was below 2×10^7 dyn/cm^2 (285 psi). The latter part of the 40 kpsi series yields meaningless results, however. Applied shear stresses were above $2\ 10^7$ dyn/cm^2. High shear stress measurements were attempted. at 50 kpsi with capillary 0 without giving meaningful results. This explains the missing high shear stress in Figure 14 of the flow curve for capillary 0 at 50 kpsi. The sapphire capillary, capillary 0, was taken out and inspected after such experiments. No damage to the sapphire or its seals was ever observed.

The siloxane was investigated also at 32°F. Figure 16 shows the results. In order to investigate high shear stress behavior, only capillary 0 experiments were performed.

Measurements at 50 kpsi could not be carried out. A partial solidification was observed at 40 kpsi above shear stresses of about 3×10^6 dyn/cm^2 (43 psi). The siloxane seemed to be in a stable condition in that lower shear stresses applied after a high stress situation gave results consistant with earlier results within the same series.

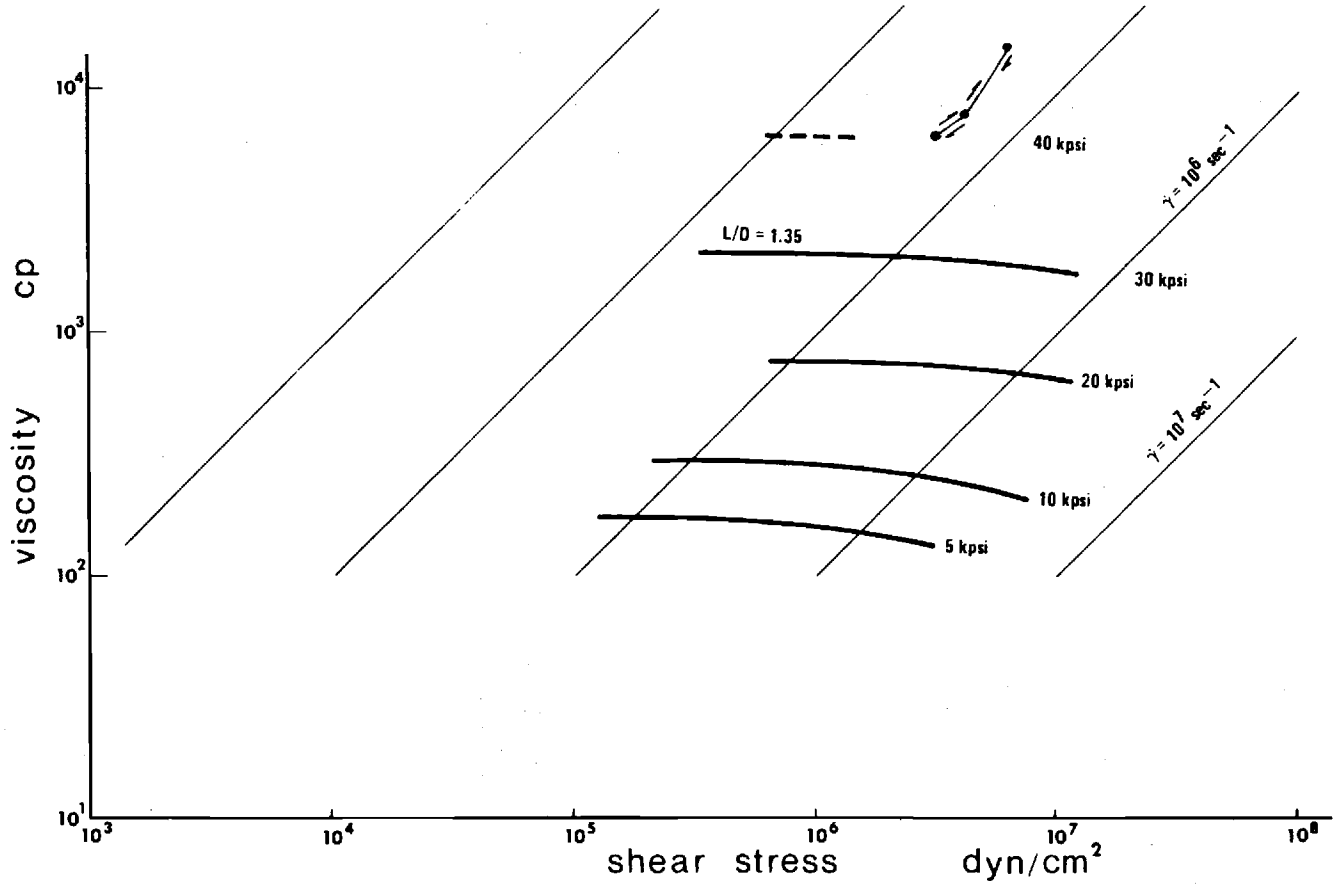

Figure 16. Non-Liquid Behavior of Siloxane at 40 kpsi, High Shear Measurements. (Apparent reversible behavior T = 32°F.)

The flow curves for siloxane, at $75^{\circ}F$, show smaller deviation from the Newtonian characteristic than the curves of diester as shown in Figure 8. This is consistant with the dissipation heating hypothesis and expectations based on the significantly smaller Q-factor for siloxane.

The flow curves of Figure 16 at 5 and 10 kpsi show greater deviation from the Newtonian characteristic than previously observed. This greater deviation is consistant with a slightly greater slope (greater Q) in the temperature region 32° - 75° as seen from Figure 13 compared with Figure 11.

The experiment was repeated under identical conditions as the previous measurements, $32^{\circ}F$ capillary 0 only. The results are found in Figure 16. Non-liquid behavior was again observed at 40 kpsi and shear stresses above 3×10^{6} dyn/cm^{2}. A gradual process toward complete solidification seemed to prevail, however. No definite explanation was found for this slightly altered behavior under otherwise identical conditons.

The siloxane measured at $100^{\circ}F$ with capillary 4 in order to establish a connection with low shear stress data previously measured. The results are plotted in Figure 18. The results of capillary 4 measurements were found to be of slightly larger magnitude than expected (see Figure 13 and Figure 11). The reason for this deviation was not pursued further because the discrepancy was considered insignificant for the general conclusions of the work.

Several investigations were performed into the solidification of the siloxane. The more rugged capillary 1 was mounted in the system during these investigations. The temperatures were $75^{\circ}F$ and $32^{\circ}F$. Pressure was increased in steps of 10 kpsi with a waiting period of several minutes.

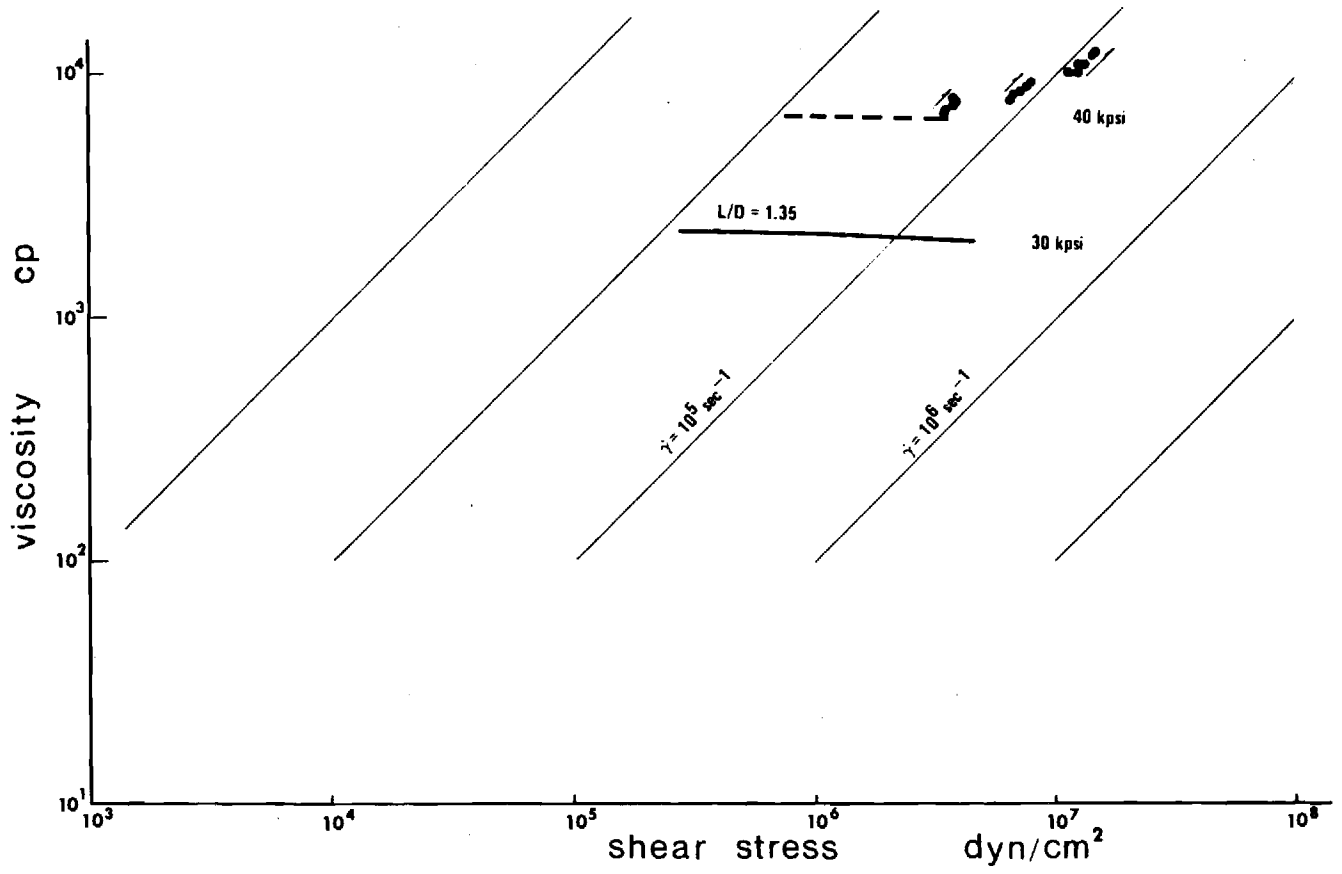

Figure 17. Non-Liquid Behavior of Siloxane at 40 kpsi, High Shear Measurements. (Apparent irreversible behavior T = 32°F.)

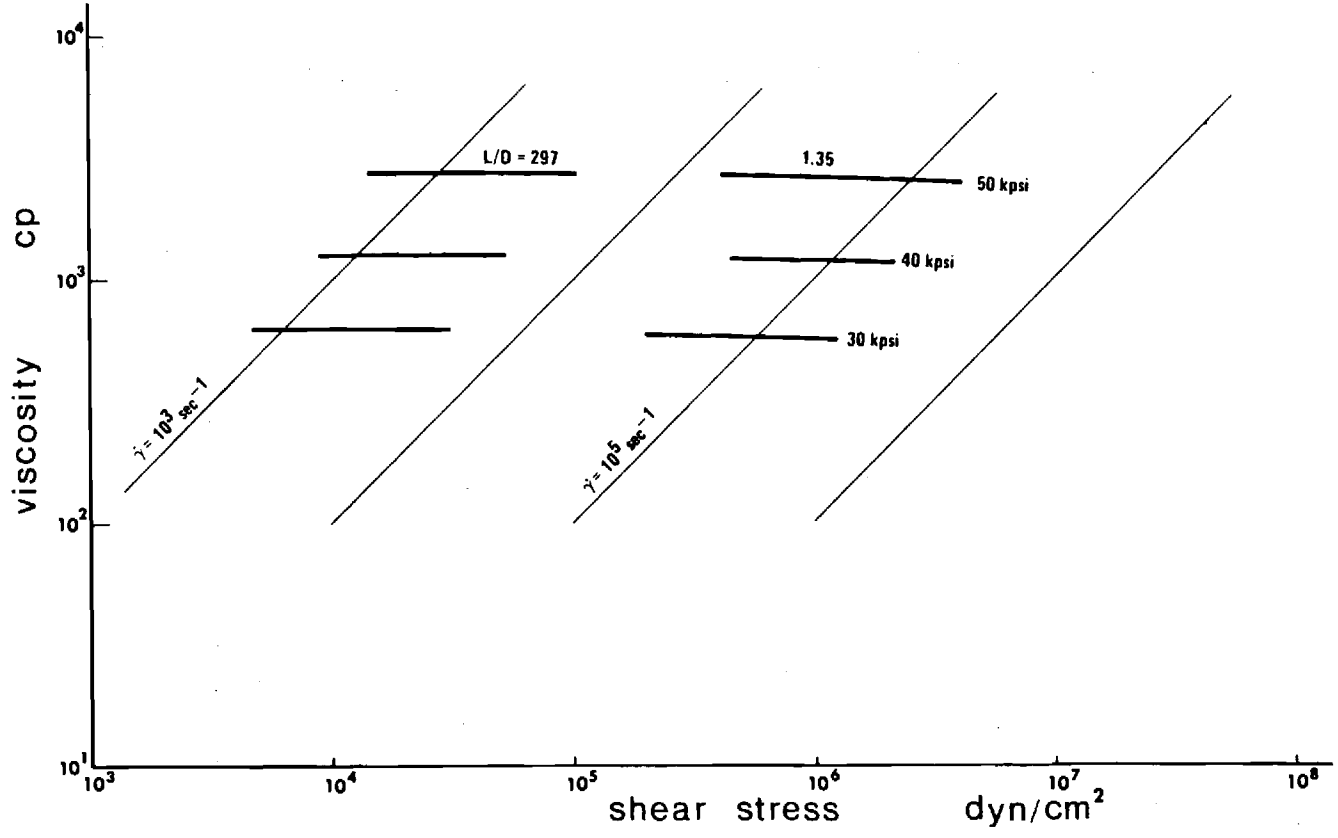

Figure 18. Low Shear Measurements (Capillary 4) and High Shear Measurements (Capillary 0) for Comparison with Previous Collected Data.

Shear stress shocks were applied at each pressure level to provoke a possible solidification. Shear stress peaks are estimated to have been of about 5×10^5 cyn/cm^2. Complete blockage of some of the tube branches of the test systems was observed at 60 kpsi for 75° and at 50 kpsi for 32°F. These observations were reproducible. A large hysteresis in reversal to complete liquid state was found. A return to the liquid state started first after the system pressure - in the still liquid branches - was lowered 25 to 35 kpsi below the blockage generating pressure. This return to the liquid state was accompanied by a slight volume increase observed as a slight pressure increase in the liquid branches. The observations of blockage pressures and the solidifications experienced at lower pressures and viscosities seem to justify a tentative viscosity - shear stress diagram (Figure 19) which predicts ranges where non-liquid behavior can be anticipated. These observations are interesting and may provide a key to a possible explanation for the anomalous behavior of some silicone oils in their ability to create an elastohydrodynamic lubrication film. Figure 19 is plotted with Figure 15 as background.

Polyalkyl Aromatic + Additive (DN 600 + Additive). High shear stress measurements of the synthetic lubricant DN600 + Additive are found in Figure 20. The flow curves show Newtonian behavior at least up to 3×10^6 dyn/cm^2 (435 psi). The general form of the flow curves suggests that Newtonian behavior persists up to the maximum employed stress of 4.2×10^7 dyn/cm^2 (610 psi). Partially non-liquid behavior was possibly encountered at 30 kpsi and certainly at 40 kpsi.

The table values of capillary 1 at 20 kpsi show some scatter around 10^6 dyn/cm^2. These data were taken with a manual traverse of the viscometer. Difficulties in maintaining steady conditions at very low speed may explain the scatter. Some low speed data points created with the constant speed

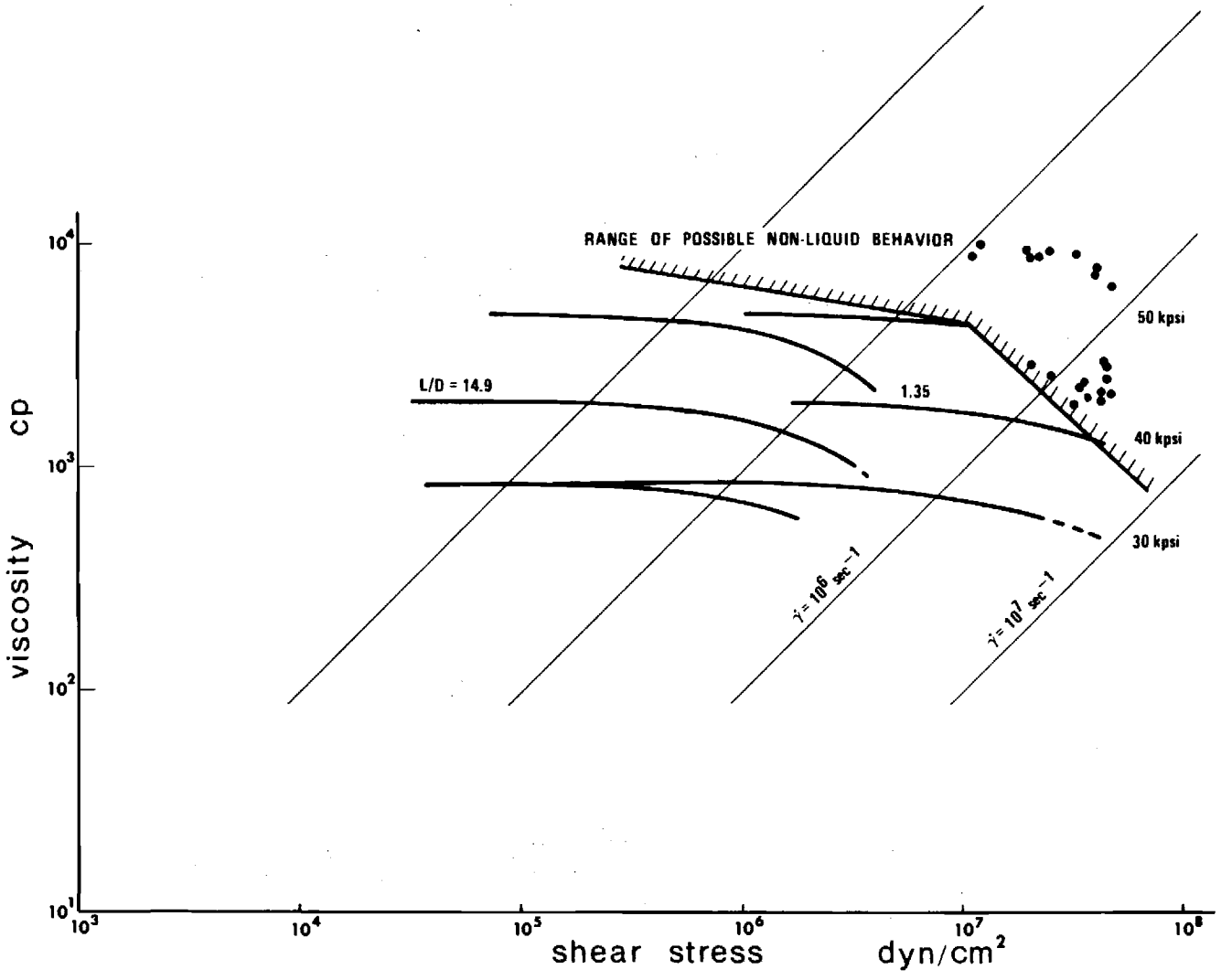

Figure 19. Range of Possible Non-liquid Behavior of Siloxane, 75°F. (This figure is plotted with Figure 15 as the background.)

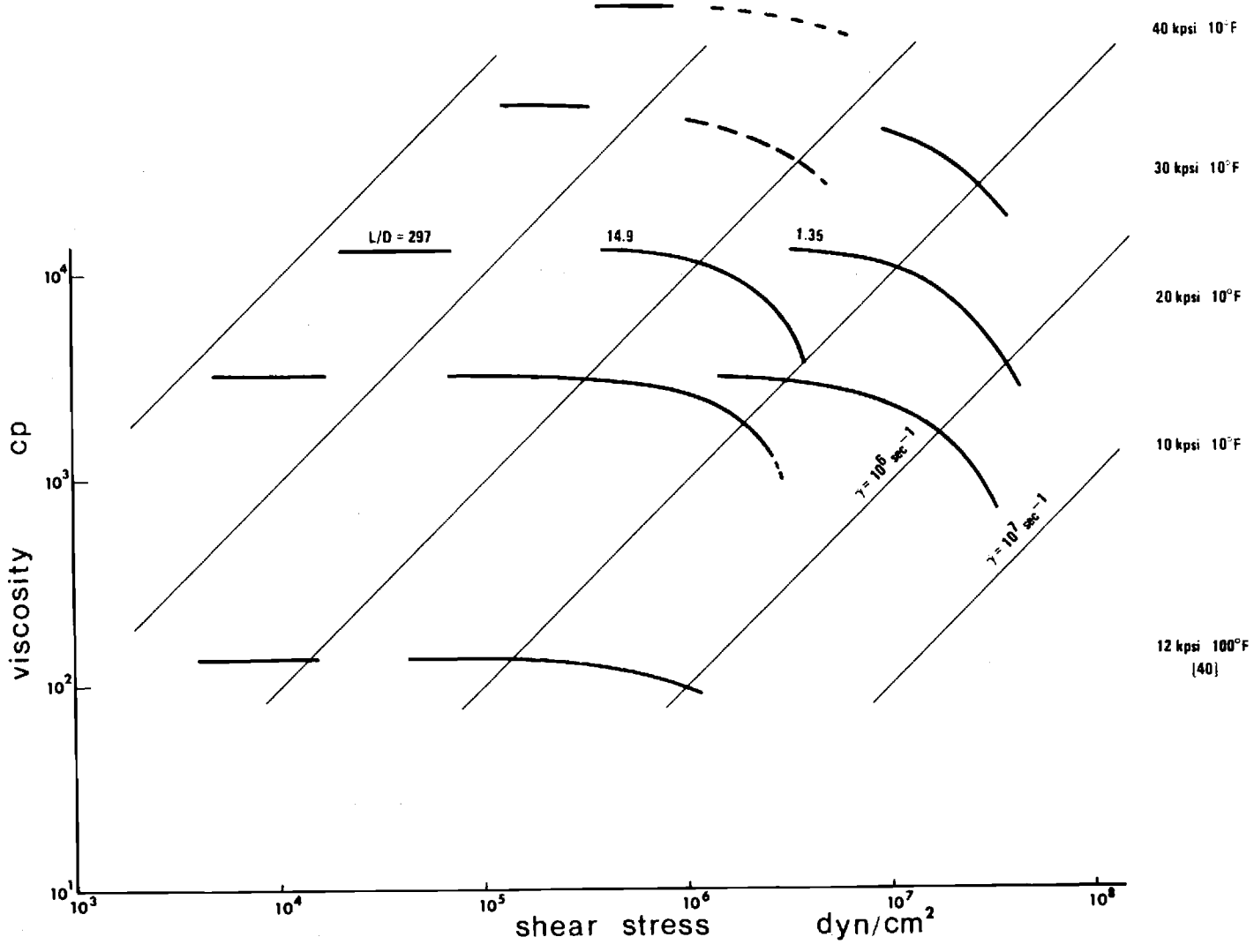

Figure 20. Flow Curves for Polyalkyl Aromatic + Additive (DN 600 + Additive). 10°F and 100°F.

drive are found at 3×10^5, 6.6×10^5, and 9.6×10^5 dyn/cm^2. Scatter for these groups is very small.

Previous measurements of DN600 + Aditive were carried out up to 1.65×10^5 cp. Conditions were 100 kspi and 100°F. Non liquid behavior was not experienced, presumably due to the higher temperature. The scatter at $1 - 2 \times 10^5$ cp (40 kpsi, 10°F) can possibly be explained as a partial solidification caused by low temperatures but not necessarily due to high shear stress.

Synthetic Paraffinic Oils XRM 109 F4 and XRM 177 F4. The lubricants XRM 109 F4 and XRM 177 F4 are essentially the same, except that XRM 177 F4 is blended with an anti-wear additive. This additive is not expected to cause significant changes in the viscosity of the blend. The base lubricant in XRM 109 F4 and XRM 177 F4 is a synthetic paraffinic oil similar to Fluid D, the synthetic paraffinic oil reported in [9], [10] and to fluid XRM 109 reported in [11].

Figures 21 - 24 along with Tables 7 and 8 show the low shear stress data. Viscosities at atmospheric pressure are equal for the two lubricants. The pressure viscosity relations at 100°F are also very nearly identical. There is a trend for XRM 109 F4 to show slightly higher viscosities than XRM 177 F4 at higher pressures and temperatures. The greatest deviation is found at 50 kpsi and 300°F. XRM 109 F4 has a viscosity which is about 8% higher than the corresponding viscosity of XRM 177 F4.

Figure 25 shows a pressure-viscosity plot of XRM 109 F4, XRM 177 F4 and Fluid D. The figure illustrates the difference between samples which are not from the same lot. The viscosity of Fluid D is consistently lower than the viscosities of the XRM fluids. The figure also shows the slightly increased viscosities for XRM 109 F4 compared with XRM 177 F4. The trend is particularly visible at 300°F. The anti-wear additive reduces the viscosity slightly compared with that of the base fluid.

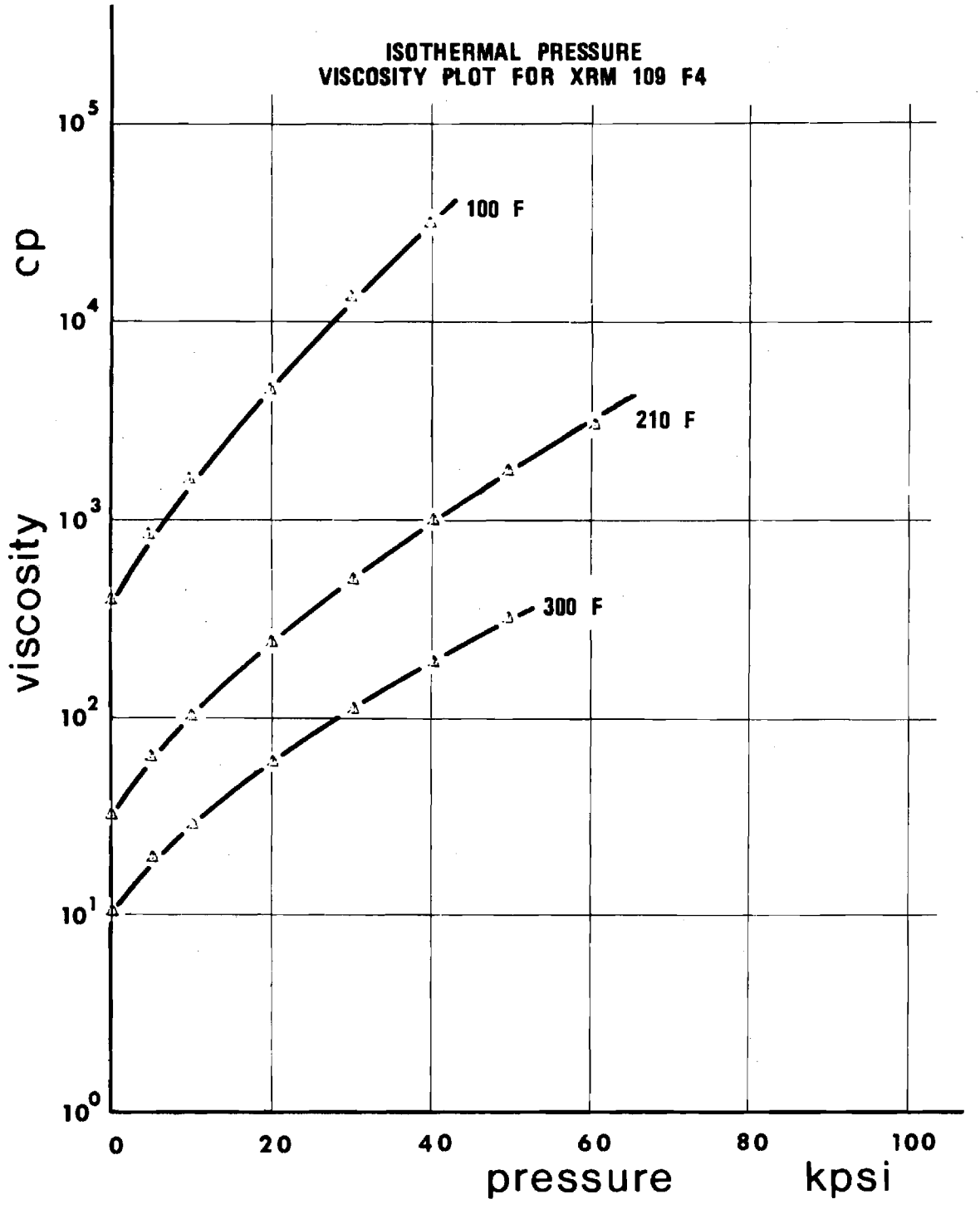

Figure 21. Isothermal Pressure Viscosity Plot for XRM 109 F4. (Semilog Presentation.)

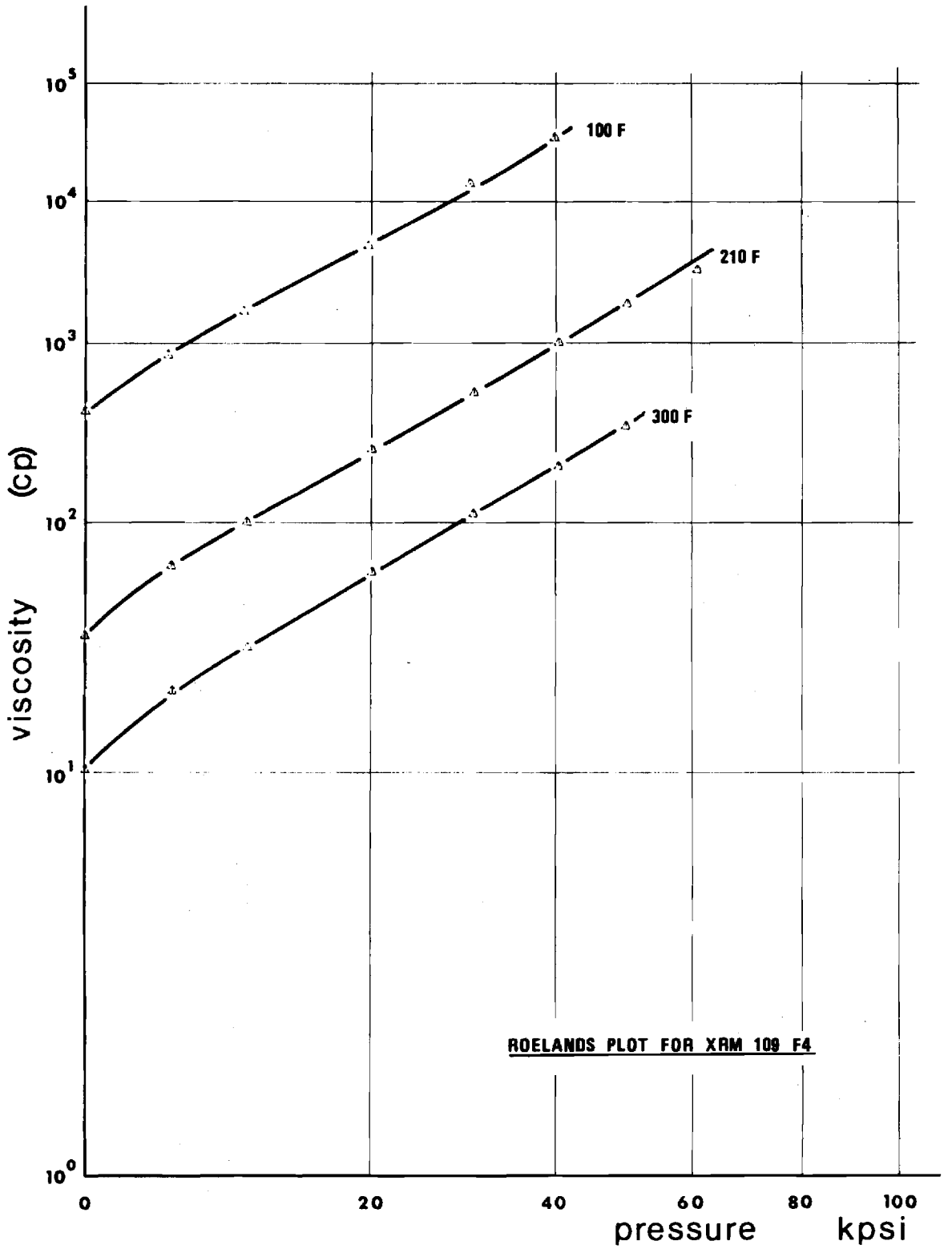

Figure 22 . Roelands Plot for XRM 109 F4.

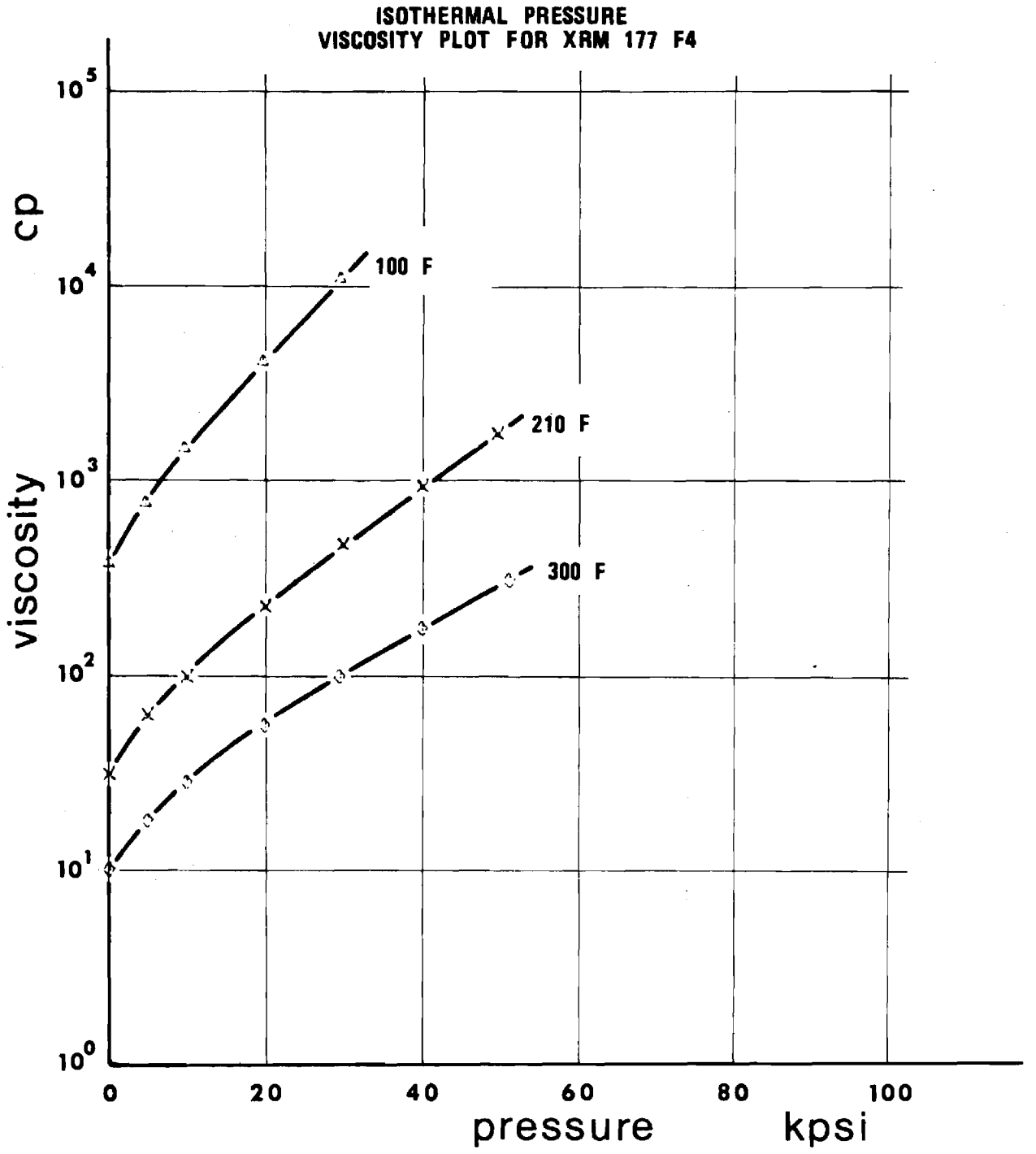

Figure 23. Isothermal Pressure Viscosity Plot for XRM 177 F4. (Semilog Presentation.)

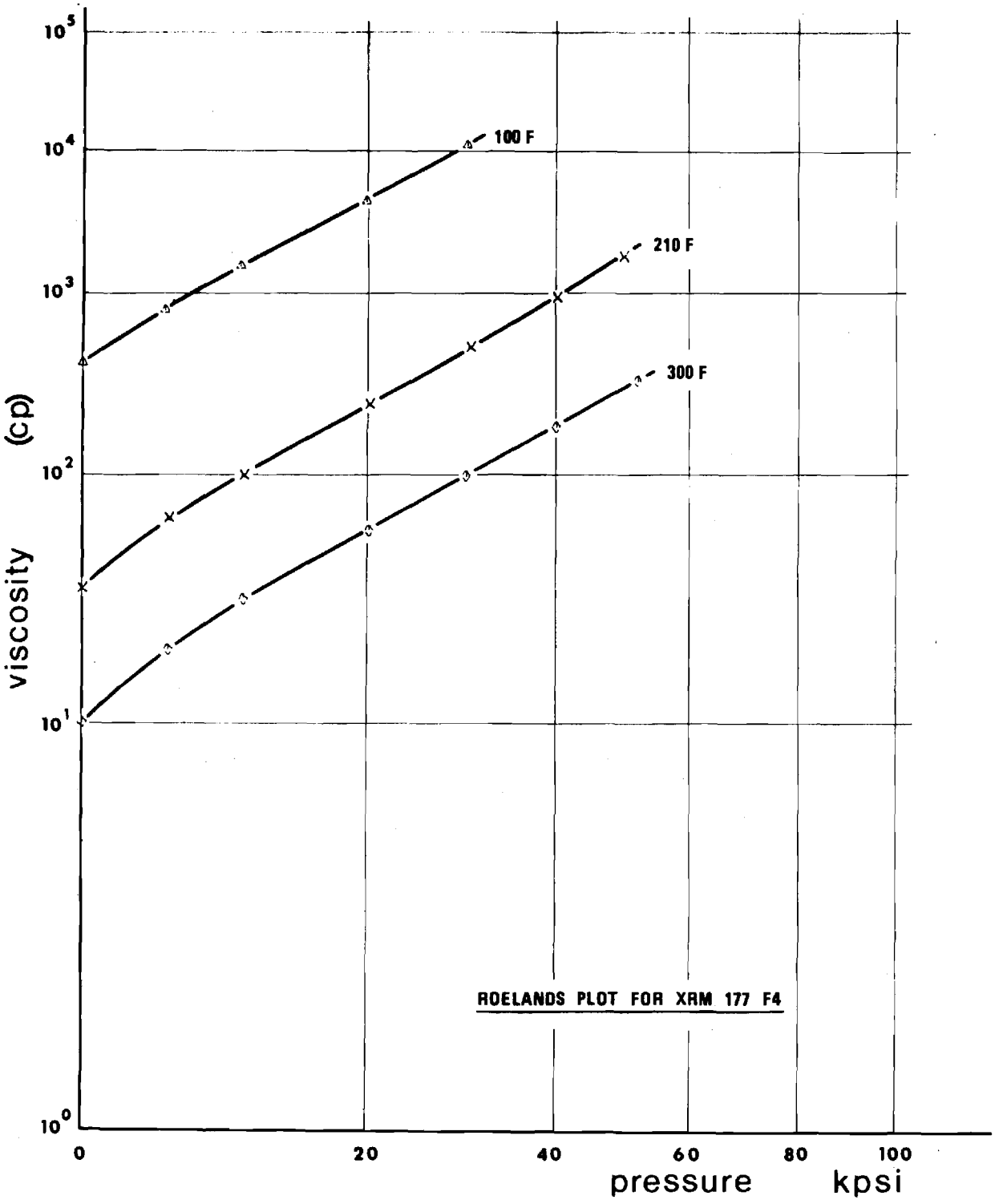

Figure 24 . Roelands Plot for XRM 177 F4.

Table 7 XRM 109 F4, Synthetic Paraffinic Oil,

Plot, L/D = 297

Averaged Data Points

XRM 109 F4 100 F

P (PSI)	V (cP)
.00000	.37600+03
.47530+04	.80367+03
.97724+04	.15267+04
.19794+05	.43194+04
.29879+05	.12829+05
.39870+05	.30525+05

XRM 109 F4 210 F

P (PSI)	V (cP)
.00000	.31600+02
.49462+04	.62895+02
.99898+04	.10047+03
.20023+05	.23623+03
.30184+05	.49047+03
.40246+05	.97936+03
.49608+05	.17384+04
.60497+05	.29581+04

XRM 109 F4 300

P (PSI)	V (cP)
.00000	.16220+02
.50313+04	.19251+02
.10065+05	.28248+02
.20112+05	.58539+02
.30257+05	.10861+03
.40363+05	.19823+03
.49687+05	.31313+03

Table 8 XRM 177 F4, Synthetic Paraffinic Oil,

Plot, L/D = 297

Averaged Data Points

FLUID XRM 177F4 100°F

P (PSI)	V (CP)
.00000	.37600+03
.47029+04	.76613+03
.96466+04	.14697+04
.19651+05	.41280+04
.29578+05	.11027+05

FLUID XRM 177F4 210 F

P (PSI)	V (CP)
.00000	.31600+02
.49475+04	.63243+02
.99268+04	.99644+02
.19991+05	.22776+03
.30020+05	.47191+03
.40206+05	.93740+03
.49704+05	.17434+04

XRM 177 F4 300 F

P (PSI)	V (CP)
.00000	.12220+02
.48992+04	.18247+02
.98698+04	.28595+02
.19905+05	.55708+02
.29546+05	.99291+02
.40126+05	.17470+03
.51372+05	.30802+03

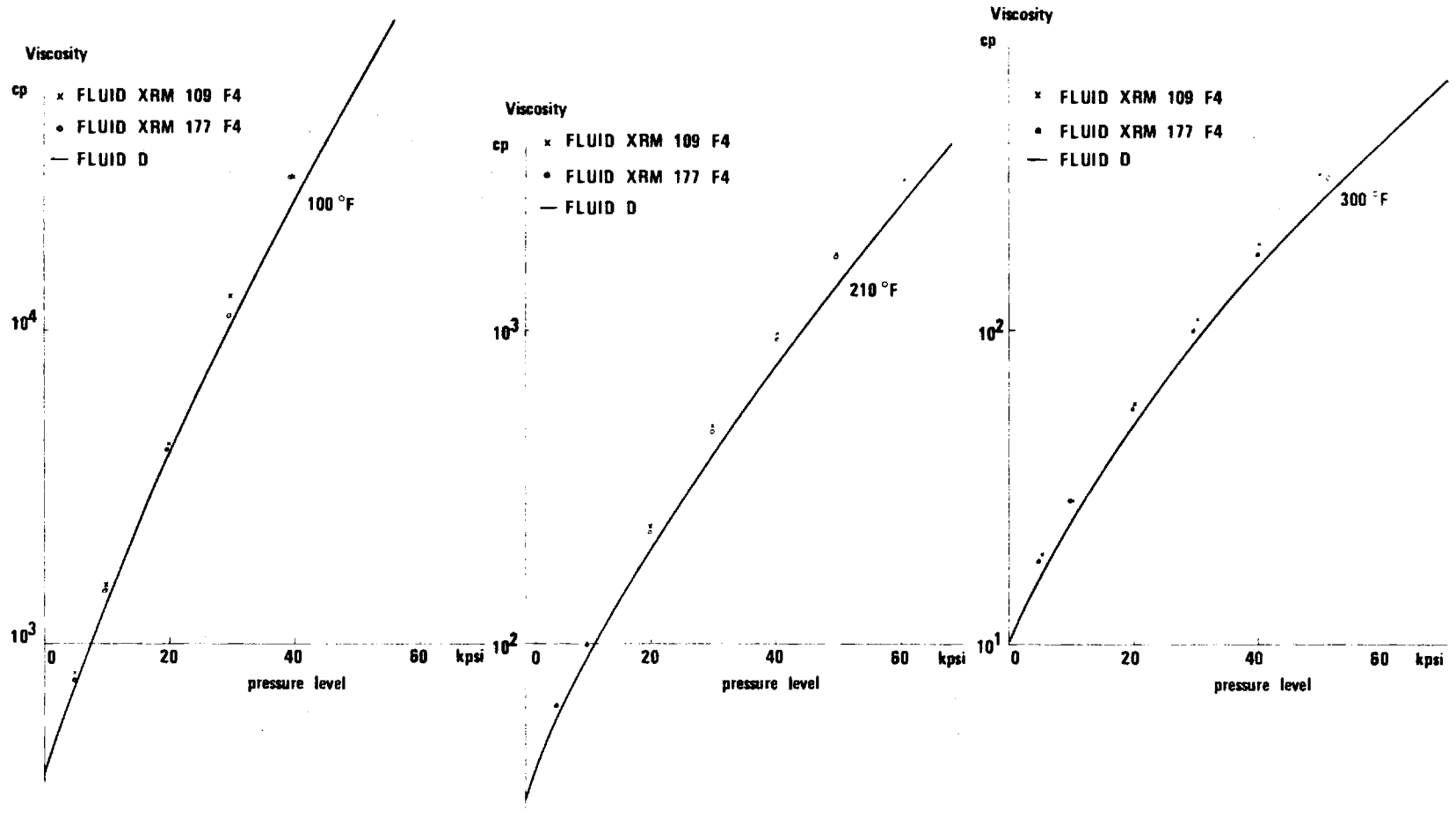

Figure 25. Isothermal Pressure Viscosity Plot of Fluid D, XRM 109 F4 and XRM 177 F4. (The effect of the antiwear additive, XRM 109 and XRM 177, and the difference in properties when the fluids are not from the same lot, fluid D and fluids XRM, are shown.)

Figure 26 shows the high shear stress measurements for fluid XRM 177 F4. The two fluids XRM 177 F4 and XRM 109 F4 were found previously during the low shear stress investigation to be very nearly identical. shear stress investigations of XRM 109 F4 would expectedly not yield significant new information and were therefore not carried out.

Some of the flow curves for a capillary cover more than two decades of shear stress. The Newtonian parts of the curves are particularly far extended into the low shear region showing good agreement with measured low shear data. The overlap zone is more than a decade wide. The heating effect of the curves of capillary 1 is distinctly seen. The general form of the flow curves suggests that the apparent non-Newtonian behavior measured with capillary 0 is caused by heating alone. The highest shear stress measured was $4.78 \times 10^7 dyn/cm^2$ (695 psi).

The operating characteristics for the lubricant in an EHD contact are also shown in Figure 26. The two vertical lines are estimated working conditions for the lubricant at a load of 15 lbf at 55 in/sec sliding speed in a steel ball and sapphire disc contact. The positions in the contact are at the center (the right vertical line) and 1/4 of the contact radius from the entrance (the left vertical line). Figure 26 shows clearly that capillary viscometry is not very far from the situation where EHD conditions for a lubricant can be created in a laboratory experiment in which the parameters of interest can be varied independently of each other.

An investigation of all the reported flow curves of the four lubricants has shown that all characteristics do fit to one general standard curve, regardless of the fluid type and for both capillary 1 and capillary 0 measurements. Deviations from this master curve are of the same magnitude as the experimental error. This observation of generality strongly indicates

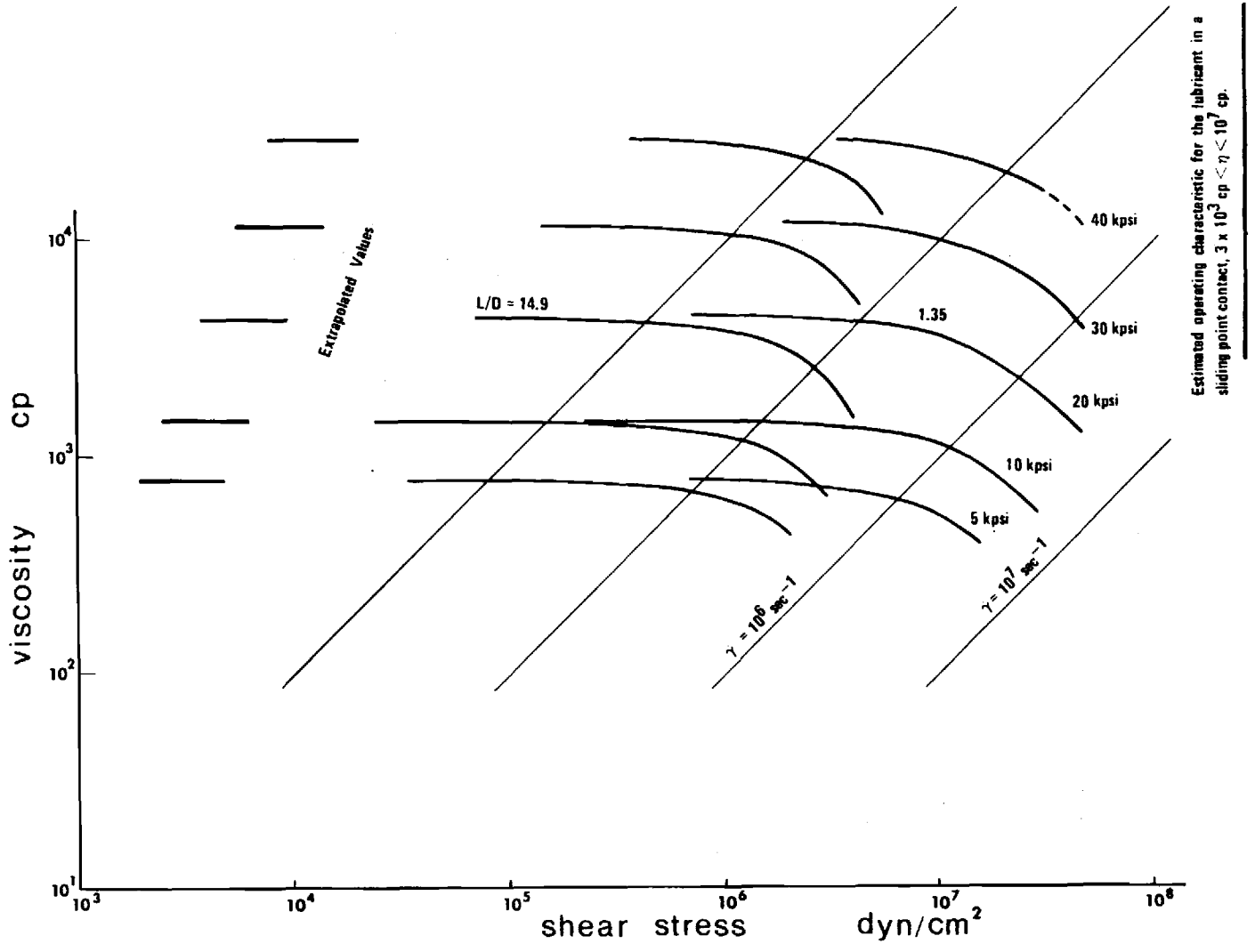

Figure 26. High Shear Measurements of XRM 177 F4, 100°F. (A maximum shear stress of about 700 psi is obtained. The figure shows the operational characteristic for the lubricant in an elastohydrodynamic contact with a maximum Hertzian pressure of 150 kpsi.)

that the same mechanism is responsible for deviation from a Newtonian characteristic. Further work on the hypothesis of dissipation heating is under way, particularly with respect to the influence of the coefficients of temperature-viscosity and heat condition.

B3J: Paraffinic Mineral Oil with 11.5% Polyalkylmethacrylate MW = $.2 \times 10^7$. Polymer blended lubricants have long been used extensively in various engineering fields, particularly the automotive industry. High shear stress investigations of a polymer mixed lubricant are therefore of interest. It was decided to select a high molecular weight polymer in a relatively high concentration with a straight paraffinic mineral base oil for such an investigation.

The base oil as well as mixtures with a lower molecular weight polymer (MW $\sim .56 \times 10^6$) have been investigated before [1], however, only up to about $10^6 dyn/cm^2$. The base oil was then found to have completely Newtonian characteristics in the investigated range.

The same base oil (R-620-12) was selected in this investigation. A polymer (Rohm and Haas PL 4523) with considerably greater molecular weight (MW $\sim .2 \times 10^7$) than used before, was used in order to produce extreme properties of the mixture. The polymer was delivered in solution with a paraffinic oil similar to the base oil. A viscosity increase of 20 times the base oil viscosity was desired. The appropriate percentage polymer, 11.5%, was predicted from [1] and [8]. A blend with this concentration was prepared and mixed vigorously for 48 hours at room temperature. The mixing was carried out by bubbling dry, filtered air through the charge from the bottom of the container.

Data obtained with capillaries 4 and 1 showed a large amount of scatter. Lack of expected consistancy of the data led to a suspicion of incomplete mixing. The viscometer was then purged. The remaining blend was agitated vigorously for another 24 hours at 160°F. Measurements with the more thoroughly mixed charge were carried out with all three capillaries at 100°F and at 5, 10 and 20 kpsi. It was found that the extra mixing operation did not improve the consistancy of the newly collected data. The results of both experiments are, therefore, considered representative for the behavior of the mixture. Figure 27 summarizes the tabulated data.

It is seen from the figure that non-liquid response sets in for a relatively low magnitude of shear stress of about $3 \times 10^5 dyn/cm^2$ (4psi). A pronounced directional effect is found for capillary 1 measurement at 20 kpsi. Apparent viscosities differ by a factor 2-3 for capillary 0 measurements at 10 kpsi and for the same shear stress or the same shear rate. The method of generating the data was different, however. The 10 kpsi series at $2 \times 10^6 dyn/cm^2$ was produced with the constant speed unit. The 10 kpsi data from 7×10^6 to $3 \times 10^7 dyn/cm^2$ were produced manually.

The data from capillary 4 may be regarded as second Newtonian viscosities. A pronounced viscosity increase ($\sim$ 30%) occurs for increasing shear stresses before apparent non-liquid response sets in at about 3×10^5 dyn/cm^2. Such viscosity increases as well as the non-liquid behavior were not observed in previous measurements [1] in the same shear stress range. The concentration of polymer and the molecular weight were, however, significantly lower.

Figure 28 and 29 and Table 9 show the pressure-temperature-viscosity relations at shear stresses believed to correspond to the second Newtonian

Table 9 B3J: Paraffinic Mineral Oil R-620-12 + 11.5 per cent Polyalkylmethacrylate PL 4523 (MW = .2 + 07), Plot, L/D = 297

FL 33J 75 F

P (PSI)	V (CP)
.00000	.10000+04
.47541+04	.40180+04
.96455+04	.19524+05

FL 33J 100 F

P (PSI)	V (CP)
.00000	.42000+03
.47652+04	.10053+04
.97187+04	.22384+04
.19797+05	.94024+04

FL 33J 150 F

P (PSI)	V (CP)
.00000	.15500+03
.47369+04	.29473+03
.96952+04	.51290+03
.19735+05	.13066+04
.29838+05	.35385+04

FL 33J 190 F

P (PSI)	V (CP)
.00000	.10000+03
.47804+04	.17128+03
.97525+04	.27204+03
.19772+05	.58191+03
.29778+05	.13774+04
.39625+05	.28990+04

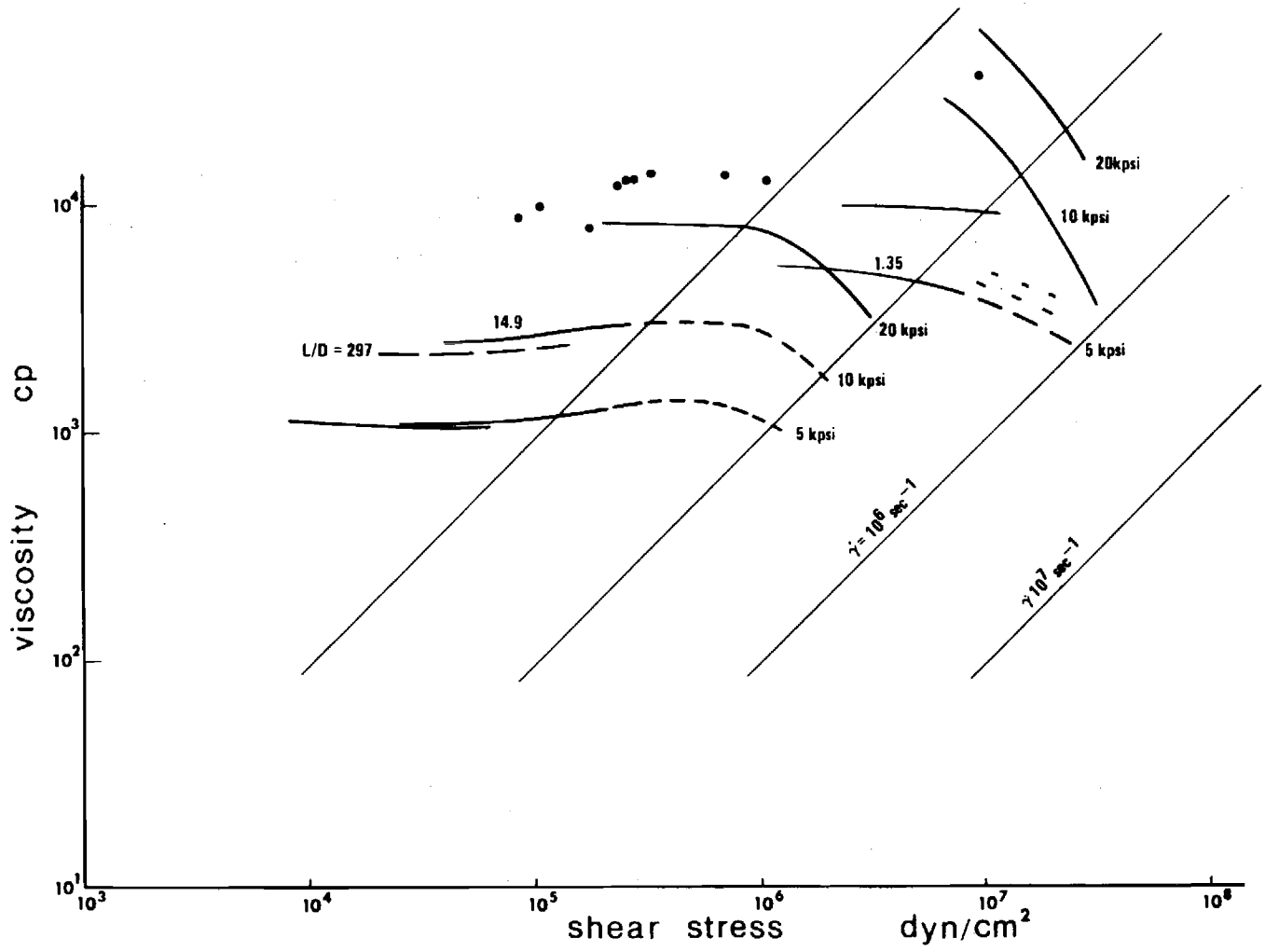

Figure 27. High Shear Measurements of Fluid B3J. (Paraffinic mineral oil with 11.5 per cent polyalkylmethacrylate (MW = 2 x 10^6).)

viscosities. The temperature-pressure-viscosity characteristics plotted on an ASTM D 341-43 chart show a pronounced curvature. Viscosities at atmospheric pressure (in Table 10) are estimated from an ASTM type rectifying chart. The viscosities at atmospheric pressure were measured with a Cannon Fenske Routine Glass Viscometer No. 400. The applied shear stress is about 60 dyn/cm^2 for $\rho \sim 0.85$, whereas the lowest shear stresses reported in Table 9 are approximately 10^4 dyn/cm^2. The measured viscosities at the very low level of shear stress were about 2.5 times greater than the viscosities at 10^4dyn/cm^2. Table 10 summarizes these viscosities at atmospheric pressure. The tabular values are believed to represent the first Newtonian state (column 1) and the second Newtonian viscosity level (column 2).

Fluid B3J shows the expected flow curve characterized by a first Newtonian viscosity η_1 at low shear stress ($\sim 10^2$dyn/cm^2) and a second Newtonian viscosity η_2 at a shear stress of about 10^4dyn/cm^2. The ratio η_1 / η_2 is approximately 2.5. The second Newtonian viscosity η_2 never approaches the viscosity η_b of the base liquid. The ratio η_2 / η_b is of the order of 10. The second Newtonian viscosity level does not significantly exceed 10^4dyn/cm^2. The apparent viscosity increases with increasing shear stress in the range 10^4 - 10^5dyn/cm^2. The increase in viscosity amounts to about 30%. Distinct non-liquid behavior appears shortly above 10^5dyn/cm^2 (1.4 psi) and continues to the highest shear stress $\sim 3.5 \times 10^7$ dyn/cm^2 (500 psi). It is significant that non-liquid behavior sets in at stresses (1.4 psi) which are more than 10^3 times smaller than the average shear stress in a moderately loaded elastohydrodynamic point or line contact. These shear stresses (1.4 psi), where transition to non-liquid

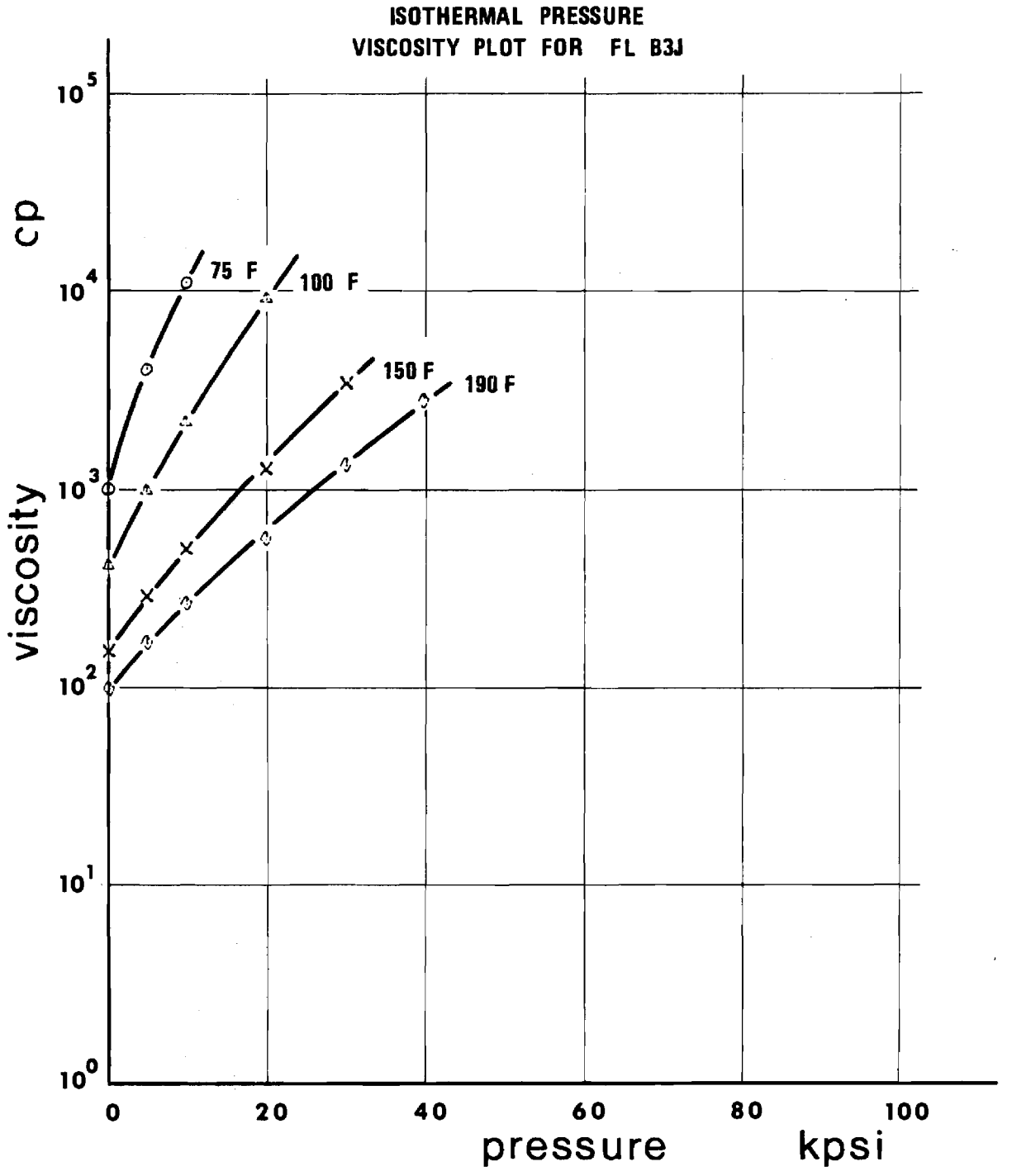

Figure 28. Isothermal Pressure Viscosity Plot for Fluid B3J. (Paraffinic mineral oil with 11.5 per cent polyalkylmethacrylate (MW = 2 x 10^6). Measurements with capillary 4. Semilog presentation.)

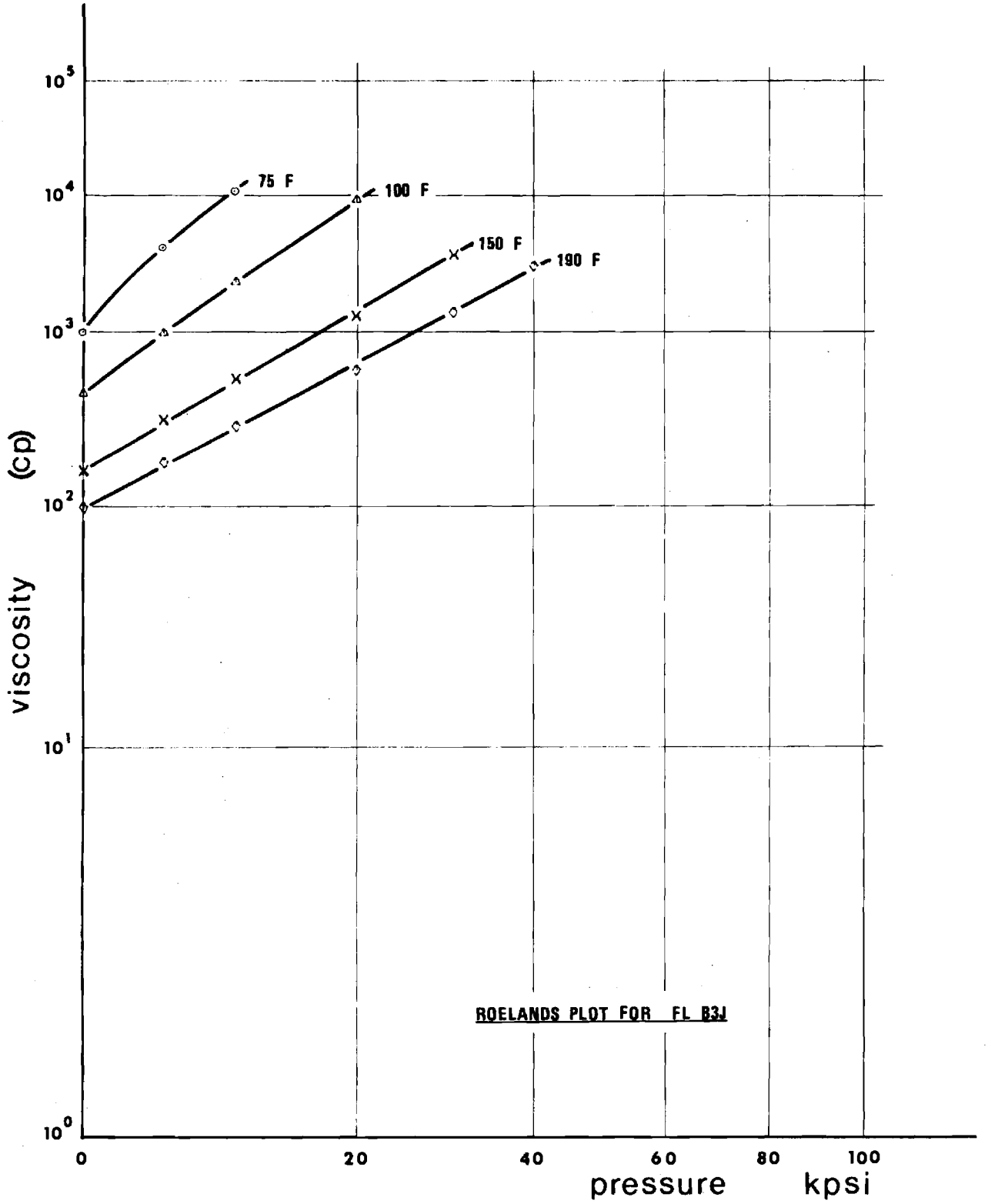

Figure 29. Roelands Plot for Fluid B3J. (Paraffinic mineral oil with 11.5 per cent polyalkylmethacrylate (MW = 2 x 10^6). Measurements with Capillary 4.)

Table 10

Paraffinic Mineral Oil with 11.5% Polyalkylmethacrylate MW = $.2 \times 10^7$. Viscosities at Atmospheric Pressure.

	1 $\simeq$ 60 dyn/cm^2 Capillary No 400	2 $10^4 - 10^5$ dyn/cm^2 Cap 4 + Cap 1 *
75 °F	-	1000 cp
100 °F	1010 cp	420 cp
150 °F	384 cp	155 cp
190 °F	221 cp	100 cp

* Table values are estimated from extrapolated characteristics on ASTM D 341 - 43 type charts.

behavior appears for the material B3J, are found far into the inlet zone of an elastohydrodynamic contact. At this location, the pressures are low, film thicknesses are many times the centerline film thickness and temperatures are very nearly equal to ambient temperatures.

b. Revised Pressure Viscosity Coefficients

In last year's progress report a complete set of pressure-viscosity data on all the fluids investigated for NASA was presented. Included were pressure-viscosity coefficients for each fluid. Both α_{OT} and α^* were presented where

$$\alpha_{OT} \equiv \frac{d\ln\mu}{dp}\Bigg|_{T,P=0} \quad ; \quad \alpha^* \equiv \left[\mu_o \int_o^\infty \frac{dp}{\mu(p)}\right]^{-1}$$

These were computer processed for the viscosity-pressure data. As is to be expected, the value of α^* should be more reliable because it involves the integration of experimental data over the entire range of data obtained. However, the values of α_{OT} are obtained by the differentiation of experimental data at one end of the range of the data, which inherently introduces the possibility of significant errors. Further, it was found after last year's progress report was submitted that the algorithm employed in calculating the values of α_{OT} introduced additional errors in the values of α_{OT} when the viscosity or viscosity-pressure coefficient were in certain ranges.

Therefore, the values of α_{OT} were recalculated by plotting the data and obtaining the slope of the log viscosity-pressure isotherm at atmospheric pressure by the best visual fit to the data. The revised data are presented in Table 11 and Figure 30 and replace Table 1 (p.25) and Figure 5 (p.28) respectively in the last year's progress report. To the best of our knowledge, the other data presented in that report are correct.

Table 11. Revised Table 1 - PRESSURE VISCOSITY CHARACTERISTICS [1] - α_{oT} - of 1972 Progress Report

Fluids	$\alpha_{oT} \times 10^4$ (psi)$^{-1}$ 100°F	210°F	300°F	75°F [2]
Advanced Ester	1.05	0.95*	0.92*	1.08
Formulated Advanced Ester	1.27	1.02*	0.84*	1.32*
Naphthenic Mineral Oil Plus Additive	1.84*	1.48*	1.25*	1.95*
Synthetic Paraffinic Oil Plus Additive	1.40*	1.25*	1.02*	1.44*
DN-600 Plus Additive	1.42	1.25*	1.03*	1.43
DN-600	1.40*	1.20*	1.00*	1.43
FN-2961	2.12	1.25	0.92*	2.53
MCS-418	1.00*	0.63*	0.51*	1.18*
MCS-460	2.17	0.94	1.03	3.00
Krytox	3.07*	3.02	3.00*	3.08*
XRM-109	1.40*	1.53*	0.97	1.25

1) To obtain the pressure viscosity coefficient in $[N/m^2]^{-1}$, divide the entry by 6.894×10^3.
2) Extrapolated data from Figure 6.

* numbers that have been changed.

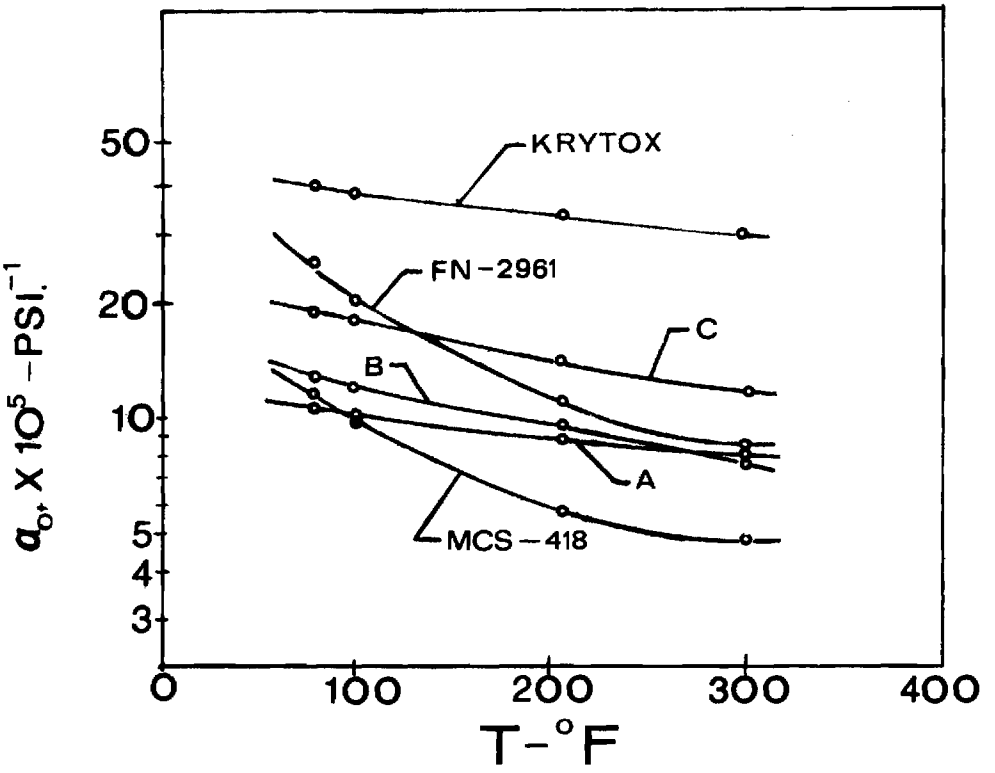

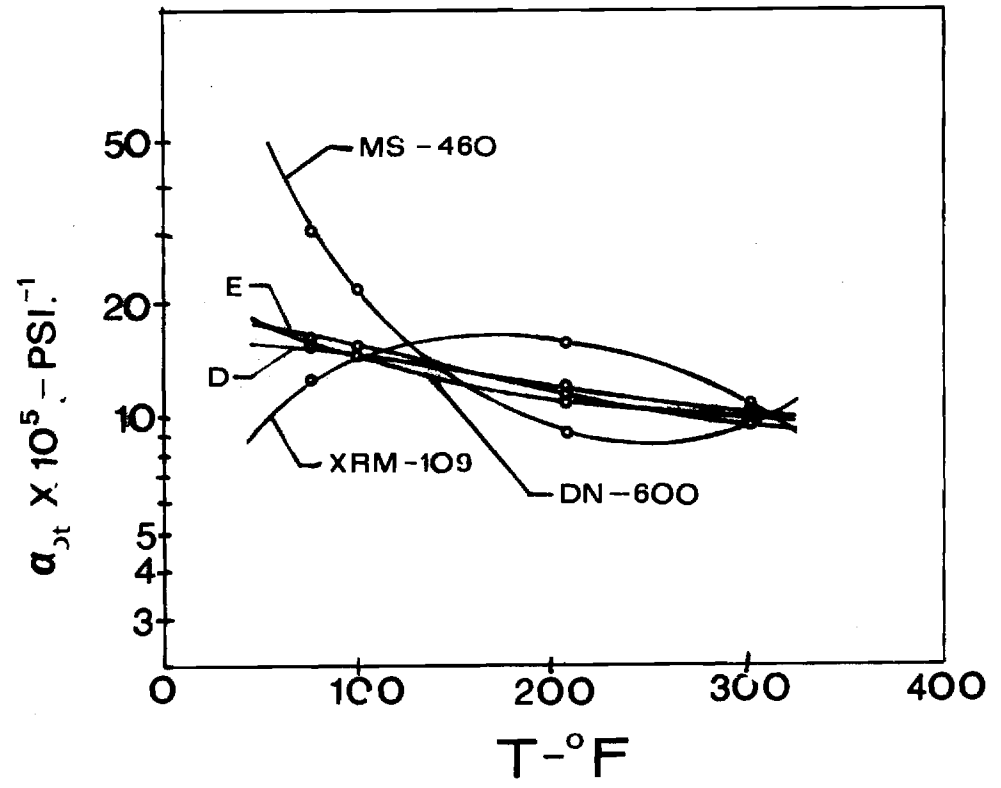

Figure 30 - Revised Figure 6. (1972 Report) - Viscosity-Pressure Characteriistic σ_{oT} as a Function of Temperature (0 - measures, ■ - extrapolated).

III. ELASTOHYDRODYNAMIC LUBRICATION INVESTIGATIONS

a. EHD Pressure Measurement Investigations

A study was conducted to determine the feasibility of a technique to measure the pressure profile in a sliding EHD point contact. The pressure measurement technique employed a transducer consisting of a 9.0 x 10^{-5} m (.0035 in.) diameter piston attached to a cantilever load cell and allowed to move in a 9.0 x 10^{-5} diameter orifice in the sapphire bearing plate.

The equipment (Figure 31) that was used is basically the same as that used in previous EHD investigations (12,13). The spherical bearing surface is a steel ball of 3.18 x 10^{-2} m (1.25 in) diameter. The sphere is rotated through a flexible coupling cemented to its surface. The sphere is supported and loaded against the bearing sapphire by three radial ball bearings and located in a lubricated bath. A significant amount of inertia was incorporated into the drive mechanism in order to maintain a nearly constant sliding velocity between the spherical bearing and sapphire.

The upper surface of the contact is a synthetic sapphire disc having one of its plane surfaces directed toward the contact. The sapphire bearing used to determine the pressure distribution has dimensions as shown in Figure 32 .

The needle, designed to slide as a piston in the orifice of the sapphire, was processed from a steel rod whose end was ground in the sapphire orifice. A diamond polishing compound with a particle size of 0.25 micron was used for grinding. The length of the needle in the sapphire was ground to 2.504 x 10^{-4} m (0.010 in) and to a corresponding diameter of 9.0 x 10^{-5} m (0.0035 in) (Figure 33). The needle was cemented to a holder rigidly attached to a micrometer screw mounted in the cantilever

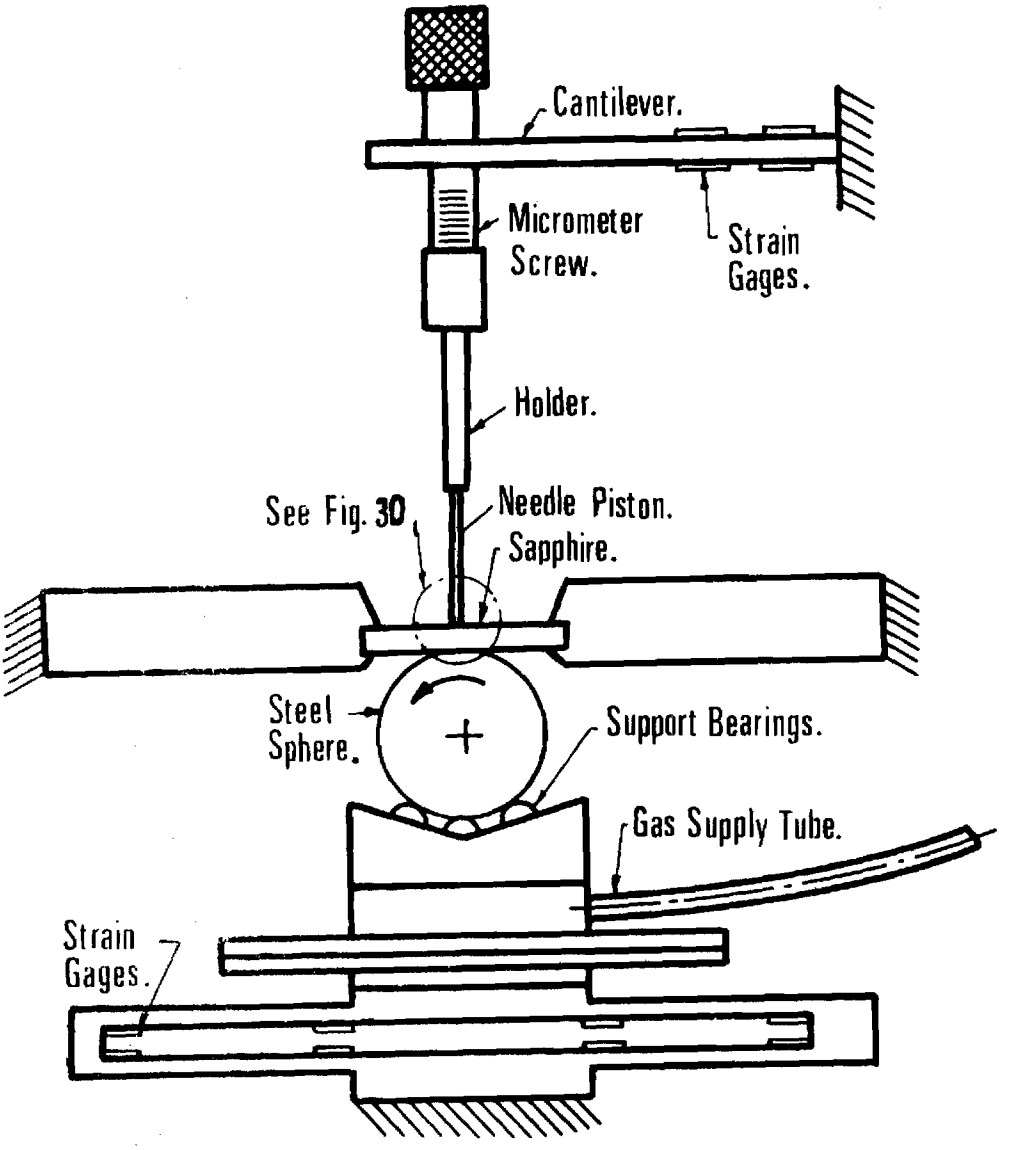

Figure 31. Schematic Diagram of the Experimental Apparatus for Pressure Measurement.

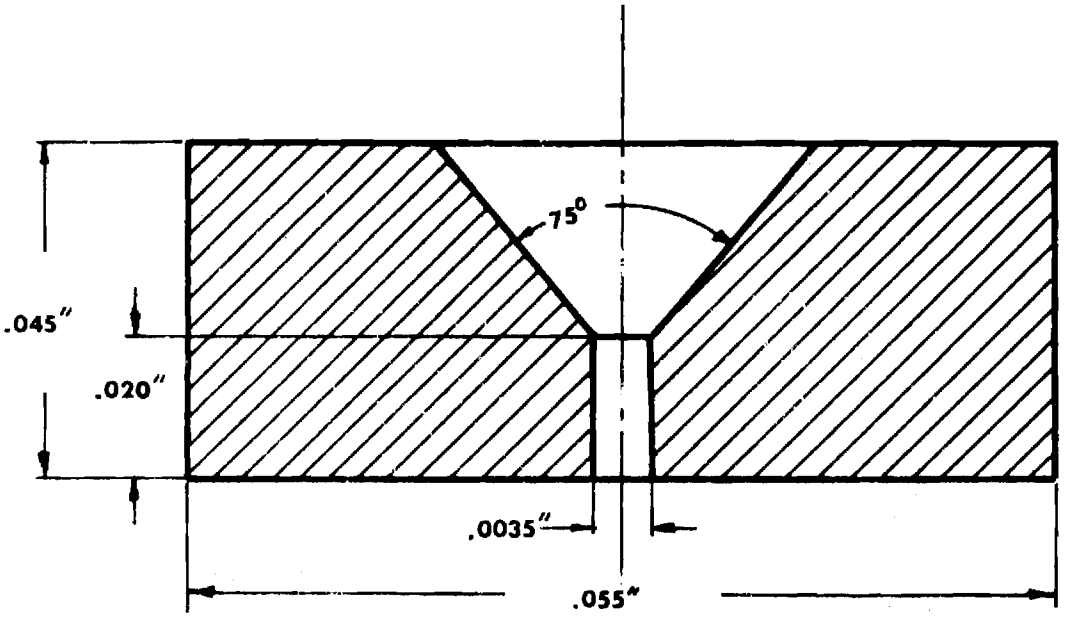

Figure 32. Geometry of the Bearing Sapphire.

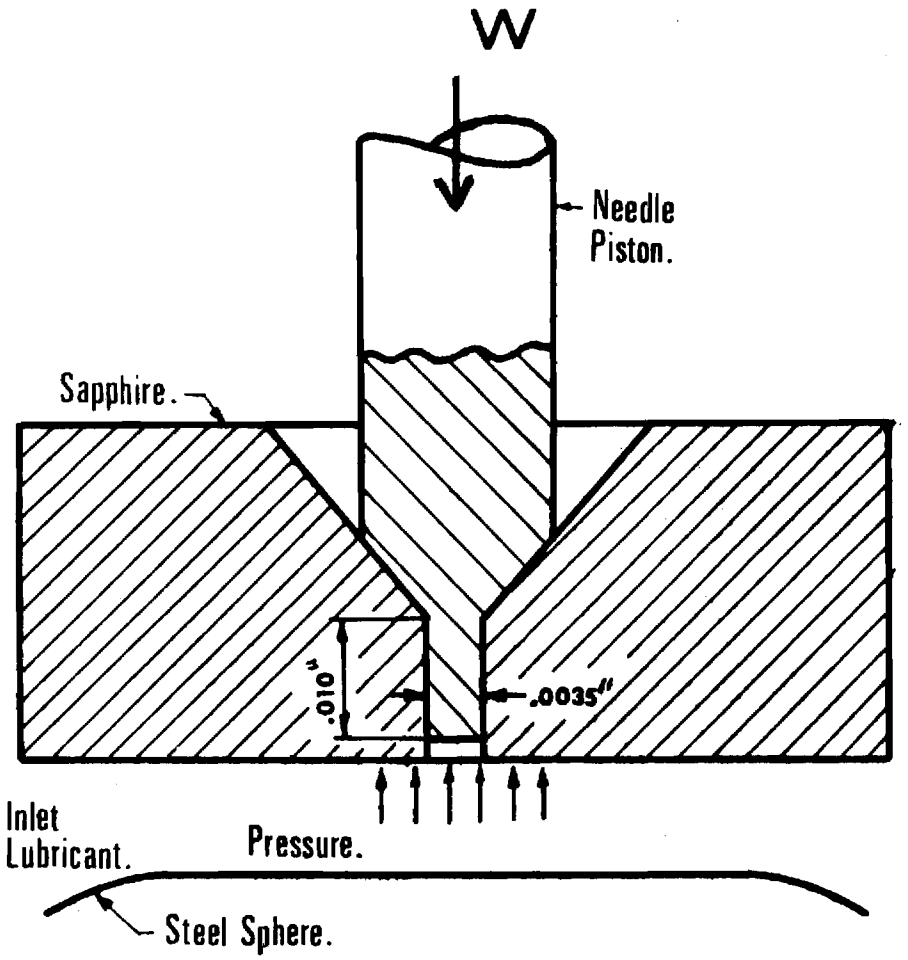

Figure 33. Detail of the Needle - Sapphire Assembly.

beam (Figure 31).

Four silicon semi-conductor strain gages were cemented on the cantilever beam. The strain gages were connected in a four gage bridge circuit. The sensitivity of this transducer was determined to be 0.072 mV/kpsi. The deflection of the cantilever beam is approximately 0.001 in/lbf.

A pneumatic system has been used to apply the normal load of 15 lbf (150,000 psi Hertz) between the bearing surfaces. The normal force load cell was calibrated statically by placing known weights on the sapphire support. A linear response up to 30 lbf normal load was obtained.

The transducer was calibrated in a separate mounting as shown in Figure 34 . Lubricant oil at a known pressure was fed into the fitting. The pressure acting on the end of the needle resulted in a normal force on the needle causing a deflection of the cantilever load cell. The output voltage (see Figure 35) was plotted against each value of pressure $0 - 0.69 \times 10^9$ N/m^2 (0 - 100 kpsi). During the calibration experiment no leakage of lubricant from the system was observed.

The location of the orifice in the sapphire bearing relative to the elastohydrodynamic contact was observed through a Leitz metallurgical microscope. The upper plate of the apparatus in which is mounted the sapphire bearing offers a two direction freedom of movement by means of micrometer screws in each direction.

Many attempts were made to record an output signal from the transducer while passing the sapphire orifice through the elastohydroydnamic contact. None of them was successful. However, an immediate explanation of failure to record pressure could not be determined because the conditions

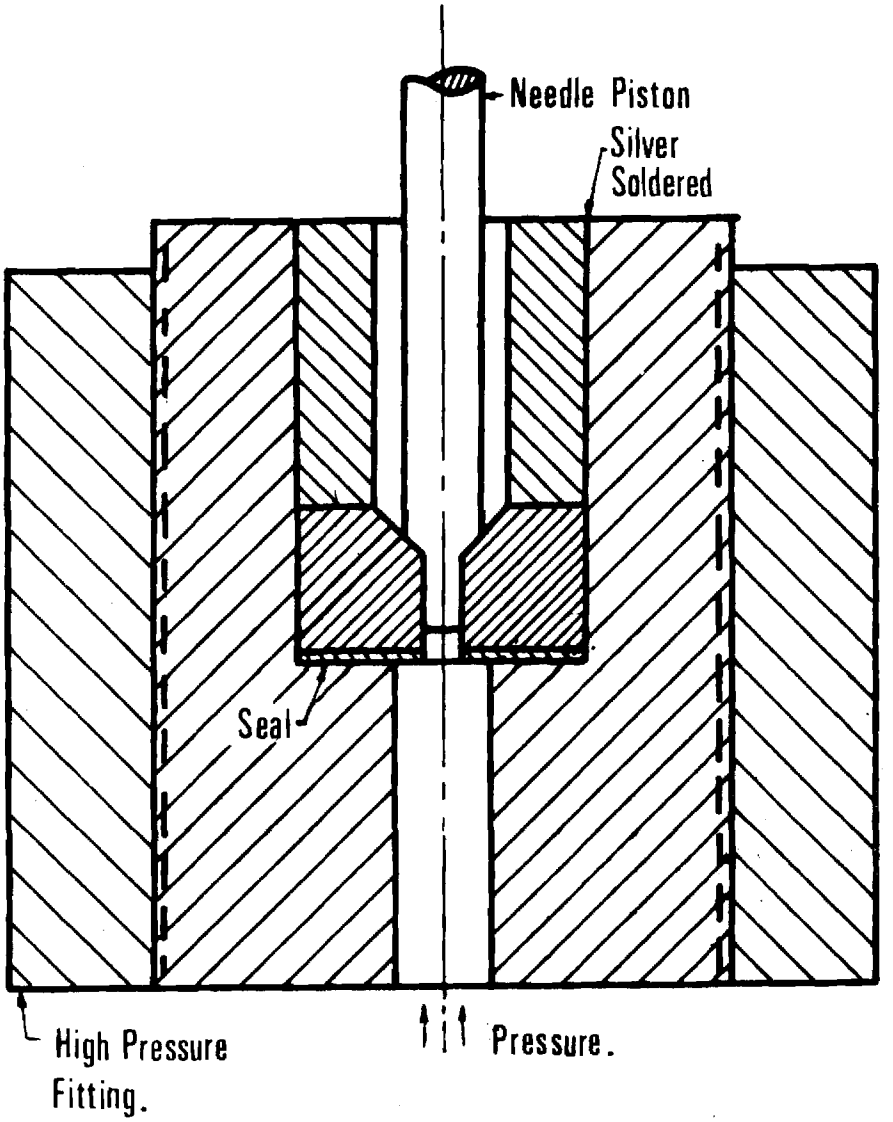

Figure 34. Needle - Sapphire Assembly Used for Pressure Calibration.

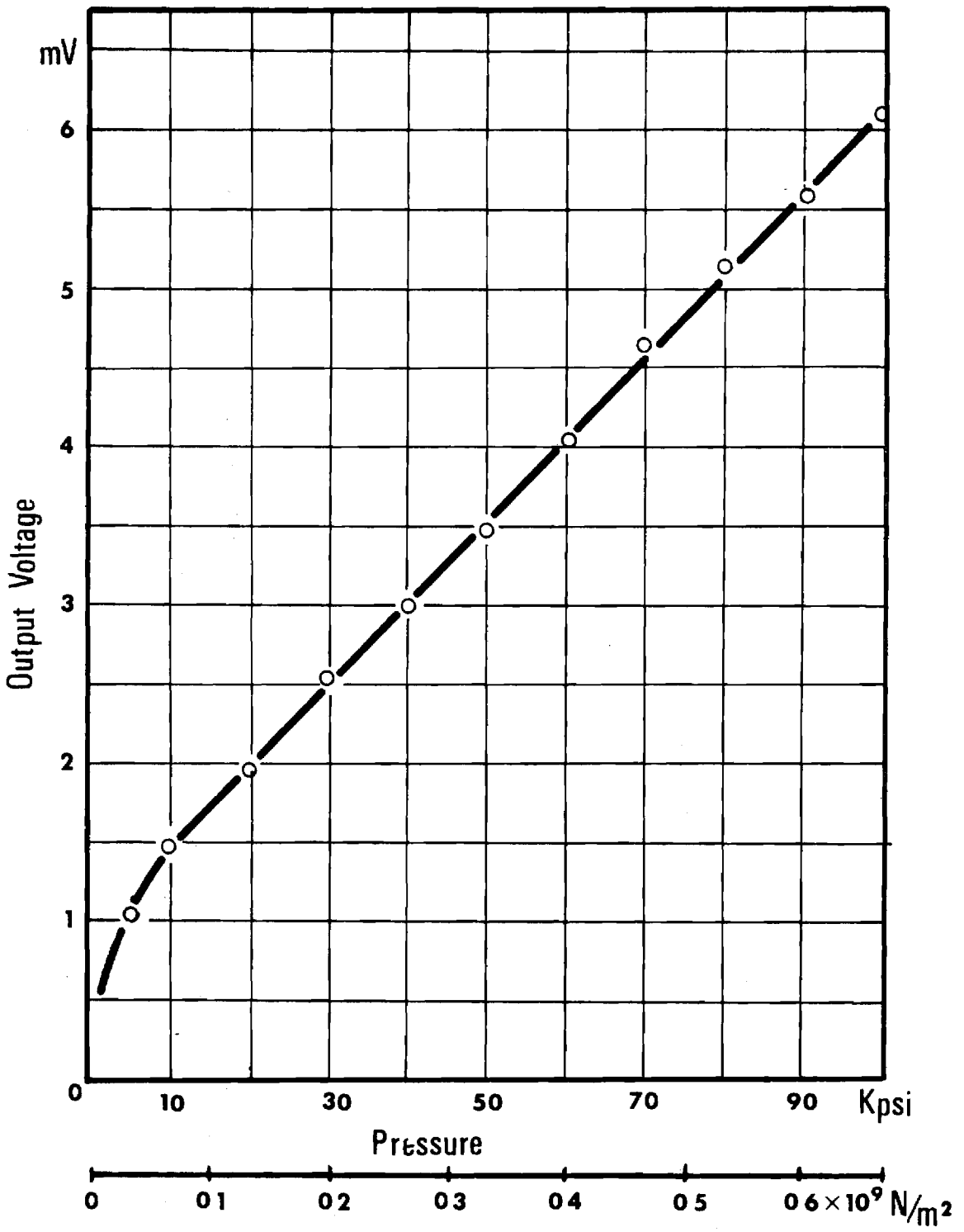

Figure 35. Calibration Curve for the Pressure Transducer.

during the successful calibration appeared to be similar to those of the elastohydrodynamic contact.

During repeated experiments, a leakage of the lubricant oil between the needle and the wall of the orifice in sapphire bearing was observed. This leakage was not noticed during the calibration experiment. The radial clearance between the needle and orifice remained the same as during calibration at a value $\geq$ 0.25 micron (10^{-5} in) due to the particle size of the diamond compound used to grind the piston portion of the needle. The hydrocarbon oil used during the experiment has a viscosity of 100 cp at a pressure of 0.69×10^{8} N/m^2 (10 kpsi). Under these conditions the leakage flow rate would be 3.5×10^{-5} in^3/sec, for an isothermal annular flow with pressure dependent viscosity. The fluid flow rate in the elastohydrodynamic contact passing by the orifice is only 3.0×10^{-6} in^3/sec, however, at a sliding speed of approximately 50 in/sec. As the pressure builds the viscosity increases and, therefore, at very high pressures the leakage flow rate will decrease with increasing pressure. This was the case during the calibration where the fluid flow rate available was very large compared to the leakage flow rate.

Because the annular leakage flow rate is greater than the flow rate of the fluid entering the EHD contact, the pressure will never build up to levels where the viscosity reaches values where the leakage can be neglected as an important factor in pressure measurement.

An additional difficulty in the elastohydrodynamic contact is the elevated temperature which causes the viscosity to be low compared to conditions during high pressure calibration.

The technique presented in this chapter to determine a pressure profile across the elastohydrodynamic contact was found not to be feasible. It has also been determined that more accurate machining of the needle-

sapphire assembly will not make the technique feasible. The clearance between the needle and orifice is already very small and significantly smaller clearances would be difficult to produce.

A technique employing two sapphires is under consideration at this time. One sapphire would have a small orifice and a conical opening as shown in Figure 32. A second sapphire having a manganin strain gage evaporated on its surface would be mounted above the first with the manganin gage positioned over the conical hole. This method combines two of the most widely used techniques in experimental research to determine the pressure distribution; the orifice technique and that of evaporated manganin strain gage. This method appears to solve the difficulties which were encountered in each of the separate techniques. The leakage flow rate from the piston - orifice technique would be eliminated by not using a piston and the manganin strain gages would no longer be exposed directly to the severe stress conditions of the elastohydrodynamic contact. The orifice in the sapphire could further be enlarged at its upper exit to allow the use of a coil strain gage rather than an evaporated one.

The orifice adjacent to the contact could be made much smaller than that used previously since a mating piston would not be required. The reduction in orifice diameter would increase the pressure measurement resolution.

b. EHD Temperature Measurements.

A technique has been developed for obtaining a map of the steel ball surface temperature and the lubricant temperature averaged across the film in an EHD contact. The temperature measurement system consists of an infrared micro-detector used to collect infrared radiant energy

from the elastohydrodynamic contact and, thereby, allowing the deduction of the local temperature. The problem of separating the infrared radiation contributions from the ball, lubricant film and sapphire bearing plate has been solved by collecting the infrared radiation under three different conditions, two of them using steel spheres with different emissivities and one using a filter consisting of a calibrated fluid sample "cell" placed between the infrared detector and sapphire bearing plate.

Because the surfaces used for the EHD contact are steel and sapphire, the pressures in the contact are in the range of current design practice. The maximum Hertz pressure is 1.034×10^{9} N/m^2 (150,000 psi) for the data reported. These data are for a sliding contact. For a given set of conditions the ball surface temperature reaches a maximum of 115°C and the average fluid temperature reaches a maximum of 360°C, both occurring near the side lobes. The experiment was performed at room temperature with sliding velocities of 1.39 m/sec (54.9 ips).

The sliding EHD point contact is formed using a 3.18×10^{-2} m (1.25 in) diameter steel ball rotating and loaded against a 1.52×10^{-3} m (0.060 in) thick sapphire flat. The system has been used previously in extensive investigations of film thickness [12], traction [13] and pressure measurement as mentioned in section IIIa.

It is shown in Figure 36, that the pressure transducer has been replaced by an infrared radiometric detector (Barnes Engineering Company, Model RM-2A). The purpose of this detector is to measure the infrared radiation emitted from the contact and, therefore, allow the contact temperatures to be deduced.

The radiometric detector has been equipped with a 15X reflecting objective which allows a spot size resolution of 3.56×10^{-5} m (0.0014 in.).

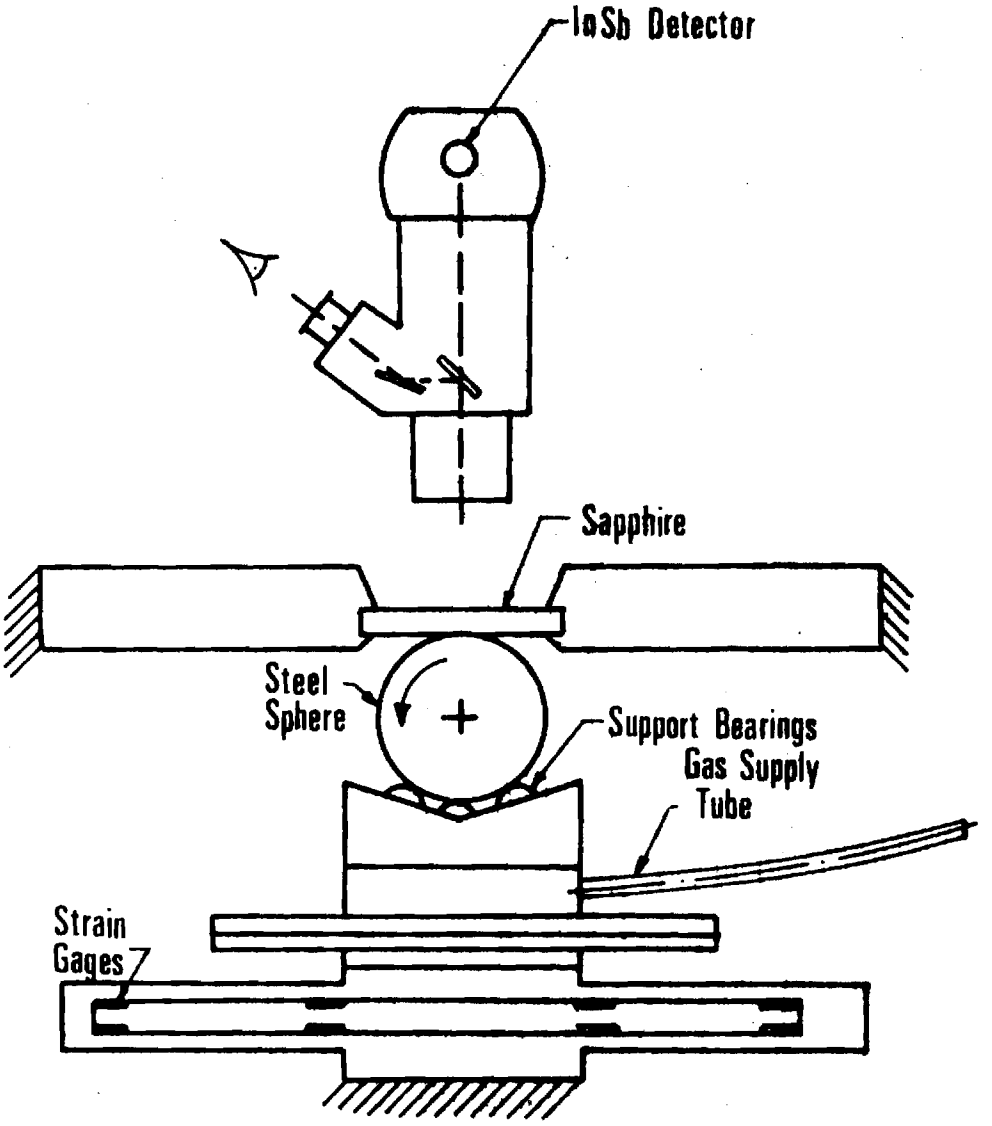

Figure 36. Schematic Diagram of the Experimental Equipment.

The radiation from this spot plus that from a related solid angle (Figure 36) between this spot and the objective are focused onto a liquid nitrogen cooled indium antimonide detector. This detector has a spectral response of 1.8 to 5.5 x 10^{-6} m (1.8 to 5.5 microns). The sapphire has a transmissivity of 0.90 over this same range thus allowing the steel ball and oil film radiation to reach the detector. The visible light also collected by the objective is separated from the IR and is directed toward a visual eyepiece. The visual and IR systems are parfocal, and the visual field of view is twenty times as large in diameter as the area which is covered by the IR detector. The area covered by the detector is located in the center of the visual field of view and is indicated by intersecting cross hairs. This allows one to focus on the oil film by visually searching for the interference fringe pattern characteristic of the EHD contact. The detector will then respond to radiation from the 3.56 x 10^{-5} m (0.014 in.) diameter oil film and steel ball surface plus a volume of the sapphire disk (see Figure 36). Since the temperatures of the lubricant film and the bearing surfaces are desired separately, rather than an average contact temperature, experimental techniques have been devised to isolate the radiation contributions from the sapphire, lubricant film, and steel ball.

Figure 37 shows the components of the radiation received by the In-Sb detector. The radiation emitted from a surface per unit time, area and solid angle is called areal radiant intensity and has units of watts · cm^{-2} · $ster^{-1}$. There are four areal radiant intensity sources: N_o - due to reflected ambient background radiation, N_s - due to emission from the sapphire, N_b - due to emission from the steel ball, and N_f - due to emission from the lubricant film. There is also an attenuation factor

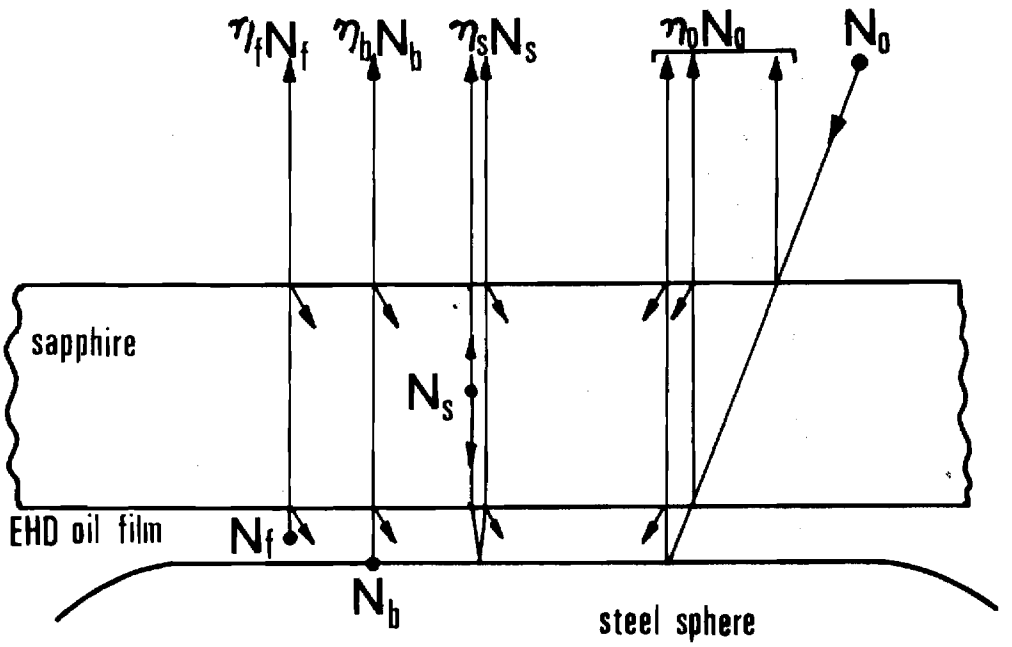

Figure 37. Radiation Incident on the Detector (Angles Exaggerated for Clarity).

associated with each of these components. Under the conditions listed below, these factors are:

$$\eta_0 = 0.082 + 0.683\ \rho b$$
$$\eta_s = 1. + 0.830\,\rho b \qquad (1)$$
$$\eta_b = 0.830$$
$$\eta_f = 0.830$$

based on

1. Fresnel reflection losses of 0.076 at the sapphire-air interface and 0.0064 at the sapphire - oil interface [14].

2. sapphire transmissivity of 0.90 for the 1.52×10^{-3} m (0.060 in.) thick disk [14],

3. that the sapphire radiates to both hemispheres and a portion of the radiation initially directed toward the oil film is reflected back to the detector.

4. absorptivity of the oil film is negligible due to its thickness of approximately 2.54×10^{-7} m (10^{-5} in.), and

5. that, although the oil film also radiates to both hemispheres, the effect has been accounted for in the value of emissivity assigned to the film.

The IR radiometric detector contains a black body source at ambient temperature. A mechanical chopper in the detector alternately exposes the detector to the total incident radiationand then to the black body reference. The output signal, therefore, is a function of the difference between these values

$$E = k(N_{TOTAL} - N_o) \qquad (2)$$

where k is a known instrument constant. It can be seen from Figure 37 that the total incident radiation is given by

$$N_{TOTAL} = \eta_f N_f + \eta_b N_b + \eta_s N_s + \eta_o N_o \qquad (3)$$

therefore, combining equations 1 - 3 ,

$$E/k = 0.830\ (N_f + N_b) + (1. + 0.830\ \rho_b)\ N_s$$

$$+ (0.683\ \rho_b - 0.918)\ N_o \qquad (4)$$

The reflectivity of the ball surface ρ_b can be measured with the radiometric detector. The quantity N_o is dependent on the ambient temperature only and can be evaluated. The individual areal radiant intensity values N_f, N_b and N_s are known functions of the source emissivity and temperature.

The sapphire which is 1.52×10^{-3} m (0.060 in.) thick will have a large temperature gradient due to the viscous heating in the oil on one side and ambient air on the other. Radiation is emitted from throughout the thickness rather than just at a surface. Because the temperature distribution of the sapphire is unknown a sapphire surface temperature has not been determined thus far.

Since the steel ball is opaque, a surface emissivity and temperature can be associated with the areal radiant intensity N_b. The Emissivity of the ball surface has been determined at several temperatures using the radiometric detector. The technique is to paint a small spot of flat black paint ($\varepsilon \simeq 0.95$) on the ball surface, heat the ball to an elevated temperature and then compare the areal radiant intensities at adjacent points on the ball surface - one on and one off the painted section. This technique gave a surface emissivity of 0.28 for the 52100 chrome steel ball. This value was reproducible at several temperature levels.

The emissivity of the oil film must be determined before a film temperature can be calculated. Since the oil film is an absorbing medium with anticipated high temperature gradients, the temperature which will be

assigned to the oil film will be an average temperature across the film. Because the areal radiant intensity is related to the fourth power of temperature, however, this average value will be skewed toward the maximum temperature in the film. In general, the emissivity of the oil film is a function of oil chemistry, wavelength and film thickness. The emissivity, therefore, must be determined for the lubricant being used with the same detector to be used in temperature measurements. Once the dependence on film thickness is known, film thickness profiles previously obtained [12] can be used to obtain a local emissivity value. McMahon [15] presents a relation between effective emissivity and film thickness of a semi-transparent material. For a lubricant film thickness h, considered as a heated, reflecting, partially transparent body, the relation is

$$\varepsilon = \frac{(1 - \rho^*)(1 - e^{-\lambda h})}{(1 - \rho^* e^{-\lambda h})} \qquad (5)$$

where λ is an absorption coefficient for the oil film and ρ^* is the effective reflectivity of the oil film. In a separate experiment in which a stationary ball was placed in a constant temperature bath of the test lubricant with the sapphire resting on top of the ball, the areal radiant intensity was measured near the contact between the surfaces. An oil film occupied the space between the ball and sapphire. Since the dimensions of the gap can be determined from geometry alone, the areal radiant intensity data at a known fluid temperature can be transformed into a local emissivity value. The data obtained resulted in an emissivity of 0.352 for a film thickness of 5.08×10^{-5} m (0.002 in.). Solving equation (5) for λ yields $\lambda = 9.43 \times 10^{3}$ m^{-1} (240 in^{-1}). For EHD film thicknesses on the order of 10^{-7} m (10^{-5} in.), the quantity

$\lambda \cdot h$ is of the order 10^{-3}, allowing equation (5) to be accurately approximated by

$$\varepsilon_f = \lambda h \tag{6}$$

For a given experiment, temperature is a function only of areal radiant intensity and emissivity, therefore,

$$T_b = f\ (N_b,\ \varepsilon_b) \tag{7}$$

$$T_f = f\ (N_f,\ \varepsilon_f) \tag{8}$$

Since the film thickness at any point in the contact can be determined using the optical interference technique [12] ε_b and ε_f can be found. However, there remain three equations (4,7,8) with five unknowns (N_f, N_b, N_s, T_b, T_f). Clearly, two additional independent relations must be found. This has been done by the following two alterations to the experiment described thus far.

In order to determine the ball surface temperature, the EHD experiment was repeated under identical conditions, but with a ball having an emissivity of 0.47 compared with that of 0.28 used in the first experiment. The increase in emissivity was accomplished by allowing the ball surface to react in a high temperature oil bath. A comparison of film thickness values taken using each ball indicated that the conditions in the contact were identical regardless of which ball was used. All other variables remaining constant, the higher ball emissivity will give a higher ball areal radiant intensity N_b. We have shown through an order of magnitude analysis (see Appendix D) that the increased radiation from the ball surface will have a negligible effect on the film and surface temperatures. Therefore, for a given point in the contact, the data from the two experiments using a low and high emissivity ball will result in two different output signals E_1 and E_2. Since the transmissivity of the

ball is zero [16]

$$\rho_b + \alpha_b = 1 \tag{9}$$

but at equilibrium [16]

$$\alpha_b = \varepsilon_b \tag{10}$$

therefore

$$\rho_b = 1 - \varepsilon_b \tag{11}$$

Equation (4) may now be rewritten for the experiments using balls with low and high emissivity

$$E_1/k = 0.830\ (N_f + N_{b1}) + 1.598\ N_s - .426\ N_o \tag{12}$$

$$E_2/k = 0.830\ (N_f + N_{b2}) + 1.440\ N_s - .556\ N_o \tag{13}$$

where the subscript 1 refers to the low emissivity ($\varepsilon_{b1} = .28$, $\rho_{b1} = .72$) and 2 refers to the high emissivity ball ($\varepsilon_{b2} = .47$, $\rho_{b2} = .53$). Subtracting equation (12) from (13)

$$\frac{E_2 - E_1}{k} = 0.830\ (N_{b2} - N_{b1}) - 0.158\ N_s - .130\ N_o \tag{14}$$

The black body areal radiant intensity is a function of temperature only with

$$N = \varepsilon\ N^{BB} \tag{15}$$

Since the ball surface temperatures are assumed equal in cases 1 and 2, equation (14) may be rewritten as

$$\frac{E_2 - E_1}{k} = 0.158\ N_b^{BB} - .158\ N_s - .130\ N_o \tag{16}$$

With an ambient temperature of 20°C, $N_o = 3.7 \times 10^{-3}$ watts/cm^2 - ster. A conservative estimate of N_s (see Appendix E) is on the order of 0.4×10^{-3} watts/cm^2 - ster or about 2 percent of N_b^{BB} and has, therefore, been neglected. The value of N_b^{BB} is typically of the order 20×10^{-3} watt/cm^2 - ster. The only unknown in equation (16) is N_b^{BB}. The temperature can be obtained from the black body areal radiant intensity through the calibration curve supplied with radiometric detector.

Although the two experiments described above allow the determination of the ball surface temperature they are not sufficient to allow the film temperature to be deduced. The technique devised to isolate the film areal radiant intensity consists of an experiment in which the low emissivity ball is used. The detector output signal E_1 is then compared with the signal E_3 obtained with a filter placed between the upper sapphire surface and the detector objective (see Figure 36). The filter consists of a sandwich of two sapphire disks and a 5×10^{-5} m (0.002 in.) thick film of oil identical in composition to that being used in the EHD contact. Hence the radiation from the EHD oil film is absorbed by the oil in the filter. As can be seen from Figure 38, those contributions other than $\eta_f N_f$ shown in Figure 37 have been attenuated by a filter attenuation factor η_F. Because of a strong absorption band (C-H bond) in the aliphatic oil at 3.4μ, the EHD oil film will emit primarily at this wave length. Since a much thicker film of the same oil is used in the filter, the filter will absorb the entire contribution $\eta_f N_f$ from the EHD oil film. A reflecting shield is placed between the upper surface of the EHD contact sapphire and the filter until just prior to recording the total radiation to maintain the filter at ambient temperature. Otherwise, the absorption of $\eta_f N_f$ would raise the filter temperature to some unknown value. Figure 38 also shows that the filter itself is emitting at T_o and that some of the background radiation

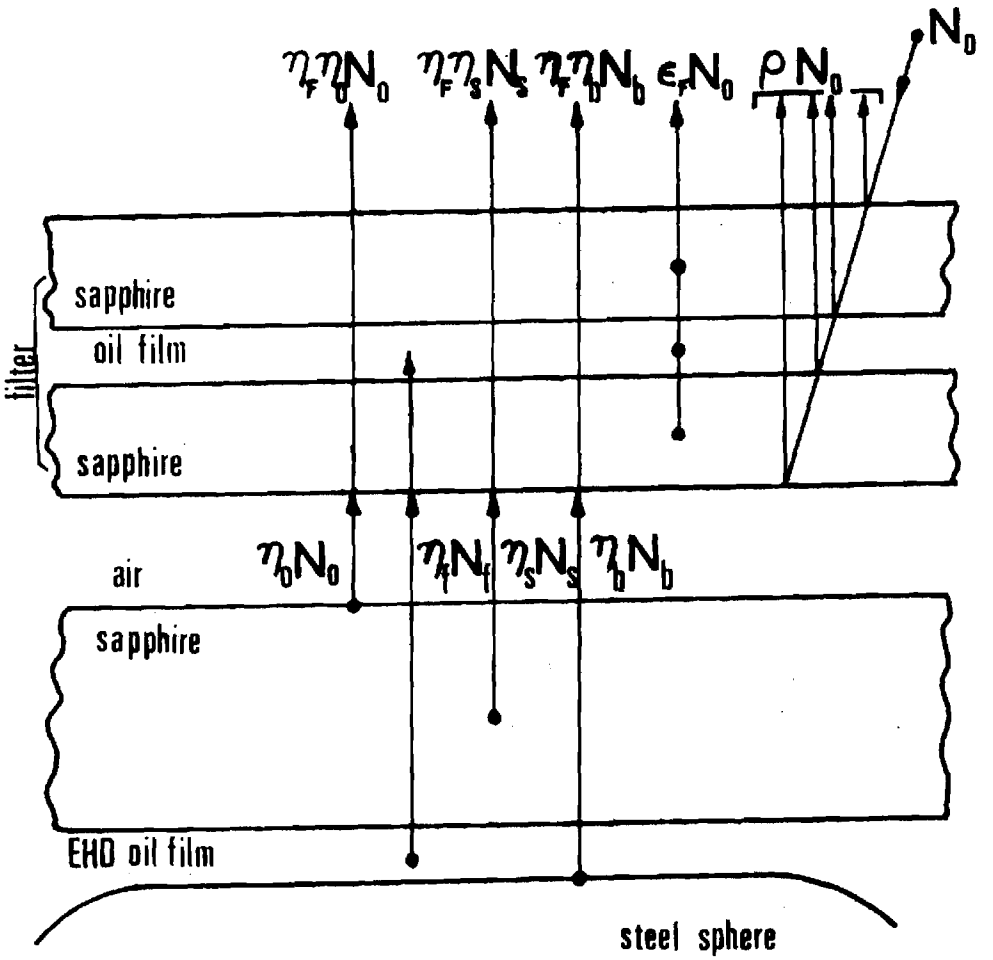

Figure 38. Oil Film Filter (Not to Scale).

is also reflected from the filter. The total areal radiant intensity received in this third experiment is, therefore,

$$(N_{TOTAL})_3 = \eta_F (\eta_{b1} N_{b1} + \eta_s N_s + \eta_o N_o) + \varepsilon_F N_o + \rho_F N_o \qquad (17)$$

Substituting equations (1) and (17) into equation (12) we get,

$$E_3/k = \eta_F (.830 N_{b1} + 1.598 N_s + .574 N_o) - (1 - \rho_F - \varepsilon_F) N_o \qquad (18)$$

Since for transparent medium [16]

$$t_F + \rho_F + \varepsilon_F = 1 \qquad (19)$$

the last term in equation (18) may be written as $t_F N_o$. The transmissivity of the filter t_F can be related to the attenuation factor η_F which includes transmission and reflection losses

$$\eta_F = (1 - \rho_F)\, t_F = 0.850\, t_F \qquad (20)$$

where the reflection losses are calculated Fresnel reflections at the sapphire-air and sapphire-oil interfaces. Substitution of equation (20) into (18) and subtracting from equation (12) yields,

$$(E_1 - \frac{E_3}{\eta_F}) \frac{1}{k} = 0.830 N_f + 0.176 N_o = 0.830 \varepsilon_f N_f^{BB} + 0.176 N_o \qquad (21)$$

The quantities E_1 and E_3 are the output signals, and k and N_o are known. The film emissivity ε_f can be obtained from equation (6) since the film thickness profile has also been obtained throughout the contact [17]. The filter attenuation factor has been found experimentally by placing the filter between the detector objective and a calibrated black body source (Barnes, Model RM 121). Because of the spectral shift in peak

power wavelength with increasing temperature, this attenuation factor is a function of the equivalent black body source temperature. Using the black body source, a calibration curve of η_F as a function of temperature was obtained.

Based on an initial estimate of the EHD film temperature T_f, a value of η_F is inserted in equation (21) which is then solved for N_f^{BB}. The film temperature is then determined directly from this value. A better estimate of η_F can be used in equatior (21) until convergence on a film temperature is obtained. Because the variation of η_F in the range of interest is small, convergence is rapid.

The procedure needed to obtain a mean film temperature and ball surface temperature, therefore, requires that data from four separate experiments be obtained: the film thickness using optical interference methods and radiation data for the low emissivity ball with and without the oil film filter and the high emissivity ball without the filter. The success of the procedure is based on the fact that the data in the EHD experiment are reproducible [17] thereby assuring identical conditions in each of the four experiments.

In order to collect a large amount of data in a short period of time so that the contact temperatures will not change significantly, a scanning system has been built into the detector mount which permits the detector to scan through the contact area in the direction of the surface velocity. Data were taken continuously in the direction of the scan at a constant detector speed of 0.0075 in/sec. The infrared detector has a temperature resolution of 5°C corresponding to 0.01 sec response time. The temperature resolution improves to 0.5°C for a response time of 1.0 sec. Successive passes were made at 2.5×10^{-5} m (0.001 in.) increments. From

these data points, the contour maps shown in Figures 39 and 40 were developed. The recorded output E/k of the detector, after analysis, can then serve directly as a map of total areal radiant intensity as a function of contact position.

Experimental Results

The lubricant used during this investigation is a naphthenic mineral oil used in previous EHD studies [12,13 ,17] and viscometric studies [2] in this laboratory. The fluid has been shown to be Newtonian [2] at shear rate and pressure levels approaching those anticipated in the EHD contact. The atmospheric pressure viscosity is 0.0217 Ns/m^2 (21.7 cp) at 37.8 C and 0.0032 Ns/m^2 (3.2 cp) at 98.9 C and the pressure-viscosity characteristic α^* is 2.32×10^{-8} m^2 (1.60×10^{-4} in^2/lbf).

All data was obtained with a peak Hertz contact pressure of 1.034×10^9 N/m^2(150,000 psi). Sliding velocities of 0.35, 0.69 and 1.39 m/s (13.7, 27.4 and 54.9 in/sec) were used in the investigation.

Using the infrared techniques developed in the previous section, contour maps of the steady state film and ball surface temperatures have been obtained and are shown in Figures 39 and 40 for the maximum sliding velocity. In each of these figures the boundary of the Hertzian contact region is shown for reference. Since the EHD contact is assumed to be symmetric about the centerline only one half of the contact area has been studied. Figure 41 shows the interference fringe pattern for the same conditions (1.39 m/s, 1.034×10^9 N/m^2) as used in Figures 36 and 37 .

In all these figures, the lubricant is entering the contact at the top of the figure. Referring to Figure 39 , it can be seen that along the contact centerline, the lubricant is at 30°C just ahead of the contact

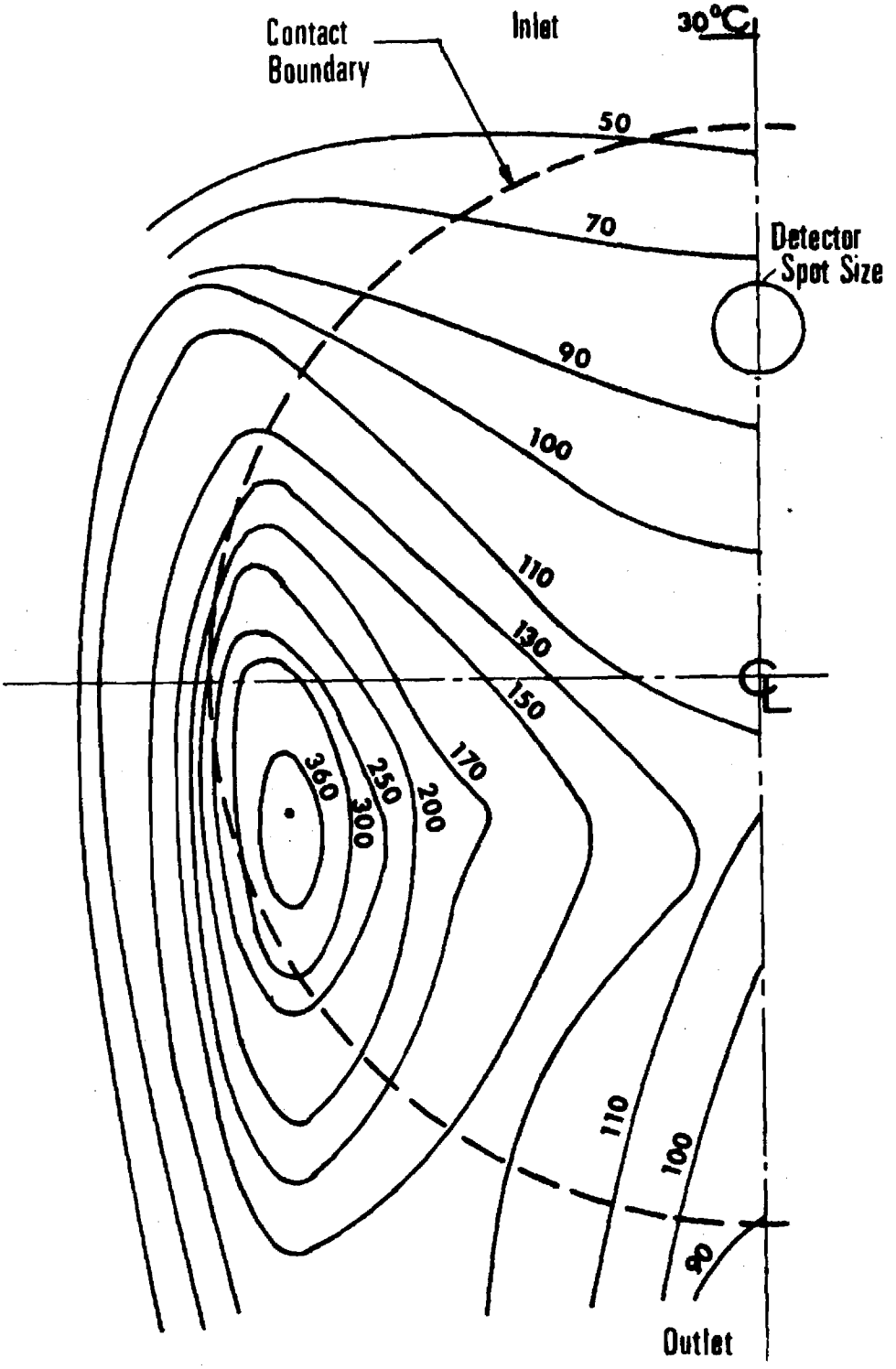

Figure 39. Steady State Film Temperature in the EHD Contact at 1.39 m/sec (54.9 ips) Sliding Speed.

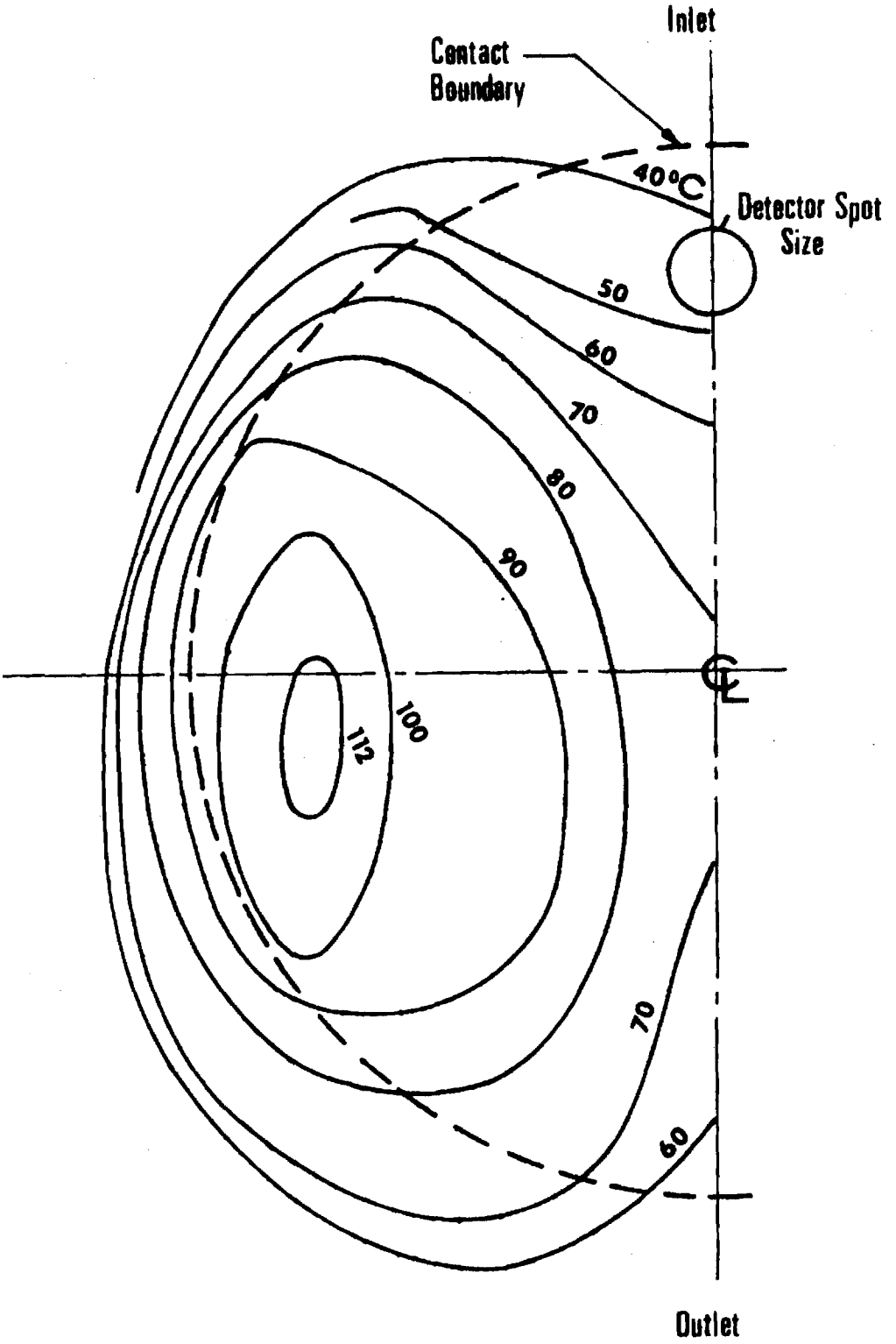

Figure 40. Ball Surface Temperature in the EHD Contact at 1.39 m/sec (54.9 ips) Sliding Speed.

Figure 41. Interference Fringe Pattern of the EHD Contact at 1.39 m/sec (54.9 ips) Sliding Speed.

inlet and increases in temperature to almost 50°C as it crosses the Hertzian contact boundary. The film reaches a maximum of 115°C just beyond the contact center and exits from the contact region at 75°C. The most striking feature about Figure 39, however, is the fact that the maximum film temperature (≃ 360°C) occurs at the minimum film thickness location (See Figure 38) in the EHD side lobe constriction. Based on previous measurements [17] the film thickness at this location is only 6.35×10^{-8} m (2.5×10^{-6} in.).

Figure 40 is a plot of the ball surface temperature distribution. The ball surface temperature is less than 40°C at the contact inlet, rises to over 70°C just beyond the contact center and exits the contact at just under 60°C. As is the case for T_f, the maximum ball surface temperature occurs in the side lobe constriction. The maximum values of T_f and T_b do not appear to be at precisely the same locations, however. The maximum ball temperature is only 115°C compared with 360°C for the lubricant film.

The temperature contours shown in Figures 39 and 40 were the maximum steady state values obtained during the investigation. Figures 42 and 43 show the variation with sliding velocity of steady temperature, T_f and T_b along the contact centerline. At each position in the contact and at each speed, the mean film temperature is substantially higher than the ball surface temperature. This is consistent with the fact that there is internal heat generation in the film due to viscous shear and that conduction to the boundaries is a primary heat transfer mechanism.

Finally, Figure 44 is a plot of maximum ball surface temperature in the contact as a function of sliding velocity. As was mentioned above, the maximum temperature is found in the EHD side lobe constriction.

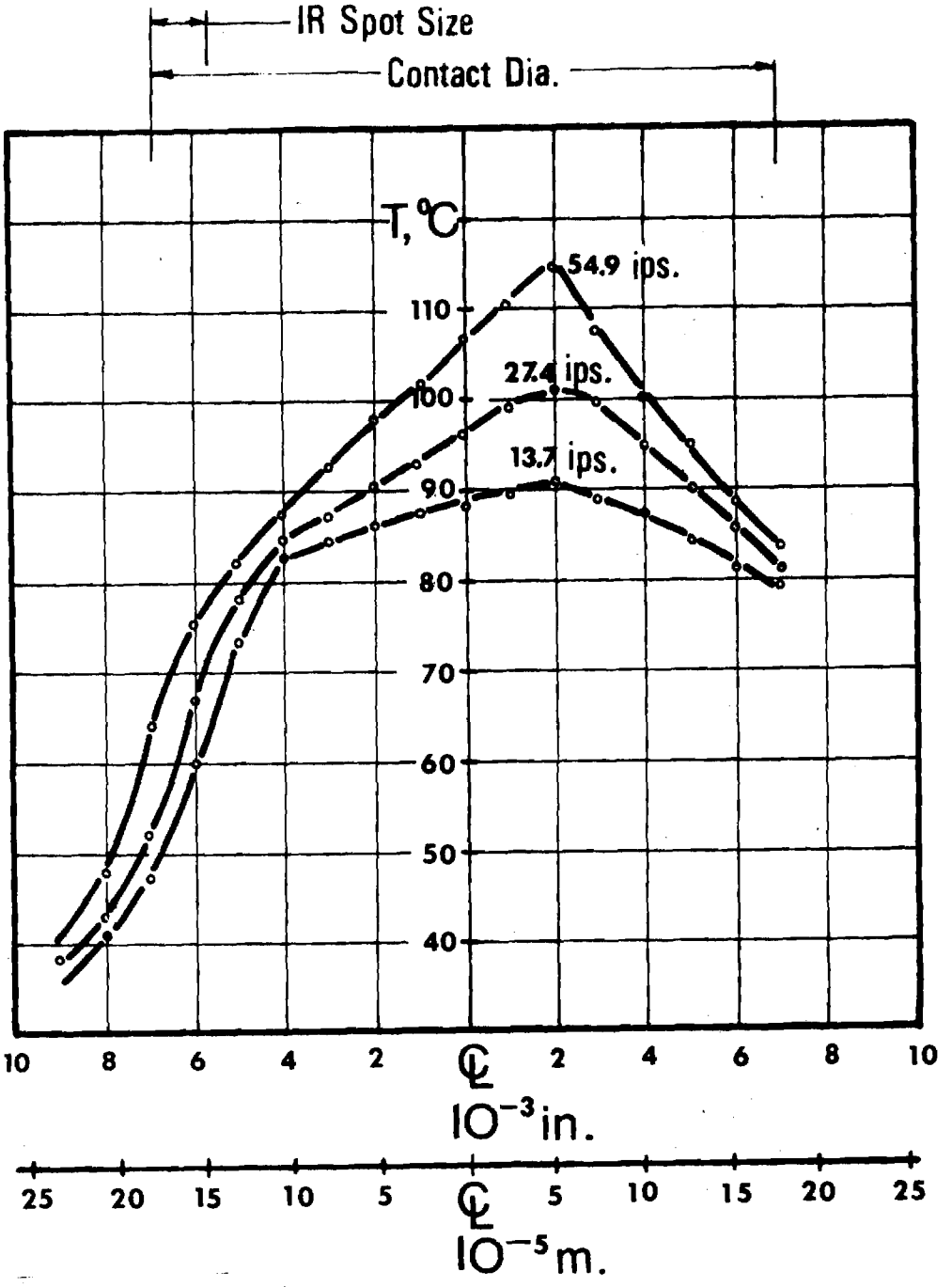

Figure 42. Steady State Film Temperature Distribution along the Contact Centerline as a Function of Sliding Speed.

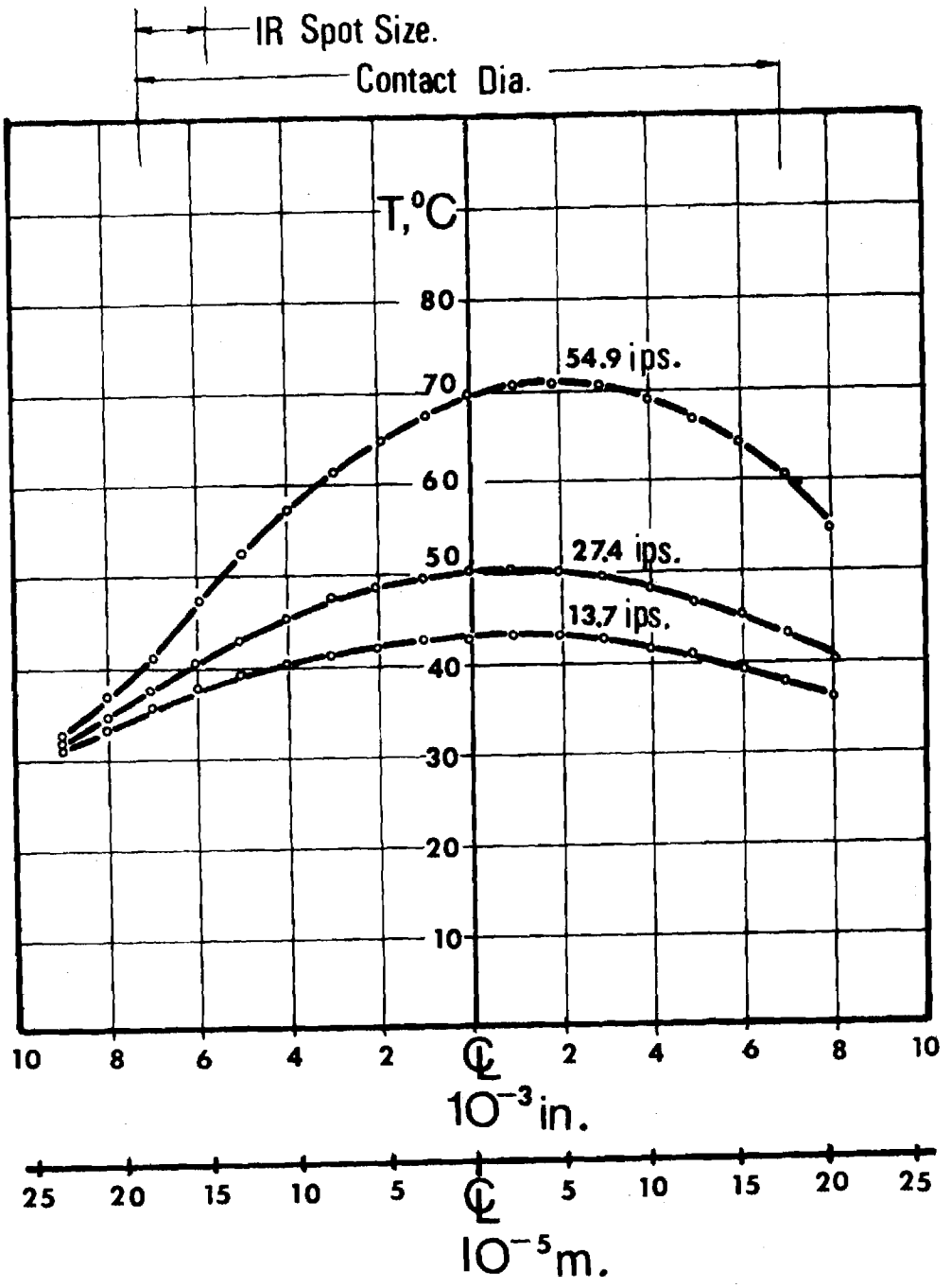

Figure 43. Ball Surface Temperature along the Contact Centerline as a Function of Sliding Speed.

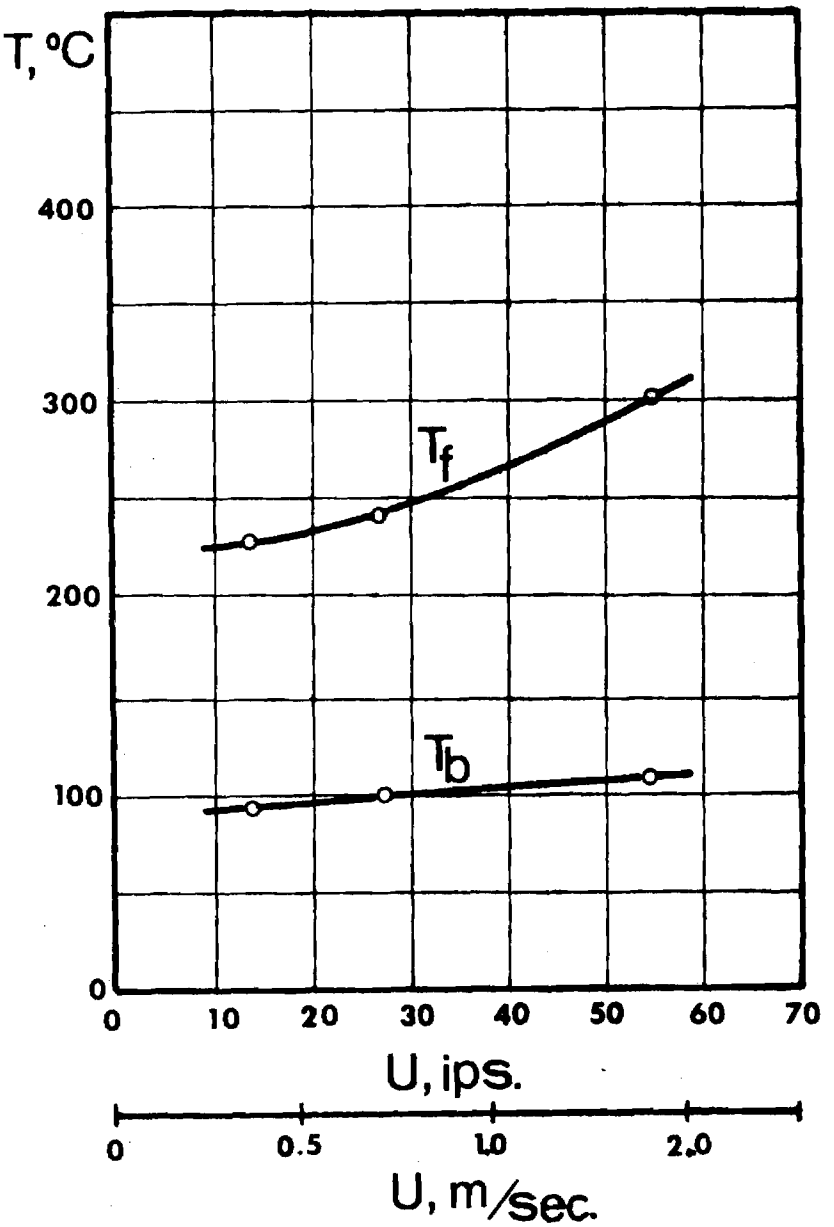

Figure 44. Maximum Ball Surface Temperature and Film Temperature as a Function of Sliding Speed.

Figure 43 also shows the film temperature variation with sliding velocity at the same contact location where the maximum ball temperature was found. Due to significant film emissivity variation throughout the contact, this location, which is the point of maximum radiation is not necessarily the point of maximum T_f. Except for the highest sliding velocity experiment, sufficient data were not obtained to find the maximum fluid temperature in the side lobe constriction.

Discussion of Results

The most useful temperature data which could be obtained for an EHD contact would be the sapphire and ball surface temperatures plus the temperature profile through the lubricant film. We have presented a technique wherein the actual ball surface temperature and a fourth power average fluid temperature taken through the film can be determined. The fact that the fourth power average is determined means that the peak film temperatures will be somewhat higher than the data presented.

Throughout the above discussion film thickness data has been used which was taken in a separate experiment with essentially the same apparatus. In the film thickness investigations, a 3.18×10^{-3} m (.125 in.) thick sapphire was used whereas a 1.52×10^{-3} m (.060 in.) sapphire was used in IR investigations. Because the thickness of the sapphire may influence its temperature distribution, thus changing the thermal boundary condition in the contact, film thickness and traction data were taken using both sapphires and were found to be identical.

The detector has been calibrated over the temperature range of interest using a radiometric calibration source (Barnes, Model RM-121). The detector resolution under the conditions of the experiment is 0.5C

according to manufacturer's specifications. Because of this relatively high resolution, the accuracy of the temperature data reported is primarily a function of the emissivity values and the proportion of received radiation assigned to each source in equations (15 , 16 , 21). The measured emissivity values for the ball surface used are believed to be correct to well within 10%. If this $\pm$ 10% error is carried through the above equations it amounts to an error in ball temperature of $\pm$ 4 ^{o} C at the maximum contact temperature of 115 ^{o} C. At locations where the temperature is less than this maximum the error will be lower. Also, if any of the calculated coefficients in quations (16) and (21) are in error by $\pm$ 10%, a similar error in ball temperature will result.

The most significant possible error is in the emissivity assigned to the oil film. From equation (6) it is seen that the emissivity is proportional to film thickness. Unfortunately, the error in film thickness is an absolute quantity (depending on fringe order interpretation (see Figure 41) rather than a percentage of the film thickness. This yields a maximum relative error at points of minimum film thickness, which are located at the points of maximum film temperature. The maximum error in film thickness has been assessed at $\pm$ 1.8 x 10^{-8} (0.7 x 10^{-6} in.) corresponding to misreading a contour on the film fringe pattern. At the point of maximum film temperature (360^{o}C) this $\pm$ 1.8 x 10^{-8}m error in minimum film thickness (6.4 x 10^{-8} m) results in an error in temperature of $\pm$ 30 ^{o}C. At all other locations within the contact, this error is substantially less because the film thickness is larger and the error in reading represents in this case only a fraction of its actual value. Also, for investigations in which the minimum film thickness is greater than 6.4 x 10^{-8} m, which includes most cases previously investigated in

this laboratory [12, 13, 17], the error is expected to be less.

The extremely high local fluid temperatures found in this investigation are thought to be a result of the high shear rates (10^7 sec^{-1}) at minimum film thickness locations in the Hertzian contact. The question does arise, however, whether the shearing is viscous with complete separation of the surfaces, or there is actually some asperity contact at the minimum film thickness locations. This is a possibility for the cases reported above since the minimum film thicknesses in the side lobes are of the order of the surface roughness values for the ball and sapphire. It is not obvious if asperity contact is occurring, however, since the ball surface shows no surface damage after running under load for several minutes. An investigation is currently under way [18] to determine which mechanism is causing these extreme temperature values.

In this research [18] a model was developed to determine the relationship between the adiabatic stationary wall temperature T_{mw}, which is the maximum fluid temperature and the moving wall temperature T_1. This model is based on the assumptions that the only heat source is the viscous dissipation at constant shear stress rate. It results in a relationship of the form,

$$\int_{T_1}^{T_{mw}} K_T \frac{dT}{\eta(p,T)} = U^2 \qquad (22)$$

where:

K_T = thermal conductivity
= 0.0167 lbf/sec °F

$\eta(p,T)$ = fluid viscosity function of the local pressure and temperature

U = sliding speed

It should be noticed that the average fluid temperature, mapped in the Figure 39, has to be at any time smaller than that of the adiabatic stationary wall temperature, unless some additional heat sources other than viscous dissipation in the fluid are present. The equation (22) was solved graphically for the maximum wall temperature due to viscous dissipation. The temperature obtained from the analysis was found to be less than the lubricant temperature experimentally deduced in some regions. The findings indicate the existence of a region in the contact area where a heat source, other than viscous dissipation, influences the lubricant temperature (Figure 45). In the conditions under investigation the asperity contact is assumed to be the additional energy source causing the high fluid temperature.

As seen in Figure 45, part of the area where the asperity contact may be present corresponds to that expected as a result of small film thicknesses in the side lobes. The roughness of the sphere used is 3.18×10^{-8} m (1.3×10^{-6} in.) and the minimum film thickness for a speed of 1.30 m/sec (54.9 in.sec) and load of 6.8 Kgf (15 lbf) is 6.35×10^{-8} m (2.5×10^{-6} in.).

If the asperity contact plays an important role in causing the high fluid temperature, the infrared technique can be an useful tool in detecting incipient film failure in highly loaded contacts.

Conclusions

We have presented a technique for mapping the temperature distribution in a sliding EHD contact. Both the ball surface temperature and a fourth power average lubricant film temperature have been obtained

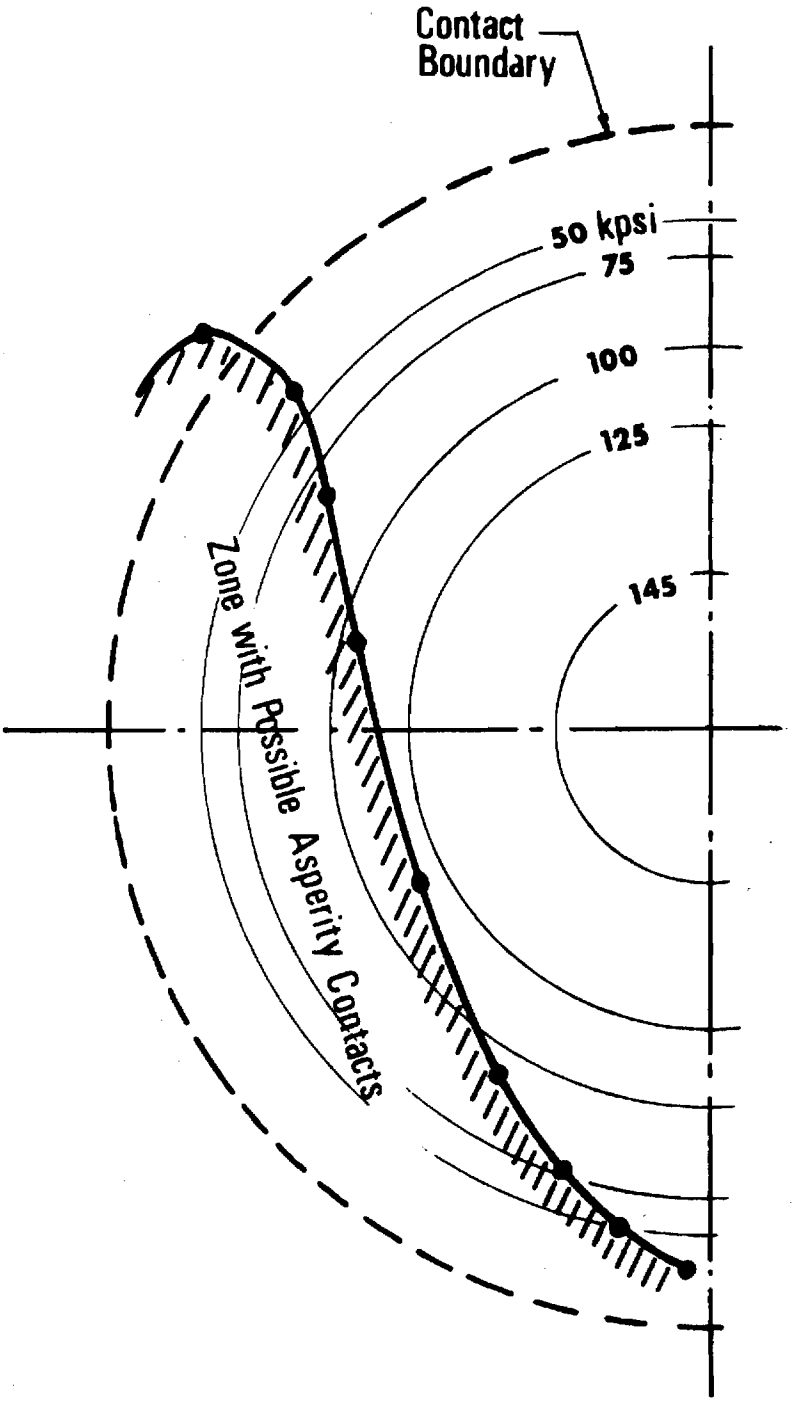

Figure 45. Contact Region with External Heat Source (Asperity Contacts).

at points throughout the contact. Under a specific set of experimental conditions, ball temperatures as high as 115°C and average fluid film temperatures as high as 360°C have been reported. Both temperature peaks were found to occur in the contact side lobes where the film thickness is a minimum. It was also observed that at each point in the contact, both temperatures increased significantly as the sliding velocity was increased.

Although only a limited amount of data was collected, it is sufficient to show that the technique reported can be useful in obtaining detailed temperature data in the EHD contact. In addition, it also suggests additional experiments using the IR microdetector; namely extensions to rolling contact experiments, to a determination of the sapphire surface temperature, to a spectral analysis of the materials in the contact, to aid in evaluating lubricant constitutive equations under EHD conditions, and to an investigation of the mechanisms leading to film failure.

c. The General Viscous Lubrication of Rolling and Sliding Rigid Cylinders

Introduction

The objective of the research in this section is to develop a general theory of the viscous lubrication of sliding and rolling cylinders. The fluid behavior considered is restricted to the case of the rheological behavior of the fluid being completely described by a viscosity function which is time independent. That is, the rheological model of the fluid excludes either normal stress effects or shear viscoleasticity. To date, and in the next six months, the isothermal case only is considered. The load range being studied spans the complete range from the lightly loaded case characterized by rigid cylinders to the highly loaded elastic cylinder case of full elastohydrodynamic lubrication.

This report is of the completion of the first phase; that of rigid cylinders and shear thinning fluids which do not exhibit a second Newtonian in their viscosity shear stress relation. The cases of the fluid with a second Newtonian and that of elastic cylinders with the full range of fluid behavior are both nearly completed and a complete report on those is expected in the next year.

Problem Formulation

A description of the system considered and its mathematical representation is discussed in detail in the previous annual report. This representation will only be briefly reviewed here. The system geometry and kinematics are shown in Figure 46. Let (R) be the equivalent radius of the system and (h_o) be the centerline spearation. Let (u_1) and (u_2) be the lower and upper surface velocities. Let (x_a) and (x_b) be

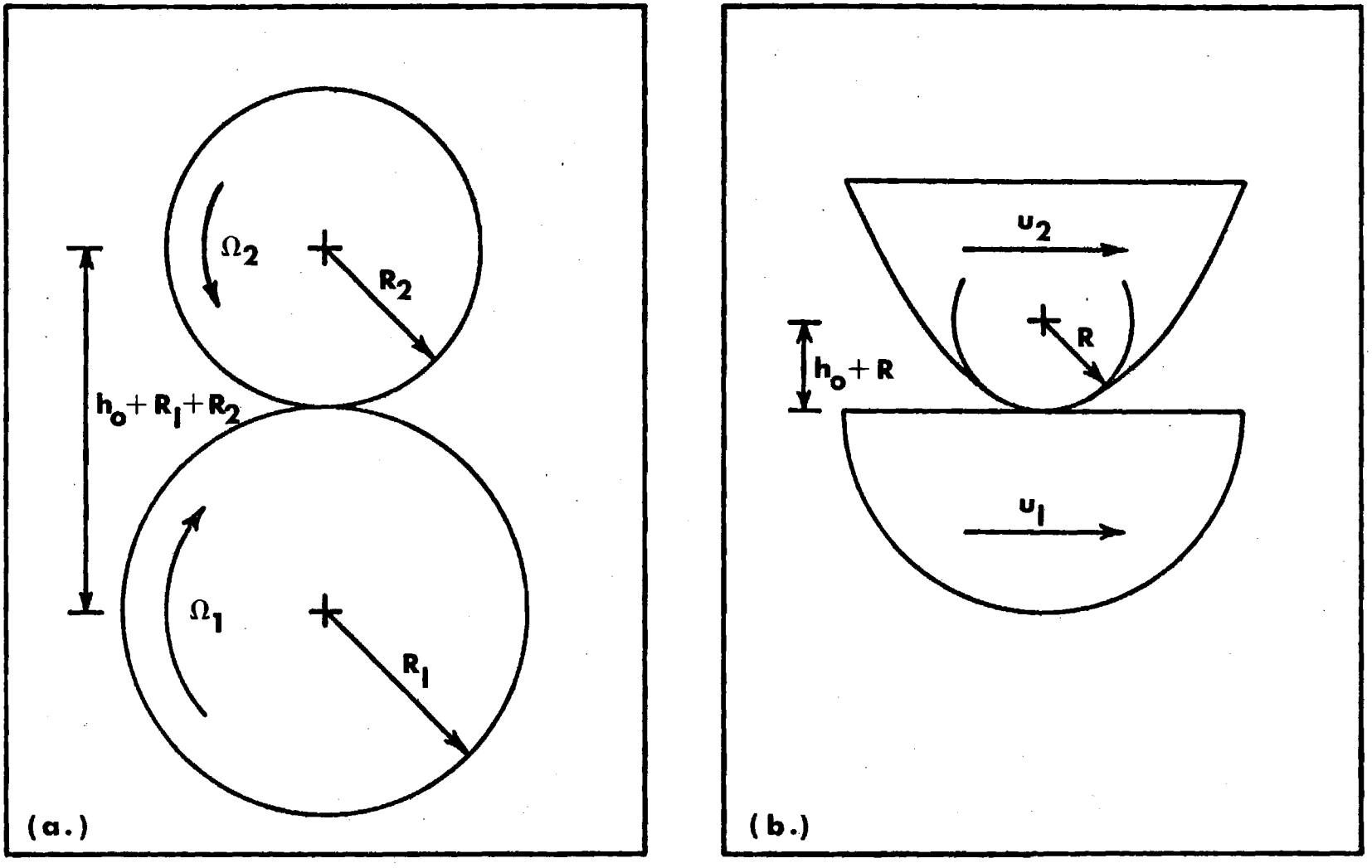

Figure 46. System Geometry & Kinematics. (a.) Original Geometry & Kinematics. (b.) Equivalent Geometry & Kinematics.

the inlet and outlet coordinates of the film. Let (h) be the film thickness, (s) be the shear stress on the lower surface and (p) be the pressure. Let (d) be the density and (z) be the viscosity of the fluid. The density and viscosity functions may be expressed in the form

$$d = d_0 \ (1 + dn)^{-1} \tag{23}$$

$$z = z_0 \ e^{b\ p} \ (1 + zn)^{-1} \tag{24}$$

where (d_0) and (z_0) are respectively the base density and viscosity, (b) is the log viscosity pressure coefficient and (dn) and (zn) are the density and viscosity deviation functions. The term (dn) is a function of pressure only while the term (zn) is a function of shear stress only. Then the shear stress on the lower surface and the pressure are given by

$$S(s,t) = s - s_0 - sn(s,t) = 0 \tag{25}$$

$$T(s,t) = t - t_0 - tn(s,t) = 0 \tag{26}$$

subject to the boundary conditions

$$x_a = 0 \tag{27}$$

$$x_b = 0 \tag{28}$$

and where

$$s_0 = 6 \ U \ z_0 \ e^{b\ p} \ (-\ (1 + A)\ h + (1 + dn)\ h_b)\ h^{-2} \tag{29}$$

$$t_0 = 12 \ U \ z_0 \ e^{b\ p} \ (h - (1 + dn)\ h_b)\ h^{-2} \tag{30}$$

$$t = h \ (\frac{dp}{dx}) \tag{31}$$

$$sn(s,t) = -4 \ SIn(s,t) - 6 \ TIn(s,t) \tag{32}$$

$$tn(s,t) = 6 \ SIn(s,t) + 12 \ TIn(s,t) \tag{33}$$

$$SIn(s,t) = t^{-1} \int_{s}^{s+t} Z\ zn\ (Z)\ dZ \tag{34}$$

$$TIn(s,t) = t^{-2} \int_{s}^{s+t} Z\ (s - Z)\ zn(Z)\ dZ \tag{35}$$

$$h = h_0 + .5\ R^{-1}\ x^2 \tag{36}$$

$$h_b = h_0 + .5\ R^{-1}\ x_b^2 \tag{37}$$

$$U = .5\ (u_1 + u_2) \tag{38}$$

$$A = (-u_1 + u_2)\ (6\ U)^{-1} \tag{39}$$

The equations (25) through (39) represent the system behavior for fluids described by equations (23) and (24). For evaluation of the system, the density and viscosity deviation functions must be specified. A large class of fluids is described by

$$dn = e\ p\ (1 + f\ p\ )^{-1} \tag{40}$$

$$zn = (k\ t)^m \tag{41}$$

where (e) and (f) are reciprocal pressures and (k) is a reciprocal shear stress. The exponent (m) is assigned a value of 2 in this investigation. Such a specification is in agreement with observations of the density and viscosity behavior of a variety of fluids of interest. Such fluids as common petroleum oils, silicone oils and various bulk polymers are adequately described over a wide range of pressures and shear stresses by this specification. The values of (e) and (f) are of the order 5×10^{-6} psi^{-1}. Such a value of (k) implies that the viscosity of the fluid has been reduced by 50% at a shear stress of 5 psi. A plot of the nondimensional log viscosity vs. the nondimensional log shear stress is shown in Figure 47 .

For the above choice of viscosity deviation functions (zn), equations (32) and (33) reduce to

$$sn(s,t) = k^{-2}\ (-s^3 + .5\ s\ t^2 + .2\ t^3) \tag{42}$$

$$tn(s,t) = k^{-2}(-3\ s^2\ t - 3\ s\ t^2 - .9\ t^3) \tag{43}$$

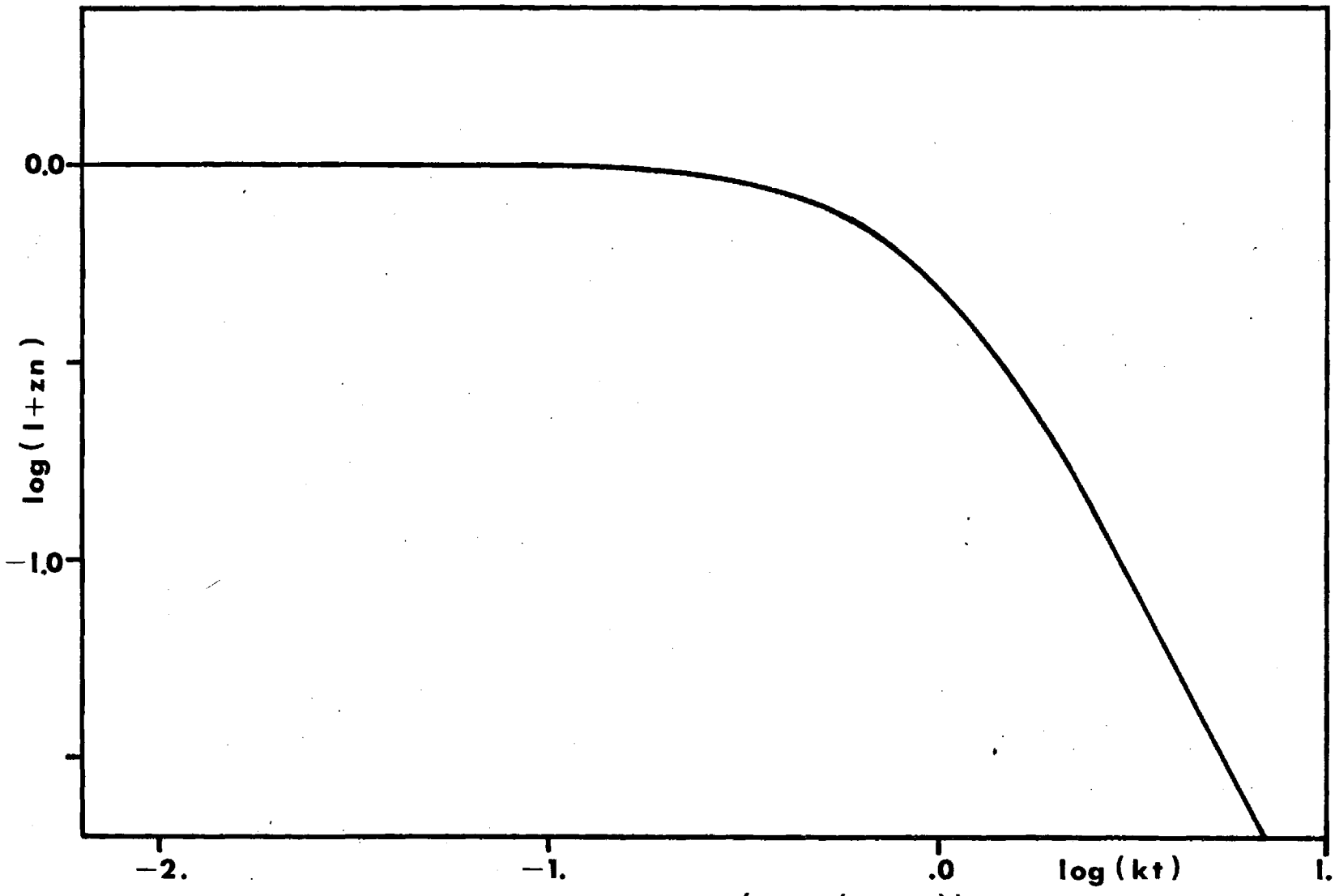

Figure 47. Nondimensional Log Viscosity ($-\log(1+zn)$) vs Nondimensional Log Shear Stress ($\log(kt)$).

Problem Solution

This system of equations is essentially a nonlinear first order differential equation with a free boundary. An approximate solution of such equations can be obtained as the solution of the related system of finite difference equations. These are nonlinear algebraic equations and may be solved by a variety of well-known iterative methods.

A direct application of the Newton-Raphson method is ineffective and a modified method is shown schematically in Figure (48). The grid spacing is variable. The inlet and outlet regions are separated and solved separately. The variables (s) and (t) are treated separately and equations (25) and (26) are solved for s and t respectively.

These latter modifications do not effect the accuracy of the solution of the finite difference system. The maximum error for computation was set at 0.1%. Comparison of pressure distributions from increasingly dense grid spacings indicates that a variable spacing of 50 points in the (x_a, x_b) interval is sufficient for an error of less than 1% in the pressure distribution due to the finite difference representation.

Results

Two objectives were pursued in this investigation. The first was to determine the details of the distribution of shear stress on the lower surface and the distribution of pressure for a typical fluid in a typical operation. The second objective was to map out the system parameters over the entire range of fluids and operations.

For the first investigation a fluid was chosen with $d_o = 1.\times 10^{-3}$ slugs in $^{-3}$, $z = 2. \times 10^{-5}$ reyn, $b = 0.0$ psi^{-1}, $e = f = 0.0$ psi^{-1} and $k = 0.0$ psi in case A, $k = .1$ psi^{-1} in case B. The operation was chosen with $R = 2.0$ in, $h_o = 3 \times 10^{-4}$ in, $u_1 = u_2 = 100$ in/sec in case I and $13\ u_1 = 7\ u_2 = 910$ in/sec in case II. The resulting distribution in all cases $x_a = .75$ in./s of shear stress on the lower surface and of pressure are shown in Figures 49 through 51. This fluid was chosen to eliminate the effects of pressure on either the density or viscosity functions.

The results of the second investigation follow from the first by varying the fluid and operation parameters. In addition the previously introduced independent parameters, the dependent parameters of load per unit length (W) and traction in the lower surface per unit length (TR) are of interest. In accordance with standard conventions (TR) is positive when it is to the

Computational Flow Chart

(Subscript (i) refers to inlet region and subscript (e) refers to outlet region. (JAC) is the jacobian of the set of equations in the first argument with respect to the set of variables in the second argument. (ERR) is the relative error function of the set of variables in the argument. (eps) is the error criterion. (g.t.) is (greater than).)

1. Read system parameters (x_a, R,U,A,d_0,e,f,z_{0b},k)
2. Read state parameter (h_0)
3. Read grid spacing $(dx_I)^T = (dx_{Ii}, dx_{Ie})^T$
4. Read or calculate starting solution $(s_I^0, p_{I+1}^0, x_b^0)^T$
5. Set $(s_I^*, p_{I+1}^*, x_b^*)^T = (s_I^0, p_{I+1}^0, x_b^0)^T$
6. Calculate $(A_{Ii,Ji+1}) = (JAC(T_{Ii}^*, p_{Ji+1}^*)$
7. Solve $(T_{Ii}^*)^T = (A_{Ii,Ji+1})(p_{J+1} - p_{J+1}^*)$
8. Calculate $(s_{Ii})^T$
9. Set $(s_{Ii}^*, p_{Ii+1}^*)^T = (s_{Ii}, p_{Ii+1})^T$
10. If $(ERR((s_{Ii}^*, p_{Ii+1}^*)^T))$ g.t. (eps), go to (6)
11. Calculate $(A_{Ie,Je+1}) = (JAC(T_{Ie}^*, p_b^*), (p_{Je+1}^*, x_b^*)))$
12. Solve $(T_{Ie}^*, p_b^*)^T = (A_{Ie,Je+1})(p_{Je+1} - p_{Je+1}^*), (x_b - x_b^*))^T$
13. Calculate $(s_{Ie})^T$
14. Set $(s_{Ie}^*, p_{Ie+1}^*, x_b^*)^T = (s_{Ie}, p_{Ie+1}, x_b)^T$
15. If $(ERR((s_{Ie}^*, p_{Ie+1}^*, x_b^0)^T))$ g.t. (eps), go to (11)
16. Set $(s_I^0, p_{I+1}^0, x_b^0)^T = (s_I^*, p_{I+1}^*, x_b^*)^T$
17. If $(ERR((s_I^0, p_{I+1}^0, x_I^0)^T))$ g.t. (eps) go to (5)
18. Write $(s_I, p_{I+1}, x_b)^T$

Figure 48

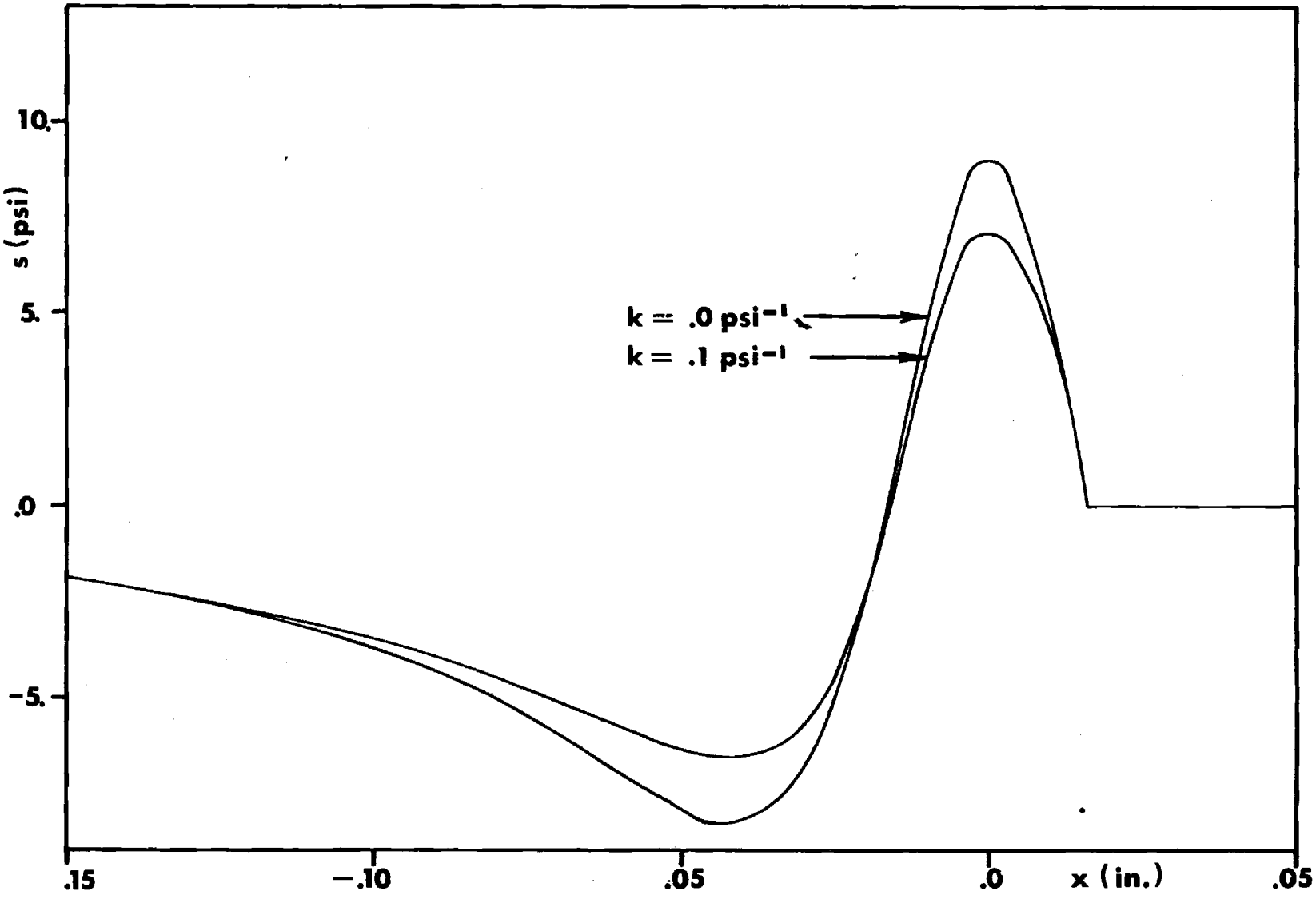

Figure 49. **Distribution of Shear Stress on the Lower Surface for 0 % Slip.**

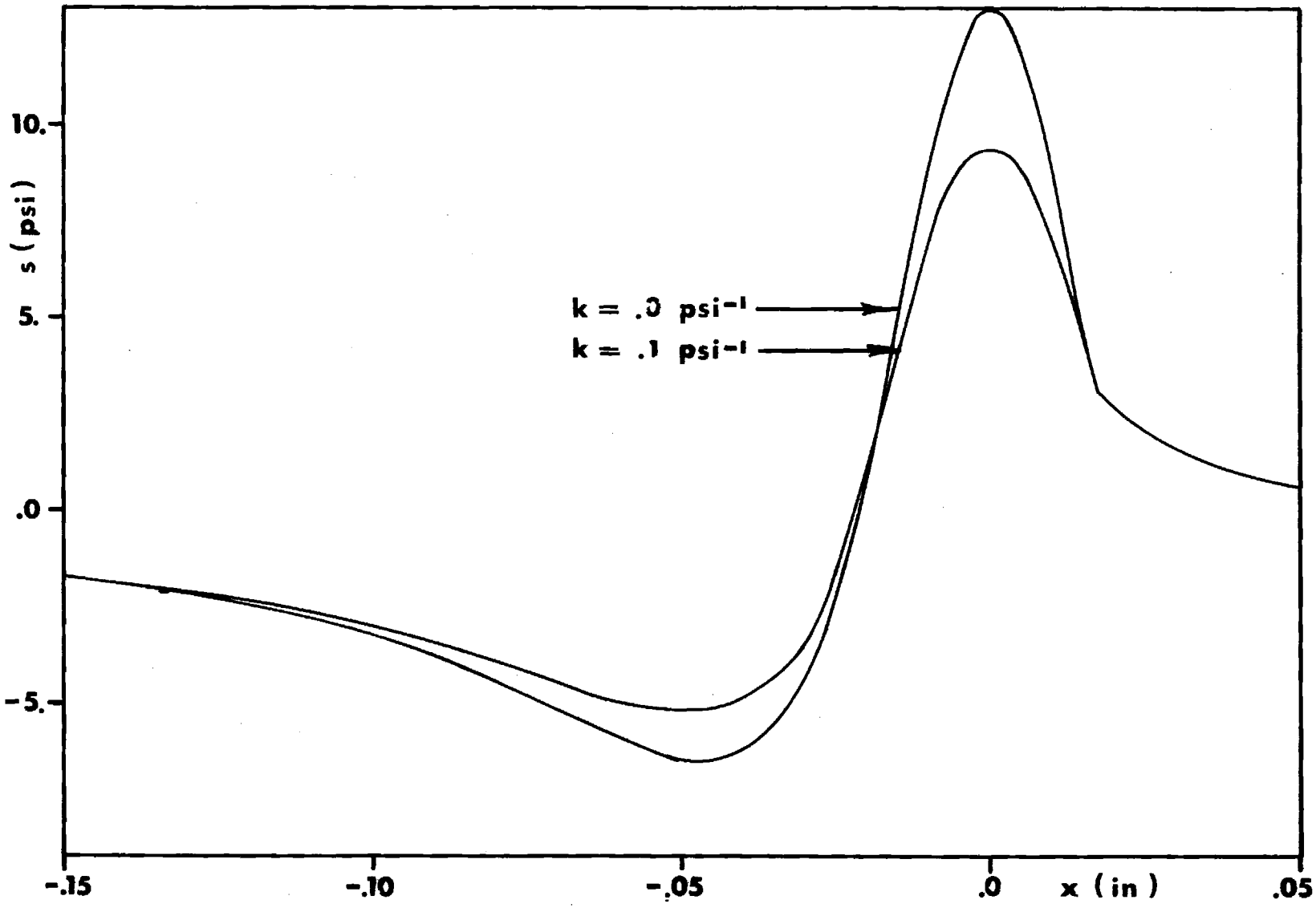

Figure 50 . Distribution of Shear Stress on the Lower Surface for 60 % Slip.

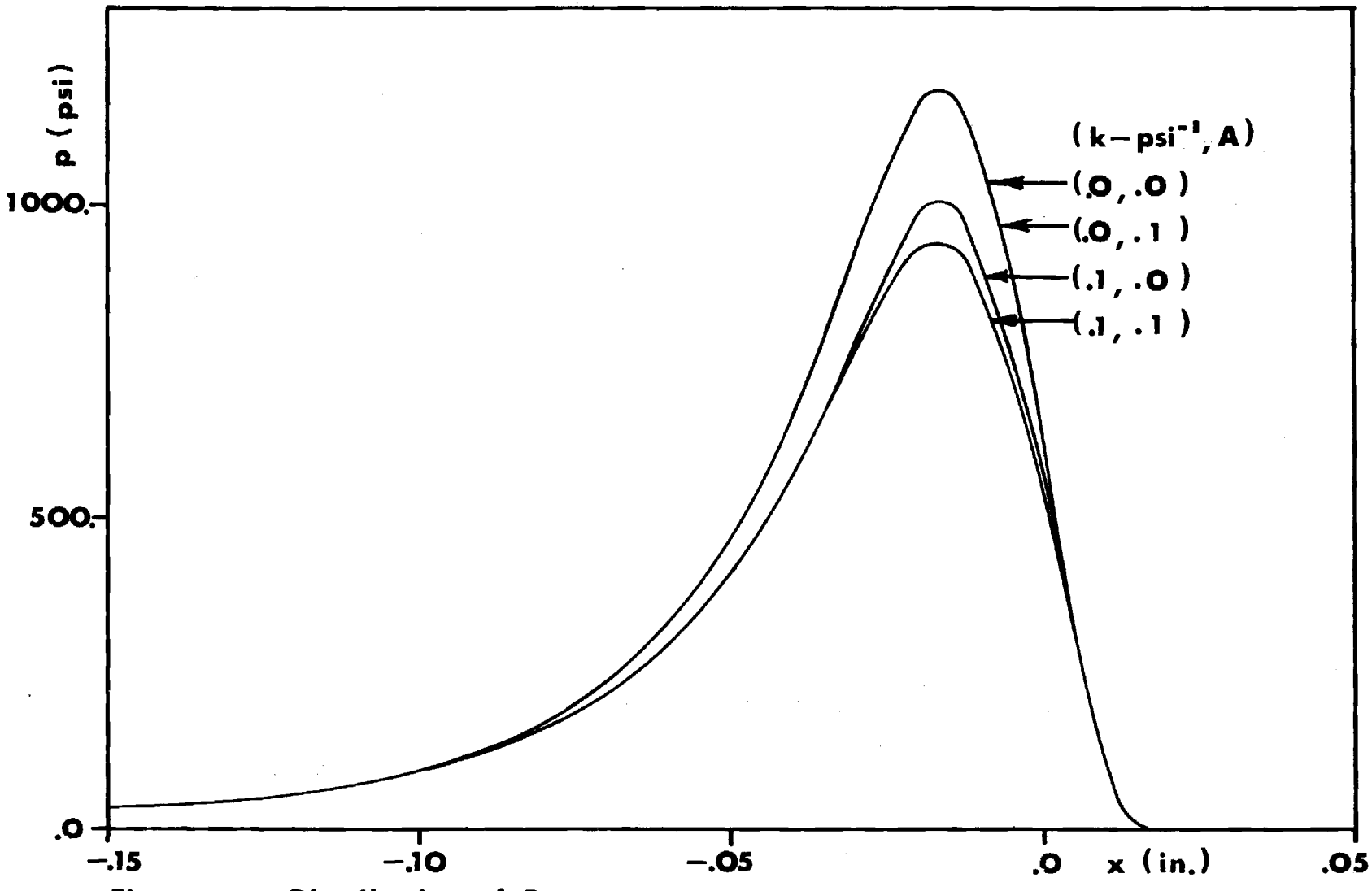

Figure 51 Distribution of Pressure.

right in Figure 46. For convenience and economy of display the following nondimensional parameters are introduced

$$GI = b\,(2\,k\,h_o^{-1})^{\frac{1}{2}}\,z_o\cdot\,U\,h^{-1} \qquad \text{(operation parameter)}$$

$$G2 = k\,z_o\cdot\,U\,h_o^{-1} \qquad \text{(fluid parameter)}$$

$$G3 = A \qquad \text{(slip parameter)}$$

$$WT = .5\,W\,R^{-1}\,(z_o\cdot\,U\,h_o^{-1})^{-1} \qquad \text{(load parameter)}$$

$$TRT = .5\,TR\,R^{-1}\,(z_o\cdot\,U\,h_o^{-1}) \qquad \text{(traction parameter)}$$

$$TRC = T/W = TRT/Wt \qquad \text{(traction coefficient)}$$

Nondimensional curves for (WT) and (TRC) are shown in Figures 52 and 53. These curves were calculated for a fluid with $e = f = 0.0\ psi^{-1}$ (i. e. constant density).

Discussion

The solution of the system for a given set of data requires 50-100 seconds of CPU time on the Univac 1108. Not all solutions can be obtained from a fixed starting solution such as a linearized system. However, the continuation of solutions yields solutions in all cases of interest. The solutions for $b = 0.0\ psi^{-1}$ (GI = 0) and $h_o = 0.0003$ indicate a large reduction in peak pressure in cases B compared with cases A (i. e. shear thinning compared to constant viscosity fluids). This results in loss of load capacity. This loss may be significant at high values of the operation parameter (GI). Similarly, there is a large reduction in the peak shear stress on the lower surface and the traction on the lower surface as the fluid parameter (G2) increases. Such behavior is typical for this class of fluids. The maximum pressures are maintained at a low level (under 2000 psi) throughout this investigation so as not to invalidate the assumption of rigid cylinders. At these pressure levels the effects of fluid compressibility are negligible.

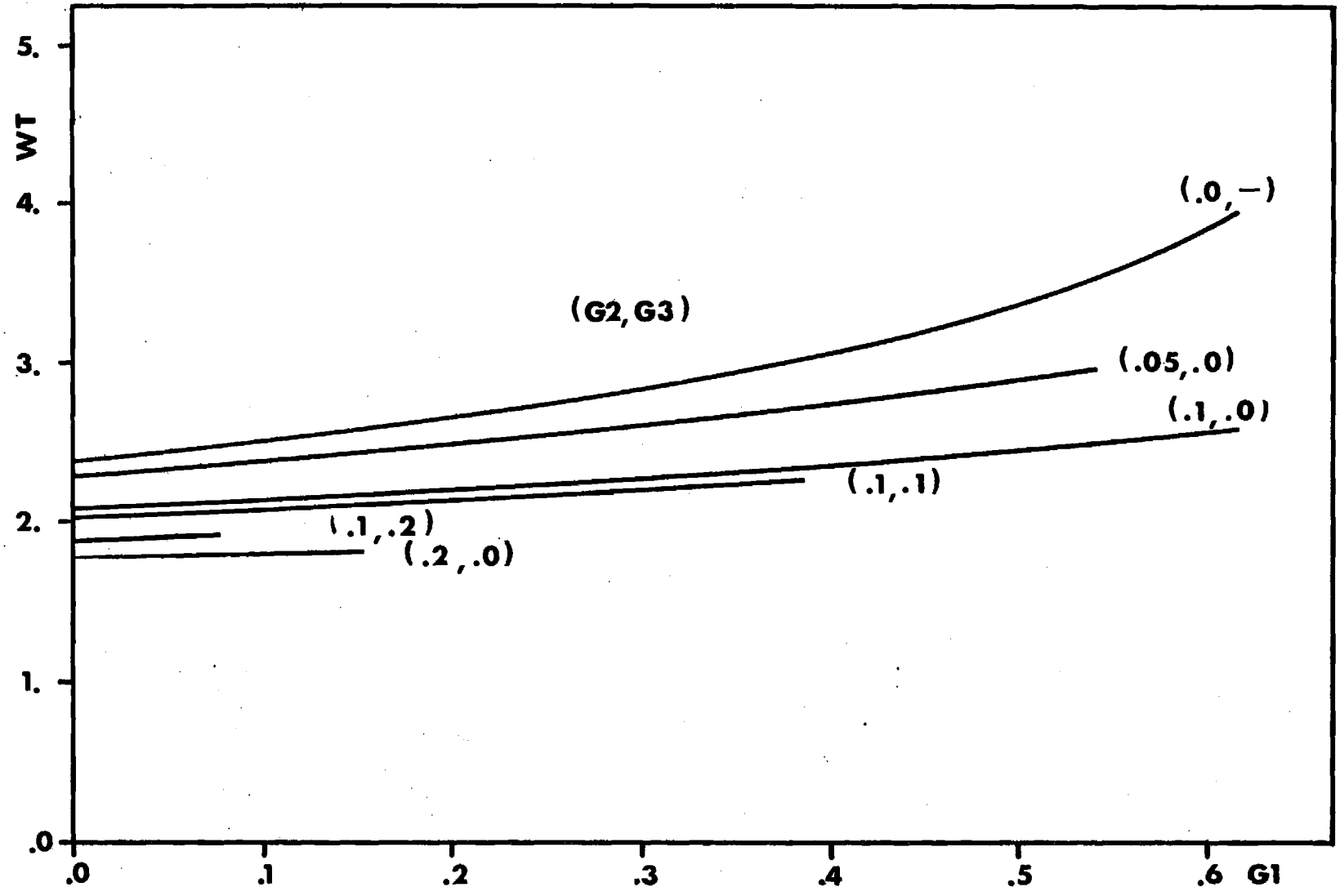

Figure 52. Nondimensional Load (WT) as a Function of Operation Parameter (G1) & Shear Stress Parameter (G2) & Slip Parameter (G3).

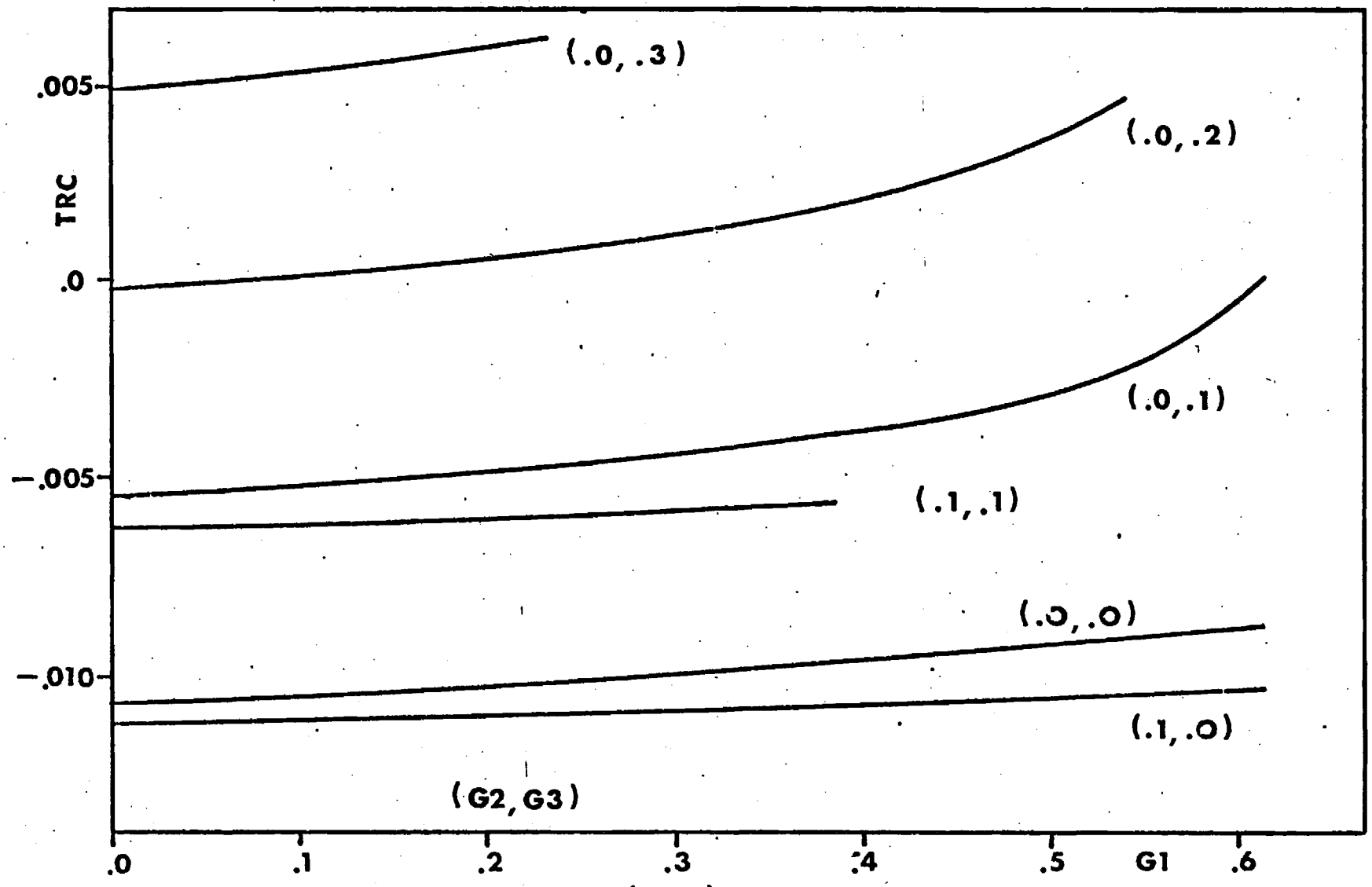

Figure 53. Traction Coefficient (TRC) as a Function of Operation Parameter (G1) & Shear Stress Parameter (G2) & Slip Parameter (G3).

The non-dimensional charts indicate the expected general behavior and are useful as a rough guide to the designer. Such information for the case $k = 0.0\ psi^{-1}$ and $b = 0.0\ psi^{-1}$, i. e. for fluids with a constant viscosity function has been presented by Peppler (19) and Cameron (20). The points on the GI = 0 axis of these charts are in agreement with the results for conditions of G1 = G2 = 0. It is interesting to note the large range of negative traction coefficients indicating conditions under which cylinder 1 cannot drive cylinder 2. These charts also allow the measurement of fluid properties, i. e. k, through measurements of the load and traction coefficients.

The methods developed here are readily applied to other fluid models, such as those of the Ree-Eyring, Maxwell, and Reiner-Philippoff type. Similar results have already been obtained for fluids of the Reiner-Philippoff type, but are not reported here. Further, the methods are not restricted to viscosity deviations expressible as combinations of elementary functions.

The objective of this program is to extend these investigations to consider the general viscous lubrication of rolling and sliding elastic cylinders. This work is making progress and results should be forthcoming in the next few months. Calculations for the elastic deformation due to an arbitrary surface pressure have been successfully carried out. It is only necessary to introduce these computational procedures into the programs used for the rigid cylinders.

Conclusion

Preliminary results in the investigations of the general viscous lubrication of rolling and sliding elastic cylinders have been presented. These are only valid under light loads but indicate the direction of the

investigation and the results to be obtained. The problem formulation and the method of solution will remain essentially the same under heavy loads. These preliminary results have value in themselves. The non-dimensional charts allow the evaluation of lubricants in terms of their shear stress behavior and also allow the rational design of systems employing such fluids.

d. Energy Dissipation

There is a large variation in the amount of energy dissipated in a lubricant at various locations in gas turbine or reciprocating engines. The amount of energy dissipation can influence the effective viscosity of the lubricant both by increasing its temperature and, in some cases, by molecular degradation.

With respect to shear rates, engine lubrication conditions fall into three catagories which will be designated A, B and C. Region A has low shear rates which occur in the oil pump inlet and drainage galleries and corresponds to the shear rates commonly encourtered in kinematic viscosity measurements. Typically film thicknesses are large (>.01m). Behavior in this shear rate range is very important for lubricant circulation particularly at low temperature.

Region B corresponds to what might be called typical hydrodynamic lubrication as occurs in crankshaft journal bearings and other hydrodynamic sleeve bearings in engines and transmissions. Depending on operating speed, the surface velocities are of the order 1-10 m/s and the film thickness is typically on the order of 10^{-5}m resulting in shear rates of $10^5 - 10^6 s^{-1}$. Shear stresses will be on the order of 10^4 N/m^2.

Region C corresponds to elastohydrodynamic lubrication (EHD) conditions such as might be expected in gears, cams, tappets, and other concentrated load contacts in the system. These are mechanically the most severe conditions to which the lubricant is subjected. The surface velocities of these contacts are about the same or somewhat lower than those of the journal bearing, but the film thicknesses are typically 100 times smaller, resulting in shear rates of at least an order of magnitude larger. Shear stresses are not as easily estimated for EHD conditions because the

pressures are very high causing an increase in viscosity, but EHD experiments done in this laboratory suggest that average shear stresses are 10^7 N/m^2.

Because of the magnitude of the shear stresses in regions B and C, mechanical degradation of the lubricant is possible. The field of mechanical degradation of polymers has been reviewed recently by Casale, Porter and Johnson [21]. They show that although mechanical degradation does occur in polymer solutions, it is a very inefficient process when viewed from energy considerations. In some cases, the energy per mole required to break molecular bonds is as much as a million times the activation energy of C-C bonds.

Table 12 compares typical shear rates, shear stresses, energy dissipation rates and friction power factors for regions A, B and C. The energy dissipation rate can be defined either as the energy dissipated per unit time per unit volume or per mass of lubricant passing through the contact. The friction power factor is simply the energy dissipated per unit time per unit bearing area. To calculate these quantities, the simple model of a lubricated contact shown in Figure 54 is assumed. The shear stress, shear rate and film thickness (h) of the shaded volume of fluid have already been mentioned and are entered in Table 12. The energy dissipation rate per unit volume is simply the shear stress times the shear rate and it too is entered in Table 12. However, what is more important for mechanical degradation is the energy dissipated per unit mass of the fluid passing through the volume. This is obtained by multiplying the dissipation rate per unit volume times the volume and dividing by the mass flow rate through the volume.

The energy dissipation rate per gram-mole is obtained by

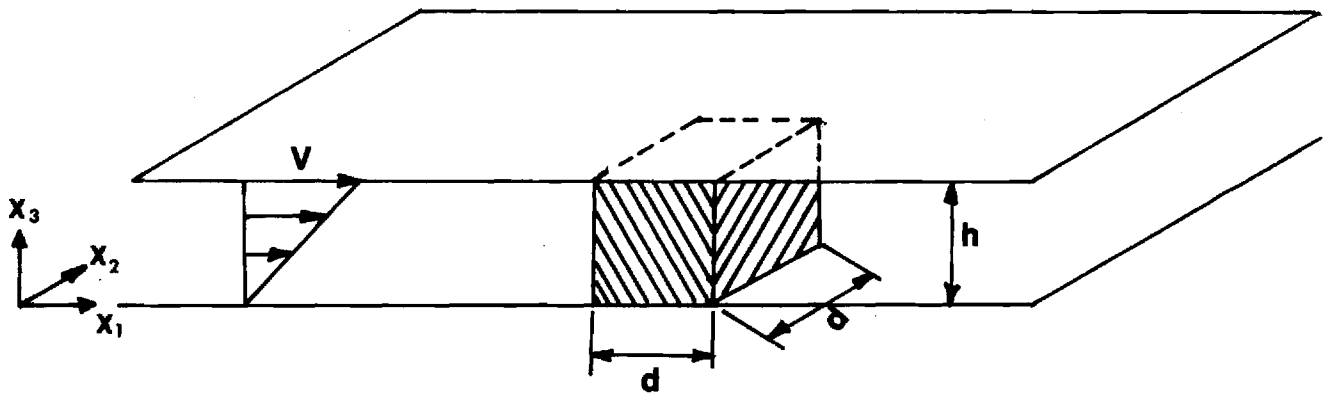

Figure 54 Simplified Model of a Lubricated Contact.

Table 12. Typical Conditions in Lubrication Regimes as Relating to Mechanical Degradation of Polymers

Variable	Units	A Low Shear	B Hydrodynamic Lubrication	C Elastohydrodynamic Lubrication
$\dot{\gamma}$ = shear rate	s^{-1}	$\leq 10^3$	$10^5 - 10^6$	$10^6 - 10^7$
τ = shear stress	N/m^2	$\leq 10^2$	10^4	10^7
$\tau\dot{\gamma}$ = energy dissipation rate per volume	W/m^3	$\leq 10^5$	$10^9 - 10^{10}$	$10^{13} - 10^{14}$
$\frac{2\tau d}{\rho h}$ = energy dissipation rate per mass flow	J/kg	$\leq 10^{-1}$	10^5	10^8
$\frac{2\tau d(MW)}{\rho h}$ = energy dissipation rate per kmole	J/kmole	$\leq (MW)10^{-1}$	$(MW)\cdot 10^5$	$(MW) \cdot 10^8$
$2\dot{\gamma}h$ = friction power factor	W/m^2	10^3	$10^4 - 10^5$	10^7

multiplying the dissipation rate per unit mass by the molecular weight. Finally, the friction power factor is simply the energy input rate per unit volume multiplied by the film thickness. These values have also been entered in Table 12.

Table 13 lists the shear rate, shear stress, energy input rate per unit volume, friction power factor and energy input rate per gram mole of lubricant for the fluids supplied by NASA for examination in this laboratory. If one recalls that the activation energy for a kmole of carbon-carbon bonds is 3.4×10^8 J/kmole, it is not surprising that some degradation occurs in region C and possibly even region B.

In fact, what is surprising when viewed in light of the numbers in Table 13, is that more degradation does not occur. However, in the review paper by Casale et al. [21] several studies on the mechanical degradation of polymers are cited which indicate that mechanical degradation is a very inefficient process, requiring as much as a million times (10^6) more energy than the activation energy for the bond. Clearly, in the EHD areas (regime C) some mechanical degradation is to be expected and it is probably these (EHD) conditions which cause the degradation observed in the engine tests of Wright and Johnson (22) and Selby and West (23).

An investigation has recently been conducted in this laboratory under sponsorship of the National Science Foundation to study molecular degradation in a single EHD sliding point contact. Several fluids including polymer blends and silicones have been investigated. The permanent loss of viscosity and the change in molecular weight distribution of the sample have been determined. Analysis of the fluids was made on a few micro-liter sample extracted from the exit region of the EHD contact.

Table 13 Typical Elastohydrodynamic Lubrication Conditions for NASA Supplied Fluids. *

Fluid	U m/s	$\dot{\gamma}$ x10^{-6} s^{-1}	τ_{avg} x10^{-6} N/m^2	$\dot{\gamma}\tau_{avg}$ x10^{-12} W/m^3	$\dot{\gamma}\tau_{avg}$ hx10^{-6} W/m^2	$\frac{2\tau d(MW)}{\rho h}$ x10^{-6} J/kmole
Advanced Ester	.35	9.5	42	400	14	860(MW)
	1.4	9.3	25	230	34	120(MW)
Formulated Advanced Ester	.35	7.6	51	390	18	780(MW)
	1.4	8.2	29	240	41	120(MW)
Naphthenic Mineral Oil Plus Additive	.35	1.4	58	81	20	190(MW)
	1.4	2.7	35	95	48	55(MW)
Synthetic Paraffinic Mineral Oil Plus Additive	.35	.89	40	36	14	86(MW)
	1.4	1.9	24	46	35	27(MW)
DN600 Plus Additive	.35	5.0	38	190	13	460(MW)
	1.4	7.3	29	210	40	130(MW)
FN 2961	.35	1.4	50	70	18	160(MW)
	1.4	3.2	38	120	51	71(MW)
MCS 460	.35	2.7	69	190	25	410(MW)
	1.4	5.1	51	260	70	140(MW)
MCS 418	.35	3.5	53	190	19	320(MW)
	1.4	6.3	40	250	55	110(MW)
DN-600	.35	5.0	34	170	12	400(MW)
	1.4	7.3	26	190	36	110(MW)
XRM-109F	.35	.97	47	46	17	110(MW)
	1.4	1.8	21	38	23	23(MW)
KRYTOX	.35	.92	68	62	24	68(MW)
	1.4	1.8	40	72	55	20(MW)

*for 67N normal load, 3.53 × 10^{-4}m contact diameter, pure sliding.

Results indicate that a single pass through an EHD contact is sufficient to significantly alter the rheology of many lubricants.

REFERENCES

1. Novak, J. D. An Experimental Investigation of the Combined Effects of Pressure, Temperature and Shear Stress Upon Viscosity. Doctoral Thesis, Univ. of Mich., 1968.

2. Winer, W. O., and Novak, J. D., "Some Measurements of High Pressure Lubricant Rheology", Journal of Lubrication Technology, Trans. ASME, Series F., Vol. 90, No. 3, July 1968, pp. 580-591.

3. Pressure-Viscosity Report, Vols. I and II, a report prepared by the ASME Research Committee on Lubrication, ASME, New York, 1953.

4. Hersey, M. D. Theory and Research in Lubrication, New York, Wiley and Sons, Inc. 1966.

5. Appledoorn, J. K., Physical Properties of Lubricants, Chap. 8, Boundary Lubrication, An Appraisal of World Literature, The ASME Committee on Lubrication, New York, 1969.

6. Eckert, E. R. G., and Drake, R. M., Jr., Analysis of Heat and Mass Transfer, McGraw-Hill , 1972.

7. Winer, W. O., Sanborn, D. M., and Jakobsen, J., Investigations of the Rheology of a Series of Silicones as Related to Elastrohydrodynamic Lubrication, a Report Prepared for Dow Corning Corporation, Midland, Michigan. Georgia Institute of Technology, Atlanta, Georgia, November 1972.

8. Wright, W. A. and Crouse, W. W. Jr., "A New Concept in Generalizing Non-Newtonial Fluid Flow Data", ASLE-ASME Lubrication Conference, Washington, D. C., Oct. 1964, Reprint No. 64-LC-11.

9. Winer, W. O., Fluid Measurements NASA Report No. NAS3-15383. Georgia Institute of Technology, Atlanta, Georgia, January 1972.

10. Winer, W. W., Sanborn, D. M., Lee, D., Jakobsen, J., Carlson, S., and Bohn, M. Investigations of Lubricant Rheology as Applied to Elastohydrodynamic Lubrication, NASA Report No. 11-002-133, Georgia Institute of Technology, Atlanta, June 1970.

11. Winer, W. O. and Ehya, H., High Pressure Rheology of Four Solutions of Polytetene in Paraffinic Base Oil, NASA Report No. C-57357-B, University of Michigan, Ann Arbor, Michigan 1969.

12. Sanborn, D. M. and Winer, W. O., "Fluid Rheological Effects in Sliding Elasthydrodynamic Point Contacts with Transient Loading: 1 - Film Thickness", Trans. ASME, Journal Lubrication Technology, Vol. 93, pp. 262-271, 1971.

13. Sanborn, D. M., and Winer, Wo. O., "Fluid Rheological Effects in Elastohydrodynamic Point Contacts with Transient Loading II - Traction", Trans. ASME, Journal of Lubrication Technology, Vol. 93, pp. 342-348, 1971.

14. Kebler, R. W., "Optical Properties of Synthetic Sapphire", Linde Company, 30 East 42nd St., New York, New York.

15. McMahon, H. O., "Thermal Radiation From Partially Transparent Reflecting Bodies", Journal of the Optical Society of America, Vol. 40, No. 6, pp. 376-380, 1950.

16. Kreith, F., Principles of Heat Transfer, International Textbook Company, pp. 177-180, 1964.

17. Sanborn, D.M., An Experimental Investigation of the Elastohydrodynamic Lubrication of Point Contacts in Pure Sliding, Ph.D. Dissertation, University of Michigan, Dec. 1969 and University Microfilms, Inc., Ann Arbor, Michigan.

18. Jakobsen , J., Lubricant Rheology at High Shear Stress, Ph.D. Dissertation, Georgia Institute of Technology, 1973 (to be completed).

19. Peppler, W., "Druckubertragung an Geschmieter Zylindrischen Gleit - und Walzflachen," VDI - Forschungsheft 391 (1938), VDI-Verlag A.M.B.H., Berlin, pp. 1-24.

20. Cameron, A., "Hydrodynamic Theory in Gear Lubrication", Journal of The Institute of Petroleum," J. 38 (1952), pp. 614-622.

21. Casale, A., Porter, R. S., and Johnson, J. F., "The Mechano-chemistry of High Polymers," Rubber Chemistry and Technology, 44, April 1971.

22. Wright, W. A., and Johnson, R. H., "Rheological Properties of Automatic Transmission Fluid", SAE Paper, May 1968

23. West, J. P. and Selby, T. W., "The Effect of Engine Operation on the Viscometric Properties of Multigraded Engine Oils", May 1965, SAE Paper No. 650445.

APPENDIX A

DESCRIPTION OF FLUIDS

The table summarizes the investigated fluids and gives characteristic data for each fluid.

Experimental Fluids

Diester-Plexol 201 bis-2-ethyl hexyl sebacate

Dimethyl Siloxane DC-200-50

Polyalkyl Aromatic plus additive

Synthetic Paraffinic Hydrocarbon plus antiwear additive

Paraffinic Base Oil R-620-12 plus 11.5% Polyalkylmethacrylate (MW = $.2 \times 10^6$).

Characterization

Diester

Source - Rohm and Haas Company

Data supplied with the sample

Viscosity at 210°F	3.32 cs
Viscosity at 100°F	12.75 cs
Viscosity at -65°F	7988 cs
Viscosity Index (D-2270)	150
Neutralization number (D-974)	0.02
Cloud Point (D-2500)°F	below -65

Data transferred from literature sources

Heat conductivity at	100°F	.087 Btu/h ft °F
	37.8°C	
		.0188 lbf/°F sec
		.0154 kp/°C sec
Specific Heat per unit mass		0.46 Btu/lbm °F
	at 100°F	0.46 cal/gramm °C
	37.8°C	4295 lbf in/lbm °F
Density at	77°F	.0328 lbm/in^3
	25°C	
		.91 gramm/cm^3
Specific Heat per unit volume		.01303 Btu/°F in^3
		.416 cal/°C cm^3
		139.5 lbf/in^2 °F
Heat diffusivity		1.35×10^{-4} in^2/sec
		8.69×10^{-4} cm^2/sec

Data measured

Kinematic viscosity at	at	100°F	12.65 cs
		37.8°C	
	at	210°F	3.33 cs
		98.9°C	
	at	300°F	1.775 cs
		148.9°C	
Density	at	100°F	.903 gramm/cm^3
		37.8°C	

	at 210°F 98.9°C	.86 gramm/cm^3
	at 300°F 148.9°C	.825 gramm/cm^3
Viscosity	at 100°F 37.8°C	11.41 cp
	at 210°F 98.9°C	2.86 cp
	at 300°F 148.9°C	1.46 cp
	at 32°F 0°C	57.5 cp
	at 10°F -12.2°C	130 cp
Pressure viscosity Coefficient (Roelands)	at 32°F 0°C	Z = .51

Elastohydrodynamic film thickness and traction data taken at 15 lbf load (150 kpsi peak Hertzian pressure) 1 1/4 inch diameter steel ball loaded against a sapphire anvil

Sliding speed	13.7 ips	27.4 ips	54.8 ips	92.1 ips
h_c (μ-inch)	.4	.8	2.1	3.3
h_m (μ-inch)	.4	.8	1.3	1.3
TC	.046	.032	-	.025

Dimethyl Siloxane DC-200-50

Source Dow Corning Corporation, Midland, Michigan,

Data supplied with the sample

Degree of polymerization 43

Data measured

Viscosity	at 77°F	25°C	50 cs	48 cp
	at 100°F	37.8°C	41.5 cs	39.1 cp
	at 210°F	98.9°C	17 cs	15.7 cp
	at 300°F	148.9°C	8.6 cs	7.3 cp
Density	at 77°F	25°C	.954 gramm/cm^3	
	at 100°F	37.8°C	.943 gramm/cm^3	
	at 210°F	98.9°C	.894 gramm/cm^3	
	at 300°F	148.9°C	.850 gramm/cm^3	

Pressure viscosity characteristics

			α_{OT} psi^{-1}	α^* psi^{-1}	Z
at	75°F	23.9°C	1.28×10^{-4}	$.98 \times 10^{-4}$	.52
at	100°F	37.8°C	1.36×10^{-4}	$.96 \times 10^{-6}$	.51
at	210°F	98.9°C	1.53×10^{-6}	$.96 \times 10^{-4}$	.44
at	300°F	148.9°C	1.53×10^{-4}	$.96 \times 10^{-6}$	.43

Roelands temperature viscosity slope index

S = .55 re atmospheric pressure.

Elastohydrodynamic film thickness and traction.

Data taken at 15 lbf load (150 kpsi peak Hertzian pressure)

1 1/4 inch diameter steel ball loaded against a sapphire anvil.

Sliding speed	13.7 ips	27.4 ips
h_c(μ-inch)	2	3
h_m(μ-inch)	1	2
TC	.069	.061

Polyalkyl Aromatic plus additive.

Source NASA Lewis Research Center, Cleveland, Ohio.

Data supplied with the sample

Kinematic viscosity	at 100°F	37.6 cs
	at 210°F	6.1 cs

Data measured (40)

	100°F	210°F	300°F
	37.8°C	98.9°C	148.9°C
Viscosity cp (p = atm)	32.2	5.0	2.1
α_{OT} psi^{-1}	1.41×10^{-4}	1.39×10^{-4}	-
α^* psi^{-1}	1.17×10^{-4}	$.88 \times 10^{-4}$	-

Elastohydrodynamic film thickness and traction

Data taken at 15 lbf load (150 kpsi peak Hertzian pressure)

1 1/4 inch diameter steel ball loaded against a sapphire anvil.

Sliding speed	13.7 ips	27.4 ips	54.8 ips
h_c (μ-inch)	3	4	8
h_m (μ-inch)	2	2	4
TC	.055	.048	.042

Synthetic Paraffinic Hydrocarbon (XRM 109 F4)

Source NASA Lewis Research Center, Cleveland, Ohio.

Data measured

	100°F	210°F	300°F
	37.8°C	98.9°C	148.9°C
Viscosity cp	376	31.6	10.2
α_{OT} psi^{-1}	1.52×10^{-4}	1.37×10^{-4}	1.11×10^{-4}
α^* psi^{-1}	1.37×10^{-4}	1.04×10^{-4}	$.89 \times 10^{-4}$
Z	.44	.46	.47

Synthetic Paraffinic Hydrocarbon plus Antiwear Additive (XRM 177 F-4)

Source NASA Lewis Research Center, Cleveland, Ohio

Data measured

	100°F	210°F	300°F
	378°C	98.9°C	148.9°C
Viscosity cp	37.6	31.6	10.2
α_{OT} psi^{-1}	1.52×10^{-4}	1.37×10^{-4}	1.11×10^{-4}
α^*	1.35×10^{-4}	1.07×10^{-4}	$.86 \times 10^{-4}$
Z	.44	.46	.46

Fluid XRM 177 F4 is of the same composition as the previous investigated fluid D. The base fluid is however not from the same lot.

Elastohydrodynamic film thickness and traction for fluid D. Data taken at 15 lbf load (150 kpsi peak Hertzian pressure) 1 1/4 inch diameter steel ball loaded against a sapphire anvil

Sliding speed	13.7 ips	27.4 ips	54.8 ips
h_c(μ-inch)	15	23	30
h_m(μ-inch)	7	13	19
TC	.058	.045	.035

Paraffinic Base Oil R-620-12 plus 11.5% Polyalkylmethacrylate (MW = $2.\times10^6$).

Data supplied with the sample

Base oil R-620-12

Source: Sun Oil Company

Viscosity 33.33 cs at 100°F (37.8°C) 5.336cs at 210°F (98.9°C)

SUS/100 156.2 SUS/210 43.74

Viscosity index (ASTM D-2270)	102
Flash point	410°F
Fire point	470°F
Pour point	5°F
Refractive index	1.4754
Density gramm/cm^3	.8596
Molecular weight (MW)	401 *

Polyalkylmethacrylate PL 4523. (PAMA)

Source Rohm and Haas Company

The polymer was in solution with a paraffinic base oil, a 150 neutral carrier oil similar to the base oil R-620-12. Their chemical composition are alike. They differ only in their molecular weight. The solution contains 19% polymer. It has a kinematic viscosity of 773 cs re 210°F (98.9°C). The molecular weight is 4.51×10^6 as measured with a permeation chromatography method, GPCM. An estimated molecular weight of $2. \times 10^6$ is however found by extrapolating from viscosity and molecular weight data for lower MW polyalkylmethacrylates, MW = 1.28×10^6, $.828 \times 10^6$ and $.5 \times 10^6$. It is believed that the GPP technique is not suitable for materials with high molecular weights. The molecular weight of $2. \times 10^6$ determined with viscosity measurements are therefore adhered to. The amount polymer reported, 11.5% is the volume concentration in the final solution.

*Calculated from viscosity data using the method of A. E. Hirschler, J. Inst. Petroleum, 32, 133-61, 1946.

Data measured

	100°F	210°F	300°F
R-620-12	37.8°C	98.9°F	148.9°C
Viscosity (cp)	29.2	4.5	1.9
Density (gramm/cm^3)	.849	.809	.777

Appendix B

An estimate of the equivalent length of a cone can be arrived at as follows:

In a capillary $\Delta p = \phi(\eta 128/\pi)\ (L/D^4) = (K/D^4)L$

and $d(\Delta p) = (K/D^4)dL$

where ϕ is the volume flow per sec, then

$$\Delta p_{cone} = \int_{p_{D_o}}^{p_\infty} d(\Delta p) = (K/2tg\Psi)\int_{D_o}^{\infty} D^{-4}dD = (K/D_o^{-4})\ (D_o/tg\Psi)$$

in that

$$dD_o = 2tg\Psi dL$$

For $\Psi = 45°$ the equivalent length of the cone is 0.167 D_o

APPENDIX C

The Effect of Ball Radiation Change on Film Temperature

The energy dissipation rate in the EHD contact can be determined from film thickness and traction measurements previously obtained (12,13). For the most severe conditions imposed in this investigation (1.39 m/s velocity and 67N normal load) the traction force was observed to be 4.7N. This results in an energy input rate (fU) of 6.53 watts.

From radiation measurements made with each of the two balls, the change in ball radiation is of the order 10^2 watts/ m^2-steradian for a 3.6×10^{-5}m diameter spot size. For radiation to one hemisphere (2π steradians) and for an EHD contact diameter of 3.6×10^{-4}m, the radiation heat transfer rate is of the order 10^{-5} watts. Therefore, the heat transfer through the film due to ball radiation is negligible compared to the 6.53 watts dissipation rate. The effect of different ball surface emissivity on film temperature should therefore be negligible.

APPENDIX D

Relative Contribution of Sapphire Radiation

As an order of magnitude approximation it has been assumed that the upper sapphire surface is at ambient temperature (25 ^{o}C) and that the lower surface is at a temperature equal to that of the average fluid temperature (115 ^{o}C). These temperatures correspond to black body areal radiant intensity values of 37 and 400 watts/m^2 - ster respectively. This data represents the maximum temperature condition on the contact centerline. The radiation characteristic of the sapphire should be less than the average of the surface radiation values, due to the fourth power relation between temperature and areal radiant intensity. For an average black body areal radiant intensity of 220 watts/m^2 - ster and a sapphire emissivity of 0.018, the sapphire areal radiant intensity becomes 4 watts/m^2 - ster, which is 2% of the black body ball radiation shown in equation (16). The 2% maximum error resulting from omitting the contribution from the sapphire will result in an error in ball temperature of less than 2 ^{o}C.

E-25-620

APR

GEORGIA INSTITUTE OF TECHNOLOGY
School of Mechanical Engineering
Atlanta, Georgia

Investigations of Lubricant Rheology as Applied to Elastohydrodynamic Lubrication

NASA GRANT No.
11-002-133

by:

S. Carlson
J. Jakobsen
H. S. Nagaraj
M. A. Molina - C.
Graduate Students
D. M. Sanborn, Assistant Professor
W. O. Winer, Professor
Co-Principal Investigators

For

NASA-LEWIS RESEARCH CENTER
21000 Brookpark Road
Cleveland, Ohio 44135

September, 1974

GEORGIA INSTITUTE OF TECHNOLOGY
School of Mechanical Engineering
Atlanta, Georgia

INVESTIGATIONS OF LUBRICANT RHEOLOGY AS APPLIED TO ELASTOHYDRODYNAMIC LUBRICATION

Ward O. Winer
Principal Investigator

David M. Sanborn
Principal Investigator

Stothe P. Kezios, Director
School of Mechanical Engineering

September, 1974

1. Report No. NASA CR-134730	2. Government Accession No.	3. Recipient's Catalog No.
4. Title and Subtitle INVESTIGATIONS OF LUBRICANT RHEOLOGY AS APPLIED TO ELASTOHYDRODYNAMIC LUBRICATION		5. Report Date September, 1974 6. Performing Organization Code
7. Author(s) D. M. Sanborn, W. O. Winer, et al.		8. Performing Organization Report No. 10. Work Unit No.
9. Performing Organization Name and Address School of Mechanical Engineering Georgia Institute of Technology Atlanta, Georgia 30332		11. Contract or Grant No. NGR11-002-133 13. Type of Report and Period Covered Contractor Report
12. Sponsoring Agency Name and Address National Aeronautics and Space Administration Washington, D. C. 20546		14. Sponsoring Agency Code

15. Supplementary Notes

Project Manager, William R. Jones, Jr., Fluid System Components Division
NASA Lewis Research Center, Cleveland, Ohio

16. Abstract

This is the annual progress report for NASA Grant No. 11-002-133. The research under this grant consists of high pressure-high shear stress studies of lubricant rheology, and elastohydrodynamic lubrication (EHD) simulation, analysis and application studies intended to gain understanding of lubricant rheology in EHD lubrication. An analysis of the high pressure-high shear stress flow of lubricants in short capillaries has been completed and shows the predominant phenomena causing a reduction in apparent viscosity to be viscous heating. The infrared technique for measuring temperatures in an EHD contact has been further developed and ball surface and fluid temperatures are reported for sliding speeds of 0.35 to 12.7 m/s at 1 GN/m^2 maximum pressure. An analysis of the thermal phenomena in a sliding EHD contact is presented. An analysis of lubrication of rolling and sliding cylinders with a general viscous fluid having a range of pressure viscosity coefficients is presented for the transition region from rigid to elastic cylinders. An analysis is also presented in which the dynamics of roller bearings subject to EHD forces is investigated.

17. Key Words (Suggested by Author(s)) Elastohydrodynamic Lubrication Pressure Viscosity Measurements Liquid Lubricants Lubricant Rheology	18. Distribution Statement Unclassified - unlimited

19. Security Classif. (of this report) Unclassified	20. Security Classif. (of this page) Unclassified	21. No. of Pages 95	22. Price*

TABLE OF CONTENTS

TABLE OF CONTENTS (cont'd)

ABSTRACT

This is the annual progress report for NASA Grant No. 11-002-133. The research under this grant consists of high pressure-high shear stress studies of lubricant rheology, and elastohydrodynamic lubrication (EHD) simulation, analysis and application studies intended to gain understanding of lubricant rheology in EHD lubrication. An analysis of the high pressure-high shear stress flow of lubricants in short capillaries has been completed and shows the predominant phenomena causing a reduction in apparent viscosity to be viscous heating. The infrared technique for measuring temperatures in an EHD contact has been further developed and ball surface and fluid temperatures are reported for sliding speeds of 0.35 to 12.7 m/s at 1 GN/m^2 maximum pressure. An analysis of the thermal phenomena in a sliding EHD contact is presented. An analysis of lubrication of rolling and sliding cylinders with a general viscous fluid having a range of pressure viscosity coefficients is presented for the transition region from rigid to elastic cylinders. An analysis is also presented in which the dynamics of roller bearings subject to EHD forces is investigated.

I. Summary

During the past year research in the areas listed below has progressed and is reported herein:

High Pressure High Shear Stress Viscometry:

An analysis has been undertaken to predict and help understand the high pressure-high shear stress data reported in the previous project report (1). It was found that the predominant phenomena involved in the high shear stress measurements was the result of viscous heating and not non-Newtonian behavior of the lubricants studied. This conclusion appears to be valid to shear stresses to within a factor of three of those occuring in a typical sliding elastohydrodynamic contact and to include those occuring in a typical rolling contact. The significance of these results for pressure viscometry of lubricants is that the shear stress at which the measurement is made is not important provided it is in the second Newtonian region for polymer solutions and is not in a region high enough to cause viscous heating for the particular capillary/fluid combination. The most significant measurements are of the viscosity variation with pressure and temperature.

Elastohydrodynamic Simulation and Analysis:

a. Infrared Temperature Measurements: The equipment modifications to insure more reliable data have been completed and preliminary data are reported. The system modifications include the use of a two filter arrangement on the infrared detector optics. Each filter permits a specific bandwidth of infrared radiation to pass on to the detector. One filter covers a bandwidth in which the fluid is transparent and does not

emit, hence, with this filter in place the steel surface temperature is reliably determined. The second filter covers the C-H emission band of the test lubricant and, upon calibration of the system to include the effect of temperature and lubricant film thickness on emissivity, permits the reliable determination of the oil film temperature. The system has also been modified to permit control of the bath oil temperature over long periods of time. With these modifications ball surface and fluid temperatures over the elastohydrodynamic contact have been mapped at a Hertz pressure of 1 GN/m^2 (150,000 psi), six sliding speeds ranging from 0.35 to 12.7 m/s (13.7 to 500 ips), and a bath temperature of 40C. The maximum fluid temperature in the contact remains substantially constant ($\pm$ 12C) while the ball surface temperature increases with speed from 75C at 0.3 m/s to 133C at 5 m/s and then is constant at 133C to 12.7 m/s.

b. Elastohydrodynamic Thermal Shearing Analysis: An analysis of the thermal behavior of a sliding elastohydrodynamic contact employing a simplified model has been completed. The formulation and solution for the shear stress and temperature in heavily loaded sliding elastohydrodynamic contacts are presented. The results are given in dimensionless design charts. Integration over the contact area will yield the traction. Accuracy is expected to be very good over the nearly flat part of the contact area where the majority of the sliding traction is generated. The procedure presented is not appropriate for thick film hydrodynamic lubrication, for the inlet region, or for the rolling friction of elasto-hydrodynamic contacts.

c. Elastohydrodynamic Analysis of Rolling and Sliding Cylinders with a General Viscous Fluid: During the past year, effort has been directed to successfully obtaining solutions in the transition region from rigid to elastic heavily loaded cylinders for a range of pressure viscosity coefficients from 0 to 1.4×10^{-8} m^2/N. In the higher pressure-viscosity coefficient range this work was hampered by what was later discovered to be a region where the central film thickness actually increases with increasing load because of the initial elastic deformation process. This may explain why in the past other workers have failed to obtain solutions in this transition region. In the highly loaded regions a well defined pressure spike was obtained even though the solution technique is different from those employed by others and a uniform solution technique is employed over the entire contact region and range of operating parameters.

Dynamics of Roller Bearings Considering Elastohydrodynamic Forces: An analytical investigation has been completed which models the behavior of a roller bearing considering elastohydrodynamic forces on the rollers. A computational model was developed to predict traction forces, forces on the cage and sliding and spinning speeds of the rollers. The model accounts for operating conditions including centrifugal forces on the rollers, roller-cage friction, cage drag and race elasticity. Results given by the model for a 65mm roller bearing lubricated with XRM-109 predict that for a given set of conditions, if the shaft speed is continuously increased, the cage speed increases to a maximum and then decreases.

II. High Pressure High Shear Viscometry

In the last status report (1) high pressure, high shear stress measurements on five lubricants were reported. Measurements were reported to shear stresses of 5×10^6 N/m^2 which cover the shear stress range occuring in most rolling elastohydrodynamic contacts and is within a factor of three of the average shear stress in most sliding elasto-hydrodynamic contacts. The five fluids for which measurements were reported were: 1) diester (Di-2-ethyl hexyl sebacate), 2) polyalkyl aromatic plus additive, 3) synthetic paraffinic hydrocarbon plus anti-wear additive, 4) dimethyl siloxane (50 cs), 5) paraffinic mineral oil plus 11.5% polyalkylmethacrylate polymer (MW = 2.0×10^6). The first three exhibited very similar behavior which is believed explainable in terms of viscous heating at the high shear rates. The following analysis was undertaken to substantiate this belief and to more clearly understand capillary flow at high shear stresses.

The viscous flow of a fluid through a capillary tube generates a temperature increase, due to the dissipation heating, and a corresponding viscosity decrease of the fluid. The shear stress and the shear rate both reach their greatest value at the wall and are zero at the axis. The heat generation, which is the product of the shear stress and the shear rate, is greatest at the wall of the capillary tube and zero at the axis. The temperature after the inlet will therefore remain low at the axis and increase in radial direction with increasing distance from the axis until the cooling effect of the wall is noticeable. The temperature near the wall will remain low due to the relatively high heat

conductivity of the wall material compared with the conductivity of the fluid. The temperature profiles are axisymmetric assuming a uniform inlet temperature. The radial temperature distribution immediately after the inlet is thus characterized by an annular maximum near the wall and low temperatures at the center and the wall of the capillary tube. The temperature at the axis increases slowly in the downstream direction due to radial heat conduction towards the axis of the capillary tube. The radius of the annular maximum decreases with increasing distance from the inlet.

The viscous flow of a fluid into a cylindrical capillary tube from a reservoir also has associated with it a pressure drop originating from the velocity gradients in the contraction of streamlines before the inlet. The pressure drop ahead of the inlet is independent of the length of the capillary tube. The flow from the exit of the cylindrical capillary tube to a receiving reservoir generates an additional pressure drop. The stream lines of the exit flow will at sufficiently low Reynolds number be expected to assume a configuration equal to the configuration of the streamline of the inlet flow because the stream function, at $R_e = 0$, and the boundary conditions are symmetric with respect to the axial coordinate. The pressure drop at the exit and at the inlet are therefore identical under such conditions. The sum of the pressure drop outside the capillary tube cavity must be subtracted from the measured, total pressure change in order to calculate a correct stress in the fluid. The correction is often carried out as a number added to the geometrically determined ratio of capillary tube length and diameter. The magnitude of the correction may be found experimentally. The inlet and exit pressure drop generate temperature increases and corresponding

viscosity decreases of the fluid due to dissipation heating.

High shear rate capillary viscometry has been the subject of several studies (cf. 2,3-8). The effect of temperature increase and resulting viscosity decrease have been studied by several authors (3,4-9). However, they have not focused on the possible reduction of those effects and the consequent increasing of the upper limit of shear stress that can be attained in capillary viscometry.

The purpose of this presentation is twofold. It is an attempt to establish criteria to distinguish dissipative heating effects from effects of non-Newtonian properties in capillary tube measurements. It is also to indicate the possibility of attaining in capillary tube viscometry, fluid shear stresses approaching the average shear level experienced in an elastohydrodynamic film. The pressure level and temperature level are principally independent of the imposed shear stress in such an experiment and the time duration of shear load on a fluid particle is of the same order of magnitude as the contact time for the moving surfaces of an elastohydrodynamic contact. Rheological investigations of lubricant properties may thus be performed under simulated elastohydrodynamic conditions and under terms of mutual independency among the most important parameters;pressure, temperature and shear stress.

Problem Formulation: Flow in the Capillary Tube.

In a capillary tube experiment the volume flow rate and the pressure drop are the measurable quantities. The experiment can be designed such that the Reynolds number for the flow is sufficiently small that the entrance length, calculated according to the method of Schiller (10), can be neglected in comparison to the capillary length even for very short capillaries. The flow rate for a given pressure drop is dependent on the

temperature distribution within the flow which in turn is dependent on the shear stress resulting from the applied pressure drop.

The following analysis is to determine the temperature distribution and the resulting effect on the flow rate for a given pressure drop across the capillary. The analysis assumes the flow is fully developed throughout the capillary and therefore inertia effects are neglected. The flow is steady, laminar, and axisymmetric with the velocity zero at the wall and a function of radius only. The pressure is a linear function of the axial distance in the tube and the density, specific heat and thermal conductivity are assumed to be constant. Energy transport by axial convection and radial conduction only are considered. As will be seen axial convection is the most important mode of energy transport with radial conduction important primarily near the tube wall. Axial conduction is small compared to convection and is also small compared to radial conduction unless $(L/D)^2 \leq 1$ and even then the convection term is more important than either radial or axial conduction. The fluid temperature is a function of radial and axial dimensions and is a constant, T_o, at the inlet and at the tube walls. The geometry is shown in Figure II-1.

Under the above conditions the equation of mass continuity is satisfied identically and the equations of motion reduce to

$$r \frac{\partial p}{\partial z} = \frac{\partial}{\partial r} \left(\eta r \frac{\partial u_z}{\partial r}\right) \qquad \text{(II-1)}^*$$

The energy equation reduces to

$$\rho c u_z \frac{\partial T}{\partial z} = k\left[\frac{\partial^2 r}{\partial r^2} + \frac{1}{r} \frac{\partial T}{\partial r}\right] + \eta\left[\frac{\partial u_z}{\partial r}\right]^2 \qquad \text{(II-2)}$$

* The nomenclature for this section is listed in Table II-1 at the end of the section.

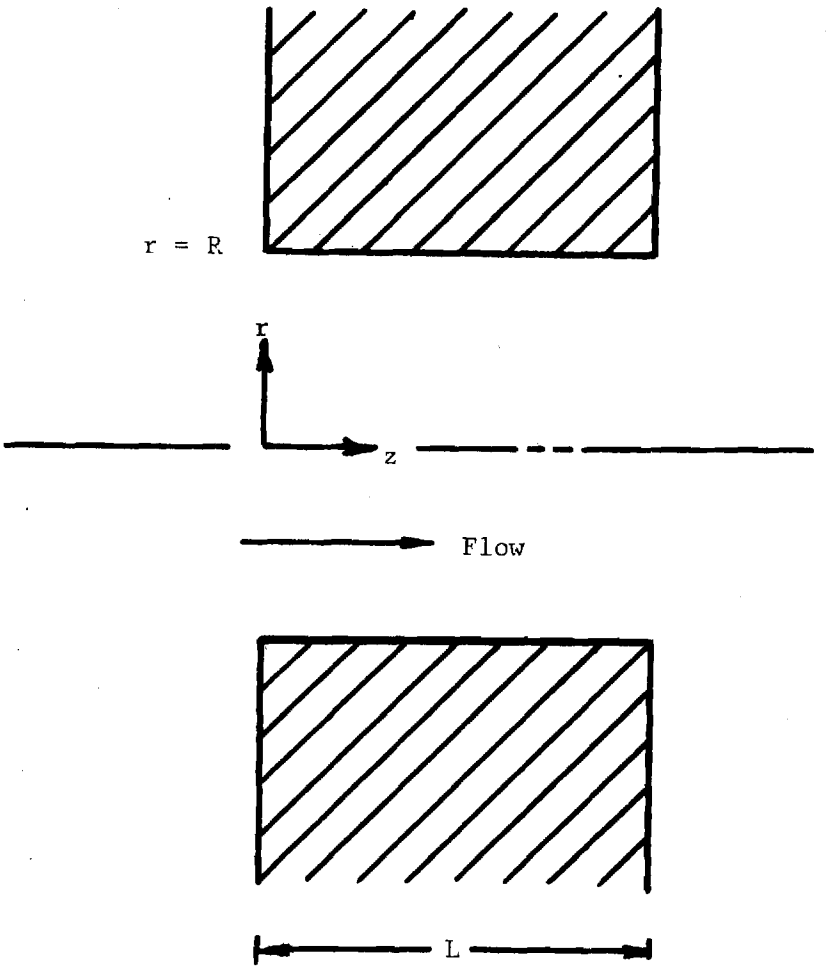

Figure II-1 Flow Geometry of a Viscous Lubricant through a Cylindrical Capillary.

Because $\frac{\partial p}{\partial z}$ is not a function of r, the velocity gradient $\frac{\partial u_z}{\partial r}$ is zero at the center (r = 0), and equation (II-1) is integrated to give

$$\frac{\partial u_z}{\partial r} = \frac{r}{2\eta} \frac{\partial p}{\partial z}$$

and

$$u_z = \frac{r^2 - R^2}{4\eta} \frac{\partial p}{\partial z}$$

which can be substituted into equation (II-2) to give

$$\rho c \frac{r^2 - R^2}{4\eta} \frac{\partial p}{\partial z} \frac{\partial T}{\partial z} = k\left[\frac{\partial^2 T}{\partial r^2} + \frac{1}{r} \frac{\partial T}{\partial r}\right] + \frac{r^2}{4\eta} \left(\frac{\partial p}{\partial z}\right)^2 \qquad \text{(II-3)}$$

The boundary conditions for Equation (II-3), the energy equation, are

$$T(r,0) - T_o, \quad T(R,z) = T_o \qquad \text{(II-4)}$$

$$\frac{\partial T}{\partial r}(0,z) = 0$$

that is the temperature at the inlet and walls remains constant and the symmetry condition on the temperature at the center.

Equations (II-3) and (II-4) can be non-dimensionalized to be

$$\hat{q} \frac{\partial \theta}{\partial \omega}(1 - \bar{\rho}^2) = \frac{\partial^2 \theta}{\partial \bar{\rho}^2} + \left(\frac{1}{\bar{\rho}}\right) \frac{\partial \theta}{\partial \bar{\rho}} + \hat{q}\bar{\rho}^2 \frac{\partial \hat{p}}{\partial \omega} \qquad \text{(II-5)}$$

and

$$\theta(\bar{\rho},0) = \theta_o, \quad \theta(1,\omega) = \theta_o, \quad \frac{\partial \theta}{\partial \bar{\rho}}(o,\omega) = 0 \qquad \text{(II-6)}$$

where

$$\bar{\rho} \equiv \frac{r}{R}, \quad \theta = \frac{T}{E}, \quad \omega = \frac{z}{L}$$

and

$$\hat{p} \equiv \frac{-p}{c\rho E}, \quad \hat{q} \equiv + \frac{(c\rho)^2 E R^4}{4L^2 \eta k} \frac{\partial \hat{p}}{\partial \omega}.$$

The temperature is normalized with respect to the material parameter E (the absolute temperature at which the fluid viscosity is 2.718×10^{-3} Nsm^{-2}) because this permits a convenient method for expressing the fluid viscosity over a range of temperatures. This should become more apparent in Section IV of this report where a method is presented for determining the value of E for a given fluid.

Solution Technique

First, the temperature distribution in the capillary tube due to dissipation is estimated for the case of axial convection and constant viscosity but no radial conduction. The deviation of the flow curves will be evaluated assuming the estimated temperature distribution but using a temperature dependent viscosity function in the calculations of flow rates.

The procedure is then repeated incorporating radial conduction. The temperature distribution is estimated assuming axial convection, radial conduction and constant viscosity. The flow curves are then evaluated using the estimated temperatures but assuming temperature dependent viscosity in the calculations of flow rates.

No Heat Conduction

The special case of no heat conduction in the fluid, is of interest because it gives an approximate description of the expected temperature profiles immediately after the inlet. This case also gives a particularly good description of the temperatures of the fluid following streamlines near the capillary axis. When heat conduction is absent equations (II-5,6) reduce to:

$$\frac{\partial \theta}{\partial \omega} = \frac{\bar{\rho}^2}{(1-\bar{\rho}^2)} \frac{\partial \hat{p}}{\partial \omega} \qquad \text{(II-7)}$$

$$\theta(\bar{\rho},0) = \theta_o$$

Because the right hand side of II-7 is not a function of ω, this is readily integrated to give the solution

$$\theta - \theta_o = (\bar{\rho}^2/(1 - \bar{\rho}^2))(\frac{\partial p}{\partial \omega})\ \omega \qquad \text{(II-8)}$$

Because conduction was neglected, the order of the equation is reduced and the boundary condition of fixed wall temperature can not be satisfied.

The temperature in the capillary tube increases linearly with the axial coordinate when no conduction occurs. The temperature is constant along the axis and increases without bound when $\bar{\rho} = 1$. The temperature profiles as a function of the relative radius are shown in Figure II-2. The temperatures depend only on the pressure drop over the length L, the specific heat per unit volume and on the location in the capillary. Fluid viscosity, shear rate or capillary tube diameter do not enter in to the determination of the temperatures. For a typical pressure drop of 3.45 MN/m^2 over the length L with a lubricant of 1.74 MN/m^2K specific heat per unit volume ($C\rho$), equation (II-8) gives the temperature rise profile at the exit:

$$T - T_o \simeq 2.0\ (\bar{\rho}^2/(1 - \bar{\rho}^2))\ K \qquad \text{(II-9)}$$

A temperature dependent viscosity can be introduced in order to estimate the character of the flow curves. The increase in volume flow, and thereby the decrease in apparent viscosity, due to heat dissipation, can be evaluated. Shear rates and fluid velocities can be determined when

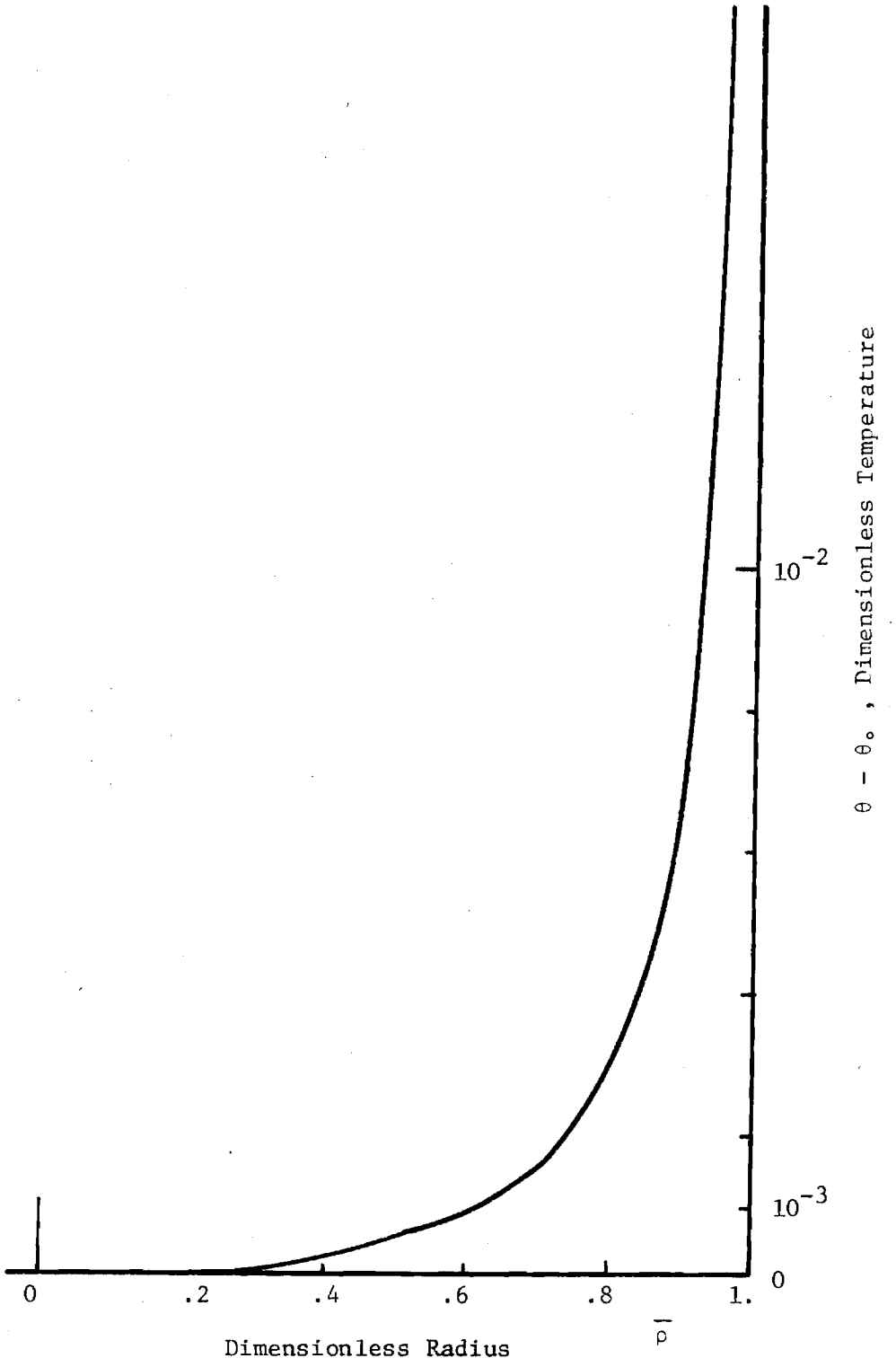

Figure II-2

Temperature Distribution in Capillary Tubes for the Case:
No Heat Conduction in the Fluid. (ω=1, Δp=3.45 MN/m^2, Cp=1.74 MN/m^{2}K, E=1366K).

the temperatures as described by equation (II-8) are assumed. An increased flow rate can then be found from integration of the velocities. The decrease in apparent viscosity can be found by the ratio between pressure drop and increased flow rate. The assumption of an unchanged temperature profile represents an approximation which can be justified only within a certain interval of applied pressure drop. It is shown in the following that the flow curves will be congruent in the range of interest of the experimental parameters when capillary tube configuration, viscosity level and fluid type are varied. The velocity profile determined by assuming the temperatures of equation (II-8) and an arbitrary temperature viscosity relation does not depend on capillary tube dimensions or materials. The relative increase in flow rate of the same fluid through different capillary tubes will therefore depend on the pressure drop alone over the capillary tubes. The measured apparent viscosity, which is proportional to the ratio of pressure drop and volume flow rate, plotted as a function of shear stress, will consequently have the same configuration in a logarithmic presentation but will be displaced in the direction of the shear stress axis according to the actual length over diameter ratio for the capillary tube in question.

The temperature profiles are independent also of the viscosity of the fluid, as seen in equation (II-8). Distortion of the velocity profiles from the parabolic form, change in volume flow rate and the change in measured apparent viscosity are therefore also independent of viscosity level. The flow curves are thus of the same congruent form for different viscosity levels but are displaced through a translation along the viscosity axis alone. The flow curves for a fluid will thus have the same form independent of capillary tube dimensions and viscosity level of the

fluid.

In comparison between fluids, different material properties must be assumed. An exponential temperature viscosity relation is of sufficient generality to describe properly the viscosity behavior of fluids for temperature changes of the order of 5 - 10°K which is approximately the range of interest for the temperature increase. The linear relation between temperature increase and the ratio of pressure drop and specific volumetric heat capacity, equation (II-8), and the assumed exponential temperature viscosity dependency imply a constant ratio of pressure drop for two fluids when equal decreases in apparent viscosity are generated. Fluids with the smaller ratio of temperature viscosity coefficient and specific volumetric heat capacity will show the same temperature profile in the capillary cavity as fluids with greater ratios but at greater pressure drop. The flow curves for different fluids will therefore have congruent forms in logarithmic presentation but will be positioned along the shear stress axis in accordance with actual temperature viscosity coefficients and specific heats per unit volume.

The conformity of the flow curves can be expected over a greater range of temperature differences. The exponential power temperature viscosity relation

$$(\mu = e^{\theta^{-\pi}_{3}}) \Big|_{p} \qquad \text{(II-10)}$$

yields a more nearly accurate description of the viscosity behavior within a range of temperature change of 40 - 100°K for many fluids. The ratio of the local temperature increases for two fluids under comparison is approximately constant for relation (II-10), proportional with the ratio of the power exponents, in the range of interest of temperature increases

and pressure drop. The ratio of pressure drop necessary to produce equal changes in apparent viscosity for two fluids is therefore also approximately constant. The conformity of the flow curves can thus be expected over greater range of temperature changes than approximately $10^{o}K$.

The flow curves of apparent viscosity will be of identical form irrespective of the dimensions of the cylindrical capillary tube, the viscosity level of the fluid and the type of fluid in the range of interest when no heat conduction is present.

Flow with Radial Conduction.

It is clear from the above that radial conduction will be important especially near the wall. The general form on the flow curves will be modified to some extent when heat conduction is present. The temperature profiles can be achieved through solution of equation (II-5) with the collocation method. A series expansion of the form

$$\theta - \theta_o \simeq \omega \sum_{1}^{n} a_n (1 - \rho^{2n}) \quad n \text{ positive integer} \qquad \text{(II-11)}$$

has been selected to generate the approximate solution. This assumed expansion satisfies the boundary conditions, Equation (II-6). The number of terms, n, in the expansion function, Equation (II-11), must be equal to the number of collocation points selected. The method of solution is to substitute the expansion function, Equation (II-11), into the equation to be solved, Equation (II-5), and require that the constants, a_n, be selected such that Equation (II-5) is satisfied at each collocation point. The above substitution transforms Equation (II-5) into a linear algebraic equation with n unknowns (the a_n). Requiring this algebraic equation to be satisfied at eachof n collocation points for any axial position of interest, yields a set of n linear algebraic equations in n unknowns which can readily

be solved for the constants a_n.

Eight radially and variably positioned collocation points were employed at each axial location. That is, n = 8 and the expansion series, Equation (II-11) was an eight term approximation to the temperature profile. Temperature profiles for typical flow situations in a cylindrical capillary tube with a diameter of 88μm and a ratio of length and diameter of 1.35 are shown in Figure II-3, and E = 1366 K, ρc = 1.74 MN/m^2K, k = 0.118 $\frac{N}{sK}$. The viscosity of the fluid is 3 Ns/m^2. The maximum temperatures are found at $\bar{\rho} \simeq .9$. The magnitude is 4.9 K at the exit for a pressure drop of 3.4 MN/m^2 over the capillary tube. This gives approximately 2.5 K average temperature increase and 5 - 10% decrease of viscosity. The total change in apparent viscosity will however be much smaller. The figure shows also the temperature profile at $\omega = .5$. The maximum temperature rise is $3.1^{o}K$ at $\bar{\rho} = .93$.

The selected series expansion (II-11) gives the expected trend, in the solutions obtained via collocation, of decreasing radius of the annular maximum when axial distance from the inlet increases. It can also be seen from the figure that the magnitude of the temperature peak is not proportional with axial position ω. This is in general true at all radial positions, for $\bar{\rho}$ greater than about .7, where heat conduction is not significant. Heat conduction is not significant in a center core $\bar{\rho} < \sim .7$, and temperature increases are seen to be proportional to axial displacement in this region. The figure shows also the temperature profile for a pressure drop of 6.7 MN/m^2 over the capillary. Temperatures in the center core region are doubled compared to the temperatures for a pressure drop of 3.4 MN/m^2. The temperature peak at Δp = 6.7 MN/m^2 is more pronounced with a maximum of approximately 12.7 K at $\bar{\rho} \sim .92$.

Figure II-4 shows the contribution from convection, conduction and

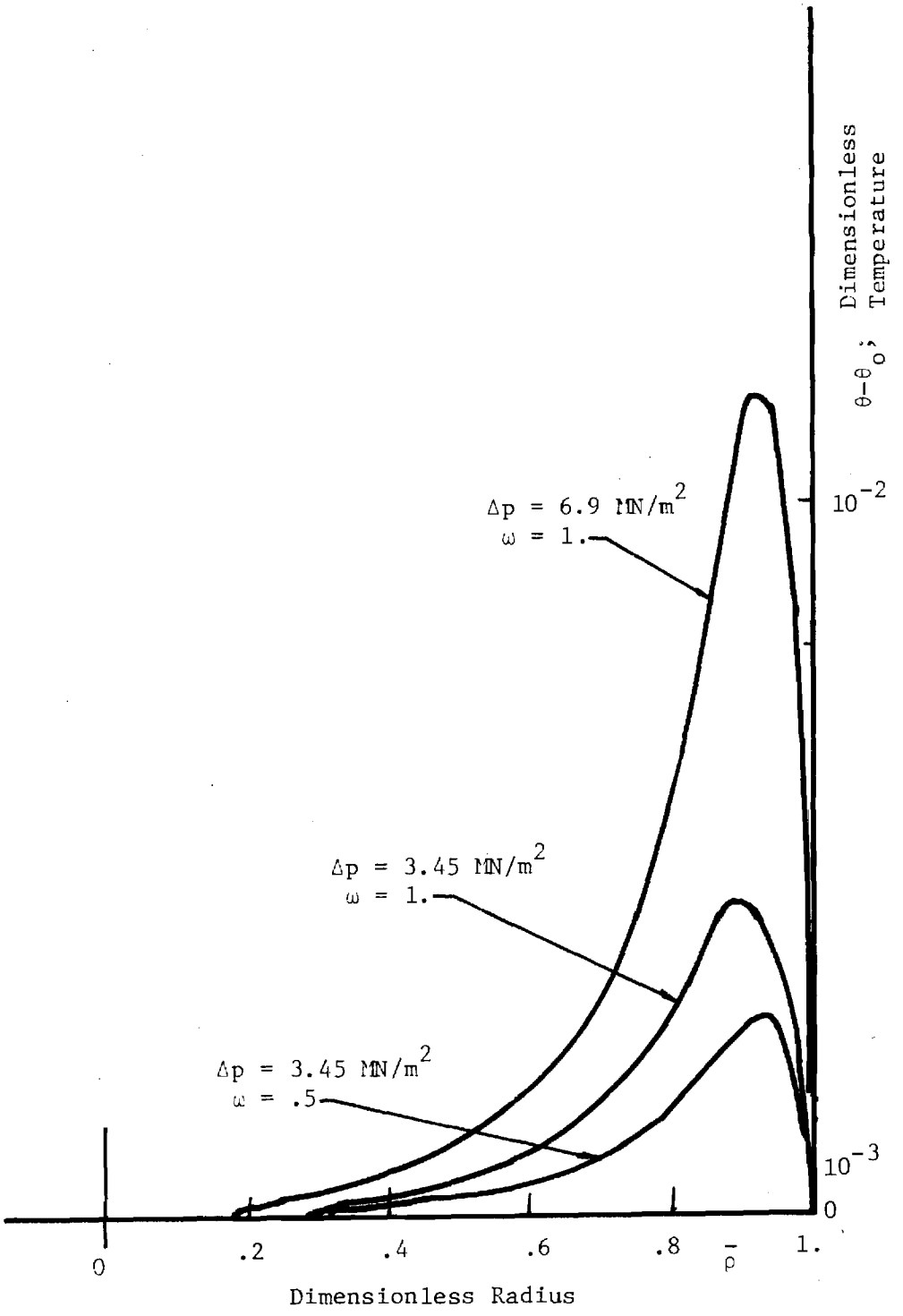

Figure II-3. Temperature Distribution in a Capillary Tube, Heat Conduction Present, (D = 88μm, L/D = 1.35, η = 3 NS/m^2, k = 0.118 $\frac{N}{sK}$, $C\rho$ = 1.74 MN/m^{2}K. E=1366K

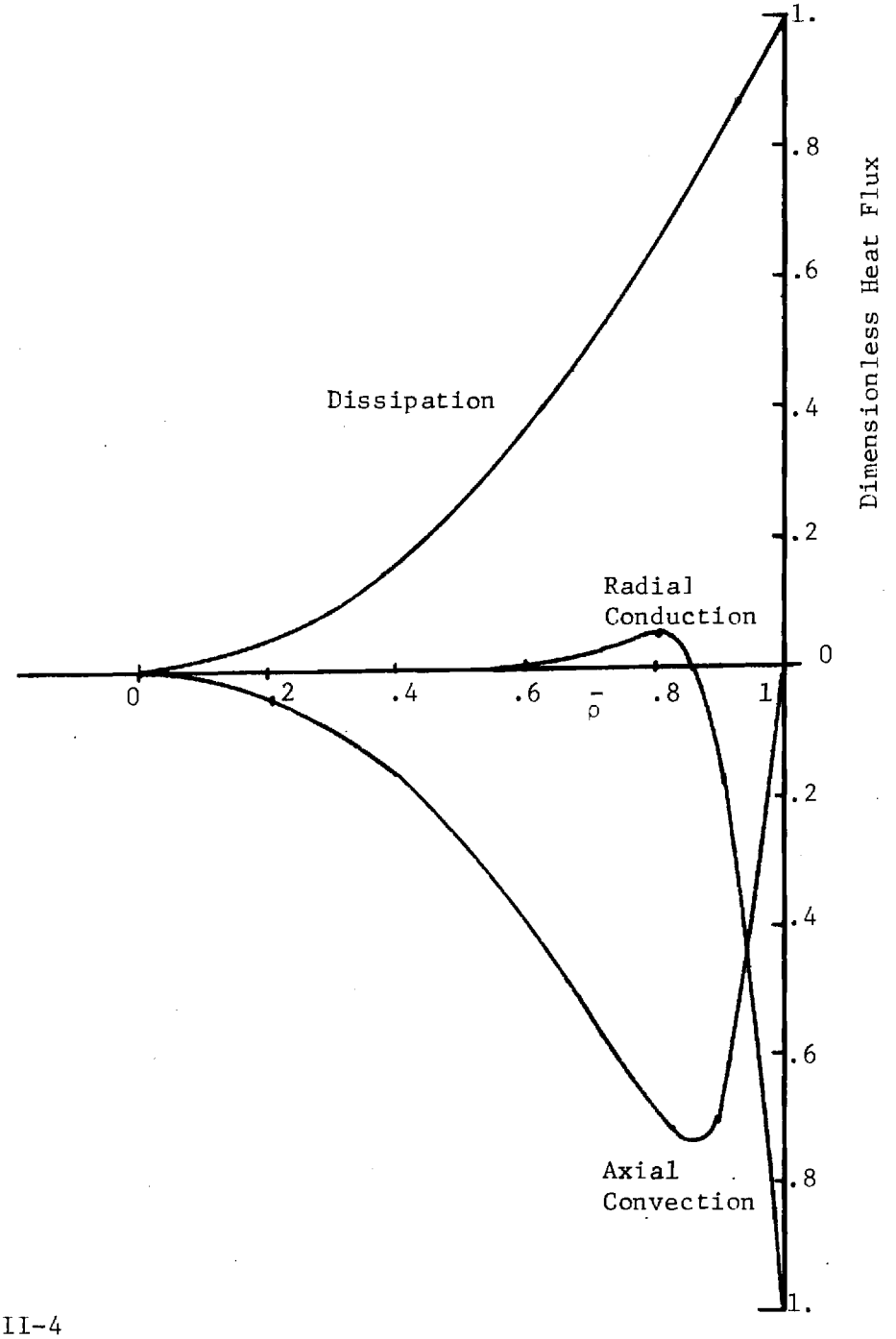

Figure II-4

Heat Balance. Contributions from Convection, Conduction and Dissipation. ($L/D=1.35$, $\omega=1$, $\eta=3$ NS/m^2, $k=0.118$ N/sK, $C\rho=1.74$MN/m^{2}K, $E=1366$ K, $\Delta p=6.9$ MN/m^2; quantities are non-dimensionalized with respect to the dissipation at $\bar{\rho}=1$).

dissipation from equation (II-5). The pressure drop is 6.7 MN/m^2. The profiles are calculated at $\omega = 1$. The dissipation profile is the same when $\omega = 0$ as for $\omega = 1$. The convection profile is a mirror picture about the $\bar{\rho}$-axis of the dissipation profile when $\omega = 0$. Convection removes therefore the total amount of generated heat when $\omega = 0$. The generated heat is seen to be removed primarily also by convection even at the exit, $\omega = 1$. Conduction, in the radial direction, sends an estimated 15% of the total dissipated energy to the capillary wall when $\omega = 1$. This happens in the region $\bar{\rho} > .86$. The total amount of heat conducted away to the walls can be estimated to be of the order of 7.5% for the total capillary length assuming as an approximation that the conduction contribution increases linearly with ω position. It is seen, at $\omega = 1$, that a small amount of heat is conducted inwards when $\bar{\rho} < .86$. The heat conducted away to the walls is a relatively small proportion of the total generated heat. The generality of the flow curves when heat conduction is absent will, therefore, expectedly transfer to the case when heat conduction is present with some slight modifications. The small amount of heat conducted away suggests also that the capillary measurements are relativelyinsensitive to the degree to which the desired condition of isothermal wall is satisfied.

The flow rate at $\omega = 1$ can be estimated under the assumption that the shear rate from the constant viscosity case is modified by exp ($\beta\Delta T$) where β is the temperature viscosity coefficient for an exponential viscosity dependency of the fluid temperature and ΔT is the temperature increase determined above. Expected flow curves of two model fluids similar to dimethyl siloxane and a synthetic paraffinic oil have been determined for capillary tubes of ratios of length and diameter of 14.9 and 1.35. Exponential temperature viscosity relations were assumed for both fluids with coefficients $\beta = 0.027\ K^{-1}$ for the siloxane and $\beta = 0.054\ K^{-1}$ for the

synthetic paraffinic oil. Equal specific volumetric heat capacity and equal exponential-power base temperatures E were assumed for the two fluids. Figure II-5 shows the expected behavior of the model fluids. The four flow curves are congruent in the range of obtained shear stress. The less temperature viscosity sensitive siloxane shows a smaller drop in apparent viscosity than the synthetic paraffinic oil at comparable shear stress. The curves from the shorter length capillary tube are located at higher shear stress than the curves from the longer capillary tubes. The gain in obtained shear stress with the use of the short capillary tube is less than expected from the length and diameter ratios of the capillary tubes. It might be speculated that the relatively better performance of the longer capillary tube can be ascribed to better cooling conditions.

Pressure Drop for the Inlet and Exit Flow

The pressure drop associated with highly viscous laminar flow, $R_e \simeq 0$, from a semi-infinite reservoir to a cylindrical capillary, on to a circular hole in a flat wall, can be expected to depend only on viscosity η, volumetric flow rate q and diameter D of the entrance. The pressure drop will, analogous with Poiseuille flow, $\Delta p/L = 128q\eta/\pi D^4$, be proportional with the viscosity and with the flow rate. Dimensional considerations lead to the expression

$$\Delta p_i = \text{const } q\eta/D^3 \qquad \text{(II-12)}$$

where the constant is dimensionless. The investigations of Sampson 1891 (11), Roscoe 1949 (12) and Happel and Brenner 1965 (13) gave this expression and the value 12 for the constant. Wurst 1954 (14) estimated the constant to be slightly lower possibly due to the displacement of a numerical factor. The analyses for the solution of the differential equation for the stream function ψ, utilized oblate spheroidal coordinates. The boundary conditions

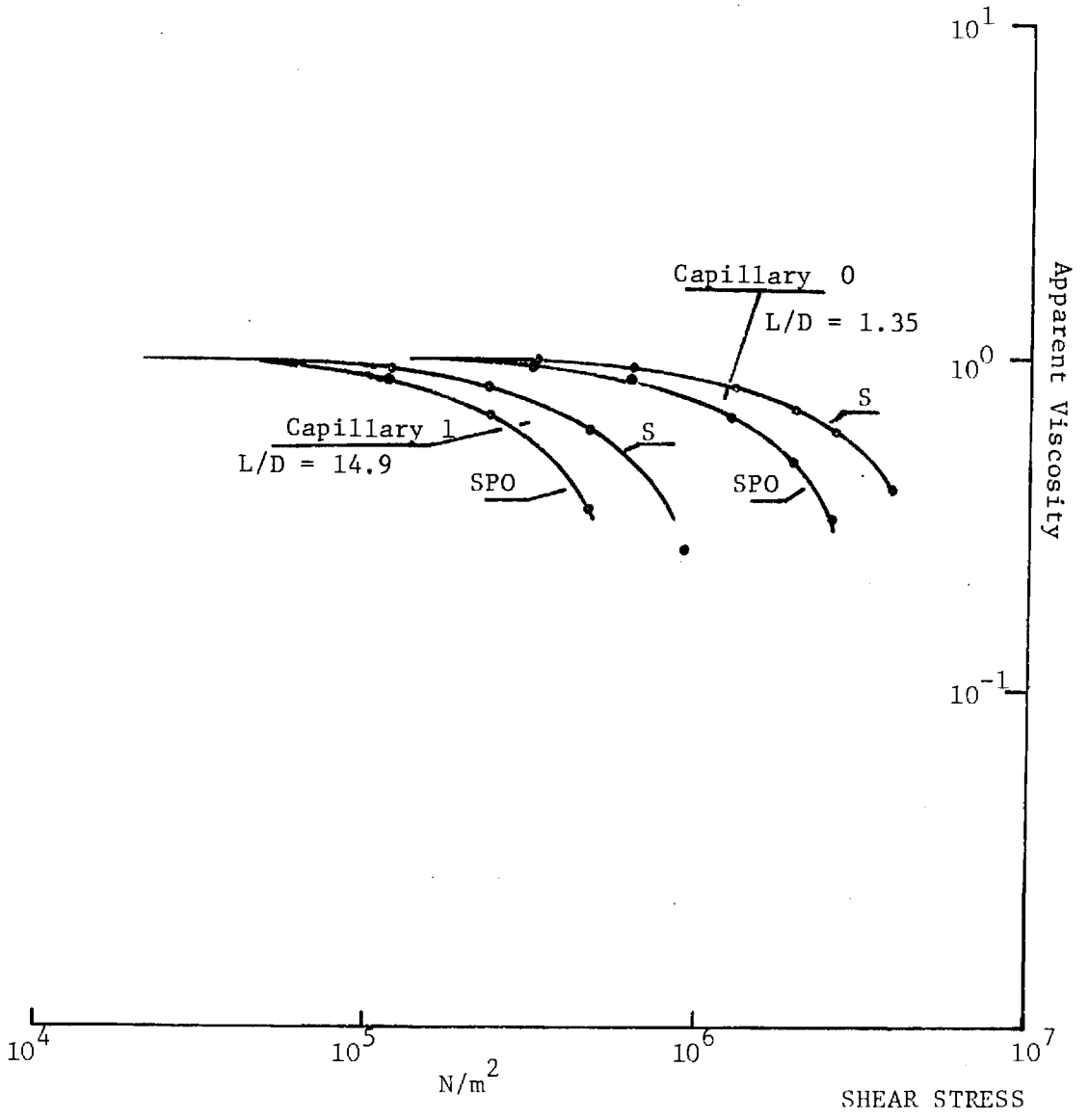

Figure II-5. Calculated Flow Curves for the Model Fluids. (SPO=synthetic paraffinic oil, S=dimethylsiloxane, apparent viscosity normalized with respect to the low shear viscosities).

were zero tangential fluid velocity at the wall and volume flow equal to -2π times the stream function at the wall. The stream function at the axis of rotational symmetry was zero. The solution, in terms of stream surfaces, is presupposed to be confocal hyperboloids of one sheet. The velocity distribution at great distance from the hole is similar to the velocity distribution for a point sink in the plane wall. The velocities over the inlet area of the hole are circularly distributed and proportional to $\sqrt{1 - r^2}$. The pressure along the axis of rotational symmetry is a monotonically decreasing function with an inflection point at the origin of the coordinate system. The pressure along the boundary wall is a steady increasing function with infinite slope at the edge of the hole. The edge is a singularity. The assumption of very small inertia terms compared with the viscous terms of the Navier-Stokes equations are thus not fulfilled in a certain small neighborhood of the edge, although the Reynolds number for the total flow is low.

Experimental verification, in some respects, of the expression (II-12) are given by Bond 1921 (15) and 1922 (16). A verification can also be deduced from the experimental work reported by Johansen 1930 (17). The measured values of the constant are near the analytic value 12. The determination by Bagley (18) of the value of the constant appears to be most nearly the analytic value although the orifice was bevelled at 45^{o} which gave divergent flow. Proportionality between pressure drop and volumetric flow rate was found in both workers reports when the Reynolds number for the total flow situation was below about 3.

The inlet pressure drop, equation (II-12), the pressure drop from the Poiseuille flow in the capillary tube and the exit pressure drop amount to the total change of pressure measured in a capillary tube viscometric experiment. The inlet and exit flow have identical stream surfaces. The

pressure drops are therefore of the same size. Their sum, $\Delta p_{ic} = 24q\eta/D^3$, is equivalent to the pressure drop over a capillary tube of length

$$L_e = (24\pi/128)\ D = \frac{3\pi}{16} D \simeq 0.59D \qquad \text{(II-13)}$$

in Poiseuille flow, which can be seen by comparison of equation (II-12) with the expression for pressure drop of viscous flow in a tube. The expression (II-13) is the theoretical, total end correction to the length of a flat ended capillary tube viscometer in Newtonian flow.

The velocity distribution and pressure drop for inlet-exit flow follow the same general expressions in the appropriate coordinate systems as those of Poiseuille flow in the cylindrical system. The heat generation will therefore have approximately the same effect on the flow curves from short length capillary tubes as the effect of an extension L_e on the capillary tube length. The flow curves from an actual, physical system and from a cylindrical capillary tube will therefore appear nearly identical.

The circularly distributed velocities at the inlet resulting from the flow from an semi-infinite reservoir do not fit the parabolic velocity profile of fully developed flow in a cylinder. The concept of an inlet length must therefore still be accounted for. The conditions are less severe than the conditions of a uniform, flat, inlet velocity profile usually assumed in the literature for flow at low Reynolds number. The exit flow will presumably impress a similar velocity profile upstream of the exit. The actual average shear rate at the wall will be slightly greater than the shear rate calculated from fully developed flow. The shear stress imposed on a fluid with a known viscosity will therefore also be correspondingly greater and interpretation of measurements in terms of parabolic velocity profiles will be a lower bound for the shear stress and shear rate.

The shear stress per unit pressure drop obtainable in a short cylindrical capillary can be evaluated as a function of the ratio of diameter and length of the capillary. The total pressure drop Δp_t over the inlet, capillary and exit system is the sum of the individual pressure drop. Equations (II-12), (II-13) and the expression for pressure drop in the capillary tube, $\Delta p = 128Lq\eta/\pi D^4$, give the ratio

$$\tau/\Delta p_t = 1/(4(L/D) + (3\pi/4)) \qquad \text{(II-14)}$$

where $\tau = \Delta p/4(L/D)$. Hence the shear stress is, in the limit as $\frac{L}{D}$ approaches zero, 42% of the total applied pressure drop. When the length-to-diameter ratio is one, the shear stress is 16% of the total applied pressure. As the length to diameter ratio gets large, the shear stress-pressure drop ratio approaches the classical relationship of $\tau = \frac{\Delta p}{4(L/D)}$. The traditional concept of a capillary tube seems to vanish when the diameter approaches or exceeds the length. Neither the mechanisms nor the governing equations do, however, exclude such a parameter combination. Some experimental work report furthermore the use of short tubes in capillary viscometry; Bagley 1957 (18) and Schnurmann 1962 (5). The expression (II-14) indicates the possibility to create experimental shear loads of the order of magnitude of 10 MN/m^2 on the fluid with a total pressure drop of only about 25 MN/m^2.

Conclusions

The highly viscous, steady laminar flow through a short cylindrical capillary tube has been investigated. Low Reynolds number conditions were assumed. A shear stress range with the upper limit approaching the average shear stress in a sliding elastohydrodynamic film was investigated, Figure II-5.

The flow curves for Newtonian fluids will show constant viscosity at

sufficiently low shear stress. An apparent viscosity lower due to dissipation heating will be measured at high shear stress. The decrease in apparent viscosity increases rapidly with increasing shear stress.

It was found that the flow curves will have an identical configuration for Newtonian fluids, independent of the parameters of the problem, shear rate, viscosity level, etc. An identical flow curve configuration cannot be expected for non-Newtonian fluids.

The location of the flow curves in the logarithmic presentation depends on viscosity level, the ratio of length and diameter of the capillary, the exponential temperature viscosity coefficient, the specific volumetric heat capacity and, to a minor degree, on the coefficient of heat conduction of the fluid.

The condition of no heat conduction in the fluid or isothermal wall appears to be of only moderate significance for high shear stress capillary viscometry under conditions of low Reynolds numbers because convection is the primary mechanism in removal of the dissipated heat.

Temperature profiles in the capillary cavity show, for isothermal wall conditions, pronounced annular peaks near the wall, and low temperatures at the axis and at the wall. The peaks tend to move inwards as the axial location increases. The peaks remain, however, for short capillary tubes in the range 0.9 to 1.0 of dimensionless radius.

Inlet and exit corrections for pressure drop over the capillary tube have been deduced for Newtonian behavior of the fluid. Only the flow from a semi-infinite reservoir into a circular hole in a flat wall has been considered. The inlet and exit pressure drop thus determined have the functional appearance of a Poiseuille flow situation. The correction can be expressed as the length of an equivalent cylindrical capillary tube with

diameter D. The heating effects are of the same character as the heating effects of the flow in the capillary tube cavity.

Determination of end corrections enables an estimate to be made of an upper limit of shear stress attainable in high shear capillary tube viscometry. The estimate shows a shear stress limit of the order of magnitude of 10 MN/m^2. This is near the level of average shear stress experienced in a sliding elastohydrodynamic film. High pressure, high shear viscometry can therefore be useful in lubricant rheological investigations of interest for elastohydrodynamic lubrication.

Table II-1

NOMENCLATURE FOR SECTION II

c	Specific heat per unit mass, $Nm(kgK)^{-1}$
k	Coefficient of heat conduction, $wm^{-1}K^{-1}$
p	Pressure, N/m^{-2}
$\hat{p}$	Dimensionless pressure, $\hat{p} = p/c\rho E$
q	Volumetric flow rate, m^3s^{-1}
$\hat{q}$	Dimensionless volume flow rate, $\hat{q} \equiv \frac{(c\rho)^2 ER^4}{4L^2 \eta k} \frac{\partial \hat{p}}{\partial \omega}$
r, z	Coordinates in cylindrical coordinate system
u_z	Velocity in axial direction, ms^{-1}
D	Diameter of the capillary tube $D = 2R$, m
E	A lubricant material parameter, the temperature ^oK at which the viscosity is 2.718×10^{-3} Nsm^{-2} (see Appendix, Section IV)
L	Length of the capillary tube, m
L_e	Length equivalent, m
R	Capillary Radius, m
R_e	Reynolds number
T	Temperature, K
T_o	Fluid inlet and wall temperature for capillary flow, K
Δp	Pressure drop, Nm^{-2}
Δp_i	Pressure drop ahead of the inlet area, Nm^{-2}
Δp_{ie}	Sum of pressure drop ahead of the inlet and after the exit area, Nm^{-2}

Δp_t	Total pressure drop over inlet, capillary tube and exit $\Delta p_t = \Delta p_{ie} + \Delta p$, Nm^{-2}
η	Viscosity, Nsm^{-2}
μ	Dimensionless viscosity
π_3	A lubricant material parameter, see Appendix Section IV.
ρ	Density, kg m^{-3}
$\bar{\rho}$	Dimensionless radius $\bar{\rho} = r/R$
τ	Shear stress at the wall of a cylindrical capillary tube, Nm^{-2}
ω	Dimensionless axial coordinate $\omega = z/L$
θ	Dimensionless temperature, T/E
θ_o	Dimensionless temperature, T_o/E
β	Temperature viscosity coefficient, $\frac{\partial \ell n \mu}{\partial T}$, K^{-1}

III. Infrared Temperature Measurements in EHD Contacts

Equipment Modifications

Several significant modifications have been made to the experimental equipment and associated instrumentation used in the investigations reported previously [1,19]. As before, the sliding EHD contact is formed using a .0318m diameter chrome steel ball rotating and loaded against a sapphire flat [19-22]. The infrared radiation emitted at this contact is measured with an infrared radiometric detector (Barnes Engineering Company, Model RM-2A) having a spot size resolution of 3.8×10^{-5}m.

The modifications made during the past year include adding a dead weight loading system in place of the pneumatic system used previously. Since only constant load data was of interest, the new system provided improved repeatability and also extended the normal load range. Figure III-1 shows a schematic diagram of the modified apparatus.

The second improvement consisted of adding a temperature controlled lubricant supply system. This sytem was needed in order to maintain an adequate supply of lubricant to the bearing reservoir at a constant temperature. Without such a system, each test run resulting in a different amount of energy dissipation would have a different equilibrium reservoir temperature. The reservoir temperature is periodically measured by a thermocouple. This system is also shown in Figure III-1.

The third and most important improvement in the sytem is the use of two filters, a narrow band pass and a wide band pass, to distinguish ball surface radiation and lubricant film radiation from the total radiation

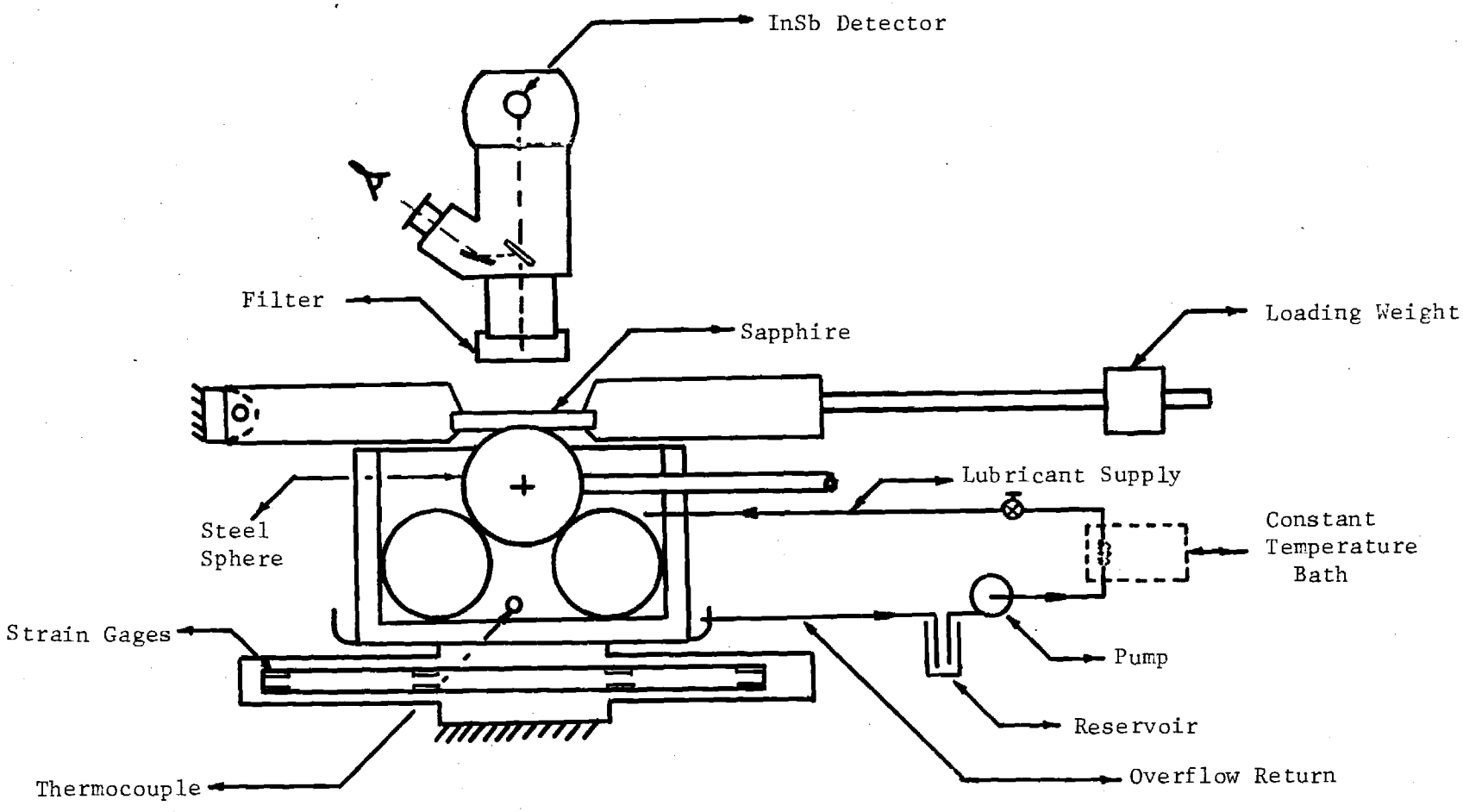

Figure III-1. Schematic Diagram of the Experimental Apparatus.

received by the infrared detector. Previously [1,19] it had been necessary to perform three separate experiments, one each with a low emissivity and high emissivity ball without a filter and one with the low emissivity ball and a special filter. In addition to reducing the amount of time needed to collect data, the two filter technique should yield more accurate results since many of the simplifying assumptions made in the first work [1,19] have not been needed.

Experimental Technique

There are four contributions to the radiant energy collected by the micro-detector; (1) from the ball surface N_b*, (2) from the lubricant film N_F, (3) from the sapphire N_s and (4) from reflected ambient radiation N_o. Using the same arguments as before [1,19], contribution (3) has been neglected and contribution (4) can be accounted for knowing the optical properties of the system and the ambient temperature. From the detector response, therefore, the sum of contributions (1) and (2) at any point in the EHD contact can be determined. The technique for separating the two components consists of using filters which take advantage of the different spectral characteristics of the two contributions.

The fluid used in this investigation is a naphthenic base oil having a peak in the emission spectra at 3.4μm, with significant emission in the band 3.0 to 3.7μm. The ball surface on the other hand emits as a grey body. Figure III-2 shows these emission characteristics along with the spectral characteristics of the narrow and wide band filters. The detector and sapphire will only respond to radiation in the band 1.8 to 5.5μm. The narrow band filter has been chosen such that essentially all of the radiation emitted by the oil film is transmitted along with a portion of the

* Nomenclature for Section III is found in Table III-2 at the end of the section.

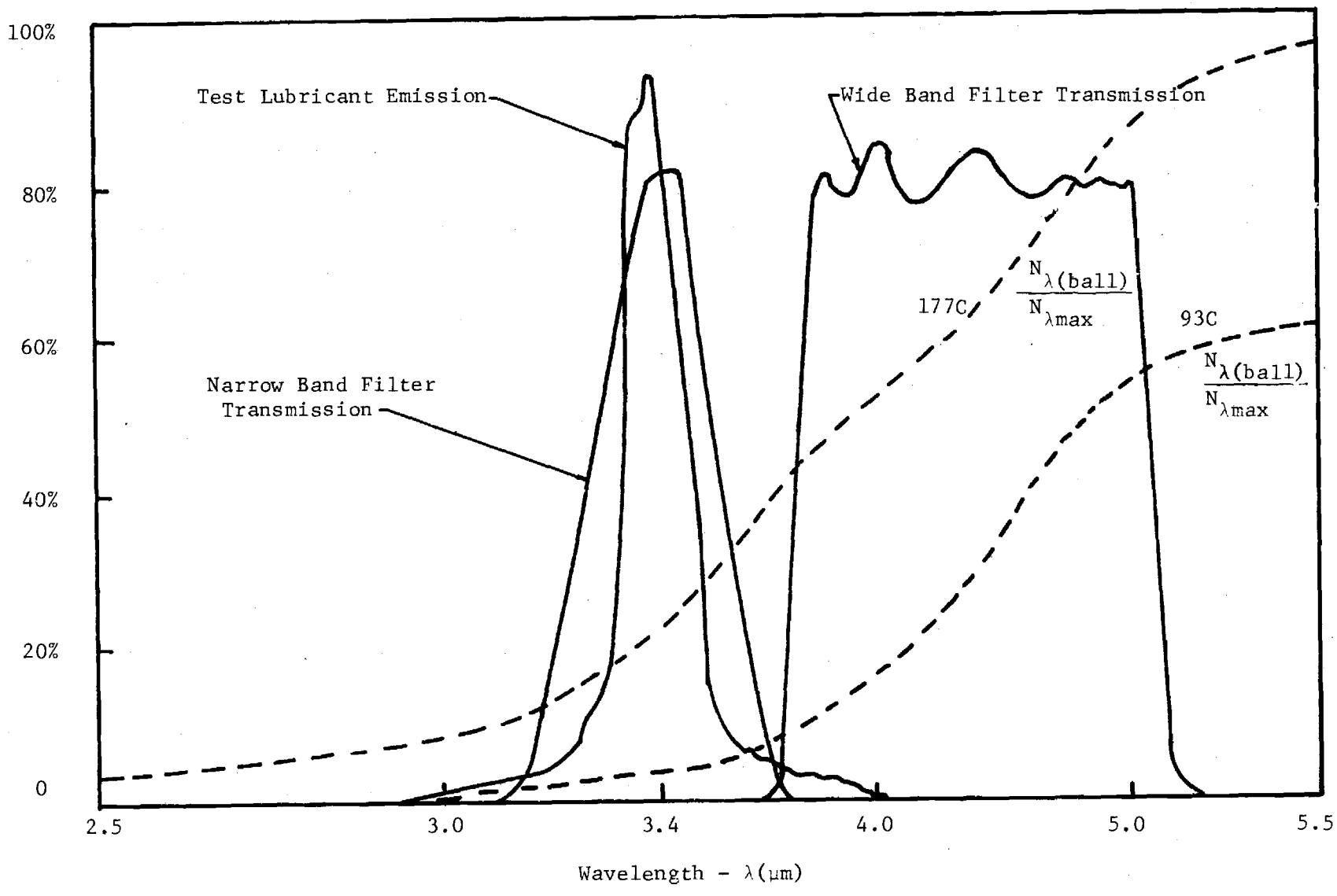

Figure III-2. Spectral Characteristics of the Fluid Film, Ball and Filters.

grey body ball radiation. The wide band filter, on the other hand, transmits only radiation from the ball surface. When using one filter or the other, the influence of the filter will be assigned to the detector rather than the radiation source, i.e. the detector calibration curve of temperature vs. radiation received will now depend on which filter is used and on both the temperature and spectral characteristics of the radiation source.

Figure III-3 shows the radiation contributions and the signal attenuation before passing through the filter. The total radiation N is, therefore,

$$N = \eta_b N_b + \eta_F N_F + \eta_s N_s + \eta_o N_o \qquad \text{(III-1)}$$

where the attenuation factors include losses due to reflection and absorption.

Wide Band Filter Analysis

As seen in Figure III-2, the wide band filter eliminates the film contribution reducing equation (III-1) to

$$N = \eta_b N_b + \eta_s N_s + \eta_o N_o \qquad \text{(III-2)}$$

The radiation emitted from the ball (a grey body) is a function of ball emissivity ϵ_b and ball temperature T_b only. Therefore,

$$N_b = \epsilon_b N_{BB}(T_b) \qquad \text{(III-3)}$$

where N_{BB} is the black body radiation received by the detector with the wide band filter. Using a standard black body calibration source (Barnes Model RM-121) the calibration curve shown in Figure III-4 was obtained.

The ball radiation attenuation is determined by reflection losses at the sapphire surfaces and absorption in the sapphire. The fluid film does

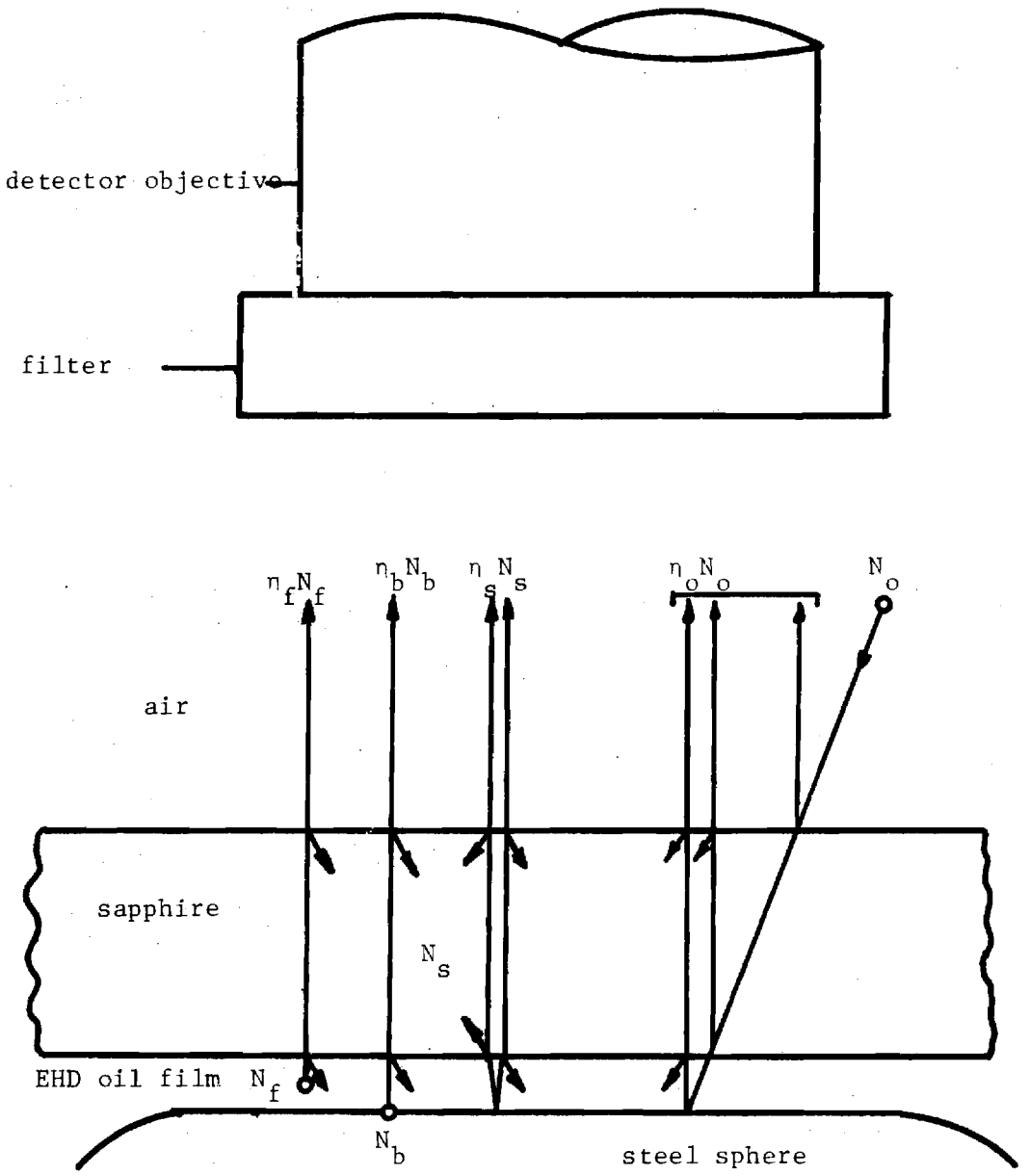

Figure III-3. A Schematic Diagram of Radiation Contributions and Attenuations.

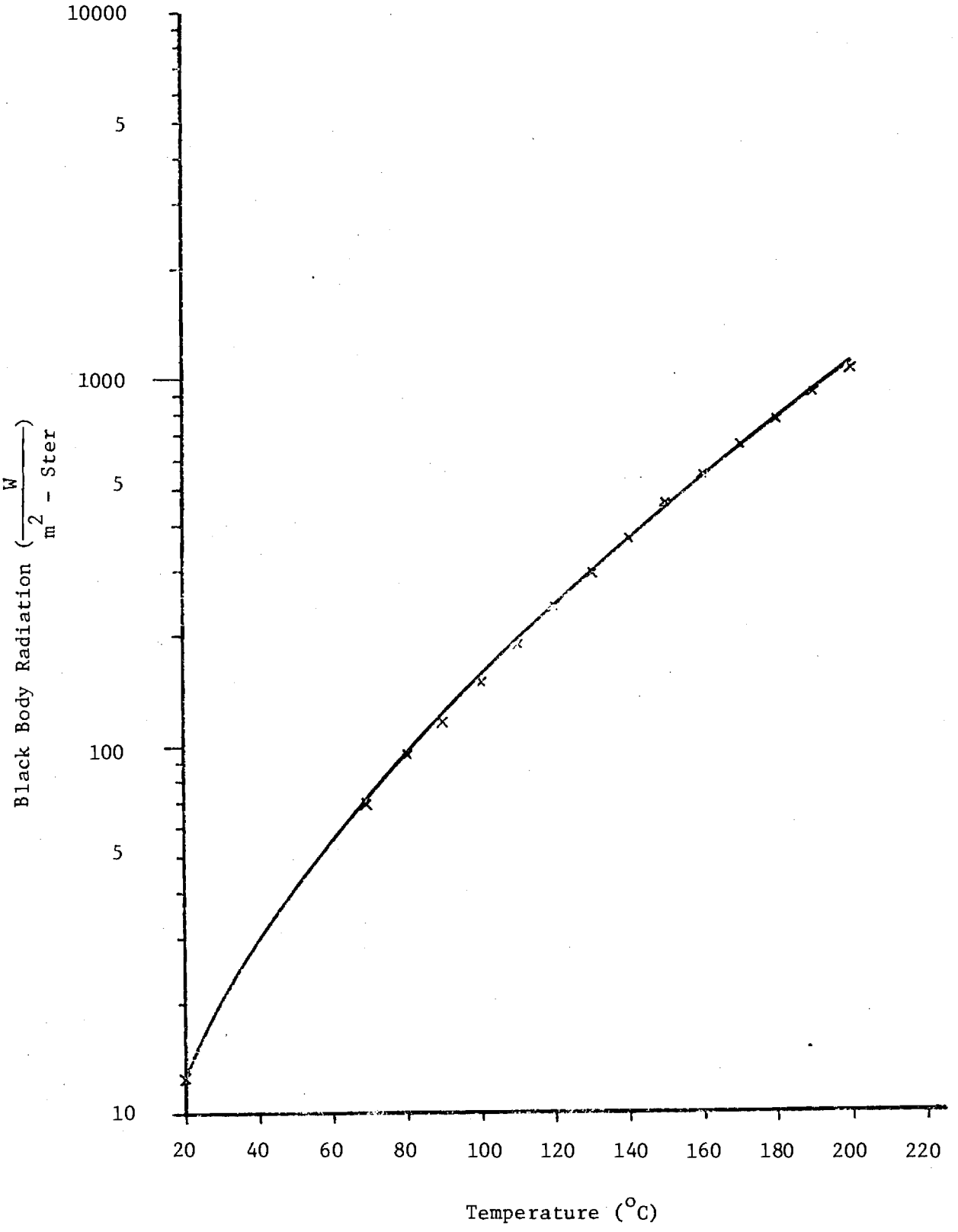

Figure III-4. Wide Band Filter Calibration for Black Body Radiation.

not absorb in the wavelengths transmitted by the wide band filter. Therefore,

$$\eta_b = \tau_s (1-\rho_1)(1-\rho_2) \qquad \text{(III-4)}$$

where τ_s is the sapphire transmissivity and ρ_1 and ρ_2 are the Fresnel reflections at the upper and lower sapphire surfaces respectively. The attenuation factor η_b is 0.83 as before [1,19].

The ball emissivity ε_b in equation III-3 was measured using both types of filters and was found to be essentially constant at 0.28. With these values, and N determined by measurement, the ball temperature can be found using equations (III-2,3,4) and Figure III-4 if the terms $\eta_s N_s$ and $\eta_o N_o$ could be found.

Because the sapphire emissivity is low (0.018), it has previously been argued [1,19] that the contribution $\eta_s N_s$ is less than 2% of the ball contribution $\eta_b N_b$. Since this omission would cause only a small error in calculated temperature, it has been omitted.

The ambient radiation N_o is assumed to be black body radiation at the temperature of the surroundings. Knowing the room temperature, Figure III-4 can be used to determine N_o. The attenuation factor η_o takes into account reflection at the upper sapphire surface, absorption in the sapphire, reflection at the lower sapphire surface and reflection at the ball surface. The net attenuation factor η_o is, therefore,

$$\eta_o = \rho_1 + \tau_s(1-\rho_1)^2 \rho_F + \rho_b \eta_b^2 \qquad \text{(III-5)}$$

where ρ_F and ρ_b are the lubricant and ball reflectivities respectively.

The above analysis was checked by taking measurements through the wide band filter of a stationary ball in a circulating oil bath at known temperature. In these measurements, the film thickness was representative

of EHD conditions and the circulating lubricant insured that the ball and fluid were at the same temperature. The trial measurements showed that varying the film thickness had no discernable effect on the total radiation and that calculated ball temperatures were consistently within 2 C of the bath temperature as measured with a thermocouple.

Narrow Band Filter Analysis

The narrow band filter analysis is considerably more complicated than the wide band analysis due to the emission and absorption of the oil. The spectral characteristics of the oil vary with lubricant chemistry, temperature and film-thickness. The total fluid radiation which would be observed without attenuation is

$$N_F = \varepsilon_F(h, T_F)\ N_{BB}(T_F) \qquad \text{(III-6)}$$

where ε_F is the fluid emissivity and is a function of film thickness and fluid temperature and where N_{BB} is the black body radiation from a relatively thick layer of the lubricant at temperature T_F.

Equation III-1 is an expression of the total radiation received when the system contains the narrow band filter. The terms $\eta_s N_s$ and $\eta_o N_o$ can be handled in the same manner as with the wide band analysis except that aborption of N_o by the lubricant must now be included. The film temperature T_F can then be determined from equation III-1 and III-6 after necessary calibration to determine the quantities η_b, η_F and N_{BB}.

In a determination of η_F, the spectral dependence of lubricant transmissivity must be considered. For a monochromatic source at wavelength λ the radiation emitted at a lower film surface and exiting at the upper surface is

$$N_{\lambda F} = N_{\lambda BB}(\lambda, T_F) \left\{ 1 - e^{-\alpha'(\lambda, T_F)h} \right\} \qquad \text{(III-7)}$$

where α' is an absorption coefficient dependent on both wavelength and film temperature, h is the local film thickness and $N_{\lambda BB}$ is the monochromatic black body radiation at temperature T_F detected through the narrow band filter. In using equation III-7 the approximation will be made that T_F is uniform across the lubricant film. This will result in reported film temperatures being an integrated value through the film. The term in brackets in equation III-7 is the monochromatic emissivity. The monochromatic transmissivity is then

$$\tau_\lambda = 1 - \varepsilon_\lambda = e^{-\alpha'(\lambda, T_F)h} \qquad \text{(III-8)}$$

Accounting for radiation initially emitted upward toward the sapphire and that component emitted toward the ball, reflected at the ball surface and then partially absorbed by the film, the net monochromatic fluid radiation is, therefore,

$$N_{\lambda F} = \varepsilon_\lambda N_{\lambda BB} + \rho_b \tau_\lambda \varepsilon_\lambda N_{\lambda BB} \qquad \text{(III-9)}$$

The exponential expressions in the terms τ_λ and ε_λ have arguments sufficiently small to allow a series approximation using only the first few terms.

In order to determine the total fluid radiation, the monochromatic radiation $N_{\lambda F}$ must be integrated over the narrow band filter band width. Therefore,

$$N_F = \int_{3.1\mu m}^{3.7\mu m} N_{\lambda F} \, d\lambda \qquad \text{(III-10)}$$

and from the monochromatic black body radiation $N_{\lambda BB}$ (equation III-7)

$$N_{BB} = \int_{3.1\mu m}^{3.7\mu m} N_{\lambda BB}\, d\lambda \qquad \text{(III-11)}$$

The attenuation of the fluid radiation by the sapphire, η_F, is determined by calibration. This attenuation is of essentially the same form as η_b in equation III-4 (wide band filter analysis).

The unattenuated ball radiation N_b in equation (III-1) for the narrow band filter measurements is the same as for the wide band analysis (equation III-3). The attenuation factor for the ball radiation η_b is the same as for the wide band analysis except that the fluid transmissivity must now be included. Therefore,

$$\eta_b = \tau_F \tau_s (1 - \rho_1)(1 - \rho_2) \qquad \text{(III-12)}$$

where τ_F is a function of film thickness and temperature. Equation (III-8) may be used to determine the dependence $\tau_F (T_F, h)$ over the narrow band wavelengths, through a calibration experiment.

Since many of the terms comprising the total radiation received (equation III-1) contain parameters dependent on the unknown T_F, an iterative solution procedure is necessary. For example, assuming an initial temperature and knowing the film thickness, η_b, ε_F, and τ_F can be determined from calibration curves and $N_{BB}(T_F)$ can be obtained from the narrow band black body calibration curve shown in Figure III-5. Equations III-1 and III-3 can then be used to obtain a calculated N_{BB} value. This value is compared with that obtained from Figure III-5 and the assumed temperature. If they are different, the temperature corresponding to the

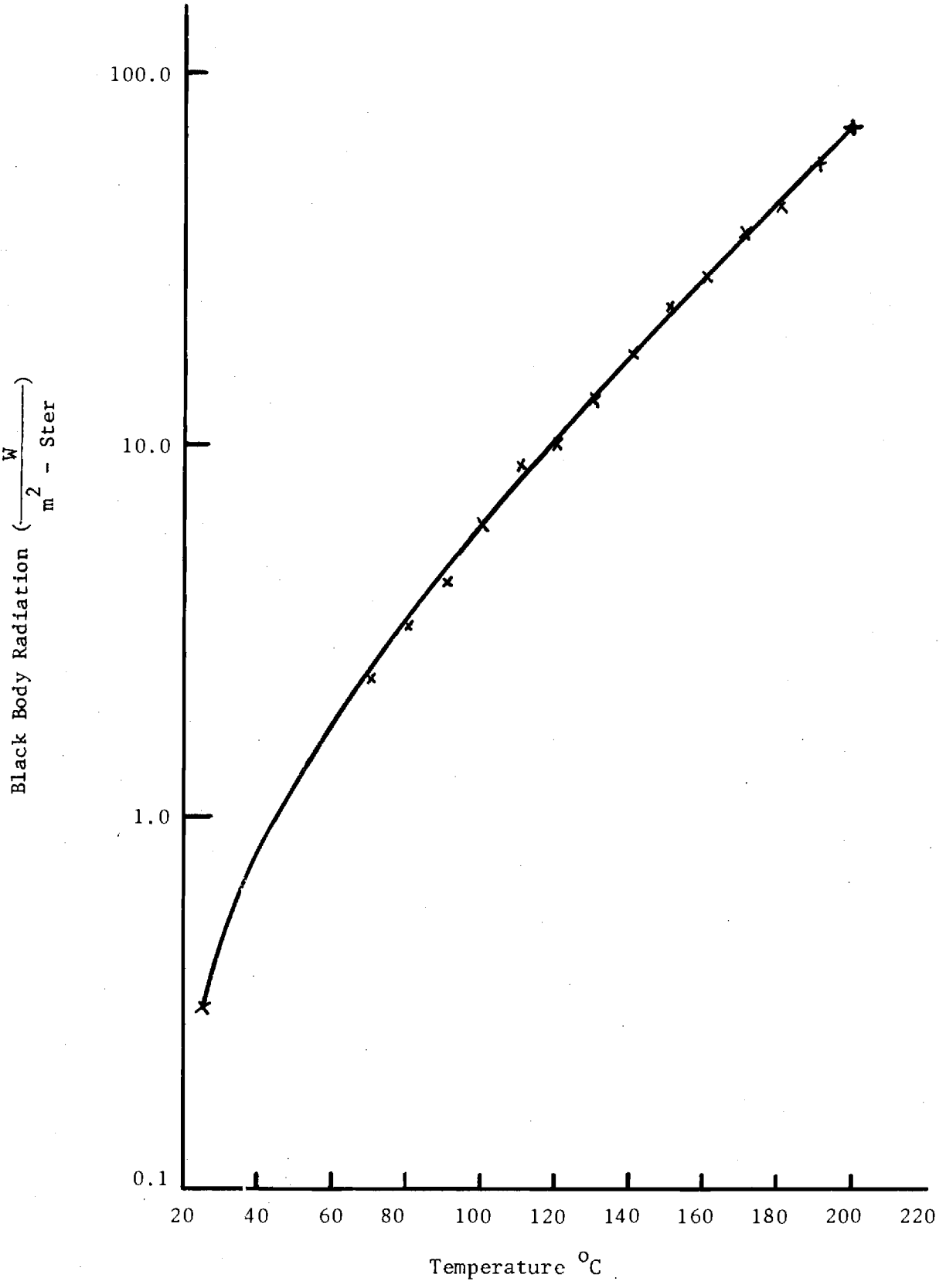

Figure III-5 Narrow Band Filter Calibration for Black Body Radiation

computed N_{BB} is used in the next iteration.

Experimental Results

Table III-1 and Figure III-6 show the most significant portions of the results obtained. All data was taken with the naphtenic base oil used previously [1,19] with a reservoir temperature of 40°C and a peak Hertz stress of 1 GN/m^2. The only independent variable in this set of data was the sliding speed, which varied from 0.35 to 12.7 m/s. Table III-1 shows the pertinent film thickness data along with the ball and lubricant temperatures at four points in the contact: the contact inlet, the contact center, the maximum temperature along a contact centerline parallel to the sliding velocity, and the maximum temperature in the contact side lobe constrictions. Figure III-6 shows essentially the same data plotted as a function of sliding speed.

Conclusions

The equipment modifications to insure more reliable data have been completed and preliminary data are reported. The system modifications include the use of a two filter arrangement on the infrared detector optics. Each filter permits a specific bandwidth of infrared radiation to pass on to the detector. One filter covers a bandwidth in which the fluid is transparent and does not emit, hence, with this filter in place the steel surface temperature is reliably determined. The second filter covers the C-H emission band of the test lubricant and, upon calibration of the system to include the effect of temperature and lubricant film thickness on emissivity, permits the reliable determination of the oil film

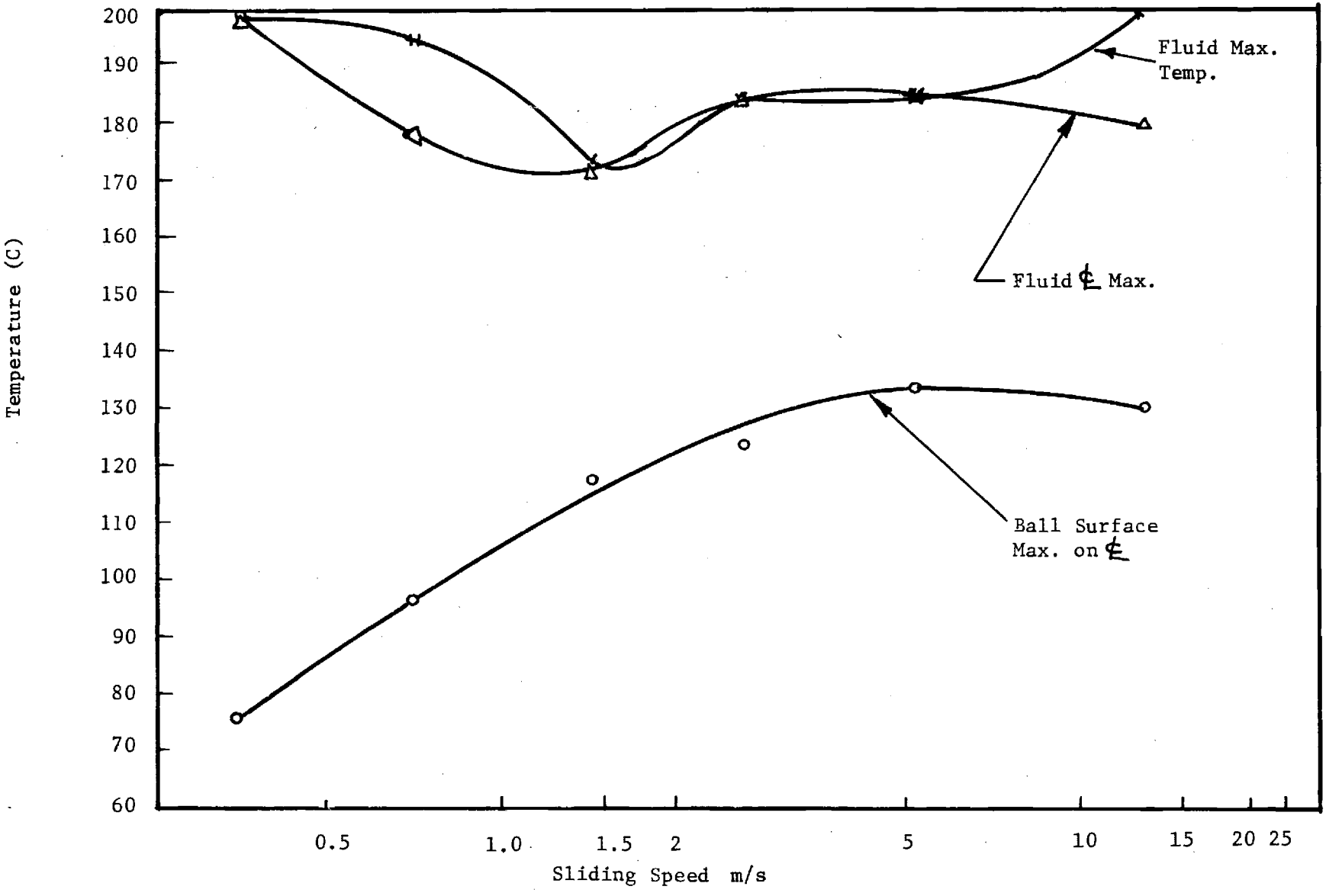

Fig. III-6. Ball Surface and Fluid Temperature Maximum as a Function of Sliding Speed.

temperature. The system has also been modified to permit control of the bath oil temperature over long periods of time. With these modifications ball surface and fluid temperatures over the elastohydrodynamic contact have been mapped at a Hertz pressure of 1 GN/m^2 (150,000 psi), six sliding speeds ranging from 0.35 to 12.7 m/s (13.7 to 500 ips) and a bath temperature of 40C. The maximum fluid temperature in the contact remains substantially constant (within $\pm$ 12C) while the ball surface temperature increases with speed from 75C at 0.35 m/s to 133C at 5 m/s and then is constant at 135C to 12.7 m/s.

Table III-1: Summary of Experimental Results

(Fluid: N1, Load 67N, Hertz Pressure 1 GN/m^2, Bath Temperature 40 $\pm$ 1C)

Speed m/s	h_c μm	h_o Side Lobe Min. μm	h_o Min. μm	Temp. at Inlet C		Temp. At Center C		Temp. Max C		Temp. Side Lobe Max C	
				Ball	Oil	Ball	Oil	Ball	Oil	Ball	Oil
12.7	0.35	0.16	0.25	67	124	102	154	130	180	116	200
5.08	0.22	0.11	0.13	56	102	120	179	133	185	78	155
2.54	0.18	0.07	0.09	56	115	113	132	123	185	88	177
1.4	0.13	0.05	0.09	54	125	98	156	117	171	60	173
0.7	0.09	0.05	0.08	46	120	83	166	96	178	58	194
0.35	0.07	0.05	0.05	45	155	67	188	76	198	46	162

Table III-2

NOMENCLATURE

h	Lubricant film thickness (μm)
N	Total radiation received by detector ($W/sr\text{-}m^2$)
N_{BB}	Black body radiation ($W/sr\text{-}m^2$)
N_b	Ball radiation received ($W/sr\text{-}m^2$)
N_F	Lubricant radiation received ($W/sr\text{-}m^2$)
N_o	Ambient radiation received ($W/sr\text{-}m^2$)
N_s	Sapphire radiation received ($W/sr\text{-}m^2$)
$N_{\lambda BB}$	Monochromatic black body radiation ($W/sr\text{-}m^3$)
$N_{\lambda F}$	Monochromatic lubricant radiation received ($W/sr\text{-}m^3$)
T_b	Ball surface temperature (C)
T_F	Mean lubricant temperature (C)
α'	Lubricant absorptivity (m^{-1})
ϵ_b	Ball emissivity
ϵ_F	Lubricant emissivity
ϵ_λ	Monochromatic lubricant emissivity
η_b	Attenuation factor for ball radiation
η_F	Attenuation factor for lubricant radiation
η_o	Attenuation factor for ambient radiation
η_s	Attenuation factor for sapphire radiation
λ	Radiation wavelength (μm)

ρ_1	Air/sapphire interface reflectivity
ρ_2	Lubricant/sapphire interface reflectivity
ρ_b	Ball reflectivity
ρ_F	Lubricant reflectivity
τ_s	Sapphire transmissivity
τ_λ	Monochromatic lubricant transmissivity

IV. Thermal Shearing Phenomena in Sliding Elastohydrodynamic Contacts

In an attempt to understand lubricant rheological behavior in elastohydrodynamic contacts an analysis was undertaken. Based on conclusions from the high shear viscometry, namely that thermal effects predominate in high energy dissipation flow, a model has been developed to account for viscous dissipation and consequent reduction in viscosity in the sliding EHD contact.

The formulation and solution for the shear stress and temperature in heavily loaded sliding elastohydrodynamic contacts is presented. The solutions are presented in dimensionless design charts. Integration over the contact area will yield the traction. Accuracy is expected to be very good over the nearly flat part of the contact area where the majority of the sliding traction is generated. The procedure presented is not appropriate for hydrodynamic lubrication, for the inlet region of an elastohydrodynamic contact, or for the rolling friction of elastohydrodynamic contact. In these cases the convective component of energy transport, which is neglected in the analysis, may be large relative to the conductive component.

The high shear, high pressure flow in a sliding elastohydrodynamic contact of a lubricant with known pressure, temperature, shear, viscosity relation can be described by a general analysis which predicts the maximum temperature and the shear stress of the film. Other film quantities can be derived therefrom. The results are of interest for prediction of traction coefficients of sliding elastohydrodynamic contacts.

A simplified, analytic method for shear stress determination in the high pressure area of a sliding elastohydrodynamic contact is presented. A general pressure-temperature-shear-viscosity relation for the lubricant is assumed. Solutions in terms of shear stress can be obtained directly with the use of dimensionless diagrams. Sliding speed and thermal conductivity of the lubricant must be known. Lubricant viscous properties, pressure distribution and film thickness of the high pressure part of the contact must be known from calculations or measurements. The Hertzian pressures can be used for a first estimation of the traction. A realistic model for the viscous behavior of many lubricants is also presented.

Problem Formulation

The variation of film thickness over the major part of an elastohydrodynamic contact is small compared to the film thickness particularly for highly loaded contacts. The shear stress component generated by the pressure gradient is also small over a great part of the contact area compared with the shear stress component from the sliding action. The effect of convection along the film is small compared with the heat conduction perpendicular to the film. Therefore, a unidirectional steady laminar flow, with pointwise constant pressure and temperature between parallel surfaces may be assumed as a good approximation for the flow: $u_1 = u_1(x_3)$, $U_3 = 0$, p - constant, $T = T(x_3)$. The flow model is shown in Figure 1 which also shows the boundary conditions and the nomenclature given in Table IV-1 at the end of the section. Surface 2 is moving with constant velocity $u_1 = (UN)$ in the x_1 direction. Constant thermal conductivity is assumed. The justification of these assumptions are discussed further in (23).

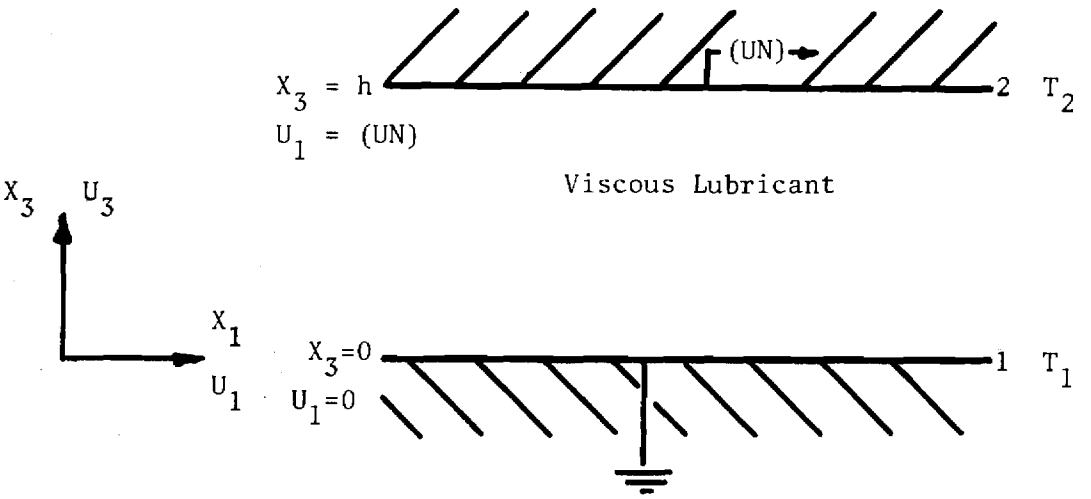

Figure IV-1 Flow Model.

The governing equations for conservation of momentum and energy respectively are reduced to:

$$\tau_{13} = \tau = \text{constant} = \eta \frac{\partial u_1}{\partial x_3} \quad \text{and} \quad k \frac{\partial^2 T}{\partial x_3^2} + \eta\left[\frac{\partial u_1}{\partial x_3}\right] = 0 \qquad \text{(IV-1)}$$

The boundary conditions are

$$\begin{aligned} u_1(0) &= 0 & T_1 &= T_1(0) = \text{constant} \\ u_1(h) &= (UN) & T_2 &= T_2(h) = \text{constant} \end{aligned} \qquad \text{(IV-2)}$$

Although the analysis of these equations can be done with any general viscosity relation $F(p,T,\tau,\eta) = 0$, a particular form of this relation will be introduced which will be used in selecting parameters with which to non-dimensionalize the governing equations. The so-called power exponential viscosity description (23)

$$\ell n \quad \ell n \frac{\eta}{\eta_o} = \pi_3 (\ell n\, E - \ell n\, T)\Big|_{\tau,p} \qquad \text{(IV-3)}$$

where E and π_3 are functions of pressure, has been found to give a reasonably accurate description of the viscosity behavior within a temperature range of 39C - 100C for many fluids. The method for determining E and π_3 are presented in Appendix IV-A, p. 61 . The range is the same magnitude as the temperature range expected in elastohydrodynamic films. The temperature-viscosity relation (IV-3) can be written as

$$\mu = \exp\left(\left(\frac{E^{+\pi_3}}{T}\right)\right) \qquad \text{(IV-4)}$$

The introduction of this form will also permit the graphical presentation of the results to facilitate their utilization.

The expressions (IV-4), (IV-1), and (IV-2) become in nondimensional form

$$\mu = \exp(\theta^{-\pi_3}) \tag{IV-5}$$

$$\mu \frac{\partial u}{\partial z} = \pi_5 \tag{IV-6}$$

$$\frac{\partial^2 \theta}{\partial z^2} + 2\pi_4 \pi_5 \frac{\partial u}{\partial z} = 0 \tag{IV-7}$$

$$\begin{aligned} u(0) &= 0 \qquad \theta(0) = \pi_1 \\ u(1) &= 1 \qquad \theta(1) = \pi_2 \end{aligned} \tag{IV-8}$$

with the variables, dimensionless temperature, velocity and film thickness, introduced as

$$\theta = T/E \qquad u = u_1/(UN) \qquad z = x_3/h \tag{IV-9}$$

and the operational parameters of the problem combined as the dimensionless quantities

$$\begin{aligned} \pi_1 &= T_1/E & \pi_2 &= T_2/E \\ \pi_4 &= \eta_o (UN)^2/2k\,E & \pi_5 &= \tau h/\eta_o (UN) \end{aligned} \tag{IV-10}$$

The products π_4 and π_5 can be regarded as dimensionless velocity and shear stress parameters, respectively.

The Maximum Attainable Temperature and the Shear Stress

The assumptions imply that the film is convectionless and also that the direction of heat conduction is perpendicular to the film plane. Equation (IV-1) shows that the shear stress, τ and hence π_5, is constant through the

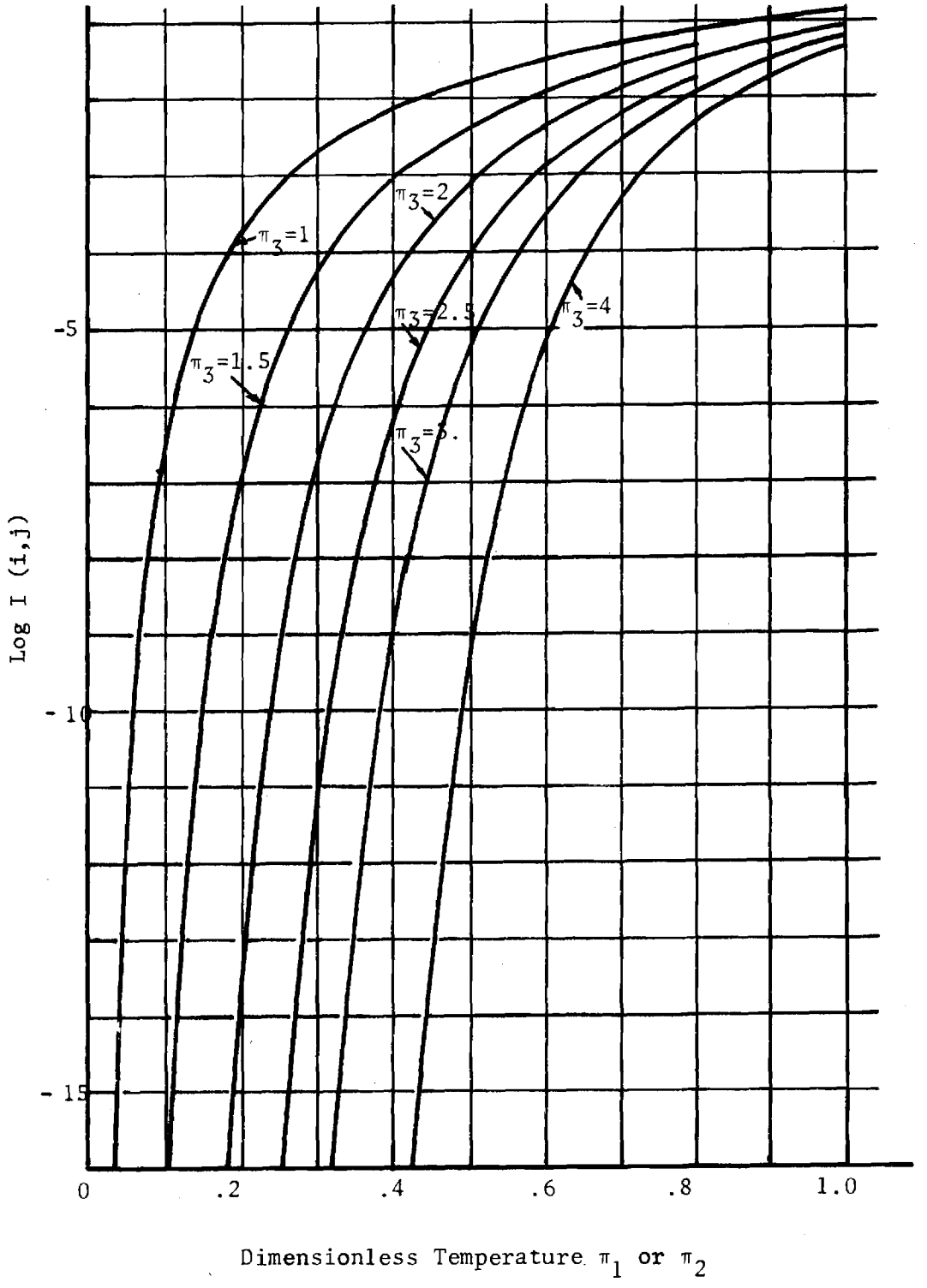

Figure IV-2 Determination of I(i,j) for Maximum Film Temperature.

film, because $\frac{\partial p}{\partial x_1}$ is assumed insignificant.

The local heat generation, due to viscous dissipation, is proportional to the shear rate, or film thickness, and the heat conduction is inversely proportional to thickness. The temperature distributions, and thereby the temperature extrema, are thus independent of the film thickness. The temperature profiles are symmetric about the adiabatic plane of the film. Considering the adiabatic plane located at the stationary surface is a good approximation for sliding elastohydrodynamic situations.

If we integrate equation (IV-7) across the film from the stationary (adiabatic) surface to some arbitrary location in the film, we obtain

$$\frac{\partial \theta}{\partial z} + 2\pi_4\pi_5 u = 0. \qquad \text{(IV-11)}$$

Substituting π_5 from equation (IV-6), rearranging and integrating across the film gives,

$$\pi_4 = \int_{\pi_2}^{\pi_1} \frac{d\theta}{\mu(\theta_1, \pi_3)} \equiv I(1,2) \qquad \text{(IV-12)}$$

By introducing an arbitrary base temperature $\pi_o < \pi_1$ or π_2 this can be written as

$$\pi_4 + I(2,0) = I(1,0) \qquad \text{(IV-12a)}$$

These integrals can be evaluated and graphically presented for a given viscosity function $\mu(\theta,\pi_3)$. For the particular viscosity function described above (equation (IV-4) or (IV-5)), these integrals are plotted in Figure IV-2.

The integrals, from π_0 to π_i, are plotted in the figure for π_3 = 1.0, 1.5, 2.0, 2.5, 3.0 and 4.0. Entrance to the diagram is through the lower temperature π_2. Intersection of the vertical line π_2 with the

appropriate interpolated π_3 value gives the value of the integral term I(2,0). The value of π_4 is added to I(2,0) which gives I(1,0) as shown in equation (IV-12a). Intersection of the horizontal line of I(1,0) with the appropriate π_3 value gives the desired π_1 of maximum temperature.

The displacement of the adiabatic plane to the stationary surface does not reduce the generality primarily because the film behavior is symmetric about the adiabatic plane. The film thickness does not participate in the determination of the maximum temperature. The influence of the temperature π_2 of the moving, cold wall, $\pi_2 < \pi_1$, on the magnitude of the maximum temperature π_1 is found in many situations to be of only minor importance because the temperature dependent integrand is small at low temperatures compared with the magnitude of the integrand when the temperature is near the maximum temperature. The maximum temperature depends therefore mainly on the velocity parameter π_4, the power exponent π_3 and the characteristic temperature E.

Auxiliary diagrams to determine the material properties π_3 and E from viscosity data for the lubricant are presented in an Appendix to this section. Approaches to the determination of the local temperature π_2 of the moving, colder bearing surface are found in Carslaw and Jaeger (24) 1962 which also contains further references to the original papers of Blok 1937 and of Jaeger 1942.

To obtain an expression for the shear stress in the case where the stationary wall is adiabatic we again substitute π_5 from equation (IV-6) into (IV-11) and integrate from the stationary wall to an arbitrary location in the film to obtain

$$\int_{\pi_1}^{\theta} \frac{d\xi}{\mu(\xi, \pi_3)} + \pi_4 u^2 = 0$$

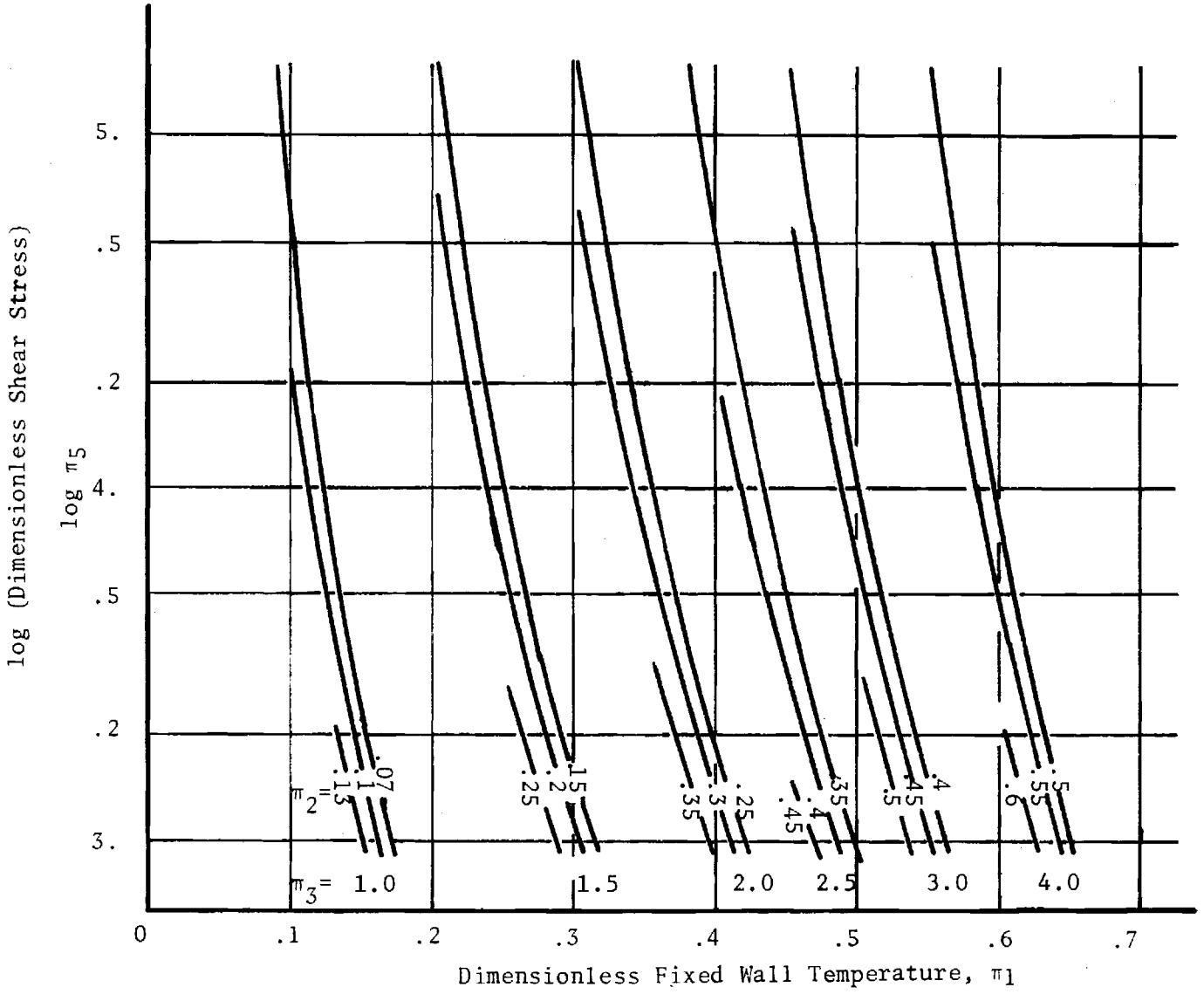

Figure IV-3. Determination of π_5. The Dimensionless Shear Stress.

which gives

$$u(\theta) = \frac{1}{\sqrt{\pi_4}} \left\{ \int_{\theta}^{\pi_1} \frac{d\xi}{\mu(\xi,\pi_3)} \right\}^{1/2} = \frac{1}{\sqrt{\pi_4}} \left\{ I(\pi_1,\theta) \right\}^{1/2} \qquad \text{(IV-13)}$$

Substituting (IV-13) into (IV-11) and integrating from one surface to the other and rearranging yields,

$$\pi_5 = \frac{1}{2\sqrt{\pi_4}} \int_{\pi_2}^{\pi_1} \left\{ I(\pi_1,\theta) \right\}^{-1/2} d\theta = \pi_5(\pi_1,\pi_2,\pi_3) \qquad \text{(IV-14)}$$

which is the dimensionless shear stress.

The dimensionless shear stress, π_5, depends on three dimensionless parameters only, π_1, π_2, π_3 . The dimensionless velocity parameter π_4 depends on the same set of parameters through equation (IV-12).

Thus the shear stress π_5 of equation (IV-14) depends on the same operational quantities as the maximum temperature of the film. The shear stress τ depends also on the film thickness h. Information about the thickness must be available, from measurements or from calculations, in order to determine the shear stress.

The dimensionless shear stress function, equation (IV-14), can be evaluated and graphically presented for a given viscosity function $\mu(\theta,\pi_3)$. For the particular viscosity function mentioned above (equation (IV-4) or (IV-5)), the function π_5 has been evaluated and plotted in Figure IV-3. It shows the presentation for π_3 = 1.0, 1.5, 2.0, 2.5, 3.0, and 4.0, and for appropriate π_2 values. The range of π_5 in the figure covers the expected operation of elastohydrodynamic films.

The interpolation procedure can be carried out as shear stress determinations for two slope exponents, π_3, of the diagram values which are nearest to the π_3 exponent of the lubricant. A straight line between the two determined stress values, π_5, will intersect with the actual π_3 curve of the lubricant and give an approximation to the desired dimensionless shear stress π_5 of the film. The shear stress can then be calculated from equation (IV-10).

The traction coefficient is determined as the summation of the shear stress distribution over the contact area. The traction coefficient may be determined also in the case of non-adiabatic walls using the symmetry properties of the film. The temperatures of the walls, Figure IV-1, must be estimated, (24). The dimensionless velocity of the adiabatic plane is found as $u_a = 1/2 + (I(2,1)/2\pi_4)$. The two parts of the film, divided by the plane, are considered individually assuming the relative velocity, with respect to the adiabatic plane, contained in two new velocity parameters. Iteration for the two parts of the film with the diagram, Figure IV-3, may be continued until satisfactory agreement with the wall temperatures is achieved.

Conclusions

The shear stress and the temperatures in the high pressure part of a sliding elastohydrodynamic point or line contact can be determined directly with the design charts presented. The applicability is dependent on 1) the ratio of the shear stress due to the pressure gradients to the shear stress due to sliding and 2) the ratio of heat convection along the film to heat conduction perpendicular to the film plane. The

accuracy of the procedure is best where these ratios are small, << 1. This is the case over 80 - 90% of the Hertzian area in elastohydrodynamic contacts where the major part of the sliding traction is generated. The procedure is not valid for hydrodynamic lubrication or to inlet-exit zones of elastohydrodynamic contacts.

Table IV-1

NOMENCLATURE

E	Lubricant material parameter, the temperature (K) at which the viscosity is 2.718×10^{-3} Nsm^{-2}
h	film thickness, m
$I(i,j) \equiv \int_{\pi_j}^{\pi_i} (\mu(\xi,\pi_3))^{-1} d\xi$	
k	Thermal conductivity of lubricant, $wm^{-1}K^{-1}$
p	Pressure, Nm^{-2}
T	Temperature, K
T_o	Arbitrary base temperature, K
UN	Velocity of moving surface in x_1 direction, ms^{-1}
u_1	Velocity of fluid in x_1 direction, ms^{-1}
u	Dimensionless velocity, u_1/UN
x_1, x_3	Dimensioned coordinates, m
x, z	Dimensionless coordinates, $\frac{x_1}{h}$ and $\frac{x_3}{h}$ respectively
η	Viscosity, Nsm^{-2}
η_o	Dimensional constant = 10^{-3} Nsm^{-2}
η_{38}	Viscosity at 38C, Nsm^{-2}
η_{100}	Viscosity at 100C, Nsm^{-2}
θ	Dimensionless temperature = T/E
μ	Dimensionless viscosity = η/η_o
π_1	Dimensionless fixed wall temperature = T_1/E
π_2	Dimensionless moving wall temperature = T_2/E

π_3 Dimensionless lubricant material parameter

π_4 Dimensionless velocity parameter = $\eta_o (UN)^2 (2kE)^{-1}$

π_5 Dimensionless shear stress parameter = $\tau h(\eta_o (UN)^{-1} = \mu \frac{\partial u}{\partial z}$

τ Shear stress, Nm^{-2}

APPENDIX IV-A

Method of Determining Constants for Viscosity-Temperature Relationship, Eq. (IV-4)

Figures IV-A1, IV-A2 and IV-A3 are prepared in order to facilitate the determination of π_3 and E. Figure A1 shows the slope parameter π_3 as a function of the viscosities $\eta_{38}|_p$ and $\eta_{100}|_p$. Entrance to the figure is the two viscosities measured at constant pressure, at the temperature of 38C and 100C, in the units of Nsm^{-2}. An ASTM chart (D 341-43) or similar charts may be used to determine the viscosities η_{38} and η_{100} if existing data were at other temperatures. Figures IV-A2 and A3 show the temperature E, in Rankine and Kelvin as function of η_{38} and π_3. Figure IV-A2 gives relatively high resolution for lubricants with the slope parameter π_3 in the range 1 to 2. Figure IV-A3 gives relatively high resolution for lubricants with the parameter π_3 in the range 2 to 4.

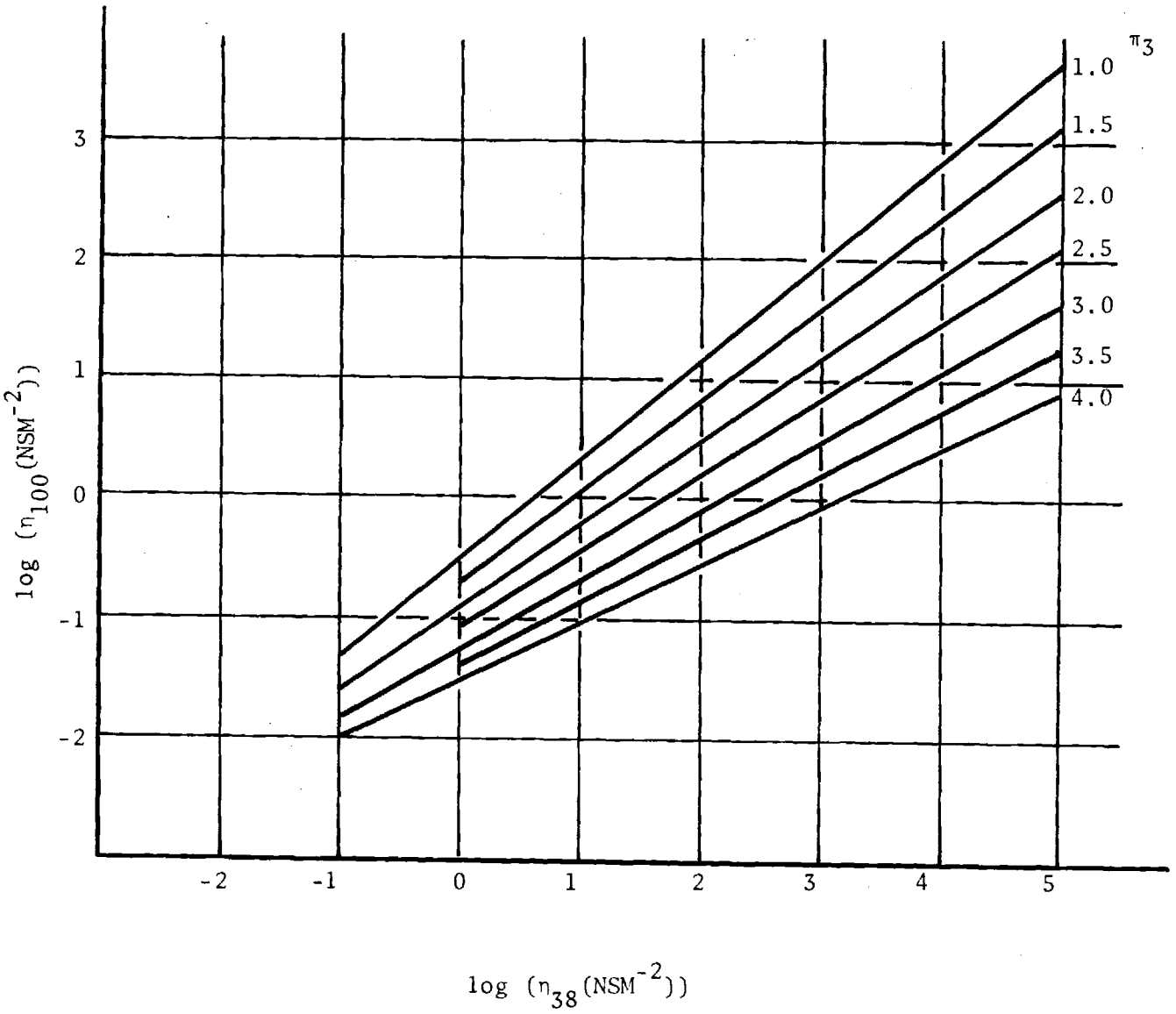

Figure IV-A1. The Temperature Viscosity Coefficient π_3.

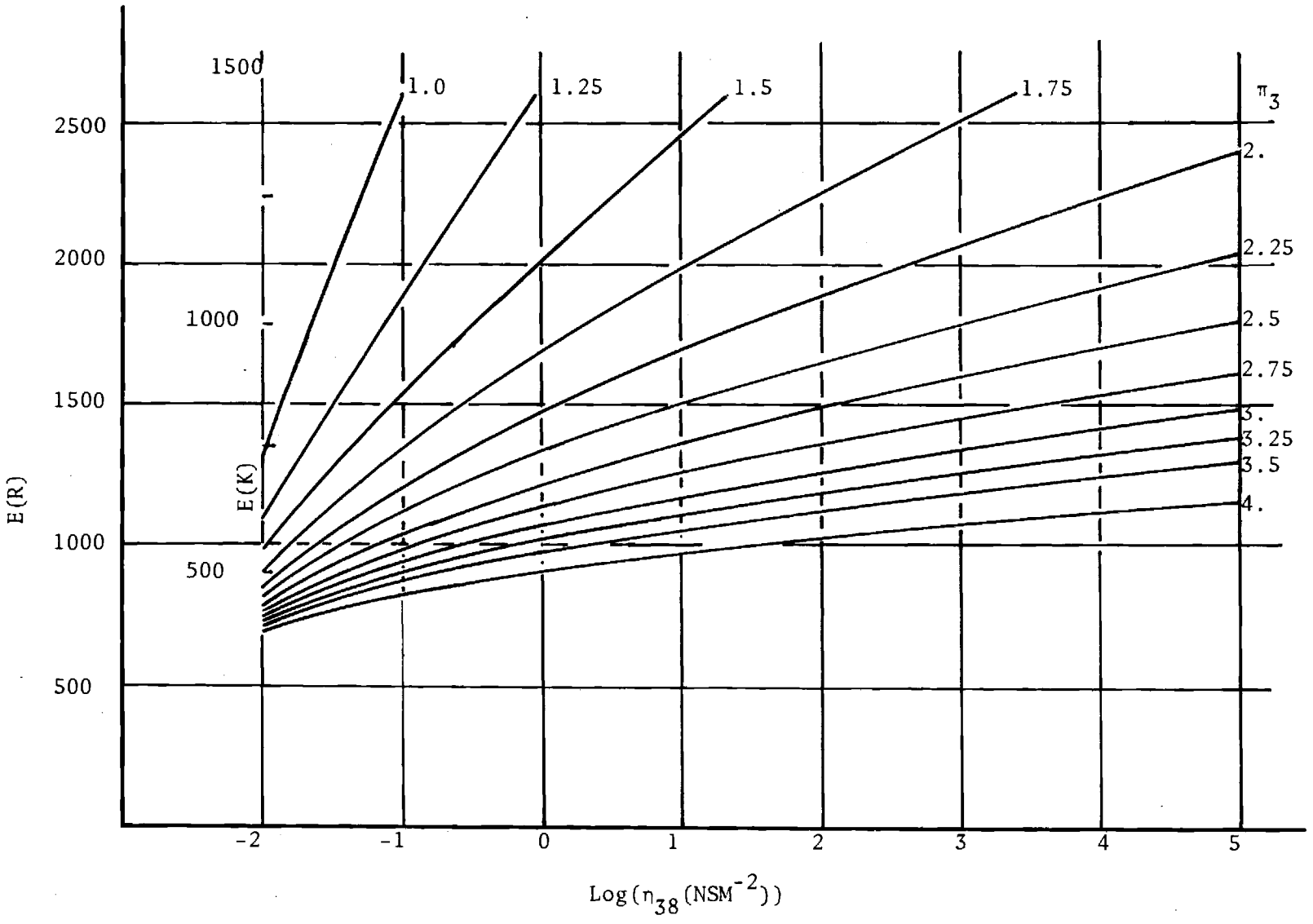

Figure IV-A2. The Temperature E (R or K).

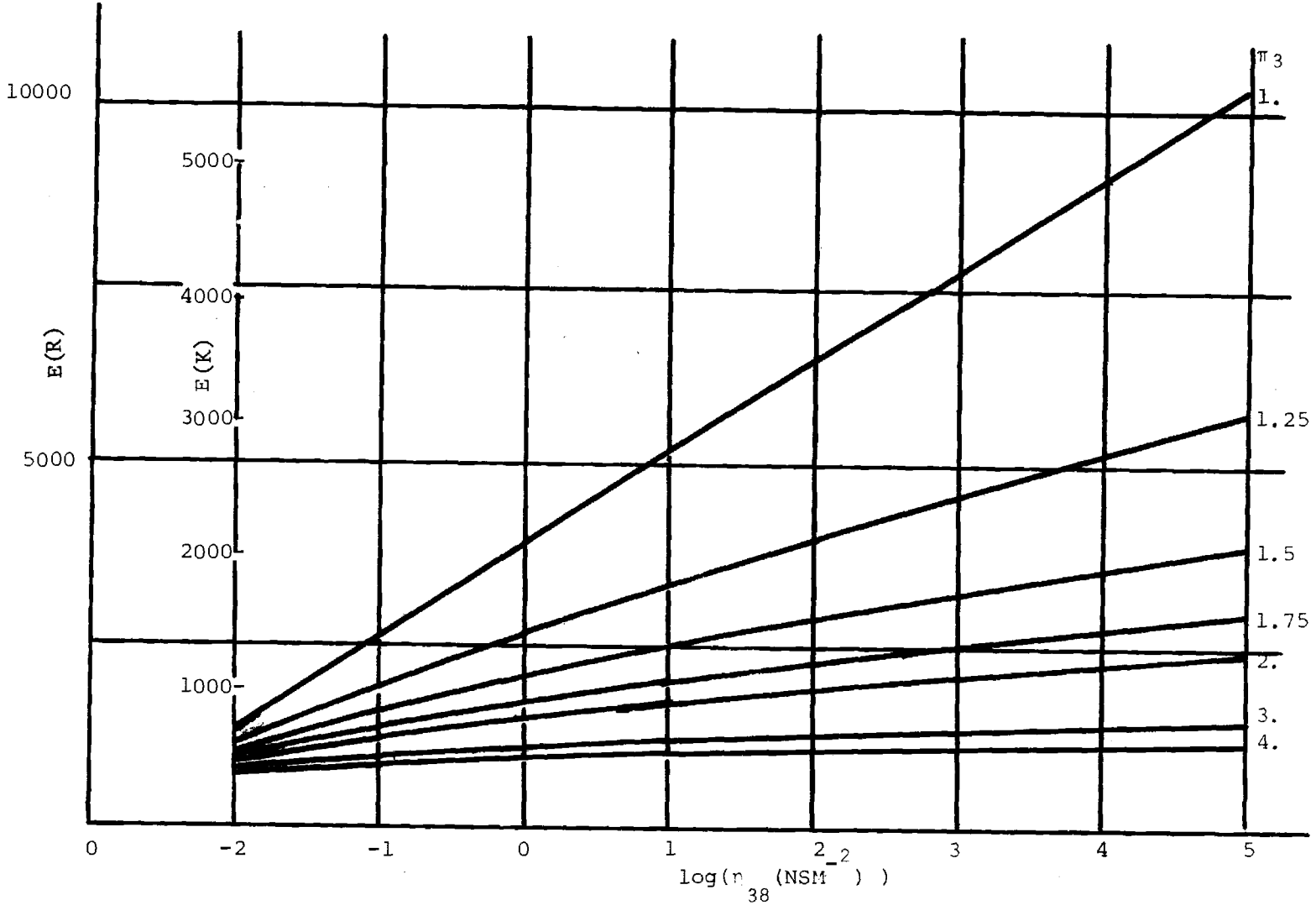

Figure IV-A3. The Temperature E (R or K).

V. Elastohydrodynamic Analysis of Rolling and Sliding Cylinders with a General Viscous Fluid.

During the past year pressure distributions have been obtained for elastic cylinders and a linear fluid under moderate loads. The results cover a range of viscosity-pressure coefficients, $\alpha \equiv \frac{1}{\mu}\frac{\partial u}{\partial p}\Big|_{T,p=atm.}$ from 0.0 to 1.4×10^{-8} m^2/N (from 0.0 to 1.0×10^{-4} psi^{-1}). This transition region is now well-explored. Several observations are of interest. First, the centerline film thickness actually increases with increasing load over certain ranges of load and α. As expected the minimum film thickness does decrease. This may explain the difficulty of some investigators in obtaining pressure distributions in the transition region. Second, secondary maximums are noted at heavy loads and intermediate values of the viscosity-pressure coefficient. The primary maximum or "spike" is formed first. However, the "spike" is not sharp. Third, at heavy loads and large values of the viscosity-pressure coefficient, sharp "spikes" occur but no secondary maximum is observed. Some special consideration of this "spike" appears necessary to efficiently continue the computation of distributions at heavy loads. In summary, however, it is important to note that the solution technique has proven adequate for the problem and has allowed the resolution of detail of the pressure distribution without special assumptions.

Previous reports have detailed the theory and solution technique employed on this project (1). Effort during the past year has been expended in the computation of specific distributions. The results cover behavior of the system up to heavy loads and large values of the viscosity-pressure coefficient. The specific system parameters are given

in Table V-I.

Figures V-1 and V-2 describe the behavior of the system parameters of most practical interest. The centerline film thickness is taken as the independent parameter and both the exit coordinate and the load are plotted as dependent parameters for various indicated values of the viscosity-pressure coefficient. The variation of both the exit coordinate and the load is no longer monotonic at larger values of the viscosity-pressure coefficient. This phenomenon was unexpected but appears reasonable upon reflection on the actual process of deformation. The dependent parameters remain monotomic if plotted against the minimum film thickness as independent parameter.

Figures V-3,4,5 and 6 indicate the behavior of the pressure distribution and the film thickness distribution. Any solution is similar to one of these basic types of distributions. Figure V-3 shows a lightly loaded case with little deformation. Figure V-4 shows a heavily loaded case with a small value of the viscosity-pressure-coefficient. No secondary maximum is observed and the primary maximum is the Hertzian maximum. Figure V-5 shows a heavily loaded case with a moderate value of the viscosity-pressure coefficient. A second maximum does occur. This is the upstream maximum and is the Hertzian maximum. The primary maximum, i.e., the absolute maximum, appears to develop into the "spike" but is not sharp. In loading the system from light loads, the primary maximum is always present and the secondary maximum develops only at heavy loads. This is again unexpected but not unreasonable. Figure V-6 shows a moderately loaded case with a large value of the viscosity-pressure coefficient. No secondary maximum is observed but the primary maximum has become a "spike" and is sharp. Increased loading will probably produce a secondary maximum, and the resulting distribution

composed of a sharp primary maximum and a rounded secondary maximum would correspond to other computations (25).

Although this investigation is yet incomplete, the solutions obtained indicate unexpected behavior which must be accounted for in any study of the transition region from light to heavy loads. Such behavior introduces significant computational difficulty and may have impeded research in this area. Use of the solution technique developed in this project and the introduction of some special techniques where necessary yields accurate results in all cases. Computations are now being extended to heavier loads and to consideration of nonlinear viscous fluids. The introduction of a nonlinear viscous fluid generally reduces the value of the primary maximum and facilitates computation.

Table V-1

Radii of both cylinders	4.00 in.	1.02×10^{-1} m
Velocity of both cylinders	1.00×10^{2} in/s	2.54 m/s
Modulus of elasticity of both cylinders	3.00×10^{7} psi	2.07×10^{11} N/m^2
Poisson's ratio of both cylinders	0.333	0.333
Base density of lubricant (considered incompressible)	3.25×10^{-2} lbm/in^3	9.02×10^{2} kgm/^{3}
Base viscosity of lubricant (considered linearly viscous)	2.00×10^{-5} lbf.s/in^2	1.38×10^{-1} N.s/m^2

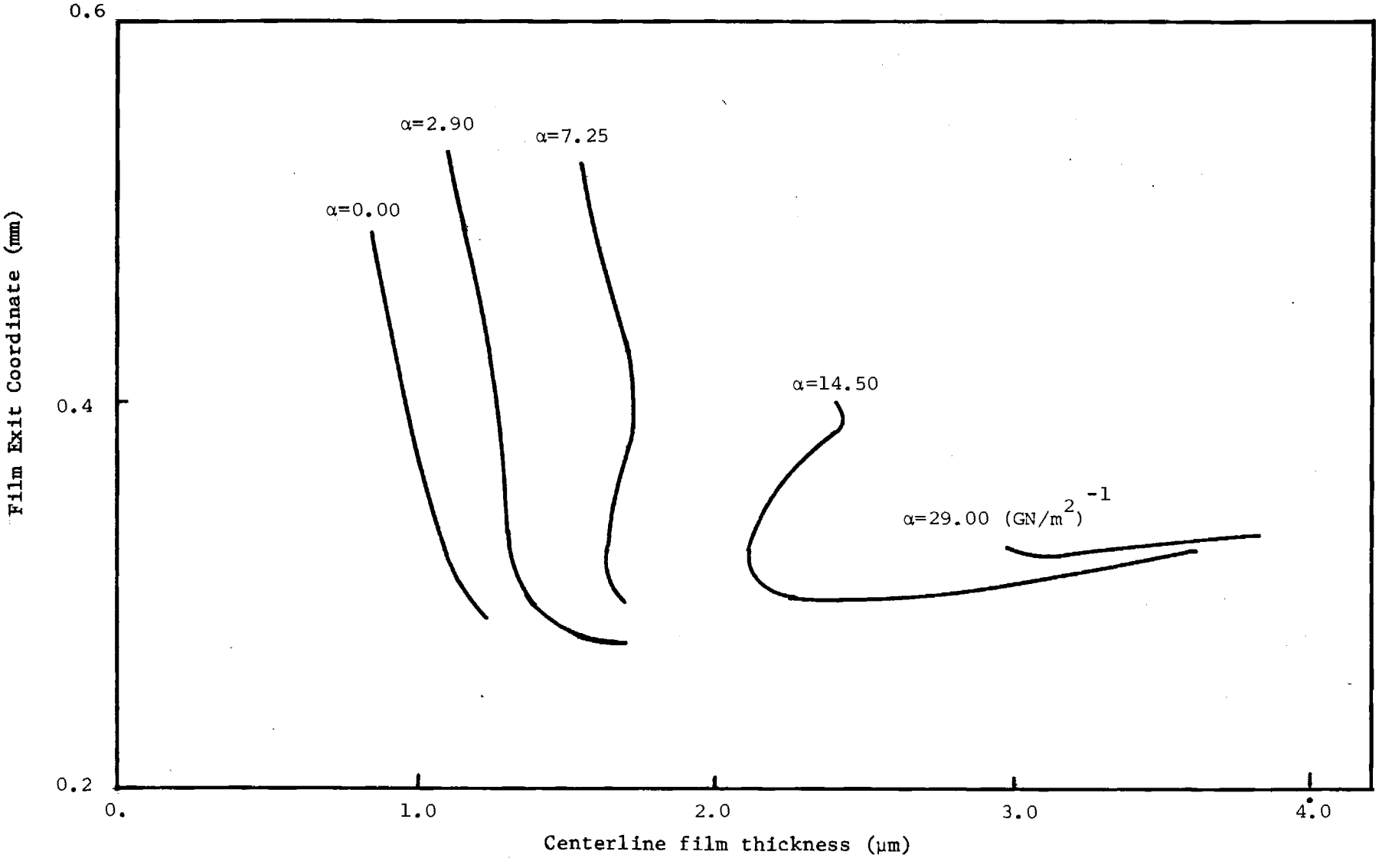

Figure V-1. Exit coordinate vs. Centerline Film Thickness for Various Viscosity-Pressure Coefficients, α.

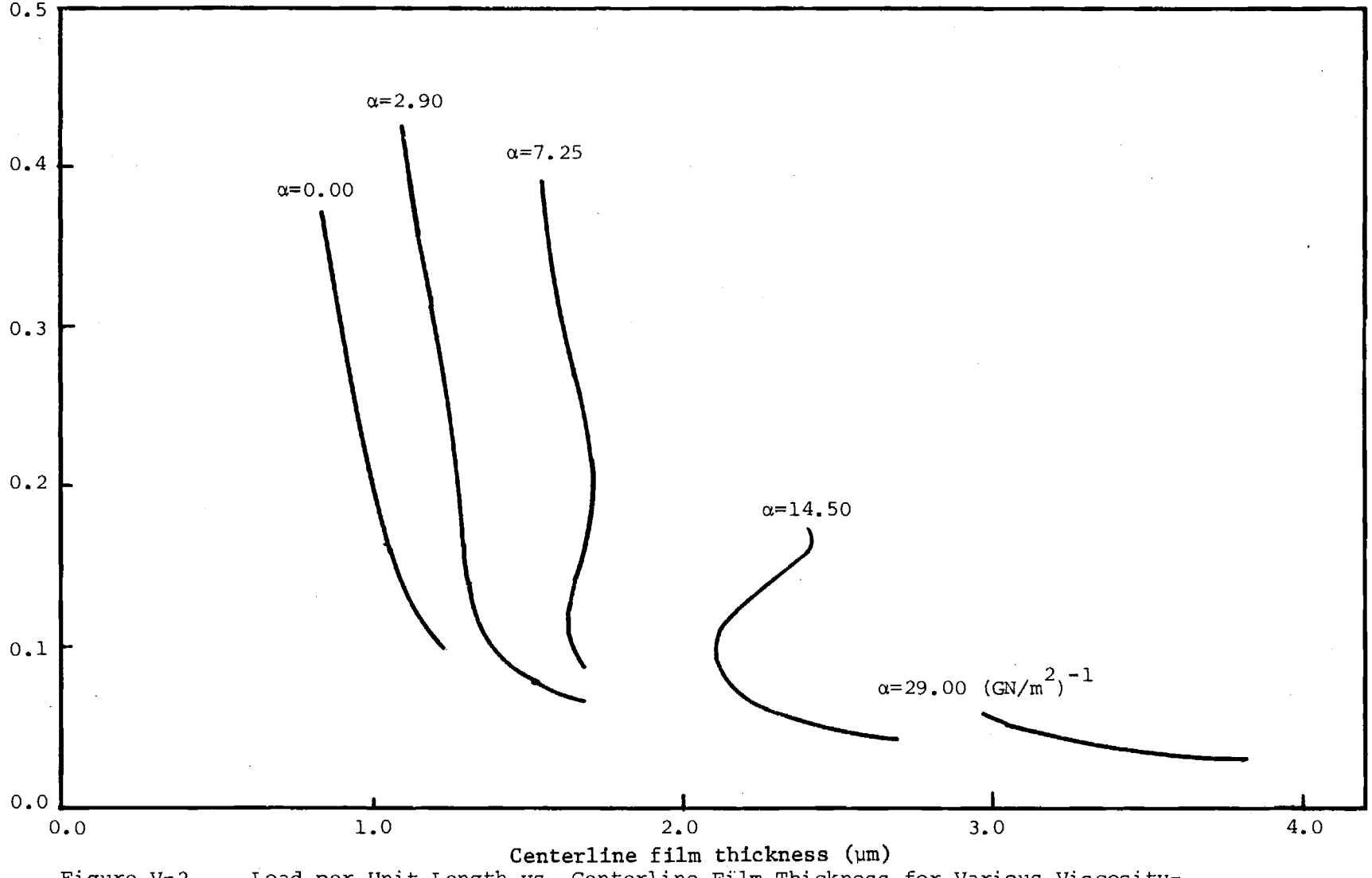

Figure V-2. Load per Unit Length vs. Centerline Film Thickness for Various Viscosity-Pressure Coefficients.

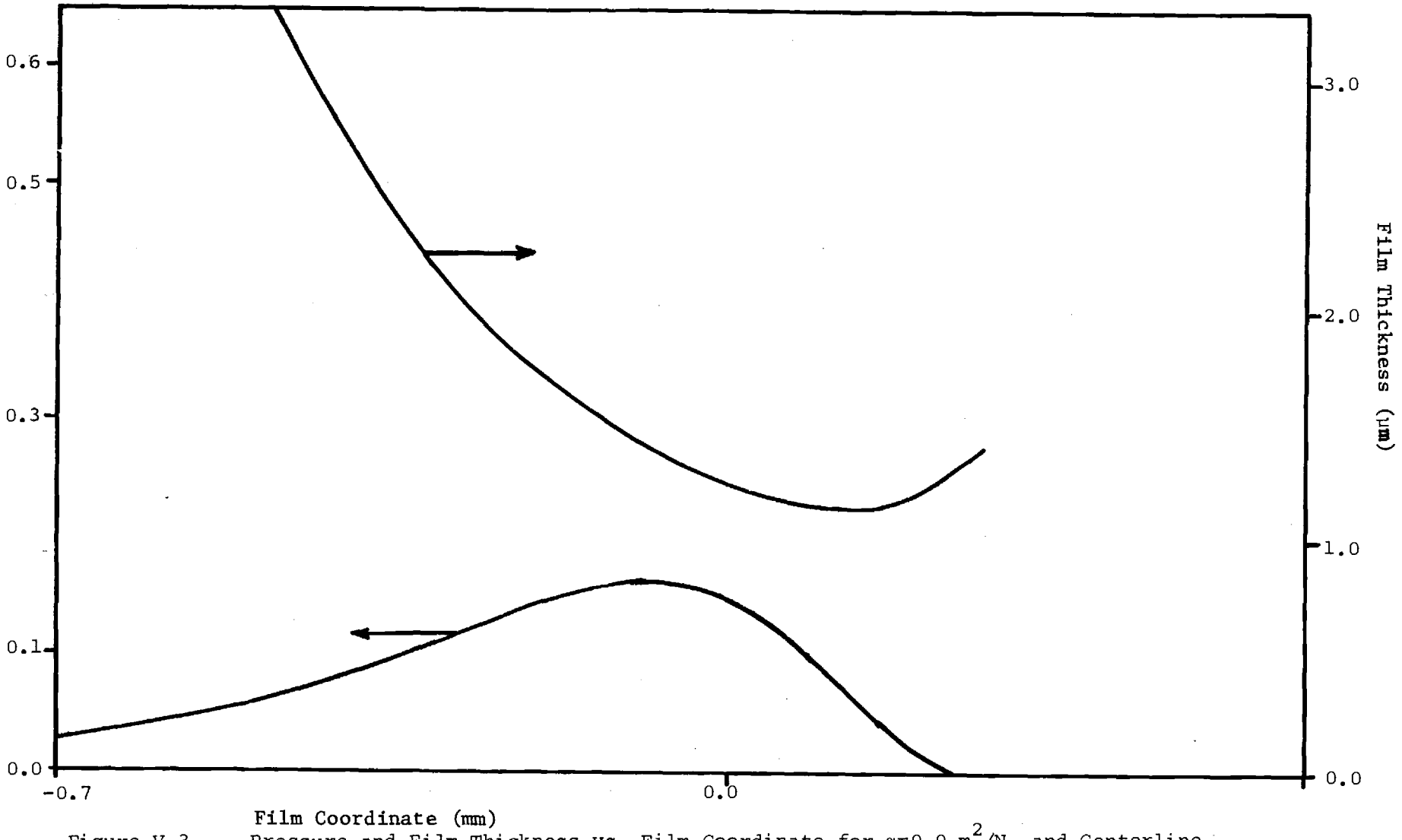

Figure V-3. Pressure and Film Thickness vs. Film Coordinate for α=0.0 m^2/N, and Centerline Film Thickness of 1.22 μm.

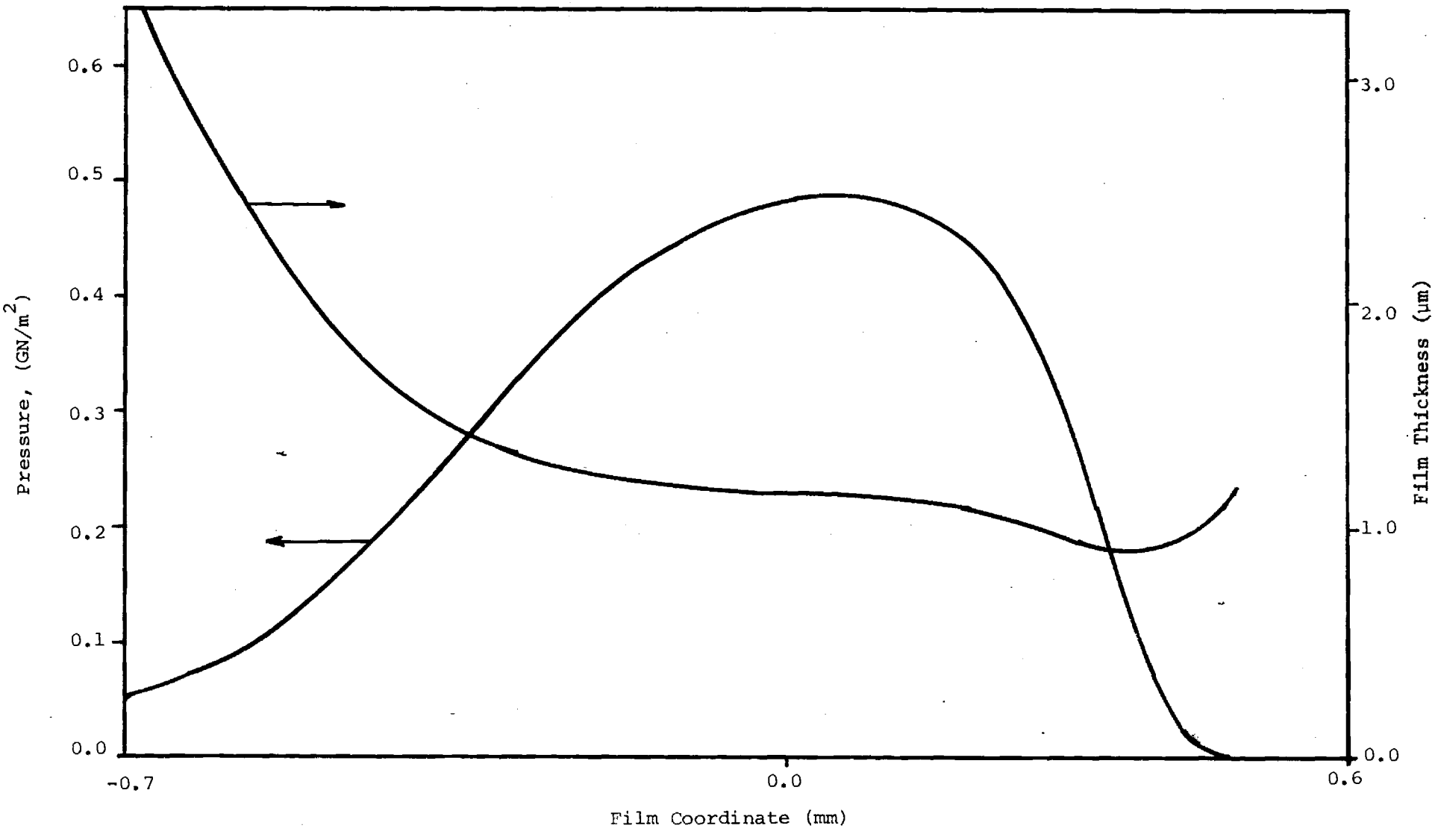

Figure V-4. Pressure and Film Thickness vs. Film Coordinate for $\alpha=2.90(GN/m^2)^{-1}$, and centerline film thickness of 1.14 μm.

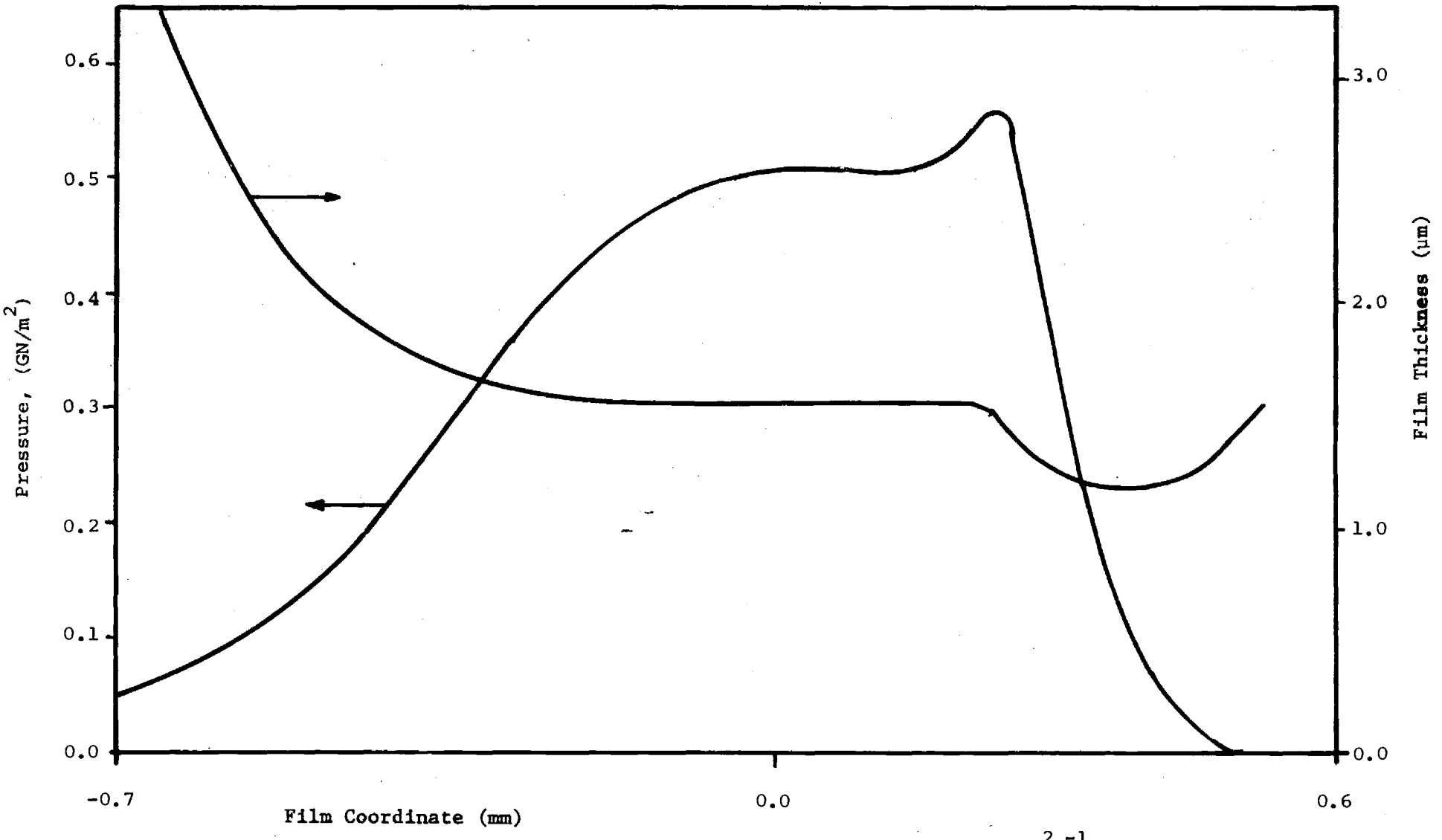

Figure V-5. Pressure and Film Thickness vs. Film Coordinate for α=7.25(GN/m^2)$^{-1}$, and centerline film thickness of 1.53 μm.

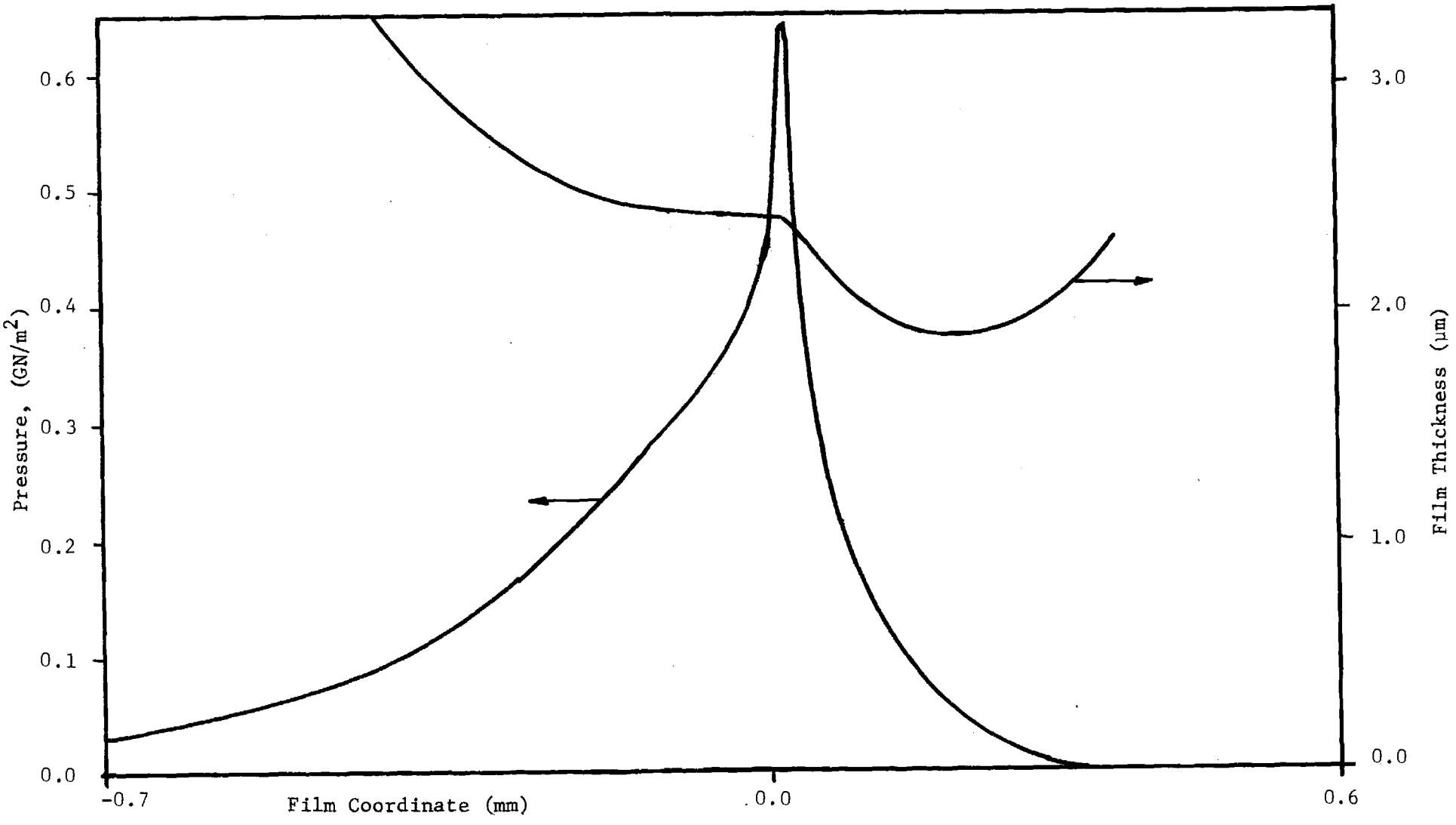

Figure V-6. Pressure and Film Thickness vs Film Coordinate for α = 14.5 $(GN/m^2)^{-1}$ and Centerline Film Thickness of 2.41μm.

VI. Dynamics of Roller Bearings Considering Elastohydrodynamic Forces.

Consistent with the goal of applying recent research findings to problems of concern to the designer, an analytical investigation was undertaken to model the behavior of a roller bearing considering EHD forces. An understanding of the dynamics of an individual roller might explain certain modes of failure.

The life and load carrying capacity of roller bearings are highly influenced by the sliding velocities at the contacts between rollers and races. In this investigation a computational model was developed to predict traction forces, forces on the cage and the sliding and spinning speeds of the rollers when the bearing is lubricated with a fluid of known traction characteristics as a function of pressure and velocity. The model takes into account the actual operating conditions of bearings. Furthermore, it may be used at high speed and/or low loads as well because the centrifugal force effects are considered.

Results given by the model when applied to a 65 mm roller bearing lubricated with XRM-109, a synthetic oil, predict that for a given set of working conditions, if the shaft speed is continuously increased, the cage speed increases up to a maximum value and then it decreases. The model also predicts the influence of cage speed and load variations on working characteristics of interest such as lubricant film thickness, elastic deflections and spinning speed of the rollers.

Many analytical and experimental investigations on this topic have been done. However, some of the recently published papers [26-29] analyze and present solutions to this problem which are valid under circumstances

not always found in practical applications. Poplawski [28] and Rumbarger, et al. [29] presented solutions considering that the cage is stationary (or with load rotating at cage speed). This assumption is consistent with Bonnes's [27] measurements of spinning speeds, but it is not representative of the normal practice wherein the load is stationary while cage and rollers rotate.

Two main characteristics of the model used in this investigation make it quite different from previous approaches:

(a) The load and outer ring of the bearing are considered stationary while the cage and inner ring rotate. As the rollers are moving with the cage, the spinning and acceleration of a roller at a given position is no longer zero. This acceleration depends on the traction forces at the contacts which in turn are determined by the radial load and the velocities. As radial forces are a function of the radial position of the roller, the acceleration will be some function of the position if the bearing is in steady state. Using this approach, the spinning speed of the roller is a periodic function of its position.

(b) Due to the movement of cage and rollers in a fluid, there exists a drag force which tends to accelerate the cage. The magnitude of the drag force depends on many factors: geometry, cage speed, temperature, fluid surrounding the moving element, etc. It is very difficult to estimate this drag accurately. In this work a varying drag coefficient is used to determine a functional relation between cage drag and cage speed, so that if the proper drag coefficient is known for a given application, the operating velocities may be found and conversely. The cage force calculated using Rumbarger's model [29] was also used.

The main assumptions and limitations under which this work is carried out are listed below, although some others will be stated when used in the

derivations below:

1. Imbalances and geometric imperfections are negligible.
2. Clearance between roller and cage is zero.
3. Cage is not accelerated at any moment.
4. Outer ring and load are stationary or they rotate at the same speed, and the reference system is fixed on the outer ring.
5. The fluid has an exponential pressure - viscosity relation.
6. The assembly clearance between rollers and races are known.
7. The working temperatures of inner and outer rings and assembly temperatures are known. These temperatures determine the working clearance.
8. The friction between rollers and cage is of the Coulomb type.
9. Dowson and Higginson's [30] elastohydrodynamic relations among U, V, G, W and traction forces are accepted at low Hertzian pressures.
10. Higginson's expression for the film thickness is modified as proposed by Cheng [31] to take into consideration the oil temperature rise through the contact. Side leakage is negligible.
11. The load sharing among rollers is determined by the elastic deformations, their compatibility and the static equilibrium conditions.
12. Velocities and accelerations of the axes of the rollers are the same as the centroidal line of the cage.
13. The spinning speed of the rollers is not affected by drag forces from the surrounding gases.

Force Analysis

According to assumption 11, the part of load taken by each roller is determined by considering the elastic deformation of the rollers and races,

the condition of static equilibrium and the geometrical compatibility of the deformations. Following the development of Harris [32], it can be shown [33] that due to an applied load P, there results a set of equations to be solved simultaneously relating loads and deflections of each roller. The number of equations to be solved is one greater than the number of rollers in the bearing. The initial clearances in the bearing were determined on the basis of given unmounted bearing clearances, standard mounting practices and operating temperatures of 88C (190 F) and 65C (150 F) at the inner and outer races respectively.

As the roller speed changes during a revolution, so do the forces between roller and cage which may change in both magnitude and direction. These forces cause friction which is assumed to be of the Coulomb type. It is also assumed that the sum of all radial friction forces on the cage is zero.

For the steady state operation of the bearing it may be assumed that the cage is not accelerated. On the average this is true, and it is also true at least Z times (the number of rollers) in each revolution. For an asymmetric position of the rollers in respect to the load, the load distribution and the traction force distribution is also asymmetric. This fact may cause some accelerations on the cage. In any case, these accelerations must be periodic.

The dimensionless groups and film thickness relation proposed by Dowson and Higginson [30] and modified by Cheng [31] to account for side leakage and thermal effects were used exclusively. In addition, an exponential pressure viscosity relation for fluid XRM-109 with a Hertzian pressure distribution was assumed.

The selection of the proper model to estimate the traction forces at the contacts presented some difficulties due to the lack of a theory or

correlation simple enough to be handled effectively. In the course of the investigation two models were used to calculate the forces between rollers and races: the first one used current EHD theory, while the second model was the result of a correlation made of the data published by Trachman and Cheng [34] for the fluid XRM-109. The traction formula proposed by Dowson and Higginson [30] predicts unrealistically high traction forces for most of the higher contact pressures of interest. Therefore, when the radial loads on a roller reached a predetermined point (60,000 psi), the experimental data [34] was used.

Roller Bearing Dynamics

The goal of this work is to determine the velocities of all elements in the bearing. Throughout the analysis, it was assumed that the outer ring was stationary. A cage speed N_c was then selected, from which individual roller speeds N_j and an inner ring speed N were deduced. From an analysis viewpoint, this was considerably easier than starting with N and deducing N_j and N_c. Expressions were writeen for the rolling and sliding velocity component at the EHD contact formed by the roller and outer race as well as that formed at the inner race in terms of a given N_c and unknowns N_j and N.

The forces on an individual roller acting in the radial direction with respect to the outer ring include:

a). A centrifugal component depending only on N_c.

b). A Coulomb friction component between roller and cage, depending on the contact force at this interface.

c). The radial component of the normal load at the outer race contact.

d). The radial component of the normal load at the inner race contact.

The forces on an individual bearing acting perpendicular to the above

forces include:

a). The traction force at the outer race contact.

b). The traction force at the inner race contact.

c). The tangential component of the normal load at the outer race contact.

d). The tangential component of the normal load at the inner race contact.

e). The normal force between roller and cage.

An unbalance in the torques resulting from these forces will cause an angular acceleration of the roller.

Method of Solution

Obtaining the roller spinning speeds and the inner ring speed requires the use of successive approximations because the forces and accelerations are functions of the velocities desired. In the present study the spinning speed acceleration for a given roller (at a given position) is not equal to zero, but is constant at each position if the bearing is in a steady state, as it is assumed. The change in acceleration from one position to another must be such that the new velocity and acceleration in the new position be the result of the previous values. Furthermore, this change must be continuous and periodic with a period equal to that of the cage.

The following is a summary of the algorithm used in this investigation.

1. The radial load distribution was obtained for a given applied load and cage speed.
2. The system velocities were determined from -
   a) assuming a roller velocity at a position directly under the applied load, tangential forces and then angular acceleration

are calculated. The roller velocity at an incremental change in position is then known from this acceleration and previous velocity. The acceleration integration continues, step by step through a complete revolution. Keeping the first value constant, this routine is repeated until the change in the last value of N_j between two successive iterations is less than 0.01 percent.

b) when the above loop converges, the initial value of roller velocity previously held constant is changed using a successive replacement method [10-12] and the loop of part a is repeated. This outer loop is repeated until convergence is obtained for an initial roller speed.

c) the spinning speed distribution found above is the correct one only if it results in a cage drag and the resultant of $\underline{z}$ cage/roller contact forces being in equilibrium. In general, this requires that the inner ring velocity be changed and the above two loops repeated until convergence is obtained.

3. The friction forces between roller and cage are now included. Their effect on steps 1 and 2 above is small.

Analysis of Results

The particular roller bearing used in this investigation is described in Table VI-1.

Table VI-1. Bearing Characteristics

Bore diameter	65.0 mm
Outer diameter	140.0 mm
Width	33.0 mm
Number of rollers	12
Roller diameter	21.0 mm
Roller length	17.0 mm
Pitch diameter	102.5 mm

The bearing was operated using lubricant XRM-109 at seven radial loads 890 - 10,675 N (200 - 2400 lbf) and at nine different cage speeds (400 - 6000 rpm).

Figures VI-1 - 3 show the two forces acting on the roller cage as a function of slip. Slip is defined as the ratio of actual cage speed to epicyclic (zero sliding) cage speed minus 1.0. For steady state operation the driving and drag forces must be equal. Note that the driving force, which is a result of traction in the EHD contact, is primarily a function of slip and load whereas the drag force is a function of cage speed. It is also interesting to note that in many cases two operating points are possible. In Figure VI-2b for example, the cage can be in equilibrium at approximately 1% or 3% slip at a 5338 N (1200 lbf) load. The inner race speed N needed to produce a certain slip at a given cage speed is also shown.

Figure IV-4 is a plot showing the locations of the peaks in the curves shown in Figures VI-1 - 3 in terms of slip and inner ring speed. Therefore, for a given load, the driving force remains essentially constant with increasing inner ring speed (Figures VI-1 - 3), but occurs at decreasing amounts of slip (Figure VI-4).

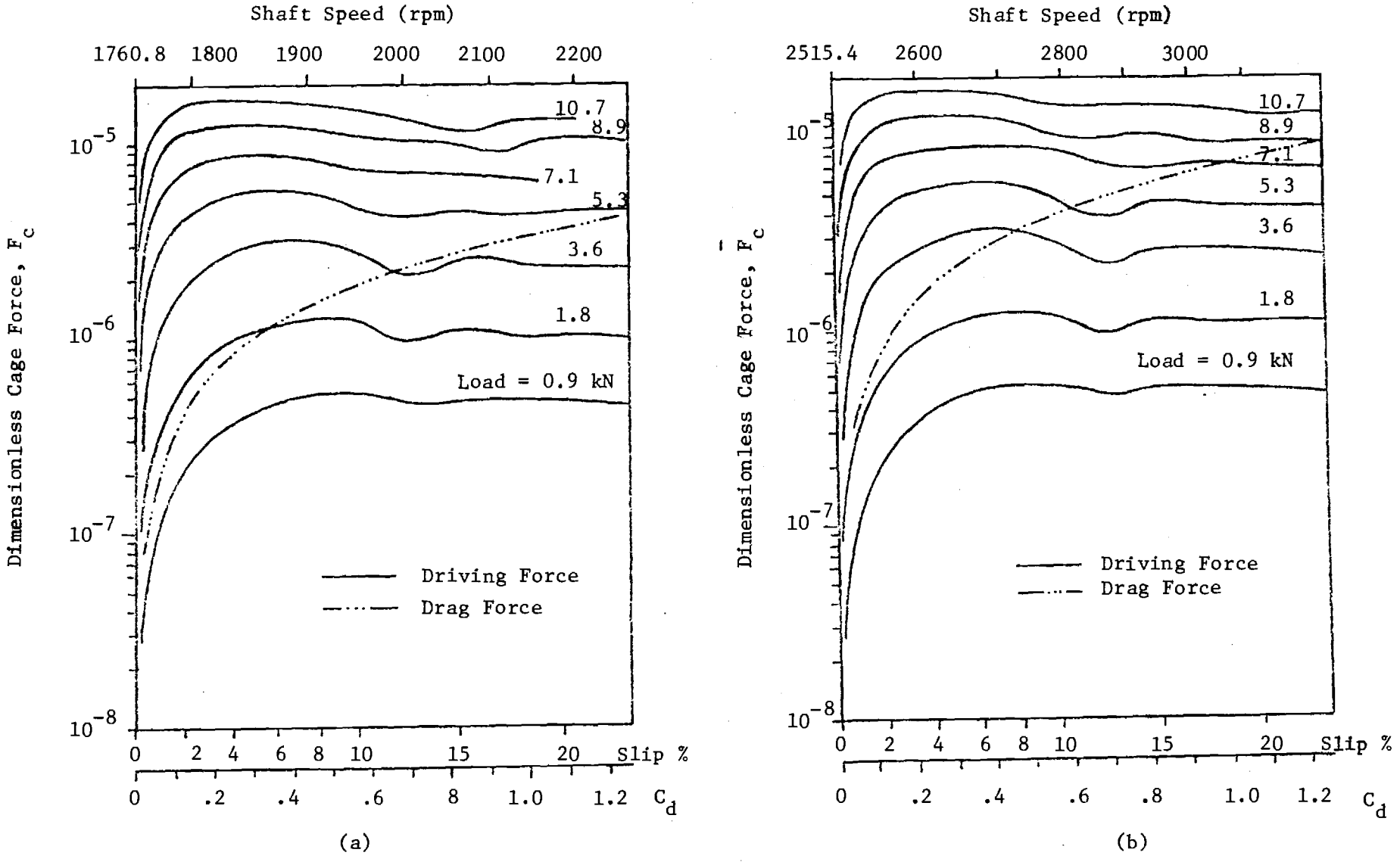

Figure VI-1. Cage and Drag Forces. Cage Speed is (a) 700 rpm, (b) 1000 rpm.

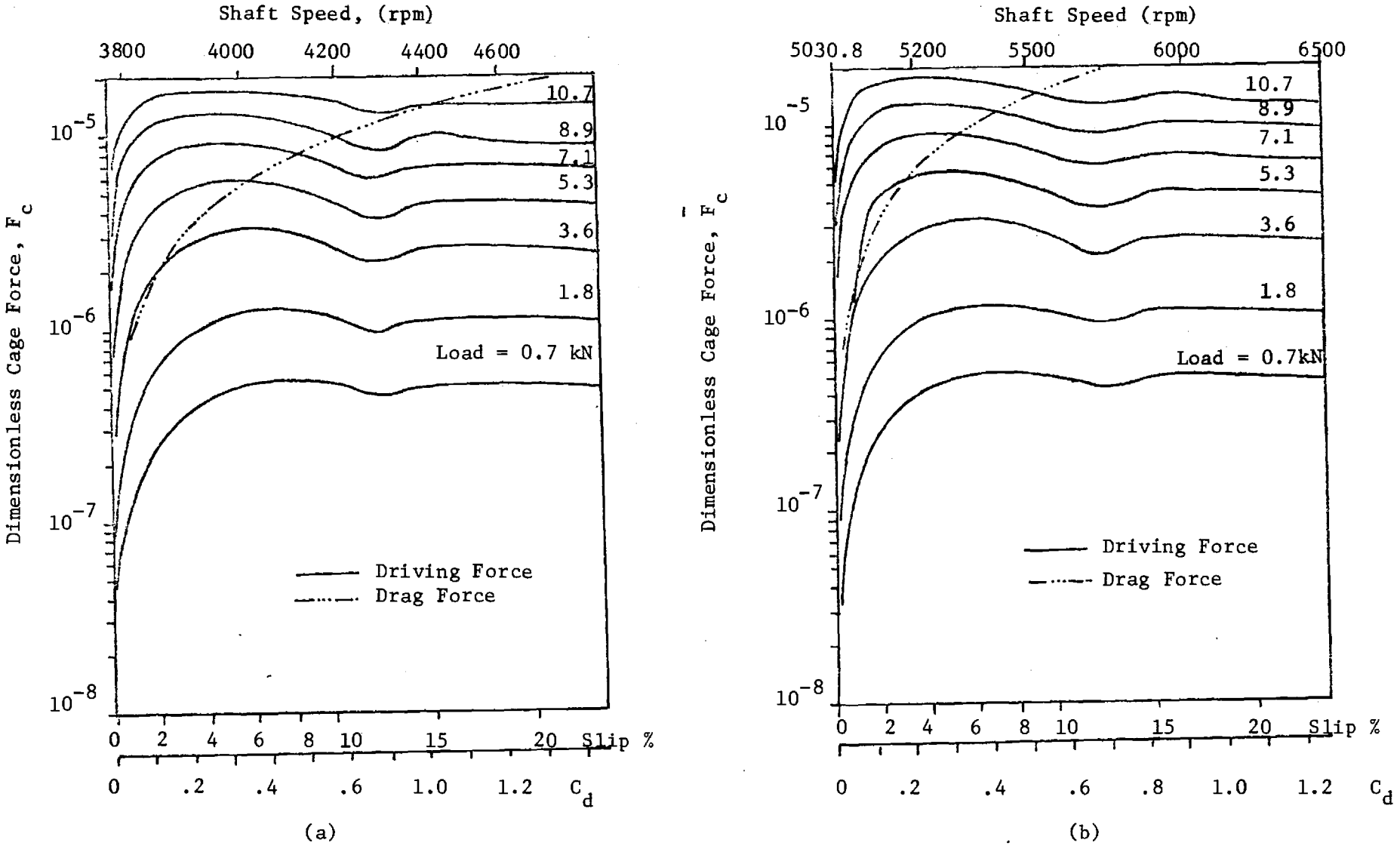

Figure VI-2. Cage and Drag Forces. Cage Speed is (a) 1500 rpm, (b) 2000 rpm.

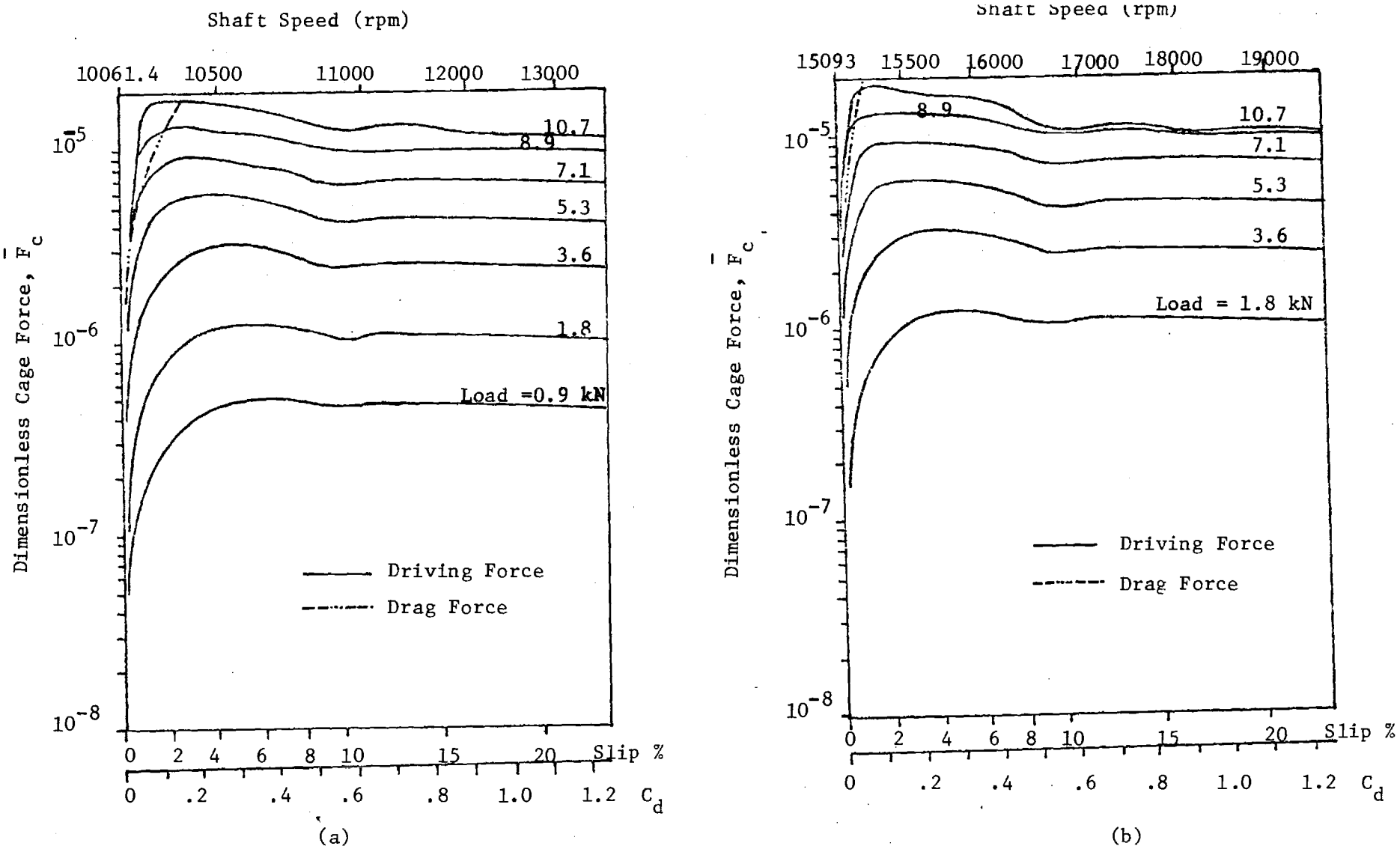

Figure VI-3. Cage and Drag Forces. Cage Speed is (a) 4000 rpm, (b) 6000 rpm.

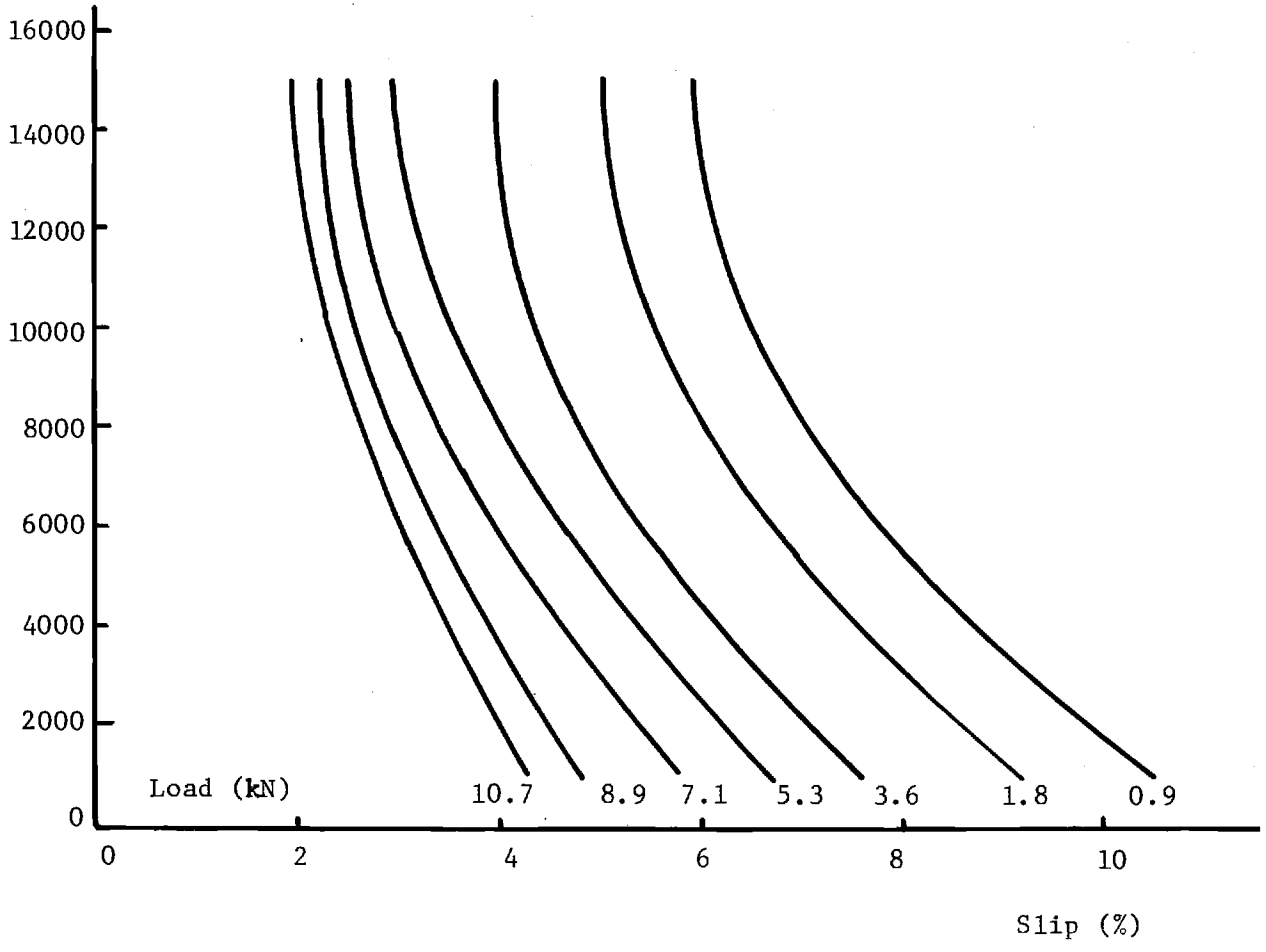

Figure VI-4. Slip at Which Maximum Driving Cage Force is Obtained.

Figure VI-5 shows the elastic deformation at the inner race as a function roller position (ψ=2 denotes the position of roller number 2 when roller number 1 is under the applied load or the position of number 1 roller after 30^{o} of cage rotation).

Figure VI-6 shows the dimensionless film thickness of the inner race as a function of roller position. As expected, the minimum film thickness occurs at the load line. Figure VI-6 also shows that the minimum film thickness is on the order of 3.8μm (150 μ-in) for the 10,675 N (2400 lbf) load.

Finally, Figure VI-7 gives the variation of roller spinning speed with roller position for a number of different operating conditions. Referring to Figure VI-7b, it is interesting to note that increasing the load at constant cage speed results in decreased slip, i.e. lower inner ring speeds are required and higher roller speeds result. Although the roller speed fluctuates, the variation is on the order of only 5%. It appears that in general, the rollers are accelerated for the 60^{o} cage rotation prior to the line of load application and then decelerate over the next 300^{o} rotation. This behavior is in sharp contrast to the results of Poplawski [28] but agrees with the trends reported by Bonnes [27].

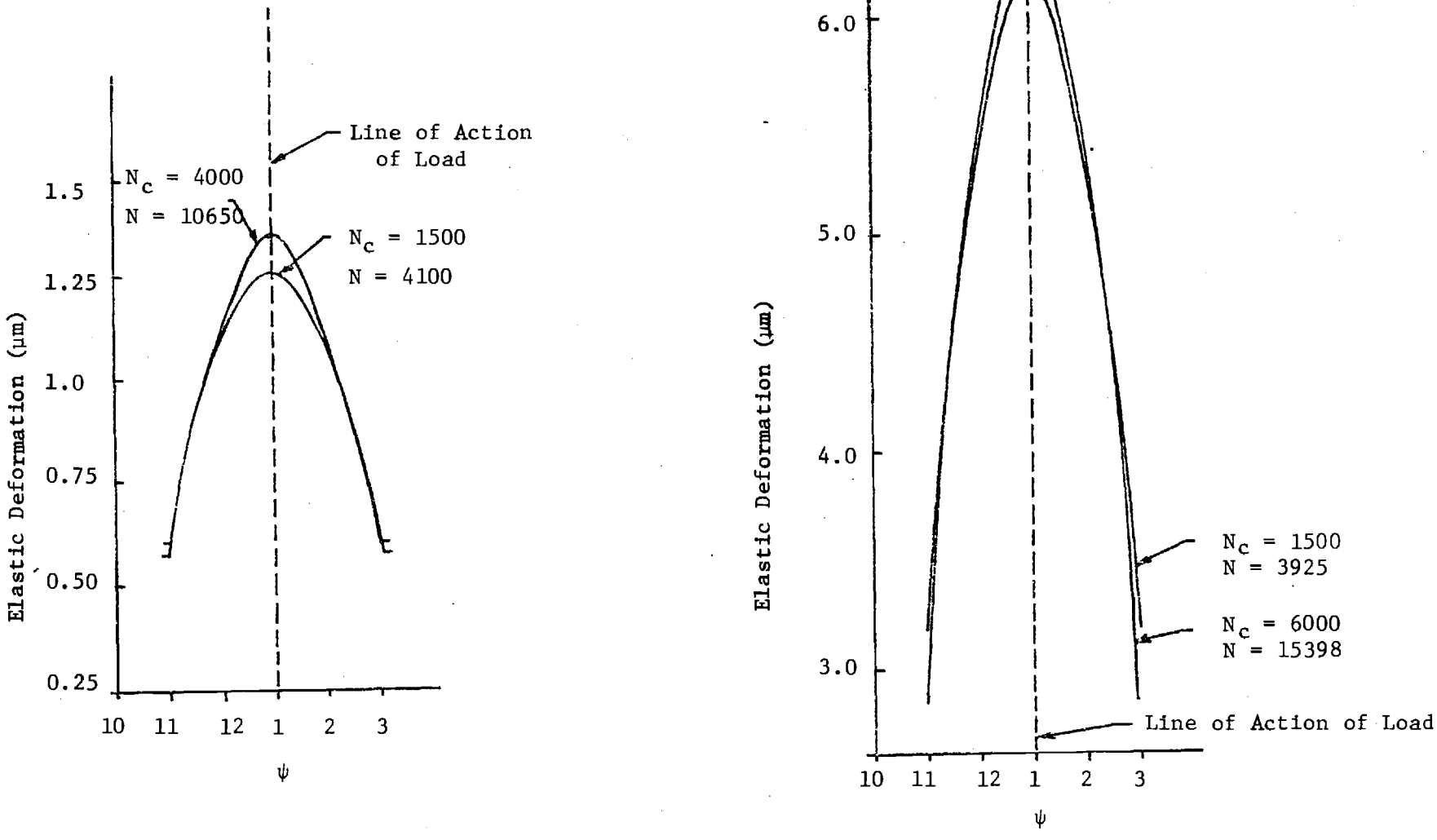

Figure VI-5. Elastic Deformation of Inner Race as a Function of Roller Position. Applied is (a) 1.78 kN, (b) 10.6 kN.

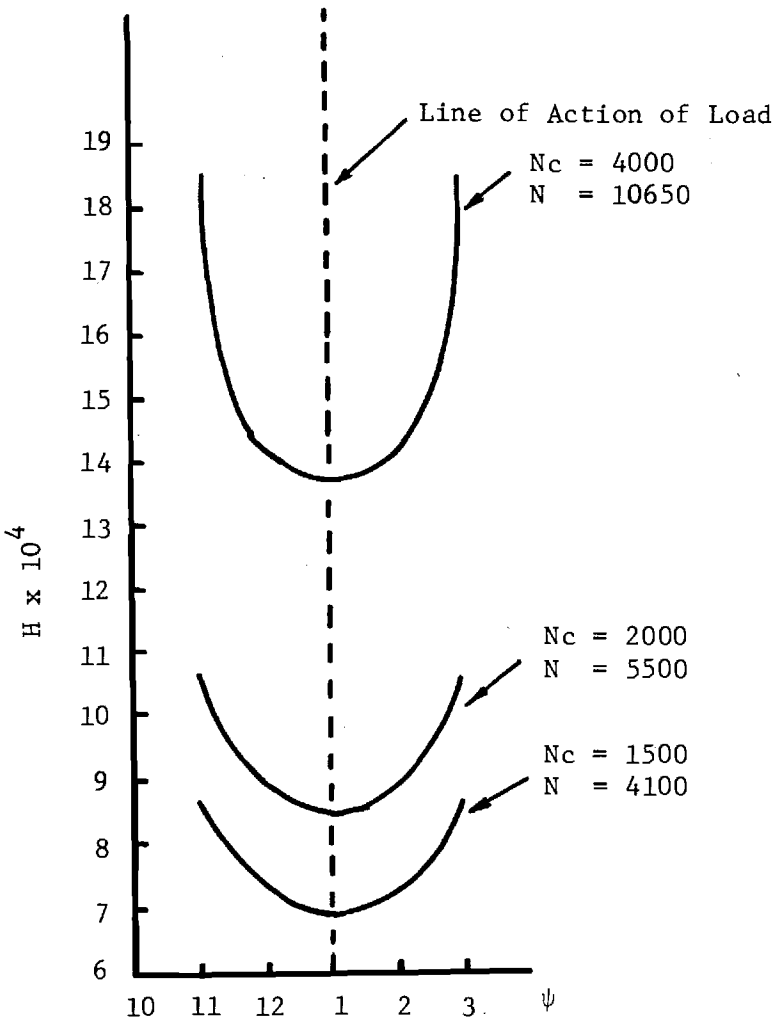

(a)

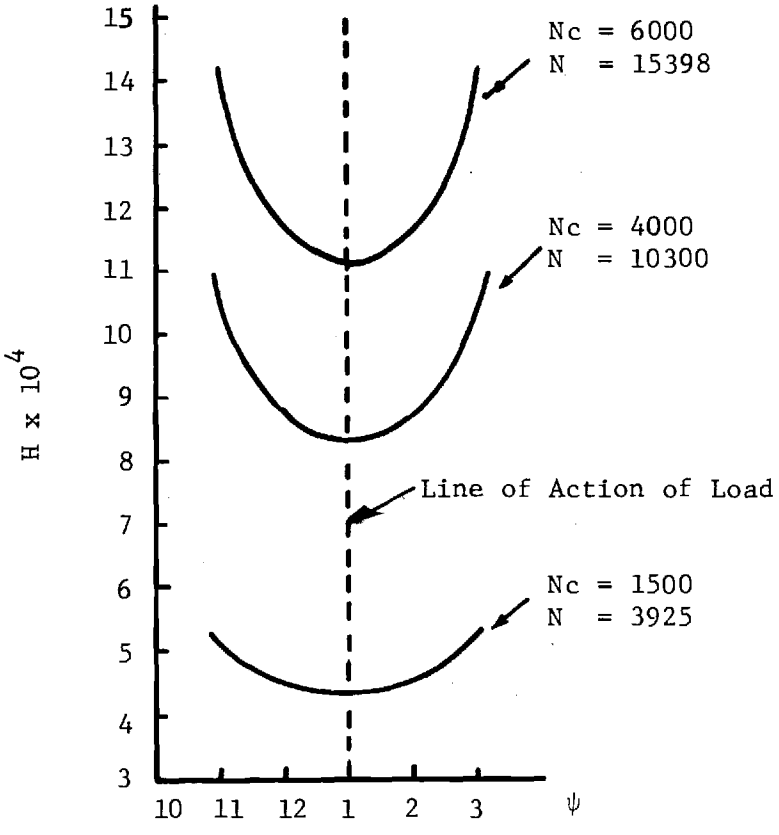

(b)

Figure VI-6. Dimensionless Film Thickness at Inner Race as a Function of Roller Position. Applied Load is (a) 1.8 kN (400 lbf) (b) 10.6 kN (2400 lbf).

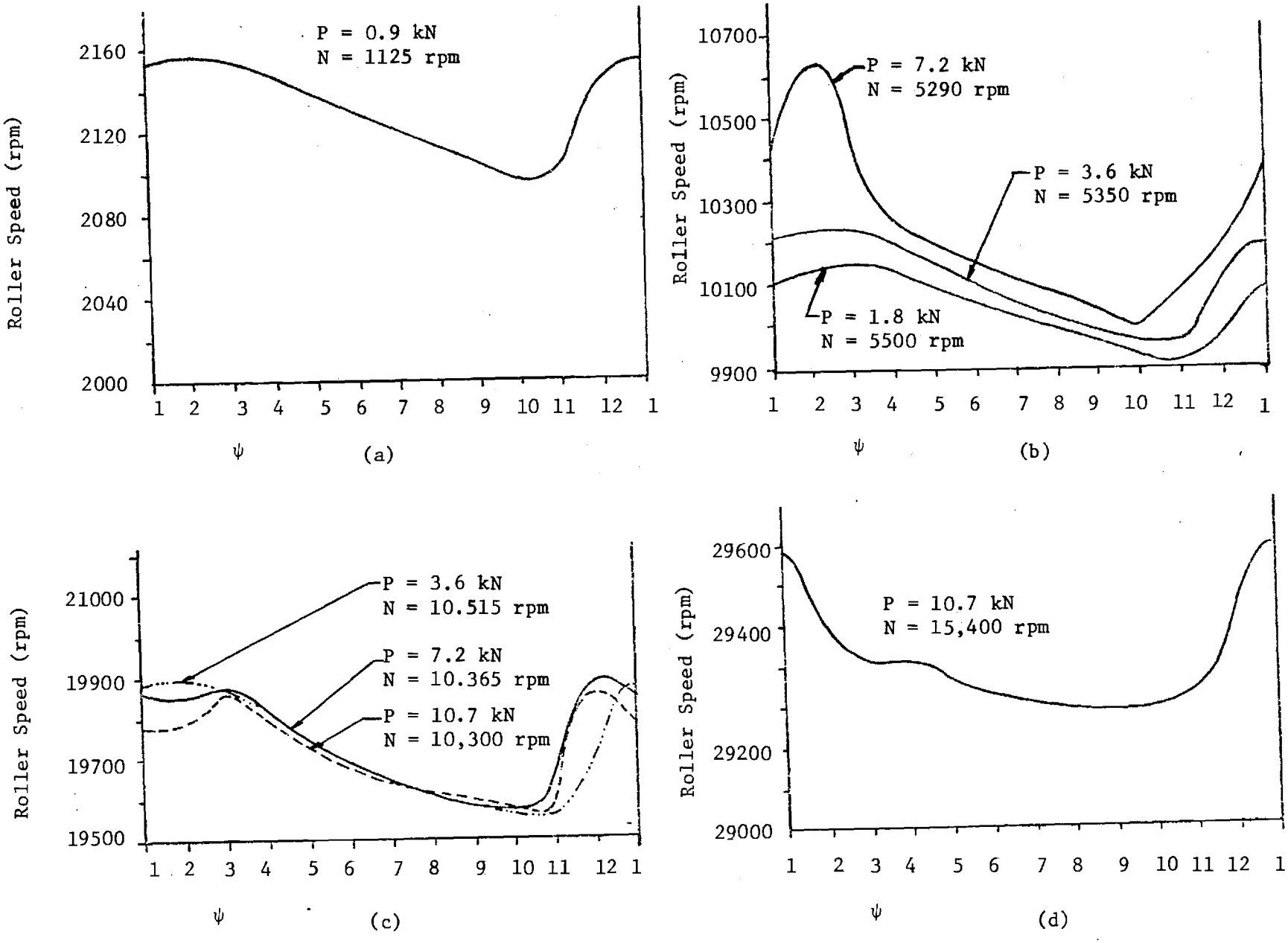

Figure VI-7. Roller Spinning Speed (Nj) as a Function of Relative Position (ψ). Cage speed is (a) 400 rpm, (b) 2000 rpm, (c) 4000 rpm, (d) 6000 rpm. (ψ is the relative roller position in 30° increments)

Table VI-2

Nomenclature for Section VI.

C_d	cage drag coefficient; $C_d \equiv \frac{\text{Cage Drag}}{\frac{\pi^3}{450} \rho R R_p^3 N_c^2}$
E	equivalent elastic modulus; $E \equiv 2\left[\frac{1-\sigma_1^2}{E_1} + \frac{1-\sigma_2^2}{E_2}\right]^{-1}$ N/m^2
E_1, E_2	modulus of elasticity of race and roller respectively, N/m^2
F_c	cage force, N
$\bar{F}_c$	dimensionless cage force, $\bar{F}_c \equiv \frac{F_c}{L_e R_i E}$
H	dimensionless film thickness; H ≡ film thickness/R_2.
L_e	effective length of roller, m
N	shaft or inner race speed, rpm
N_j	spinning speed of roller, rpm
N_c	cage speed, rpm
P	radial load supported by the bearing, N
R	roller radius, m
R_i	equivalent radius of inner contact, $R_i = (R_r^{-1} + R^{-1})^{-1}$, m
R_r	radius of inner race
R_p	radius to the center of roller, m
δ	elastic displacement, μm
ρ	lubricant density, kg/m^3
ψ	roller angular position, ψ = 0 at load line
σ_1, σ_2	Poisson's ratio for race and roller respectively
slip	(cage speed - epicyclic cage speed)/epicyclic cage speed.

VII. References

1. Carlson, S. F., Turchina, V., Jakobsen, J., Sanborn, D. M., and Winer, W. O., "Investigations of Lubricant Rheology as Applied to Elastohydrodynamic Lubrication", NASA CR-134539, October, 1973.

2. Hersey, M. D., Theory and Research in Lubrication, Wiley and Sons, New York, 1966.

3. Philippoff, W., Uber das Fliessen in Kapillaren bei extrem hohen Schubspannungen, Physikalisch Zeitschrift, 43 Jahrgang, Nr. 19/20, 1942.

4. Fritz, W., and Hennenhofer, J., "Stromung zaher Ole in Kapillaren bei hohen Schergeschwindigkeiten and hohen Reinbungsleistungen", Angew. Chem.B 19 Jahrgang, Nr. 5/6.

5. Schnurmann, R., "Das Verhalten von Schmiermitteln bei hohen Schergefallen", Erdol und Kohle, Erdgas, Petrochemie, Nr. 6, 15 Jahrgang, June 1962.

6. Gerrard, J. E., and Philoppoff, W., "Viscous Heating and Capillary Flow", 4th International Congress of Rheology, 1963, Paper 51.

7. Gerrard, J. E., Steidler, F. E., and Appeldoorn, J. K., "Viscous Heating in Capillaries: The Adiabatic Case". ACS Petroleum Division Meeting, Chicago, Illinois, Sept. 1964.

8. Gerrard, J. E., Steidler, F. E., and Appeldoorn, J. K., "Viscous Heating in Capillaries: The Isothermal-Wall Case", ACS Petroleum Division Meeting, Atlantic City, N.Y., Sept. 1965.

9. Brinkman, H. C., "Heat Effects in Capillary Flow I", Applied Science Research A2, 120-124, 1951.

10. Schiller, L., "Die Entwicklung der Laminaren Geschwindigkeitsverteilung", Zeitschrift fur Angewandte Mathematik und Mechanik, Band 2, 1922.

11. Sampson, R. A., "On the Stoke's Current Function", Phil. Trans. Roy. Soc., A182, 1891, 449-518.

12. Roscoe, R., "The Flow of Viscous Fluids round Plane Obstacles", Phil. Mag. 40, 1949, 338-351.

13. Happel, J., and Brenner, H., Low Reynolds Number Hydrodynamics with Special Applications to Particulate Media, Prentice-Hall, Inc. Englewood Cliffs, N.J. 1965.

14. Wurst, W., "Stromung durch Schlitz - und Lochblenden bei kleinen Reynolds - Zahlen", Ingenieur-Archiv, XXII Band, Sechstes (Schluss-) Heft, 1954.

15. Bond, W. N., "The Effect of Viscosity on Orifice Flows", Proc. Phys. Soc. 33, 1921, 225-230.

16. Bond, W. N., "Viscosity Determination by Means of Orifices and Short Tubes", Proc. Phys. Soc. 34, 1922, 139-144.

17. Johansen, F. C., "Flow through Pipe Orifices at Low Reynolds Numbers", Proc. Roy. Soc. A126, 1930, 231-245.

18. Bagley, E. B., "End Corrections in the Capillary Flow of Polyethylene", J. Appl. Phys., 28, No. 5, 1957, 624-627.

19. Turchina, V., Sanborn, D. M. and Winer, W. O., "Temperature Measurements in Sliding Elastohydrodynamic Point Contacts", Trans. ASME, Journal of Lubrication Technology, Vol. 96, pp.464-471, 1974.

20. Sanborn, D. M., and Winer, W. O., "Fluid Rheological Effects in Sliding Elastohydrodynamic Point Contacts: Part I - Film Thickness", Trans. ASME Journal of Lubrication Technology, Vol. 93, pp. 262-271, 1971.

21. Sanborn, D. M., and Winer, W. O., "Fluid Rheological Effects in Sliding Elastohydrodynamic Point Contacts: Part II - Traction", Trans. ASME, Journal of Lubrication Technology, Vol. 93, pp. 342-348, 1971.

22. Lee, D., Sanborn, D. M., and Winer, W. O., "Some Observations of the Relationship Between Film Thickness and Load in High Hertz Pressure Elastohydrodynamic Contacts", Trans. ASME, Journal of Lubrication Technology, Vol. 95, pp. 386-390, 1973.

23. Jakobsen, J., Lubricant Rheology at High Shear Stress, Doctoral Thesis, Georgia Institute of Technology, Sept. 1973, and University Microfilms, Ann Arbor, Michigan, 1973.

24. Carslaw, H. S., and Jaeger, J. C., Conduction of Heat in Solids, Oxford at the Clarendon Press, 1962.

25. Cheng, H. S. and B. Sternlicht, "A Numerical Solution for the Pressure, Temperature, and Film Thickness Between Two Infinity Long, Lubricated Rolling and Sliding Cylinders under Heavy Loads", ASME Trans. S. D. v. 87, pp. 695-707, 1965.

26. Harris, T. A., "An Analytical Method to Predict Skidding in Thrust-loaded Angular - Contact Ball Bearings", ASME Trans., J.O.L.T., Vol. 93, No. 1, 17-24, Jan. 1971.

27. Bonnes, R. J., "The Effect of Oil Supply on Cage and Roller Motion in a Lubricated Roller Bearing", ASME Trans., J.O.L.T., Vol. 92, No. 1, 39-53, Jan. 1970.

28. Poplawski, J. V., "Slip and Cage Forces in a High-Speed Roller Bearing", Trans. ASME, J. Lubr. Tech., Vol. 94, 143-54, April 1972.

29. Rumbarger, J. H., Filletti, E. G., Gubernick, D., "Gas Turbine Engine Mainshaft Roller Bearing System Analysis", ASME Trans., Vol. 95, Journal of Lubrication Technology, No. 4, Oct. 1973, pp. 401-416.

30. Dowson, D. and Higginson, G. R., Elastohydrodynamic Lubrication - The Fundamentals of Roller and Gear Lubrication, Pergamon Press, London, 1966.

31. Cheng, H. S., "Calculation of Elastohydrodynamic Film Thickness in High Speed Rolling and Sliding Contacts", Mechanical Technology Incorporated 67TR24.

32. Harris, T. A., Rolling Bearing Analysis, John Wiley & Sons, New York, 1966.

33. Molina, M. A., Dynamics of Roller Bearings Considering Elasto-hydrodynamic Forces, M. S. Thesis, Georgia Institute of Technology, 1974.

34. Trachman, E. G. and Cheng, H. S., "Traction in Elastohydrodynamic Line Contacts for Two Synthesized Hydrocarbon Fluids," to be published Trans. ASLE, Paper No. 73LC-4A-1.

35. Lieberstein, H. M., A Course in Numerical Analysis, J. Wiley & Sons, New York, 1966.

36. Berezin, I. S. and Zhidkov, N., Computing Methods, Vol. II, Pergamon Press, London, 1965.

37. Townsend, D. P., Allen, C. W. and Zaretsky, E. V., "Study of Ball Bearing Torque Under Elastohydrodynamic Lubrication", Paper presented to the ASLE-ASME Joint Conference, Atlanta, Oct. 16-18, 1973. ASME Paper No. 73-LUB-39.

Appendix I

Publications of Grant Sponsored Research

I. Student theses completed and published through University Microfilm and abstracted in Dissertation Abstracts.

1. Valentin Alexandru Turchina, "Pressure and Temperature Measurement Techniques in Elastohydrodynamic Contacts", M.S. Thesis, Georgia Institute of Technology, June 1973.

2. Manual A. Molina C., "Dynamics of Roller Bearings Considering Elastohydrodynamic Forces", M.S. Thesis, Georgia Institute of Technology, June 1974.

3. Jorgen Jakobsen, "Lubricant Rheology at High Shear Stress", PhD Thesis, Georgia Institute of Technology, September 1973.

II. Technical Papers

1. Winer, W. O., "A Viscometer for High Pressure Use, and Some Results", Trans. ASME, Vol. 94, No. 3, Series D, The Journal of Basic Engineering, pp. 586-589, 1972.

2. Lee, D., Sanborn, D. M., and Winer, W. O., "Some Observations of the Relationship Between Film Thickness and Load in High Hertz Pressure Elastohydrodynamic Contacts", Trans. ASME, Journal of Lubrication Technology, Vol. 95, pp. 386-390, 1973.

3. Jakobsen, J., Sanborn, D. M., and Winer, W.O., "Simulation of Severe Shear Conditions in Lubrication", Society of Automotive Engineers, SP-382, pp. 59-67, 1973.

4. Turchina, V. A., Sanborn, D. M., and Winer, W. O.,"Temperature Measurements in Sliding Elastohydrodynamic Point Contacts", Trans. ASME, Journal of Lubrication Technology, Vol. 96, pp. 410-417, 1974.

5. Jones, W. R., Johnson, R.L., Sanborn, D. M., and W. O. Winer, "Viscosity-Pressure Measurements for Several Lubricants to 5.5×10^8 N/m^2 (8×10^4 psi) and 149C (300F)", ASLE Paper No. 74-LC-4C-1, (to be presented at the 1974 ASME/ASLE Joint Lubrication Conference).

6. Jakobsen, J., and Winer, W. O., "Traction of Elastohydrodynamic Contacts with Thermal Shearing Flow", ASME Paper No. 74-LUB-28, (to be presented at the 1974 ASME/ASLE Joint Conference).

7. Jakobsen, J., and Winer, W.O., "Dissipative Heating Effects and End Corrections for Viscous Newtonian Flow in High Shear Capillary Tube Viscometry", ASME Paper No. 74-LUB-40, (to be presented at the 1974 ASME/ASLE Joint Lubrication Conference).

8. Jakobsen, J., and Winer, W. O., "High Shear Stress Behavior of Some Representative Lubricants", ASME Paper No. 74-LUB-41, (to be presented at the 1974 ASME/ASLE Joint Lubrication Conference).

9. Carlson, S. F., and Winer, W.O., "The Viscous Lubrication of Rolling and Sliding Rigid Cylinders", ASME Paper No. 74-LUB-15, (to be presented at the 1974 ASME/ASLE Joint Lubrication Conference).

DISTRIBUTION LIST

NASA Grant NGR 11-002-113

ADDRESSEE	NUMBER OF COPIES
NASA Lewis Research Center 21000 Brookpark Road Cleveland, Ohio 44135	
Attn: Contract Section A, MS 500-206	1
Technology Utilization Office, MS 3-19	1
Director of Aeronautics, MS 3-3	1
Library, MS 60-3	2
Report Control Office, MS 5-5	1
N. T. Musial, MS 500-118	1
A. Ginsburg, MS 5-3	1
R. L. Johnson, MS 23-2	1
W. R. Jones, MS 23-2	10
W. R. Loomis, MS 23-2	1
L. D. Wedeyen, MS 23-2	1
H. E. Sliney, MS 23-2	1
W. J. Anderson, MS 23-2	1
E. V. Zaretsky, MS 6-1	1
Lt. Col. G. J. Weden, MS 77-5	1
NASA Headquarters Washington, D.C. 20546	
Attn: N. F. Rekos (RLC)	1
J. Maltz (RWM)	1
Office of Naval Research Code 411 Arlington, Va. 22217	
Attn: Lt. R. Miller	1
Air Force Aero Propulsion Laboratory Wright Patterson AFB, Ohio 45433	
Attn: Howard Jones, APFL/SFL	1
Air Force Materials Laboratory Wright Patterson AFB, Ohio 45433	
Attn: Major L. Fehrenbacher, AFML/MBT	1
Battelle Memorial Institute Columbus Laboratories 505 King Avenue Columbus, Ohio 43201	
Attn: C. M. Allen	1

ADDRESSEE	NUMBER OF COPIES
Chevron Research Company 576 Standard Avenue Richmond, Calif. 94802 Attn: D. Godfrey	1
Exxon Research & Engineering Company P. O. Box 51 Linden, N.J. 07036 Attn: A. Beerbower	1
Midwest Research Institute 425 Volker Blvd. Kansas City, Mo. 64110 Attn: V. Hopkins	1
Mobil Research & Development Corp. P. O. Box 1025 Princeton, N.J. 08540 Attn: C. N. Rowe P. E. Fowles	1 1
Southwest Research Institute P. O. Box 28510 San Antonio, Texas 78284 Attn: P. M. Ku	1
Carnegie-Mellon University Dept. of Chemical Engineering Schenley Park Pittsburgh, Pa. 15213 Attn: T. Fort, Jr.	1
Pennsylvania State University Dept. of Chemical Engineering University Park, Pa. 16802 Attn: E. E. Klaus	1
Mr. E. E. Bisson 20786 Eastwood Avenue Fairview Park, Ohio 44126	1
Northwestern University The Technology Institute Evanston, Illinois 60201 Attn: H. S. Cheng	1
Texaco Research Center Research & Technical Department Fundamental Research Station Beacon, N.Y. 12508 Attn: R. Fein	1

ADDRESSEE	NUMBER OF COPIES
University of Virginia Thornton Hall Charlottesville, Va. 22091	
Attn: J. J. Kauzlarich	1
W. Jamison	1
University of Michigan Dept. of Mechanical Engineering Ann Arbor, Michigan 48105	
Attn: K. Ludema	1
Imperial College Dept. of Mechanical Engineering Exhibition Road London SW7 2BX England	
Attn: A. Cameron	1
National Engineering Laboratory East Kilbride, Glasgow Great Britain	
Attn: D. Scott	1
The Catholic University of America Vitreous State Laboratory Washington, D.C. 20017	
Attn: J. F. Dill	1

E-9562
APR
NASA CR-134882

GEORGIA INSTITUTE OF TECHNOLOGY
SCHOOL OF MECHANICAL ENGINEERING
Atlanta, Georgia

Investigations of Lubricant Rheology as Applied to Elastohydrodynamic Lubrication

NASA GRANT No.
11-002-133

By:
R. K. Kunz
H. S. Nagaraj
Graduate Students
D. M. Sanborn, Associate Professor
W. O. Winer, Professor
Co-Principal Investigators

For

NASA-LEWIS RESEARCH CENTER
21000 BROOKPARK ROAD
CLEVELAND, OHIO 44135

AUGUST, 1975

1. Report No.	2. Government Accession No.	3. Recipient's Catalog No.
NASA CR-134882		

4. Title and Subtitle	5. Report Date
INVESTIGATIONS OF LUBRICANT RHEOLOGY AS APPLIED TO ELASTOHYDRODYNAMIC LUBRICATION	August, 1975
	6. Performing Organization Code
7. Author(s)	8. Performing Organization Report No.
D. M. Sanborn, W. O. Winer, et al.	
	10. Work Unit No.
9. Performing Organization Name and Address	
School of Mechanical Engineering Georgia Institute of Technology Atlanta, Georgia 30332	11. Contract or Grant No. NGR11-002-133
	13. Type of Report and Period Covered Contractor Report
12. Sponsoring Agency Name and Address	
National Aeronautics and Space Administration Washington, D. C. 20546	14. Sponsoring Agency Code

15. Supplementary Notes

Project Manager, William R. Jones, Jr., Fluid System Components Division
NASA Lewis Research Center, Cleveland, Ohio

16. Abstract

This is the annual progress report for NASA Grant No. 11-002-133. The research under this grant consists of an analytical study of traction prediction in sliding EHD contacts and an elastohydrodynamic lubrication simulation study of the effects of load and speed on temperatures in the EHD contact. An existing shear stress theory and lubricant rheological model were studied and evaluated by applying them to traction prediction. Results obtained using measured film thickness and surface temperature data, were compared with measured traction values. The infrared technique for measuring temperatures in an EHD contact has been further developed and ball surface and fluid temperatures are reported for sliding speeds of 0.35 to 5.08 m/s at 0.52 to 2.03 GN/m^2 maximum pressure and surface roughnesses of .011 to .381 μm c.l.a. The relationship between asperity interaction, as measured by relocation surface profilimetry and high frequency temperature measurements, and the ratio of film thickness to surface roughness has also been studied.

17. Key Words (Suggested by Author(s))	18. Distribution Statement
Elastohydrodynamic Lubrication Pressure Viscosity Measurements Liquid Lubricants Lubricant Rheology	Unclassified - unlimited

19. Security Classif. (of this report)	20. Security Classif. (of this page)	21. No. of Pages	22. Price*
Unclassified	Unclassified	53	

NASA CR-134882

GEORGIA INSTITUTE OF TECHNOLOGY
School of Mechanical Engineering
Atlanta, Georgia

Investigations of Lubricant Rheology as Applied to Elastohydrodynamic Lubrication

NASA GRANT No.
11-002-133

by:

R. K. Kunz
H. S. Nagaraj
Graduate Students
D. M. Sanborn, Associate Professor
W. O. Winer, Professor
Co-Principal Investigators

For

NASA-LEWIS RESEARCH CENTER
21000 Brookpark Road
Cleveland, Ohio 44135

August, 1975

GEORGIA INSTITUTE OF TECHNOLOGY
School of Mechanical Engineering
Atlanta, Georgia

INVESTIGATIONS OF LUBRICANT RHEOLOGY AS APPLIED TO ELASTOHYDRODYNAMIC LUBRICATION

Ward O. Winer
Principal Investigator

David M. Sanborn
Principal Investigator

Stothe P. Kezios, Director
School of Mechanical Engineering

August, 1975

TABLE OF CONTENTS

subscripts

1	Stationary surface
2	Moving surface
b	Ball surface
c	Contact center value
f	Fluid
H	Hertzian conditions
o	Ambient conditions or minimum value
s	Sapphire surface

I. SUMMARY

During the past year research in the areas listed below has progressed and is reported herein:

Prediction of Traction in Sliding EHD Contacts

The shear stress theory proposed in the previous report when applied to the sliding EHD point contact using a naphthenic oil was found to yield results consistent with experimental findings for the high end of the speed range studied. The particular speed at which this theory yields reasonable results depends on the normal load and film thickness. At lower speeds, the calculated tractions exceeded the measured values. This is possibly due to either the onset of asperity interaction as the film thickness decreased or the breakdown of the Newtonian fluid model at high shear stress.

Calculations based on the theory indicated that the traction tends to increase with an increase in base viscosity and a decrease in temperature viscosity dependence of the lubricant. A weaker traction increase resulted from an increase in the pressure-viscosity dependence of the fluid. Variation in the thermal conductivity was found to have very little effect on the traction.

Experimental Investigations in Sliding EHD Contacts

A complete mapping of the average fluid and ball surface temperature has been obtained for the relatively high Hertz pressure level of 1.51 GN/m^2. The previous report contained similar data for 1.05 GN/m^2 Hertz pressure. These data are compared to yield a qualitative dependence of fluid temperature levels on Hertz pressure. Further studies of the ball surface temperature only were made at pressure levels from 0.521 to 2.03 GN/m^2.

II. THE PREDICTION OF TRACTION IN SLIDING EHD CONTACTS

A. Introduction

The determination of the traction force in elastohydrodynamic contacts is of primary importance in the understanding of many lubricated mechanisms. The traction is defined as the force generated in the contact which resists relative motion of the bearing surfaces. This is directly related to the power loss in mechanical components such as gears, cams, and rolling element bearings. Traction studies are also motivated by a need to predict the onset of skidding in rolling element bearings. However, due to the physical complexity of the problem, no simple model describing quantitatively the generation of traction in an EHD contact has yet been generally accepted. Complications caused by the large role of thermal effects and by difficulties in finding a rheological model which is adequate at high pressures and shear stress have hindered simplified theoretical analysis.

A number of models for predicting traction have been proposed. Crook (1), Kannel and Walowit (2), and Allen, Townsend and Zaretsky (3) all assumed isothermal bearing surfaces in their models. Based on temperature measurements by Turchina, Sanborn and Winer (4) this condition appears to be physically violated, particularly when a great deal of sliding is present. Cheng and Sternlicht (5) and Cheng (6) included thermal effects in a numerical analysis dealing primarily with line contacts in the prediction of film thickness, pressure, and temperature. While these investigations give a great deal of insight into the effects of thermal behavior in the analysis, the complexity of the numerical iteration technique

B. Application of the Theory

The assumptions which form the basis for this theory are summarized here in the context of their application to a sliding EHD contact. The flow geometry, with major assumptions, is shown in Figure 1. Surface 1 is stationary, and surface 2 moves with constant velocity in the x_1 direction. According to both theory and experiment, the change in film thickness over most of an EHD contact is very small compared with the size of the contact. The bearing surfaces are therefore assumed parallel in the vicinity of the point at which the shear stress is being calculated, although the film thickness is allowed to vary from point to point. While temperature variations are recognized to exist in the x_1 and x_2 directions, the gradients of temperature in these directions are smaller than in the x_3 direction by about four orders of magnitude. Therefore, temperature is assumed to be pointwise independent of x_1 and x_2.

Because surface 2 is moving, the major portion of heat generated in the contact is carried away by this surface which justifies the assumption that the stationary surface is adiabatic. Over the major portion of the contact, the component of shear stress due to the pressure gradient is much smaller than that due to sliding motion. Consequently, the pressure is assumed pointwise constant. Detailed discussion of these assumptions is found in Jakobsen (9). In addition, body forces are neglected, and density and thermal conductivity of the lubricant are assumed constant.

A Newtonian rheological model of the lubricant, employing a linear relationship between shear stress and shear rate, is used. The viscosity-temperature dependence is expressed by the power-exponential relation

$$\eta = C \exp [(E/T)^{Q}] \tag{1}$$

both E and Q are functions of pressure. Jakobsen (9) has shown that this equation gives a reasonable description of lubricant viscosity within the range of temperature and shear stress normally found in an elastohydrodynamic contact.

Through integrations of the energy equation and the equations of motion, reduced by the above assumptions and the given rheological model, the theory provides a means of calculating the shear stress τ at any point in a sliding EHD contact. The condition of an adiabatic stationary wall yields the relation

$$\int_{T_1}^{T_2} \eta(T,Q)^{-1} dT = - \frac{V^2}{2k} \tag{2}$$

which is used to determine the temperature of the stationary surface, T_1. The shear stress at a point in the contact is then determined from the equation

$$\tau = - \frac{1}{2h} \int_{T_1}^{T_2} \left[- \frac{1}{2k} \int_{T_1}^{\hat{T}} [\eta(\xi,Q)^{-1} d\xi]^{-1/2} \, d\hat{T} \right] \tag{3}$$

The following parameters must be known: the temperature of the moving surface, T_2; the film thickness, h; the thermal conductivity of the fluid, k; the sliding speed, V; and the viscosity parameters Q and E. These latter two are calculated from the above equation and from viscometric data on the lubricant at the pressure of the point under consideration.

distribution of film thickness in the contact area was also known from measurements made using the optical interference method of Sanborn and Winer (15). The required pressure-viscosity data for the fluid N1 was obtained from Novak (16). Because viscosity data was only available at pressures up to 1.38×10^8 N/m^2, it was necessary to extrapolate the experimental curves up to the maximum Hertzian pressure of 1.0×10^9 N/m^2 for the 67N load, and 1.7×10^9 N/m^2 for the 334N load. This extrapolation was performed using Roelands' (17) pressure-viscosity correlation.

Figure 2 shows a plot of both calculated and measured tractions against sliding speed for the 67 N load. The traction is represented in the form of a traction coefficient, defined as the ratio between the traction force and the normal load. Figure 3 is a similar plot for the 334 N load. Figures 2 and 3 both indicate that the agreement between calculated and measured traction becomes better as the sliding speed increases. Because the film thickness decreases as the sliding speed decreases, there is a possibility that the divergence at lower speeds is related to asperity interaction. Such interaction could affect the contact in basically two ways which would tend to decrease the actual traction below the calculated values, as is observed in the figures. First, the contact between asperities could act as an additional source of heat which would raise the film temperature, and in turn lower the lubricant viscosity and therefore the traction. The traction model used in the calculations assumes that the only source of heat in the EHD contact is that due to viscous shearing of the lubricant. Therefore, one could expect calculated tractions to exceed the measured values. In addition, as the film thickness decreases and asperities come into contact, the asperities themselves would be

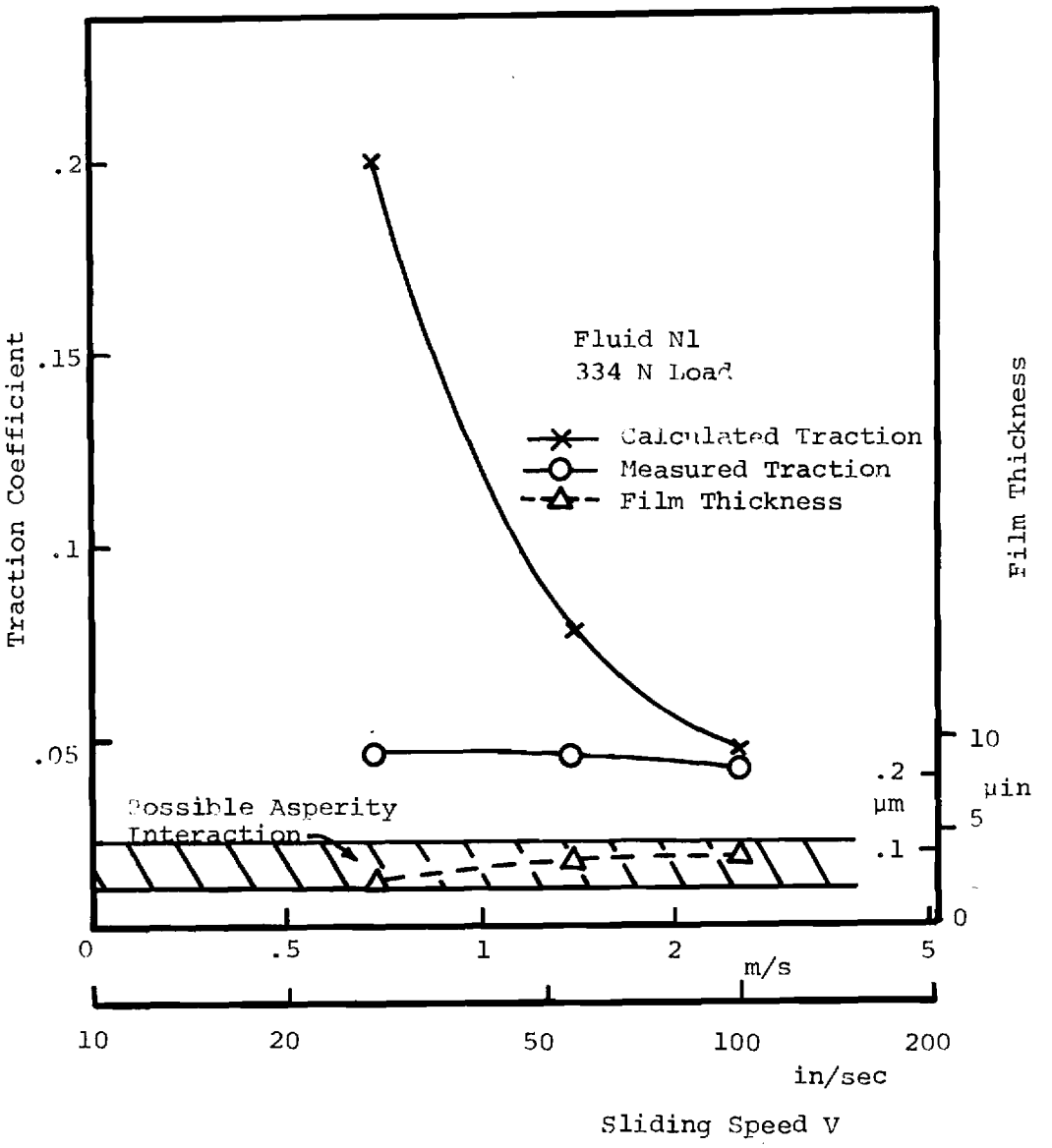

Figure 3. Calculated and Measured Traction - 1.7 GN/m^2 Hertz Pressure.

limiting value. The Johnson and Roberts limiting shear stress model would result in tractions closer to the measured values than the present model if the limiting shear stress of the fluid is less than the values calculated with the present model.

For the 67 N load, the maximum shear stress calculated at 1.40 m/s was in the neighborhood of 8.0×10^7 N/m^2. Similarly, for the 334 N load at 2.54 m/s, the maximum shear stress in the contact was calculated to be 8.1×10^7 N/m^2. Each of these two cases corresponds to the transition speed at which calculated and measured tractions began to deviate as the speed decreased. At higher speeds, calculated shear stresses were lower than these values throughout the contact. At speeds lower than the transition speeds, these shear stresses were exceeded by the calculated value. The fact that these maximum shear stresses are essentially the same for the two loads lends credence to the possibility that the Newtonian rheological model of the lubricant used in the calculations fails to adequately describe fluid behavior at extremely high shear stresses.

D. The Effect of Material Parameters on Traction

The effects on the traction of variations in the lubricant material parameters: temperature-viscosity dependence, pressure-viscosity dependence, base or inlet viscosity, and thermal conductivity were studied. These quantities were varied independently in calculations using the measured surface temperature and film thickness found for Fluid N1 (the naphthenic base oil (15)). The results were then compared with the calculations for Fluid N1.

In order to examine the effect of temperature-viscosity dependence on the calculated traction, a model fluid having the same pressure dependence

Another model fluid was used, having the same pressure and temperature dependence as Fluid N1, but having a viscosity at inlet conditions three times that of Fluid N1. As before, all other system parameters were held constant. The resulting traction coefficient was greater than that for Fluid N1 by a factor of 1.75. The traction therefore increases as the inlet viscosity increases.

The only other lubricant material parameter involved in the traction calculation is the thermal conductivity. Variations in this property appear to have very little effect on the traction. In addition, the thermal conductivities for most hydrocarbon and dimethyl siloxane lubricants fall within a very narrow range.

Traction measurements would not be expected to be as sensitive to material property differences as the above calculations indicate. This is primarily because the surface temperatures for Fluid N1 were used in the calculations. Using a more viscous fluid, for instance, would increase the energy dissipation in the contact, thus increasing the temperature and decreasing the traction until a lower steady state value is reached with higher surface temperatures. Temperatures and film thicknesses for Fluid N1 were used only so as to allow independent variation of the material parameters. Consequently, the results of the calculations of this section should be viewed as relative variations only, rather than as absolute magnitudes to be expected in actual lubrication situations.

E. Conclusions

The shear stress theory of Jakobsen and Winer (11), when applied to a sliding EHD point contact, was found to yield realistic values for the traction at high sliding speeds. The particular speed at which the

III. EXPERIMENTAL INVESTIGATIONS IN SLIDING EHD CONTACTS

A. Temperature Distributions at a 215N Normal Load

The distribution of the average fluid film temperature and ball surface temperature, for a load of 67 N (1.05 GN/m^2 maximum Hertz pressure) have been obtained using the test apparatus shown in Figure 4 and the results were reported previously [10,21]. Similar measurements for the case of a normal load of 215N (1.51 GN/m^2 maximum Hertz pressure) were made and the most important results are given in Table I. It can be seen from Table I that the film thickness at the center of the EHD conjunction, at the side lobes and at the contact exit are all essentially the same. This constant film thickness tends to give more symmetric temperature distributions than previously observed.

In addition, at the higher load (215N), the maximum ball surface and fluid temperatures always occurred on or near the contact centerline at a point downstream of the contact center. The reason for this is that the pressure, and thus viscosity, is greatest at the contact center, and consequently, for a uniform film thickness, viscous dissipation is a maximum at the center. However, since the fluid residence period increases as it moves toward the exit, the position of the maximum temperature could be between the contact center and exit depending on the effectiveness of heat transfer at the bearing surfaces. At lower loads [10], the maximum contact temperature may occur off the contact center line, for example, at the side lobe constriction. This is attributable to the very low film thicknesses at the side lobes compared to other locations.

Also, the position of the maximum fluid film temperature is upstream of the position of the maximum ball surface temperature. Keeping in mind

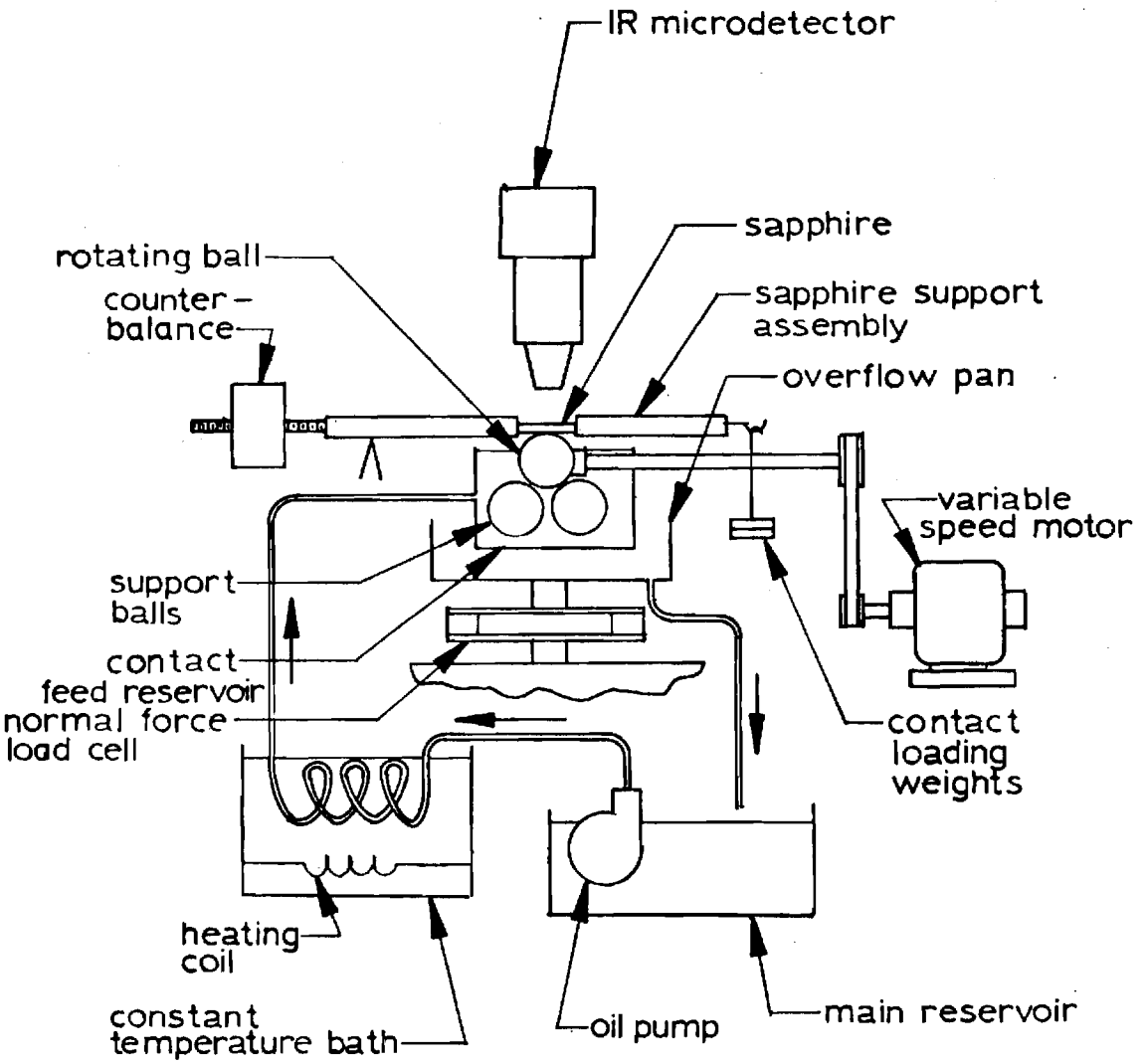

Figure 4. Sliding EHD Test Apparatus.

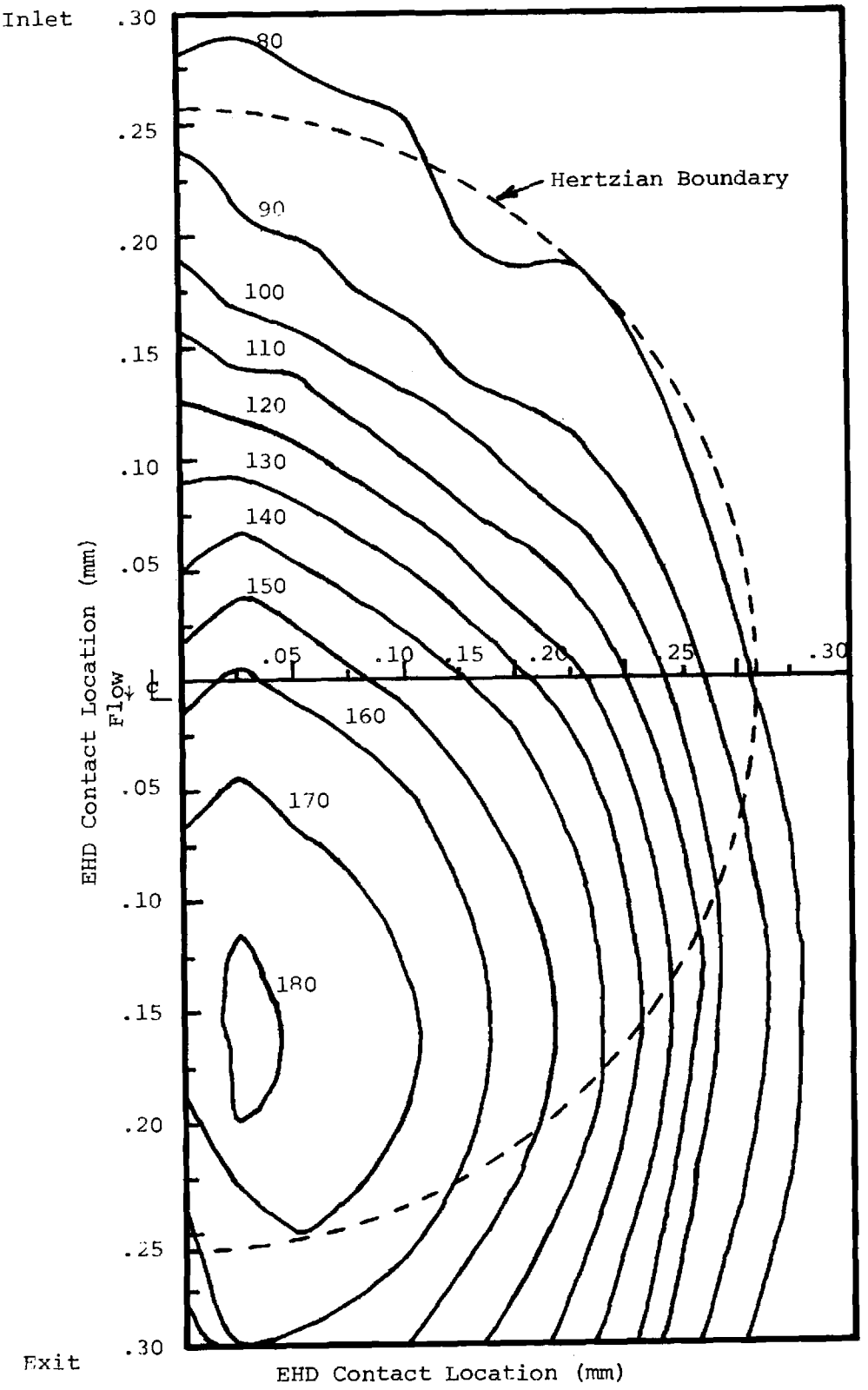

Figure 5. Ball Surface Temperature (^{o}C) - 1.05 GN/m^{2} Hertz Pressure, Naphthenic Base Oil, 40^{o}C Bath Temperature, 1.39 m/s Sliding Speed, Smooth Ball (0.011 μm c.l.a.)

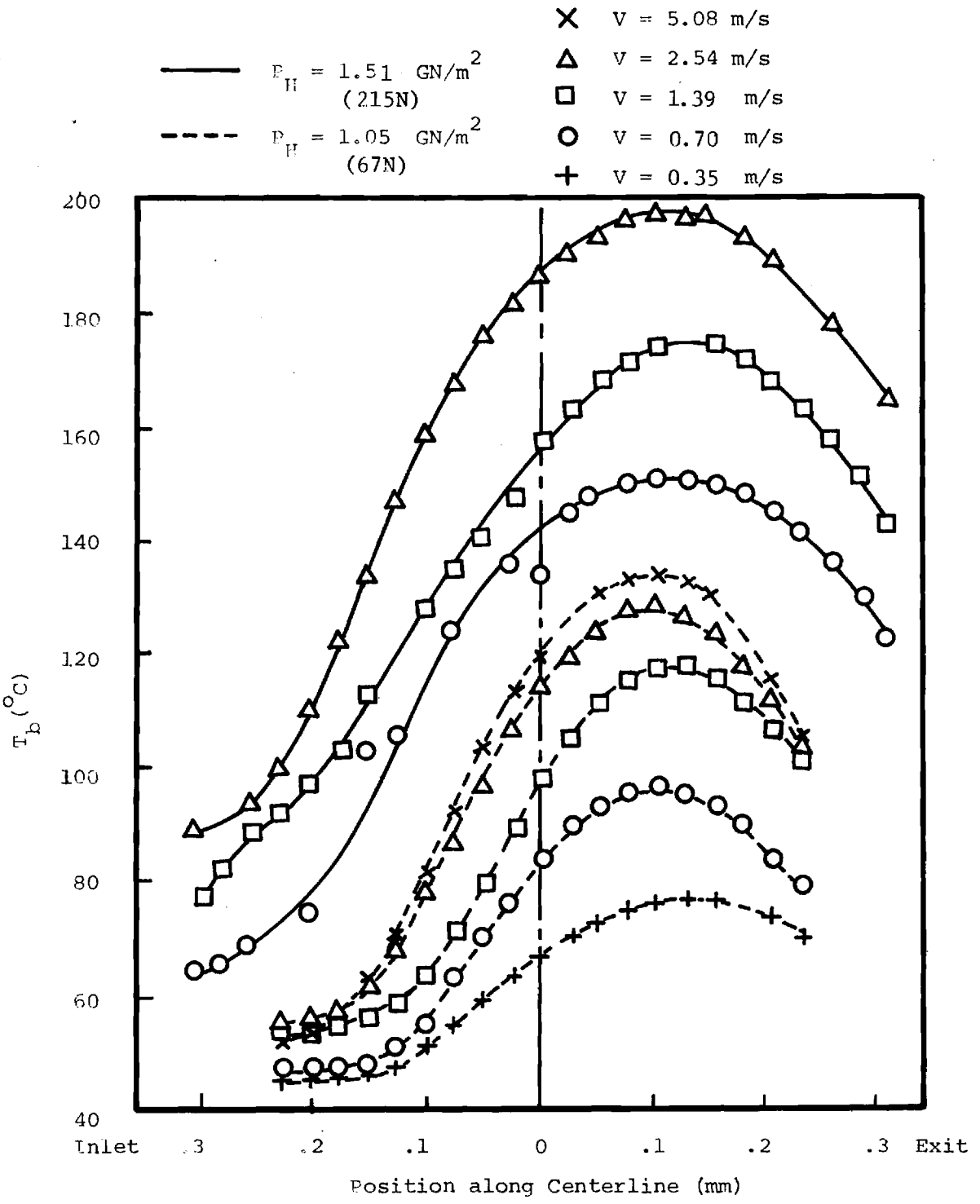

Figure 7. Ball Surface Temperature Along Centerline as a Function of Speed and Load -- Naphthenic Base Oil N1, 40°C Bath Temperature, Smooth Ball (.011 μm c.l.a.).

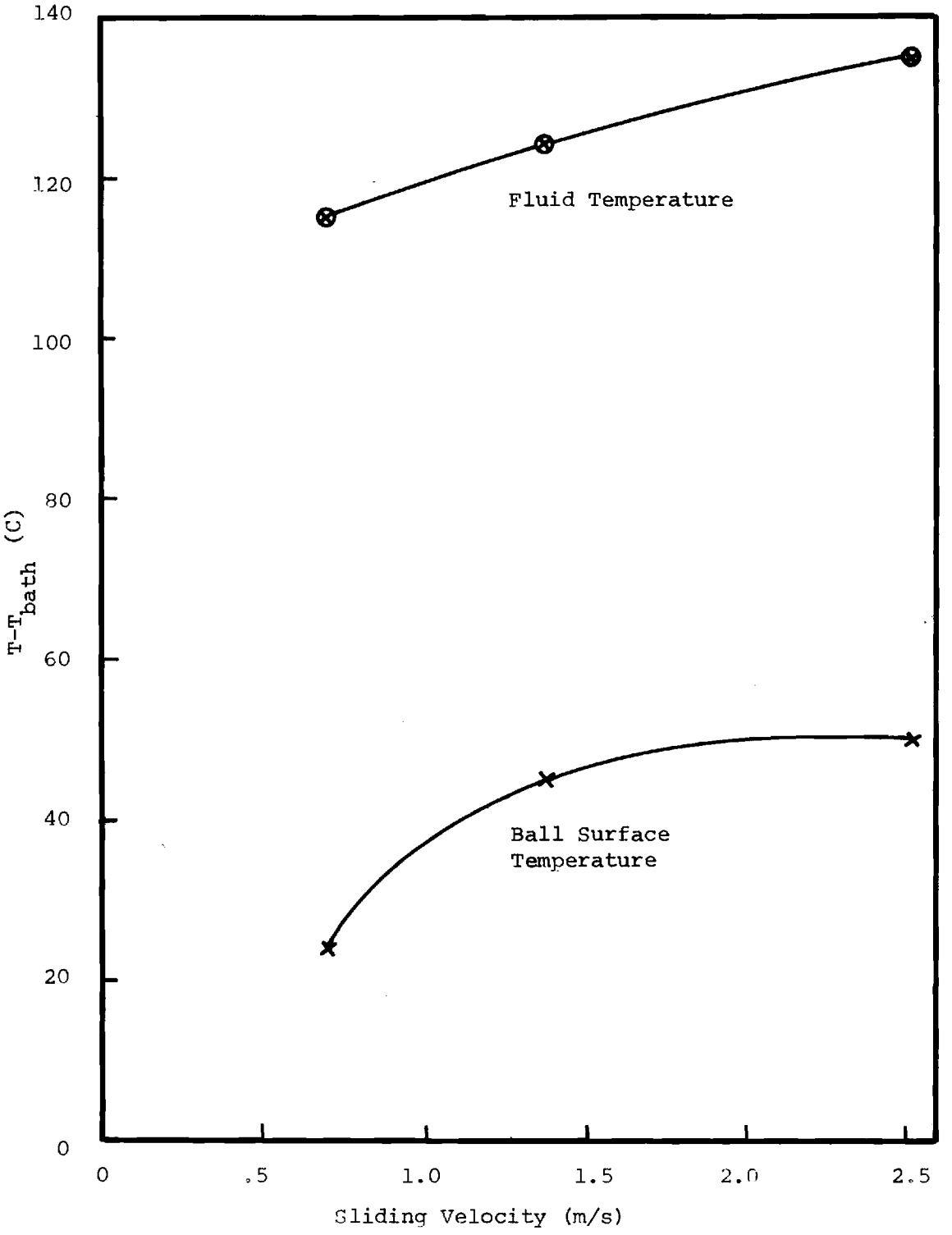

Figure 9. Temperature Increase above Bath Temperature at Contact Inlet - 1.51 GN/m^2 Hertz Pressure, Naphthenic Base Oil (N1), Smooth Ball (0.011 μm c.l.a.).

B. Ball Surface Temperature Measurements Under Severe Conditions

In order to understand the failure of elastohydrodynamic films and the behavior of the contact temperatures, it is necessary to examine the EHD contact under conditions which result in relatively thin films, i.e. films of the same thickness as the composite roughness of the bounding surfaces. Under such circumstances, the fluid film may be locally discontinuous, resulting in ambiguous fluid temperature readings. Therefore, during this study, only the ball surface temperature was measured. In addition, for convenience, measurements were taken only at the center of the Hertzian contact. The temperature at the contact center is near the maximum (see Figure 7) and is, therefore, representative of the most severe conditions in the EHD contact.

Figure 10 shows a plot of the ball temperature rise at the contact center above the bath temperature, as a function of sliding velocity for peak Hertz pressures ranging from 0.52 to 2.03 GN/m^2. For a given Hertz pressure, the data plotted on log-log coordinates falls on one straight line for velocities up to a certain value and then on another line, of lower slope, for higher velocities. This decreasing dependence of temperature on velocity is supported, by the arguments of Archard [22] and Jaeger [23]. Applying Archard's analysis to a point contact results in the temperature difference between the fluid midplane temperature (assumed to be the maximum fluid temperature) and the ball surface temperature given by

$$T_f - T_b = \left(\frac{W}{4k_f \pi a^2}\right) (TC \cdot V \cdot h) \qquad (4)$$

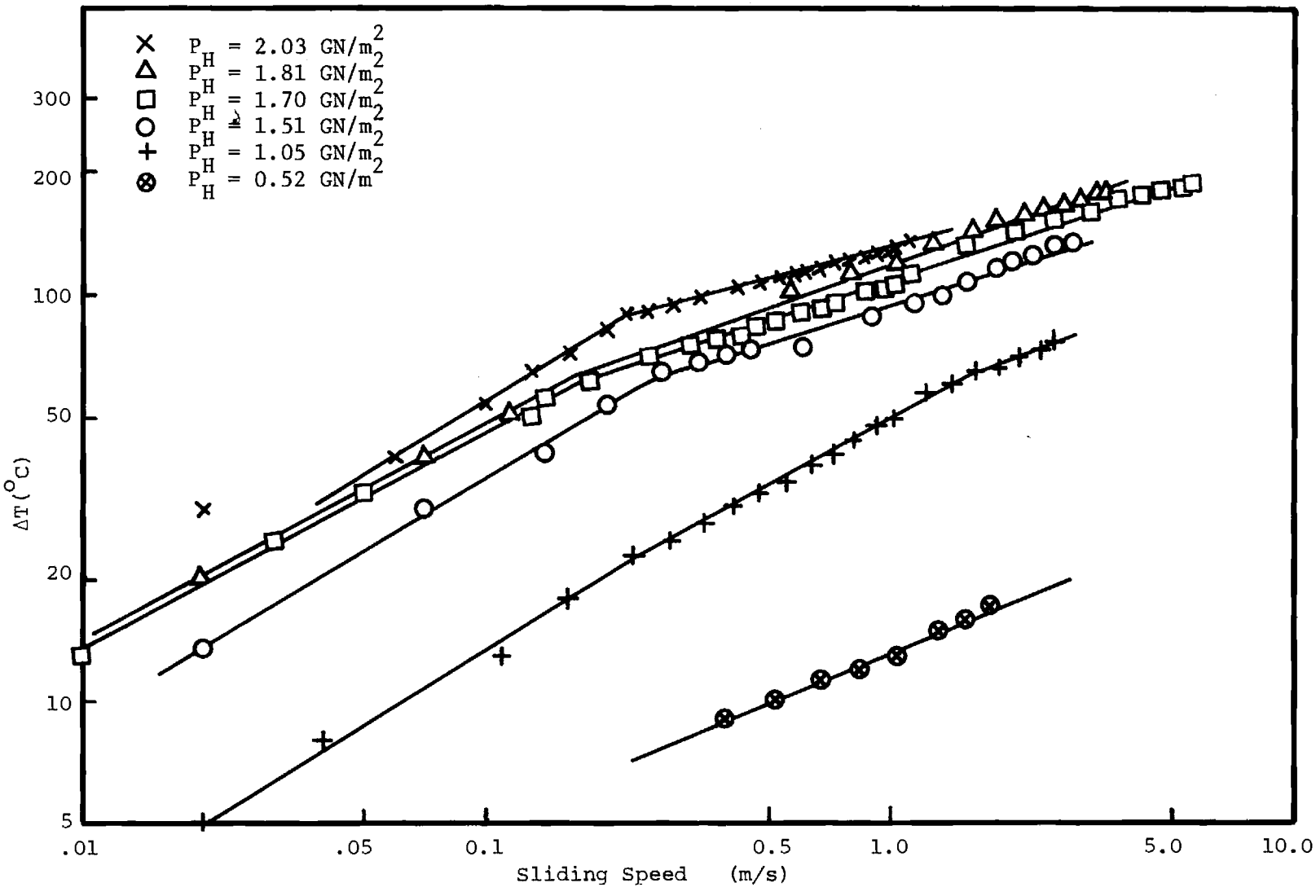

Figure 10. Ball Surface Temperature Rise at Contact Center, Smooth Ball (.011 μm c.l.a.), $1 < \Lambda < 2$ for P_H = 2.03 GN/m^2, otherwise $\Lambda > 2$.

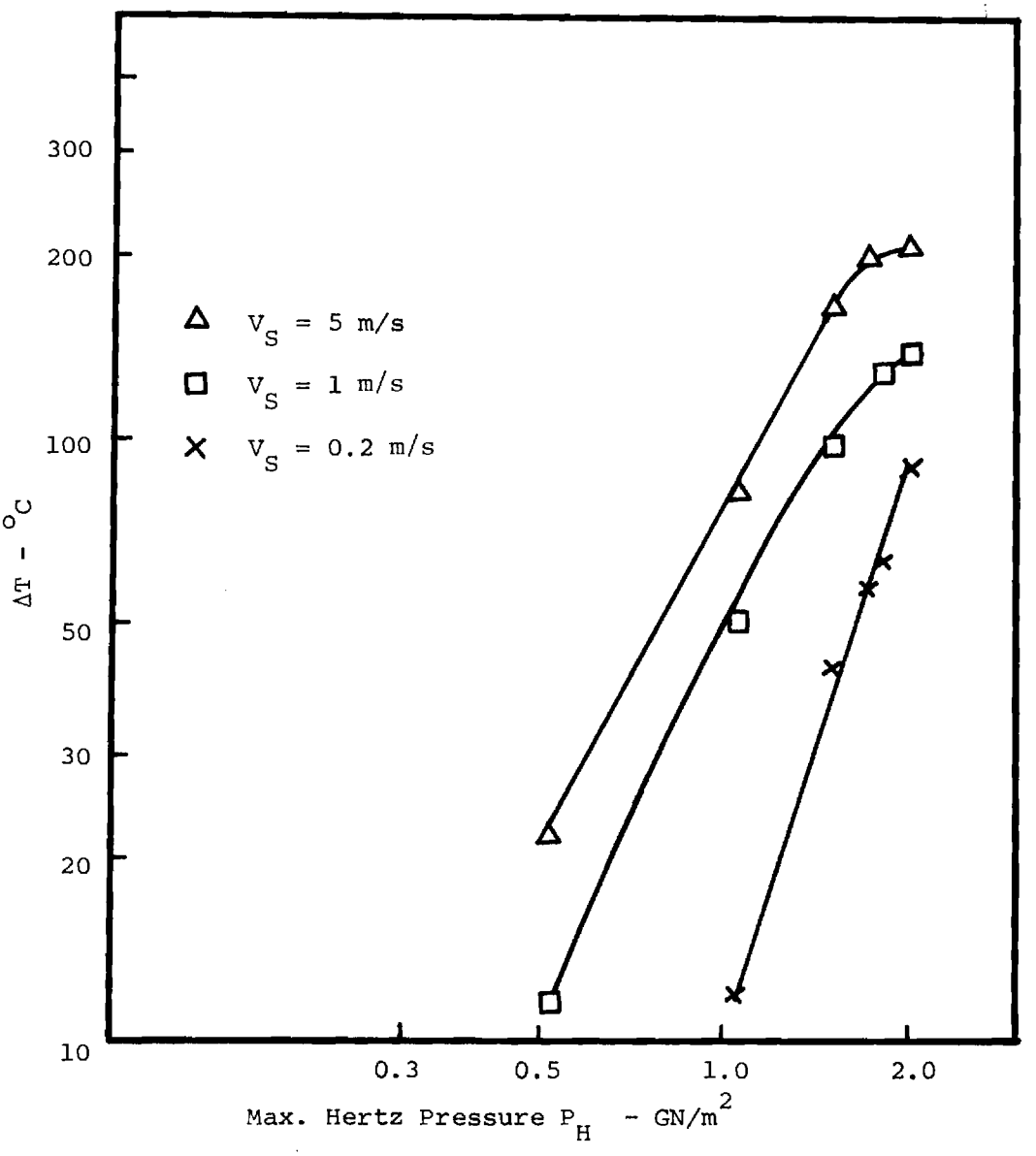

Figure 11. Surface Temperature Rise at Contact Center Versus Maximum Hertz Pressure, Smooth Ball (0.011 μm c.l.a.).

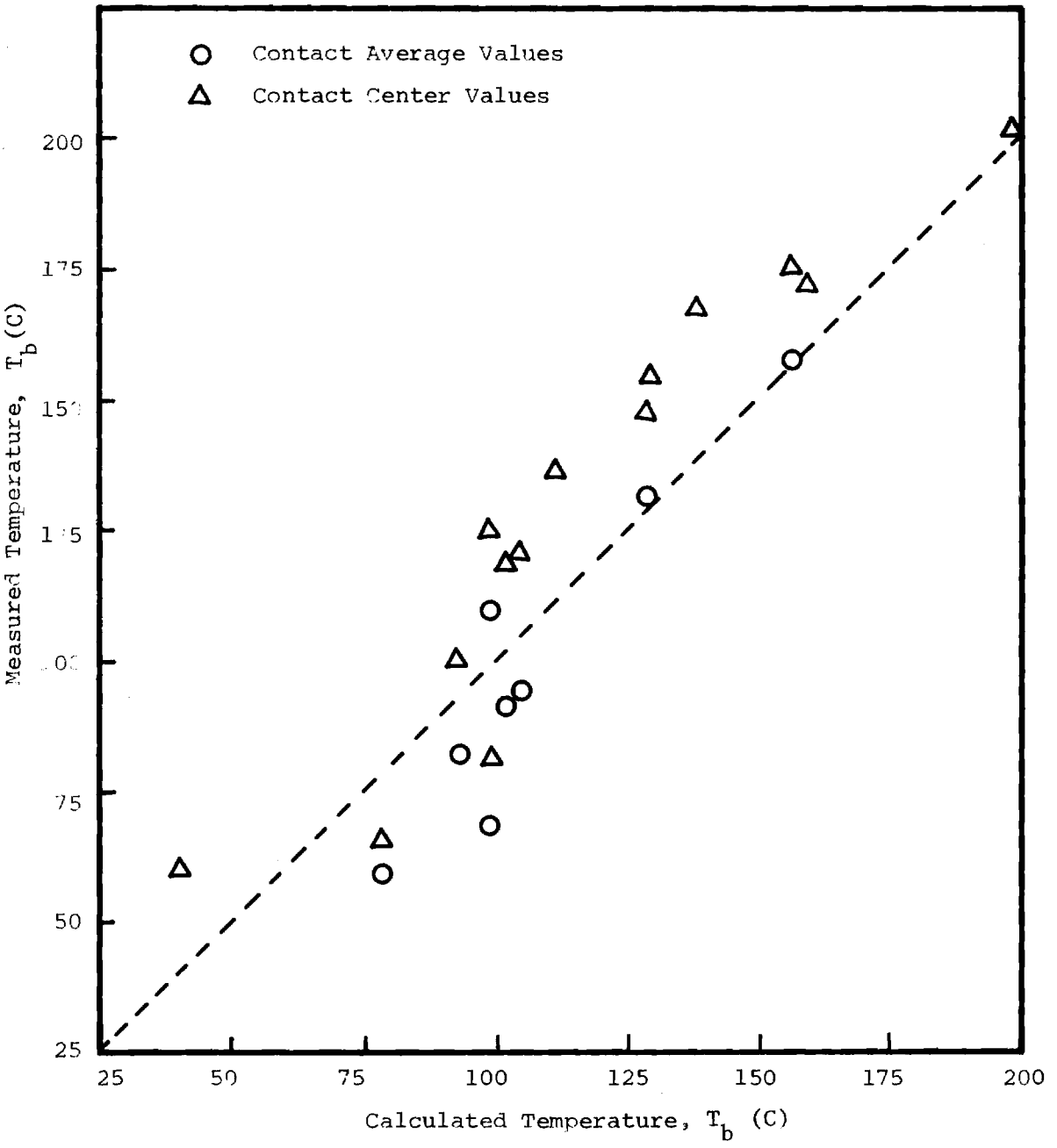

Figure 12. Comparison of Average Contact Temperatures Calculated Using the Blok Jaeger-Archard Theory and Measured Temperatures, Smooth Ball (0.011 μm c.l.a.).

In these cases, the ratio of contact length to height is the greatest thereby making conduction more significant. This trend is supported by the data for P_H = 1.51 GN/m^2 and 1.05 GN/m^2, in which contact average measured temperatures have been determined. The average deviation between calculated and measured temperatures was 4.8% for the 1.51 GN/m^2 data and 17% for the 1.05 GN/m^2 data using a Celsius temperature scale.

Although the flash temperature concept offers a means of estimating the contact surface temperature it is subject to substantial limitations. The average value obtained can be significantly in error, but more important, the method yields only an average. The peak temperature, which may be more important in determining contact behavior, is often much higher than the average.

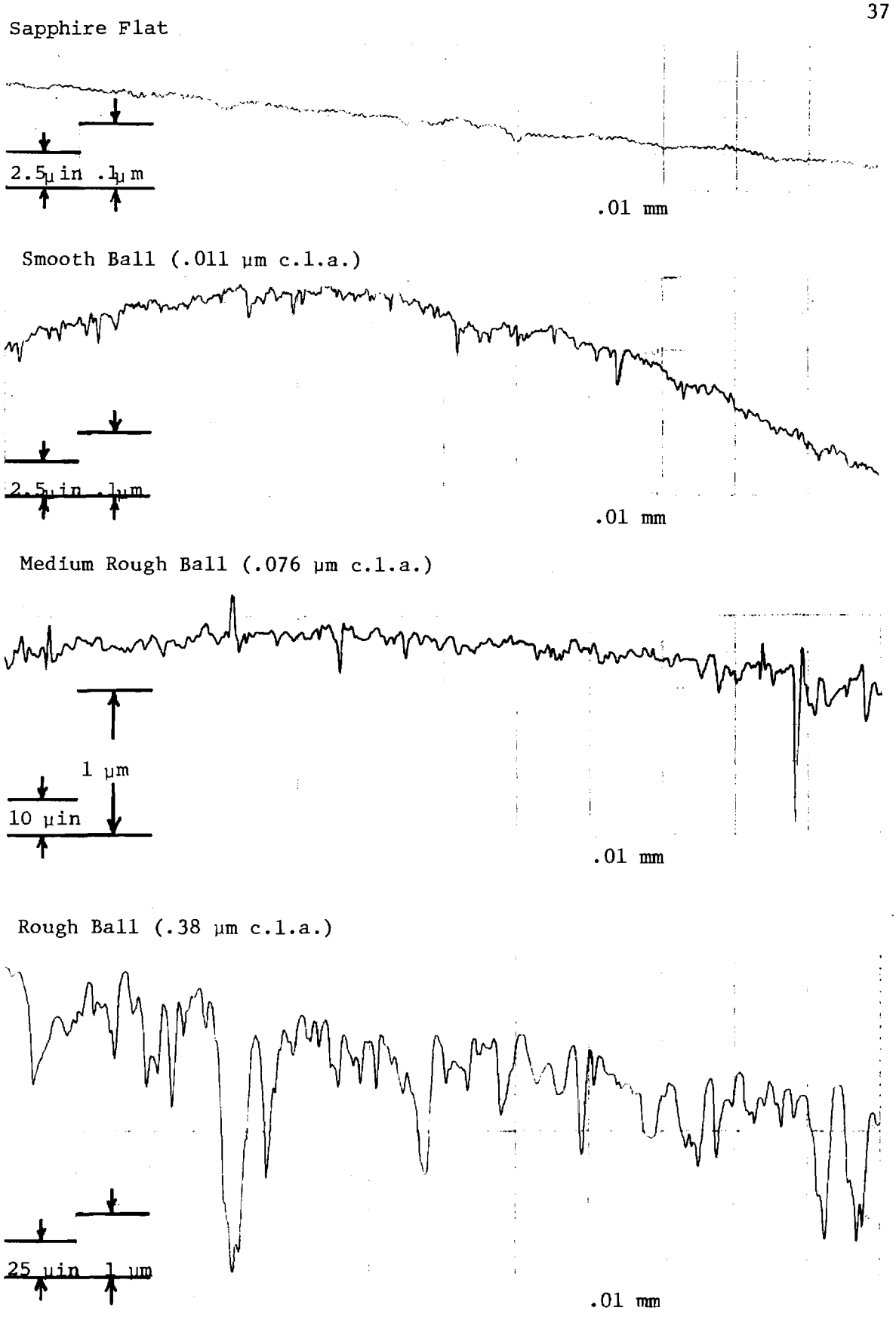

Figure 13. Surface Roughness Profiles.

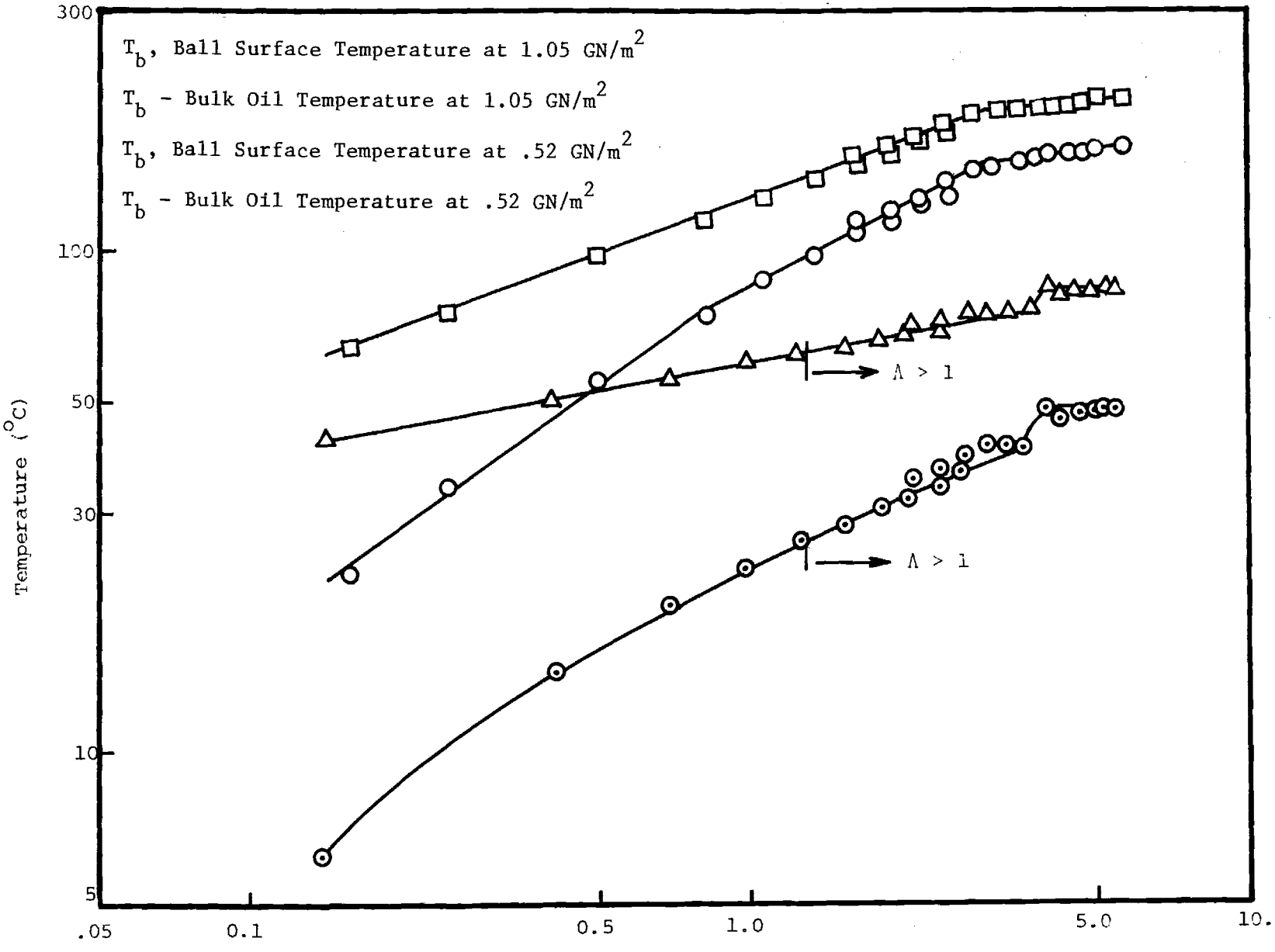

Figure 15. Maximum Ball Surface Temperature - Rough Ball (0.381 μm c.l.a.), (Λ < 1, except as noted).

at the contact center. It was necessary to make this procedural change because the contact center could not be located when the rough ball was used. This is due to the disappearance of the interference fringe pattern because of light scattering at the relatively large surface asperities. Therefore, the contact was scanned for the maximum surface temperature in each case.

The temperatures for the smooth and medium rough balls are only slightly different throughout the range of operating conditions. The surface temperatures for the rough ball appear to be significantly higher than those of the smoother balls. To put all temperatures on an equivalent basis the rough ball data in Figures 15 and 16 should be reduced by approximately $10^{o}C$. This is the difference between the maximum and center surface temperatures for the smooth ball (see Figure 3) .

The parameter Λ, which is the ratio of EHD film thickness h to the composite surface roughness σ, is a recognized parameter for predicting EHD contact performance [25]. For values greater than 2, no asperity interactions are expected. At Λ less than 1, severe asperity interaction is anticipated. The range $1 < \Lambda < 2$ is a transition region. Surface roughness measurements made on the sapphire and ball surfaces in this laboratory are c.l.a. values. The values of Λ obtained using c.l.a. rather than r.m.s. roughnesses are not sufficiently different that the transition values noted above are significantly altered [25]. Also, in computing the parameter Λ, the film thickness value used is that measured for the smooth ball. This is necessitated for two reasons. First of all the interference fringe pattern used to determine film thickness disappears as the roughness is increased. Secondly, the meaning of film thickness

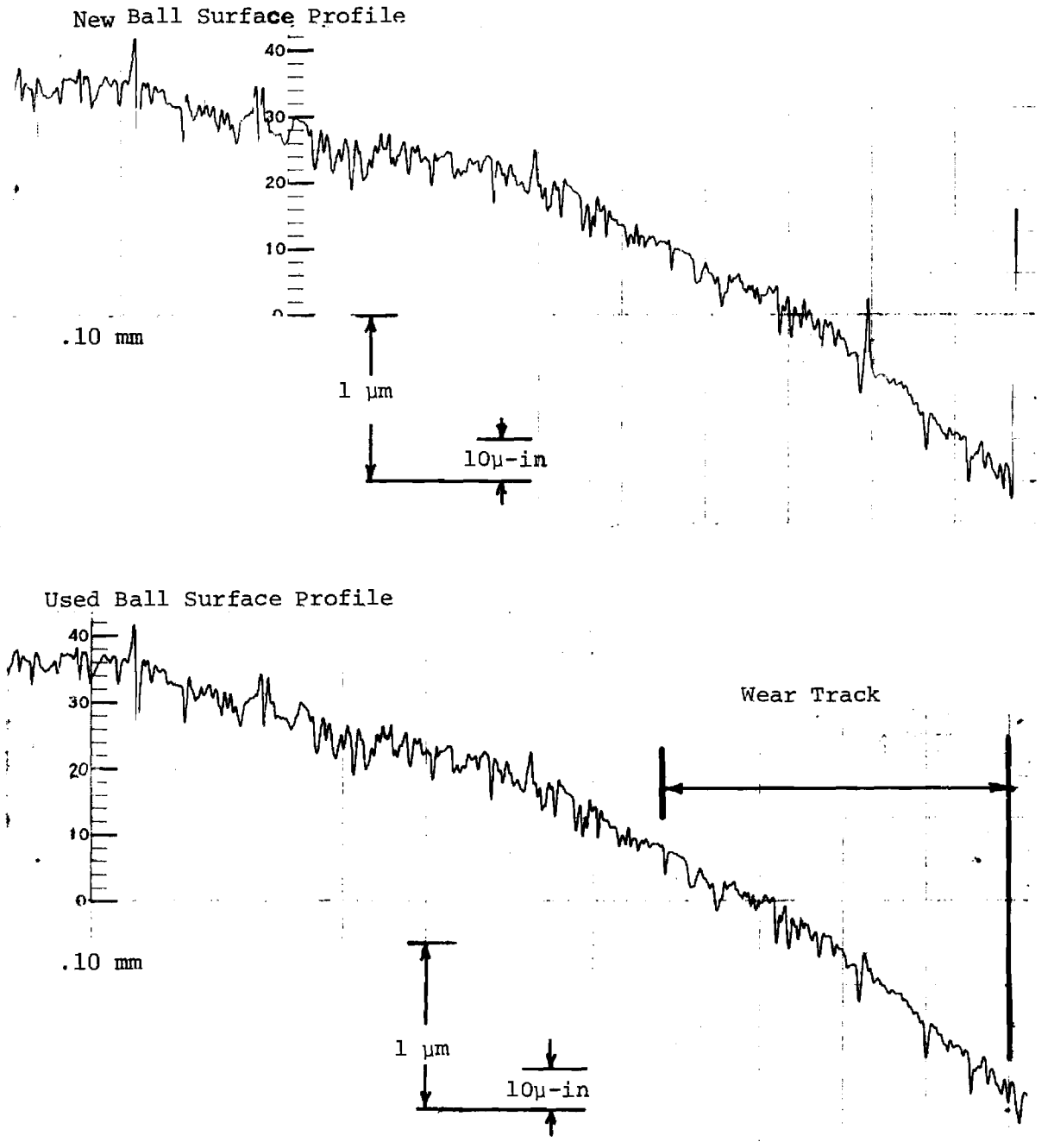

Figure 17. Relocation Profile for the Medium Rough Ball (.076 µm c.l.a.), (P_H = 1.70 GN/m^2, 0.83 $\leq$ V $\leq$ 5.0 m/s).

E. Relocation Profilimetry

Figure 19 shows two photographs of the specimen rotation attachment with a relocation stage fitted to a Bendix Group XV surface measuring system. Because of the curvature of the ball surface, it was necessary to modify the standard Bendix system to allow measurements over an adequate arc length at high vertical magnification. This has been accomplished by rotating the ball about its axis under a fixed stylus.

A relocation mechanism is incorporated in the rotation attachment. In order to detect any change in the surface profile, it is necessary to measure the profile at precisely the same point on the ball surface before and after being used in the EHD contact. Four of the possible six degrees of freedom are removed by using a pair of V-blocks to support the ball by two cylindrical collars cemented to the ball surface on opposite sides of the ball. The centerlines of the collars and ball are made as nearly coincident as possible. Since one of the collars is used to rotate the ball in the EHD contact simulator, the plane containing the wear track will be normal to this centerline. The other two degrees of freedom are removed by providing stops to limit motion along the axis of rotation and the amount of rotation about this axis.

As can be seen from Figure 17, the method has been successful in relocating the same area on the ball surface for re-examination. However, since it is not practical to obtain profiles of the entire wear track region before and after running in the EHD contact, an indication of no asperity interaction is inconclusive. Asperity interaction may have taken place at locations other than those measured.

F. High Frequency Temperature Fluctuations

It has been demonstrated in the previous sections that asperity interaction can significantly alter the ball surface temperature level. The results given thus far, however, are time-averaged temperatures obtained with the infrared detector in the DC mode. In this mode of operation, the frequency response is 400 Hertz. From the surface profile measurements (Figures 17 and 18) it has been determined that only a single asperity can occupy the detector's field of view (.036 mm diameter) at any one time. However, at 1.0 m/s sliding velocity, the residence time is only 36 μs. The DC mode, therefore, cannot respond to a temperature rise caused by a single asperity interaction. The available AC mode of operation, however, can detect such temperature transients. The liquid nitrogen cooled detector has a response time of 8 μs. The differences in the AC and DC modes of operation are shown in Figure 20.

An important consequence of operating in the AC mode is that the reference signal is absent. Instead the instrument will produce a voltage difference proportional to the variation in target radiation emitted. Through an independent experiment, using an external chopper, it has been determined that the variation indicated in the AC mode is centered on the signal received in the DC mode. From this information a plot of time-averaged surface temperature along with the maximum and minimum values can be obtained.

Electrical noise problems were encountered when using the AC mode. A satisfactory solution was obtained, however, by using a variable electrical band pass filter. Although the noise and signal could not be entirely separated due to the closeness of their frequencies, a pass

band of 1.0 to 20 KHz proved effective, since the high peaks in the signal are within 20 KHz for most of the sliding speeds.

Figure 21 shows a plot of the ball surface temperature at the contact center as a function of Hertz pressure. The .076 μm c.l.a. surface roughness ball was used at a sliding speed of 1.0 m/s. The plot shown was constructed using the DC mode data at five different Hertz pressures. In addition, the AC mode was used at the four highest Hertz pressure levels. As is shown in Figure 21, the AC data shows no fluctuation about the DC level at P_H = 1.05 GN/m^2, but shows an increasing amount of fluctuation as the pressure is increased. The upper and lower curves represent the range of temperatures detected. It is believed that the peak values represent individual asperity interactions. Figure 21 also shows the significance of the parameter Λ in predicting the onset of asperity interaction. Figure 22 is a graph of the same data, along with data from higher sliding speeds. In all cases, the center value represents the DC (time averaged value). From this data it appears that the range of temperatures detected in the AC mode of operation increases significantly as more of the normal load is supported by individual asperities. This corresponds to a condition of decreasing Λ values.

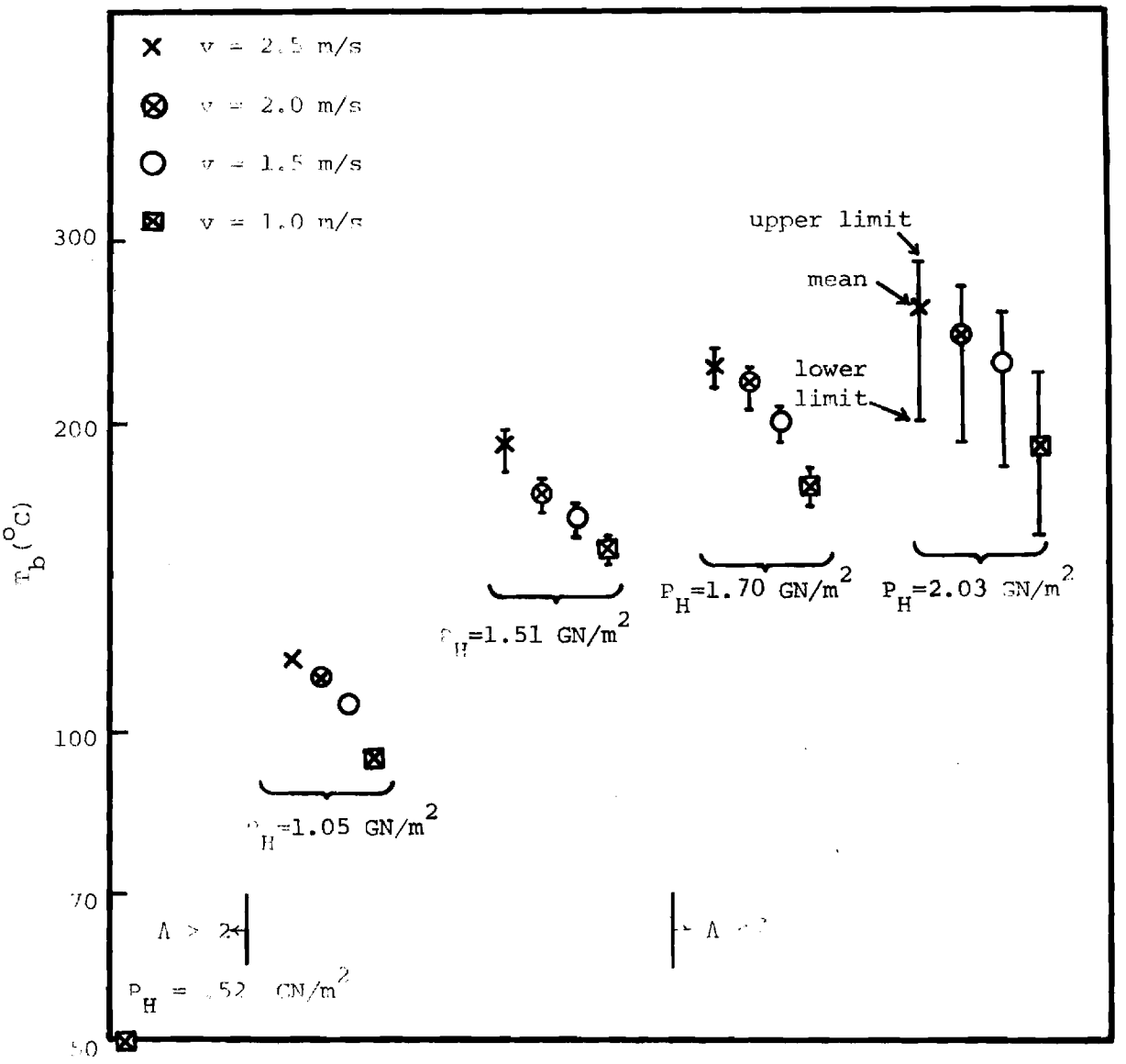

Figure 22. Average Value and Range of Ball Surface Temperature Fluctuations - Medium Rough Ball (.076 μm c.l.a.).

13. Kunz, R. K., "Thermal and Traction Behavior in Sliding Elastohydrodynamic Contacts," M.S. Thesis, Georgia Institute of Technology, Atlanta, 1974.

14. Sanborn, D. M., and Winer, W. O., "Fluid Rheological Effects in Sliding Elastohydrodynamic Point Contacts with Transient Loading: 2-Traction," Trans. ASME, JOLT, Series F, Vol. 93, No. 3, 1971.

15. Sanborn, D. M. and Winer, W. O., "Fluid Rheological Effects in Sliding Elastohydrodynamic Point Contacts with Transient Loading: 1-Film Thickness," Trans. ASME, JOLT, Series F, No. 2, 1971.

16. Novak, J. D., "An Experimental Investigation of the Combined Effects of Pressure, Temperature, and Shear Stress upon Viscosity," Ph.D. Dissertation, University of Michigan, Ann Arbor, 1968.

17. Roelands, C. J. A., "Correlational Aspects of the Viscosity-Temperature-Pressure Relationships of Lubricating Oils," Doctor Ingenieur Dissertation, Technische Hogeschool te Delft, 1966.

18. Sibley, L. B., "EHD Techniques and Application to the Design of Roller Bearings," Report No. A171Q010, SKF Industries, Inc., Research Laboratory, 1971.

19. Johnson, K. L. and Roberts, A. D., "Rheology of Oil Films at High Contact Pressure," Nature, Vol. 240, No. 5383, 1972.

20. ASME, Pressure-Viscosity Report, Vols. I and II, a report prepared by the ASME Research Committee on Lubrication, N. Y., 1953.

21. Ausherman, V. K., Nagaraj, H. S., Sanborn, D. M., and Winer, W. O., "Infrared Temperature Mapping in Elastohydrodynamic Lubrication," ASME Paper to be presented at Joint ASME-ASLE Lubrication Conference, Miami Beach, Florida, October 1975.

22. Archard, J. F., "The Temperature of Rubbing Surfaces," Wear, Vol. 2, No. 6, October 1959, pp. 438-455.

23. Jaeger, J. C., "Moving Sources of Heat and the Temperature at Sliding Contacts," Proc. Roy. Soc. N.S.W., Vol. 56, 1942, p. 203.

24. Blok, H., "Surface Temperatures under Extreme-Pressure Lubricating Conditions," Second World Petroleum Conference, Paris, June 1937, Vol. 3, Section 4.

25. Bamberger, E. N., et al., "Life Adjustment Factors for Ball and Roller Bearings - An Engineering Design Guide," ASME, New York, 1971.

Final Contract Tech. Rpt.

GEORGIA INSTITUTE OF TECHNOLOGY
SCHOOL OF MECHANICAL ENGINEERING
Atlanta, Georgia

Investigations of Lubricant Rheology as Applied to Elastohydrodynamic Lubrication

NASA GRANT NO.
11-002-133

D. M. Sanborn, Associate Professor
W. O. Winer, Professor
Co-Principal Investigators

G. M. Rentzepis, Associate Professor
Research Associate

S. Bair
Research Engineer

M. A. Alsaad
R. K. Kunz
H. S. Nagaraj
Graduate Students

For

NASA-LEWIS RESEARCH CENTER
21000 BROOKPARK ROAD
CLEVELAND, OHIO 44135

September, 1976

GEORGIA INSTITUTE OF TECHNOLOGY
SCHOOL OF MECHANICAL ENGINEERING
Atlanta, Georgia

Investigations of Lubricant Rheology as Applied to Elastohydrodynamic Lubrication

NASA GRANT NO.
11-002-133

D. M. Sanborn, Associate Professor
W. O. Winer, Professor
Co-Principal Investigators

G. M. Rentzepis, Associate Professor
Research Associate

S. Bair
Research Engineer

M. A. Alsaad
R. K. Kunz
H. S. Nagaraj
Graduate Students

For

NASA-LEWIS RESEARCH CENTER
21000 BROOKPARK ROAD
CLEVELAND, OHIO 44135

September, 1976

GEORGIA INSTITUTE OF TECHNOLOGY
School of Mechanical Engineering
Atlanta, Georgia

INVESTIGATIONS OF LUBRICANT RHEOLOGY AS APPLIED TO ELASTOHYDRODYNAMIC LUBRICATION

Ward O. Winer
Principal Investigator

David M. Sanborn
Principal Investigator

Stothe P. Kezios, Director
School of Mechanical Engineering

September 1976

TABLE OF CONTENTS

TABLE OF CONTENTS (Continued)

LIST OF TABLES

LIST OF FIGURES

LIST OF FIGURES (Continued)

LIST OF FIGURES (Continued)

LIST OF FIGURES (Continued)

LIST OF FIGURES (Continued)

I. INTRODUCTION

This is the final annual technical report for NASA Grant NGR-11-002-133 (March 1971 - April 1976) "Investigation of Lubricant Rheology as Applied to Elastohydrodynamic Lubrication". A brief summary of the first four years research are included in Section II. This report is primarily concerned with the research performed during the last year.

During the first four years significant progress was made in three areas; a) rheology of lubricants in a high pressure rheometer, b) observation of lubricant behavior in an elastohydrodynamic simulator, including the development of a temperature measuring technique, and c) the analytical modeling of elastohydrodynamic contacts (isothermal non-linear rheological fluid model and a linear model with thermal effects).

During the past year the research was concerned with elasto-hydrodynamic simulation and exploration of glassy state lubricant behavior. The ehd simulator research (Section III) is a continuation of the infrared temperature measurements to study the maximum surface temperatures in ehd contacts including rolling contacts with sliding. The effect of roughness on surface temperature and wear has also been studied. Correlations of surface temperature and operating variables have been developed which are suitable for use in engineering design.

Preliminary studies of the glass transition of lubricants were undertaken to determine if typical lubricants in typical ehd contacts pass through a glass transition (Section IV). They clearly indicate that some lubricants do pass into the glassy state in ehd contacts.

These results require further study and will result in a change in thinking regarding ehd lubricant rheology.

As a necessary part of the glassy state studies an analytical procedure was developed which relates the measured ehd film thickness to the pressure distribution. No assumption about lubricant rheology was necessary. This effort is presented in Section V.

In the appendices are presented a list of persons who have received support from this grant and a list of publications which were totally or in part obtained from this research.

The principal investigators wish to express their appreciation to NASA for the grant and to R. L. Johnson, W. J. Anderson, W. Jones and L. Wedeven for their support and encouragement. They can share the satisfaction which the principal investigators have for receiving the ASME Melville Award for the development of the infrared temperature technique. Acknowledgment is also made of the fact that some of the research in this report has been jointly supported by the National Science Foundation (Grant Number ENG 74-21002).

Professors Sanborn and Winer were co-principal investigators of the research reported and had overall responsibility. The other co-authors were involved in specific aspects: Dr. Alsaad conducted the light-scattering glass transition experiments which constituted his doctoral research. Mr. Bair conducted the other glass transition experiments and assisted in the ehd experiments, Dr. Nagaraj conducted the ehd temperature measurement experiments which constituted a major portion of his doctoral research, Professor Rentzepis and Mr. Kunz were responsible for the elasticity analysis of Section V.

II. SUMMARY OF RESEARCH CONDUCTED DURING 1971-1975

A brief summary of research completed during the first four years of this grant is presented in this section. For more complete details in each area the previous annual contract reports or referenced publications should be consulted.

A. High Pressure Rheology of Lubricants

Fifteen fluids have been subjected to high pressure rheological measurements. These include several fluids which consist of pairs of base fluid and base fluid plus an antiwear additive. These measurements were in two categories: 1) determination of the effect of pressure and temperature on the fluid viscosity (and pressure-viscosity coefficients) at relatively low shear stress (approximately 1kPa [1,2], and 2) determination of the effect of high shear stress upon the viscosity at modest pressures and temperature [3,4]. The pressures and temperatures chosen for the latter experiments were those which gave a low shear stress viscosity comparable to the average apparent viscosity observed in the ehd contact simulator under the sliding point contact conditions employed in this laboratory. All fifteen fluids have been subjected to the former type of measurements while six fluids have been subjected to the latter.

The pressure viscosity measurements have shown that the pressure-viscosity coefficient, important in ehd, decreases with increasing temperature in such a manner that the natural logarithm of the pressure-viscosity coefficient is approximately inversely proportional to the temperature [1,2]. Maximum differences of less than a factor of four in pressure-viscosity coefficient were observed among typical lubricants at a temperature of

37.8C (100 F). These differences are reduced considerably at 149C (300 F). Differences in viscosity and viscosity-pressure coefficients between base fluids and base fluids formulated with antiwear additives were found to be minor in all cases [1,2].

The high shear stress measurements performed on six fluids were conducted up to a shear stress within a factor of 3 to 4 of the average shear stress occurring in the sliding point contact ehd simulator employed in this laboratory (5 MPa compared to 14-20 MPa). Repeatable data explainable in terms of viscous heating only were obtained on four of the six fluids throughout the entire range of pressure, temperature and shear stress examined. The other two fluids, a polymer blended mineral oil and a 50 cs dimethyl siloxane, exhibited rheological behavior which could not be explained by viscous heating alone. The polymer blended mineral oil exhibited shear thinning behavior at relatively low shear stress as expected. Both the polymer blended mineral oil and the dimethyl siloxane exhibited "non-liquid" behavior above some characteristic threshold pressure and shear stress. In both cases the apparent viscosity during the non-liquid behavior was higher than expected from Newtonian considerations and generally was neither repeatable nor correlatable with the chronology of the measurement. In retrospect this behavior may be related to glass transition in these materials at the conditions of the experiments.

During the high shear stress measurements the average resident time of a fluid particle in the capillary, hence the time it was subjected to the high shear stress, was short (4 μs) compared to the average time the fluid particle is in an ehd contact (10^2 μs). Although the capillary residence time varied from a minimum of 4 μs up to 10^5 μs no effect of

residence time on viscosity was observed for the four fluids mentioned above suggesting time dependent effects are not important in this range. This is consistent with the oscillatory crystal research of Lamb and co-workers which indicates that the shear relaxation time for fluids in this viscosity range are of the order of 10^{-3} to 10^{-2} μs.

Viscous dissipation is an important rheological phenomena in the high shear behavior of typical liquid lubricants. This phenomena can be confused with shear thinning pseudoplastic behavior. The utilization of capillaries of different length-to-diameter ratios in performing the experimental measurements is essential in distinguishing between pseudoplastic and viscous heating effects. In addition to interpreting the experimental data, an analysis of the flow of a Newtonian fluid in a capillary including viscous dissipation and temperature dependent viscosity was performed [5]. The results of this analytical model are consistent with the experimental measurements. The analytical model was able to predict the high shear stress behavior of the lubricants whose behavior was measured with a good accuracy up to the highest shear stress measured.

Jakobsen's film thermal-shearing model[6] has been applied to point contacts[7] with emphasis on comparing predictions with existing data from this laboratory. The model appears to have some merit in conditions of high sliding. However, one result of this study has been the recognition of the possible importance of lubricant behavior in the glassy state. This possibility is discussed in Section V of this report.

B. Elastohydrodynamic Simulator Studies

All the fluids that were studied in the high pressure rheometer have also been studied in the ehd simulator where film thickness distribution

and traction were measured. Most of these measurements were at Hertz pressures in the range 1.0 - 2.0 GPa and with sliding speeds in the range 0.02 - 5.0 m/s.

The most significant advancement in these studies has been the development of the infrared emission technique for determining the fluid and ball surface temperature distributions in the ehd contact [8,9,10]. The technique utilizes an indium-antimonide liquid nitrogen cooled detector to measure the IR radiation emitted by the contact region. By suitable filtering, the radiation from the ball surface and the fluid can be separated and with the system calibration each temperature can be determined. At 1GPa Hertz pressure the temperature measurement area resolution is 1% of the contact area. Two principal applications of the technique have been studied. The first was to measure the temperature distribution for a given fluid and then employ these temperatures in an analytical model assuming a given fluid constitutive equation to predict traction which was compared with the measured value [7]. Because of the rheometer measurements mentioned above the linear constitutive model with temperature and pressure dependent viscosity was employed. The second major application of the IR temperature measuring technique was in observing the behavior of an ehd film as the severity of the contact condition increases [9,10]. The objective was to learn about failure of severely loaded ehd contacts. Based on the surface temperature mappings that have been completed to date, temperatures in some regions of the contact are higher than expected when considering viscous dissipation as the only energy source. The analytical model discussed below permits the prediction of the maximum fluid temperature through the film for a given film thickness.

Based on this model the maximum predicted temperature would be in the center of the contact. However, the measured maximum temperature may be in the lobe region and considerably higher than predicted for some operating conditions [9]. The region where measured temperatures exceed the predicted temperatures coincided with the region where the optical film thickness was equal to or less than the composite surface roughness of the surfaces utilized [9]. Thus both the film thickness and temperature measurements suggest the possibility of asperity interaction resulting in energy dissipation in addition to that due to viscous dissipation.

Throughout the experiments performed thus far, ball surface temperatures have been obtained. In addition, the fluid film temperature and ball surface profile have been determined at selected points. The ball surface temperature variations with speed are in close agreement with the results predicted by Jaeger, Blok, and later Archard, for temperature variations of run in surfaces [10]. These correlations are further developed in Section III of this report. Ball temperatures as high as 250 C for a reservoir temperature of 35 C have been observed. The lubricant temperatures have been approximately 40 C above those of the ball surface.

C. Analytical Modeling of Ehd Contacts

Two analytical models of ehd contact behavior have been developed. One was for the complete solution of the isothermal lubrication of rollers with a non-linear viscous fluid covering the load range from the lightly loaded rigid cylinder case to the highly loaded elastic cylinder case [11]. The second model is concerned only with the prediction of traction in highly loaded elastic contacts with viscous dissipation and temperature dependent linear viscosity [6,7].

The complete solution for the isothermal lubrication of rollers with non-linear fluids has been a difficult numerical problem to execute. However, solutions are now available with both linear and non-linear fluids for lightly loaded rigid cylinders and for elastic cylinders [11,12], in which case the solutions have been completed to the limit of the computing capabilities available. When this research was initiated it was thought that shear thinning of lubricants at high shear stress may be an important rheological phenomena. However, the concurrent work mentioned above of the high shear stress measurements of viscosity now indicate that shear thinning probably is not important for most lubricants. Those findings make the results of this analytical modeling less important than originally expected. The results are, however, still expected to be of value for two reasons; a) the numerical technique employed is different from most previous ehd analytical studies and therefore the results can serve as a comparison with other works for the linear fluid case, and b) because of the broad similarities between shear thinning and the effect of viscous heating the results of this model may give some qualitative insight into ehd behavior where viscous heating is present. The results will of course be useful for applications employing non-linear shear thinning fluids, however, this class of lubricants is now believed to be a relatively small portion of liquid lubricants currently employed. There may be wider application of the results to those systems employing greases, however.

The second analytical model developed [6,7] was the result of the high shear stress rheometer measurements which indicated the importance of viscous heating compared to shear thinning at high shear stress. This

model is concerned with predicting traction in the contact given a velocity, film thickness distribution and a rheological constitutive model for the fluid. The constitutive model employed is a linear model with pressure and temperature dependent viscosity. The model also accounts for the thermal effects of viscous energy dissipation. Because of the dependence upon obtaining film thickness independent of the analysis this effort is primarily useful in assessing the validity of rheological constitutive relations. Preliminary application of the model to a sliding ehd contact suggests that a linear viscous model with temperature dependent viscosity and viscous dissipation may be sufficient to describe the behavior of the fluid in an ehd contact with high sliding. However, the model fails to predict the traction as the amount of sliding decreases. This failure of the model may be the result of the lubricant behavior as a glassy solid in low sliding and rolling ehd contacts.

III. EXPERIMENTAL INVESTIGATIONS IN EHD CONTACTS

A. Introduction

The surface temperature data obtained for the case of pure sliding under the previous contract [13] was analyzed and compared to predicted flash temperatures. The surface temperature data is in good agreement with the predicted flash temperature.

Both the surface roughness profile and the AC signal from the infrared detector were analyzed in the frequency domain. It was found that only certain wavelengths in the roughness profile are important as far as asperity interaction is concerned. The parameter $\Lambda(\Lambda = h_c/\sigma)$* is shown to be a valuable means of predicting surface interaction in EHD contacts. A new method for determining the surface roughness, σ, is also proposed.

The effect of various amounts of rolling on the film thickness, traction and surface temperature was studied and the results are reported. A correlation study of the influence of sliding and rolling velocity on surface temperature was also undertaken and the results are discussed.

---

*The nomenclature used in this section is found on the following pages.

NOMENCLATURE

a	Hertzian contact radius, m
C	Auto-correlation function
d	Hertzian contact diameter = 2a,m
h_c	Film thickness at contact center, m
h_m	Minimum film thickness, m
k	Thermal conductivity, W/(mK)
L	Non-dimensional time parameter = t_1/t_2
ℓ	Length, m
$P(\omega)$	Power spectrum
P_H	Peak Hertz contact pressure, N/m^2, Pa
$\bar{q}$	Heat flux, W/m^2
r	Correlation coefficient
R^2	Coefficient of determination
t	Time, s
t_1	Thermal diffusion time = $a^2/2\alpha$,s
t_2	Characteristic resident time = a/V,s
T	Temperature, C
ΔT	Temperature rise, C
T_o	Upstream (bulk) temperature, C
TC	Traction coefficient
V	Surface Velocity, m/s
$\bar{V}$	Rolling velocity = $1/2(V_b + V_{sa})$, m/s
V_{BP}	Break-point velocity in correlation study, m/s
V_s	Sliding velocity = $V_b - V_{sa}$, m/s
W	Load, N

x Distance along surface, m

α Thermal diffusivity, m^2/s

β Length shift in computing autocorrelation function, m

β^* Correlation distance, m

K A constant = $.968\ a^{1/2}\alpha^{1/2}/k$, $m^{3/2}s^{1/2}\ C/N$

Λ h_c/σ

λ Wavelength, m

μ Viscosity, Ns/m^2

Σ Slide roll ratio = $V_s/\bar{V}$

σ Surface roughness, rms or Ra, m

τ Time, s

ω Wave numbers = $1/\lambda$, m^{-1}

Subscripts

b ball

f fluid

sa sapphire

B. Experimental Equipment and Techniques

Two EHD contact simulators were used in the studies conducted during the past year. The first (Figure III-1) is the apparatus used for film thickness, traction and temperature measurements of EHD contacts in pure sliding. It is the same as the equipment used in pure sliding EHD studies previously conducted in this Laboratory. The new equipment (Figure III-2) differs from the sliding rig primarily in that the sapphire disk may be rotated by a separate drive system to achieve various amounts of slip. The new equipment also has a simplified system for traction measurement. In the pure sliding apparatus, the traction force was isolated from the normal force by using an air bearing under the sphere support. In the new rig, the lateral motion needed to detect the traction force is obtained by mounting the ball support on sheet metal columns. The system is therefore very rigid with respect to the normal load, but is relatively flexible with respect to the traction force. Strain gages are attached to the columns such that bending strain (proportional to traction) can be detected, but compression (proportional to normal load) can not.

In each simulator, the contact is formed using a 31.8 mm diameter 52100 steel ball rotating and loaded against a sapphire flat. Lubricant film thickness was measured for the smooth ball experiments using an optical interference technique. Both monochromatic and dichromatic [14] methods were employed.

Chromium steel balls (AISI 52100) of three different roughness values have been used to study the effects of surface roughness. The

Ra values are 0.011, 0.075 and 0.38 μm and are referred to as smooth, medium rough and rough, respectively. These balls do not have a preferred roughness orientation. Because of the high loads and relatively rough surfaces used in this study, it was not always possible to accurately measure film thickness by an optical technique. The fluid temperature can not be obtained without an accurate film thickness distribution. Rough surfaces give a time dependent film thickness at a given location which prohibits the determination of film temperatures for the rough ball. Therefore, only ball surface temperatures were measured.

The technique for measuring the ball surface temperature distribution in the contact has been described earlier [9,12]. Ball surface temperature measurements are made only at the contact center for the case of smooth and medium rough balls. The center of the EHD contact is easy to locate and also, the temperature at this location is quite close to the maximum. In the experiments with the rough ball, the temperature measured is the maximum in the contact, whether or not it occurs at the contact center. It was necessary to make this procedural change because the contact center could not be located when the rough ball was used. This is due to the disappearance of the interference fringe pattern because of light scattering at the relatively large surface asperities. Therefore, the contact was scanned for the maximum surface temperature in each case.

The infrared radiation emitted at this contact is measured with an infrared radiometric detector having a spot size resolution of 38 μm with a 15X objective and a response time of 8 μs in the A.C. mode of

operation. It was necessary to monitor the oil reservoir temperature with a thermocouple and to hold it constant with a constant temperature bath and an oil circulation system.

A Bendix surface profilimeter has been equipped with a relocation device [13]. This allows the same area of the ball surface to be examined in the profilimeter both before and after use in the EHD simulator.

Fourier analysis of both the surface profile data and the high frequency I-R data was done using Hewlett-Packard Model 5451A Fourier Analyzer System. This equipment is owned by another unit of the Institute but has been made available for use on his project.

The fluid used throughout this investigation is a naphthenic base oil designated N1 in previous studies. A complete description of the fluid is given in the appendix of reference [15].

C. Flash Temperature Measurements for Pure Sliding

Ball surface temperatures for the smooth ball were reported a year ago [13], but a correlation study with existing flash temperature theories has only just been completed. Figure III-3 shows a plot of the ball temperature rise at the contact center above the bath temperature, as a function of sliding velocity for peak Hertz pressures ranging from 0.52 to 2.03 GN/m^2. For a given Hertz pressure, the data plotted on log-log coordinates falls on one straight line for velocities up to a break-point value and then on another line, of lower slope, for higher velocities. The temperature rise is the difference between the ball surface temperature at the contact center and the lubricant bath temperature as measured with a thermocouple.

The trends shown in Figure III-3 can be predicted using the

techniques of Blok [16], Jaeger [17] and Archard [18]. The energy dissipation rate in the contact is equal to the product $(W \cdot TC \cdot V_b)$. The heat flux to each surface is then proportional to the dissipation rate divided by the area of the contact, or

$$\bar{q} \propto \frac{W \cdot TC \cdot V_b}{\pi a^2} \propto TC \cdot P_H \cdot V_b \qquad (1)$$

where the constant of proportionality includes the portion of the total heat flux transferred to the ball. According to Archard [18] the temperature rise on the surface of a solid moving at velocity V_b and subjected to heat flux $\bar{q}$ can be described in terms of a non-dimensional parameter $L = t_1/t_2$. The term $t_1 = a^2/2\alpha_b$ represents the time required for the effect of $\bar{q}$ to penetrate a distance (a) below the surface, whereas $t_2 = a/V$ represents the time required for a point in the contact to move a distance (a). Therefore, for a given fluid and surface, L is proportional to $(P_H \cdot V_b)$. The variation in ΔT (ball surface temperature minus bulk oil temperature) is given as

$$\Delta T \propto \bar{q} \cdot P_H \propto TC \cdot V_b \cdot P_H^2 \qquad \text{for } L < .1 \qquad (2)$$

and

$$\Delta T \propto \bar{q} \cdot P_H^{1/2} \cdot V_b^{-1/2} \propto TC \cdot V_b^{1/2} \cdot P_H^{3/2} \qquad \text{for } L > 5 \qquad (3)$$

The parameter L has been plotted in Figure III-3 for the case of $P_H = 1.70$ GN/m^2. The values 0.1 and 5 represent points for which the full solution is in good agreement with the limiting cases of equation 2 (stationary heat source solution) and equation 3 (fast moving heat source solution) respecitvely. Most of the data shown in Figure III-3 has an L between the limiting values.

In order to determine how well the data fits the Jaeger-Archard predictions of equations (2) and (3), a multiple regression analysis of the data shown in Figure III-3 was performed. For each Hertz pressure level, the data was divided into two regions separated by a break-point velocity clearly visible in Figure III-3. This break-point velocity is a function of Hertz pressure and can be described by

$$V_{BP} = 0.53\ P_H^{-1} \tag{4}$$

with a correlation coefficient of r = 0.95. This results in a value of 3.4 for L at the break point in the experimental data. This is reasonably close to unity which is the theoretically predicted breakpoint [18]. The reason for this discrepancy is the limited amount of experimental data at low values of L. For sliding velocities below V_{BP},

$$\Delta T \propto P_H^{2.02}\ V^{0.53} \tag{5}$$

with $R^2 = .978$. For velocities above V_{BP},

$$\Delta T \propto P_H^{1.34}\ V^{0.34} \tag{6}$$

with $R^2 = .985$.

These relations were obtained neglecting the traction coefficient, since traction data was not obtained during these experiments. However, from equations 1-3 it is apparent that its influence must be included. Based on previously reported data [19,20], the traction coefficient has only a slight positive dependence on P_H in the pressure ranges studied. Furthermore, TC was found to be dependent on sliding velocity to the

power -0.29 with r = .994. The data used had $3 \leq L \leq 22$. Including this dependence in equations 5 and 6 results in

$$\Delta T \propto P_H^{2.02} V_b^{.82} V_b^{-.29} \propto P_H^{2.02} V_b^{.82} \cdot TC \tag{7}$$

and

$$\Delta T \propto P_H^{1.34} V_n^{.63} V_b^{-.29} \propto P_H^{1.34} V_b^{.63} \cdot TC \tag{8}$$

Recalling that equations 2 and 3 represent limiting cases, the experimental results appear to be in good agreement with the predicted trends (equations 2 and 3).

D. Correlations Between Surface Roughness and Temperature

In the previous report [13], a method was described wherein the surface roughness profile could be determined at the same location on the ball surface both before and after running in the EHD simulator. During the past year, a significant extension of this work has been undertaken on the frequency or wavelength aspects of the surface profile signal and its influence on surface temperature.

In order to study the ball surface profile in the frequency or wavelength domain, the profilometer output was first recorded on magnetic tape. This was done for samples of balls from the three roughness classifications, both before and after running in the EHD simulator.

The recording of the profilometer trace was transferred to a Hewlett-Packard Fourier Analyzer. The first step in any analysis performed by this instrument is an A/D conversion. After analysis

of the digital representation of the input signal, the results may be printed and/or a D/A conversion can be made and the results plotted or displayed on a CRT.

Figure III-4a shows the surface profile of the unused ball having an initial surface roughness of 0.38 μm Ra. The trace represents the signal after the A/D and D/A conversions and is an excellent replica of the original signal plotted by the Bendix profilometer. The distance along the ball surface is shown in terms of the Hertzian contact diameter, d. For the conditions of steel on sapphire at 1.24 GN/m^2 peak Hertz pressure, the calculated contact diameter is 0.43 mm.

Figure III-4b shows the same ball after running for 24 minutes in the simulator. The profile traces shown in Figure III-4 were taken in the direction of the sliding motion. No attempt was made to measure the profile at precisely the same location on the ball surface. The traces taken are of sufficient length that they should be representative of any position within the wear track. From the previous report [13], the conditions of 1.24 GN/m^2 and V_s = 1.02 m/s should result in a value of $\Lambda < 1$ based on the unused ball surface roughness. The value $\Lambda < 1$ indicates that asperity interaction should be expected. Comparing the two traces in Figure III-4, it is apparent that the 24 minute run-in period has resulted in a smoother surface. The roughness is .25 μm Ra which results in $\Lambda \simeq .4$. The 15.9 mm radius of curvature of the ball surface can also be seen.

1. Power Spectra

The primary function of the Fourier Analyzer is to perform the Fast Fourier Transform (FFT) on the time varying input signal. A convenient way of displaying the amplitudes of the component terms in Fourier

series is through the power spectrum. The input to the analyzer is a time varying voltage. After the A/D conversion, the FFT results in a complex amplitude for each of the 127 (plus a constant) terms used in the series. Each of these terms is assigned a pair of channels in the analyzer. The frequency range, and therefore, frequency increment can be selected. The frequency assigned to two adjacent pairs of channels differs by a constant. The resulting plot of the power spectrum is linear in the independent variable, frequency. The value of the ordinate at each center frequency (channel) is the product of the complex amplitude for that frequency and its conjugate. The units are, therefore, V^2 versus Hz. The D/A conversion makes the plotted results appear to be continuous, but all of the data processing was done digitally in terms of the coefficients of the first 127 terms of the Fourier series.

Although the results are plotted on a linear frequency scale, this is not a convenient representation for this study. This is due to the fact that the frequency is influenced by the profilometer stylus scanning speed and differences between magnetic tape recording and play-back speeds. In order to remove these effects, the abscissa has been changed to read wavelength. The unit of wavelength selected is d, the Hertz contact diameter of 0.43 mm. The power spectra of the profiles shown in Figure III-4 are given in Figure III-5.

The first four channels (0-3) were cleared prior to plotting. This is because the values are so large compared to the values in higher channels (see insert), that a plot would show only the very low frequency components. Therefore, only components having wavelengths $<3d$ have been plotted. In comparing the power spectra for the unused

and run-in ball surface profiles, note the factor of two change of scale in Figure III-5a versus III-5b. The most apparent contrast is the reduction of the components having wavelengths <2d. Comparing the tabular data in Figure III-5, it appears that roughness components having wavelengths >2d remain essentially unchanged after the 24 minute run-in period. The nine percent difference in DC level can be attributed to slight differences in signal amplification in obtaining the two surface profiles. The most drastic change occurs for a wavelength of one Hertz diameter. This component has been reduced by more than a factor of eight.

2. Autocorrelation Function

In addition to the power spectrum, the autocorrelation function can be useful in describing the surface profile. In fact, Whitehouse and Archard [21] and Peklinik [22] suggest the description of a real surface in terms of only σ, the rms roughness, and β^*, the correlation distance. Briefly, the autocorrelation function is obtained by comparing a time varying signal, in this case the surface profile measurement, with a replica of itself where the replica is shifted some amount of time (or distance at a given velocity). If the shift along the surface profile is β, then the autocorrelation function $C(\beta)$ becomes

$$C(\beta) = \frac{1}{\ell} \int_0^{\ell} a(x)a(x + \beta)dx \qquad (9)$$

where $a(x)$ is the amplitude of the surface profile trace at a distinct x along the surface. For a truly random signal, $C(\beta)$ will be a maximum at $\beta = 0$. If the signal is periodic, $C(\beta)$ will peak whenever β is a

multiple of the wavelength. If a Gaussian distribution of surface roughness amplitudes is considered, equation 9 results in an exponential autocorrelation function when normalized such that C(0) = 1.0,

$$C(\beta) = \exp(-\beta/\beta^*) \tag{10}$$

Therefore, when $\beta = 2.3\beta^*$, $C(\beta) = 0.10$. The value 0.10 has been arbitrarily set by Whitehouse and Archard as being sufficiently small that two points on the surface may be regarded as being independent. The power spectrum is the inverse Fourier transform of the autocorrelation function, or

$$P(\omega) = \int_{-\infty}^{\infty} C(\tau) e^{-i\omega\tau} d\tau \tag{11}$$

Substituting equation 10 into 11 results in

$$\begin{aligned} P(\omega) &= 0.5 && \text{for } \lambda = 1/\omega = \beta^* \\ P(\omega) &\tilde{-} 0 && \text{for } \lambda = 1/\omega < 0.1\beta^* \\ P(\omega) &\tilde{-} 1 && \text{for } \lambda = 1/\omega > 10\beta^* \end{aligned} \tag{12}$$

The wavelength β^* can therefore be thought of as a dividing point between those surface wavelength components having significant amplitudes and the shorter wavelengths which do not. Whitehouse and Archard have shown the model to be in good agreement with a large number of real surface profiles.

Figure III-6 shows the autocorrelation function for the unused and run-in ball surfaces shown in Figure III-4. The position shift β is shown in terms of the Hertz diameter d. If the Whitehouse-Archard

model is applied to the data in Figure III-6, the value of β^* can be found from $C(2.3\beta^*) = 0.1\ C(0)$. The correlation distance β^* is .17d (74μm) for the unused ball and .33d (142μm) for the run-in surface. It is apparent that the exponential model of equation (10) can only be used for $\beta \leq 2.3\beta^*$. The further increase in $C(\beta)$ implies that the profile is not truly random, but has strong periodic components with wavelengths > d. This can also be seen from the power spectra shown in Figure III-5.

Figure III-6 also shows that the correlation distance has doubled as a result of the run-in process. From equation 10, a doubling of β^* implies that two points on the surface must be taken twice as far apart after run-in to be considered independent. Because of the interrelationship between the power spectra and autocorrelation function (equations 11 and 12), if the surfaces were in fact random, the half power point would be shifted to a wavelength twice the value of that for the unused surface. This is the case when the high frequency components are reduced much more than the low frequency components (see Figure III-4). This is also consistent with the notion of independent points. Consider, for example, a surface comprised of only two wavelength components 2d and 0.2d. When the 0.2d wavelength component is present, the autocorrelation function would have a value of 1.0 for $\beta = 2md$ where m is an integer. However, it would also have sizable peaks for $\beta = 0.2md$ (with drops to near zero between). After run-in, however, the 0.2d wavelength component will be substantially reduced. Assuming it to be eliminated, the $C(\beta)$ now peaks only once every $\beta = 2md$ and reaches zero between the peaks. If the correlation distance

is defined as the ten percent point, it is apparent that this distance must be increased if high frequency components are reduced or eliminated.

3. Correlation between Surface Roughness and Temperature Fluctuations

The AC signal from the infrared detector obtained during the run-in process was also recorded and analyzed on the Hewlett-Packard analyzer. However, in order to eliminate noise in the detector signal, a 20 KHz, 3dB filter was used during data acquisition. The noise remaining below 20KHz had a peak power of about $5 \times 10^{-6} V^2$ whereas the detector signal had a power content on the order of $10^{-4} V^2$. Furthermore, the sampling technique used by the Fourier analyzer tends to average out the random noise while enhancing the signal.

Figure III-7 shows a normalized histogram of the AC signal from the detector obtained at the beginning of the run-in period (Figure III-7a) and after running for eight minutes (Figure III-7b). The figure shows that the voltage distributions are nearly Gaussian. Secondly, it is apparent that the amount of dispersion is decreased by the run-in process. It is interesting that both the high and low extremes in temperature signal have been eliminated as the asperity peaks were removed. The symmetry of the fluctuations supports the argument advanced previously [10] that the peak in the temperature fluctuation signal is due to local heating at an asperity; whereas the minimum signal occurs directly after this maximum and is due to the relatively low local pressure in the region following an asperity.

Figure III-8 shows the power spectra for the same IR detector signals as used in Figure III-7. The abscissa has been replotted in

terms of wavelength in units of d (Hertz diameters). It is apparent from Figure III-8 that the run-in process results in a significant reduction in power at all wavelengths. In both spectra, the peak occurs near $\lambda = 2d$, although the run-in process has reduced the peak magnitude by more than a factor of three. It should be noted that the detector signal was also filtered to remove frequency components less than 500 Hz. This corresponds to wavelengths in Figure III-8 which are greater than 5d.

4. Discussion of Results of Spectra Correlations between Temperature Fluctuations and Surface Roughness

Based on the results shown in Figures III-5 and III-8, the authors believe that the methods presently used to determine acceptable levels of the Ra or rms surface roughness may not be the most appropriate when surface roughness effects on EHD contact temperature, wear or scuffing are of interest. For example, the rms value for the surface shown in Figure III-4a (unused rough ball) is equal to the square root of the integral of the power spectrum (Figure III-5a). However, the proper limits of integration must be chosen. The Bendix instrument used to obtain the profile shown in Figure III-13a uses an upper limit of .76 mm (through electrical filtering) and has a lower limit set by the stylus radius of 13μm. If one assumes that the absence of surface temperature fluctuations is indicative of negligible asperity interaction (as shown in the previous report [13]), then as far as asperity interaction is concerned, one can determine the significant wavelengths of the surface profile. For example, Figure III-8a shows that the

temperature spectral power content during asperity interaction drops to about ten percent of its peak value for the wavelengths $\lambda \leq d/4$. However, Figure III-5a shows that there are significant roughness components down to at least $\lambda = .08d$ (the power content is essentially the square of the amplitude). The same figures show that the major components for both the roughness profile and the temperature signal are in the range $d \leq \lambda \leq 2d$. Therefore, whereas the roughness wavelength in the range $d \leq \lambda \leq 2d$ are obviously important in causing temperature fluctuations, wavelengths shorter than d/4 appear to have no effect. This, of course, is based on the premise that a temperature fluctuation is caused by an asperity interaction. Based on the power reduction to ten percent of its maximum value, the lower bound for rms determination should be $\lambda \simeq d/4$. The upper limit is set at $\lambda = 2d$ because the temperature signal drops off rapidly for $\lambda > 2d$ even though there are roughness components present with wavelengths greater than 2d (see Figure III-5).

On the basis of the data taken, it appears that the rms surface roughness to be used in a calculation of $\Lambda(\Lambda = h/\sigma)$ should consider only wavelengths in the range $d/4 \leq \lambda \leq 2d$. For this experiment, d = 0.43 mm and the applicable range is then $.11 \leq \lambda \leq .86$ mm. A roughness of about .38μm rms was obtained using the Bendix system with limits of about $.013 \leq \lambda \leq .76$ mm, and the standard filter (2CR-type). However, by integrating the power spectrum of the surface profile in the Fourier Analyzer between the limits of $0.11 \leq \lambda \leq 0.86$ mm the rms value for the surface roughness was 0.53μm. This higher value is believed to be due to significant power in range $0.76 \leq \lambda \leq 0.86$ mm.

The Bendix instrument also has available cut-offs at .25 mm and .067 mm. The use of either of these values would correspond t rms integration limits of .030d - - .58d and .030d - - .18d respectively. Since the desired range is .25d - - 2d, the resulting rms values from the profilometer using these cutoffs would not be expected to be a reliable measure of surface roughness in predicting surface interaction.

In addition to the possibility of getting a value of surface roughness which cannot reliably predict performance, the fact that wavelengths shorter than 0.25d do not appear to be significant might have an economic impact. For example, under conditions in which the Hertz diameter is relatively large, the final stages in a lapping or polishing process may not be important.

The EHD contact appears to behave like a mechanical filter in which wavelengths outside of a relatively narrow band have a negligible effect on the performance of this system. If relatively thin films are expected during the operation of a highly loaded bearing, an improvement in surface finish should be considered. However, the magnitude of the rms roughness and the processes which might best improve the surface can not be adequately chosen until the Hertz contact diameter is known so a wave length range for measuring surface roughness can be defined.

5. Wear Measurements by Ferrographic Analysis

In order to confirm the dependence of asperity interactions on Λ, a ferrographic analysis of the oil used in thetest rig was performed. In ferrographic analysis, solid particles are precipitated from the oil by a magnetic field as the oil flows slowly over a

substrate. Particles are precipitated from the oil at a rate depending on size and magnetic permeability. The resulting ferrogram yields the size distribution and concentrations of particles in the oil sample.

Using special precautions to avoid oil contamination by particles other than contact wear debris, 30 mℓ samples were taken at various Hertz pressures for 1 m/s sliding. The fluid was the same naphthenic base oil used in the temperature measurement experiments. Knowing the film thickness and surface roughnesses for each of these conditions, the ferrogram results could be interpreted in terms of the Λ parameter. Figure III-9 shows the percent area covered on the ferrogram (proportional to concentration of particles) as a function of Λ. Results are shown for experiments using the rough, medium rough and smooth balls. The two separate curves shown represent positions on the Ferrogram. The upper curve corresponds to relatively large size particles compared to the second curve.

The importance of the paramter Λ is clearly shown. Wear rates for both particle size classes (upper and lower curves) begin to increase rapidly as Λ approaches and then falls below one. Therefore, the onset of asperity interactions predicted by the occurrence of surface temperature fluctuations correlates very well with the results of the Ferrographic analysis. The calculation of the Λ value was based on a roughness cut-off of 0.76 mm, which is reasonably close to 2d, (0.86 mm), the recommended value.

E. Experiments in Rolling EHD Contacts

Prior to the investigations being reported here, all EHD

experiments conducted in this laboratory were for case of pure sliding. The pure sliding experiments were selected because of their relative simplicity and because the contact temperatures would be higher, thus aiding in the development of the infrared temperature measurement technique. However, since a majority of Hertzian contact conditions occur in devices having relatively small amounts of slip, this condition had to be investigated.

The apparatus shown in Figure III-2 was constructed to allow independent selection of the surface velocity of both the sapphire flat and the steel ball. The results presented here are primarily concerned with the influence of slip on lubricant film thickness, traction and ball surface temperature.

1. Film Thickness and Traction Measurements

The results of the film thickness and traction experiments may be obtained simultaneously, but they cannot be obtained concurrent with the temperature measurements. In addition to requiring two different microscopes (metallurgical and infrared), the film thickness measurement requires a partially reflective coating, which would interfere with the infrared microscope operation.

Table III-1 is a summary of the film thickness and traction experiments. Since only the influence of slip is being studied, a single fluid, the naphthenic oil N1, was investigated. Rolling velocity, slide-roll ratio and peak Hertz pressure were all varied. A slide-roll ratio $\Sigma = 0$ implies pure rolling and a ratio $\Sigma = 2$ implies pure sliding. In all cases, fluid N1 the naphthenic base oil and the smooth ball (.011 μm Ra) were used.

Film thickness and traction have been plotted as a function of Σ in Figures III-10 and III-11 respectively. The effect of the slide/roll ratio on film thickness is small. In fact, both the centerline and minimum film thickness depend on sliding velocity to a power in the range 0 to -0.09 depending on the Hertz pressure and rolling velocity. It is apparent from Figure III-11 that the peak normally obtained in TC vs. Σ experiments in line contacts is not present here. Wedeven's traction data for point contacts [23] also lacks such a peak.

The influence of rolling velocity on film thickness and traction under conditions of zero slip is shown in Figure III-12.

2. Surface Temperature Measurements

Table III-2 shows the results of the ball surface temperature measurements. Because of small changes in the lubricant bath temperature during the course of the experiments, the temperature rise $\Delta T(\Delta T = T_b - T_{bath})$ has been tabulated instead of the absolute temperature of the surface. Also, due to the relatively low infrared detector signal level under conditions of small amounts of sliding, only the high load conditions of those listed in Table III-1 were imposed in the temperature measurement experiments. However, these conditions are the closest to those found in normal practice.

The data from Table III-2 has also been plotted and is shown in Figures III-13-15. Figures III-13 and III-14 show the dependence of temperature rise on slide-roll ratio Σ for rolling velocities of 0.75 and 1.00 m/s respectively. A linear regression analysis of the maximum temperature rise data for both rolling velocities has resulted in

$$\Delta T = 30.3\Sigma + 1.2, \ C \tag{13}$$

with a correlation coefficient of 0.99.

Figure III-15 shows the temperature rise as a function of rolling velocity for the case of pure rolling ($\Sigma = 0$). The data fit the straight line

$$\Delta T = 5.2, \ C \tag{14}$$

with a correlation coefficient of 0.99.

The variation of surface temperature rise with position in the EHD contact is shown in Figures III-16-18 for slide roll ratios in the range 0 to 2.0. The data for $\bar{V}$ = .75 m/s (Figure III-16) and $\bar{V}$ = 1.00 m/s (Figure III-17) are quite similar and the pure sliding results ($\Sigma = 2.0$) are in good agreement with the data reported previously [13]. It is interesting to note the small amount of inlet heating present under these conditions. For example, at 1.5 Hertz radii upstream of the contact center, the surface temperature is less than 5 ^{o}C above the bath temperature. Considering that the ball surface temperature several Hertz radii upstream must be greater than or equal to the bath temperature, the 5 ^{o}C value is probably only partially due to heating in the inlet region. This relatively low value is consistent with the film temperature rise in the inlet predicted by Greenwood and Kauzlarich [24].

A second observation from Figures III-16-17 is the movement of the peak in the temperature profile toward the exit as Σ is increased.

Also, Figure III-18, which contains only zero slip data, shows that the peak occurs near the contact center and the temperature at the inlet and exit contact boundaries are nearly equal. The trend toward a symmetric temperature distribution as Σ approaches zero is a result of the primary mechanism of heat generation going from viscous shear when appreciable slip is present, to compression heating at $\Sigma \simeq 0$. Viscous shear results in a heat flux present throughout the contact region. If this flux were uniform, the ball surface temperature would continue to rise as it passed through the contact. The fact that the heat flux is very much greater at the contact center results in a temperature reduction as the exit boundary is approached. The faster the heat flux falls off, the lower the exit temperature should be. In the case of nearly pure rolling, the viscous shear component is absent in Hertzian region and the temperature rise is due to shear in the inlet and compressional heating. The latter term is a function of the pressure profile, which is nearly symmetric in the contact. The film and surface temperature should therefore rise and fall with pressure. Therefore, the trends shown in Figures III-16-18 appear to be reasonable.

3. Extension of Flash Temperature Analysis for Sliding and Rolling

The flash temperature analysis done in a previous section can be extended to consider the influence of rolling. The formulation by Archard is followed except that the influence of a second surface must be taken into account. Also, since most of the data in Table III-2 corresponds to $L > 5$, the fast moving heat source limit is applied. It is also assumed that the viscous dissipation takes place in a single

plane. This assumption is reasonable because the dissipation is inversely proportional to viscosity and the shear stress is constant through the film [18]. Since a temperature profile through the film was not calculated, it was further assumed that this adiabatic plane occurred at the center of the film. If the two surface temperatures are not substantially different, this approximation should be reasonable.

The total heat flux $\bar{q}$ is the sum of that transferred to each surface (assuming convection can be neglected). Therefore

$$\bar{q} = \bar{q}_b + \bar{q}_{sa} = \frac{TC \cdot W \cdot V_s}{\pi a^2} \tag{15}$$

Since the dissipation is assumed to occur only on the midplane, the remaining fluid merely conducts the heat to the adjoining surface. This allows a linear temperature profile to be imposed between the midplane and boundary. If T_{max} is the midplane film temperature (maximum through the thickness) and T_b and T_{sa} are the surface temperatures at the same position in the contact, then the conduction equation reduces to

$$T_{max} - T_{sa} = \frac{h}{2k_f} \bar{q}_{sa} \tag{16}$$

$$T_{max} - T_b = \frac{h}{2k_f} \bar{q}_b \tag{17}$$

The average surface temperatures can be obtained from the flash temperature theory of Archard [18]. It should be noted that the location of viscous dissipation is fixed with respect to the IR detector. Therefore, the heat source is moving with respect to points on the two surfaces with velocities equal in magnitude to the absolute surface velocities.

For L > 5,

$$T_{sa} - T_{osa} = \frac{K_{sa}}{V_{sa}^{1/2}} \bar{q}_{sa} \tag{18}$$

$$T_b - T_{ob} = \frac{K_b}{V_b^{1/2}} \bar{q}_b \tag{19}$$

where T_o is the bulk temperature assigned to each surface and $K = .968a^{1/2}\alpha^{1/2}/k$. Equations 15-19 can be combined to yield $\Delta T_b = T_b - T_{ob}$. The procedure is to eliminate T_{max} from equations 16-17 and then to substitute expressions for $\bar{q}_{sa}$ and $\bar{q}_b$ from equations 18 and 19 into the new equation and equation 15. This results in two equations in the unknowns, T_{sa} and T_b. Eliminating T_{sa} from them results in the following equation

$$\Delta T_b = \frac{\left(\frac{TC \cdot W \cdot V_s}{\pi a^2}\right)\left(\frac{h}{2k_f} + \frac{K_{sa}}{V_{sa}^{1/2}}\right) + (T_{osa} - T_{ob})}{1 + \frac{V_b^{1/2}}{K_b}\left(\frac{K_{sa}}{V_{sa}^{1/2}} + \frac{h}{k_f}\right)} \tag{20}$$

For the conditions used in this study, $(T_{osa} - T_{ob})$ is small compared to the first term in the numerator. Using an average film thickness of 0.16 μm (Figure III-10) and W = 67N, equation 20 can be evaluated for the materials used.

The ball surface temperature rise given in equation 20 assumes only viscous shear as a heat generation mechanism. However, Table III-2 shows that even when $V_s = 0$, $\Delta T_b \neq 0$. In order to account for this additional mechanism, the empirical relation for the pure rolling data

obtained earlier (equation 14) is used. Adding this temperature rise to the rise due to viscous shear (equation 20) results in

$$\Delta T_b = 5.2\bar{V} + \frac{66.7\ TC \cdot V_s}{\frac{V_{sa}^{1/2}}{5.8V_{sa}^{1/2} + 14.9} + \frac{V_b^{1/2}}{11.8}} \qquad (21)$$

Equation 21 has been evaluated using the conditions shown in Table III-2 except for the conditions of pure sliding ($\Sigma = 0$, $V_{sa} = 0$). The simple sliding data was excluded because $L_{sa} = 0$, thus not meeting one of the imposed restrictions. Also, with a stationary sapphire surface, T_b and T_{sa} are likely to be considerably different, resulting in the assumption of the adiabatic plane being at the center of the film being in error. The results are shown in Figure III-19.

It should be remembered that the predicted temperature rise is the average over the contact area whereas the measured temperature rise is the maximum from Figure III-19, it is therefore clear that the predicted values of temperature rise are higher than the measured values.

There are a number of differences in the development of flash temperature theory and the conditions found in the experiments. First of all, the theory is based on a uniform heat flux over the contact area. The heat flux distribution in the EHD contact is probably non-uniform with the maximum occurring near the center. Also because of differences in thermal diffusivities of the materials of the contact, the adiabatic plane of the fluid film may not occur at the film center. Finally, the theory assumes a semiinfinite solid with the free surface being adiabatic except under the concentrated heat flux. This is not

consistent with the conditions of the experiment. The ball and sapphire surfaces outside the contact area are constantly flooded with lubricant. The agreement shown in Figure III-19 should therefore be viewed cautiously.

Because of the apparent agreement shown in Figure III-19, equation 20 can be considered as a predictive equation for the maximum ball surface temperature.

IV. GLASS TRANSITIONS IN LUBRICANTS

A. Introduction

A preliminary investigation into the possible role of glass transition and glassy state behavior of lubricants in EHD contacts was undertaken. Part of this effort requires knowledge of the pressure and temperature distributions in the EHD contact which are the subjects of the previous sections of this report. In this section preliminary results of the glass transition of lubricants as a function of pressure by two methods are presented along with a discussion indicating possible implications of the results to EHD lubrication.

The proposition that the mechanical behavior of lubricants in EHD contacts might not be that of a viscous liquid but of an elastic solid was first presented by Smith [25] in 1960. The results of Johnson and Roberts [26], and Johnson and Cameron [27] suggest that the lubricant film responds as an elastic solid under the conditions of pressure, temperature and shear rate of their EHD experiments.

Lubricating oils contain linear and highly branched hydrocarbons. Thus, a lubricating oil can display both a glass transition which is associated with the non-crystallized (non-linear hydrocarbons) part of the lubricant oil and a phase transition which is associated with the wax in the oil (linear hydrocarbons). Regardless of the wax content in a given oil, the glass transition temperature remains unchanged [28]. When comparing the conditions to which a lubricant is subjected in a typical EHD contact to available glass transition data, it appears quite likely that the lubricant is in or near the glassy state. This appears to be certain for some bulk polymers and polymer solutions and may also

be true for low molecule weight hydrocarbons. If in or near the glassy state, the solidlike behavior and ultimate mechanical properties of the lubricant may be the controlling material characteristics in the large strain and large strain rate conditions that exist in EHD.

A preliminary review of the literature [29,30,31] of glassy solids indicates that the stress and strains occurring in EHD contacts exceed the ultimate stress and strain in many materials. The work performed in this laboratory on the molecular degradation of lubricants in EHD contacts clearly demonstrates that yielding on a molecular level does occur in these applications. The infinitesimal strain work of Lamb [32] and Litovitz and Dill [33] which is being applied to EHD through the efforts of Harrison and Trachman [34] are important in determining the extent to which the lubricant is in the glassy state, but, it seems to us, the important material properties are the ultimate or large strain properties and not the linear viscoelasticity properties.

In the early stages of this research, glass transition temperatures at atmospheric pressure were measured by the technique of Differential Scanning Calorimetry (DSC) for two lubricating oils: naphthenic base oil R-620-15, designated as N1 and five ring polyphenyl ether, 5P4E. The instrument employed was a Perkin-Elmer Model DSC-2. Glass transition temperatures were -59 C for N-1 sample and -21 C for 5P4E. Probably because these values are low compared to the operating temperatures in a typical EHD contact, the occurrence of the glass transition phenomenon and the existence of the glassy state in the contact were not investigated earlier by other researchers in this field. However, because of the fact that the glass transition temperature increases with pressure, and because

of the existence of high pressures in the EHD contacts, the glass transition temperature can be greater than the operating temperature in the contact. The ASME Pressure-Viscosity-Report [35] was used to obtain an estimate of the variation of T_g with pressure. The solidification points indicated in the ASME report were assumed to be approximate glass transition points. Since these are reported as pressures at several different temperatures, they permit an estimate of the change of glass transition temperature with pressure. Also, according to McKinny and Goldstein [36], the glass transition is an isoviscous state. This is apparently because the glass transition is a constant relaxation time state for a given process and the relaxation time is essentially proportional to the viscosity. The change in temperature with pressure required to maintain constant viscosity gives results that are consistent with the results based on solidification. Based on this approach for typical lubricants, the glass transition temperature increases with pressure at a rate ranging from 80 to 350 C/GPa. Thus, it would be expected that some lubricants will be in the glassy state in an EHD contact with average pressures of 0.7 GPa or higher at room temperature. Therefore, it would be expected that many lubricants are in the glassy state for a significant portion of the time they are in the contact.

The temperatures and pressures at which glass transition occurs and the mechanical properties of the lubricant in the glassy state may influence the two most important dependent operating variables of an EHD contact: the film thickness and the traction. Since the relaxation time of a material in the glassy state is long compared to the residence time in the contact, it is possible that once in the glassy state, the

lubricant will remain in the glassy state on the moving surface while the surface moves from one EHD contact to the next. This may happen in spite of the fact that the pressure causing the glassy state formation has been removed. It is also possible that the glassy lubricant does not have time to flow while in the EHD contact but cleaves somewhere in the film so that solid layers of lubricant adhere to the contact surfaces and slide upon each other or the lubricant may undergo large strain like a ductile solid subjected to large stresses.

Therefore, the glass transition temperature as a function of pressure is a significant material property of lubricants. The mechanical and thermal properties of a substance in the glassy state are known to be functions of $T_g(P)$ which in turn is a function of temperature, pressure, and rate of temperature and pressure changes prior to entering the glassy state.

B. Glass Transition Temperature and the Glassy State

Glass transition is characterized by certain experimental observations which occur while the imposed environment of the material is changing. Commonly experiments are performed for isobaric cooling or isothermal compression of the material. At the glass transition, many material properties change in a characteristic manner. As the temperature is reduced in the liquid region, the material contracts and the viscosity increases. If the material is capable of crystallization, a point will be reached where crystallization starts. If crystallization does not occur or can be avoided, the viscosity will continue to increase until some level of 10^7-10^{12} Pas is reached [37,38,39]. At this point, the material becomes rigid and the thermal expansion coefficient falls by

about one-half to one-third of its value in the melt or liquid state as shown in Figure IV-1.

Glass transition is also accompanied by a change in the specific heat, c_p, isothermal compressibility, β, and other secondary properties. It corresponds to a change in slope of a plot of specific volume versus temperature as shown in Figure IV-2. Thus, glass transition phenomena are a characteristic of any liquid which can be supercooled to a sufficiently low temperature without crystallization.

Glass transition phenomena are often referred to as an apparent second-order transition since it is characterized by a discontinuous change in the secondary thermodynamic quantities. These changes occur over a range of temperatures and are not strictly discontinuous. Ferry [40] and Haward [29] showed that glass transition phenomena are not true second-order thermodynamic transitions since at T_g the substance is not in thermodynamic equilibrium. This is due to the slowness of molecular rearrangements at this temperature. This absence of thermodynamic equilibrium is part of the definition of the glassy state.

Below T_g, the degree of order will appear fixed and will not vary with temperature or pressure during the time of experimental observation. Because of this, the structural degrees of freedom are said to be frozen-in and therefore, the structural contribution to α, c_p and β are absent in the glassy state.

The effect of pressure on T_g is shown in Figure IV-2. The glass transition temperature shifts upward as the pressure is increased. The increase in T_g with pressure will be sufficient to maintain an isoviscous state. A sufficiently high pressure can induce a transition from the

liquid state to the glassy state without requiring a decrease in the temperature.

The transition temperature of a material is a function of the imposed rate of change of the material's environment, and for a series of constant rate experiments, the transition temperature curve is a constant relaxation time curve. The characteristic time of the experiment is dependent on the observation time employed in the experiment. An approximate value of the relaxation time of the material when transition occurs is the observation time employed in the experiment. The range in the relaxation time of the material as it goes through the transition from liquid to glass is from about 0.1 to 10^2 times the observation time. In the transition region the material exhibits both viscous and elastic behavior relative to the process. The range of the transition region is indicated on Figure IV-1 and 2.

As a result of the non-equilibrium state, the thermodynamic history of a glass forming liquid has considerable influence on the structure, the transition and the properties in the glassy state. The rate of the imposed environmental change effects the transition point and the properties of the glassy substance. Glass transition can be reached by isobaric cooling, isothermal compression, an imposed rate change or a combination of these changes on the material. For example, the influence of the rate of cooling, K, on the shift of the glass transition temperature of poly(vinyl acetate) has been studied over a wide range of rates by Kovacs [41]. The volume-temperature response obtained from different constant rates of cooling of a glass-forming substance is shown in Figure IV-3. Since decreasing the rate of cooling increases the

effective experimental time, the glass transition temperature will be shifted to lower values. Matsouka and Maxwell [42] studied the effect of rate of compression on the compressibility curves of polysterene at 121 C. Their results indicate that glass transition pressure, P_g, shifts to lower values when a greater rate of pressure application is employed. If the pressure is increased slowly, the molecules of the material will have enough time to rearrange and the glass transition will take place at a higher pressure. On the other hand, if the rate of pressurization is increased, the time for any structural changes is smaller and the glass transition occurs at a lower pressure.

The influence of thermodynamic history on glass transition of poly(vinyl acetate) was studied by McKinney and Goldstein [36] by using three different thermodynamic histories: variable formation history (isobaric cooling at different pressures), and two constant formation histories (cooling at atmospheric pressure or 80 MPa (800 bar) followed by pressure changes in the glassy state).

Several techniques are employed for the determination of the glass transition temperature such as dilatometry [36,38,43], differential scanning calorimetry [28,44,45], thermomechanical analysis (TMA), dielectric [46,47] and light-scattering techniques [48-58]. Depending on the technique used, various methods exist for specifying the glass transition temperature within the transition region. The usual dilatometric technique is to cool the liquid at a constant rate and extrapolate the linear portions of the volume-temperature relation above and below the transition region to their intersection. The

temperature of this intersection [36] is taken as the glass transition temperature as shown in Figure IV-2. If T_g is measured by the change in the expansion coefficient or the specific heat, then T_g is taken as the mid-point in the step-change as measured from the extensions of the glass and liquid base lines as shown in Figure IV-1. While the choice is somewhat arbitrary, and other authors have suggested alternate techniques, the above methods are the most commonly used. Because of these different ways of defining T_g for different experiments, and because of the different inherent rates and histories in the different experiments, different glass transition temperatures may be measured on the same material in different experiments.

The first step in the study of the importance of the glassy state in EHD contacts is to determine if the lubricant is in or near the glassy state while in an EHD contact. This requires the determination of the glass transition temperature as a function of pressure and rate at observation times comparable to that of an EHD contact for typical lubricants. From these data, a phase diagram showing the liquid and the glassy states for the lubricant can be constructed. Based on the temperatures and pressures in the contact inferences can then be made regarding the state of the lubricant in the contact.

Knowing the temperature and pressure distributions in the EHD contact, the phase diagram will permit determination of whether or not the lubricant is in the glassy state, approximately what operating conditions result in the glassy state behavior, and over what fraction of the contact area the glassy state exists.

C. Experimental Technique

The glass transition temperature as a function of pressure based on two different techniques - light scattering and volume dilatometry - is reported. The two techniques are complimentary because the observation times are similar (about 200s) but the characteristic rates of the experiments are quite different - ($10^{+2}s^{-1}$ for dilatometry and $10^{-10}s^{-1}$ for light scattering). Therefore as the material approaches the amorphous glassy state in the case of the volumetric experiment the material is a viscous liquid while in the light scattering it is behaving as an elastic liquid.

1. Light-Scattering Method

The basic concepts of the light-scattering technique and the description of experimental equipment used for measuring the glass transition temperature are discussed.

a. Theory

When a laser beam passes through a transparent medium, a small portion of the light is scattered in all directions. This light scattering is a result of optical inhomogeneities in the scattering medium. The optical inhomogeneities are the result of fluctuations of the dielectric constant brought about by fluctuations of density due to random thermal motion of the molecules [59].

The dielectric constant, ε, of a liquid can be considered as

$$\varepsilon = \bar{\varepsilon} + \Delta\varepsilon \qquad (1)$$

where $\bar{\varepsilon}$ is the average dielectric constant and $\Delta\varepsilon$ represents the fluctuation in ε. Assuming the entropy, S, and the pressure, P, are independent variables, one can write $\Delta\varepsilon$ as a sum of two terms

$$\Delta\varepsilon = \left(\frac{\partial\varepsilon}{\partial S}\right)_P \Delta S + \left(\frac{\partial\varepsilon}{\partial P}\right)_S \Delta P \qquad (2)$$

The first term is the result of entropy fluctuations at constant pressure (isobaric) while the second term is the result of pressure fluctuations at constant entropy (adiabatic). The convenience of this choice of independent variables is obvious if one realizes that thermal sound waves are adiabatic pressure fluctuations. These pressure fluctuations represent random local compressions or rarefections which, as a consequence of the elastic properties of the medium, do not remain fixed in position but travel throughout the volume of the sample. These adiabatic fluctuations can be described by means of plane sound waves of thermal origin propagating in all possible directions.

The study of the specific heat of a solid lead Debye [60] to the conclusion that the energy which one must have in all 3N degrees of freedom associated with the atomic oscillations of the solid can be considered as the energy of 3N normal elastic waves. Thus, Debye considered the energy of thermal motion of a solid as the energy of elastic waves. The Debye representation of the energy of thermal motion can also be extended to liquids and dense gases if the damping of thermal waves is small.

A major advancement in the development of light-scattering theory was achieved when Brillouin [61] established the fact that sound waves and the Debye thermal elastic waves were the same phenomena.

Thermal fluctuations do not remain "frozen", but change continuously in time and therefore, they can modulate the scattered light. If we let the modulation function be $\Phi(t)$ and the monochromatic light wave

undergoing modulation be given by

$$E_s(t) = E_o \exp(i\omega_o t) \tag{3}$$

where $E_s(t)$ is the electric field intensity of the scattered light and E_o is its amplitude, the resulting vibration of the scattered light will have the form

$$E'_s(t) = E_s(t) \cdot \Phi(t) \tag{4}$$

Consider the modulation of the scattered light by adiabatic fluctuations of pressure. The change of pressure with time satisfies the wave equation. Neglecting the absorption of the elastic waves, we can write the wave equation in the form [59]

$$\ddot{\Phi} - V^2\nabla^2\Phi = 0 \tag{5}$$

where V represent the velocity of propagation of the elastic waves. The solution of equation (5) is given by

$$\Phi(t) = \Phi_o \cos[\Omega t - \vec{k}\cdot\vec{r}] \tag{6}$$

where Ω is the frequency of the elastic wave and equal to $\vec{V}\cdot\vec{k}$ where $\vec{k}$ is the wave vector of the elastic wave. Thus, the vibration in the scattered light wave with wave vector $\vec{k}_s$ diffracted by the elastic wave with wave vector $\vec{k}$ in the direction of $\vec{k}_s$ is given by

$$E'_s(t) = \frac{\Phi_o E_o}{2} \{\exp[i(\omega_o + \Omega)t - \vec{k}\cdot\vec{r}] + \exp[i(\omega_o - \Omega)t + \vec{k}\cdot\vec{r}]\} \tag{7}$$

The above result shows that there are two doublets in the spectrum of the scattered light with frequencies $(\omega_o + \Omega)$ and $(\omega_o - \Omega)$

symmetrically located on the two sides of the incident frequency, ω_o.

All 3N Debye waves in a body propagate in all possible directions. If such a body is irradiated by a parallel light beam with wave vector $\vec{k}_i$ and the scattered light is observed in the direction of the wave vector of the scattered light, $\vec{k}_s$, making an angle Θ with $\vec{k}_i$ as shown in Figure IV-4, then the maximum intensity of the scattered light along $\vec{k}_s$ will occur when the wave vector $\vec{k}$ of the elastic wave together with the vectors $\vec{k}_s$ and $\vec{k}_i$ satisfy the Bragg condition

$$\vec{k}_i \mp \vec{k} = \vec{k}_s$$

or

$$|\vec{k}| \equiv k = \mp |\vec{k}_s - \vec{k}_i| = 2n_i k_i \sin \frac{\Theta}{2} \tag{8}$$

where n_i is the refractive index of the scattering medium at the incident wave length. Since the wave number is the reciprocal of the wave length, equation (8) can be rewritten as

$$\Lambda = \frac{\lambda}{2n_i \sin \Theta/2} = \frac{V}{\Omega} \tag{9}$$

where Λ is the wave length of the sound wave and λ is the wave length of the incident light, while V is the sound velocity and Ω the frequency of the sound wave.

Moreover, as a consequence of the sound wave, the frequency of the incident light is altered by the Doppler effect with respect to the original value ω_o. This shift was first predicted by Brillouin [61] as

$$\omega_B = \mp 2\omega_o \left(\frac{n_i V}{c}\right) \sin \Theta/2 \tag{10}$$

where c is the speed of light.

Rearranging and using the relation $\lambda = c/\omega_o$ we can write equation (10) as

$$V = \mp \omega_B \cdot \frac{\lambda}{2n_i \sin(\Theta/2)} \tag{11}$$

Comparing equations (9) and (11) we obtain the frequency shift, ω_B, equal to the sound frequency, Ω. For scattering angle of 90^o and incident light of wavelength of 5145^oA, the frequency shift in materials having a sound velocity of the order of 3000 m/s. and a refractive index of 1.5 is about 12×10^9 Hz. This result shows that the Brillouin method deals with acoustical phenomena in the gigacycle region (hypersound). This shift represents a frequency change of less than 0.002 percent. The observation of this frequency shift is possible with a gas laser as a monochromatic light source and a Fabry-Perot interferometer as a detector. The two signs in the above equations correspond to the two opposite directions in which the sound wave may travel.

According to Landau and Placzek [62], the scattered light produced by the entropy fluctuations of $\Delta\varepsilon$ does not propagate in normal liquids and these fluctuations are the source of the central unshifted component of the scattered light. The intensity of this component, I_c, is expressed as a function of the total intensity in the Brillouin doublet, $2I_B$, by the Landua-Placzek relation [48,49]

$$\frac{I_C}{2I_B} = \gamma - 1 \tag{12}$$

where γ is the specific heat ratio.

Measurements on Brillouin spectra have been made by a number of workers such as Rank, et al. [48,50], Cummins and Gammons [51], Pinnow et al. [49], and others [52,53] who observed the Brillouin effect by using He-Ne and Argon ion laser as the light source. A typical frequency spectrum of lubricating oils is shown in Figure IV-5. The shift of the Brillouin lines from the laser frequency is of interest since it enables us to calculate the velocity of sound according to equation (11).

For a viscous medium, two types of Brillouin scattering can be observed:

(i) Scattering from longitudinal sound waves which gives a measurement of the longitudinal modulus, M, as

$$M = \rho V_{\ell}^2 \tag{13}$$

where V_{ℓ} is the longitudinal velocity of sound given by

$$V_{\ell} = \omega_{B\ell} \frac{\lambda}{2n_i \sin \Theta/2} \tag{14}$$

(ii) In highly viscous materials just as in crystals and glasses, a second set of Brillouin lines is often observed in the depolarized spectrum with a shift smaller than that of the longitudinal Brillouin lines (not shown in Figure IV-5). These new shifted components are transverse Brillouin lines due to scattering from propagating thermal transverse waves which can propagate in the medium as it becomes more viscous. Scattering from transverse waves appear in the depolarized spectrum because these waves cause anisotropic fluctuations in the local structure of the material. In lubricants at high viscosities, the material is acting in a glassy manner and the transverse Brillouin

peaks may be detected. The fact that these peaks appear in the frequency spectrum is an indication that the longitudinal waves are no longer purely compressional waves but contain a transverse component also. Scattering from transverse sound waves gives a measurement of the shear modulus, G, as

$$G = \rho V_t^2 \tag{15}$$

where V_t is the transverse velocity of sound given by

$$V_t = \omega_{Bt} \frac{\lambda}{2n_i \sin \Theta/2} \tag{16}$$

In low-viscosity liquids, the transverse elastic waves are so weak that the inner Brillouin doublet, which is brought about by the diffraction and modulation of light by the transverse wave, is difficult to observe. In this research only longitudinal frequency shifts and longitudinal sound velocities will be reported.

b. Pressure and Temperature Coefficients of the Sound Velocity

A change in the slope of the sound velocity as a function of temperature and pressure like density or specific heat also defines the glass transition and has been observed by many workers [52-55]. It has been established that the change in the temperature coefficient of the sound velocity is a manifestation of the change in the thermal expansion coefficient that occurs at the glass transition temperature [56-58]. This allows us to detect the glass transition with gigacycle sound waves. Figure IV-6 shows the variation of the sound velocity and frequency shift with temperature for atactic polystyrene [53] where a change in slope

is clearly observed at the glass transition temperature.

The dependence of the velocity of sound on the density, ρ, is seen through the relation

$$V = (M/\rho)^{1/2} \tag{17}$$

where M represents the appropriate modulus of elasticity which is a function of the density. Since the density appears explicitly in the above relation, it is clear that a change must appear in the slope of the velocity-temperature and velocity-pressure curves at the glass transition. A comparison of volume-temperature data with velocity-temperature data taken from literature [56] is consistent with the above observation. However, the expansion coefficient of polystyrene is $2.2 \times 10^{-4}\ ^{o}C^{-1}$ for $T < T_g$ and $5 \times 10^{-4}\ ^{o}C^{-1}$ for $T > T_g$ while the velocity coefficient is $8 \times 10^{-4}\ ^{o}C^{-1}$ for $T < T_g$ and 14×10^{-4} for $T > T_g$ which shows that the dependence of velocity on density is chiefly through the strong dependence of the modulus on density and only to a lesser extent through the explicit appearance of density in equation (17).

c. Light Scattering Experimental Apparatus*

The schematic arrangement of the basic components of the light-scattering experiment is shown in Figure IV-7 and consist of (1) a argon ion laser in single frequency operation and having a power of about 200 milliwatt at $\lambda = 5145^{o}A$ (single line operation is accomplished by inserting a wavelength-dispersing element (Prism) into the laser cavity), (2) a high pressure scattering cell containing the

*The assistance of Drs. D. C. O'Shea and F. D. Medina of the Georgia Tech Physics Department for the use of their light scattering equipment and guidance in this work is gratefully appreciated.

lubricant sample to be investigated, and (3) a detector which permits the spectroscopic analysis of the scattered light.

The scattered light from the lubricant sample is collected by a lens and enters a Fabry-Perot interferometer as shown in Figure IV-8. The output of the interferometer, consisting of polarized and depolarized scattered light, is focused on a screen which has a pinhole in front of a photomultiplier tube (PMT). The output signal from the PMT can be processed by a standard counting system and recorded with a multichannel analyser. The spectrum can also be recorded on X-Y recorder and/or punched on paper tape using the output of a ratemeter.

The Fabry-Perot interferometer used in the light-scattering experiment consists of a pair of highly reflective mirrors separated by a specified distance, d. The mirrors can be moved and tilted to ensure exact parallism between their surfaces. At certain wavelength [63] the amount of light transmitted through the mirrors will be many times larger than expected from the combined transmission for two highly reflective mirrors. This occurs when there is constructive interference between incident light waves with those of different reflections. Only when all the waves from the multiple reflections are in phase will there be high transmission. For incident light normal to the mirror faces, the maximum transmission will occur when

$$\lambda_m = \frac{2d}{m} \tag{18}$$

where m is the order of interference (an integer). In terms of frequency, the above equation can be written as

$$\nu_m = \frac{c}{\lambda_m} = m \frac{c}{2d} \tag{19}$$

The transmitted beams are focused by a lens onto a screen where a series of concentric interference fringes are observed. Only light travelling perpendicular to the plates obey the simple resonance condition. This light is focused to the center of the ring pattern. By placing a pin-hole at this center, only light with frequency $\nu_m = m \frac{c}{2d}$ is allowed to pass through and be detected by a photomultiplier tube. If we plot the transmission of the interferometer as a function of frequency for a monochromatic incident light of frequency f, we would obtain a curve similar to that shown in Figure IV-9. These transmission characteristics enable the device to be used as a tunable filter to display the output frequency of the laser. The frequency range which is transmitted during the Fabry-Perot scan is known as the free spectral range (FSR) which is

$$FSR = \frac{c}{2d} \tag{20}$$

Since the speed of light is approximated by 3×10^8 m/s, the frequency units can be expressed in cm^{-1} (wave number units). A frequency of 15×10^9 Hz corresponds to 0.5 cm^{-1}. Unless otherwise specified, the frequency units will be reported in cm^{-1}.

In the scanning mode, we observe the spectral content of the scattered light by moving one mirror along the interferometer axis without disturbing the parallelism of the mirrors by applying a ramp (sawtooth) voltage to a piezoelectric transducer (PZT) attached to one of the mirrors.

The temperature inside the Fabry-Perot interferometer is controlled

by a proportional controller and a thermister sensor. Two resistors (20 watt) are glued to each of the bottom and side panels of a box enclosing the interferometer and serve as heaters. The temperature is controlled to about 2-3^{o} above room temperature.

Since the Rayleigh line intensity is usually several orders of magnitude greater than that of Brillouin lines, a significant improvement of the frequency spectrums can be obtained by operating the Fabry-Perot interferometer in triple pass geometry. This is accomplished by using a pair of corner cubes (Figure IV-8).

In summary, the light-scattering technique enables one to determine the sound velocity at frequency ω_B if a monochromatic beam of light strikes the scattering medium and the frequency shift of the Brillouin scattered light at angle θ is measured. The location of the change in the slope of the sound velocity as a function of temperature and pressure is a measure of the glass transition.

d. High Pressure Equipment

The high pressure equipment consists of a scattering cell, a strain gauge pressure transducer, a 9:1 area ratio intensifier and a hand pump.

The high pressure cell* (3" x 2-3/4" x 1-3/4") is shown schematically in Figure IV-10. It was used to pressures of 0.66 GPa (100,000 psi). The test fluid in the cell was separated from the hand pump oil by an intensifier which was connected to the cell by high pressure tubing. The cell material is Vasco Max 300 CVM alloy.

*The high pressure cell was originally designed by Dr. W. B. Daniels of the University of Delaware.

Heat treatment of the cell was necessary to raise the hardness and increase the strength properties. Aging the cell by heat treatment for six hours at 480 C followed by an air quench raised the hardness to about 52-55 Rockwell "C" and increased the yield strength to 1.9 GPa.

An intensifier with a 9:1 piston area ratio was mounted between the hand pump and the high pressure scattering cell. The test fluid is contained in the high pressure side of the intensifier cavity, the high pressure tubing and the optical cell. The high and low pressure sides of the intensifier piston were sealed with Viton O-rings which were protected by anti-extrusion rings. The intensifier material is the same as that of the optical cell and it was heat treated in the same manner.

The pressure of the lubricant sample contained in the optical cell was measured with a commercial strain gage pressure transducer located as shown in Figure IV-10. The pressure transducer is a Norwood model 114 manufactured by the Advanced Technology Division of American Standard and was used in high pressure viscosity measurements conducted under this grant.

One of the important features of using the pressure transducer is that the lubricant sample pressure is measured directly in the optical cell and thus the influence of intensifier seal friction on pressure measurements is eliminated. However, when the material viscosity increases during glass formation the sample pressure may be different from the transducer pressure because of glass formation in the tube connecting them.

e. Glass Formation History

Because of the dependence of the glass properties on formation history, two standard procedures were adopted to form the glass of the materials investigated. In one formation history (history A), the

pressure was increased from atmospheric to a reference pressure in the liquid region. At the same time, the sample temperature was increased at a rate of 6.1 mC/s (22C per hour) to about 17 C above its assumed glass transition temperature. At this point the pressure and temperature were kept constant for about 30 minutes. The sample was then cooled at constant pressure and frequency spectra were taken at 2.8C (5 ^{o}F) intervals. Twenty minutes were allowed for the temperature to reach equilibrium before each spectrum was recorded. Hence, experimental measurements were started in the liquid state and the glassy state was reached by decreasing the temperature at constant pressure as shown in Figure IV-11. This procedure was repeated at different constant pressures and, therefore, the structure of the glass formed varies with the formation pressure.

In the second formation history (history B), the glass was formed by pressurizing the sample at room temperature from atmospheric pressure until the glassy state was reached. Frequency spectra for this case were taken at pressure intervals of about 20 to 27 MPa (3000 to 4000 psi). Again up to twenty minutes was allowed for the sample to reach equilibrium before the spectra were recorded.

In history A, the sample temperature was changed by controlling the voltage input to an electric tape heater wrapped around the intensifier-cell assembly which was enclosed in an oven. By controlling the input voltage to the electric heater, the cell temperature was controlled to better than $\pm$ 0.1 C. The temperature was measured with a copper-constantan thermocouple in conjunction with a direct reading digital thermometer. The thermocouple was in a brass well fitted into a hole in the cell body (Figure IV-10).

f. Data Reduction Technique and The Results for 5P4E*

The data on 5P4E will be used to illustrate the data reduction technique. Some results are also available on N1* and the phase diagram for that material based on light-scattering will be presented in the Discussion section.

All frequency spectra of scattered light were obtained at a fixed scattering angle of 90^{o}. The free spectral range for each case investigated was kept constant. This procedure was adopted to minimize the errors in measuring the separation distance of the Fabry-Perot interferometer which in turn minimized the error in the calculated frequency shift. Using the scattering angle of $\theta = 90^{o}$ in equation (9) and (11), one obtains

$$\Lambda = \frac{\lambda}{\sqrt{2}\, n_i} \tag{21}$$

and

$$V = \omega_B \frac{\lambda}{\sqrt{2}\, n_i} \tag{22}$$

The recorded spectra were used to measure the frequency shift and to calculate the sound velocity by employing equation (22).

The frequency spectrum of 5P4E recorded at 0.2 GPa (28,200 psi) and 24.4 C (76 F) (formation history B) is shown in Figure IV-12. It contains two successive orders of the interference. The center of the four Brillouin peaks were located at some height where the Brillouin

*See Appendix A for material descriptions.

components appeared to be symmetrical. The separation distance, d, of the Fabry-Perot interferometer was 0.50 cm corresponding to a free spectral range of 30 GHZ $\left(\frac{c}{2d}\right)$. The frequency shift obtained from this spectrum is equal to

$$\omega_{B,k} = \frac{\ell}{2L_k} \cdot \frac{c}{2d} \tag{23}$$

where k = 1,2. Two values of ω_B can be calculated, each corresponding to the order of interference. These are (see Figure IV-12)

$$\omega_{B,1} = \frac{\ell}{2L_1} \cdot \frac{c}{2d} = \frac{6.85}{16.50} \times \frac{3 \times 10^{10}}{2 \times 0.50} = 12.45 \text{ GHZ}$$

and

$$\omega_{B,2} = \frac{\ell}{2L_2} \cdot \frac{c}{2d} = \frac{6.85}{16.40} \times \frac{3 \times 10^{10}}{2 \times 0.50} = 12.53 \text{ GHZ}$$

Each value of ω_B together with the values of n_i(1.6873) and λ(5145 Å) is used in equation (22) to determine the velocity of sound at the indicated pressure and temperature as follow

$$V_1 = \frac{\lambda\omega_{B,1}}{\sqrt{2}\, n_i} = 12.45 \times 10^9 \times \frac{5145 \times 10^{-10}}{1.6873\sqrt{2}} = 2685 \text{ m/s}$$

and

$$V_2 = \frac{\lambda\omega_{B,2}}{\sqrt{2}\, n_i} = 12.53 \times 10^9 \times \frac{5145 \times 10^{-10}}{1.6873\sqrt{2}} = 2702 \text{ m/s}$$

The average values of $\omega_{B,k}$ and V are reported. Frequency shifts and sound velocities at other pressures and temperatures are calculated in the same manner. The results of these calculations for 5P4E at 24.4 C (76 F) (history B) are shown in Table IV-1 and plotted in Figure IV-13. From this figure, it is seen that the sound velocity and the frequency shift increase with increasing pressure and a change in the slope is apparent at 0.17 GPa (24,700 psi) corresponding to a velocity of sound of 2658 m/s. This change of slope represents the glass transition. The velocities on each side of the transition region can be represented by linear functions of pressure. The two sections of Figure IV-13 were each fit by least squares regression to a linear expression of the form

$$V = A + B\ P \tag{24}$$

where V is in m/s and P in MPa. The intersection of these lines are interpreted [52-58] as occurring at the glass transition pressure. The least square expression obtained for each section of the velocity-pressure curve shown in Figure IV-13 is

$$V_L = 2098 + 156.3\ P$$

and

$$V_g = 2397 + 72.87\ P$$

Solving these two equations for their intersection, one obtains

$$P_g = 170.3 \text{ MPa} \quad \text{and} \quad V = 2658 \text{ m/s}.$$

Frequency spectrum of 5P4E obtained by formation history A

(at 0.40 GPa (59,000 psi)) and recorded at 64.4 C (148 F) is reproduced in Figure IV-14. It is typical in general appearance of all frequency spectra obtained. The separation distance, d, was 0.725 cm corresponding to FSR of 20.7 GHZ. The frequency shifts and the sound velocities were calculated from the position of the Brillouin peaks as discussed above. The result of these calculations are shown in Table IV-2 and are plotted in Figure IV-15. The sound velocity increases as the temperature is decreased. At the transition region the dependence of sound velocity on temperature changes. This change of slope of the temperature coefficient of the sound velocity was observed at all formation pressures. Once again, the two portions of the sound velocity curves were fit by least square regression to straight lines of the form

$$V = a + b\,T \tag{25}$$

where V in m/s and T in C.

5P4E was subjected to formation history A at a total of six formation pressures. The resulting material behavior is shown in Table IV-3 and Figures IV-16 and 17.

The least square expressions for both portions of the velocity-temperature curves were solved for their intersection to determine the glass transition temperature at each formation pressure. The glass formation temperature-pressure combinations result in the phase diagram shown in Figure IV-18. The glass transition temperatures and pressures were least square fit with a straight line. The expression obtained is given by

$$T_g = 0.183\ P_g - 4.74$$

$$(T_g = 2.27\ P_g + 23.5 \text{ with } T_g \text{ in F and } P_g \text{ in kpsi})$$

with T_g in C and P_g in MPa. The glass transition temperature at 24.4 C (76 F) by history B was excluded from the fit due to the different history by which the glass was formed. However, in general, the transition obtained by History B fell near the line obtained by History A.

The scattered light frequency shift was also least square fit with straight lines and the expressions obtained were solved for their intersection to locate the glass transition. The results obtained from the frequency shift did not differ from those obtained from the sound velocity by more than 1.4 MPa (200 psi) for the glass transition pressure (History B, at 24.4 C (76 F)) nor more than 1 C (2 F) transition temperature at any formation pressure for History A. Therefore, the glass transition data were obtained from the sound velocity only.

D. Dilatometry Method

As mentioned in the introduction, dilatometry can be used to measure the glass transition at long observation times. In many respects volume dilatometry is both conceptually and experimentally less complicated than the light scattering method for determining glass transition. Dilatometry is inherently a low rate process and a change in rate shifts the glass transition in a known manner. Therefore, dilatometry data is significant in that any temperature-pressure combination placing the material in the glassy-state by dilatometry measurements will indicate glass formation in an EHD contact because of the

shorter observation time in the EHD contact.

Dilatometry measures the relative volume of the material as a function of temperature and pressure. The compressibility and thermal expansion coefficients of the material differ in the liquid and glass regions and the glass transition is defined by this change as discussed in the introduction and shown in Figures IV-1, 2, and 3.

Three dilatometers were constructed and are shown schematically in Figure IV-19, IV-20, and IV-21. The three devices were made to cover different pressure ranges. Two types of experiments can be conducted: 1) isobaric cooling (History A) and 2) isothermal compression (History B). Both the isobaric cooling and isothermal compression experiments had observation times on the order of 10^2s to 10^3s.

The formation histories in the dilatometry experiments were similar in that the material was always taken from the liquid state into the glassy state. For elevated pressure experiments this required heating and pressurizing in the liquid region well above the glass transition to some starting pressure and temperature from which the isobaric cooling or isothermal compression would start. As the experiment progressed the relative specific volume would be obtained as a function of temperature or pressure and the intersection of the curves in the liquid and glassy regions would define the glass transition. These intersections and resulting phase diagrams were obtained in the same manner as that in the section on light-scattering for the sound velocity data.

Experiments have been completed on the materials shown in Table IV-4. The phase diagram for 5P4E obtained with the volumetric method compared with that from the light-scattering is shown in

Figure IV-22. The reason for the difference in the data from the two techniques is not known at this time but the difference is small relative to the temperature and pressure ranges a material is subjected to in an EHD contact. Therefore, if 5P4E is subjected to a temperature-pressure combination in an EHD contact which is to the right of the dilatometry curve on this phase diagram, the material will be in the glassy state in the EHD contact. These data suggest that 5P4E would be in the glassy state in most EHD applications. Figure IV-23 contains similar comparisons for material N1. The same comments made regarding 5P4E are applicable to N1.

Figure IV-24 contains phase diagram data for several materials based on the isothermal compression measurements. The variation in glass forming tendencies of the materials is large. However, the typical mineral oil based lubricants studied have very similar glass forming characteristics as shown in Figure IV-25. The transition regions for the compression experiments are shown in Figures IV-26, IV-27, and IV-28. Because the observation time in these experiments was approximately five minutes the glass transition point is where the material relaxation time is approximately five minutes and the transition region represents the changes in relaxation time (τ_m) from about one tenth that value on the liquid end to about 10^2 times that on the glassy end ($0.5 \leq \tau_m \leq 500$ minutes). In this region the material exhibits both viscous and elastic behavior relative to this experiment. In the liquid region the relaxation time is much less than 0.5 minute and the material can be treated as a viscous liquid in this process. In the glassy region the relaxiation time is greater than 50 minutes and the

material can be treated as an elastic solid in this process.

Table IV-5 lists those materials which were studied but for which no glass transition was observed for the volumetric experiments in the pressure and temperature range studied. This implies that the relaxation times of these materials were much less than one half minute in the pressure and temperature range of observation.

E. Two Additional Experiments

Glass transition is accompanied by changes in all the material's physical properties including very large changes in viscosity. In the past glass transition has been defined as the point at which the viscosity of the material reaches a high value (e.g. $10^{11} Ns/m^2$). Because the approximate shear rates and shear stresses to which the material is subjected in an EHD contact are not consistent with such high viscosities, while the temperatures and pressures indicate it is in the glassy state, two simple shearing experiments were conducted. Both were conducted in a concentric cylinder device. In one experiment the torque (shear stress) was measured continuously at constant shear rate ($0.43\ s^{-1}$) while the 5P4E sample was cooled continuously. In the second experiment a crude indication of the ultimate shear strength of the material in the glassy state was obtained.

The viscosity measurement experiment was conducted in a Haake concentric cylinder viscometer and the results are shown in Figure IV-29. As expected the viscosity increases rapidly with decreasing temperature but the trend begins to change substantially as the glass transition temperature is approached. The glass transition temperature as measured by differential scanning calorimetry is -23 C and is marked on the

figure. The shear stress limit of the instrument is about 3.5 kPa. As the temperature continues to decrease below the glass transition temperature the material effectively becomes a rigid solid.

Once in the glassy state the material has solid-like properties such as sound velocity, thermal expansion coefficient, specific heat, etc., and might also be expected to have an ultimate yield shear strength. To get an estimate of this property at atmospheric pressure, a concentric cylinder device was constructed with a outer diameter of 16 mm, inner diameter of 13 mm and length of 16 mm. The outer cylinder could be held firm and the inner cylinder turned with a torque wrench when the sample was cooled below its glass transition temperature. A thermocouple was inserted into the sample through the inner cylinder and the device cooled by liquid nitrogen. The torque required to break the inner cylinder loose was then an estimate of the yield shear strength of the material. The data are shown in Table IV-6. These results suggest that yield behavior of the material in the glassy state should be studied in conjunction with the study of material behavior in EHD contacts.

F. Discussion of Results

1. Pressure Dependence of Glass Transition Temperatures in Lubricants

The glass transition results presented suggest that glass transition phenomena and rheological behavior in the glassy state are important for some lubricants in some EHD applications.

The volumetric experiments covered the widest range of pressure and temperature. As seen in Figure IV-23 for N1 at low formation pressures (up to about 0.45 GPa), the transition temperature is a linear function of pressure with a slope of about 190 C/GPa. Above 0.45 GPa, the slope

decreased gradually and the glass transition relation became linear again above 0.55 GPa with a slope of about 100 C/GPa. Figure IV-23 also includes the light scattering transition data obtained by history A for fluid N1 (slope = 120 C/GPa). The glass transition temperatures of the light scattering technique are seen to be higher (by about 19 C) than the temperatures based on the volumetric method at all pressures. The reason for this difference is unclear at present.

The glass transition temperature for N1 at atmospheric pressure was also determined by the volumetric measurements and has a value of - 81 C. This value is lower than that obtained by the DSC measurements by about 22 C. The decrease in T_g is due to the different cooling rates (28 C/hr for the volumetric measurements and 1220 C/hr for the DSC measurements) and the different formation history used in each technique.

The volumetric and light scattering transition data for 5P4E are shown in Figure IV-22 and have behavior similar to that discussed above for N1.

From the above discussion, the glass transition determined from the light scattering technique is in general agreement with glass transition measurements obtained with other techniques.

2. Relationship of Glass Transition to EHD Conditions

To obtain an impression of the relationship between glass transition for various lubricants and conditions in EHD contacts , Figure IV-30 has been prepared. Figure IV-30 contains the liquid-glass transitions for three lubricants as measured by the volumetric technique. The three lubricants selected represent a wide range of behavior with respect to glass transition. Above and to the left of each curve is the liquid

region for the material for low rate (long observation time) processes. To the right and below each curve is the glassy region. Based on limited measurements on three other hydrocarbon base oils the curve for N1 is an adequate first approximation for non-polymer containing hydrocarbon base oils. Also indicated in Figure IV-30 are the approximate ranges of pressure in the inlet and the Hertzian zones of an EHD contact. The approximate temperature ranges are also marked for an inlet temperature of about 20 C based on the IR temperature measurements reported elsewhere in this report. What this heuristic depiction shows is that glass transition most probably occurs in many practical applications of EHD contacts with many existing lubricants. The higher the contact pressure the more likely the transition to the glassy state, particularly with rolling and low slip ratio contacts. The glass transition and glassy state behavior is most likely to effect traction but may also effect film thickness if the transition occurs in the inlet zone, which can happen. The above clearly suggests the phenomena of glass transition occurs in EHD and its effects may be observable in EHD data already available.

a. Traction Measurements

Johnson and Cameron [27] measured the traction transmitted by an elastohydrodynamic film in a rolling contact with low sliding speeds and near isothermal conditions. From the traction measurements, the variation in apparent viscosity of their oil* with pressure and temperature is shown in Figure IV-31. The variation of the apparent viscosity with pressure shows a marked change above 10^3 Pas. The

*Shell Vitra 76 similar to N1 but of higher viscosity.

authors [27] remarked that it is tempting to suppose that this change indicates a change in physical properties of the oil at high pressure. To test their remarks, the linear sections of Figure IV-31 were extrapolated to obtain an intersection. Pressures of about 0.57 and 0.88 GPa were obtained at 30 and 70 C respectively. These intersection points fall near the glass transition lines of N1 fluid as shown in Figure IV 23 which is repeated with this data in Figure IV-32. The fact that the intersection points correspond to the measured glass transition points support the authors [27] remark.

b. Side Thrust Measurements

Johnson and Roberts [26] devised a rolling-contact experiment with a small amount of twist. Because of certain kinematic characteristics of their contact, no side thrust will be transmitted if the lubricant behavior is that of a liquid. If the material behaves like a solid, some side thrust will be observed. Figure IV-33 is a plot of the relative side thrust as a function of contact pressure. This transition in the behavior of their oil* is similar to that of specific heat or expansion coefficient of a material passing through a glass transition as discussed earlier. This observation raises the question of whether the behavior shown in Figure IV-33 is a glass transition. The onset of solid like behavior occurs at about 0.5 GPa and 23 C which is plotted on Figure IV-32. When the technique for determining the glass transition temperature for such a physical behavior was used, a midpoint transition pressure (see Figure IV-32) of about 0.7 GPa was obtained at 23 C. These values of pressure are seen to fall in the transition and glassy regions of Figure IV-32. This result agrees with

Johnson and Roberts' conclusion that a transition from viscous to solid behavior occurred above a contact pressure of about 0.5 GPa.

c. Contact Temperatures and Pressures

Fluid and ball surface temperature distributions in a sliding and rolling contact are shown in Section III of this report. Figure IV-34 is a plot of the ball surface temperature at the contact center versus maximum Hertz pressure at three sliding speeds. Figure IV-35 shows the ball surface temperature versus sliding speed at different Hertz pressures. Because both figures have temperature and pressure plotted, we can include the glass transition lines obtained by the light-scattering and the volumetric measurement techniques. As shown in these figures, the lubricant near the ball surface is in the glassy state at a sliding speed of 0.2 m/s. At higher sliding speeds, the glassy state exists only at high pressures. This result was expected since a sliding contact generates frictional heat and thus the temperature levels in the contact are relatively high.

The above disscussion suggests the existence of the glassy state in sliding EHD contacts at relatively low speeds or sufficiently high pressures.

Ball surface temperature distributions for fluid N1 at different slide-to-roll ratio $\left(\Sigma = 2\,\frac{(u_2 - u_1)}{(u_2 + u_1)}\right)$ are shown in Chapter III and are repeated in Figure III-36. The speed ratio, Σ, ranged from zero (pure rolling) to 2.0 (pure sliding) at a constant Hertzian pressure of 1 GPa and at constant rolling speed of 0.75 m/s. Based on the measured temperatures, assumed Hertzian pressure distributions, and the glass transition data, it can be estimated what portion of the fluid in contact with the

ball surface will be in the glassy or liquid states. The portions are shown in the bar diagrams included in Figure IV-36. The lubricant near the ball surface is in the glassy state for all speed ratios except that of $\Sigma = 2.0$. At sufficiently low speed ratios, the glassy state occupies all the contact area. This result shows that the lubricant N1 is in the glassy state in a rolling/sliding contact and the glass can occupy all the contact area at low slide-to-roll speed ratios.

G. Conclusions

The glass transition temperatures of lubricants increase sufficiently with pressure to cause glass transition in EHD contacts with many typical lubricants. The glass transition behavior of lubricants of current interest varies considerably. Some, for example 5P4E, undergo glass transition at room temperature at about 0.14 GPa while bis-2-ethyl hexyl sebacate did not undergo a glass transition down to -3C even up to 1.1 GPa.

It appears that EHD data already available in the literature are consistent with the glass transition observations reported here. Glass transition of lubricants can be expected to influence both the EHD traction and the film thickness depending on the location of the transition in the contact.

The results of the preliminary study reported here clearly suggest that further research into the glass transition of lubricants, rheological behavior of lubricants in the glassy state and further verification of glass transition in EHD contacts are needed. Analytical modeling of the mechanics of EHD contacts with glassy lubricants should be pursued. Also the study of the relationship of chemical structure to glass transition may be useful in future lubricant formulation.

V. ON THE ANALYTICAL DETERMINATION OF PRESSURE DISTRIBUTION IN EHD LINE CONTACTS FROM FILM THICKNESS DATA

A. Introduction

The objective of the investigation reported in this section is the determination, by analytic methods, of the pressure distribution to which a film is subjected in an elastohydrodynamic process. The EHD-generated pressures in the film are the surface-tractions on the solid components of the system. In this study the solid components consist of either two elastic cylinders with parallel generators, or an elastic cylinder and an elastic plate.

The interest inherent in the foregoing problem is many-fold. Firstly, the rheological properties of the film are functions of its local pressure and temperature. This dependence becomes more pronounced at the high pressures generated in the EHD-zone. Consequently the integrity of the film is tied to the understanding of this dependence. Secondly, if the intensity of the pressure field becomes large enough there is a distinct possibility that the lubricant's physical state may change. Hence an accurate description of the thermodynamic variables is needed to assess the accuracy of the currently employed theories and hypotheses of the EHD process. Thirdly, the pressure distribution is necessary for the calculation of the stress fields to which the elastic components of the system are subjected. The determination of the stress field could lead to a better understanding of the fatigue and fracture of bearing surfaces. Fourthly, since the determination of the pressure field, as developed here, is independent of

NOMENCLATURE

a	half-width of pressure distribution
$[A]$	cylinder solution corresponding to arbitrarily distributed surface load
$[B_1]$	basic solution to cylinder problem
$C(0,k\theta)$	cosine integral
F_x, F_y	surface forces
h	elastohydrodynamic film thickness
h_o	film thickness in undeformed state
h_n	Fourier coefficient of pressure on half-plane
$[H]$	half-plane solution corresponding to arbitrarily distributed surface load
$[H_{01}]$	symmetric half-plane solution
$[H_{02}]$	antisymmetric half-plane solution
i	$\sqrt{-1}$
J	set of real integers
p	pressure
p_n	Fourier coefficient of pressure
p_o	reference pressure
P	total applied load
r_o	radius of cylinder
$r_1,\ldots,r_4$	radial location of arbitrary interior point z relative to points of application of surface forces
r_i	residual
$[S_{12}]$	antisymmetric cylinder solution
$[S_{22}]$	symmetric cylinder solution
$S(0,k\theta)$	sine integral

u,v	displacement in x- and y-directions respectively
u_1,u_2	surface deformation of bodies 1 and 2
U_i,V_i	coefficient of deformation
x,y	cartesian coordinates
x_o	reference length
$\hat{x}$	distance along x-axis measured from point of contact in the undeformed state
z	complex variable $x + iy$
z_k	points on surface of body at which forces act
α	angular location of surface force
α_o	angular half-width of pressure distribution on cylinder
β	angular coordinate of arbitrary point on cylinder surface
$\tilde{\beta}$	dimensionless angle, β/α_o
γ	normal approach of two solid bodies
$\theta_1,\ldots,\theta_4$	angular location of arbitrary interior point z relative to points of application of surface forces
λ,μ	Lamé elastic constants
ξ	dimensionless coordinate x/a
σ	tangential surface traction
$\tau_{xx},\tau_{xy},\tau_{yy}$	stresses
ϕ,ψ	complex potentials
$[\ ]$	stress tensor or displacement tensor fields associated with a particular solution

Superscripts

(a), (s)	antisymmetric and symmetric solutions, respectively
$\overline{\quad}$	complex conjugate function
$'$	differentiation with respect to the argument

the state of the lubricant, one may view the EHD-process as a reasonable method for examining the behavior of fluids under high pressures.

B. Problem Statement

As stated previously, the surface tractions*, to which the elastic components of the system are subjected, are caused by the EHD generated pressure field in the thin film separating the solid components of the system. Since the region of the solid elements over which the EHD pressure is acting has dimensions which are very small by comparison to the dimensions of the solid, and furthermore the thickness of the fluid film is orders of magnitude less than its EHD-zone length, it is reasonable to assume that the variation of the EHD-pressure across the thickness of the film is negligible.

Under these circumstances the surface tractions acting on either of the two solid bodies separated by the fluid film are identical, Figures V.1 and V.2. Consequently, the problem under consideration, namely the determination of the pressure distribution in the EHD film, may be decomposed into three simpler problems.

(i) The determination of the displacement field of the first solid body subjected to the EHD-generated pressure field over a region of its surface of the order of magnitude of the EHD-zone.

(ii) The determination of the displacement field of the second solid body subjected to the same pressure field over the same region as the first solid body.

*Surface tractions are the force distributions on the surface of the solid body.

(iii) The calculation of the film thickness as a function of position for a given pressure distribution. This task may be accomplished from the determination of the displacement fields of problems (i) and (ii), the undeformed geometry of the elastic bodies, their normal approach and the total load transmitted across the film. The resulting relationships contain the film thickness and the EHD generated pressure intensity as dependent functions. The complete mathematical description of the EHD problem can be accomplished by deriving the appropriate field equations for the fluid film from the conservation equations of fluid mechanics. However, the coupling of the pressure field with the film thickness and consequently with the elastic displacements makes the resulting equation almost intractable. However, experimental techniques have been developed which make it possible to measure the fluid film thickness in an EHD process. Thus, assuming the availability of film thickness information, the complex complete mathematical problem may be bypassed in favor of the following simpler problem: the calculation of the pressure field in terms of the fluid film thickness. The resulting mathematical problem is much simpler than the complete one associated with the EHD process.

In this investigation an EHD line contact is considered. Hence the elastic bodies bounding the film are either parallel cylinders or a cylinder and a plate. Section C contains the formulation of the boundary value problem of an elastic cylinder subjected to surface tractions over a small portion of its curved boundary, and the determination of the associated displacement field as a function of the EHD-generated pressure field. In Section D the deflection of a

thick plate subjected to normal loading is examined by approximating the plate by the elastic half-space and subjecting it to the same surface tractions employed in Section C. In Sections C and D it is assumed that the length of the cylinder is large enough so that the edge effects may be neglected and that the geometry of the bodies as well as the pressure distribution variations along the axial direction are sufficiently small to be ignored. With the adoption of these assumptions the elastic deformation problem reduces to one of plane elasticity and the complex function approach is employed. The coupling between the pressure distribution and the known film thickness is accomplished in Section E.

The first phase of the problem is approached as a boundary value problem of the first kind (Sections C and D). The result of the first phase is a relationship between the surface tractions and the film thickness. The measured film thickness is then employed in the second phase of the analysis to calculate the pressure distribution (Section E). The numerical approach and its consequences are discussed in Section F. The influence of errors in the measurements of the film thickness on the pressure distribution and the method of minimizing their effect is also presented in Section F. Finally Section G deals with test cases for the evaluation of the whole analytic and numerical approach.

C. The Displacement Solutions - The Cylinder

In this section, the complex representation of the theory of plane elasticity is employed [64,65], for the purpose of formulating the solutions of an elastic cylinder under surface tractions. The surface tractions are assumed independent of the axial direction and the body

forces are ignored. Under these conditions, the stress tensor field and the associated displacement vector field may be represented in terms of two complex holonomic functions [66,67] by

$$\tau_{xx} + \tau_{yy} = 2[\Phi'(z) + \overline{\Phi'(z)}] \tag{C.1}$$

$$\tau_{yy} - \tau_{xx} + 2i\tau_{xy} = 2[\bar{z}\Phi''(z) + \Psi'(z)] \tag{C.2}$$

$$2\mu(u + iv) = \left(\frac{\lambda+3\mu}{\lambda+\mu}\right)\Phi(z) - \overline{z\Phi'(z)} - \overline{\Psi(z)} \tag{C.3}$$

where $'$ implies differentiation with respect to the argument, $\overline{\quad}$ denotes the complex conjugate function, and λ,μ are the Lamé elastic constants.

In the case of an elastic cylinder under surface forces $F_x + iF_y$, the functions $\Phi(z)$ and $\Psi(z)$ are found to be

$$\Phi(z) = \frac{1}{2\pi i}\int \frac{f\,d\xi}{\xi - z} - \frac{1}{2\pi i}\int \frac{f\,d\xi}{\xi} - \bar{a}\, r_o z \tag{C.4}$$

$$\Psi(z) = \frac{1}{2\pi i}\int \frac{\bar{f}\,d\xi}{\xi - z} - \frac{1}{z}\Phi'(z) + \frac{a}{z} \tag{C.5}$$

where

$$a = \bar{a} = \Phi'(0)$$

$$f = i\int_{\Gamma} (F_x + iF_y)ds \tag{C.6}$$

If the surface forces consist of n concentrated forces applied at points of the circumference z_k, the stress functions assume the form,

$$\Phi(z) = \frac{1}{4\pi} \sum_{k=1}^{n} (F_{kx} + iF_k y)[2\ell n(z_k - z) - z\bar{z}_k] \qquad (C.7)$$

$$\Psi(z) = \frac{1}{2\pi} \sum_{k=1}^{n} \left[(F_{kx} - iF_{ky})\ell n(z_k - z) - (F_{kx} + iF_{ky}) \frac{\bar{z}_k}{z_k - z}\right] \qquad (C.8)$$

Employing the above function for the particular case of a pair of equal and opposite forces, parallel to the real axis, acting at $z_1 = r_o e^{i\alpha}$, $z_2 = r_o e^{i(\pi-\alpha)}$, one obtains

$$\Phi(z) = \frac{p}{2\pi} \left\{\ell n \frac{z_1 - z}{z_2 - z} + \frac{\bar{z}_1 - \bar{z}_2}{2r_o^2} z\right\} \qquad (C.9)$$

$$\Psi(z) = -\frac{p}{2\pi} \left\{\ell n \frac{z_1 - z}{z_2 - z} - \frac{\bar{z}_1}{z_1 - z} + \frac{\bar{z}_2}{z_2 - z}\right\} \qquad (C.10)$$

with the associated displacement field

$$u = -\frac{p}{4\pi\mu} \left\{\frac{2(\lambda+2\mu)}{\lambda+\mu} \ell n \frac{r_2}{r_1} + \cos 2\theta_1 - \cos 2\theta_2 - \left(\frac{2\mu}{\lambda+\mu}\right) \frac{x}{r_o} \cos\alpha\right\} \qquad (C.11)$$

$$v = -\frac{p}{4\pi\mu} \left\{\left(\frac{2\mu}{\lambda+\mu}\right) (\theta_1 + \theta_2) - \sin 2\theta_1 - \sin 2\theta_2 - \left(\frac{2\mu}{\lambda+\mu}\right)\frac{y}{r_o} \cos\alpha\right\} \qquad (C.12)$$

with $p = F_2 = F_1$ and (r_1,θ_1), (r_2,θ_2) signifying the location of an arbitrary interior point z of the cylinder relative to the points of application of the surface forces. The displacement field at any point on the surface may now be expressed in terms of the intensity of the load, p, the location of its application, (r_o,α) and the arbitrary point on the surface $Q(r_o,\beta)$

$$u(\beta;\alpha) = -\frac{\lambda+2\mu}{2\pi(\lambda+\mu)\mu}\, p\left\{\ell n\, \frac{\cos\frac{1}{2}(\alpha+\beta)}{\sin\frac{1}{2}(\alpha-\beta)} - \cos\alpha\cos\beta\right\} \qquad (C.13)$$

$$v(\beta;\alpha) = -\frac{p}{2\pi(\lambda+\mu)\mu}\left\{\mu\left(\alpha+\frac{\pi}{2}\right) + \lambda\cos\alpha\sin\beta\right\} \qquad (C.14)$$

This solution forms the basis for the subsequent development of the problem and is referred to as solution $[B_1]$. The displacement field $[B_1]$ may be expanded by means of Green's method, to yield the displacement field corresponding to an arbitrarily distributed surface loading of intensity $p(\alpha)$.

In this work, however, the following procedure is adopted. Let $[S_{22}]$ denote the solution corresponding to surface loading symmetric with respect to the x- and y-axes, and $[S_{12}]$ denote the solution corresponding to loading antisymmetric with respect to the x-axis and symmetric with respect to the y-axis. Consequently the sought solution, $[A]$, corresponding to the arbitrarily distributed surface loading is given by

$$[A] = a_1[S_{12}] + a_2[S_{22}] \qquad (C.15)$$

with a_1, a_2 being constants and letters in brackets refer to the stress tensor or displacement vector fields associated with this particular solution.

Solutions $[S_{12}]$ and $[S_{22}]$ are subsequently generated by using the "basic" solution $[B_1]$ and employing Green's method with the appropriate choice of loading functions $p(\alpha)$.

1. The Symmetric Solution. $[S_{22}]$

Let two pairs of equal and opposite forces, parallel to the x-axis,

act at points z_1, z_2, z_3 and z_4 of the surface of the cylinder, with the points of application chosen in such a manner as to make the loading symmetric with respect to the x and y-axes. The displacement field associated with this loading is easily obtained from the basic solution $[B_1]$, Figure (V-3a)

$$u(\beta;\alpha) = + \frac{\lambda+2\mu}{2\pi(\lambda+\mu)\mu} p\left\{\ell n\tan\frac{1}{2}|\alpha+\beta| + \ell n\tan\frac{1}{2}|\alpha-\beta| + 2\cos\alpha\cos\beta\right\} \quad (C.16)$$

$$v(\beta;\alpha) = - \frac{p}{\pi(\lambda+\mu)} (\pi+2\alpha) \quad (C.17)$$

The displacement field for distributed loading $p(\alpha)$ over an arc $(-\alpha_o,\alpha_o)$, which adheres to the symmetry imposed in this section, is

$$u(\beta) = \frac{\lambda+2\mu}{\pi(\lambda+\mu)\mu} \int_o^{\alpha_o} p(\alpha)\left\{\ell n\tan\frac{1}{2}(\alpha+\beta) + \ell n\tan\frac{1}{2}(\alpha-\beta) + 2\cos\alpha\cos\beta\right\} r_o d\alpha \quad (C.18)$$

$$v(\beta) = - \frac{1}{\pi(\lambda+\mu)} \int_o^{\alpha_o} p(\alpha)(\pi+2\alpha) r_o d\alpha \quad (C.19)$$

Since the intensity $p(\alpha)$ is symmetric with respect to the x-axis, which is the $\alpha = 0$ ray, then $p(\alpha) = p(-\alpha)$. Hence it renders itself to the following representation

$$p(\alpha) = \sum_{n=0}^{\infty} p_n \cos\left(\frac{2n+1}{2\alpha_o}\pi\alpha\right) \quad (C.20)$$

which, in conjunction of Eqs. (C.18) and (C.19) and along with the assumption that the angles α_o and β are small and the introduction [68,69] of

$$q_n = \frac{2n+1}{2}\pi \; ; \qquad \tilde{\beta} = \frac{\beta}{\alpha_o} \tag{C.21}$$

$$S(0,k\theta) = \int_o^\theta \frac{\sin kx}{x}\,dx \; ; \qquad C(0,k\theta) = \int_o^\theta \frac{1-\cos kx}{x}\,dx$$

yields the displacement field

$[S_{22}]$:

$$u(\beta) = \sum_{n=o}^{\infty} p_n\, U_n(\beta;\alpha_o) \tag{C.22}$$

$$v(\beta) = \sum_{n=o}^{\infty} p_n\, V_n(\beta;\alpha_o) \tag{C.23}$$

where

$$\begin{aligned} U_n(\beta;\alpha_o) = \frac{(\lambda+2\mu)r_o}{\mu(\lambda+\mu)\pi}\Bigg\{ & \frac{q_n\alpha_o}{q_n^2+\alpha_o^2}\sin q_n \cos\alpha_o\cos\beta \\ & + \left(\frac{\alpha_o}{q_n}\right)\Bigg[\sin q_n\Big[\ell n(1+\tilde{\beta}) + \ell n(1-\tilde{\beta}) + 2\ell n\,\frac{\alpha_o}{2}\Big] \\ & + \sin q_n\tilde{\beta}\big[\ell n(1+\tilde{\beta}) - \ell n(1-\tilde{\beta}) + C(0,q_n(1-\tilde{\beta})) \\ & - C(0,q_n(1+\tilde{\beta}))\big] - \cos q_n\tilde{\beta}\big[S(0,q_n(1-\tilde{\beta})) + S(0,q_n(1+\tilde{\beta}))\big]\Bigg]\Bigg\} \end{aligned} \tag{C.24}$$

$$V_n(\beta,\alpha_o) = -\frac{r_o\alpha_o}{\pi(\lambda+\mu)}\left\{(2\alpha_o+\pi)\frac{\sin q_n\tilde{\beta}}{q_n}-\frac{\alpha_o}{q_n^2}\right\} \tag{C.25}$$

2. The Antisymmetric Solution, $[S_{12}]$

The loading in this case consists of two pairs of equal and opposite forces parallel to the x-axis, the $\alpha = 0$ ray. The first pair acts at the points $z_1 = r_o e^{i\alpha}$ and $z_2 = r_o e^{i(\pi-\alpha)}$ respectively, while the second pair acts at $z_3 = r_o e^{-i\alpha}$ and $z_4 = r_o e^{i(\pi+\alpha)}$ and has its sense reversed with respect to the first pair. Thus the loading is antisymmetric with respect to the x-axis and symmetric with respect to the y-axis (Figure V-3b). Taking advantage of the basic solution $[B_1]$, the displacement field associated with this type loading is found to be

$$u(\beta;\alpha) = \frac{\lambda+2\mu}{2\pi(\lambda+\mu)\mu}\, p\, \ell n\left|\frac{\sin(\alpha+\beta)}{\sin(\alpha-\beta)}\right| \tag{C.26}$$

$$v(\beta;\alpha) = -\frac{\lambda}{\pi(\lambda+\mu)\mu}\, p\cos\alpha\sin\beta \tag{C.27}$$

Subsequently the displacement field for distributed loading over an arc $(-\alpha_o,\alpha_o)$, with $p(\alpha) = -p(-\alpha)$ is simply

$$u(\beta) = \frac{\lambda+2\mu}{2\pi(\lambda+\mu)\mu}\int_o^{\alpha_o} p(\alpha)\, \ell n\left|\frac{\sin(\alpha+\beta)}{\sin(\alpha-\beta)}\right| r_1 d\alpha \tag{C.28}$$

$$v(\beta) = -\frac{\lambda}{\pi(\lambda+\mu)\mu}\int_o^{\alpha_o} p(\alpha)\cos\alpha\cos\beta\, r_o d\alpha \tag{C.29}$$

With the loading intensity $p(\alpha)$ being antisymmetric with α, its expansion is of the form

$$p(\alpha) = \sum_{n=1}^{\infty} p_n \sin \frac{n\pi\alpha}{\alpha_o} \tag{C.30}$$

Substitution of Eq. (C.30) into Eqs. (C.28) and (C.29), and adopting the notation introduced by Eqs. (C.21) along with assumption that α_o and β are small, yields the results

$[S_{12}]$:

$$u(\beta) = \sum_{n=1}^{\infty} p_n U_n(\beta;\alpha_o) \tag{C.31}$$

$$v(\beta) = \sum_{n=1}^{\infty} p_n V_n(\beta;\alpha_o) \tag{C.32}$$

where

$$\begin{aligned} U_n(\beta;\alpha_o) = \frac{(\lambda+2\mu)r_o}{2\pi(\lambda+\mu)\mu}\left(\frac{\alpha_o}{q_n}\right)\{&\cos q_n[\ell n(\tilde{\beta}-1) - \ell n(\tilde{\beta}+1)] + (\cos q_n \\ &+ \cos q_n\tilde{\beta})[\ell n(\tilde{\beta}+1) - \ell n(\tilde{\beta}-1) - C(0,q_n(\tilde{\beta}-1)) - C(0,q_n(\tilde{\beta}+1))] \\ &+ (\sin q_n\tilde{\beta})[S(0,q_n(1+\tilde{\beta})) - S(0,q_n(1-\tilde{\beta}))]\} \end{aligned} \tag{C.33}$$

$$V_n(\beta;\alpha_o) = -\frac{\lambda r_o}{\pi(\lambda+\mu)\mu}\left(\frac{q_n}{q_n^2+\alpha_o^2}\sin q_n\right)\cos\alpha_o \sin\tilde{\beta} \tag{C.34}$$

with $q_n = n\pi$.

3. The General Solution

The displacement field corresponding to an arbitrary pressure distribution is obtained by employing the solutions $[S_{22}]$ and $[S_{12}]$.

Its form is as follows

$$u(\beta) = \sum_{n=0}^{\infty} \left\{ p_n^{(s)} U_n^{(s)}(\beta;\alpha_o) + p_n^{(a)} U_n^{(a)}(\beta;\alpha_o) \right\} \tag{C.35}$$

$$v(\beta) = \sum_{n=0}^{\infty} \left\{ p_n^{(s)} V_n^{(s)}(\beta;\alpha_o) + p_n^{(a)} V_n^{(a)}(\beta;\alpha_o) \right\} \tag{C.36}$$

where superscript (s) refers to the displacement field associated with the symmetric solution $[S_{22}]$, and superscript (a) refers to the displacement field associated with the antisymmetric solution $[S_{12}]$.

D. The Displacement Solutions - The Half-Space

If one of the solid bodies that bounds the EHD zone from above or below is a thick elastic plate, whose dimensions are large by comparison to the EHD zone, then the elastic response of the plate can be represented reasonably by that of the elastic half space. If, furthermore, the other body is a sufficiently long elastic cylinder it can be assumed that the EHD-generated pressure is independent of the coordinate along the axis of the cylinder. Under these circumstances, the thick elastic plate can be substituted by the elastic half-plane. It is this case that is considered in this section and this is consistent with the formulation of the problem of section C.

Again, as in the previous section, the displacement field may be expressed [66] in terms of two complex functions $\phi(z)$ and $\psi(z)$ by

$$2\mu(u + iv) = \left(\frac{\lambda+3\mu}{\lambda+\mu}\right) \varphi(z) - z\varphi'(z) - \psi(z) \tag{D.1}$$

If the loading over the force boundary is

$$\begin{aligned} \tau_{yy} &= p(x) \\ \tau_{xy} &= \sigma(x) \end{aligned} \qquad \text{for } x \in [-a,a] \tag{D.2}$$

it can be shown [66] that the stress functions $\phi(z)$ and $\psi(z)$ are

$$\varphi(z) = -\frac{1}{2\pi}\int(\sigma + ip)\ell n(t - z)dt \tag{D.3}$$

$$\psi(z) = -\frac{z}{2\pi}\int(\sigma + ip)\frac{dt}{t-z} + \frac{1}{2\pi}\int(\sigma - ip)\ell n(t - z)dt \tag{D.4}$$

and the displacement field becomes

$$4\pi\mu(u + iv) = -\int(\sigma + ip)\left[\left(\frac{\lambda+3\mu}{\lambda+\mu}\right)\ell n(t-z) + \ell n(t-\bar{z})\right]dt$$

$$-(z-\bar{z})\int(\sigma-ip)\frac{dt}{t-\bar{z}} \tag{D.5}$$

In this problem it is assumed that the tangential surface tractions are negligible ($\sigma = 0$), thus the displacement eq. (D.5) reduces to

$$4\pi\mu(u + iv) = -i\int_{-a}^{a} p(t)\left[\left(\frac{\lambda+3\mu}{\lambda+\mu}\right)\ell n(t-z) + \ell n(t-\bar{z})\right]dt$$

$$+ i(z-\bar{z})\int_{-a}^{a} p(t)\frac{dt}{(t-\bar{z})} \tag{D.6}$$

Because any arbitrary loading function $p(x)$ can be expressed as a sum of a symmetric and an antisymmetric component, the corresponding displacement field may be given as a combination of displacements corresponding to symmetric and antisymmetric solutions

$$[H] = a[H_{01}] + b[H_{02}]$$

1. The Symmetric Solution, $[H_{02}]$

Assuming that $p(x) = p(-x)$, $p(x)$ may be expanded in the form, Figure V-4a

$$p(t) = \sum_{n=1}^{\infty} h_m \cos \frac{m\pi t}{a} \qquad m = \frac{2n+1}{2}, \quad n \in J \tag{D.7}$$

And the displacement becomes

$$4\pi\mu(v - iu) = -\left(\frac{\lambda+3\mu}{\lambda+\mu}\right) \sum_{n=1}^{\infty} h_m \int_{-a}^{a} \left(\cos \frac{m\pi t}{a}\right) \ell n(t-z)dt$$

$$- \sum_{n=1}^{\infty} h_m \int_{-a}^{a} \left(\cos \frac{m\pi t}{a}\right) \ell n(t-\bar{z})dt$$

$$+ 2iy \sum_{n=1}^{\infty} h_m \int_{-a}^{a} \left(\cos \frac{m\pi t}{a}\right) \frac{dt}{(t-\bar{z})} \tag{D.8}$$

Eq. (D.8), after some calculations and evaluating at $y = 0$, the free surface, yields

$$4\pi\mu\, u = -\sum_{n=1}^{\infty} a h_m \left\{(\theta_1 + \theta_2)\sin q_m - \left(\frac{2\mu}{\lambda+\mu}\right) \frac{1}{q_m} (\theta_1 - \theta_2)\sin q_m \xi\right\} \tag{D.9}$$

$$4\pi\mu v = -\sum_{n=1}^{\infty} \frac{2a}{q_m} h_m \left(\frac{\lambda+2\mu}{\lambda+\mu}\right) \left\{(\sin q_m) \ell n\, r_1 r_2\right.$$

$$- (\sin q_m\xi)\left[\ell n \frac{r_1}{r_2} + C(0,q_m(1+\xi)) - C(0,q_m(1-\xi)\right]$$

$$- (\cos q_m\xi)[S(0,q_m(1+\xi)) + S(0,q_m(1-\xi))]\Big\} \qquad (D.10)$$

where

$$\theta_1 + \theta_2 = \begin{cases} 0 \text{ for } x > a \\ \pi \text{ for } a > x > -a \\ 2\pi \text{ for } x < -a \end{cases} \qquad (D.11)$$

$$\xi = \frac{x}{a}, \quad r_1 = a - x, \quad r_2 = a + x \qquad (D.12)$$

$$q_m = m\pi = \frac{2n+1}{2}\pi \qquad \text{as in section C.}$$

2. The Antisymmetric Solution - $[H_{01}]$

The antisymmetric solution is characterized by Figure V-4b,

$$p(x) = - p(-x)$$

and consequently submits to the representation

$$p(x) = \sum_{m=1}^{\infty} h_m \sin \frac{m\pi x}{a} \qquad m \in J \ . \qquad (D.13)$$

Substitution of eq. (D.13) into eq. (D.6) yields

$$4\pi\mu(v - iu) = -\left(\frac{\lambda+3\mu}{\lambda+\mu}\right)\sum_{m=1}^{\infty} h_m \int_{-a}^{a}\left(\sin\frac{m\pi t}{a}\right)\ell n(t-z)dt$$

$$-\sum_{m=1}^{\infty} h_m \int_{-a}^{a}\left(\sin\frac{m\pi t}{a}\right)\ell n(t-\bar{z})dt$$

$$+ 2iy\sum_{m=1}^{\infty} h_m \int_{-a}^{a}\left(\sin\frac{m\pi t}{a}\right)\frac{dt}{(t-\bar{z})} \qquad (D.14)$$

Performing the indicated operations in eq. (D.14) and evaluating at $y = 0$, the displacement field at the free surface corresponding to the antisymmetric loading becomes

$$4\pi\mu u = -\sum_{m=1}^{\infty} h_m\left\{\frac{a}{q_m}\left(\frac{2\mu}{\lambda+\mu}\right)(\cos q_m\xi - \cos q_m)(\theta_1-\theta_2)\right\} \qquad (D.15)$$

$$4\pi\mu v = -\sum_{m=1}^{\infty} h_m \frac{2a}{q_m}\left(\frac{\lambda+2\mu}{\lambda+\mu}\right)\left\{(\cos q_m\xi - \cos q_m)\ell n\frac{r_1}{r_2}\right.$$

$$+ \cos q_m\xi\,[C(0,q_m(1+\xi)) - C(0,q_m(1-\xi))]$$

$$\left. - \sin q_m\xi\,[S(0,q_m(1+\xi)) + S(0,q_m(1-\xi))]\right\} \qquad (D.16)$$

3. The General Solution - [H]

The displacement field corresponding to an arbitrary pressure distribution in $x \in [-a,a]$ is generated from the linear combinations of $[H_{02}]$ and $[H_{01}]$. Thus

[H]: $$u(\xi) = \sum_{n=0}^{\infty} (h_m^{(s)} U_m^{(s)} + h_m^{(a)} U_m^{(a)}) \tag{D.17}$$

$$v(\xi) = \sum_{n=0}^{\infty} (h_m^{(s)} V_m^{(s)} + h_m^{(a)} V_m^{(a)}) \tag{D.18}$$

where $h_m^{(s)}$ is the pressure coefficient corresponding to the symmetric loading, while $h_m^{(a)}$ is the pressure coefficient associated with the anti-symmetric loading, and

$$U_m^{(s)} = - \frac{a}{4\pi\mu} \left\{ (\theta_1 + \theta_2) \sin q_{ms} - \frac{2\mu}{(\lambda+\mu) q_{ms}} (\theta_1 - \theta_2) \sin q_{ms} \xi \right\} \tag{D.19}$$

$$V_m^{(s)} = - \frac{a(\lambda+2\mu)}{2\pi q_{ms} \mu(\lambda+\mu)} \left\{ (\sin q_{ms}) \ell n r_1 r_2 \right.$$

$$- (\sin q_{ms} \xi) \left[\ell n \frac{r_1}{r_2} + C(0, q_{ms}(1+\xi)) - C(0, q_{ms}(1-\xi)) \right]$$

$$\left. - (\cos q_{ms} \xi) [S(0, q_{ms}(1+\xi)) + S(0, q_{ms}(1-\xi))] \right\} \tag{D.20}$$

$$U_m^{(a)} = - \frac{a}{2\pi q_{ma}(\lambda+\mu)} (\cos q_{ma} \xi - \cos q_{ma})(\theta_1 - \theta_2) \tag{D.21}$$

$$V_m^{(a)} = - \frac{a(\lambda+2\mu)}{2\pi q_{ma}(\lambda+\mu)} \left\{ (\cos q_{ma} \xi - \cos q_{ma}) \ell n \frac{r_1}{r_2} \right.$$

$$+ \cos q_{ma} \xi [C(0, q_{ma}(1+\xi)) - C(0, q_{ma}(1-\xi))]$$

$$\left. - \sin q_{ma} \xi [S(0, q_{ma}(1+\xi)) + S(0, q_{ma}(1-\xi))] \right\} \tag{D.22}$$

and

$$q_{ms} = m\pi = \frac{2n+1}{2}\pi \qquad n \in J$$

$$q_{ma} = m\pi = n\pi$$

E. The Pressure Distribution in the EHD Zone

If the film thickness in the EHD contact is known from measurements, and the elastic properties and geometric characteristics of the solid bodies are known, it is possible to calculate the pressure distribution in the EHD zone. The film thickness may be expressed as

$$h(x,p(x)) = h_o(x) - \gamma(P) + u_1(x,p(x)) + u_2(x,p(x)) \qquad (E.1)$$

where $h(x,p(x))$ is the film thickness; $h_o(x)$ is the film thickness in the undeformed state when the bodies are touching; $\gamma(P)$ is the normal approach of the solid bodies; and u_1 and u_2 are the displacements of the surface of the solid bodies at the EHD zone. The film thickness and the displacements are functions of position and of pressure distribution. The film thickness is known from measurements, and $h_o(x)$ may be calculated from the geometry of the undeformed solid surfaces. In the previous two sections, expressions have been derived that give u_1 and u_2 explicitly in terms of position and the Fourier coefficients of the pressure distribution. It remains, then, to determine the normal approach $\gamma(P)$ and the pressure coefficients.

Specifically, since at any point A in the contact zone or its near neighborhood the film thickness is known, then

$$h(x_A,p(x)) = h_o(x_A) - \gamma(P) + u_1(x_A,p(x)) + u_2(x_A,p(x)) \qquad (E.2)$$

where

$$u_1(x_A,p(x)) = \sum_{n=0}^{N-1} p_n^{(s)} U_{1n}^{(s)} + \sum_{m=1}^{M} p_m^{(a)} U_{1m}^{(a)} \qquad (E.3)$$

$$u_2(x_A,p(x)) = \sum_{n=0}^{N-1} p_n^{(s)} U_{2n}^{(s)} + \sum_{m=1}^{M} p_m^{(a)} U_{2m}^{(a)} \qquad (E.4)$$

$U_{1n}^{(s)}$, $U_{1m}^{(a)}$, $U_{2n}^{(s)}$, $U_{2m}^{(a)}$ are the symmetric and antisymmetric coefficients of the deformations of bodies 1 and 2 respectively, corresponding to a pressure distribution of the form

$$p = \sum_{n=0}^{N-1} p_n^{(s)} \cos \frac{2n+1}{2a} \pi x + \sum_{m=1}^{M} p_m^{(a)} \sin \frac{m\pi}{a} x \qquad (E.5)$$

Further information is obtained by observing that the total pressure acting on either of the solid surfaces is equal to the applied load thus

$$P = \int_{-a}^{a} p(x)dx \qquad (E.6)$$

If the film thickness is known at (N + M) points, there are (N + M + 1) equations available ((N + M) of the form of Equation (E.2), plus equation (E.6)) to determine the (N + M + 1) unknowns $\gamma(P)$, $p_n^{(s)}$, and $p_m^{(a)}$. The pressure distribution in the EHD zone is then known from equation (E.5).

It is apparent that if the EHD zone is bounded by two cylinders, both u_1 and u_2 will be given by equation (C.35). If one of the boundary

surfaces is a cylinder and the other is a plate, u_1 is obtained from equation (C.35) and u_2 from equation (D.18). The latter case is the one which will be dealt with in the following discussion; treatment of the case of two cylinders is analogous.

Figure V-5 shows the conjunction of the cylinder and the plate. The pressure zone extends from $x = -a$ to $x = a$, and $\beta = -\alpha_o$ to $\beta = \alpha_o$. Because α_o is very small, $a = r_o\alpha_o$, and $x = r_o\beta$. Since the location of the point $x = 0$ is the midpoint of the pressure distribion, it is necessary to specify the points at which the pressure goes to zero (i.e. the inlet and outlet points) in order to determined the location of $x = 0$ and the value of a. An ad hoc procedure for determining these points is discussed in a later section. It should be noted that the origin of the x coordinate in this analysis in general is not the center of the dry Hertzian contact.

F. Numerical Considerations

As developed in the previous section, the problem of determining the pressure distribution in the EHD zone reduces to the problem of solving a set of algebraic equations for the Fourier coefficients of the pressure. Since equations (C.35) and (D.18) for the displacement of the solid surfaces are linear in these coefficients, the set of algebraic equations to be solved is linear. In order to avoid an ill-conditioned numerical system of equations, equation (E.2) is solved for the total displacement,

$$u_1(x_A,p) + u_2(x_A,p) = h(x_A,p) - h_o(x_A) + \gamma(P) \quad A = 1,2,\ldots,n \qquad (F.1)$$

where the left-hand side is expressed in terms of the Fourier coefficients

p_i, $i = 1,2,\ldots,m$ by equations (E.3) and (E.4). A trial value of $\gamma(P)$ is assumed, and when $m = n$ the system (F.1) may be solved for p_i. Equation (E.6) is then evaluated to see if the total load condition is satisfied. If not, a different value for γ is selected and the process repeated. Since the system is linear, two iterations are required to find the true value of γ. Because only the right-hand side of equation (F.1) is affected by changing γ, very little extra work is incurred by this iteration scheme. If the film thickness measurements were known to be exact, the film thickness at m points would be sufficient to determine the Fourier coefficients. However, due to unavoidable inaccuracies in the measurements, certain modifications to the solution of the equations must be made.

Since the measurements at each point in the EHD zone are in error, the total error increases as the number of points used, n, increases. At the same time, a sufficient number of points must be used to adequately characterize the shape of the film thickness profile. Furthermore, the number m of Fourier coefficients to be found must be large enough that the truncated Fourier series, equation (E.5) (with $m = N + M$) may accurately represent the true pressure. To alleviate this problem, n and m are chosen, with $n > m$, and the following process used to "smooth out" the errors in the film thickness. The algebraic equations take the form

$$a_{ij}\, p_j = b_i \qquad i = 1,2,\ldots n, \quad j = 1,2,\ldots,m \tag{F.2}$$

where p_i are the unknown coefficients. Equation (F.2) represents an overdetermined system (that is, there are more equations than unknowns)

for which, in general, there is no exact solution. Accordingly, the residual, r_i, is defined as

$$a_{ij}p_j - b_i = r_i \tag{F.3}$$

The unknowns p_j are then determined so as to minimize the sum of the squares of the residuals, $r_i r_i$. This results in a system of m linear equations [70]. The minimization of the residuals has the effect of smoothing the data while coming as close as possible to solving equations (F.2), recognizing the fact that the data is a best estimate to the true film thickness. The amount of smoothing depends on the degree to which n is greater than m. If the Fourier series for the pressure is to converge to the true pressure, the coefficients must eventually go to zero as m is increased. Once n is selected, the amount of smoothing required is determined by increasing n until the Fourier coefficients begin to increase, causing the series to diverge. As a check on the acceptability of the result the magnitudes of the residuals may be compared to the expected error in film thickness measurements.

It should be noted that the calculations for the pressure are based on the displacement of the surfaces from their undeformed states, rather than on the film thickness itself. From equation (E.1), assuming $h_o(x)$ and $\gamma(P)$ may be found precisely, the magnitude of the error in total displacement, $u_1 + u_2$, is the same as that for the film thickness. Consequently, near the center of the contact where the film thickness is small and the surface deformation is large, a small relative error in film thickness results in a smaller relative error in the displacement. Therefore, the pressure calculated in the part of the

contact where deformations are large is expected to be quite accurate. On the other hand, in the inlet region where the pressure is building up gradually from zero, the film thickness is large due to the initial surface geometry while the displacements are small because of the lower pressure. Hence, a small relative error in film thickness in the inlet region may result in a large relative error in the displacement, so that the pressure calculated in this region is somewhat less reliable. Thus it is often helpful to introduce additional information in this area by requiring that the pressure gradient at $x = -a$ vanish. This is a consequence of the fact that the pressure is generated by the hydrodynamic action of the fluid, and has the effect of introducing an additional equation into the set to be solved. This procedure tends to offset somewhat the increased effect of errors in the inlet region.

Because of the method by which pressures are calculated, an error in film thickness which is constant in magnitude throughout the entire EHD zone has no effect on the computations. Such an error has the character of a rigid-body translation of one of the solid surfaces, and would therefore be absorbed in the normal approach term (γ) of equation (E.1), leaving the displacement and hence the pressure unaffected. Consequently the range of errors encountered, rather than their magnitude, determines the accuracy of the calculated pressure distribution.

G. Test Cases and Evaluation

In order to test the procedures described in the previous section, and to evaluate the effects of certain types of errors in the input data, a number of test cases were run. In the first case,

the following pressure distribution was employed

$$p(\hat{x}) = \begin{cases} 0 & \hat{x} \leq -x_o \\ p_o & -x_o < \hat{x} < x_o \\ 0 & \hat{x} \geq x_o \end{cases} \qquad (G.1)$$

where $\hat{x} = 0$ is the contact point of the undeformed surfaces. Closed-form solutions for the displacements of the cylinder and the plate for the pressure distribution were found from equations (C.13) and (D. 6). These displacements were then used as film thickness data to obtain a series expression for the pressure of the form of equation (E.5), which could be evaluated by comparison with equation (G.1). The calculated pressure curve which resulted is shown in Figure V-6, which represents equation (E.5) with 10 terms, and $a = 1.3\ x_o$. The major disagreement with equation (G.1) occurs near $\hat{x} = \pm x_o$ where the pressure is discontinuous; this is to be expected due to the nature of the series, and is not a serious drawback, since pressure discontinuities are not expected in a film. The selection of $a = 1.3\ x_o$ results in small negative pressures near the inlet and outlet. This will be discussed later in this section in more detail.

As a second case, the film thickness was taken as zero over the region $-x_o < \hat{x} < +x_o$; this is the case of two dry bodies in contact over the region, for which the pressure distribution should approximate the Hertzian semi-elliptical distribution. The results are shown in Figure V-7 for nine terms in the series of equation (E.5), with a and $x = 0$ chosen so that the pressure is zero at $\hat{x} = -1.33\ x_o$ and $\hat{x} = 1.1\ x_o$.

The agreement is good except near $\hat{x} = \pm x_o$, where there is a discontinuity in the pressure gradient. In the presence of such a discontinuity, inaccuracy in the series expansion is to be expected, since equation (E.5) implies continuous derivatives.

A third test case was examined using a pressure distribution expressed by a third-degree polynomial, shown in Figure V-8. As in the first case, a closed-form expression for the displacement of the surfaces was obtainable, and the resulting film thickness profile is also shown in Figure V-8. The values of the total load, elastic constants of the surfaces, cylinder dimensions, and minimum film thickness were selected so as to approximate those in an actual EHD contact [71]. The calculated film thickness was used to obtain a series solution for the pressure as described in the preceding section. When the inlet and outlet points ($x = \pm a$) were specified correctly, the series expression for the pressure showed negligible deviation from the polynomial expression throughout the contact. Because the pressure distribution of Figure V-8 in some ways resembles that expected in an EHD contact, this test case was examined further in order to study the effects of certain types of errors. It was estimated that, using the optical interference method of measuring film thickness, the maximum error in film thickness at a given location is .025 μm (1 μin.). Accordingly, three sets of random errors in the range (-.025, .025) μm were introduced into the film thickness data. This was a fairly severe test, because in actuality the errors would most likely be normally distributed, over the range (-0.025, 0.025 μm). The pressure distributions calculated from these three error sets are shown in Figure V-9.

Sets 1 and 3 show the largest errors on the side corresponding to the inlet of an EHD contact, as would be expected from the discussion of the previous section. The general shape of the pressure distribution is preserved in all three cases shown in the figure.

The effects of errors in location of the beginning and end of the pressure were also studied. The results of varying the point of zero pressure at the inlet of the EHD zone are shown in Figure V-10. When the inlet point is located too far in, a hump in the calculated pressure appears, and convergence of the series becomes somewhat slower. The presence of these conditions indicates that the inlet point should be moved farther out. When the inlet point was located too far out, the calculated pressure came in at zero up to the true inlet, and blended into the exact distribution almost immediately, resulting in negligible error. When the change in pressure near the inlet is more abrupt, as in Figure V-6, negative pressures may result if the inlet point is set too far out. Since the location of the point of zero pressure is not known ahead of time, these conclusions are helpful in locating the inlet point when calculating the pressure distribution. Similar conclusions may be drawn concerning the location of the outlet point; however, the determination of the location of this point in an actual EHD contact is generally less difficult, since it is known a priori that the pressure goes to zero in the vicinity of the exit constriction of the film.

In addition, small (3%) errors were introduced in the elastic constants, the total load, and the radius of the cylinder. The calculated pressure distribution was found to be relatively insensitive

($\tilde{-}$ 1%) to these errors in the elastic constants and the load, and somewhat more sensitive to errors in the radius. This is not a serious drawback, since the radius may be measured to a high degree of precision.

At present, accurate data for the film thickness in an actual EHD line contact are not available to us. Wymer and Cameron [71] show measured line contact film thickness profiles, but from their published figures it is possible to determine the film thickness only to within 2-3 μ in. at a given location in the EHD zone. Nevertheless, a pressure distribution was calculated based on their measurements, and the results shown in Figure V-11 where it is compared with the Hertzian distribution. The figure also shows a comparison between the measured film thickness used as input for the calculations, and the film thickness which would result from the calculated pressure distribution. The difference between the two is the residual, which is quite large near the exit region, as shown in the figure. In this region, the magnitude of the slope of the film thickness profile is quite large, which increases the difficulty in reading the points from the figures. Because of the large residuals near the exit and the inaccuracy of the input data used, the pressure distribution of Figure V-11 should be viewed as a rather rough approximation. In spite of the lack of precise film thickness data for a line contact, accurate data is available for the EHD point contact. Most of the foregoing numerical methods and conclusions concerning probable errors are expected to carry over into this case.

H. Summary of Computational Method

If the film thickness is known from measurements at n points x_A, A = 1,2,...,n, in the EHD zone, the set of n equations (F.1) is used

to find the Fourier coefficients of pressure as follows. The film thickness in the undeformed state is known at each point x_A, and an initial estimate for the normal approach $\gamma(P)$ is made. The right-hand side of equations (F.1) is then known. The displacements $u_1(x_A,p)$ and $u_2(x_A,p)$ are expressed in terms of the m unknown Fourier coefficients. The number of Fourier terms used (m) is arbitrary as long $m < n$. For the case of two cylinders, both u_1 and u_2 are given by equation (C.35); for the case of a cylinder and a plate, u_1 is given by equation (C.35) and u_2 by equation (D.18). Equation (F.1) is then a set of n equations in m unknowns. An additional equation is obtained from the requirement that the pressure gradient be zero at the inlet $\left(\frac{dp}{dx}\Big|_{x=-a} = 0 \text{ from equation (E.5)}\right)$. Because the system is overdetermined ($m < n + 1$) residuals are defined as in Equation F.3. The condition that the sum of the squares of the residuals be a minimum is applied, which results in a system of m equations in m unknowns. This system is solved for the m Fourier coefficients, for use in equation (E.5) for the pressure distribution. The total load P is calculated from equation (E.6), and the result compared with the known value of the load. If they are not the same, a new estimate is made for $\gamma(P)$, and the solution process is repeated. Once equation (E.6) is satisfied, the Fourier coefficients of pressure are known, and the pressure at any point in the EHD contact is determined from equation (E.5).

The calculations require knowledge of the film thickness at n locations in the EHD zone, the total load on the system, the elastic constants of the solid bodies, and the radii of the cylinders. In addition, the number of sine and cosine terms to be used in equation

(E.5) and the locations of the inlet and outlet points must be specified. On the following pages is a listing of the Fortran computer program for calculating the pressure distribution by the above method.

```
FYCM:49.
GEORGIA TECH CYBER 74.                    NOS 1.1-419/420.
USER NUMBER: ME650AC
PASSWORD
********
TERMINAL:      75,TTY
RECOVER /SYSTEM: GET,MLSDP
/LIST,F=MLSDP
```

```
      PROGRAM EHDP(DAT,INPUT,OUTPUT,TAPE5=DAT,TAPE4=INPUT,TAPE6=OUTPUT)

C     PROGRAM TO COMPUTE PRESSURE DISTRIBUTION FOR EHD LINE CONTACT
C     FROM FILM THICKNESS DATA.
      DIMENSION H(30),BETA1(30),BETA2(30),Q(30),A1(30,30),XT(80)
      DIMENSION A2(30,30),AS(30,30),X(30),U(30),P(51),XIN(51),XTIN(51)
      DIMENSION IPIVOT(30),D(30),SL(30,30),UIN(30)
      DIMENSION UC(30),HC(30),RES(30)
      REAL K1,K2
C     PRELIMINARY DATA:
C       SET IFLAG=0 FOR TWO CYLINDERS, =1 FOR CYLINDER + PLATE
C       GAM: INITIAL GUESS FOR NORMAL APPROACH OF BODIES (M)
C       F: TOTAL LOAD (N)
C       M: NO. OF COS TERMS IN SERIES FOR PRESSURE
C       N: NO. OF SIN TERMS IN SERIES FOR PRESSURE
C       L1: NO. OF FILM THICKNESS DATA POINTS TO BE INPUT
C       SP: DESIRED SPACING BETWEEN POINTS AT WHICH PRESSURE
C           IS TO BE PRINTED OUT (M)
C       X1,X2: INLET, OUTLET POINTS, MEASURED FROM POINT OF CONTACT
C              IN UNDEFORMED STATE (M)
```

```
      READ(5,*)IFLAG,GAM,F
      READ(5,*)M,N,L1,SP
      READ(5,*)X1,X2
      PI=4.*ATAN(1.)
      A=ABS((X1-X2)/2.)
      OFST=-(X1+X2)/2.
      NN=0
      MM=M-1
      L11=L1+1
      LL=M+N
C     FILM THICKNESS DATA:
C       X(I): DISTANCE OF I-TH DATA POINT FROM POINT OF CONTACT IN
C             @UNDEFORMED STATE (M)
C       H(I): FILM THICKNESS AT X(I) (M)
      READ(5,*)(X(I),H(I),I=1,L1)
      DO 13 I=1,L1
      XT(I)=X(I)+OFST
   13 CONTINUE
C     DATA ON BODY 1 - CYLINDER:
C       YM1: MODULUS OF ELASTICITY (N/M**2)
C       PR1: POISSON'S RATIO
C       R1: RADIUS (M)
      READ(5,*)YM1,PR1,R1
      K1=2.*(1.-PR1*PR1)/(PI*YM1)
      ALP1=A/R1
      DO 5 I=1,L1
      BETA1(I)=XT(I)/R1
    5 CONTINUE
      CALL CYL(ALP1,BETA1,N,M,L1,A1)
      IF(IFLAG.EQ.0)GO TO 10
C     DATA ON BODY 2: USE IF IFLAG=1
      READ(5,*)YM2,PR2
      K2=2.*(1.-PR2*PR2)/(PI*YM2)
      CALL PLATE(A,XT,N,M,L1,A2)
      RIN=0.0
      GO TO 17
```

```
C     DATA ON BODY 2: USE IF IFLAG=0
   10 READ(5,*)YM2,PR2,R2
      K2=2.*(1.-PR2*PR2)/(PI*YM2)
      ALP2=A/R2
      DO 20 I=1,L1
      BETA2(I)=YT(I)/R2
   20 CONTINUE
      CALL CYL(ALP2,BETA2,N,M,L1,A2)
      RIN=1./R2
C     COMBINE MATRICES FOR BODIES 1 AND 2. SL(I,J) IS THE MATRIX OF
C       COEFFICIENTS OF THE UNKNOWN FOURIER COEFF. OF PRESSURE.
   17 DO 25 I=1,L1
      DO 25 J=1,LL
      SL(I,J)=(A1(I,J)*K1+A2(I,J)*K2)*A/PI
   25 CONTINUE
C     INCLUDE CONDITION THAT PRESSURE GRADIENT VANISH AT INLET
      DO 70 I=1,N
      SL(L11,I)=((-1.)**I*I)*(1.E-10)
   70 CONTINUE
      DO 71 I=1,M
      SL(L11,N+I)=((-1.)**(I-1)*(2.*I-1.)/2.)*1.E-10
   71 CONTINUE
C     FROM SL, FORM MATRIX CORRESPONDING TO MINIMIZATION OF THE NORM
C       OF THE RESIDUAL.
      DO 55 I=1,LL
      DO 55 J=1,LL
      AS(I,J)=0.0
      DO 55 K=1,L11
      AS(I,J)=AS(I,J)+SL(K,I)*SL(K,J)
   55 CONTINUE
C     BEGIN PROCEDURE FOR SOLVING THE SET OF LINEAR EQUATIONS FOR THE
C       UNKNOWN FOURIER COEFF.
      DO 1 I=1,LL
      IPIVOT(I)=I
      ROWMAX=0.0
      DO 2 J=1,LL
```

```
    2   ROWMAX=AMAX1(ROWMAX,ABS(AS(I,J)))
    1   D(I)=ROWMAX
        NM1=LL-1
        DO 3 K=1,NM1
        J=K
        KP1=K+1
        IP=IPIVOT(K)
        COLMAX=ABS(AS(IP,K))/D(IP)
        DO 4 I=KP1,LL
        IP=IPIVOT(I)
        AWIKOW=ABS(AS(IP,K))/D(IP)
        IF(AWIKOW.LE.COLMAX)GO TO 4
        COLMAX=AWIKOW
        J=I
    4   CONTINUE
        IPK=IPIVOT(J)
        IPIVOT(J)=IPIVOT(K)
        IPIVOT(K)=IPK
        DO 3 I=KP1,LL
        IP=IPIVOT(I)
        AS(IP,K)=AS(IP,K)/AS(IPK,K)
        RATIO=-AS(IP,K)
        DO 3 J=KP1,LL
    3   AS(IP,J)=RATIO*AS(IPK,J)+AS(IP,J)
C       FORM RIGHT-HAND SIDE OF THE EQNS.
   90   DO 45 I=1,L1
        WIN(I)=.5*X(I)*X(I)*(1./R1+RIN)-H(I)-CAM
   45   CONTINUE
C       FROM WIN AND SL, FORM RHS OF EQNS. CORRESPONDING TO MINIMI-
C         ZATION OF THE NORM OF THE RESIDUAL. CONTINUE SOLN. OF
C         LINEAR EQNS. WITH THIS AS RHS.
        WIN(L11)=0.0
        DO 36 I=1,LL
        W(I)=0.0
        DO 36 J=1,L11
        W(I)=W(I)+WIN(J)*SL(J,I)
```

```
   36 CONTINUE
      IP=IPIVOT(1)
      Q(1)=W(IP)
      DO 9 K=2,LL
      IP=IPIVOT(K)
      KM1=K-1
      SUM=0.0
      DO 6 J=1,KM1
    6 SUM=AS(IP,J)*Q(J)+SUM
    9 Q(K)=W(IP)-SUM
      Q(LL)=Q(LL)/AS(IP,LL)
      K=LL
      DO 7 NPINK=2,LL
      KP1=K
      K=K-1
      IP=IPIVOT(K)
      SUM=0.0
      DO 8 J=KP1,LL
    8 SUM=AS(IP,J)*Q(J)+SUM
C     Q(K): DESIRED FOURIER COEFFICIENTS
    7 Q(K)=(Q(K)-SUM)/AS(IP,K)
C     IF NECESSARY, MODIFY VALUE OF GAM TO SATISFY TOTAL LOAD CON-
C       DITION, AND RE-SOLVE THE EQUATIONS WITH NEW RHS.
      FTRIAL=0.0
      DO 34 I=1,M
      T=4.*A*(-1.)**(I-1)/((2.*I-1.)*PI)
   34 FTRIAL=FTRIAL+T*Q(N+I)
      F0=FTRIAL-F
      NN=NN+1
      IF(NN.EQ.3)GO TO 100
      IF(NN.EQ.2)GO TO 110
      F1=F0
      GAM1=GAM
      GAM=GAM/2.
      GO TO 90
```

```
  110 GAM2=GAM1
      GAM1=GAM
      F2=F1
      F1=F0
      GAM=GAM1-((GAM1-GAM2)*F1)/(F1-F2)
      GO TO 90
C     COMPUTE PRESSURE AT LOCATIONS DESIRED FOR OUTPUT.
  100 NP=INT(ABS(X1/SP))+INT(ABS(X2/SP))+3
      XTIN(1)=AMIN1(X1,X2)
      XTIN(2)=INT(XTIN(1)/SP)*SP
      NP1=NP-1
      DO 40 I=3,NP1
      XTIN(I)=XTIN(I-1)+SP
   40 CONTINUE
      XTIN(NP)=AMAX1(X1,X2)
      DO 42 L=1,NP
      XIN(L)=XTIN(L)+OFST
      P(L)=0.0
      DO 32 I=1,N
      P(L)=P(L)+Q(I)*SIN(I*PI*XIN(L)/A)
   32 CONTINUE
      DO 35 JJ=1,M
      I=JJ-1
      P(L)=P(L)+Q(N+JJ)*COS((2.*I+1.)*PI*XIN(L)/(2.*A))
   35 CONTINUE
   42 CONTINUE
C     COMPUTE RESIDUALS AT EACH DATA POINT LOCATION.
      TR=0.0
      DO 91 I=1,L1
      UC(I)=0.0
      DO 92 J=1,LL
      UC(I)=UC(I)+SL(I,J)*Q(J)
   92 CONTINUE
      HC(I)=.5*X(I)*X(I)*(1./R1+RIN)-UC(I)-GAM
      RES(I)=H(I)-HC(I)
      TR=TR+RES(I)*RES(I)
```

```
   91 CONTINUE
C     OUTPUT:
C       FTRIAL: CALCULATED TOTAL LOAD (N) - USE FOR COMPARISON AS A TEST

C               OF ACCURACY OF THE CALCULATIONS.
C       GAM: NORMAL APPROACH VALUE ARRIVED AT (M)
C       FOURIER COEFF.: COEFFICIENTS OF SIN TERMS LISTED FIRST
C       RESIDUALS: LISTED IN SAME ORDER AS INPUT POINTS (M).
C                  LAST VALUE PRINTED IS SUM OF THEIR SQUARES.
C       X: DISTANCE FROM CONTACT POINT IN UNDEFORMED STATE
      WRITE(6,*)FTRIAL,GAM
      WRITE(6,150)
  150 FORMAT(5X,"FOURIER COEFFICIENTS:")
      WRITE(6,*)(Q(I),I=1,LL)
      WRITE(6,250)
  250 FORMAT(5X,"RESIDUALS:")
      WRITE(6,*)(RES(I),I=1,L1)
      WRITE(6,*)TP
      WRITE(6,550)
      WRITE(6,450)(XTIN(I),P(I),I=1,NP)
  550 FORMAT(10X,"X (M)",10X,"PRESSURE (N/M**2)"/)
  450 FORMAT(9X,F10.5,10X,E11.4)
      WRITE(6,650)
C     IF USER WANTS CALCULATED FILM THICKNESS AT EACH INPUT POINT,
C       ENTER 1.  OTHERWISE ENTER 0.
  650 FORMAT(5X,"ENTER 1 FOR FILM THICKNESS")
      READ(4,*)NP
      IF(NP.NE.1)GO TO 93
      WRITE(6,750)
  750 FORMAT(12X,"X (M) ",9X,"FILM THICKNESS (M)"/)
      WRITE(6,450)(X(I),HC(I),I=1,L1)
   93 WRITE(6,850)
C     IF USER WANTS CALCULATED FILM THICKNESS AT OTHER POINTS IN OR
C       NEAR CONTACT, ENTER 1.  OTHERWISE, ENTER 0.
  850 FORMAT(5X,"ENTER 1 FOR ADD'L FILM THICKNESS")
      READ(4,*)NP
```

```
      IF(NP.NE.1)STOP
C     ENTER LOCATION OF DESIRED FILM THICKNESS CALCULATION. TO STOP PROG
AM,                                   R
C       ENTER VALUE > 20.
   94 READ(4,*)XX
      IF(XX.GT.20.)STOP
      XT(1)=XX+OFST
      BETA1(1)=XT(1)/R1
      CALL CYL(ALP1,BETA1,N,M,1,A1)
      IF(IFLAG.EQ.0)GO TO 95
      CALL PLATE(A,XT,N,M,1,A2)
      GO TO 96
   95 BETA2(1)=XT(1)/R2
      CALL CYL(ALP2,BETA2,N,M,1,A2)
   96 DO 97 I=1,LL
      SL(1,I)=(A1(1,I)*K1+A2(1,I)*K2)*A/PI
   97 CONTINUE
      UA=0.0
      DO 98 I=1,LL
      UA=UA+SL(1,I)*Q(I)
   98 CONTINUE
      HH=.5*XX*XX*(1./R1+PIN)-UA-GAM
      WRITE(6,450)XX,HH
      GO TO 94
      STOP
      END
      SUBROUTINE CYL(ALP,BETA,N,MT,L1,A)
C     SUBROUTINE TO FILL MATRIX CORRESPONDING TO CYLINDER DISPLACEMENTS

      DIMENSION A(30,30),BETA(30)
      REAL M
      PI=4.*ATAN(1.)
      MM=MT-1
      LL=MT+N
      DO 10 L=1,L1
      NN=0
```

```
      IF(ABS(1.-ABS(BETA(L)/ALP)).LT.1.E-10)NN=1
C     CALCULATE ELEMENTS CORRESPONDING TO ANTISYMMETRIC COMPONENTS
      DO 12 I=1,N
      COEF1=I*PI/ALP
      YL=COEF1*(BETA(L)+ALP)
      CALL SICO(XL,S1,C01)
      YL=COEF1*(BETA(L)-ALP)
      CALL SICO(XL,S2,C02)
      IF(NN.NE.1)GO TO 16
      A1=0.0
      GO TO 15
   16 A1=((-1.)**I-COS(COEF1*BETA(L)))*ALOG(ABS((BETA(L)
     1+ALP)/(BETA(L)-ALP)))
   15 B1=SIN(COEF1*BETA(L))*(S2-S1)
      C1=COS(COEF1*BETA(L))*(C01-C02)
      A(L,I)=(1./I)*(A1+B1+C1)
   12 CONTINUE
C     CALCULATE ELEMENTS CORRESPONDING TO SYMMETRIC COMPONENTS
      DO 14 JJ=1,MT
      I=JJ-1
      M=(2.*I+1.)/2.
      COEF2=M*PI/ALP
      YL=COEF2*(BETA(L)+ALP)
      CALL SICO(YL,S1,C01)
      YL=COEF2*(ALP-BETA(L))
      CALL SICO(YL,S2,C02)
      A2=(2.*M*(PI)**2/(M**2*PI**2+ALP**2))*
     1SIN(M*PI)*COS(ALP)*COS(BETA(L))
      IF(NN.NE.1)GO TO 20
      B2=SIN(M*PI)*(2.*ALOG(2.*ALP)-ALOG(4.))
      C2=0.0
      GO TO 25
   20 B2=SIN(M*PI)*(ALOG(ABS((ALP+BETA(L))*(ALP-
     1BETA(L))))-ALOG(4.))
      C2=SIN(COEF2*BETA(L))*(ALOG(ABS((ALP+BETA(L))/
     1(ALP-BETA(L)))))
```

```
   25 B2=SIN(COEF2*BETA(L))*(C02-C01)
      E2=(-1.)*COS(COEF2*BETA(L))*(S2+S1)
      A(L,N+JJ)=A2+1./M1*(B2+C2+D2+E2)
   14 CONTINUE
   10 CONTINUE
      RETURN
      END
      SUBROUTINE PLATE(A,X,N,MT,L1,AN)
C     SUBROUTINE TO FILL MATRIX CORRESPONDING TO PLATE DISPLACEMENTS
      DIMENSION AN(30,30),X(30)
      REAL M
      PI=4.*ATAN(1.)
      MM=MT-1
      LL=MT+N
      DO 10 L=1,L1
      NN=0
      IF(ABS(1.-ABS(X(L)/A)).LT.1.E-10)NN=1
C     CALCULATE ELEMENTS CORRESPONDING TO ANTISYMMETRIC COMPONENTS.
      DO 12 I=1,N
      COEF1=I*PI/A
      XL=COEF1*(A+X(L))
      CALL SICO(XL,S1,C01)
      XL=COEF1*(A-X(L))
      CALL SICO(XL,S2,C02)
      IF(NN.NE.1)GO TO 16
      A1=0.0
      GO TO 15
   16 A1=((-1.)**I-COS(COEF1*X(L)))*ALOG(ABS((A+X(L))/
     1(A-X(L))))
   15 B1=(-1.)*SIN(COEF1*X(L))*(S1+S2)
      C1=COS(COEF1*X(L))*(C01-C02)
      AN(L,I)=(1./I)*(A1+B1+C1)
   12 CONTINUE
C     CALCULATE ELEMENTS CORRESPONDING TO SYMMETRIC COMPONENTS.
      DO 14 JJ=1,MT
      I=JJ-1
```

```
      M=(2.*I+1.)/2.
      COEF2=M*PI/A
      S=SIN(COEF2*X(L))
      XL=COEF2*(A+X(L))
      CALL SICO(XL,S1,CO1)
      XL=COEF2*(A-X(L))
      CALL SICO(XL,S2,CO2)
      IF(NN.NE.1)GO TO 20
      A2=ALOG(2.)*(2.*SIN(M*PI))
      B2=0.0
      GO TO 25
   20 A2=ALOG(ABS((A-X(L))/A))*(SIN(M*PI)-S)
      B2=ALOG(ABS((A+X(L))/A))*(SIN(M*PI)+S)
   25 C2=(-1.)*S*(CO1-CO2)
      D2=(-1.)*COS(COEF2*X(L))*(S1+S2)
      AN(L,N+JJ)=(1./M)*(A2+B2+C2+D2)
   14 CONTINUE
   10 CONTINUE
      RETURN
      END
      SUBROUTINE SICO(X,S,C)
C     SUBROUTINE TO EVALUATE SIN AND COS INTEGRALS
      IF(ABS(X).GT.1.E-12)GO TO 25
      S=0.0
      C=0.0
      RETURN
   25 IF(ABS(X).LT.0.1)GO TO 26
C     SICI IS A SUBROUTINE IN CDC MATH-SCIENCE LIBRARY.
      CALL SICI(S,C,X)
      S=S+1.570796
      C=.5772157+ALOG(ABS(X))-C
      RETURN
   26 S=X
      C=0.0
      N=1
      NC=1
```

```
      NS=-1
      NTC=0
      NTS=0
      FACT=1.
      COUNT=1.
      PROD=X
      DO 10 I=2,10
      COUNT=COUNT+1.
      FACT=FACT*COUNT
      PROD=PROD*X
      TERM=PROD/(COUNT*FACT)
      IF(N.EQ.1)GO TO 15
      N=1
      IF(NS.EQ.-1)TERM=-TERM
      NS=-NS
      S=S+TERM
      IF(ABS(TERM/S).LT.1.E-5)NTS=1
      GO TO 112
   15 N=0
      IF(NC.EQ.-1)TERM=-TERM
      NC=-NC
      C=C+TERM
      IF(ABS(TERM/C).LT.1.E-5)NTC=1
  112 IF(NTS.EQ.0)GO TO 10
      IF(NTC.EQ.1)RETURN
   10 CONTINUE
      RETURN
      END
 END OF INFORMATION ENCOUNTERED.

 BYE
ME650AC   LOG OFF    13.59.13.
ME650AC   SRU      0.032 UNTS.
```

VI. REFERENCES

1. Bohn, M., Carlson, S., Lee, D., Jakobsen, J., Sanborn, D. M., and Winer, W. O., "Investigations of Lubricant Rheology as Applied to Elastohydrodynamic Lubrication", NASA Grant No. 11-002-133, June 1972.

2. Johnson, R. L., Jones, W. R., Sanborn, D. M., and Winer. W. O., "Viscosity-Pressure Measurements for Several Lubricants to 5.5×10^8 N/m^2 (8×10^4 psi) and 149 C (300F)", Trans. ASLE, Vol. 97, 1975.

3. Jakobsen, J., and Winer, W. O., "High Shear Behavior of Some Representative Lubricants", Trans. ASME, Journal of Lubrication Technology, Vol. 97, No. 3, 1975, pp. 479-485.

4. Carlson, S., Turchina, V., Jakobsen, J., Sanborn, D. M., and Winer, W. O., "Investigations of Lubricant Rheology as Applied to Elastohydrodynamic Lubrication", NASA Grant No. 11-002-133, October 1973.

5. Jakobsen, J., and Winer, W. O., "Dissipative Heating Effects and End Corrections for Viscous Newtonian Flow in High Shear Stress Capillary Viscometry", Trans. ASME, Journal of Lubrication Technology, Vol. 97, No. 3, 1975, pp. 424-278.

6. Jakobsen, J., "Traction of Elastohydrodynamic Contacts with Thermal Shearing Flow", Trans. ASME, Journal of Lubrication Technology, Vol. 97, No. 3, 1975, pp. 424-429.

7. Kunz, R. K., and Winer, W. O., "Prediction of Traction in Sliding EHD Contacts", Trans. ASME, Journal of Lubrication Technology, Vol. 98, Series F, No. 3, 1975, pp. 362-365.

8. Turchina, V., Sanborn, D. M., and Winer. W. O., "Temperature Measurements in Sliding Elastohydrodynamic Point Contacts", Journal of Lubrication Tehcnology, Trans. ASME, Vol. 96, 1974, pp. 464-471.

9. Ausherman, V. K., Nagaraj, H. S., Sanborn, D. M., and Winer, W. O., "Infrared Temperature Mapping in Elastohydrodynamics Lubrication", Trans. ASME, Journal of Lubrication Technology, Vol. 98F, No. 2, 1976, pp. 236-243.

10. Nagaraj, H. S., Sanborn, D. M., and Winer, W. O., "Effects of Load, Speed and Surface Roughness on Sliding EHD Contact Temperatures", To be published, Trans. ASME, Journal of Lubrication Technology, Presented at the Joint ASME-ASLE Lubrication Conference, Boston, Mass., October 1976.

11. Carlson, S. F., and Winer, W. O., "The Viscous Lubrication of Rolling and Sliding Rigid Cylinders", ASME Transactions, Journal of Lubrication Technology, Vol. 97F, No. 2, April 1975, pp. 180-186.

12. Carlson, S., Jakobsen, J., Nagaraj, H. S., Molina-C., M. A., Sanborn, D. M., and Winer, W. O., "Investigations of Lubricant Rheology as Applied to Elastohydrodynamic Lubrication", NASA CR-134730, September 1974.

13. Kunz, R. K., Nagaraj, H. S., Sanborn, D. M., and Winer. W. O., "Investigations of Lubricant Rheology as Applied to Elastohydrodynamic Lubrication", NASA CR-134882, August 1975

14. Foord, C. A., Wedeven, L. D., Westlake, F. J., Cameron, A., "Optical Elastohydrodynamics, Proc. Instr. Mech. Engrs. 184, Part 1, 1969/70.

15. Sanborn, D. M. and Winer. W. O., "Fluid Rheological Effects in Sliding Elastohydrodynamic Point Contacts with Transient Loading: 1 - Film Thickness", Trans. ASME, Journal of Lubrication Technology, Vol. 93, pp. 262-271, 1971.

16. Blok, H., General Discussion on Lubrication, Vol. 2, Institute of Mechanical Engineers, p. 222, 1937.

17. Jaeger, J. C., "Moving Sources of Heat and the Temperature at Sliding Contacts," Proc. Roy. Soc. N.S.W., Vol. 56, 1942, p. 203.

18. Archard, J. F., "The Temperature of Rubbing Surfaces", Wear, Vol. 2, No. 6, October 1959, pp. 438-455.

19. Sanborn, D. M., "An Experimental Investigation of the Elastohydrodynamic Lubrication of Point Contacts in Pure Sliding", Ph.D. Thesis, University of Michigan, 1969.

20. Sanborn, D. M. and Winer, W. O., "Fluid Rheological Effects in Sliding Elastohydrodynamic Point Contacts: II - Traction, Trans. ASME, Journal of Lubrication Technology, Vol. 93, pp. 342-348, 1971.

21. Whitehouse, D. J. and Archard, J. F., "The Asperities of Random Surfaces of Significance in their Contact", Proc. Roy. Soc. Lond. A., 316, 97-121, 1970.

22. Peklenik, J., "New Developments in Surface Characterization and Measurements by Means of Random Process Analysis", Proc. Inst Mech Engr, Vol. 182, Pt. 3K, 1967-1968.

23. Wedeven, L. D., "Traction and Film Thickness Measurements Under Starved Elastohydrodynamic Conditions", Trans, ASME., Journal of Lubrication Technology, Series F, No. 2, pp. 321-329, April 1975.

24. Greenwood, J. A., and Kauzlarich, J. J., "Inlet Shear Heating in Elastohydrodynamic Lubrication", Journal of Lubrication Technology, Trans. ASME, Series F, Vol. 95, pp. 417-426, October 1973.

25. Smith, F. W., "Lubricant Behavior in Concentrated Contact - Some Rheological Problems", ASLE Transaction, 3, 18, 1960.

26. Johnson, K. L., and Roberts, A. D., "Observation of Viscoelastic Behavior of an EHD Lubricant Film", Proc. Roy. Soc. Lond. A-337, 217, 1974.

27. Johnson, K. L., and Cameron, R., "Shear Behavior of Elasto-hydrodynamic Oil Films at High Rolling Contact Pressures," Proc. Inst. Mech. Engrs., 182, Pt. 1, 307, 1967-1968.

28. Noel, F., "Thermal Analysis of Lubricating Oils", Thermonica Act., 4, 377, 1972.

29. Haward, R. N., The Physics of Glassy Polymers, New York, Wiley and Sons, Inc.

30. McCrum, N. G., Read, B. E., and Williams, G. E., Anelastic and Dielectric Effects in Polymeric Solids, John Wiley and Sons, New York, 1967.

31. Rosen, Bernard. Fracture Processes in Polymeric Solids - Phenomena and Theory, John Wiley and Sons, Interscience Publishers, New York, 1964.

32. Lamb, John, "Experimental Linear Viscoelastic Measurements for Liquids", ACS Symposium on Lubricant Properties in Thin Lubricating Films, April 1976. (to be published)

33. Dill, J. F., Drake, P. W., and Litovitz, T. A., "The Study of Viscoelastic Properties of Lubricants Using High Pressure Optical Techniques", ASLE, 18(3), 202, 1975.

34. ASME, Pressure-Viscosity Report, I, II, A Report Prepared by the ASME Research Committee on Lubrication, New York, ASME, 1953.

35. McKinny, J. E., and Goldstein, M., "PVT Relationships for Liquid and Glassy Poly(Vinyl Acetate)", Journal of Research of the NBS-Physics and Chemistry, 78A, 331, 1974.

36. Turnbull, D., Contemp. Phys. 10, 473, 1969.

37. Gee, G., "The Glassy State in Polymers", Contemp. Phys., 11(4).

38. Harrison, G., The Dynamic Properties of Supercooled Liquids, Academic Press, New York 1976.

39. Ferry, J. D., Viscoelastic Properties of Polymers, New York, Wiley and Sons, Inc., 1961.

40. Kovacs, A. J., J. Polym. Sci., 30, 131, 1958.

41. Matsuaka, S., and Maxwell, B., J. Poly. Sci., 32, 131, 1958.

42. Yourtee, J. B., and Cooper, S. L., "Properties of Densified Amorphous Polystyrene", J. Appl. Poly. Sci., 18, 897, 1974.

43. Greet, R. J., and Turnbull, D., "Glass Transition in O-Terphenyl", J. Chem. Phys., 46(4), 1967.

44. Barrall, E. M., II, Porter, R. S., and Johnson, J. F., "Heat of Transition for Some Cholesteryl Esters by Differential Scanning Calorimetry", J. Phys. Chem., 71(5), 1224, 1967.

45. Johari, G. P., and Goldstein, M., "Viscous Liquids and the Glass Transition", J. Chem. Phys., 55(9), 4245, 1971.

46. Yano, O., and Wada, Y., "Dynamic and Dielectric Relaxations of Polysterene Below the Glass Temperature", J. Poly. Sci., 9(A2), 669, 1971.

47. Rank, D. H., Kiess, E. M., and Fink, U., "Brillouin Spectra of Viscous Liquids", J. Opt. Soc. Am. 56(2), 103, 1966.

48. Pinnow, D. A., Candau, S. J., LaMacchia, I. T., and Litovitz, T. A., "Brillouin Scattering: Viscoelastic Measurements in Liquids", J. Acoust. Soc. Am., 43, 13, 1968.

49. Rank, D. H., Kiess, E. M., Fink, U. and Wiggins, T. A., J. Opt. Soc. Am., 54, 1286, 1964.

50. Cummins, H. Z., and Gammon, R. W., "Rayleigh and Brillouin Scattering in Liquids: The Landau-Placzek Ratio", J. Chem. Phys., 44(7), 2785, 1966.

51. Stevens, J. R., Jackson, D. A., and Champion, J. V., "Evidence for Ordered Regions in P ly(n-butyl) Methacrylate from Light Scattering Studies", Molecular Physics, 29(6), 1893, 1975.

52. Coakley, R. W., Mitchel, R. S., Stevens, J. R., and Hunt, J. L., "Rayleigh-Brillouin Light Scattering Studies on Atactic Polystrene", A paper presented at the American Physical Society Conference, Atlanta, Georgia, April, 1976.

53. Jackson, D. A., Pentecost, H. T. A., and Powels, J. G., "Hypersonic Absorption in Amorphous Polymers by Light Scattering", Molecular Physics, 23(2), 425, 1972.

54. Romberger, A. B., Eastman, D. P., and Hunt, J. L., "Evidence for Structure in Plastics from Light Scattering", J. Chem. Phy., 51(9), 3723, 1969.

55. Work, Richard N., "On the Discontinuity in the Temperature Coefficient of the Velocity of Ultra Waves in Polymeric Materials", J. Appl. Phys., 27(1), 69, 1956.

56. Mitchell, R. S., and Guillet, J. E., "Brillouin Scattering in Amorphous Polymeric Solid", J. Polymer Sci.: Polymer Phys. Ed., 12, 713, 1974.

57. Friedman, E. A., Ritger, A. J., and Andrews, R. D., "Brillouin Scattering Near the Glass Transition of Polymethyl Methacrylate", J. Appl. Phys., 40(11), 4243, 1969.

58. Fabelinskii, I. L., Molecular Scattering of Light, Plenum Press, New York, 1968.

59. Debye, P., Ann. Physik, 39, 789, 1912.

60. Brillouin, L., Ann. Phys. (Paris) 17, 88, 1922.

61. Landau, L., and Placzek, G., Z. Phys. Sowjetunion, 5, 172, 1934.

62. O'Shea, D. C., Callen, W. R., and Rhodes, W. T., A Laser Textbook-An Introduction to Lasers and their Applications, Georgia Institute of Technology, 1973.

63. Love, A. E. H., A Treatise on the Mathematical Theory of Elasticity, Cambridge University Press, 1927.

64. Timoshenko, S., and Goodier, J. N., Theory of Elasticity, McGraw-Hill Book Company, New York, 1951.

65. Milne-Thomson, L. M., Plane Elastic Systems, Springer-Verlag, Berlin, 1968.

66. Muskhelishvili, N. I., Some Basic Problems of the Mathematical Theory of Elasticity, Noorhoff, Groningen, 1953.

67. Carrier, G. F., Krook, M., Pearson, C. E., Functions of a Complex Variable, McGraw-Hill Book Company, New York, 1966.

68. Jahnke, E., and Ende, F., Tables of Functions, Dover, New York, 1945.

69. Sheid, F., "Theory and Problems of Numerical Analysis", Schaum's Outline Series, McGraw-Hill Book Company, New York, 1968.

70. Wymer, D. G., and Cameron, A., "Elastohydrodynamic Lubrication of a Line Contact", Proc. of the Institute of Mechanical Engineers, Vol. 188, pp. 221-238, 1974.

Table III-1. Summary of Rolling Experiments
Film Thickness and Traction.

$\bar{V}$	Σ	V_s	P_H	T_{BATH}	h_c	h_m	TC
m/s	-	m/s	GN/m^2	^oC	μm	μm	--
0.5	2.00	1.00	0.81	34	.18	.076	.061
"	0.60	0.30	"	37	"	"	.056
"	0.40	0.20	"	38	"	"	.055
"	0.20	0.10	"	38	"	"	.050
"	0.00	0.00	"	39	"	"	.017
"	-.20	-.10	"	38	"	"	--
"	-.40	-.20	"	40	"	"	--
"	-.88	-.44	"	41	"	"	--
0.75	2.00	1.50	"	39	.19	.089	.058
"	1.20	0.90	"	"	.20	"	.058
"	0.67	0.50	"	"	.20	"	.055
"	0.13	0.10	"	"	.22	"	.049
"	0.00	0.00	"	38	.22	"	.024
"	2.00	1.50	0.66	33	.22	.15	.051
"	1.20	0.90	"	34	.24	.18	.051
"	0.67	0.50	"	34	"	"	.051
"	0.19	0.14	"	35	"	"	.051
"	0.00	0.00	"	"	"	"	.014
"	-.10	-.08	"	"	"	"	.041
"	2.00	1.50	1.02	40	.15	.064	.061
"	.27	.20	"	38	.18	.076	.059
"	0.00	0.00	"	37	.22	"	.020
"	-.27	-.20	"	"	.17	"	.057
0.51	0.00	0.00	"	"	.18	"	.020
0.72	0.00	0.00	"	"	.22	"	.023
1.00	0.00	0.00	"	"	.24	.127	.023
1.25	0.00	0.00	"	"	.28	.178	.027

Table III-2. Summary of Rolling Experiments
Ball Surface Temperature Rises.
(P_H = 1.02 GN/m^2)

$\bar{V}$	Σ	V_s	T_{BATH}	CENTER ΔT	MAX. ΔT
m/s	-	m/s	^oC	^oC	^oC
0.75	2.00	1.50	42	54	64
0.75	1.20	0.90	42	35	36
0.75	0.99	0.74	43	26	26
0.75	0.56	0.42	42	14	15
0.75	0.27	0.20	40	6	6
0.75	0.13	0.10	41	4	4
0.75	0.00	0.00	41	4	4
0.75	-.27	-.20	40	6	6
1.00	2.00	2.00	44	53	62
1.00	1.50	1.50	45	42	46
1.00	1.30	1.30	45	37	39
1.00	1.04	1.04	44	36	37
1.00	0.60	0.60	43	21	21
1.00	0.40	0.40	43	10	10
1.00	1.12	0.12	42	6	6
1.00	0.00	0.00	41	5	5
0.50	0.00	0.00	41	2	2
1.25	0.00	0.00	41	7	7

Table IV-1. Frequency Shift and Velocity of Sound as Function of Pressure for 5P4E at 24.4C (76F) (History B).

Date: December 26, 1975
Separation Distance - 0.50 cm
Resulting P_g = 24,700 psi
= 0.17 GPa

Spectrum Number	Pressure kpsi*	Frequency Shift cm^{-1}	Frequency Shift GHZ	Refractive Index	Velocity of Sound, m/s
1	4.78	0.33194	10.00	1.6405	2208
2	7.2	0.34034	10.21	1.6453	2258
3	10,460	0.35364	10.61	1.6518	2337
4	14,250	0.36805	11.04	1.6594	2421
5	16,800	0.37819	11.35	1.6645	2480
6	20,840	0.39429	11.83	1.6726	2573
7	23,125	0.40259	12.08	1.6772	2620
8	26,050	0.41204	12.36	1.6829	2672
9	28,200	0.41642	12.49	1.6873	2695
10	29,950	0.42067	12.62	1.6909	2715
11	31,500	0.42347	12.70	1.6939	2729

*Multiply entry by 6.894×10^{-3} to get pressure units of GPa.

Table IV-2. Frequency Shift and Velocity of Sound as a Function of Temperature at 0.40 GPa (59,000 psi) for 5P4E Oil (History A).

Date: March 2, 1976

Separation Distance = 0.725 cm

Resulting: T_g = 70.3 C

Spectrum Number	Temperature C	Frequency Shift cm^{-1}	Frequency Shift GHZ	Refractive Index	Velocity of Sound m/s
64	82	0.43966	13.19	1.7222	2787
65	80	0.44236	13.27	1.7233	2801
66	77	0.44618	13.39	1.7246	2823
67	75	0.44973	13.49	1.7258	2844
68	72	0.65369	13.61	1.7271	2867
69	70	0.45511	13.65	1.7280	2875
70	67	0.45691	13.71	1.7292	2883
71	65	0.45789	13.74	1.7303	2888
72	63	0.45910	13.77	1.7313	2894
73	59	0.46064	13.82	1.7328	2901
74	56	0.46216	13.86	1.7343	2908

Table IV-3. Least-Square Expressions for Sound Velocity, Temperatures and Sound Velocity at Transition for Different Constant Pressures: 5P4E History A.

Formation Pressure, MPa	Range of Measurements C	Least-Square Expression for Sound Velocity	Glass Transition Temperature (T_g) C	Sound Velocity at T_g, m/s
210	48-27	$V_L = 2961 - 7.99T$ $V_g = 2798 - 3.15T$	34	2692
248	49-27	$V_L = 3043 - 7.49T$ $V_g = 2856 - 2.88T$	41	2739
276	58-32	$V_L = 3138 - 7.94T$ $V_g = 2903 - 2.88T$	46	2769
321	68-43	$V_L = 3172 - 6.79T$ $V_g = 2942 - 2.43T$	53	2812
355	72-46	$V_L = 3259 - 6.95T$ $V_g = 3015 - 2.48T$	59	2848
407	82-54	$V_L = 3410 - 7.60T$ $V_g = 3032 - 2.23T$	70	2875

Table IV-4. Experimental Fluids* in Volumetric Glass Transition Experiments.

5P4E	XRM-177-F4
N1, N2	DN 600
P1	FN 2961
MCS 460	S2-Polybutene
MCS 1218	S1-Diester
Sanotrac 50	S3-DC200-Blend I
Formulated Advanced Ester	DC 200-50

*Detailed descriptions are given in Appendix A.

Table IV-5. Fluids for Which No Transition was Observed by the Volumetric Method in the Indicated Temperature and Pressure Ranges (Isothermal Compression).

SAMPLE	MAXIMUM PRESSURE (GPA)	TEMPERATURE (^{o}C)
DIESTER (S1)	1.13	-3.3
DC 200 BLEND II	** .61	7.2
DC 200 - 50 (S3)	* .92	21.1
ADVANCED ESTER	*1.07	16.9

* PISTON SEIZED
** DISPLACEMENT LIMITED

Table IV-6. Approximate Yield Shear Strength at Atmospheric Pressure

FLUID	T	T_g	$\tilde{=}$ τ yield, MPa
5P4E	- 60C	- 23C	5.38
N1	$< T_g$	- 62C	3.24
XRM	$< T_g$	N.A.	2.96

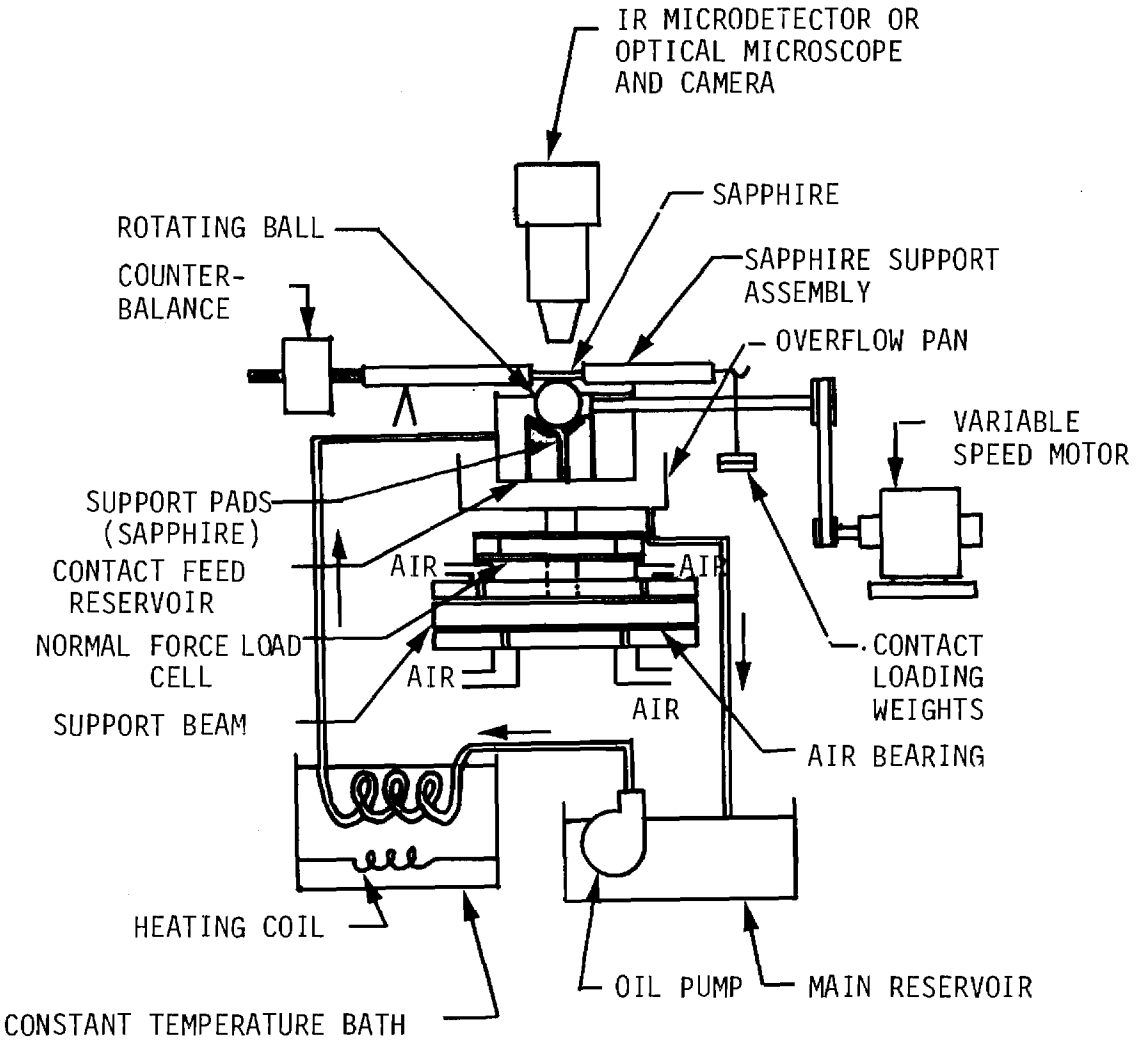

Figure III-1. Schematic of Sliding EHD Contact Simulator.

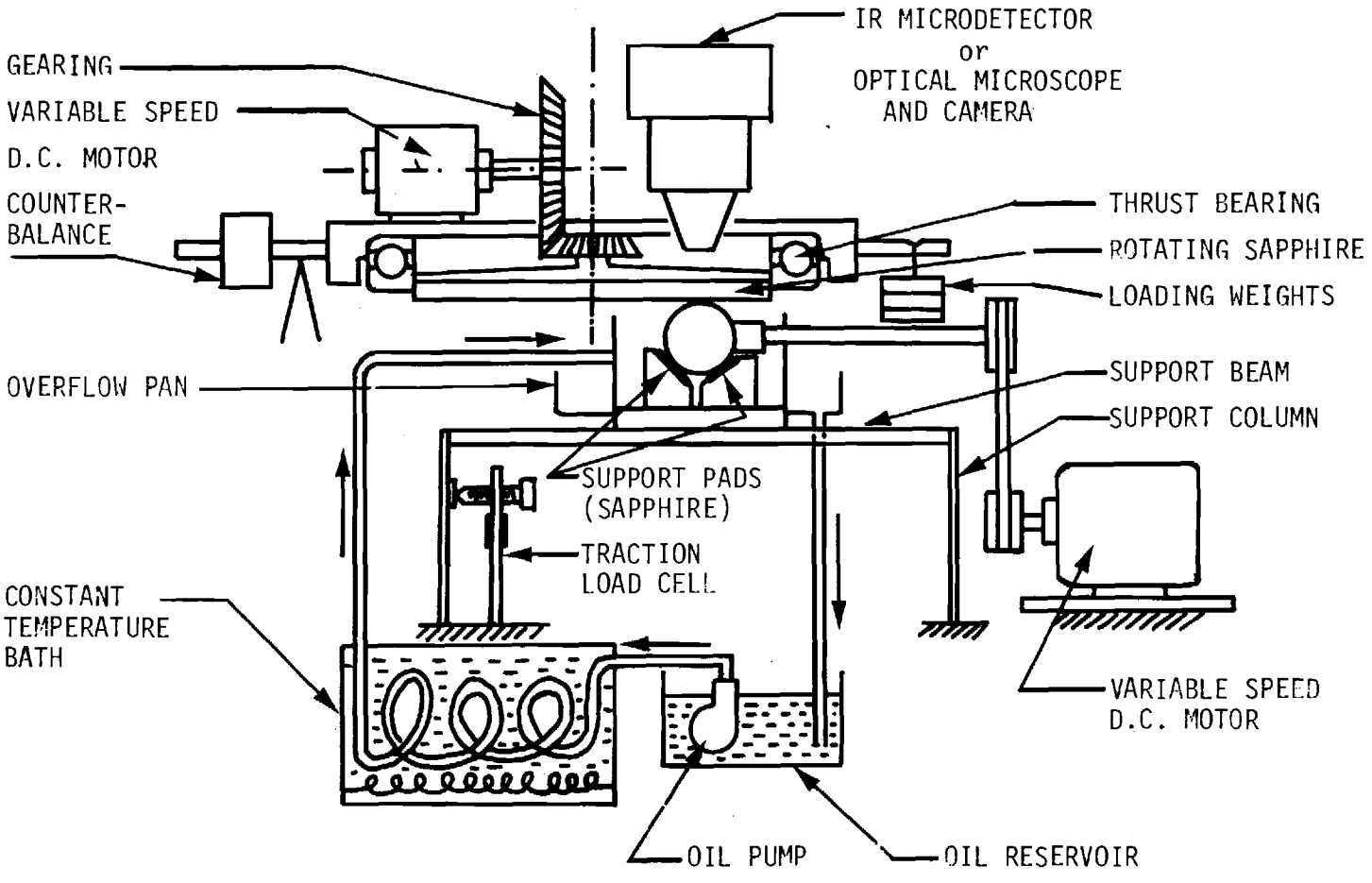

Figure III-2. Schematic of the Combined Rolling and Sliding EHD Contact Simulator.

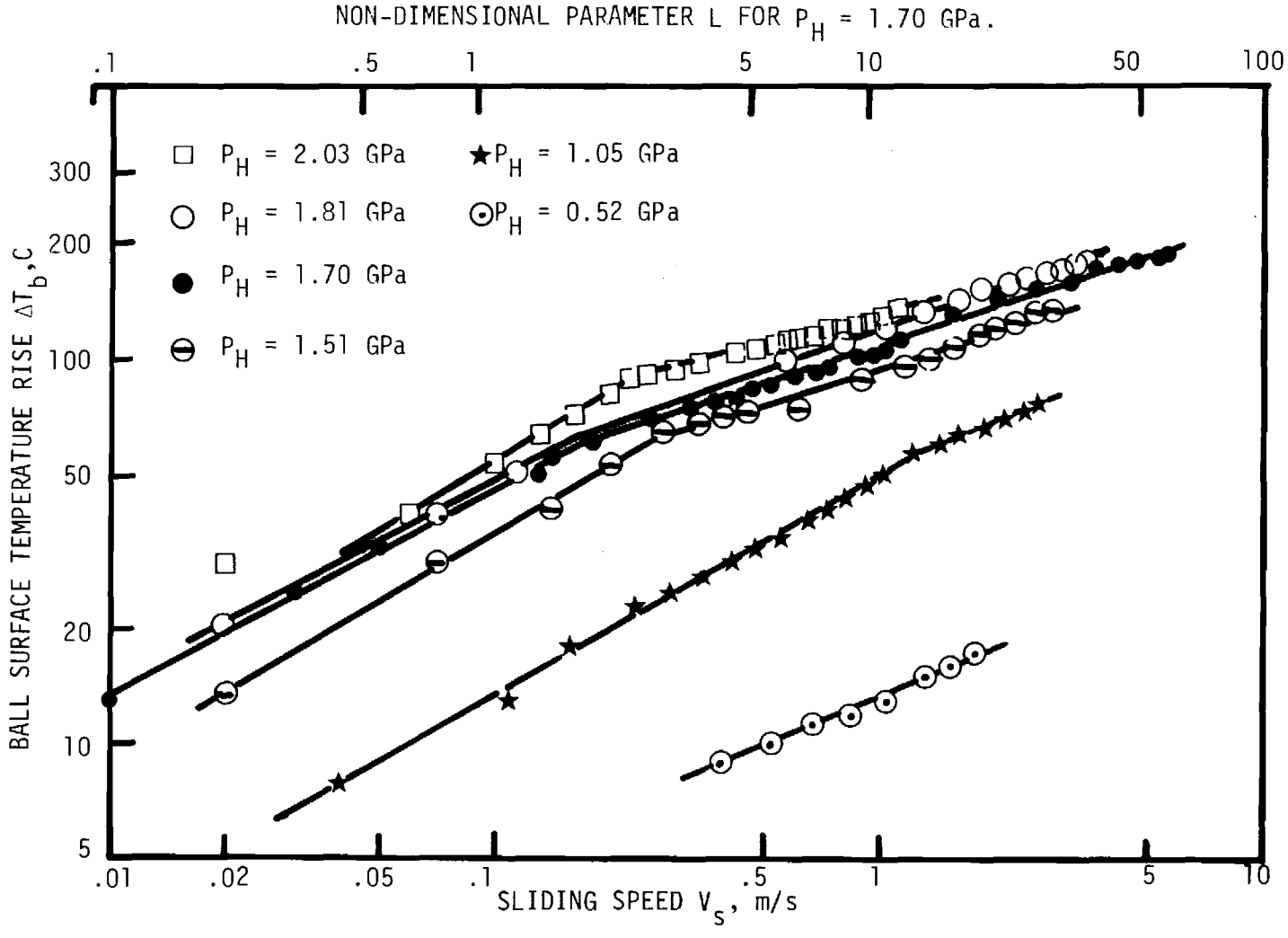

Figure III-3. Ball Surface Temperature Rise at Contact Center (.011 μm Ra roughness, $1 < \Lambda < 2$ for P_H = 2.03 GPa, otherwise $\Lambda > 2$).

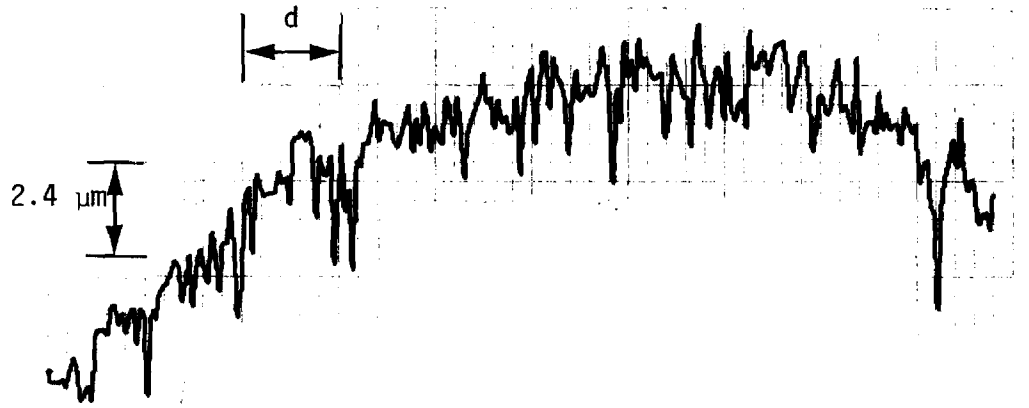

a) Unused ball surface (.38 μm Ra roughness).

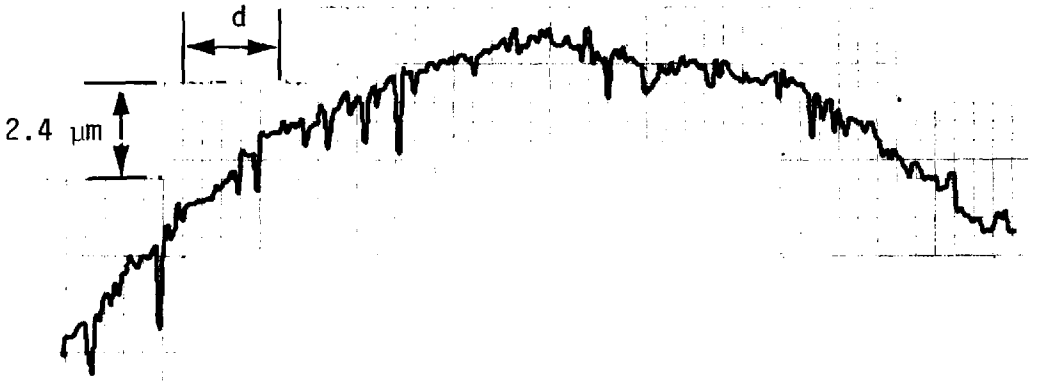

b) Ball surface after running 24 minutes (.25 μm Ra roughness).

Figure III-4. Surface Profiles in Direction of Sliding (P_H = 1.24 GN/m^2, V_s = 1.02 m/s, Hertz Diameter d = 0.43 mm, pure sliding).

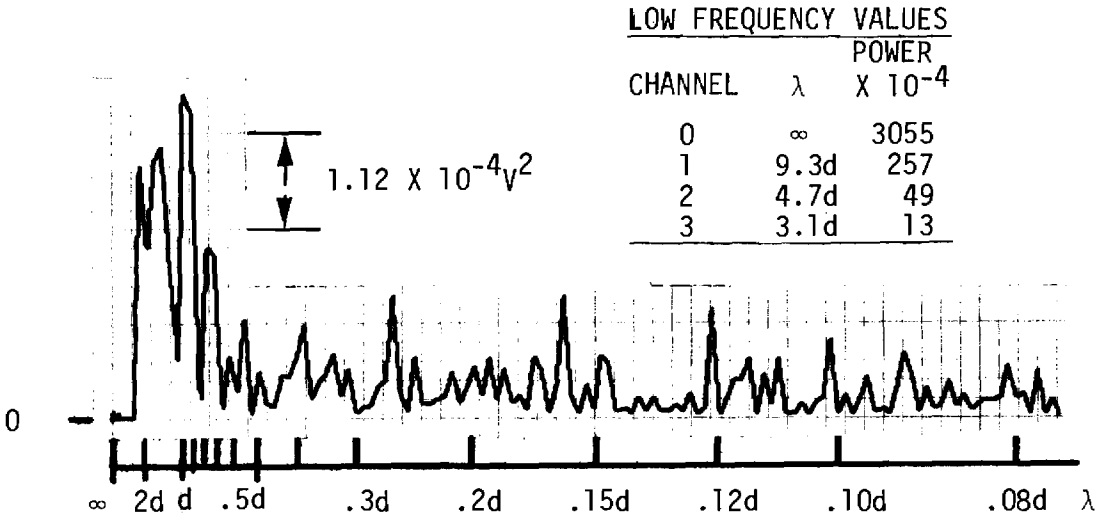

a) Unused ball surface.

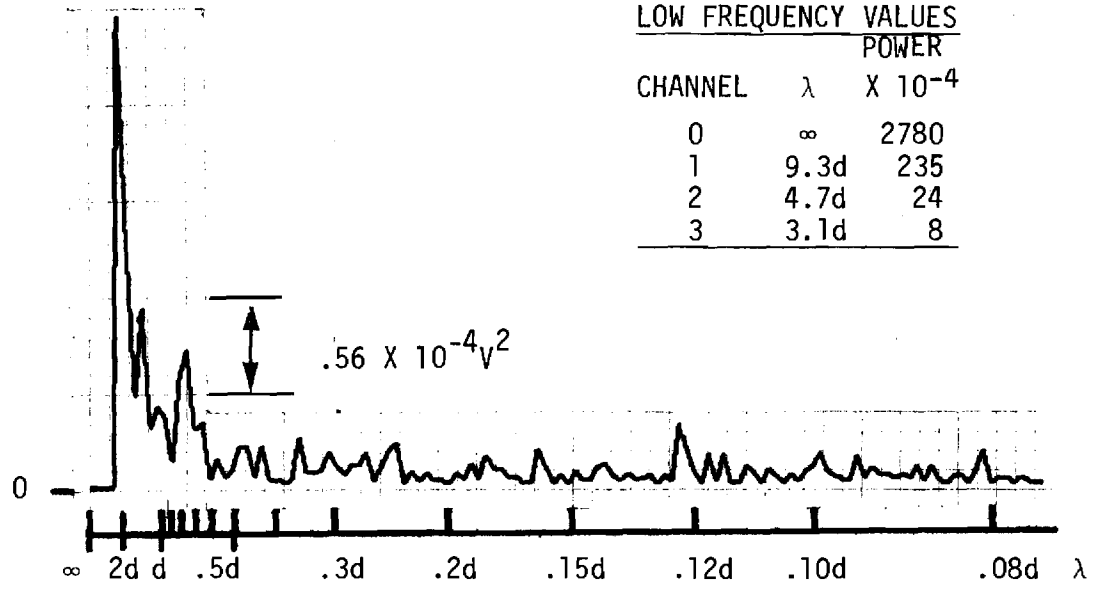

b) Ball surface after running 24 minutes.

Figure III-5. Power Spectra of the Surface Profiles (P_H = 1.24 GN/m^2, V_s = 1.02 m/s, Hertz diameter d = 0.43 mm, pure sliding.)

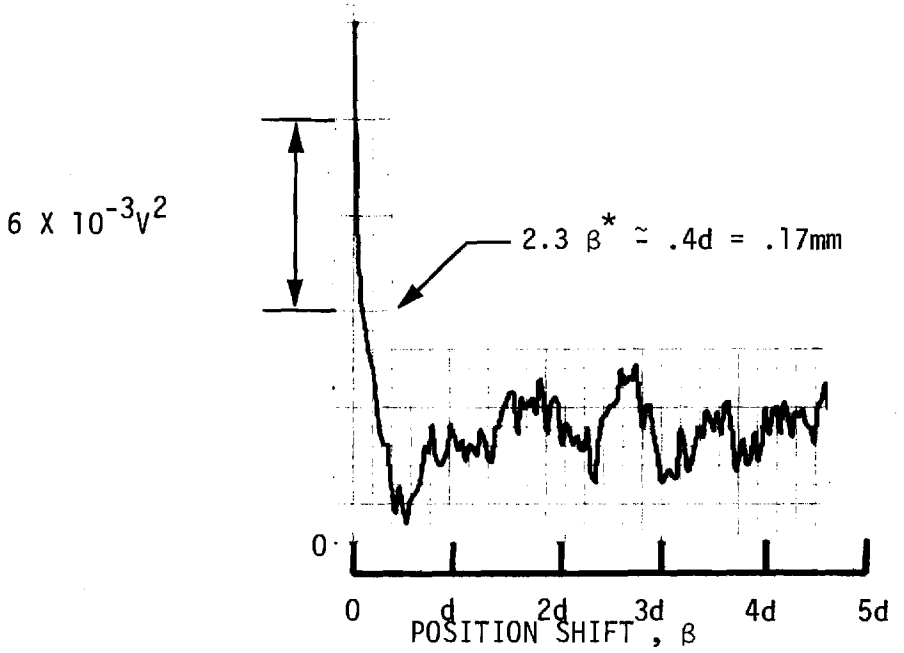

a) Unused ball surface (.38 μm Ra roughness).

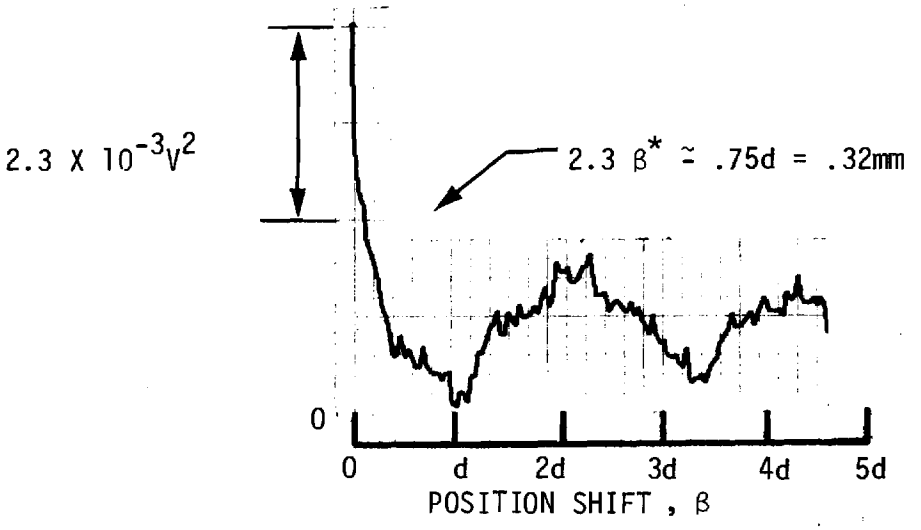

b) Ball surface after running 24 minutes.

Figure III-6. Autocorrelation Functions of the Surface Profiles. (λ > 3d not included, P_H = 1.24 GN/m^2, V_S = 1.02 m/s, Hertz diameter d = 0.43 mm, pure sliding)

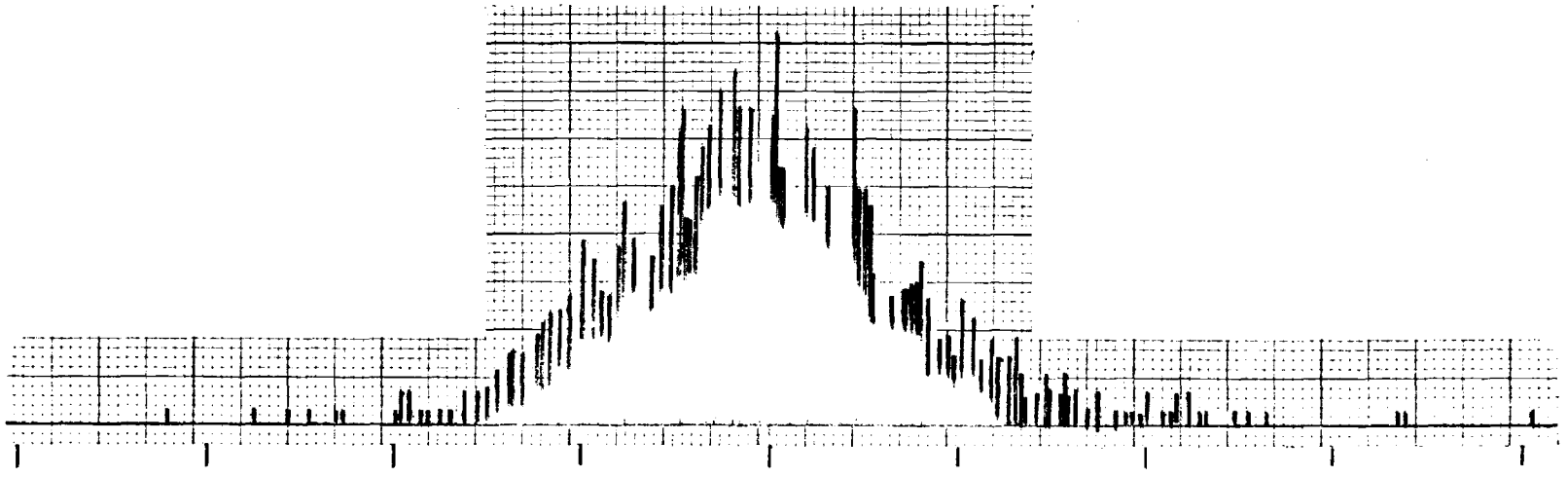

a) Initial Ball Surface Radiation Fluctuations.

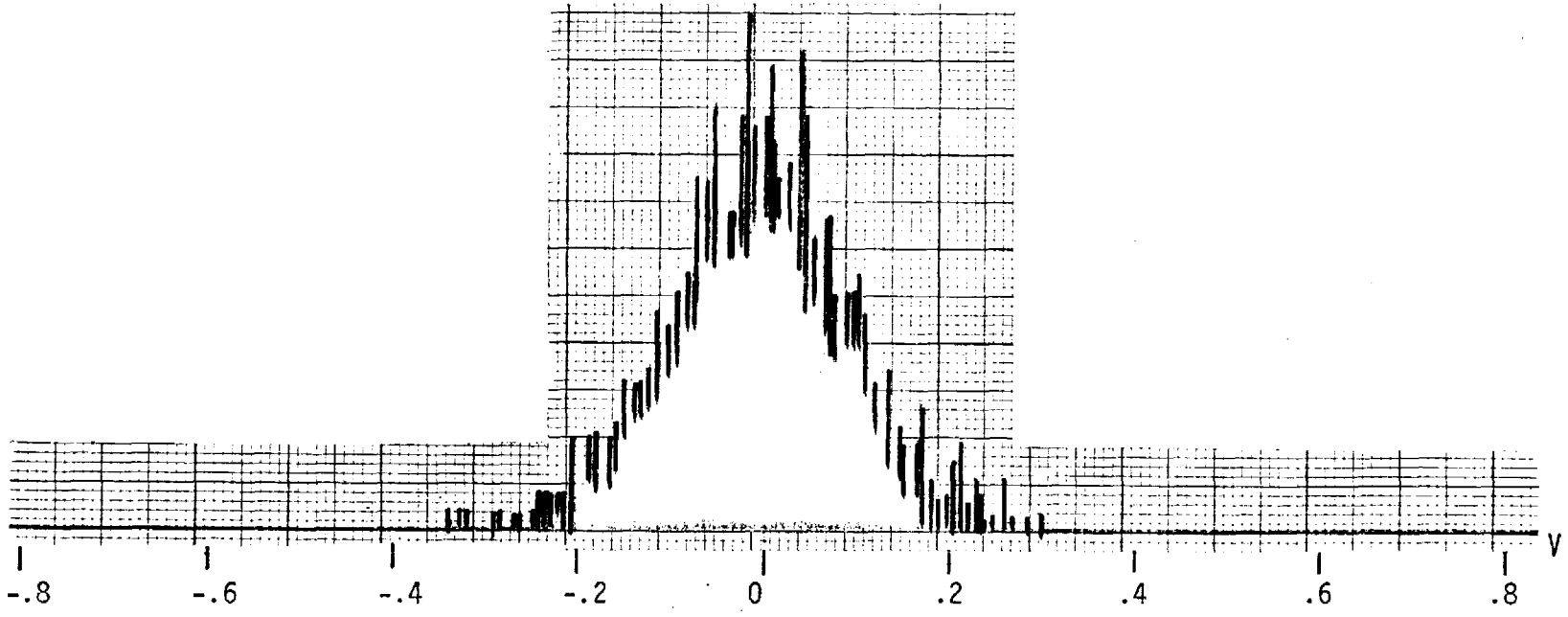

b) Ball Surface Radiation Fluctuations after Running 8 Minutes.

Figure III-7. Normalized Histograms of Ball Surface Radiation Fluctuations (.38 μm R_a initial roughness, P_H = 1.24 GN/m^2, V_s = 1.02 m/s, Hertz diameter d = 0.43 mm, pure sliding).

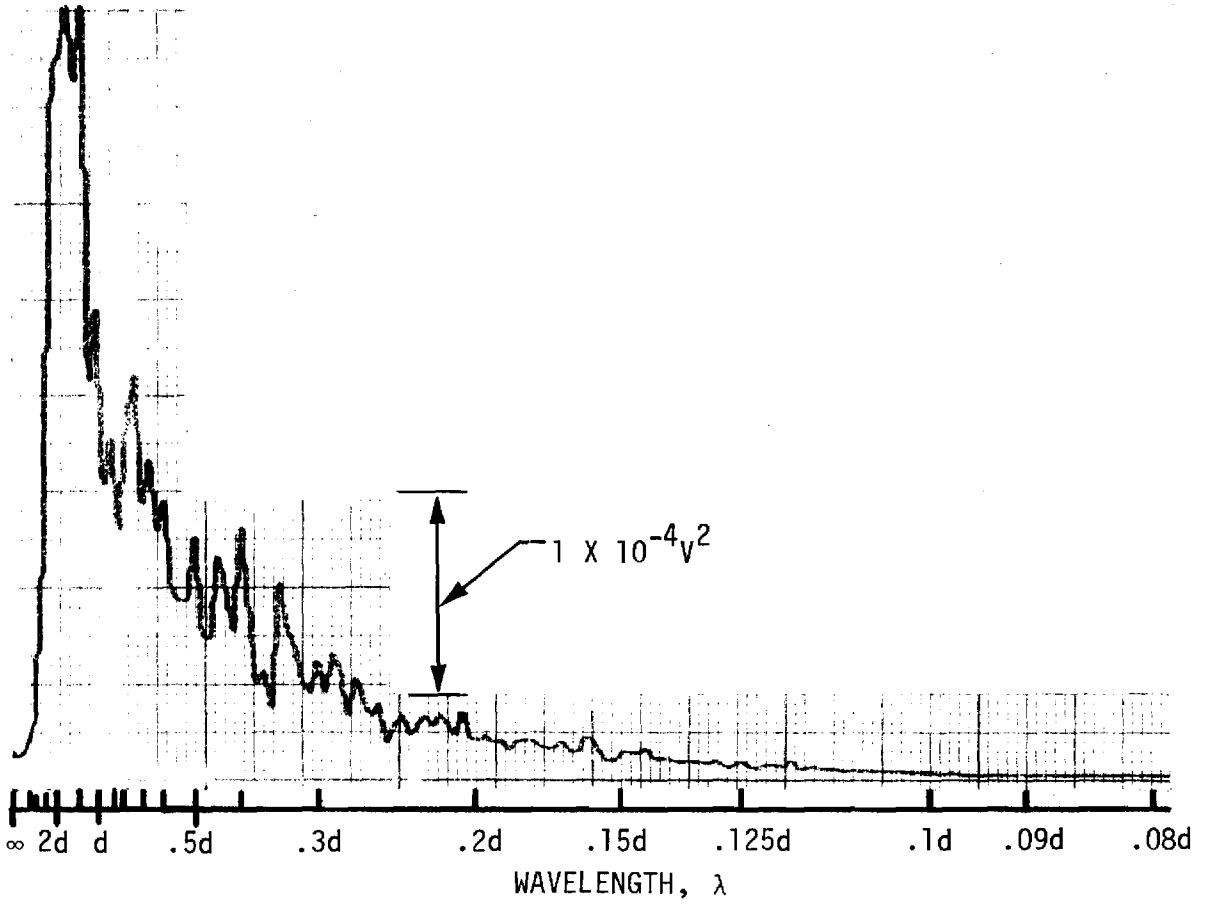

a) Ball Surface Temperature Fluctuations at Start of Run-in.

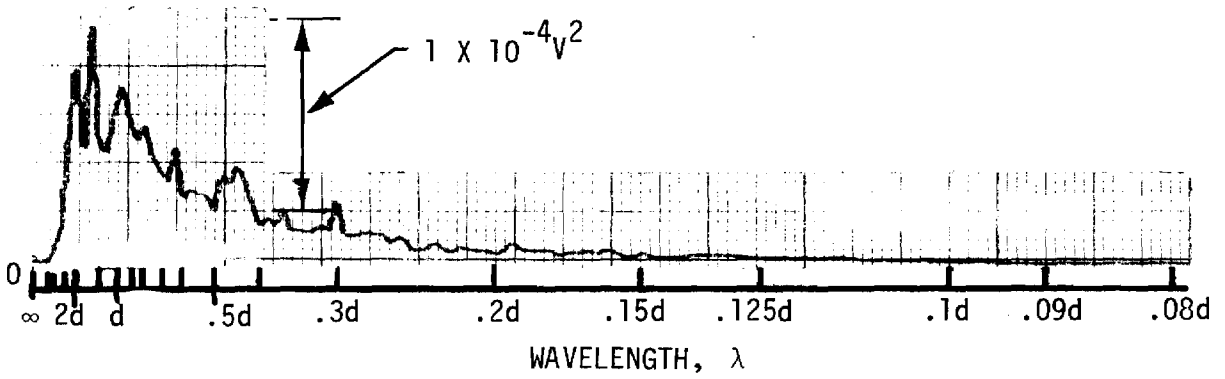

b) Ball Surface Temperature Fluctuations after 8 Minutes Run-in.

Figure III-8. Power Spectra of Ball Surface Temperature Fluctuations (.38 μm Ra initial roughness, P_H = 1.24 GN/m^2, V_s = 1.02 m/s, Hertz diameter = 0.43 mm, pure sliding).

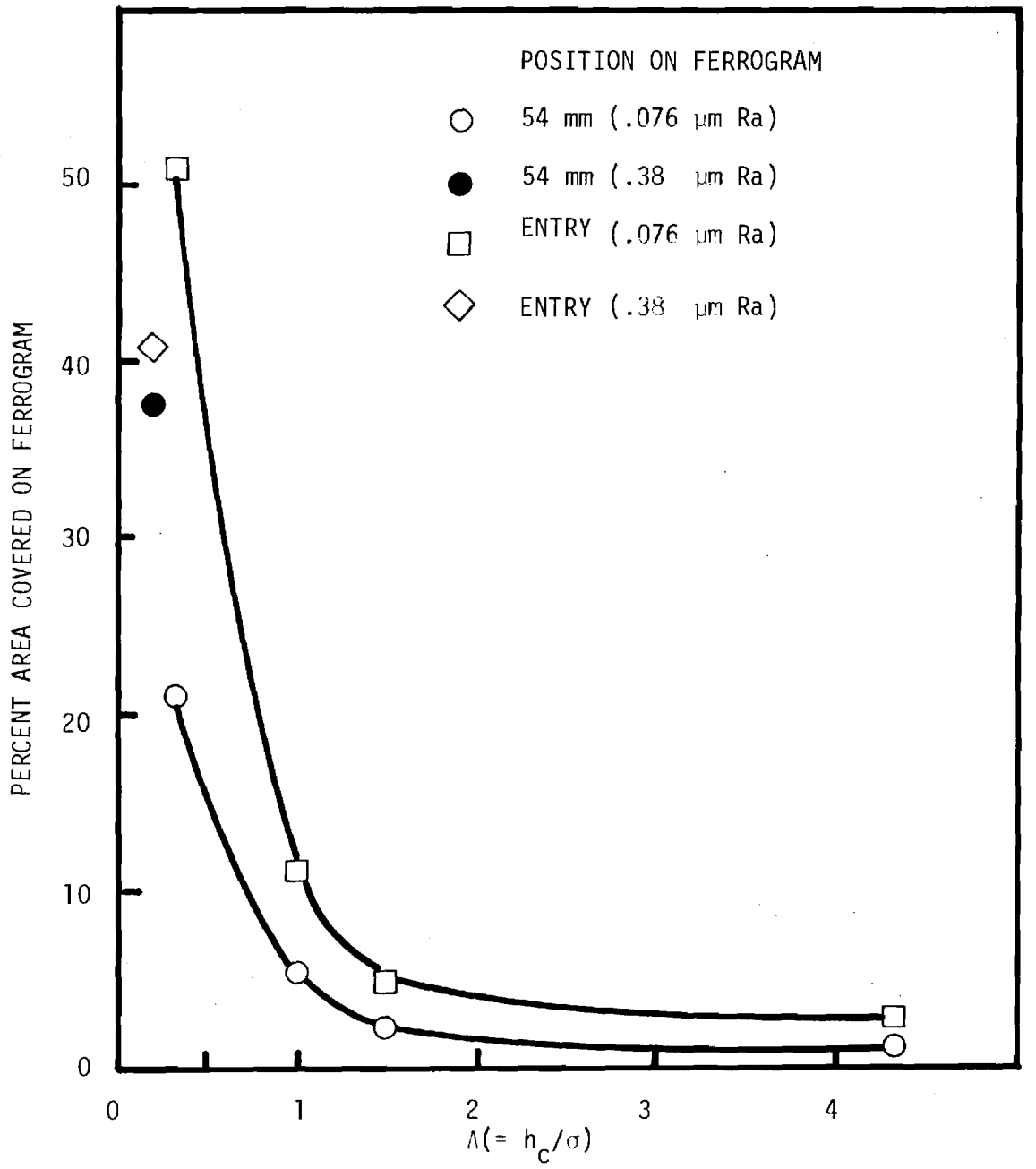

Figure III-9. Debris Concentration Dependence on Λ.

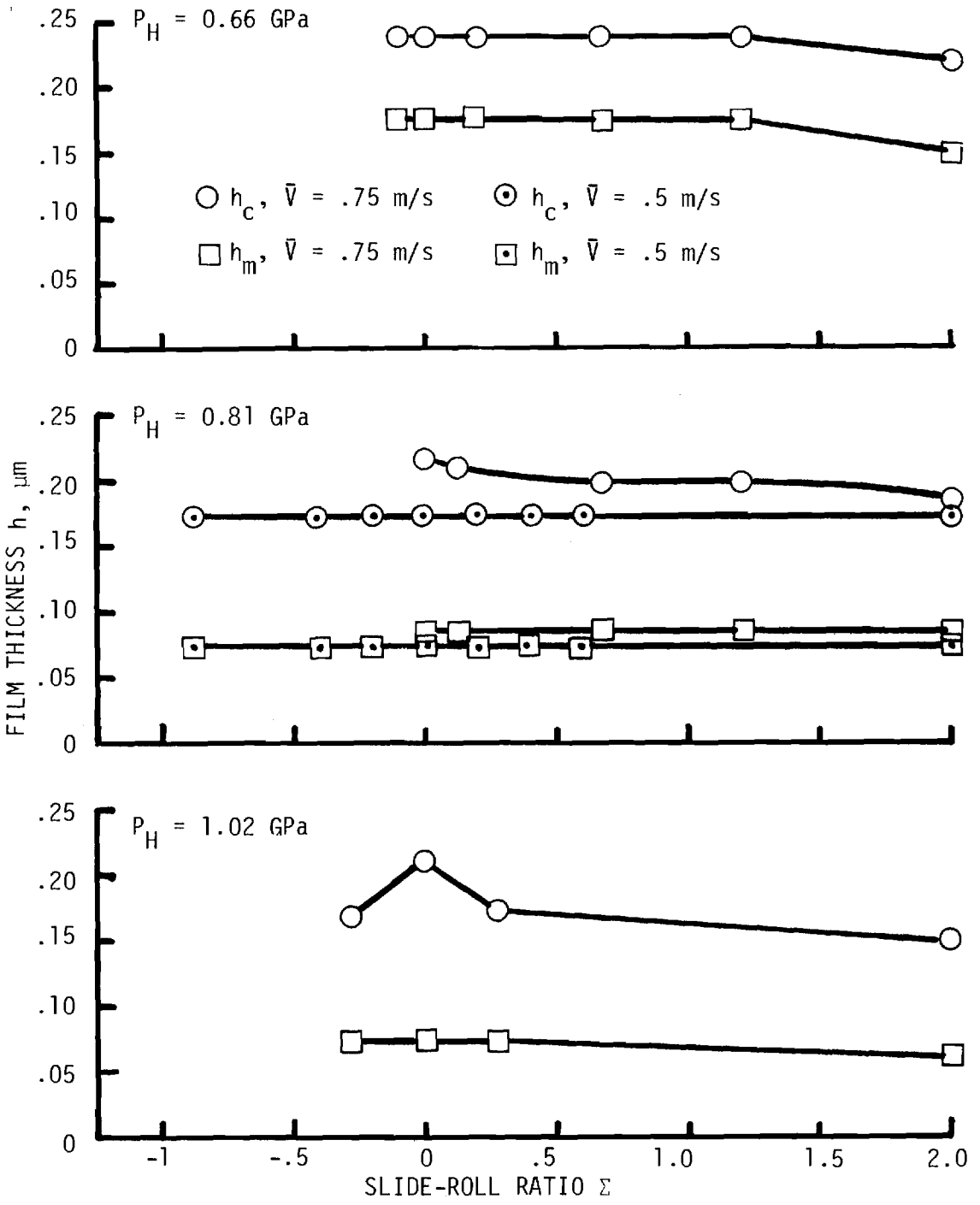

Figure III-10. Film Thickness as a Function of Slide-Roll Ratio (.011 μm Ra roughness).

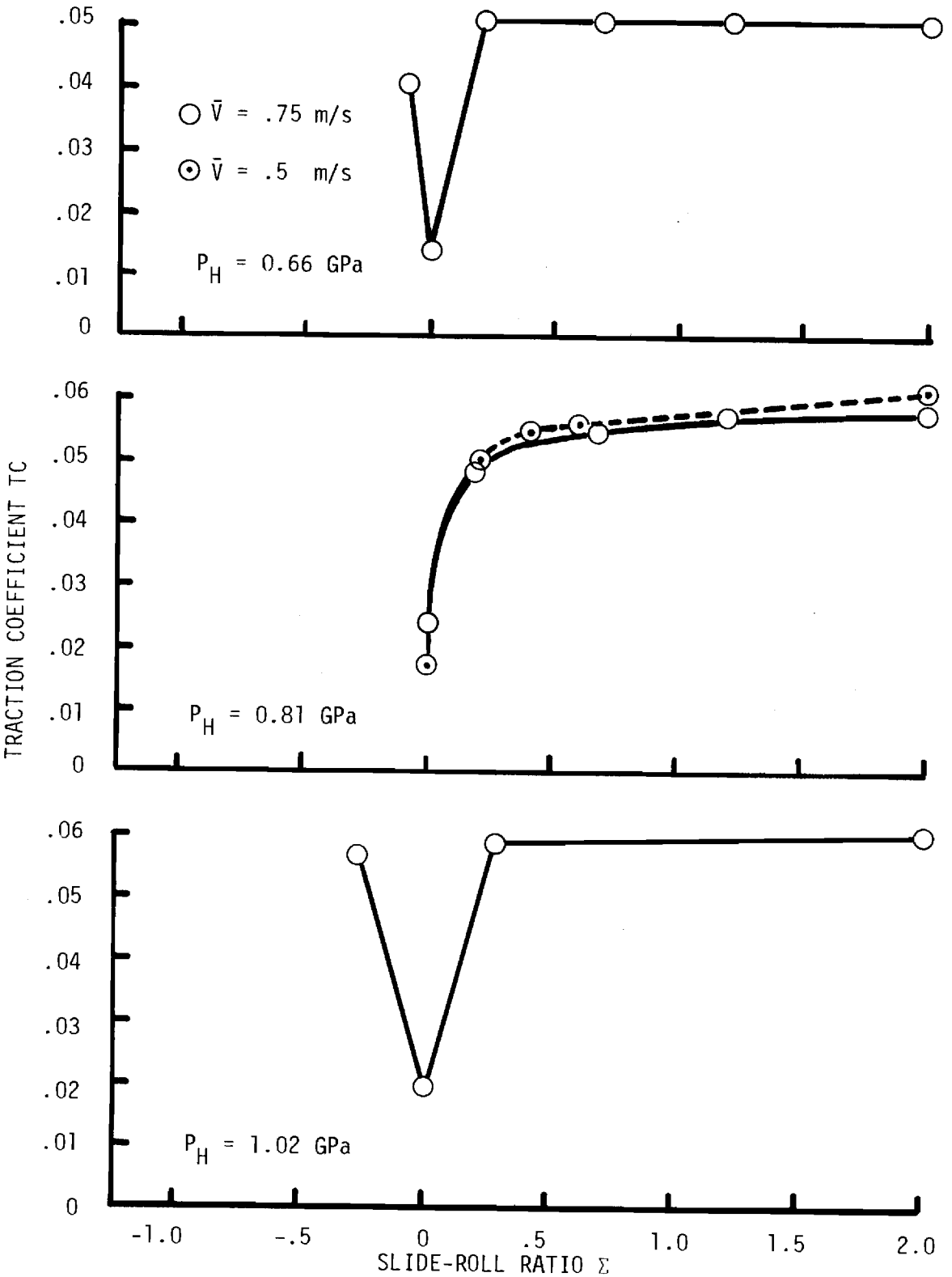

Figure III-11. Traction Coefficient as a Function of Slide-Roll Ratio (.011 μm Ra roughness).

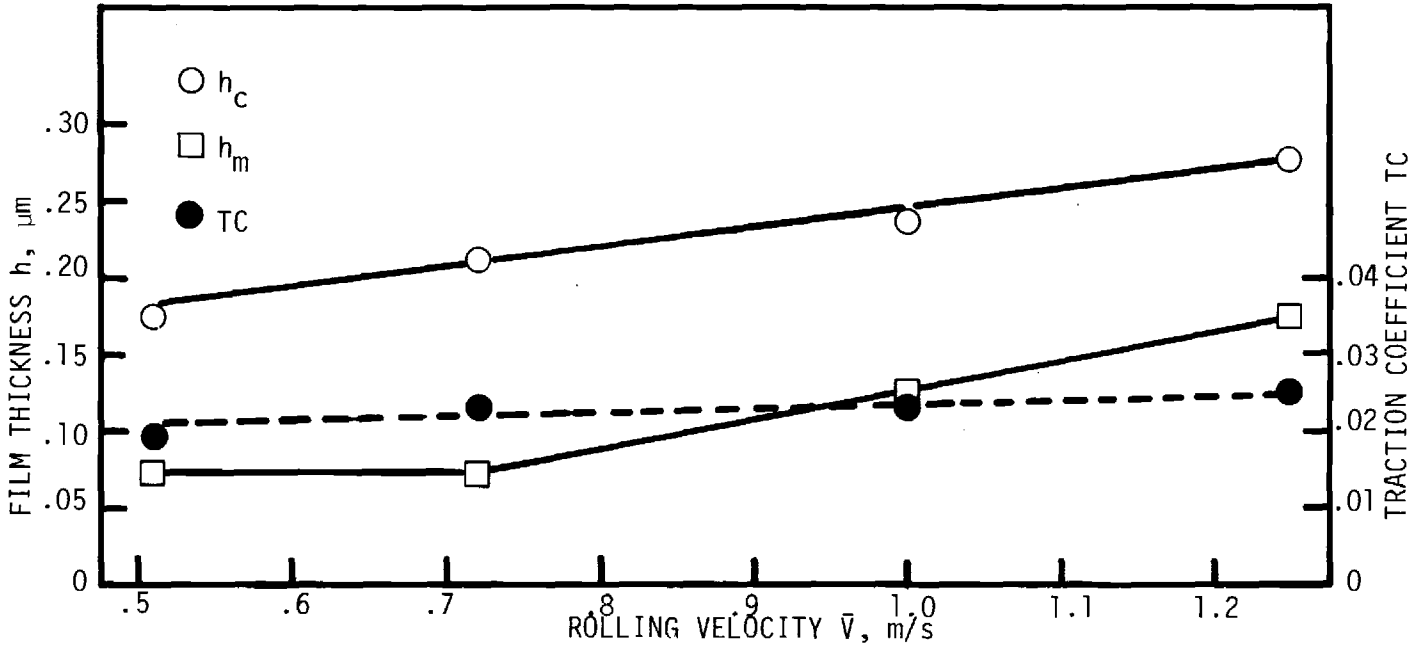

Figure III-12. Film Thickness and Traction Coefficient as a Function of Rolling Velocity (Σ = 0, .011 μm Ra Roughness, P_H = 1.02 GPa).

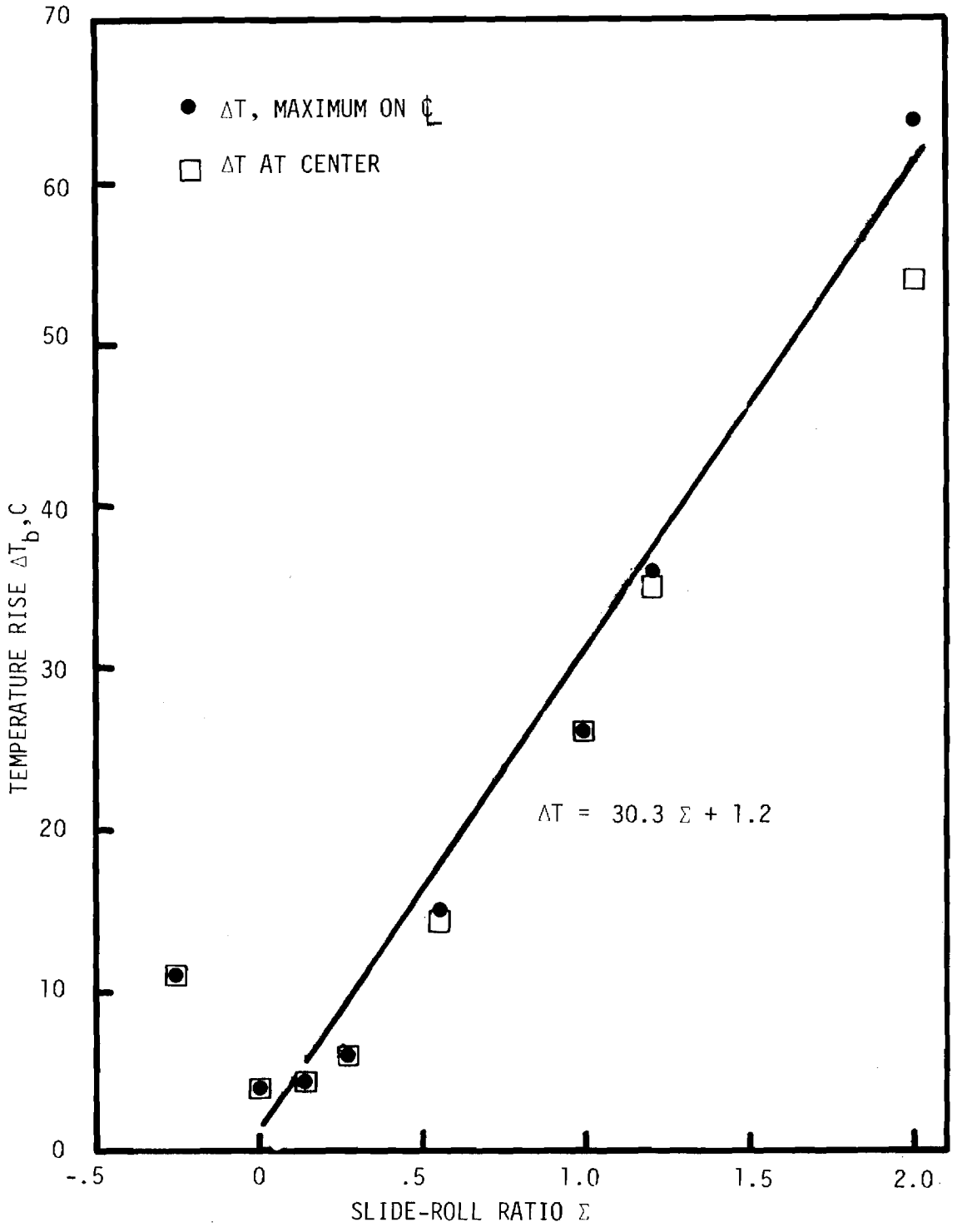

Figure III-13. Ball Surface Temperature Rise as a Function of Slide-Roll Ratio (.011 μm Ra Roughness, P_H = 1.02 GPa, $\bar{V}$ = 0.75 m/s).

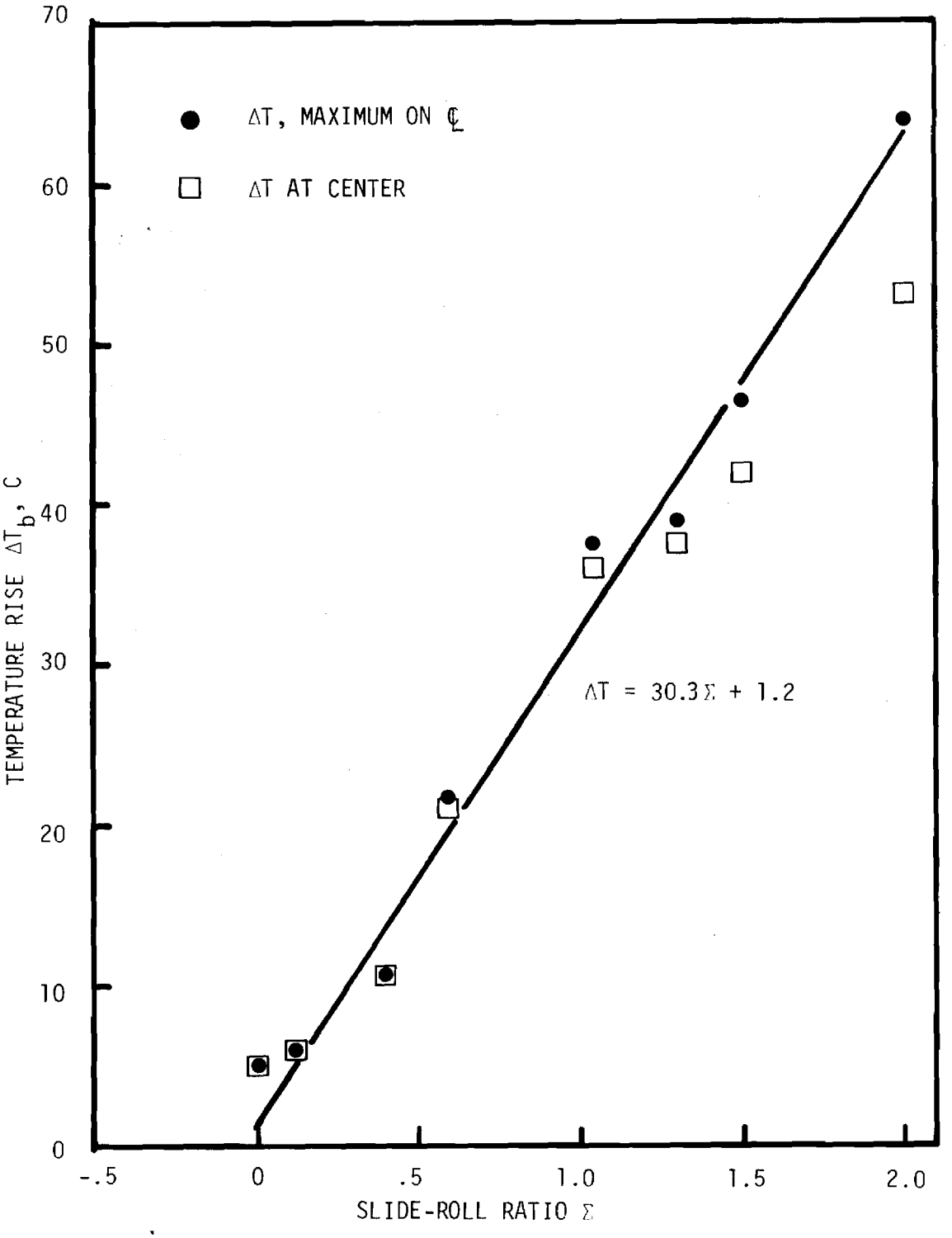

Figure III-14. Ball Surface Temperature Rise as a Function of Slide-Roll Ratio (.011 μm Ra Roughness, P_H = 1.02 GPa, $\bar{V}$ = 1.0 m/s).

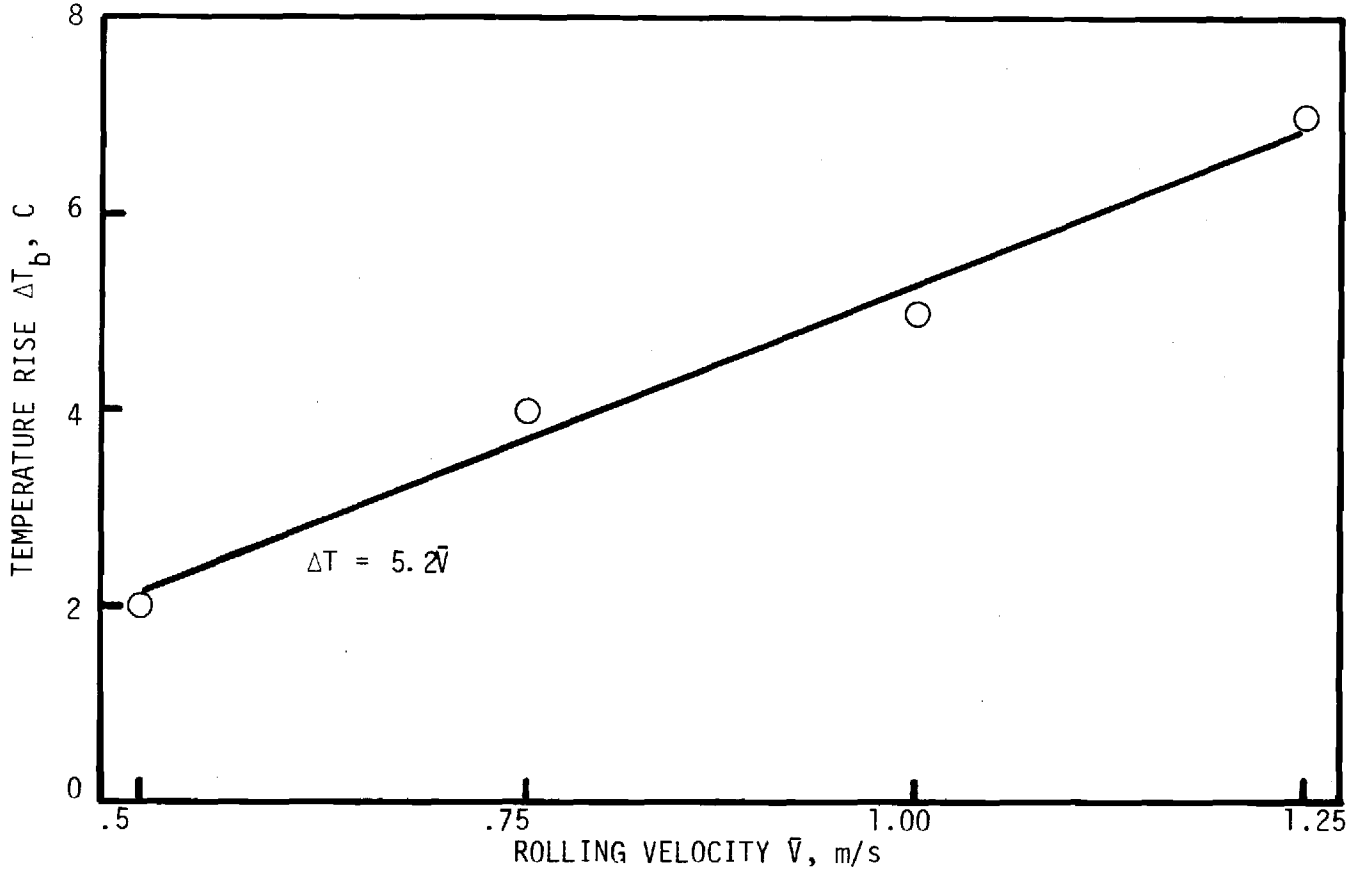

Figure III-15. Ball Surface Temperature Rise as a Function of Rolling Velocity (.011 μm Ra Roughness, P_H = 1.02 GPa, Σ = 0, Maximum ΔT_b Occurs at Contact Center).

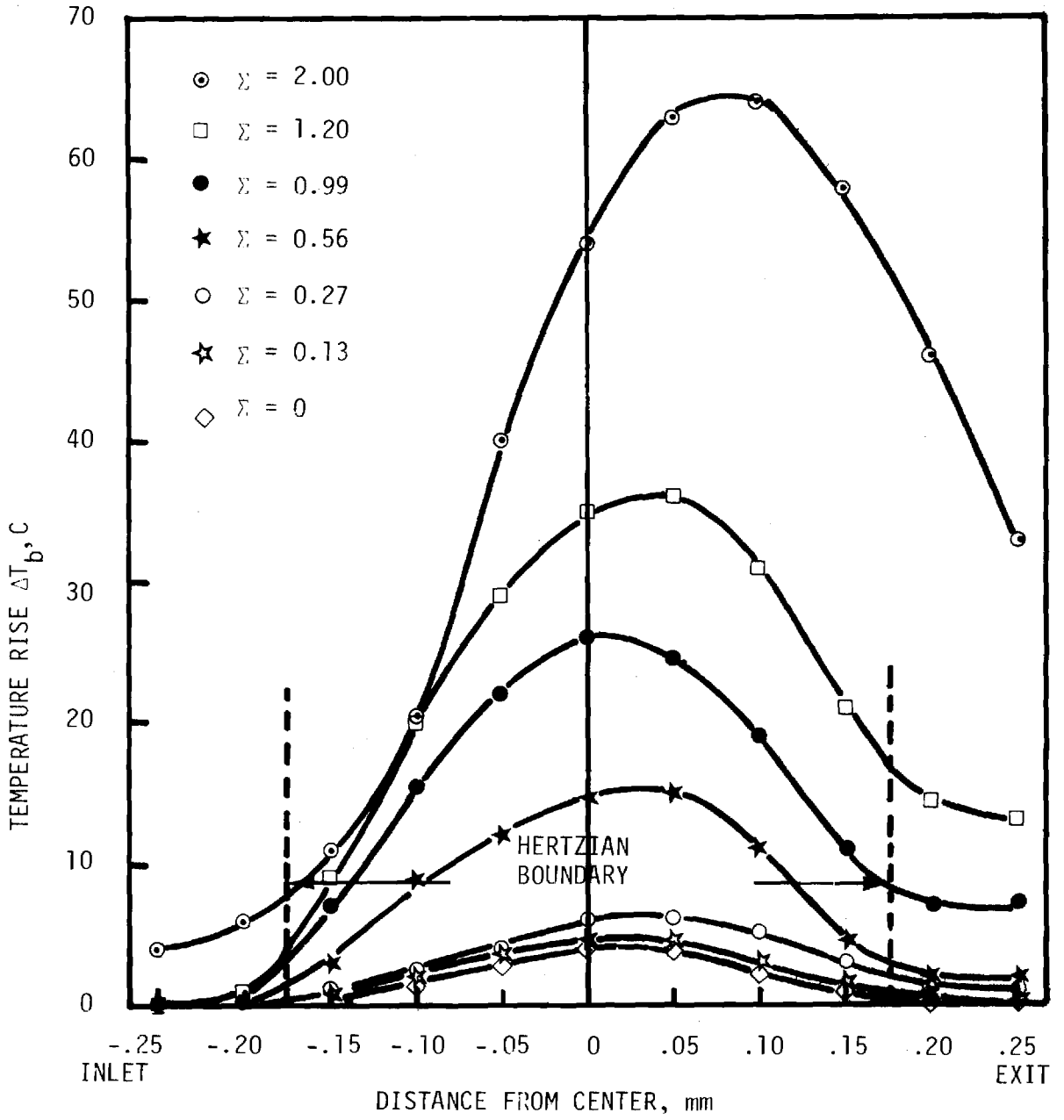

Figure III-16. Ball Surface Temperature Rise Along the Contact Centerline (.011 μm Ra Roughness, P_H = 1.02 GPa, $\bar{V}$ = .75 m/s).

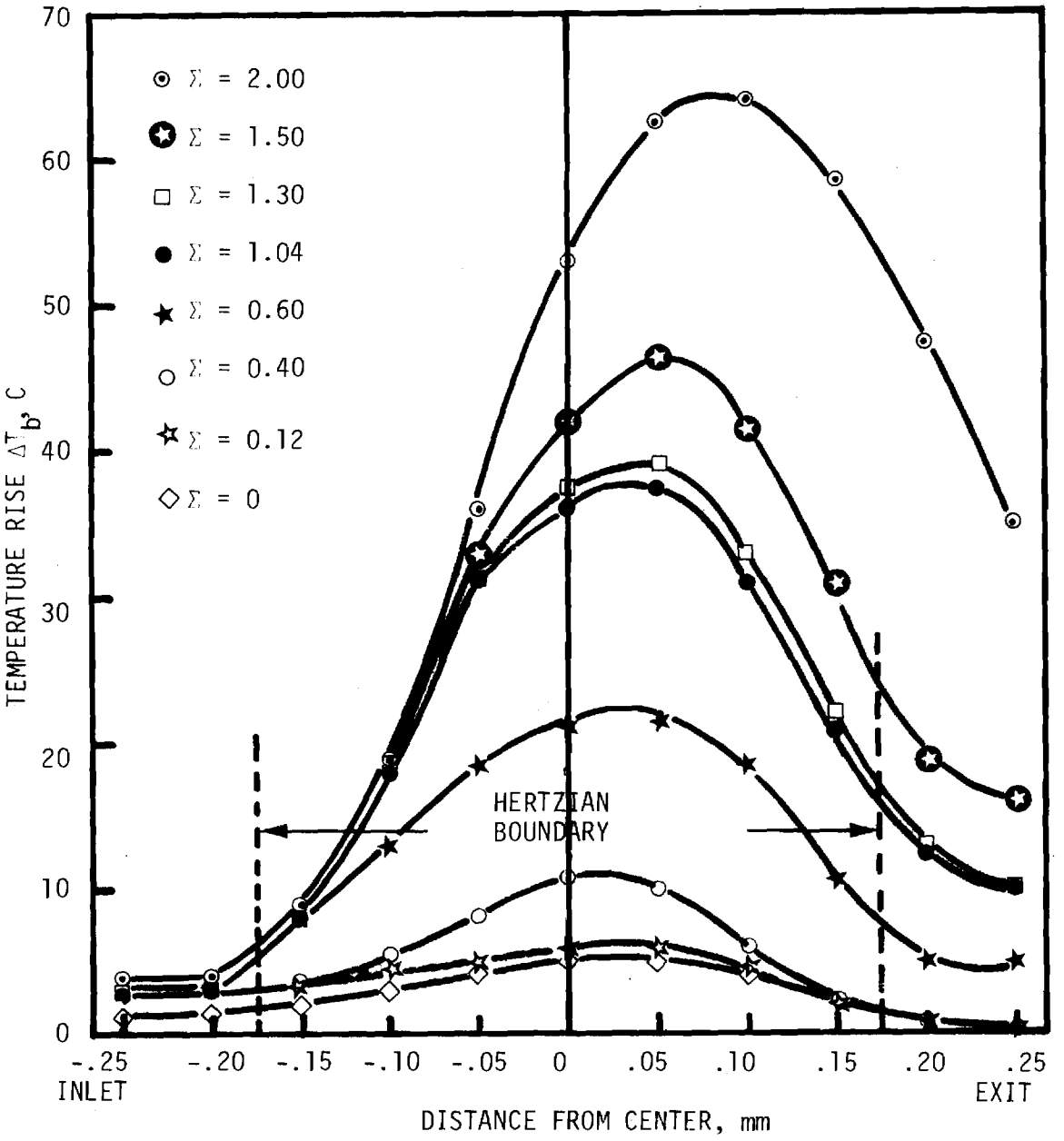

Figure III-17. Ball Surface Temperature Rise Along the Contact Centerline (.011 μm Ra Roughness, P_H = 1.02 GPa, $\bar{V}$ = 1.00 m/s).

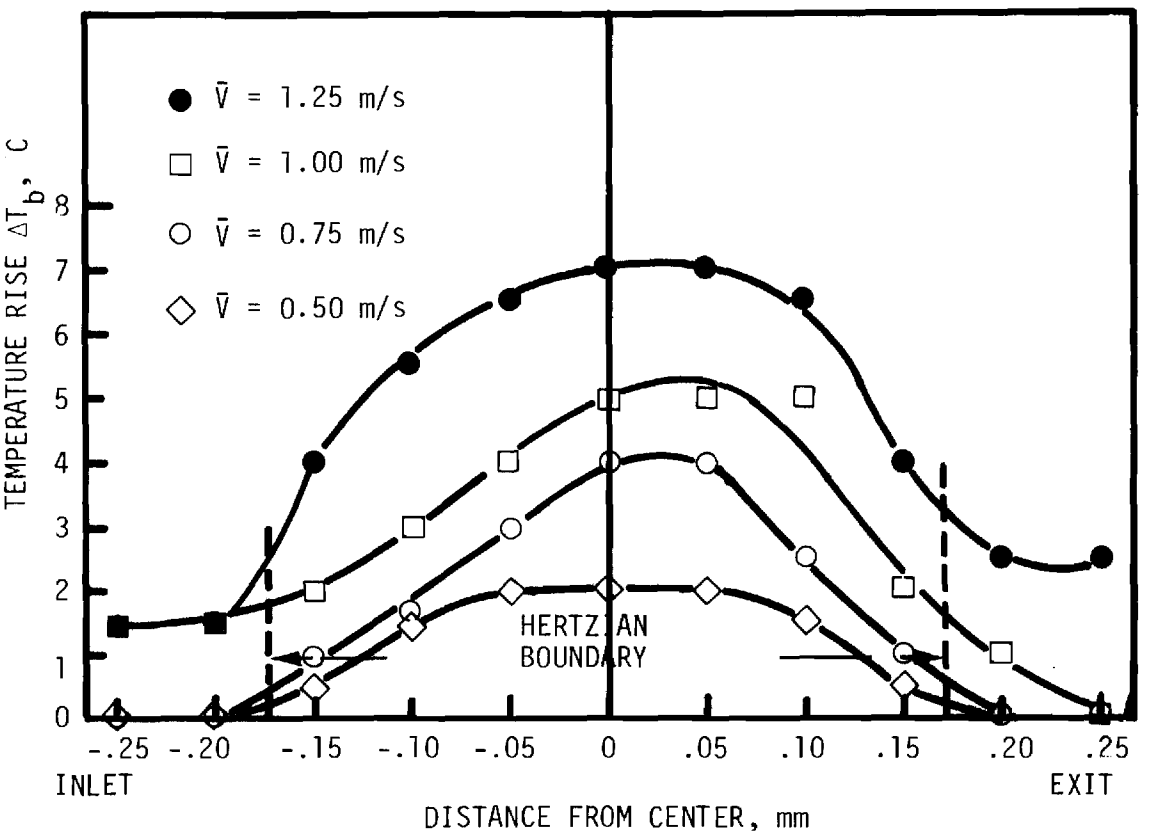

Figure III-18. Ball Surface Temperature Rise Along Contact Centerline (.011 μm Ra Roughness, P_H = 1.02 GPa, Σ = 0).

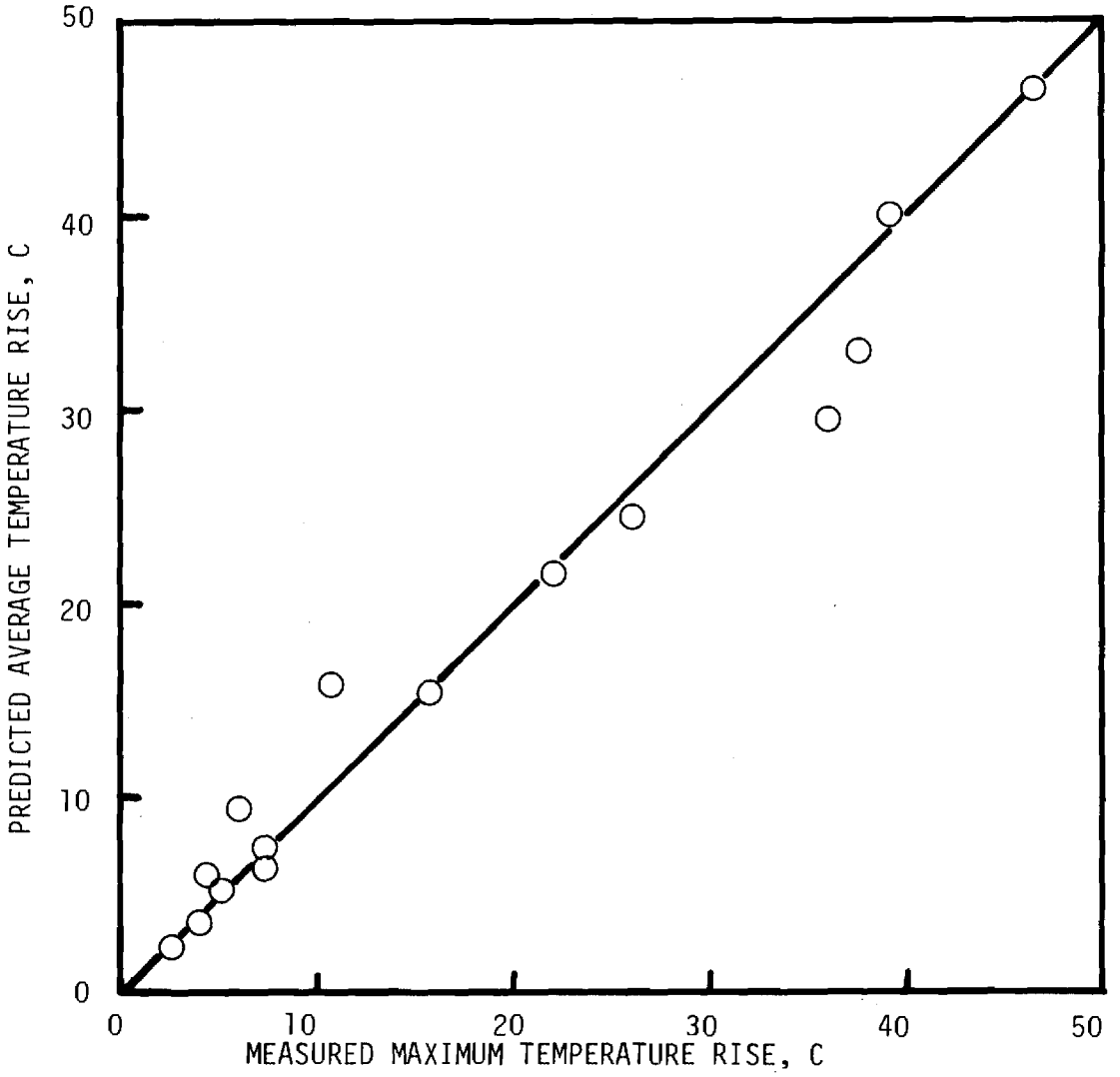

Figure III-19. Comparison of Predicted Average and Actual Maximum Ball Surface Temperature Rises for $L > 5$. Combined sliding and rolling as per Equation 21.

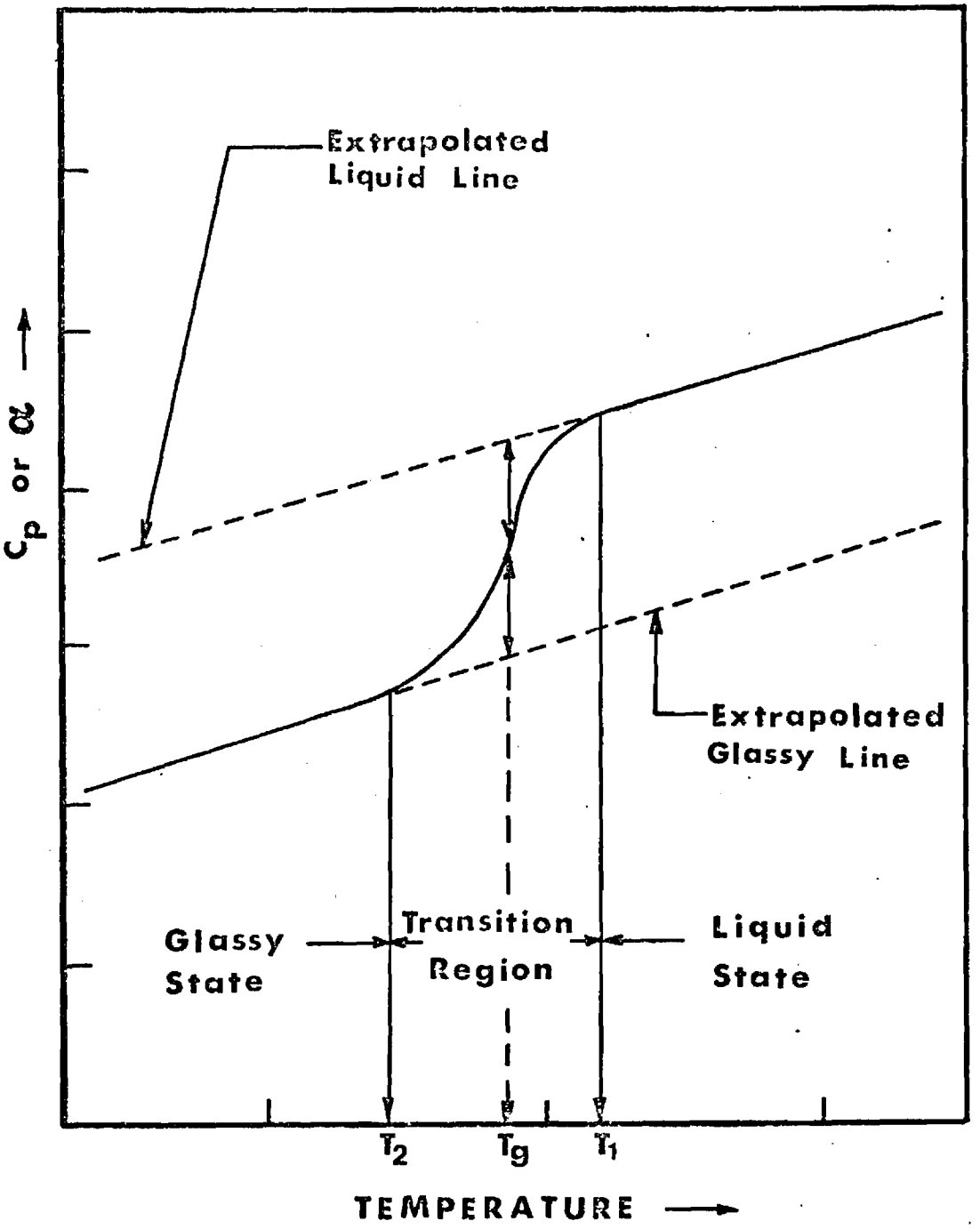

Figure IV-1. Thermal Expansion Coefficient or Specific Heat for a Typical Glassy Material.

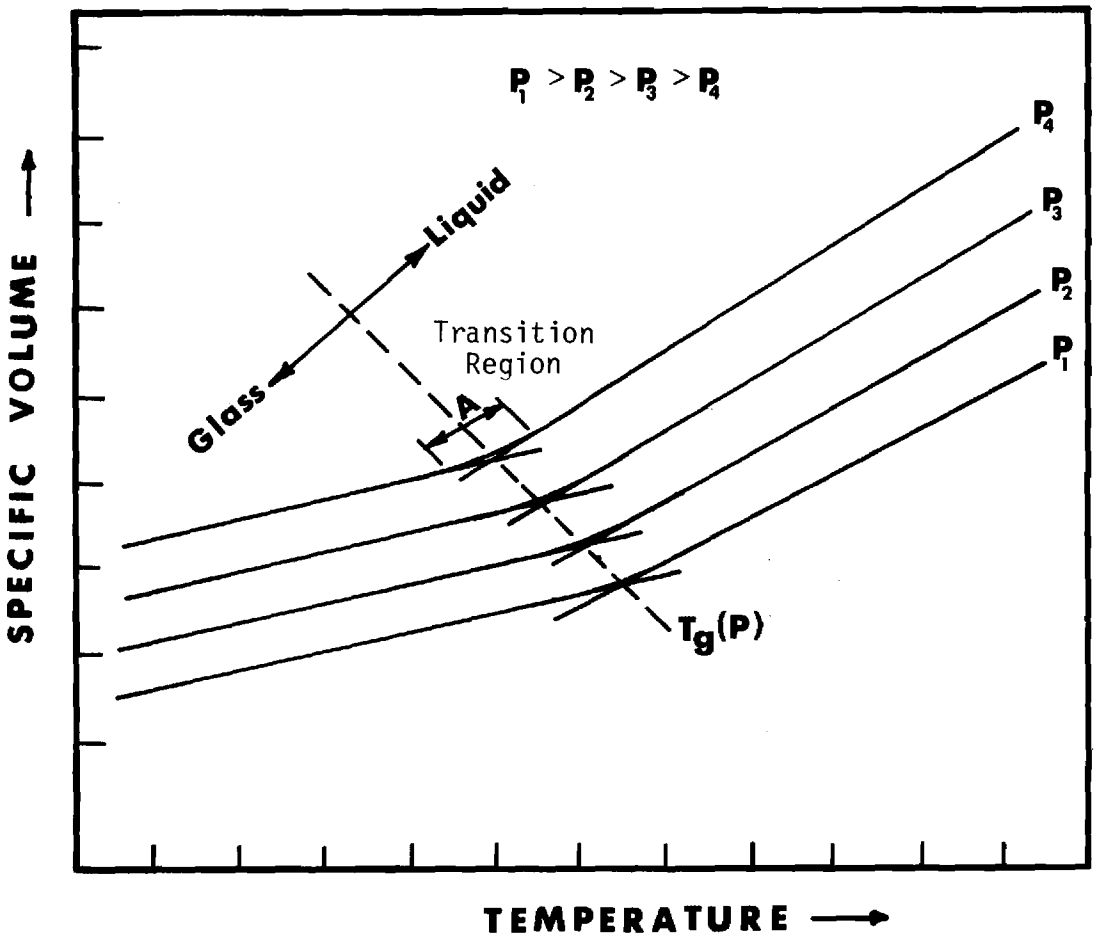

Figure IV-2. Typical Plot of Specific Volume Versus Temperature for a Glassy Material at Different Formation Pressures.

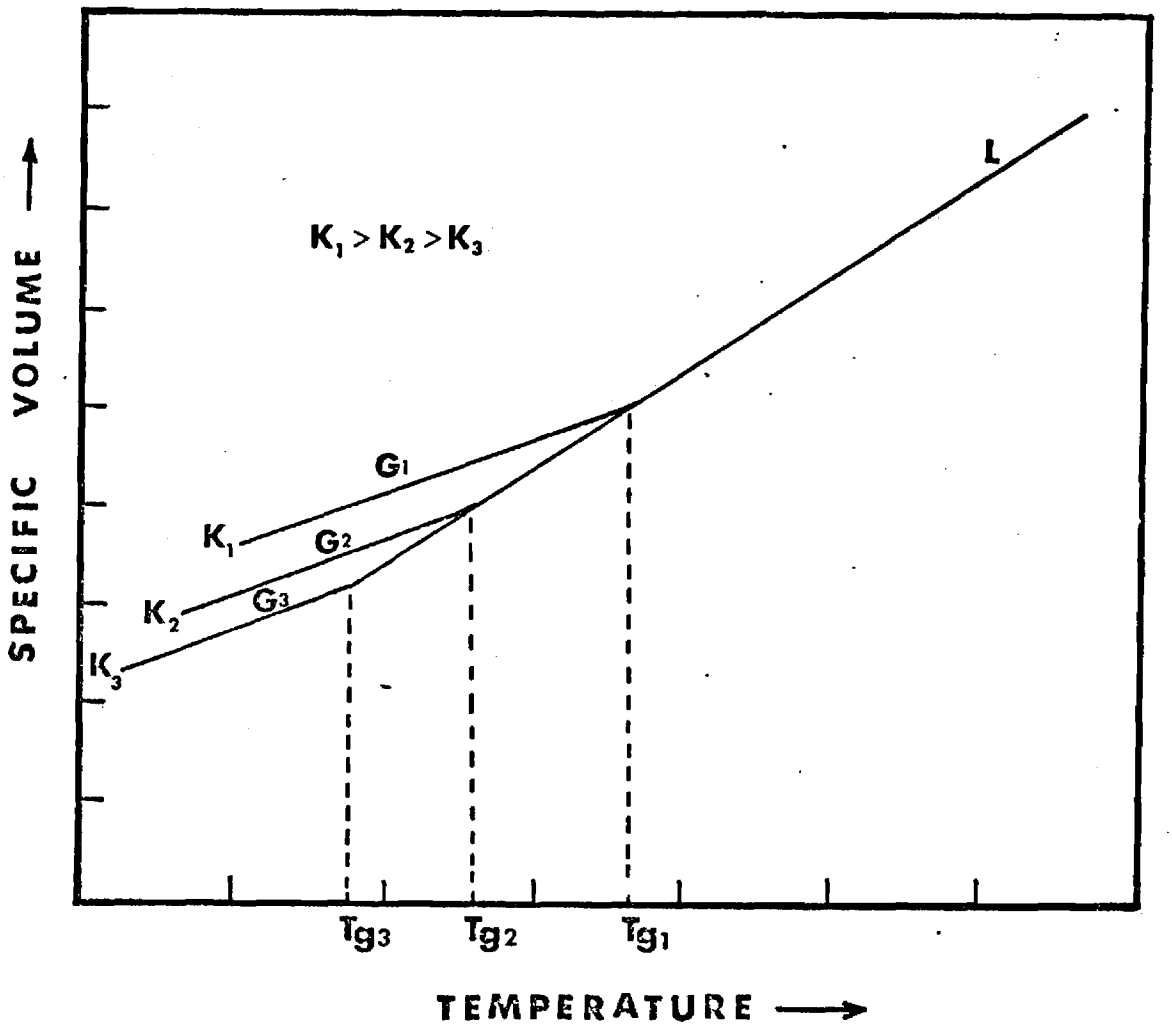

Figure IV-3. Dependence of the Glass Transition Temperature on the Cooling Rate, K_i. L = Liquid and G = Glass.

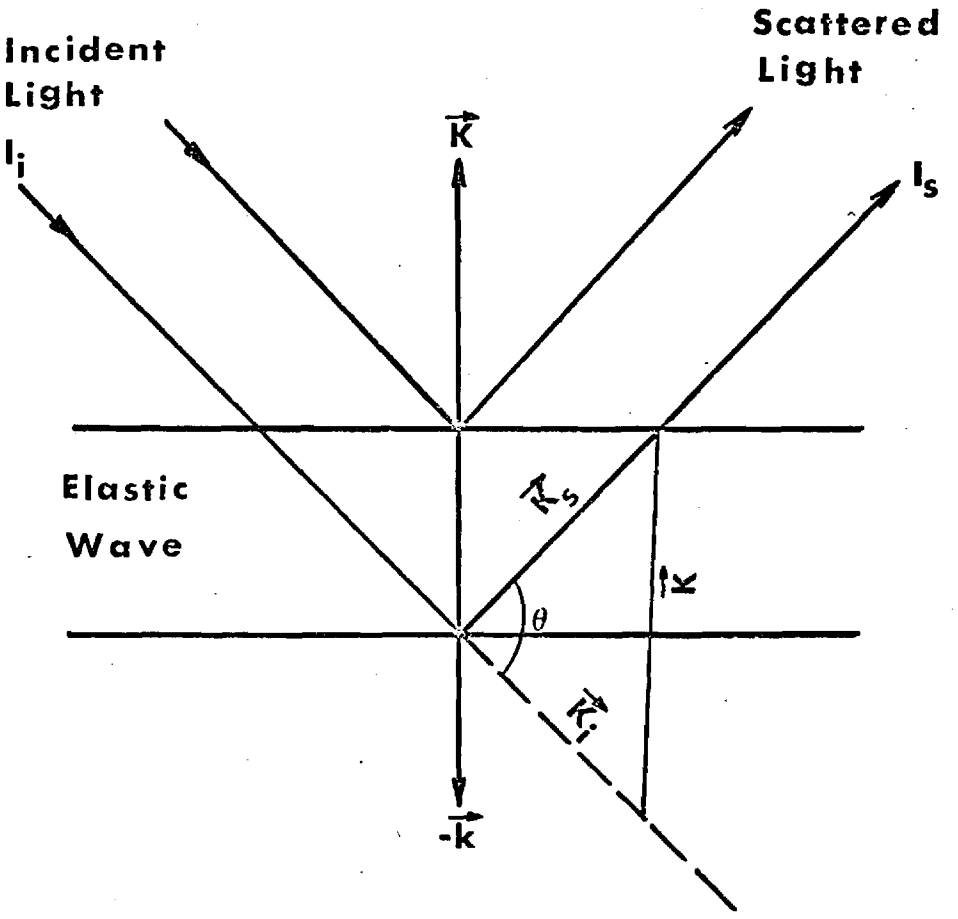

Figure IV-4. Bragg Condition of Light Scattered at an Angle θ Relative to the Incident Light Beam.

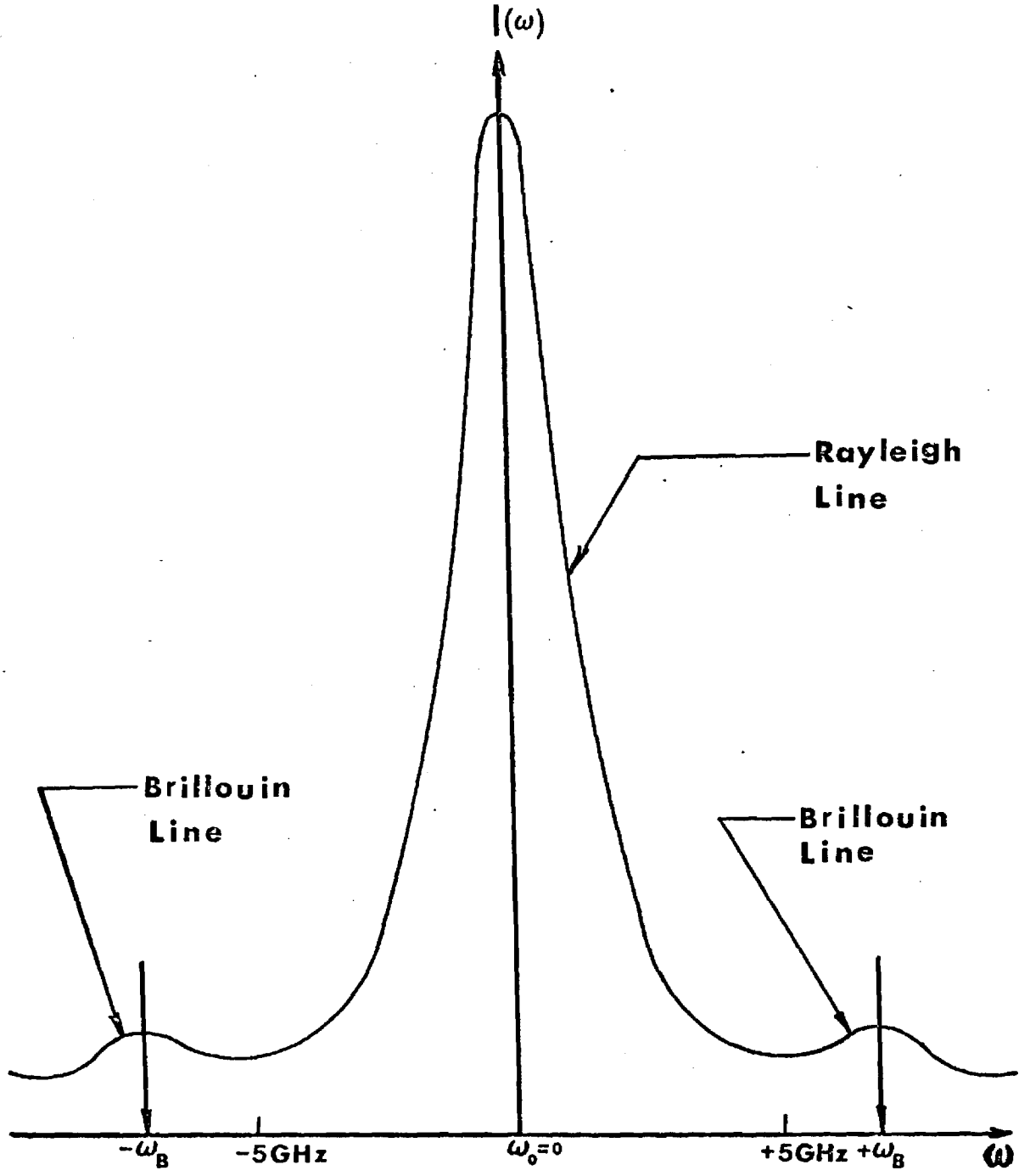

Figure IV-5. Frequency Spectrum of a Naphthenic Base Oil at 24.4C and Atmospheric Pressure.

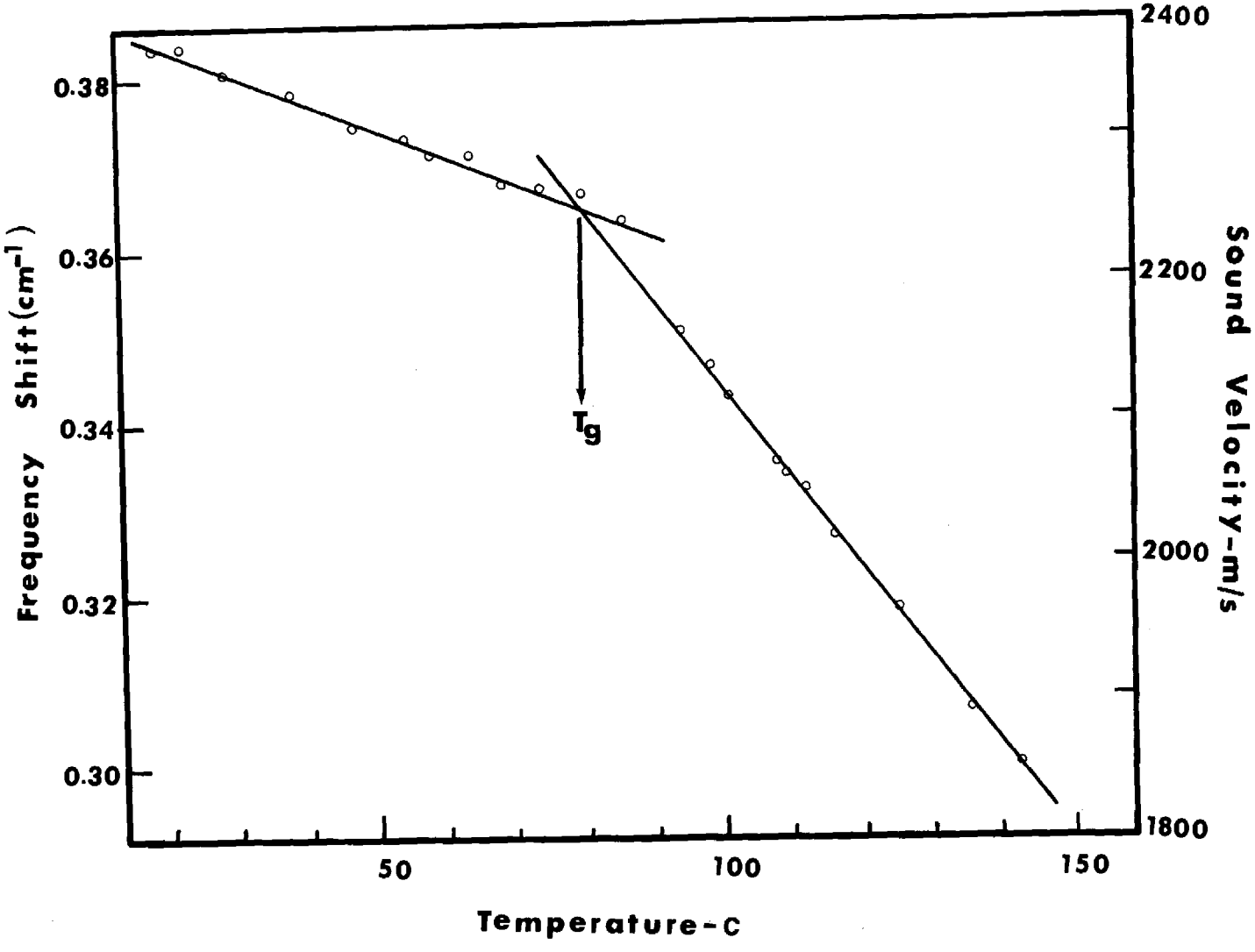

Figure IV-6. The Variation of the Brillouin Frequency Shift and the Sound Velocity with Temperature at Atmospheric Pressure for Atactic Polystyrene [53].

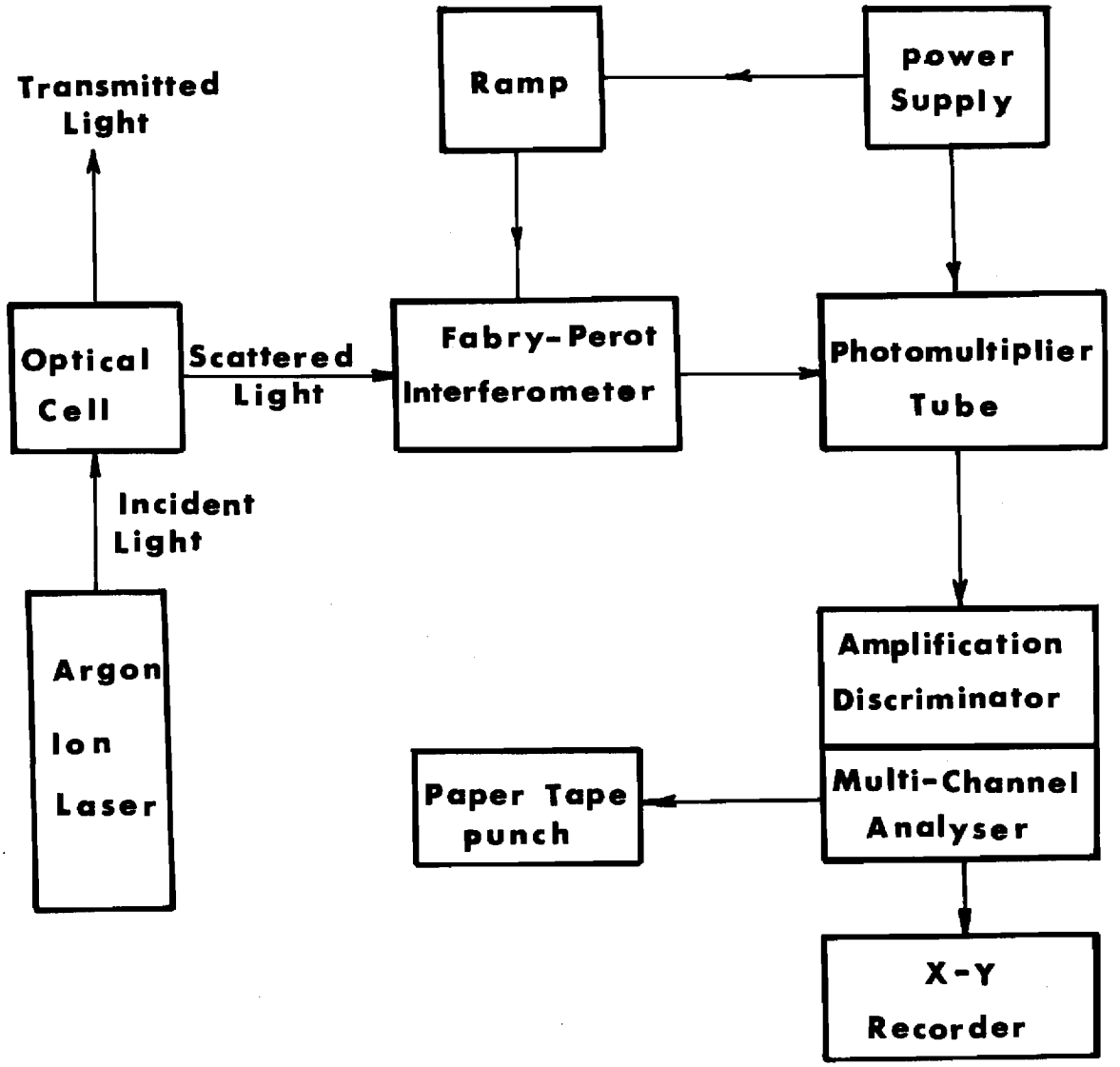

Figure IV-7. Schematic Arrangement of the Light-Scattering Experiment.

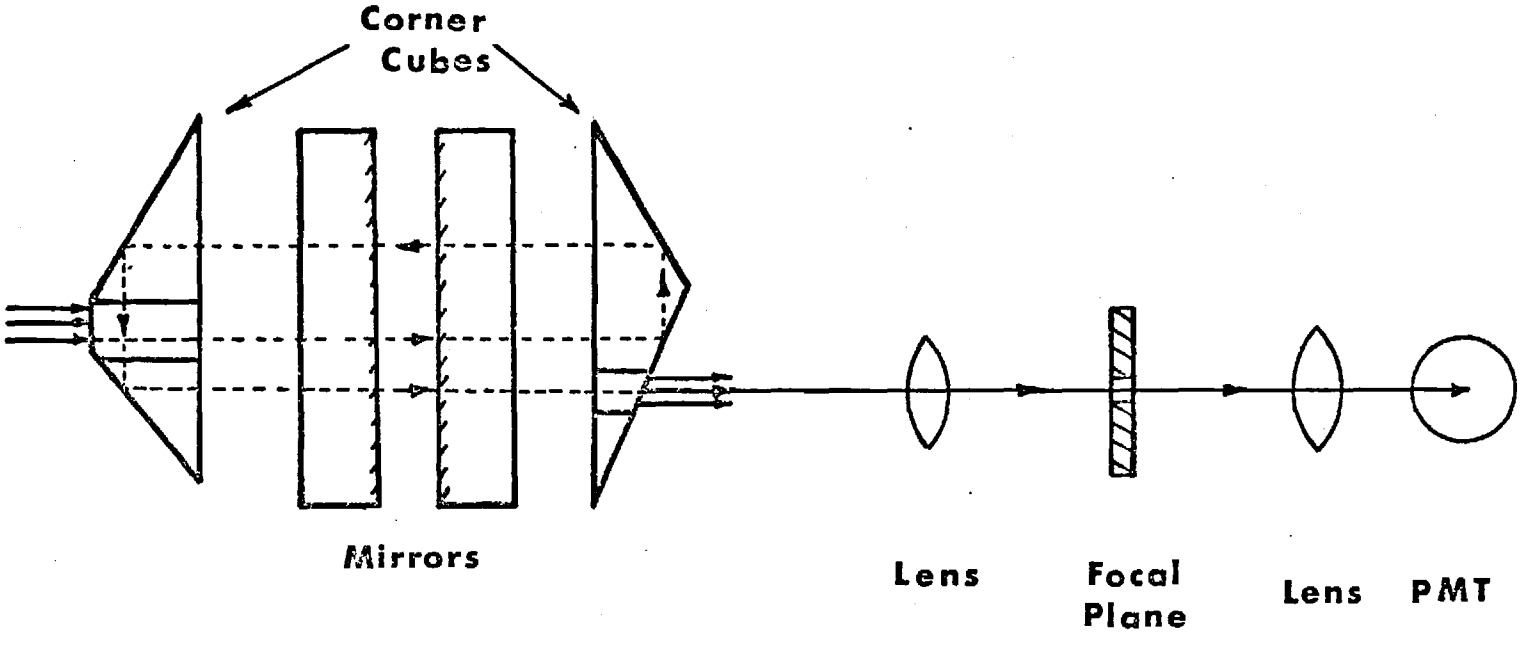

Figure IV-8. Schematic Arrangement of the Fabry-Perot Interferometer.

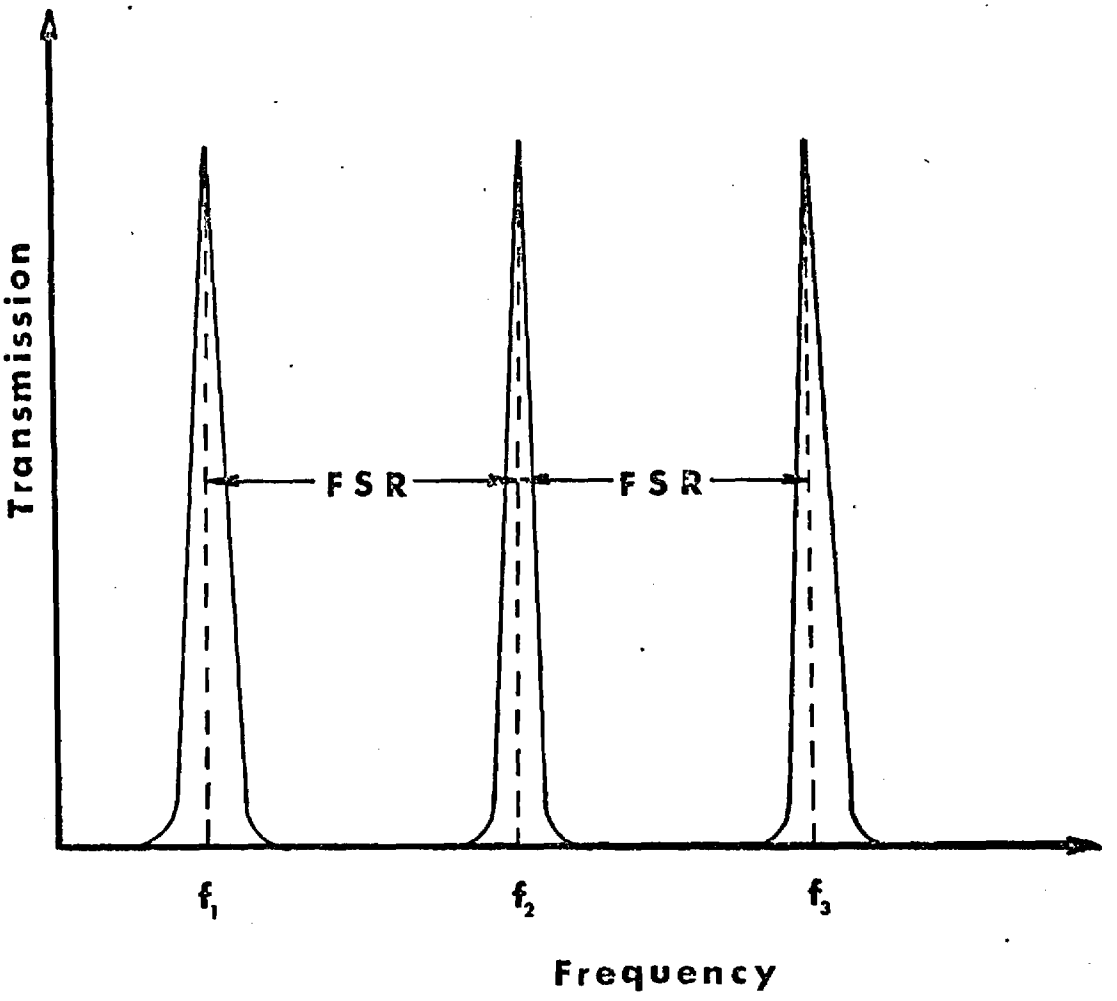

Figure IV-9. Transmission of the Fabry-Perot Interferometer as a Function of Light Frequency.

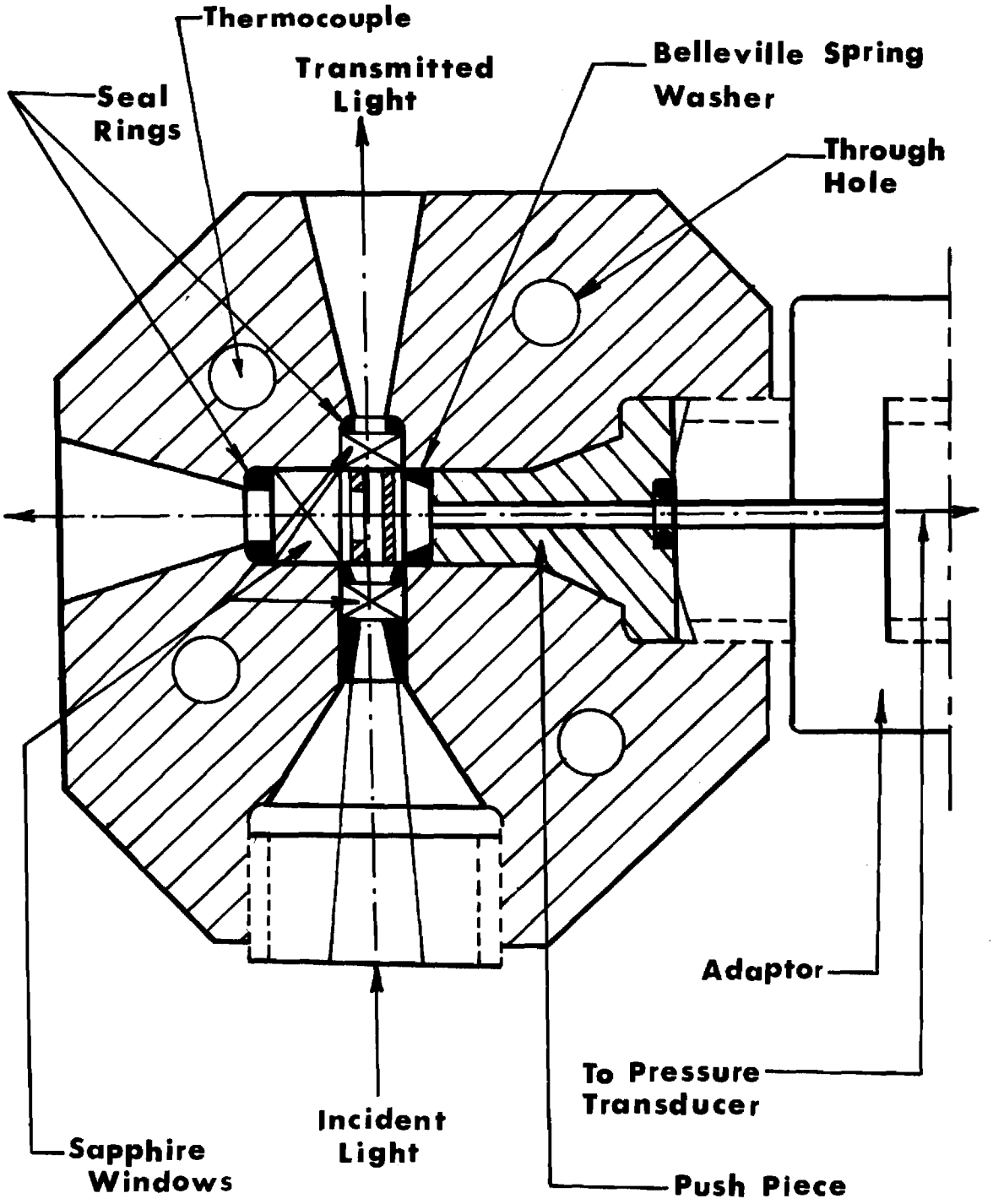

Figure IV-10. Schematic of Light-Scattering Cell. The Intensifier is Attached Perpendicular to the Paper Plane at the Centerline of the Cell.

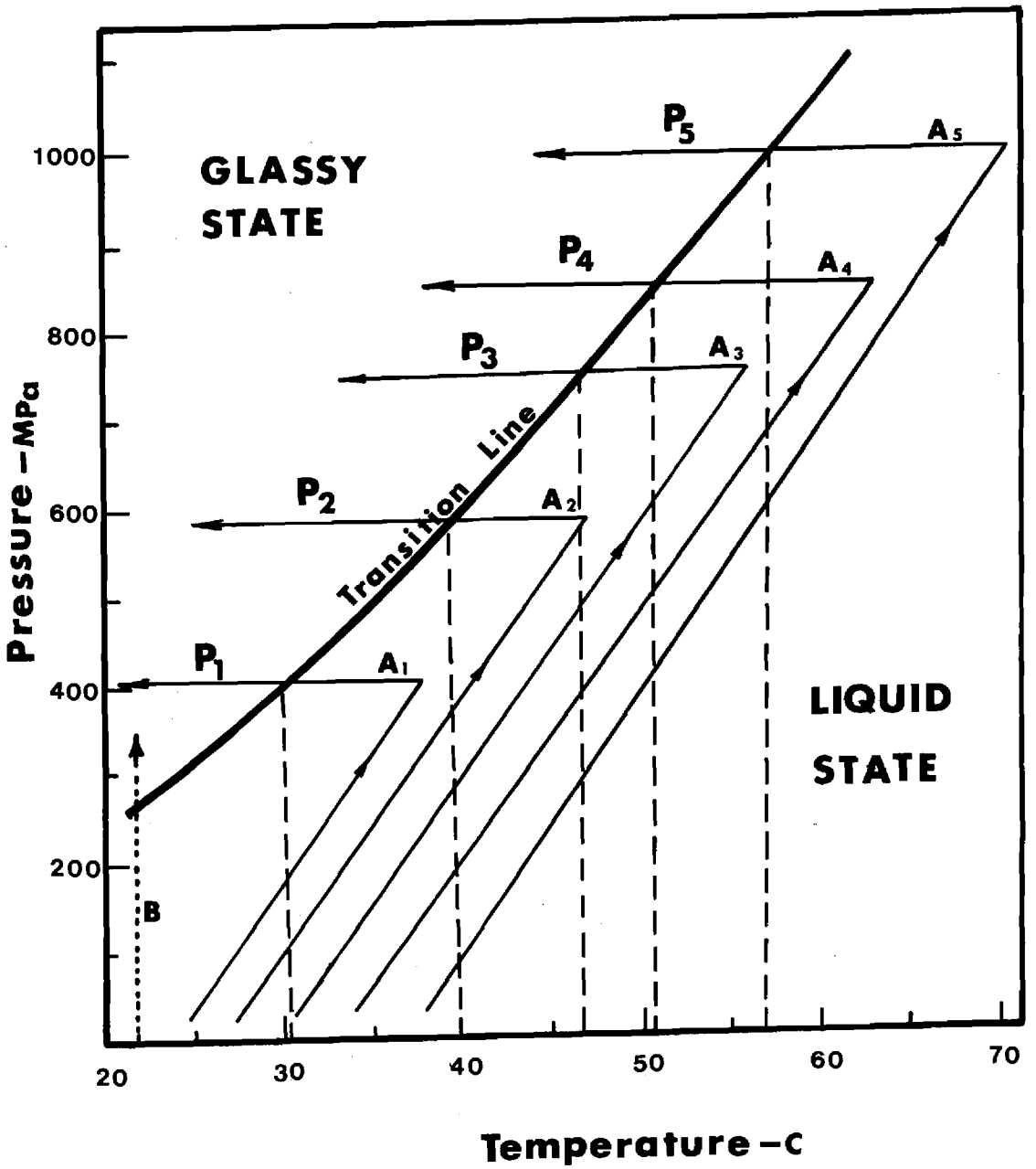

Figure IV-11. Schematic of Formation Histories Used to Form the Glass. A_i and B Represent Constant Formation Histories at Pressure P_i and Room Temperature Respectively.

Figure IV-12. Frequency Spectrum for 5P4E Fluid Recorded at 0.19 GPa and 24.4C (History B). B and R represent the Brillouin and Rayleigh Components Respectively.

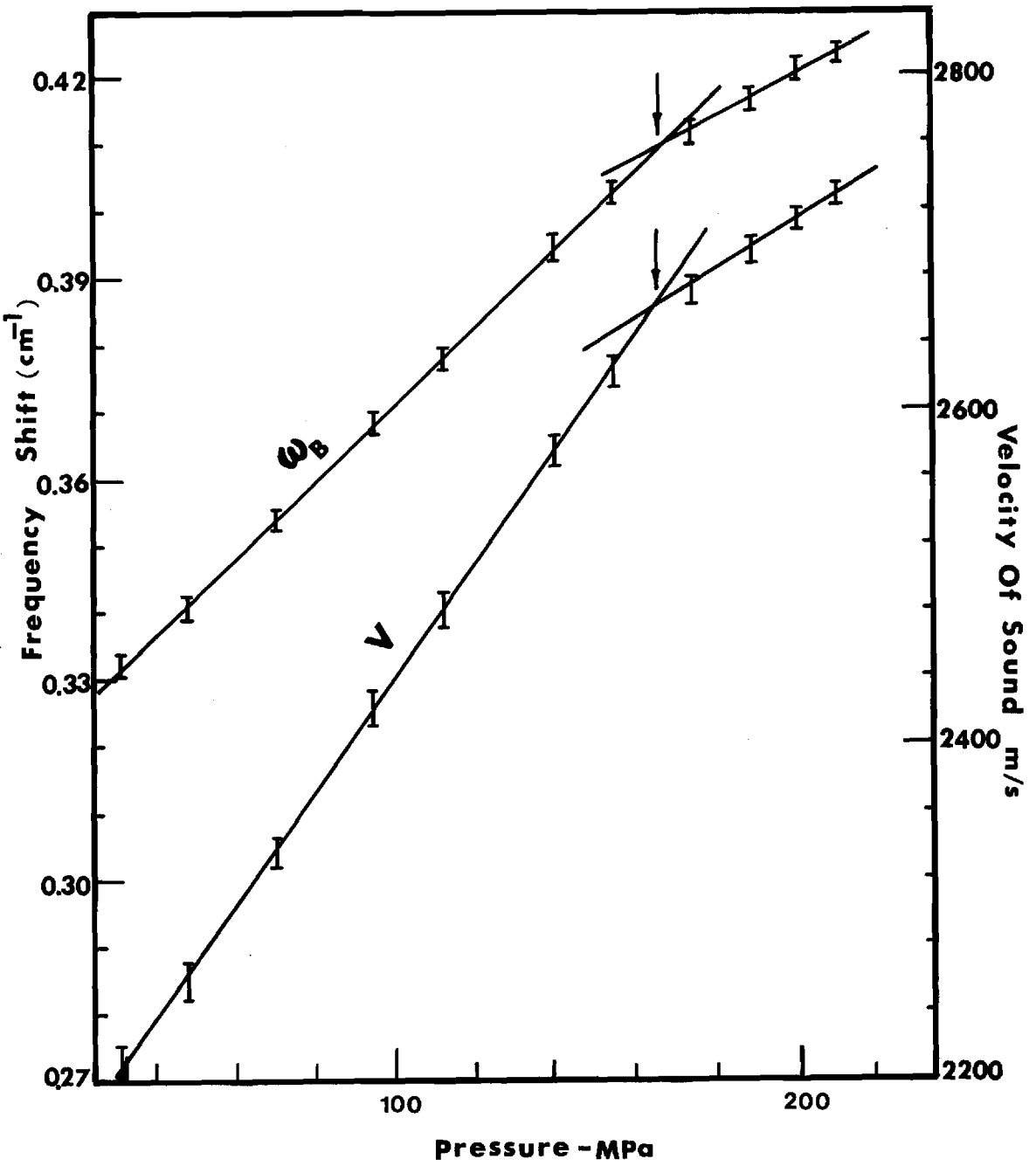

Figure IV-13. Variation of Frequency Shift and Velocity of Sound with Pressure at 24.4C (76 F) for 5P4E Fluid (History B). Arrows Indicate Glass Transition.

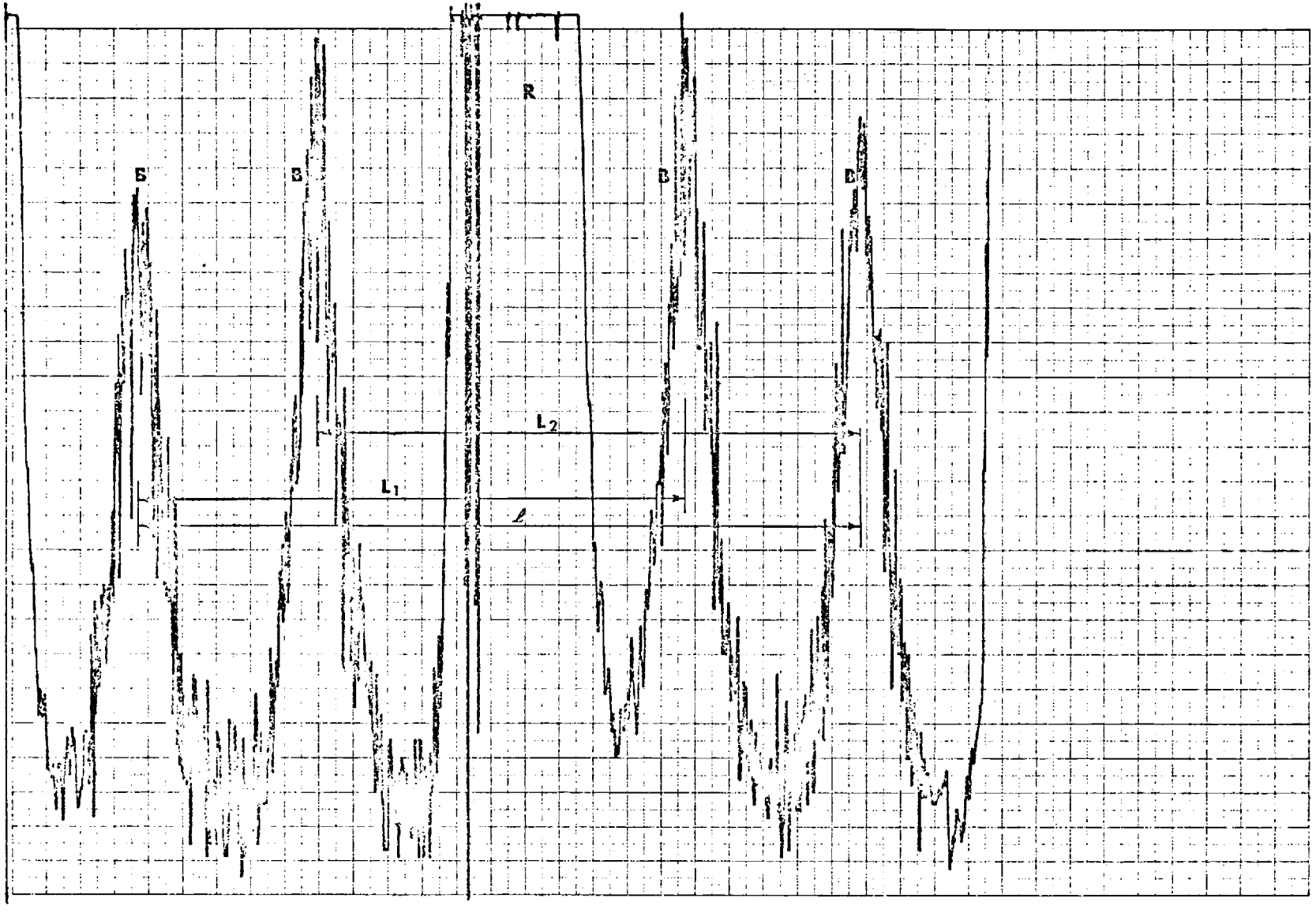

Figure IV-14. Frequency Spectrum for 5P4E Fluid Recorded at 0.40 GPa (59,000 psi) and 64.4C (148F) (History A). B and R Represent the Brillouin and Rayleigh Components Respectively.

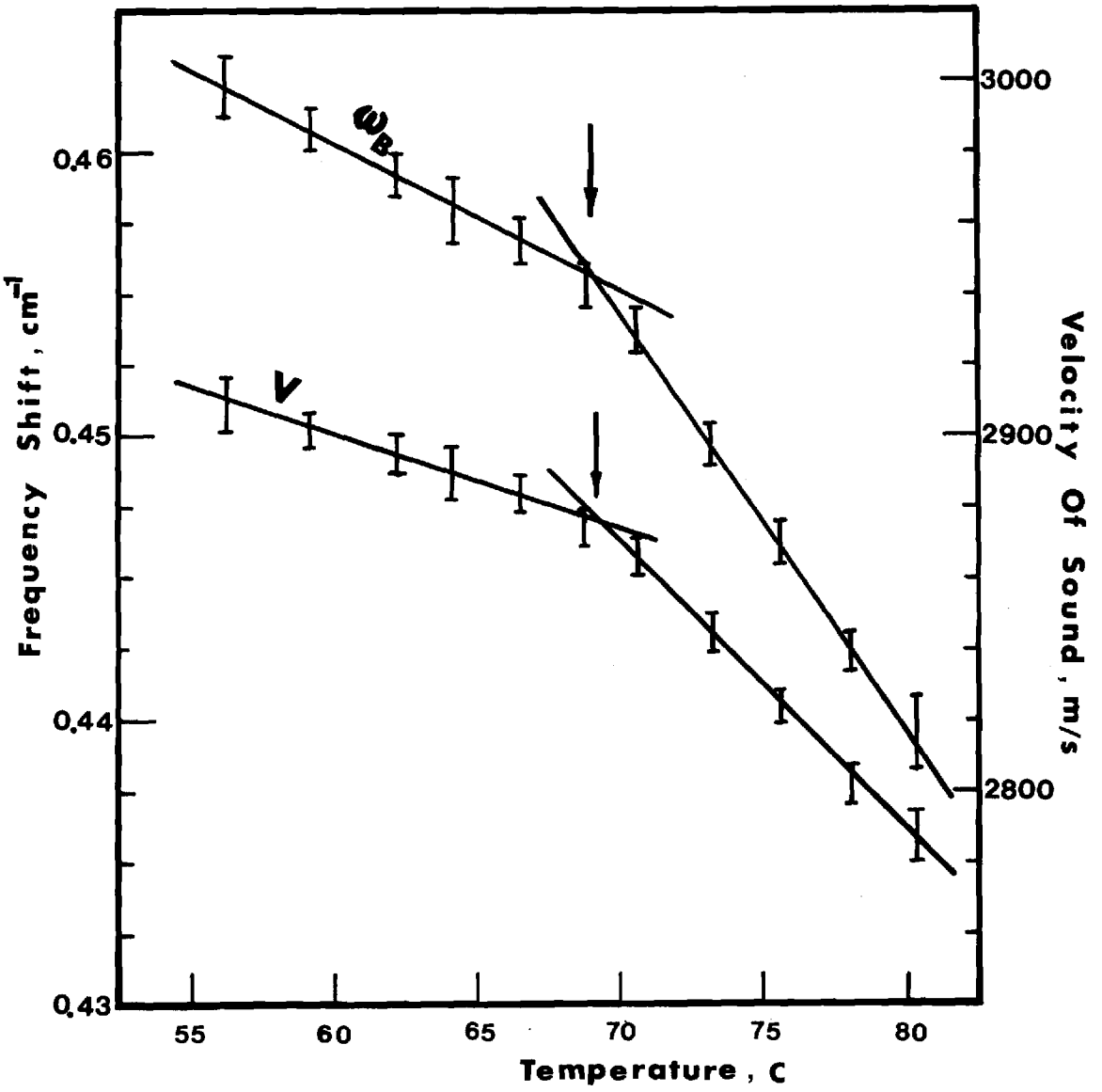

Figure IV-15. Variation of Frequency Shift and Velocity of Sound with Temperature at 0.40 GPa (59,000 psi) for 5P4E (History A). Arrows Indicate Glass Transition.

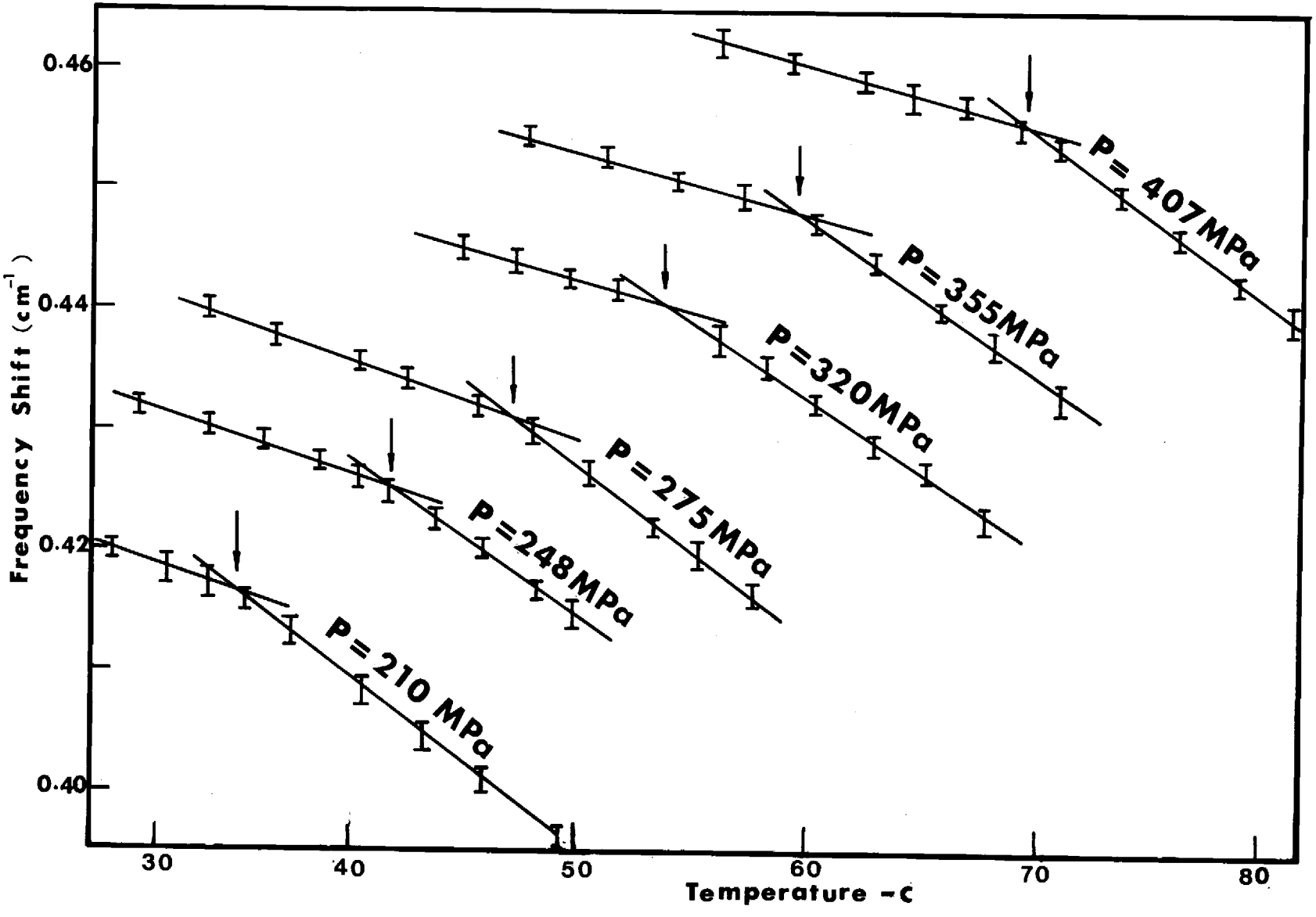

Figure IV-16. Frequency Shift Dependence on Temperature at Different Constant Pressures for 5P4E Fluid (History A). Arrows Indicate T_g.

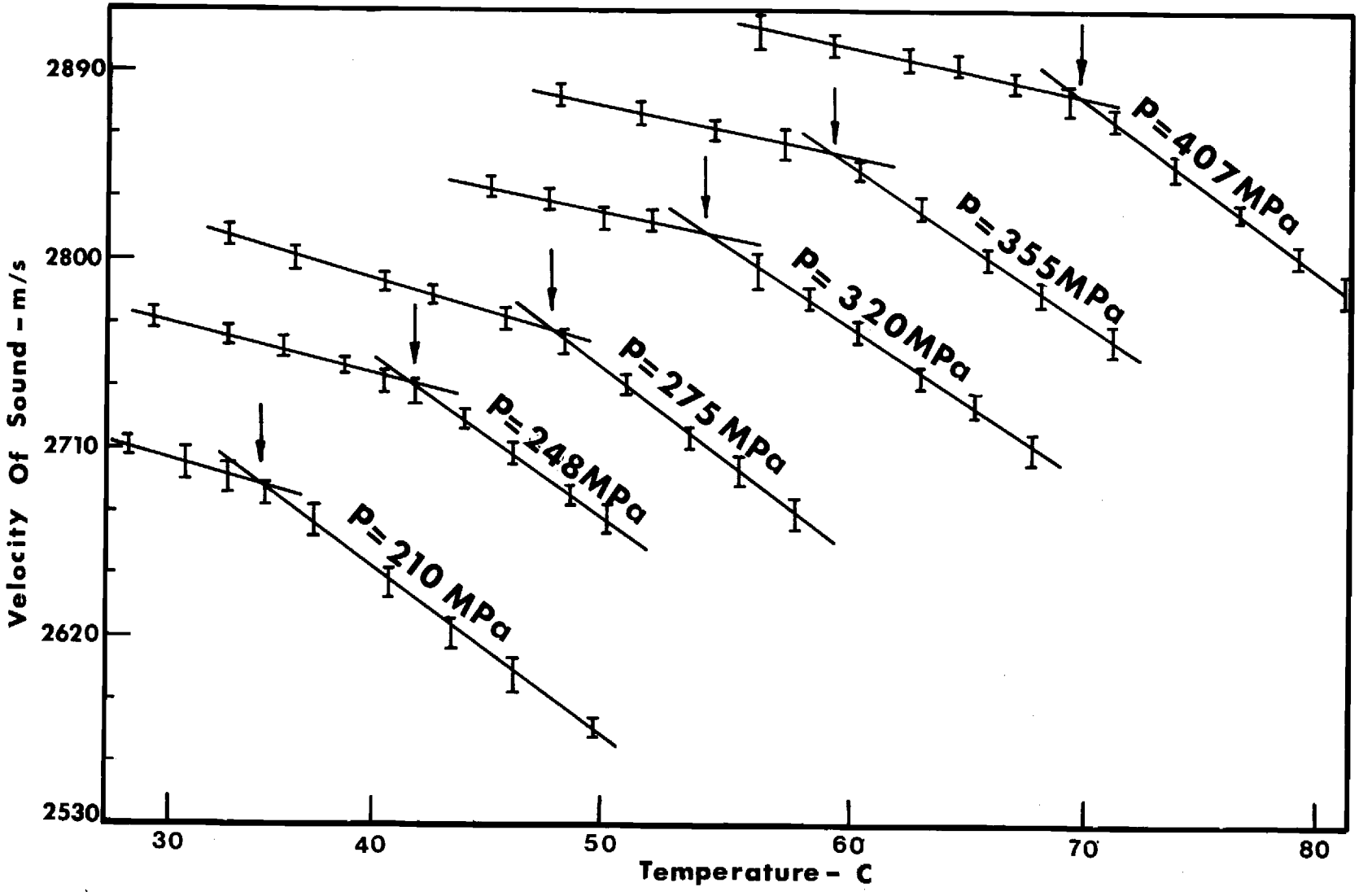

Figure IV-17. Velocity of Sound Dependence on Temperature at Different Constant Pressures for 5P4E Fluid (History A). Arrows Indicate T_q.

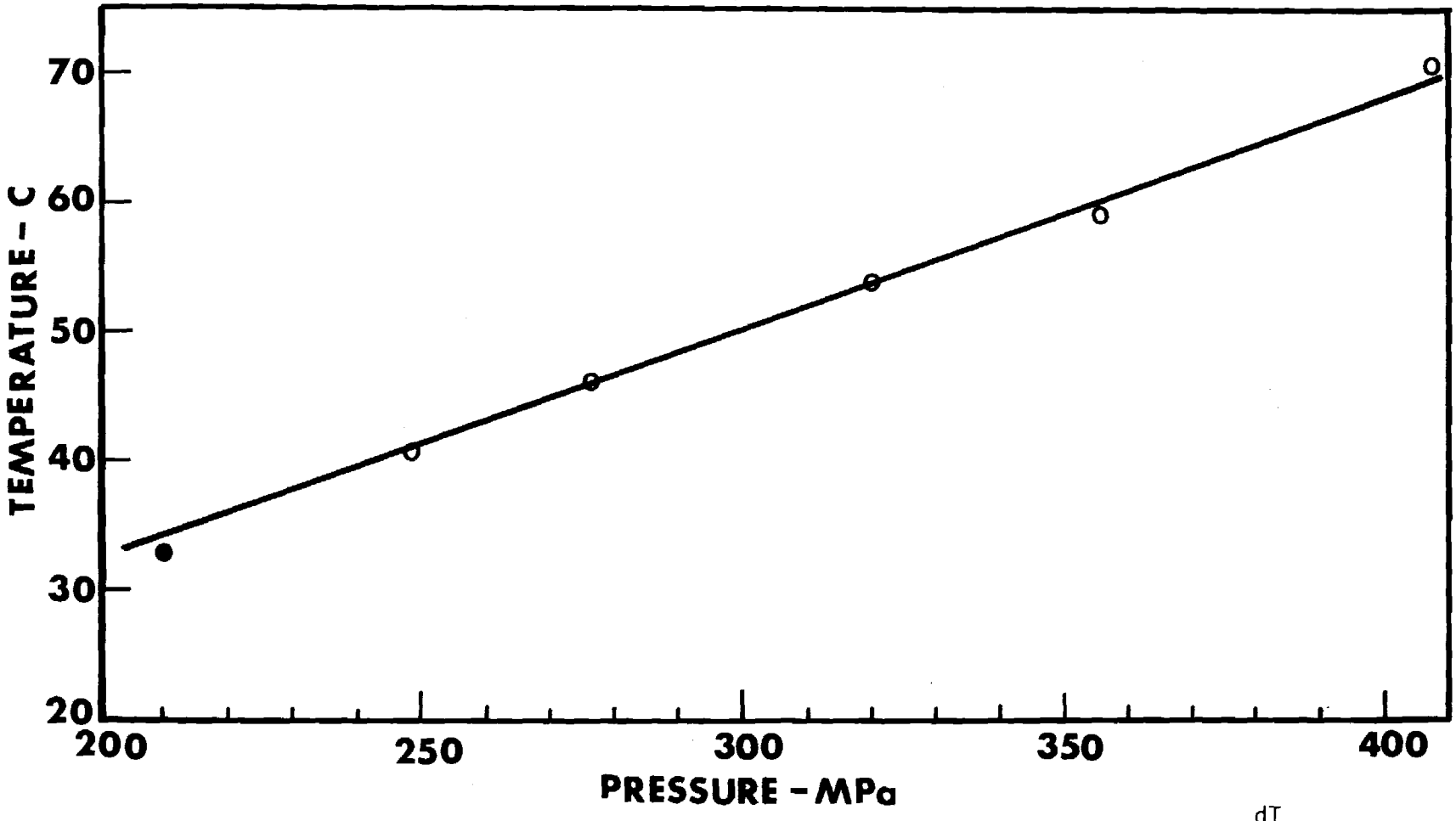

Figure IV-18. Phase Diagram for 5P4E Fluid Based on Light Scattering Experiment. $\frac{dT_g}{dP}$ = 183 C/GPa. History A. History B.

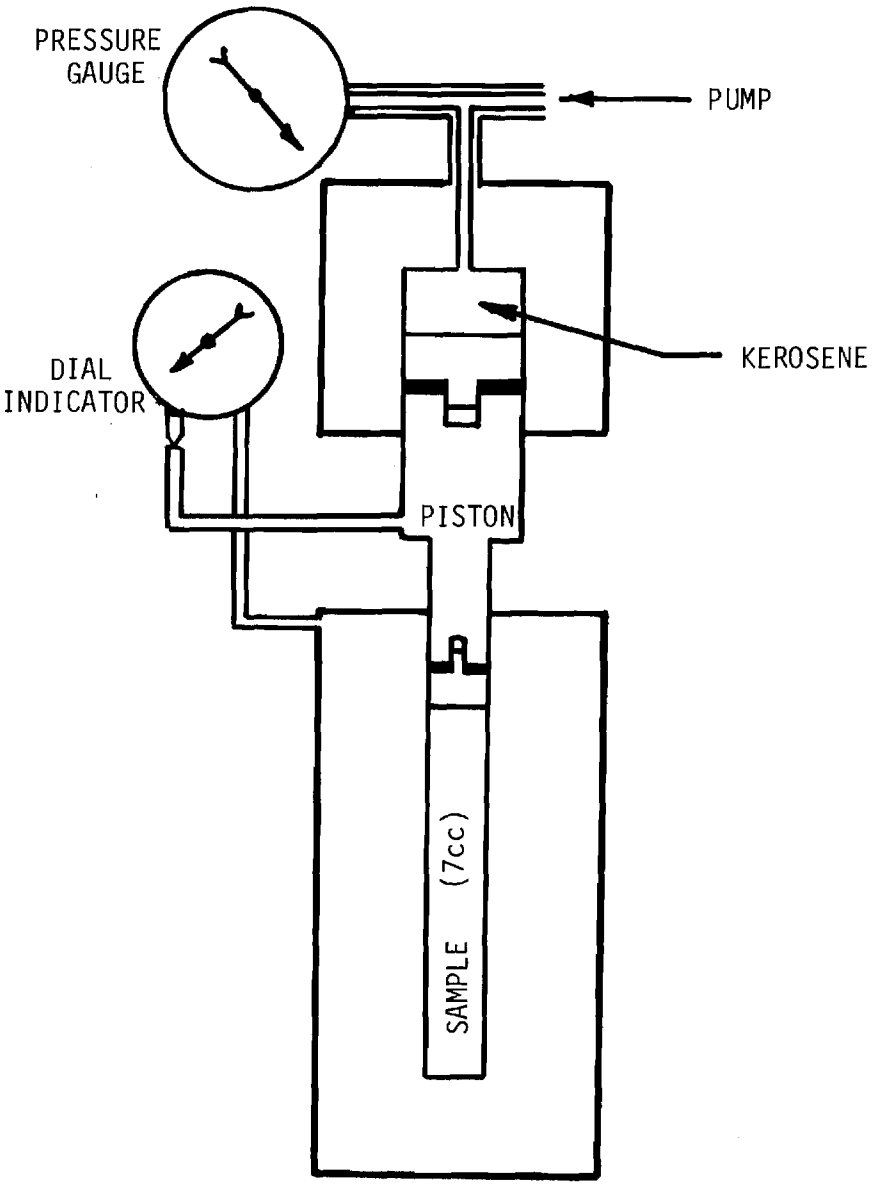

Figure IV-19. High Pressure Dilatometer (.13 to 1.2 GPa).

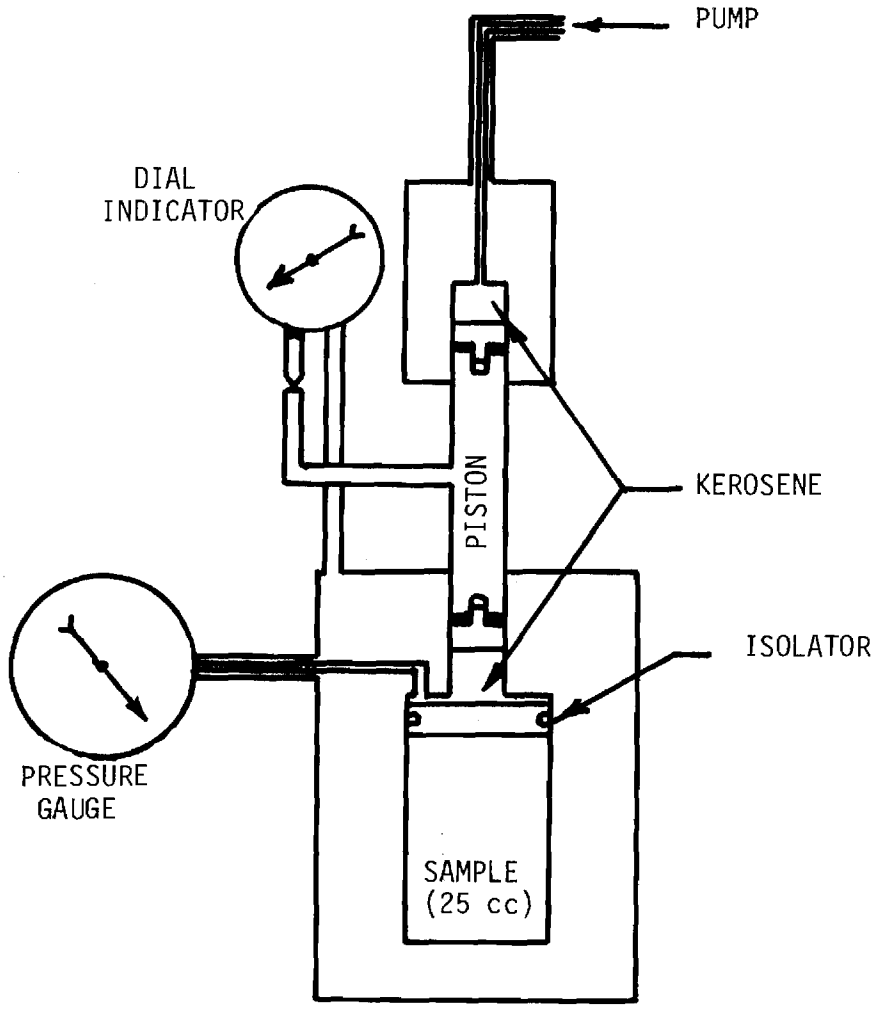

Figure IV-20. Low Pressure Dilatometer.
(.014 to .27 GPa)

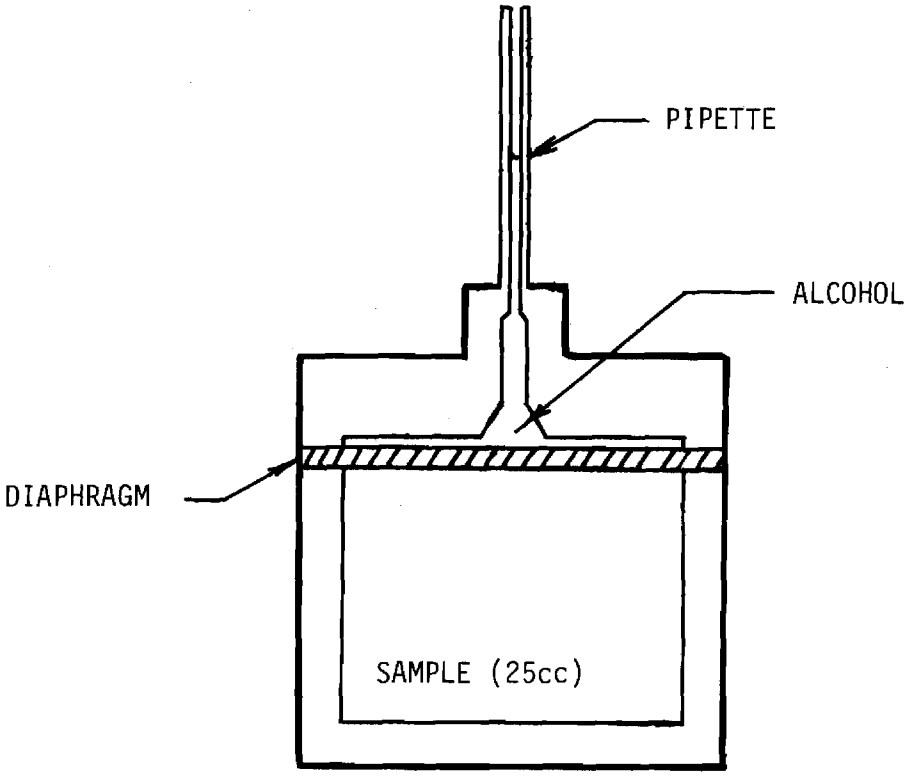

Figure IV-21. Atmospheric Pressure Dilatometer.

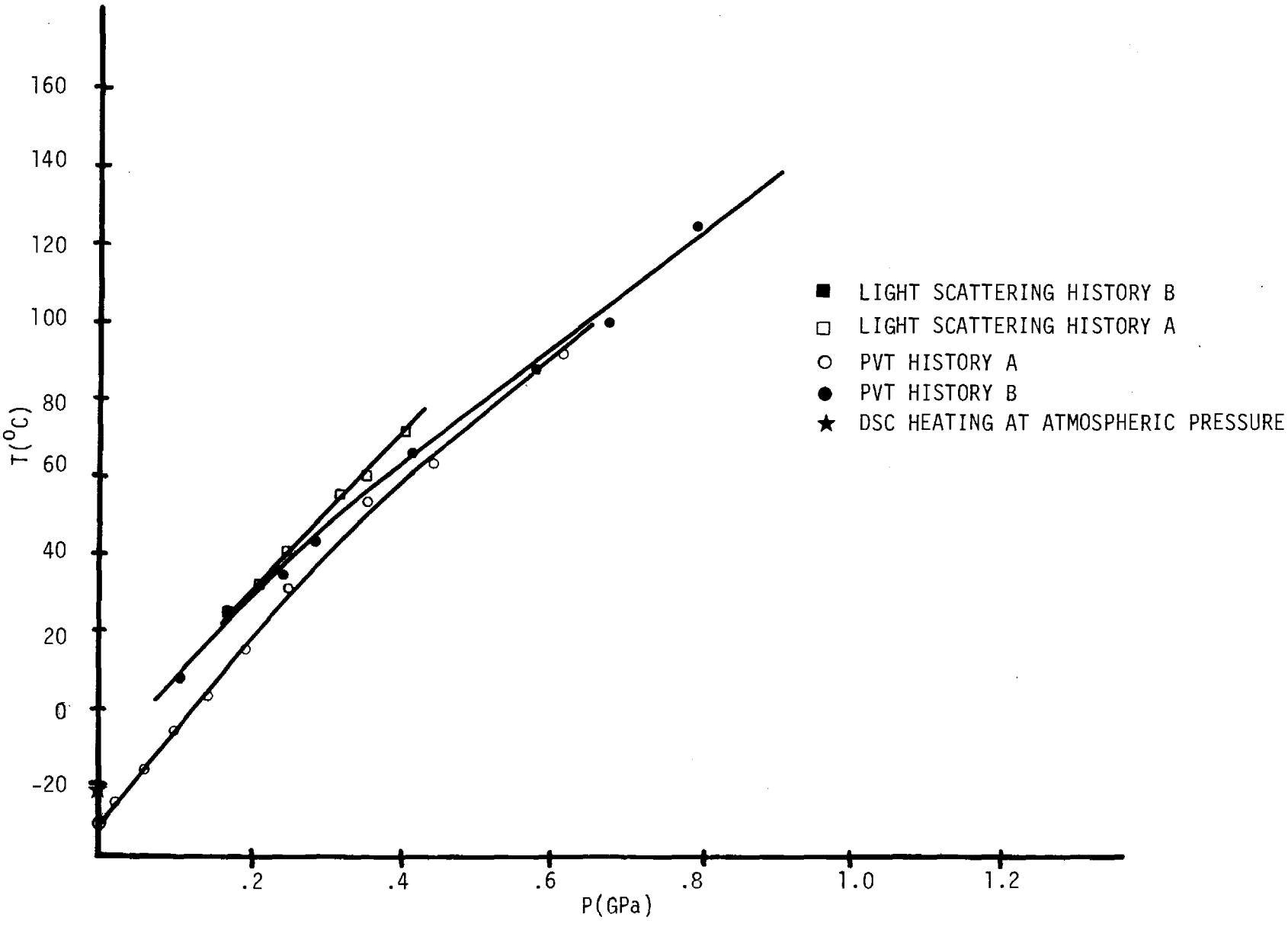

Figure IV-22. Comparison of Glass Transition of 5P4E by Various Methods.

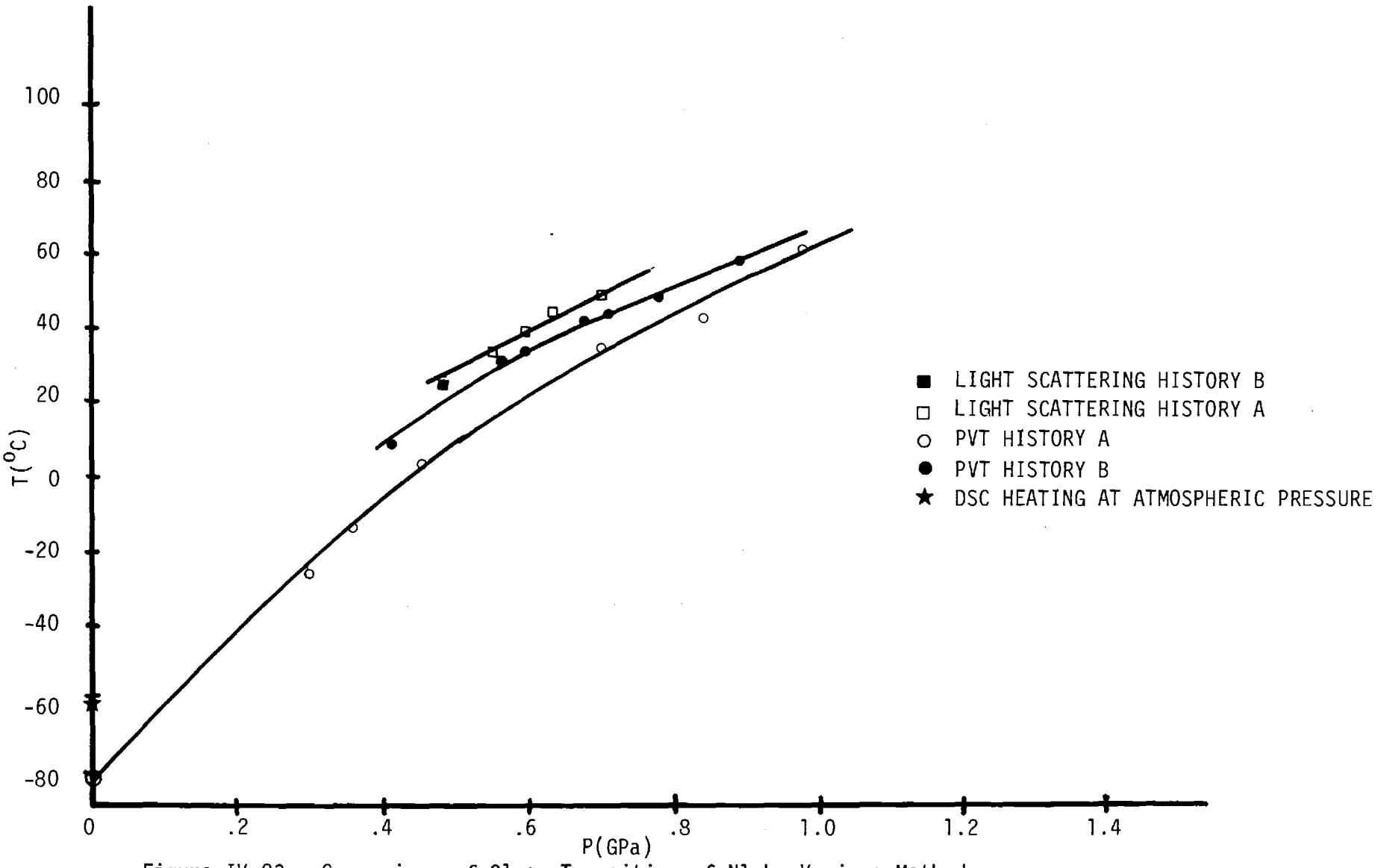

Figure IV-23. Comparison of Glass Transition of N1 by Various Methods.

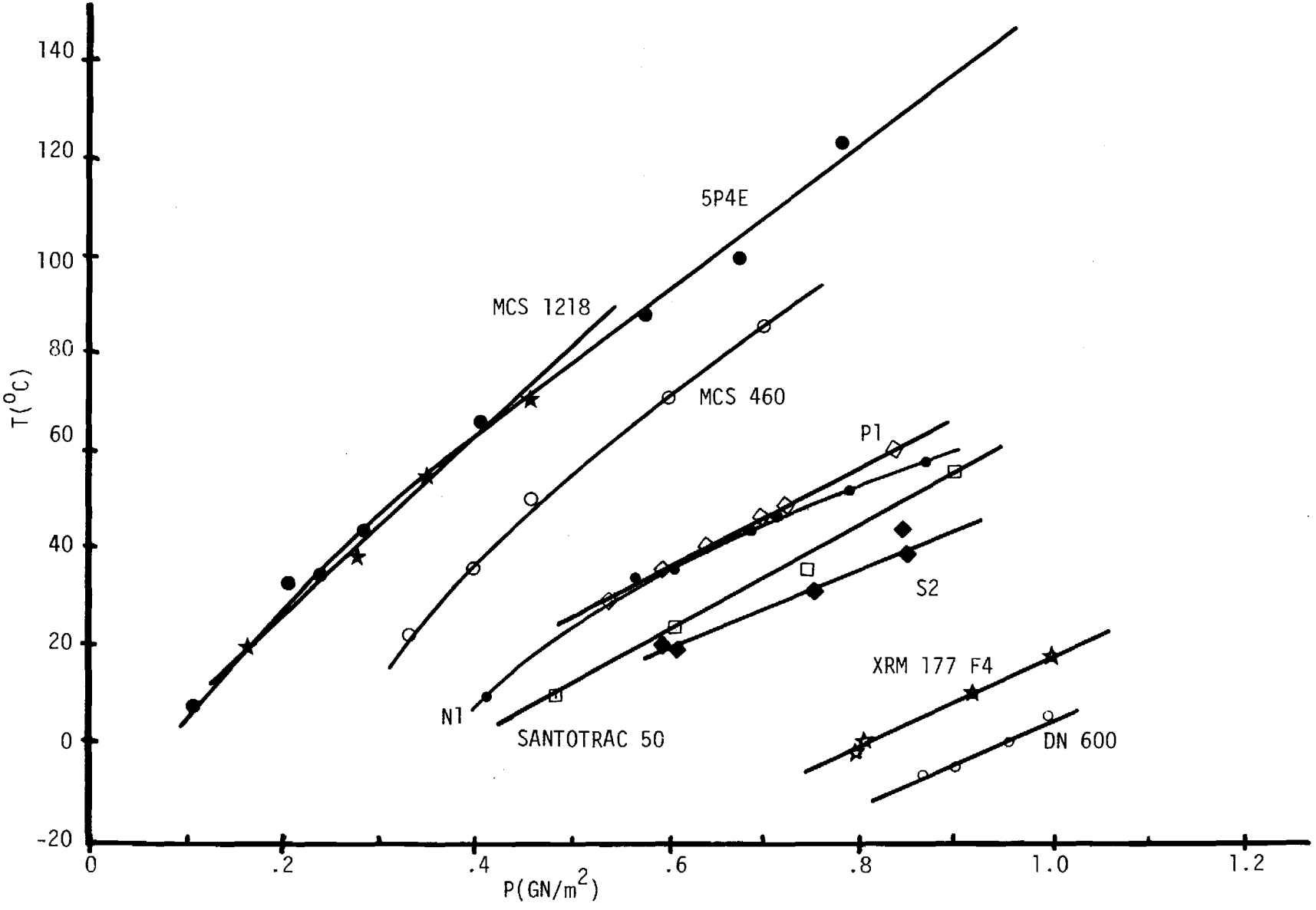

Figure IV-24. Glass Transition by Isothermal Compression from Liquid (Dilatometry).

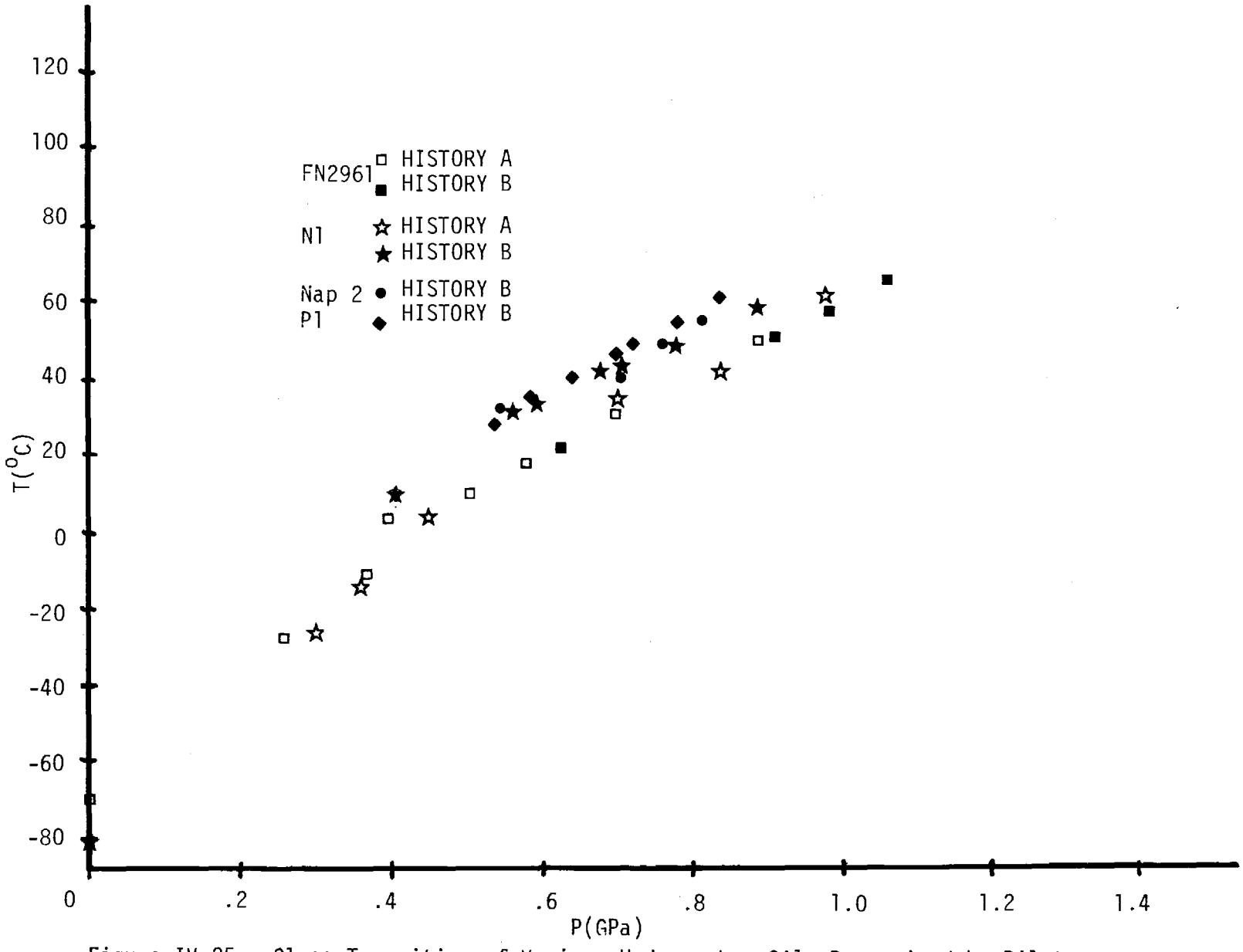

Figure IV-25. Glass Transition of Various Hydrocarbon Oils Determined by Dilatometry.

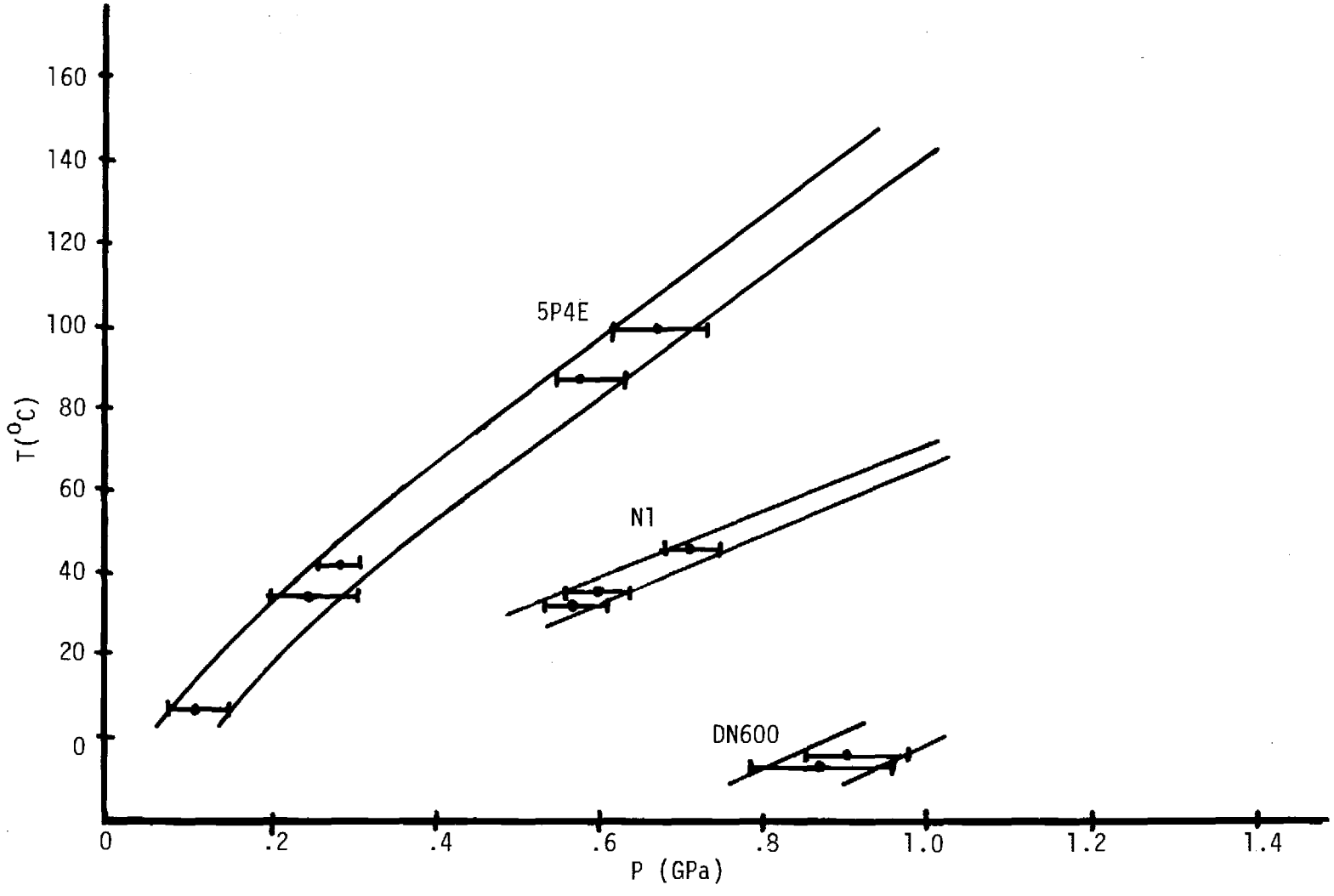

Figure IV-26. Dispersion Region in Isothermal Compression by Dilatometry.

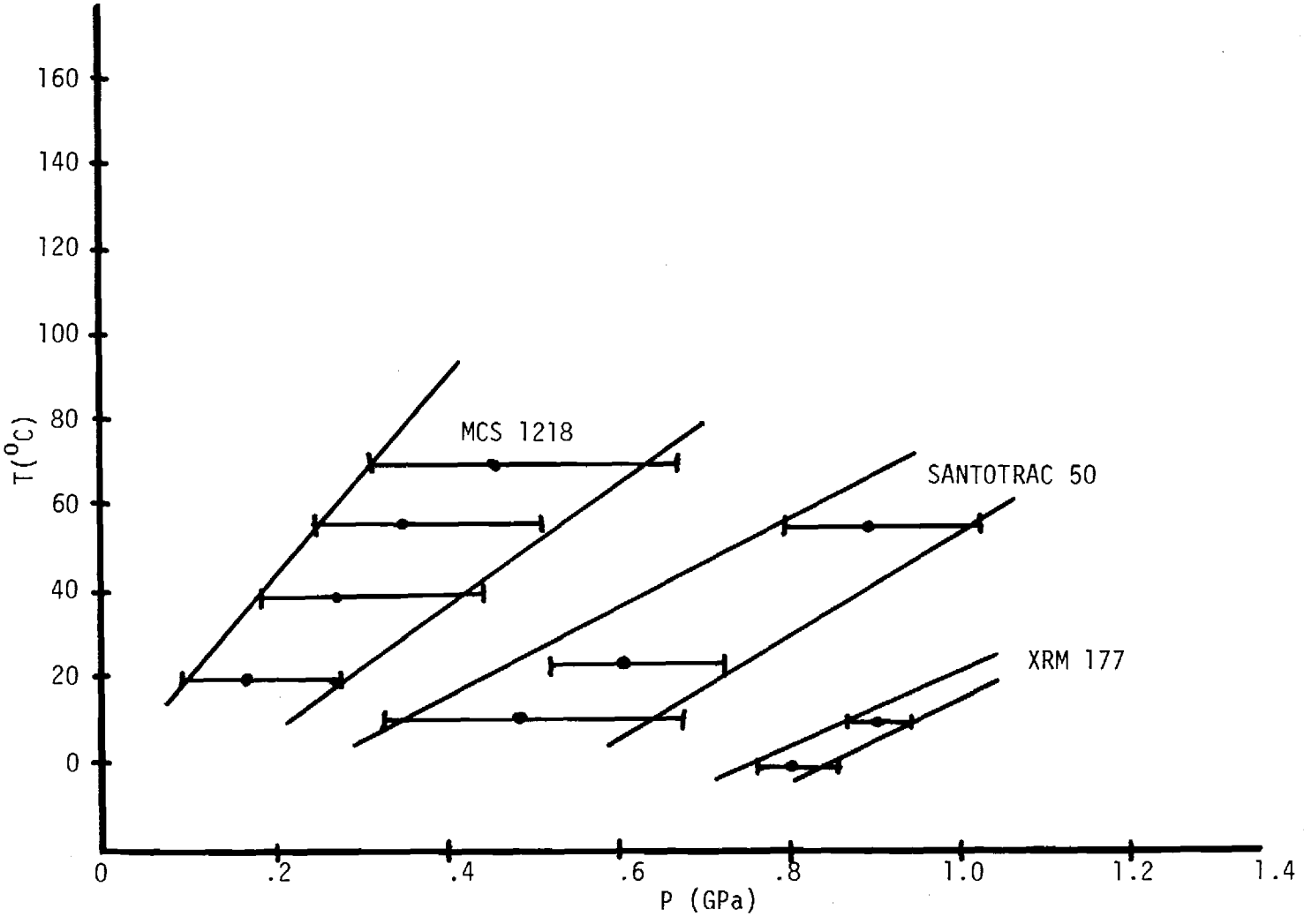

Figure IV-27. Dispersion Region in Isothermal Compression by Dilatometry.

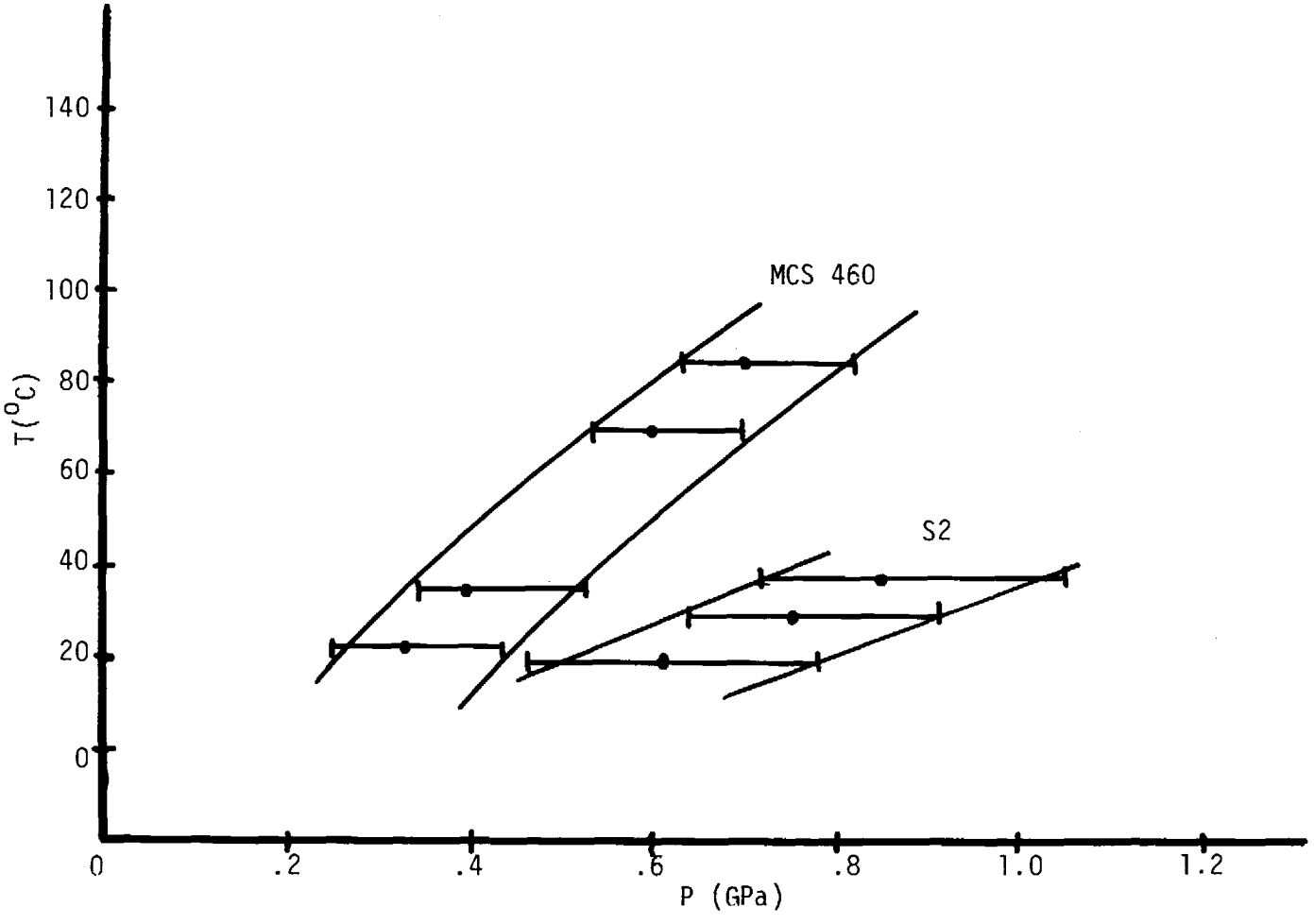

Figure IV-28. Dispersion Region in Isothermal Compression by Dilatometry.

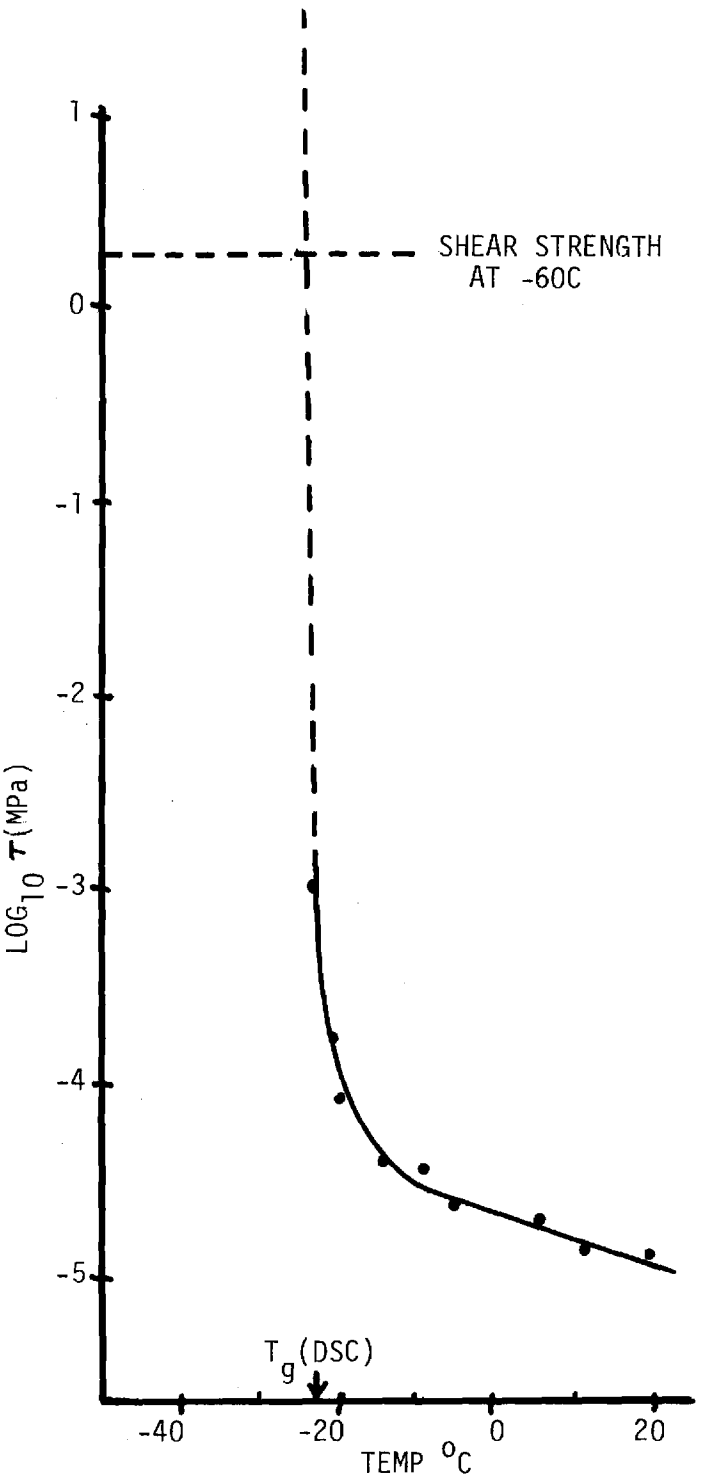

Figure IV-29. Shear Stress Between Concentric Cylinders for 5P4E Cooled at 2.75 C/min., Shear Rate $\dot{\gamma}$ = .435 sec^{-1}.

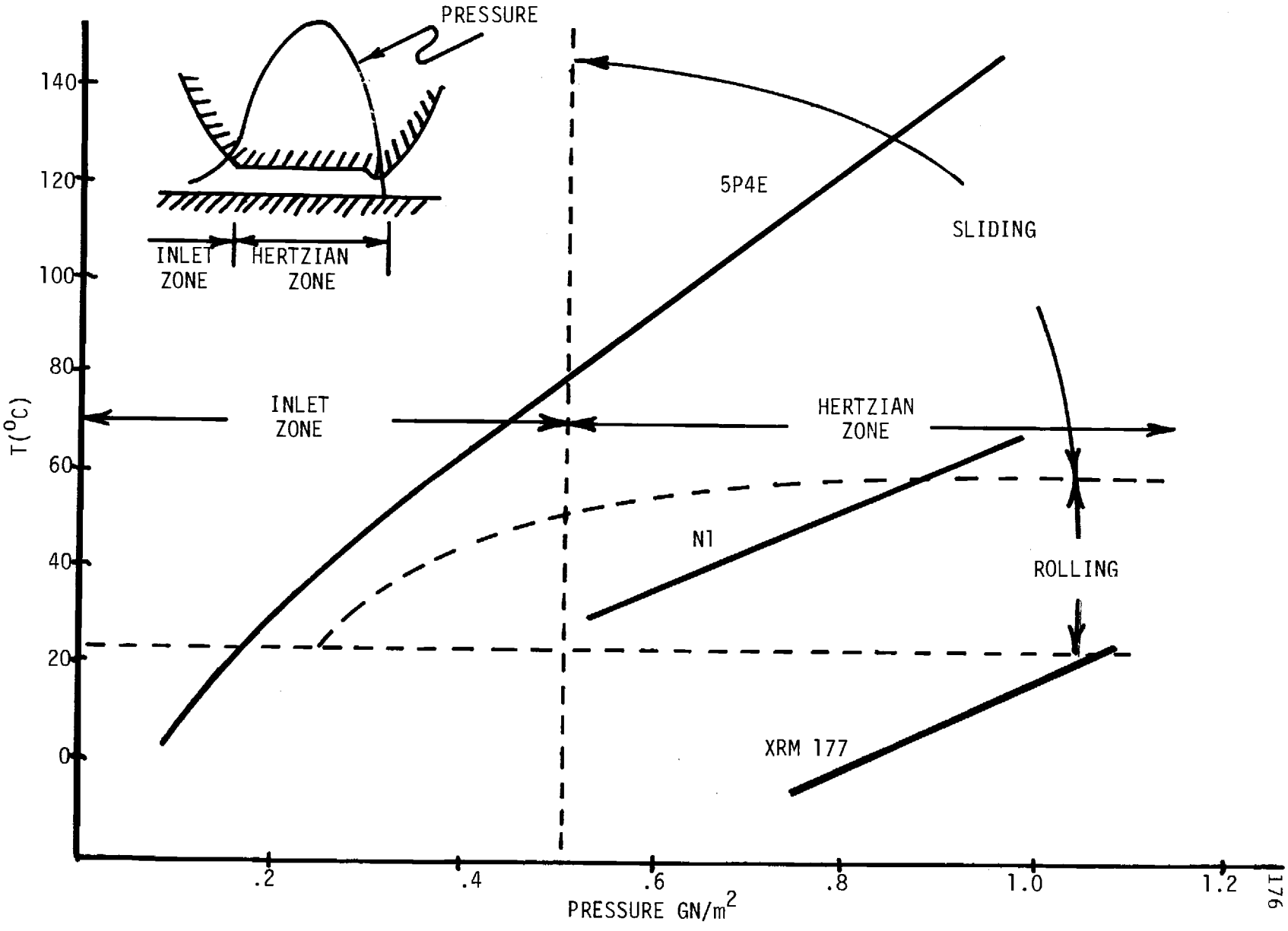

Figure IV-30. Heuristic Estimates of the Relationship Between Conditions in an EHD Contact and Glass-Liquid Phase Diagram of Some Lubricants (Lubricant Supply Temperature about 20C).

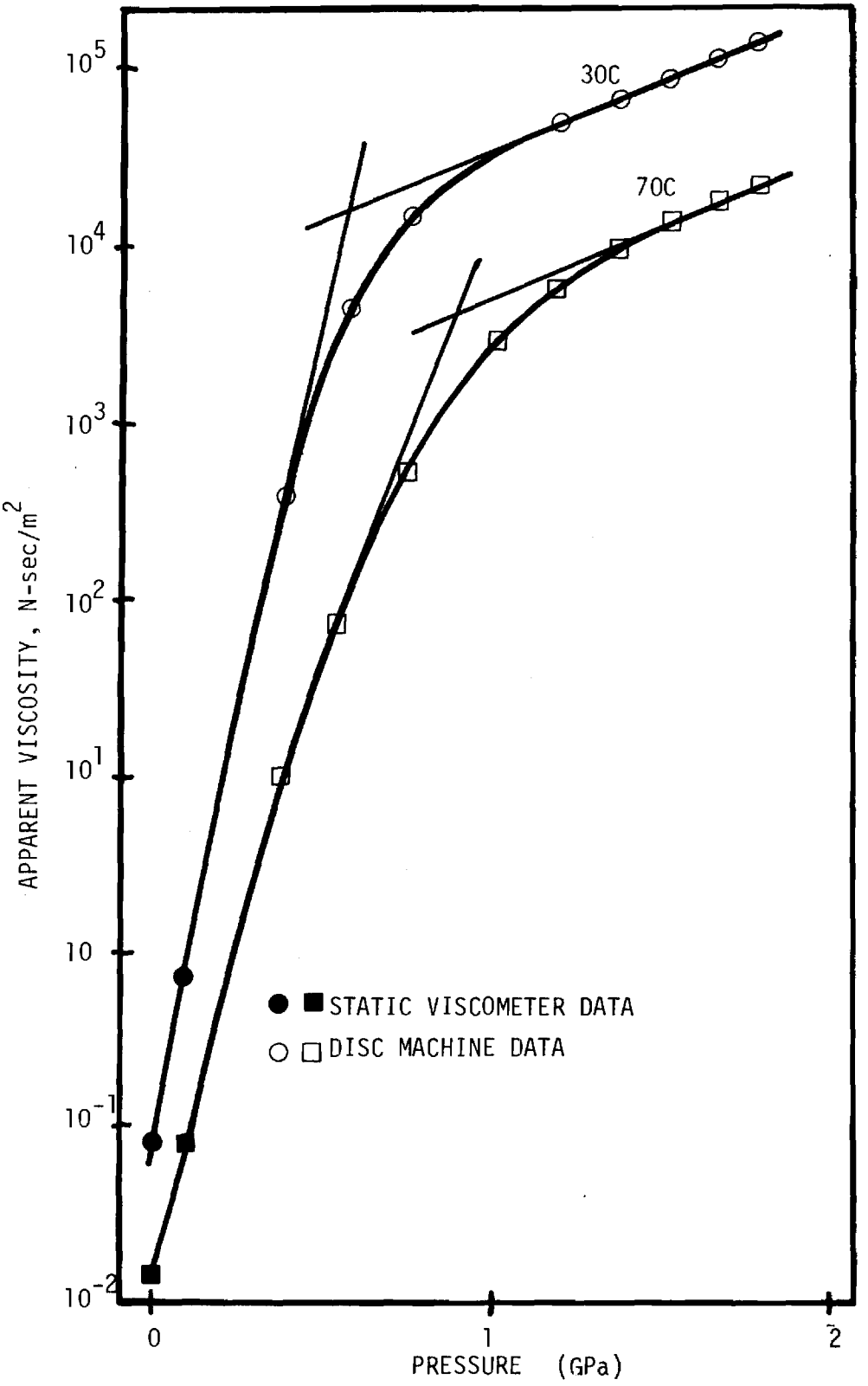

Figure IV-31. The Variation of Apparent Viscosity with Pressure and Temperature.

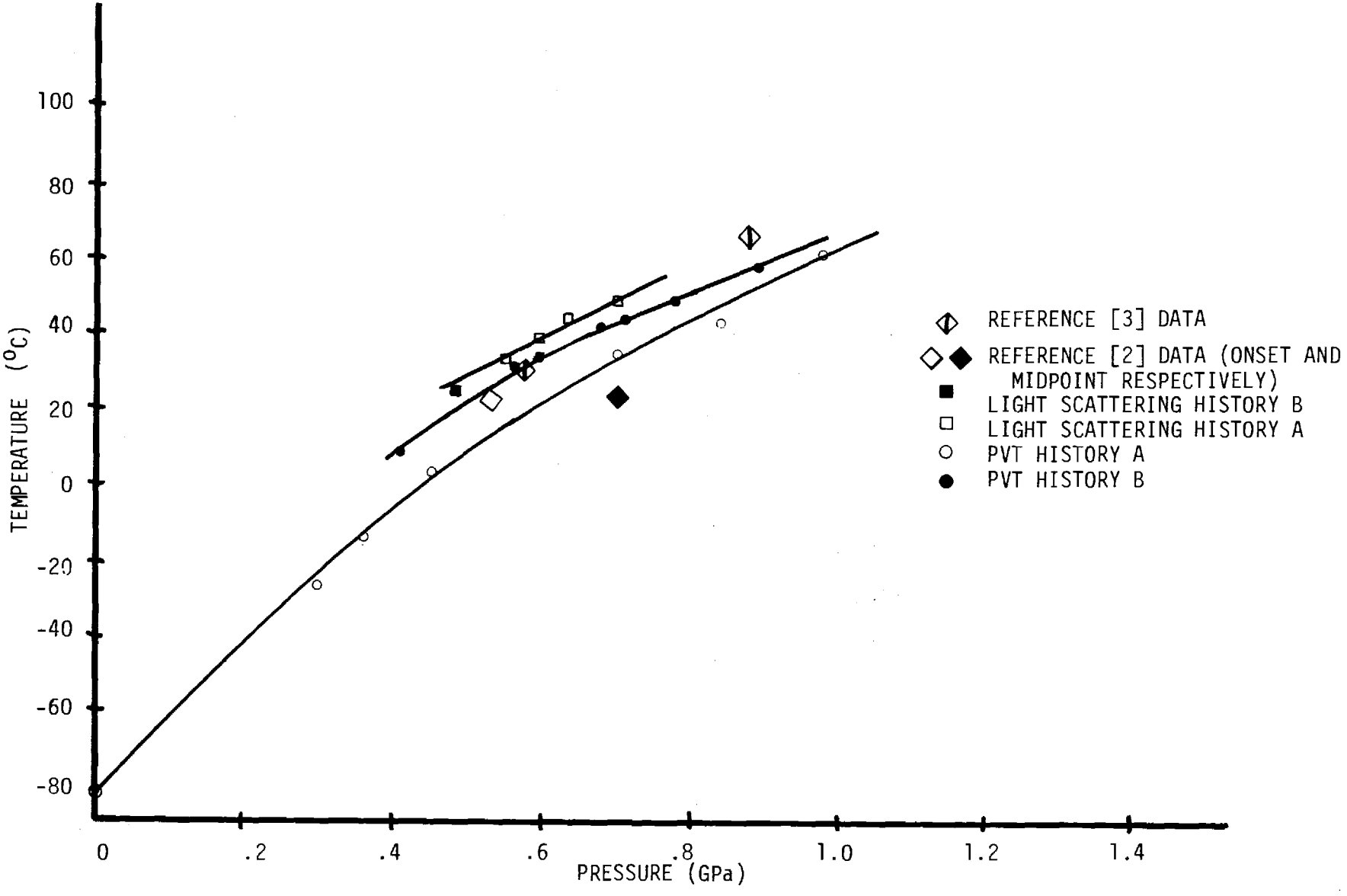

Figure IV-32. Comparison of Glass Transition of N1 by Various Methods.

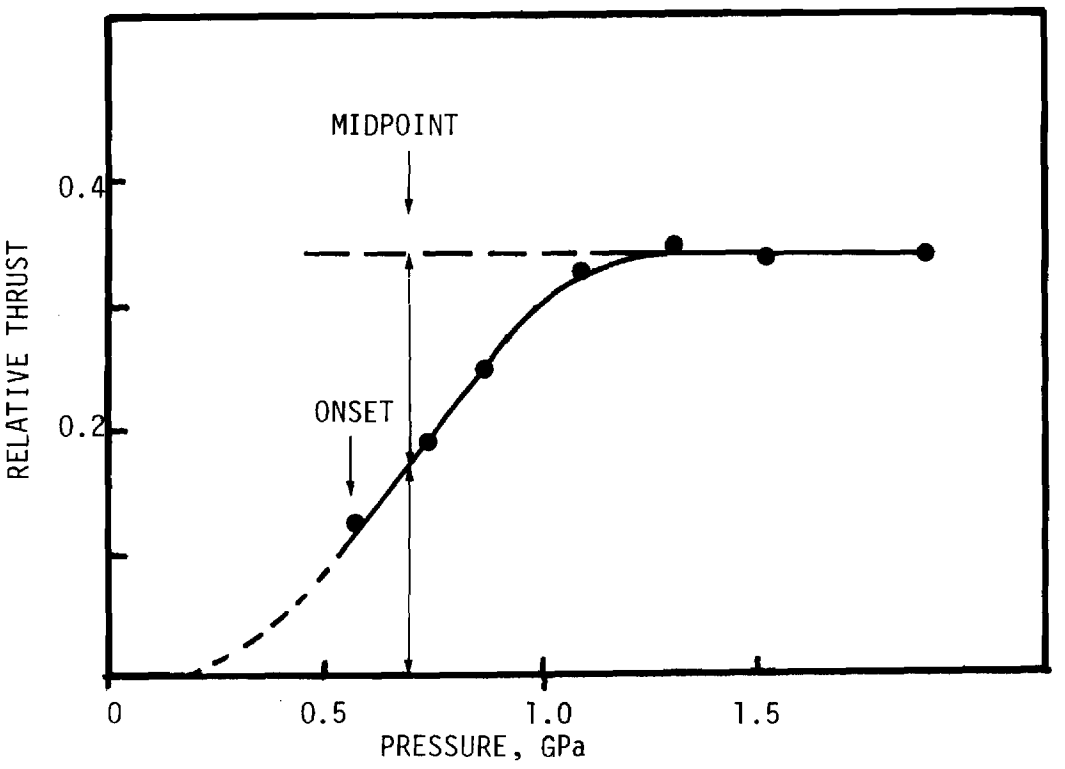

Figure IV-33. Variation of the Relative Side Thrust with Contact Pressure at 23C and 0.1 m/s [26].

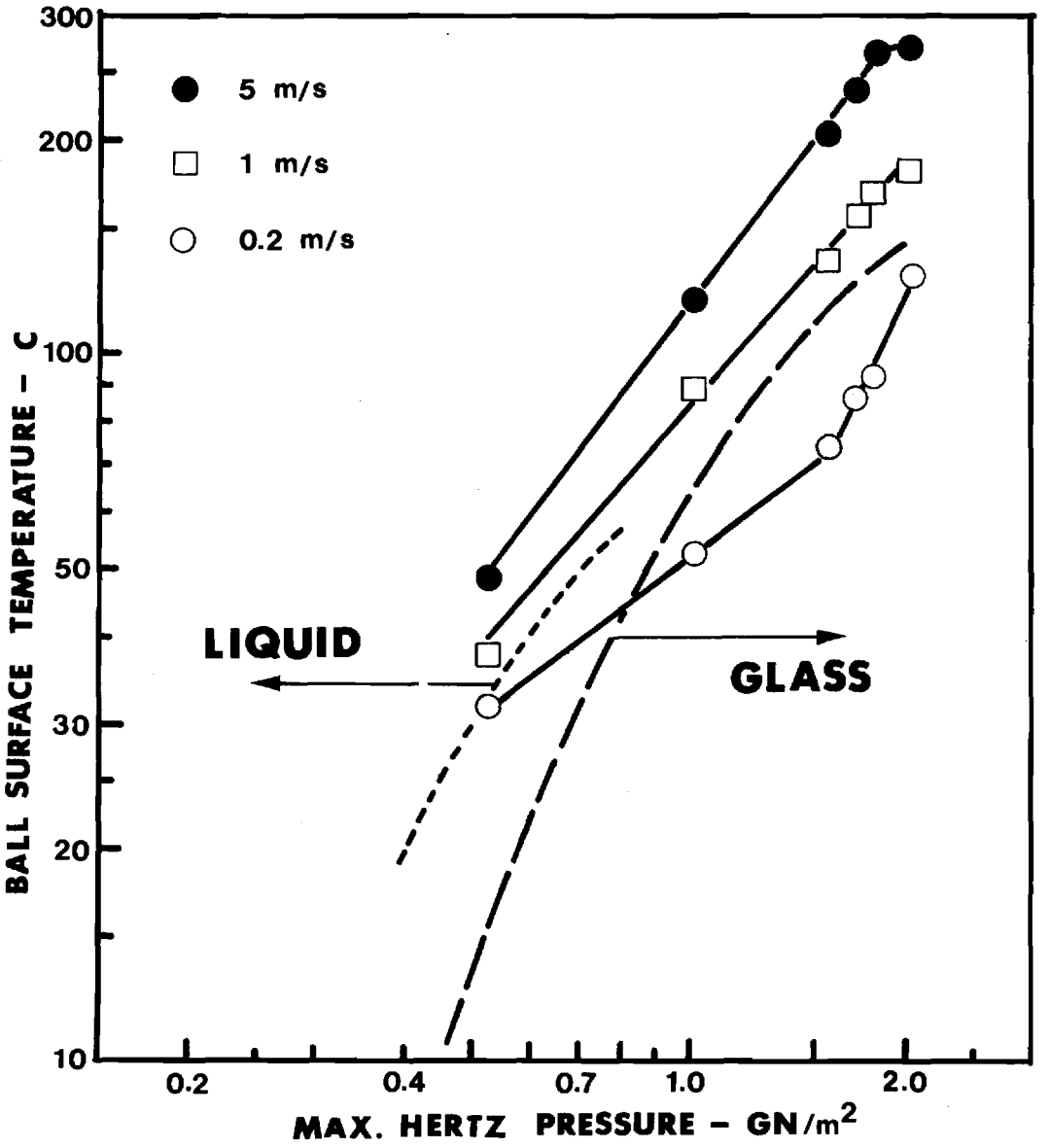

Figure IV-34. The Physical State of N1 Lubricant in the Center of a Sliding Contact at Various Speeds and Hertz Pressures (Reference [9]) ------- ------- and ——— ——— Represent the Light-Scattering and the Volumetric Glass Transition Lines Respectively.

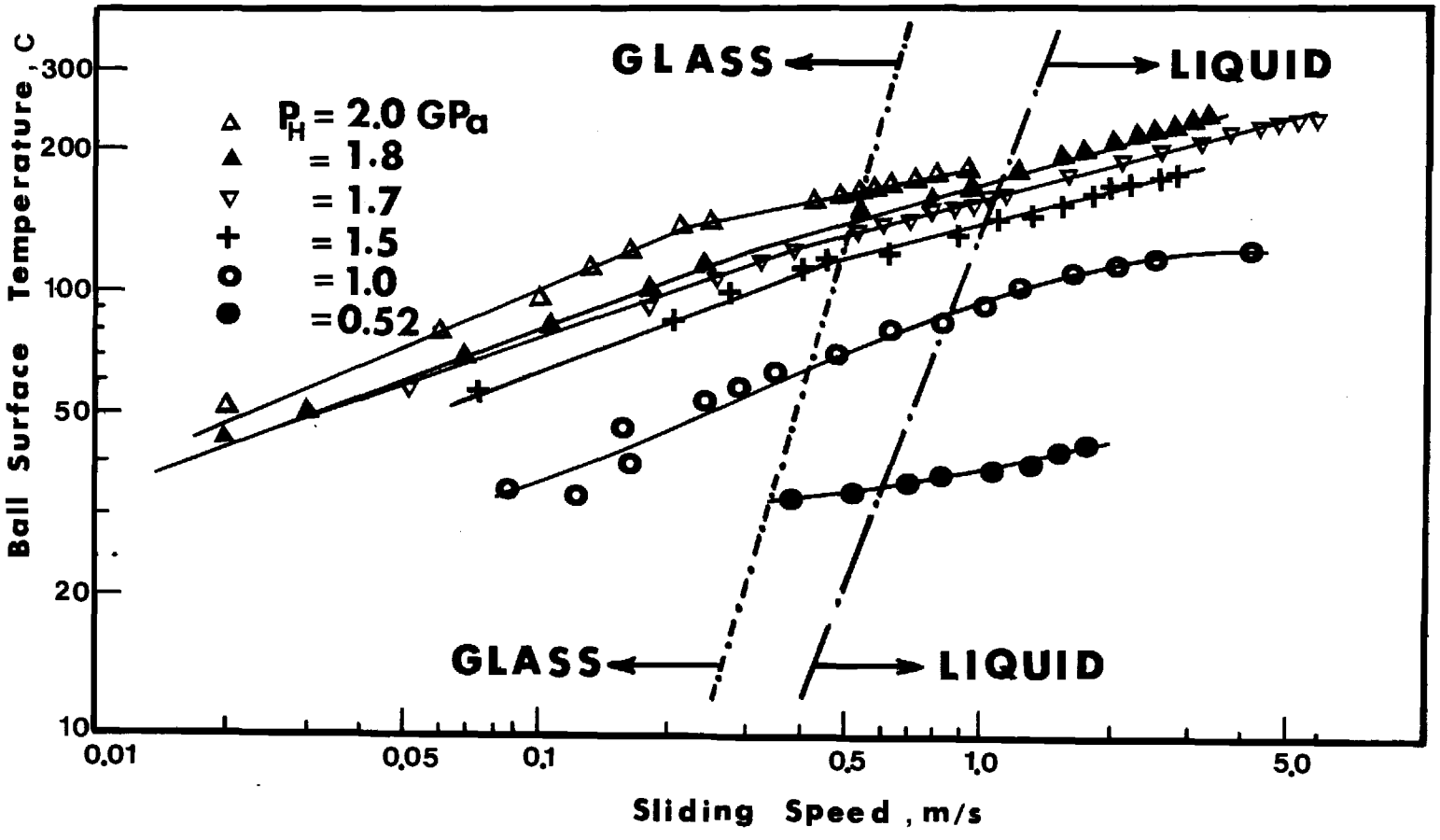

Figure IV-35. The Physical State of N1 Lubricant in the Center of a Sliding Contact at Various Speeds and Hertz Pressures ·-·-·- and —·— Represent the Light-Scattering and the Volumetric Glass Transition Lines.

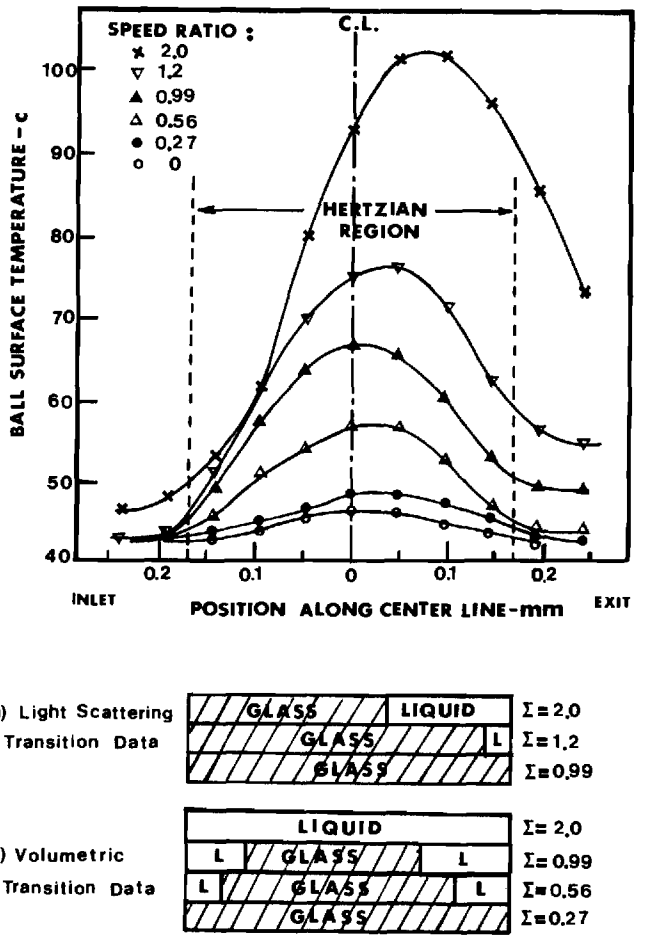

Figure IV-36. Ball Surface Temperature Distribution Along the Contact Centerline at Constant Hertzian Pressure of 1.0 GPa and Constant Rolling Speed of 0.75 m/s. (a) and (b) Represent the Physical State of the Lubricant in the Contact Area as Determined by the Light Scattering and Volumetric Transition Data Respectively.

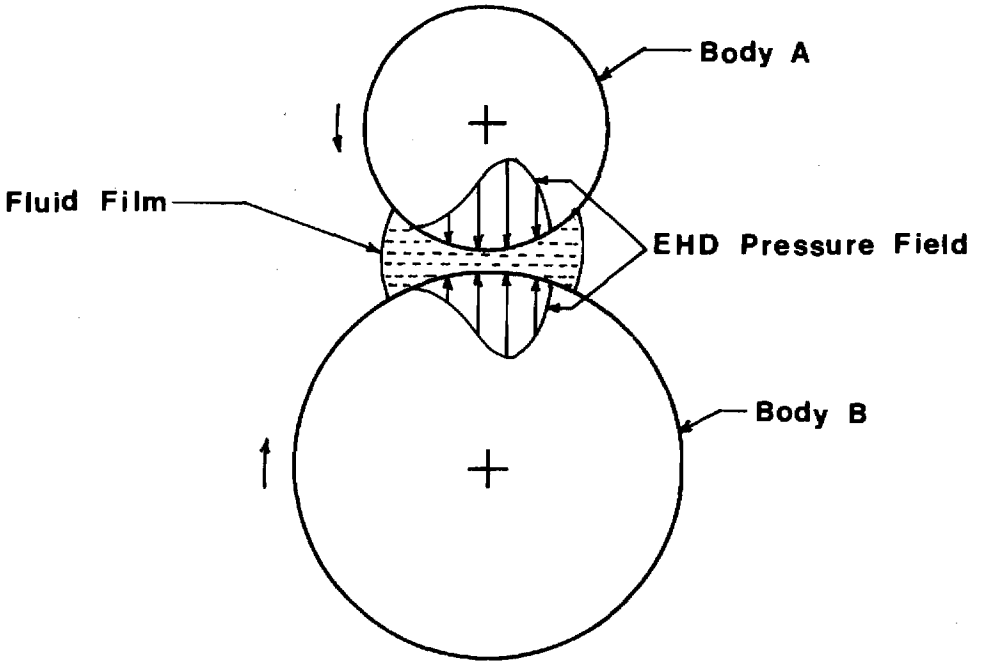

Figure V-1. Two Cylinders.

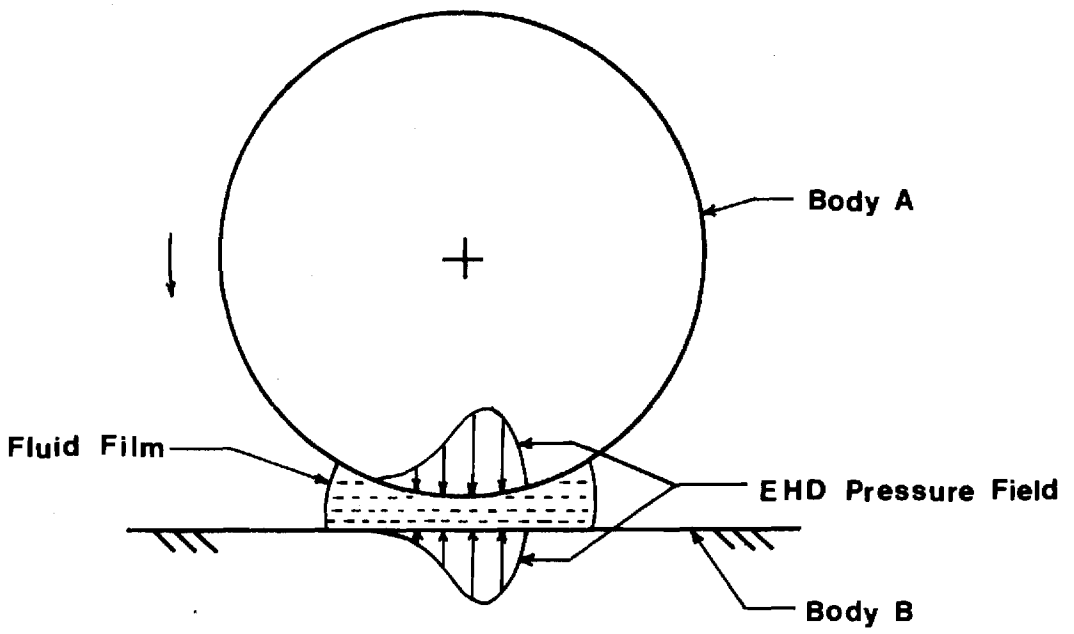

Figure V-2. Cylinder Plate.

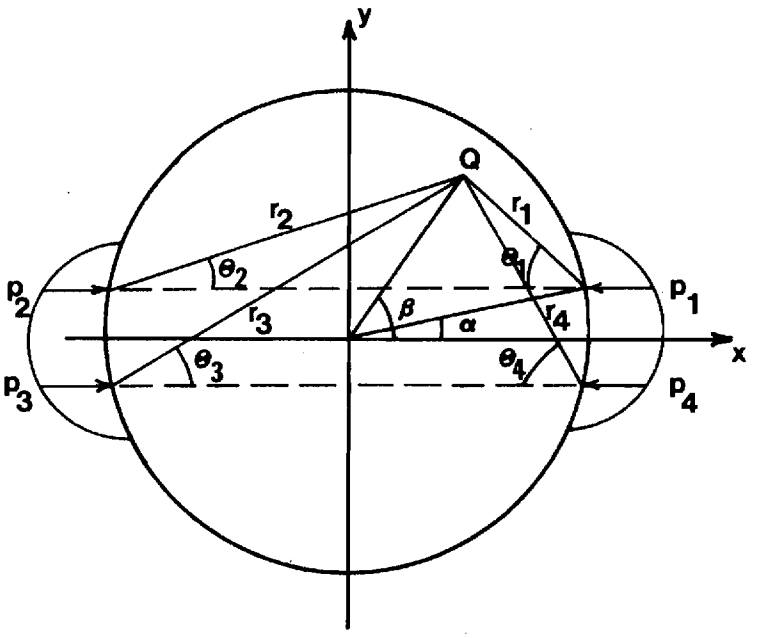

a) Symmetric Pressure Distribution.

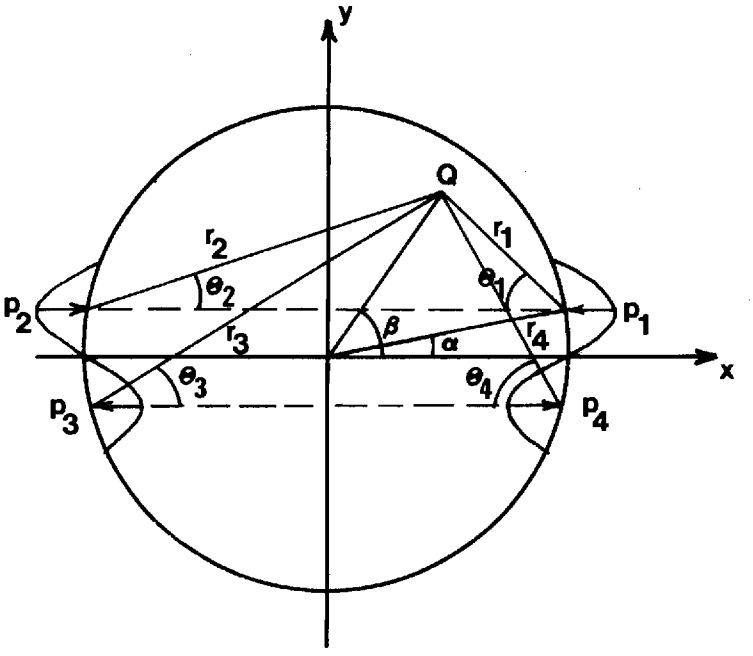

b) Antisymmetric Pressure Distribution.

Figure V-3. Decomposition of the EHD Pressure-Cylinder.

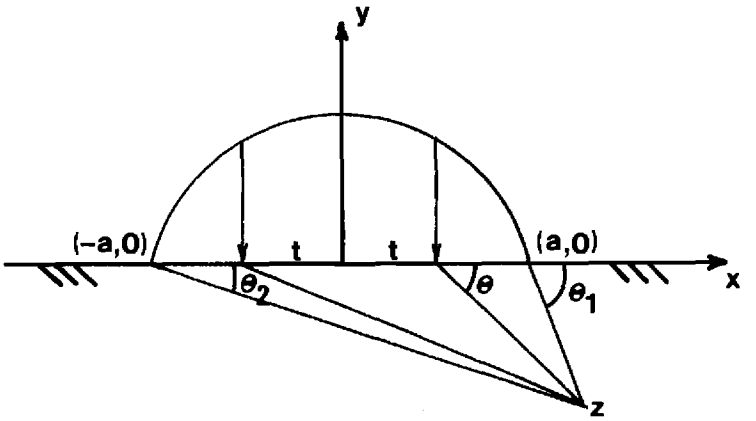

a) Symmetric Pressure Distribution.

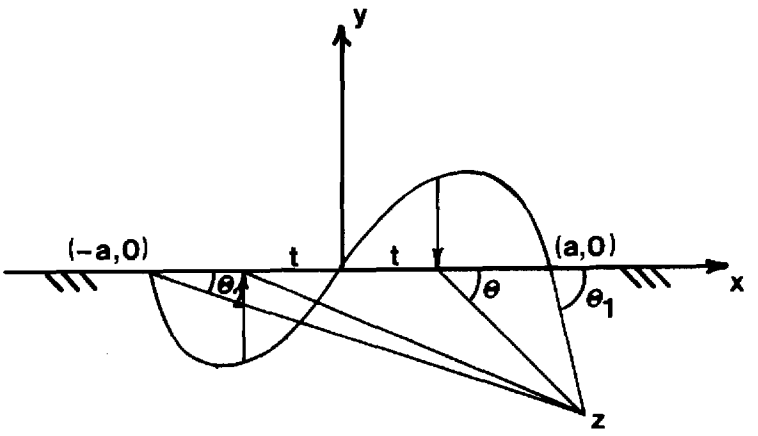

b) Antisymmetric Pressure Distribution.

Figure V-4. Decomposition of the EHD-Pressure-The Plate.

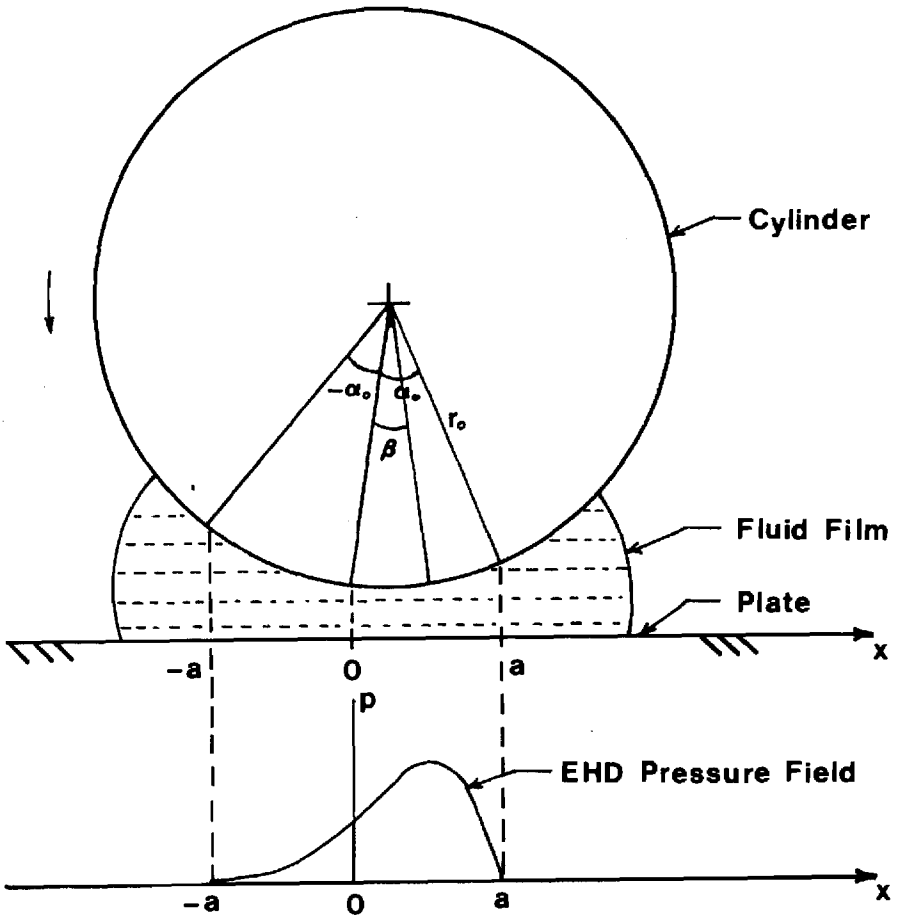

Figure V-5. Schematic Diagram of EHD Contact Zone.

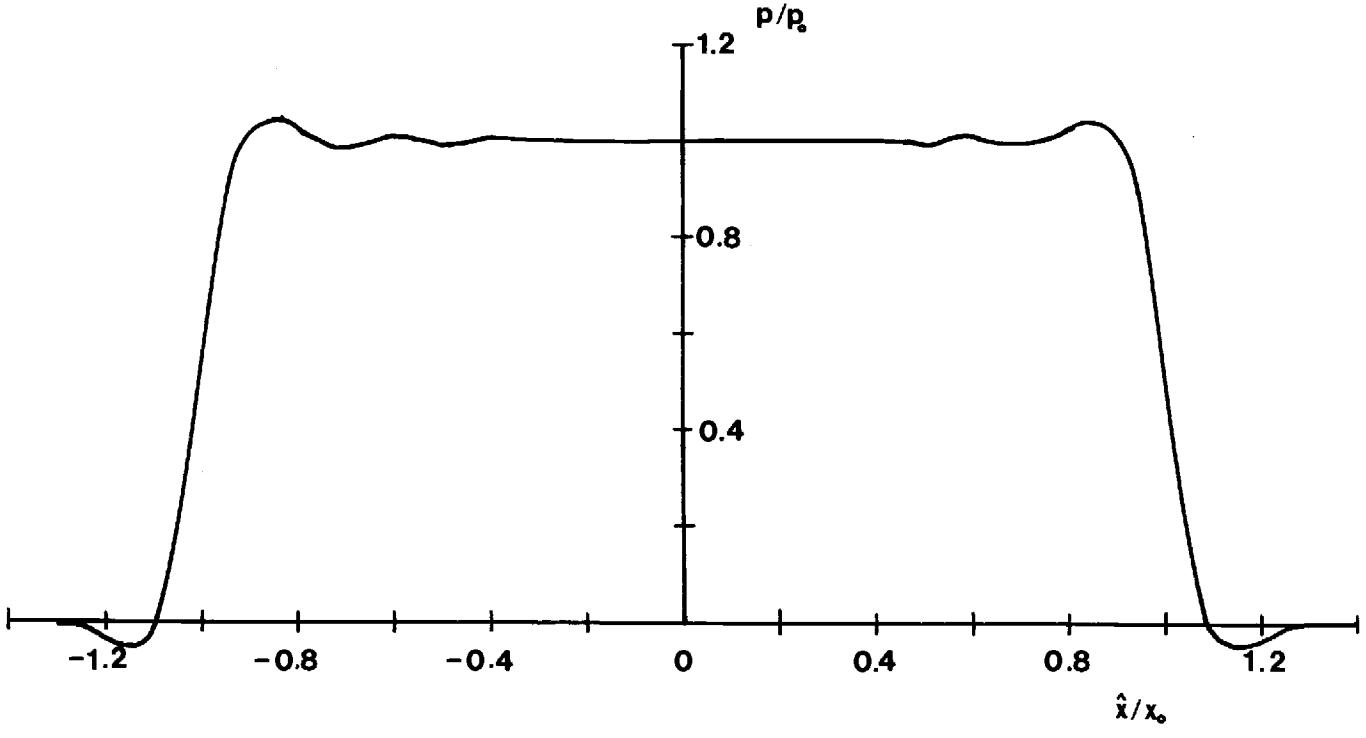

Figure V-6. Test Case 1 - Uniform Pressure Distribution.

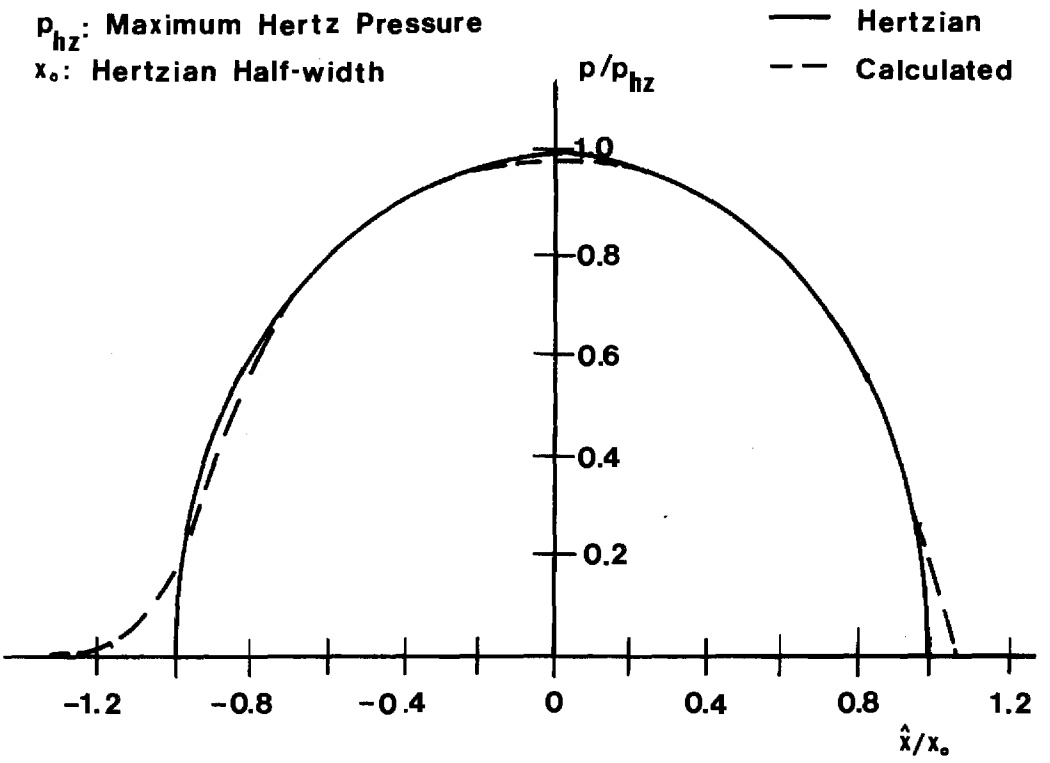

Figure V-7. Test Case 2 - Hertzian Contact.

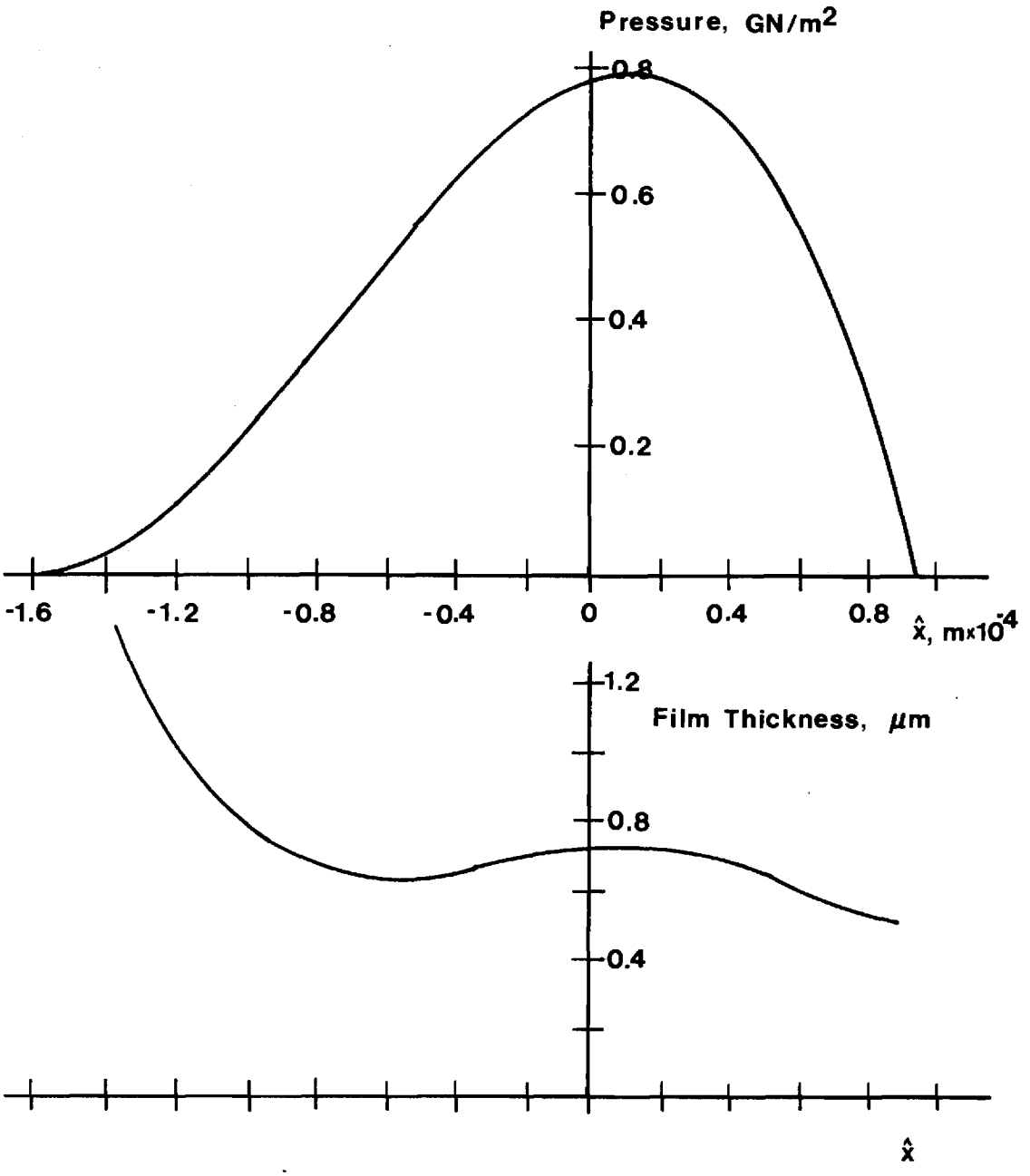

Figure V-8. Test Case 3 - Polynomial Pressure Distribution.

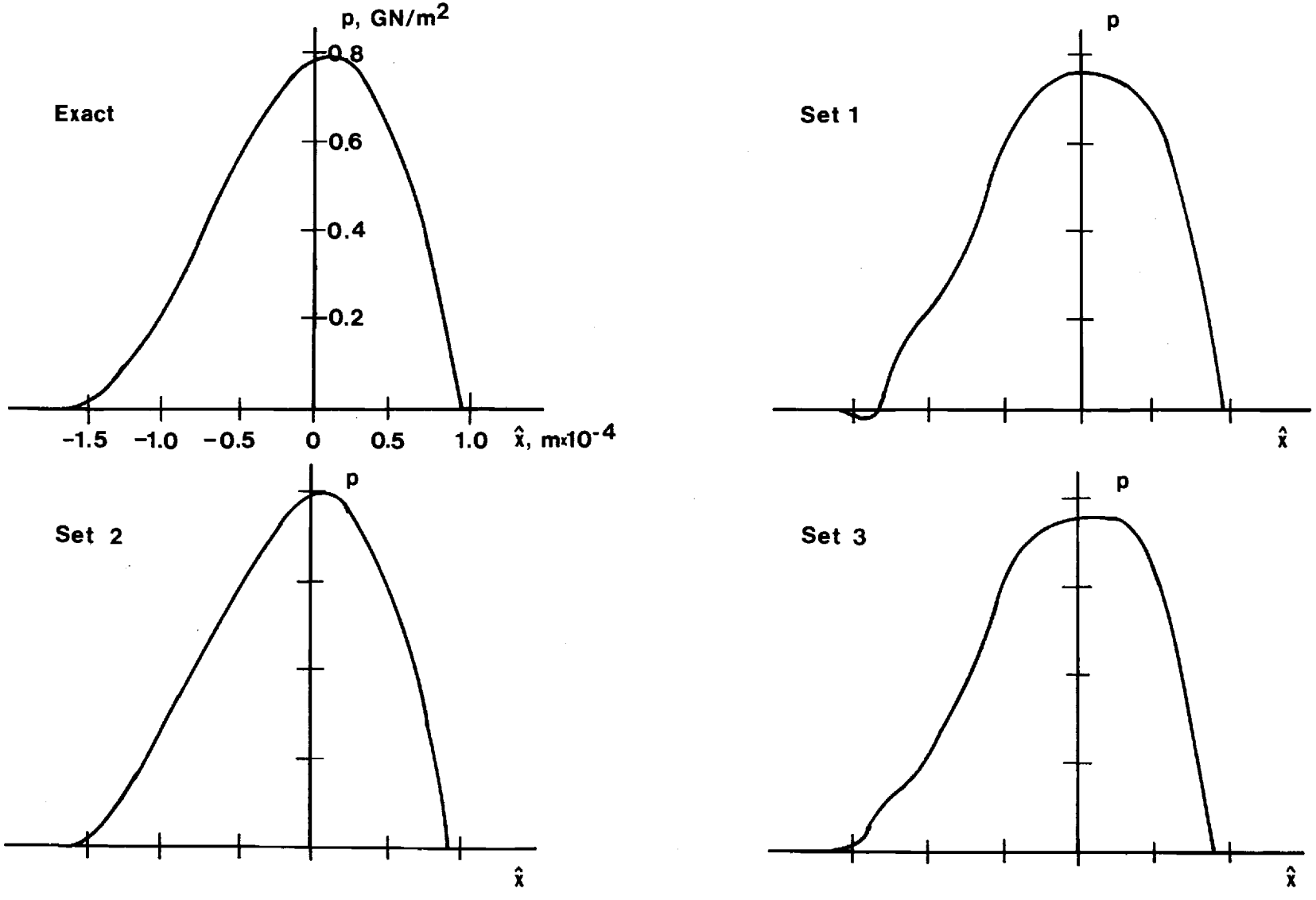

Figure V-9. Test Case 3 - Random Errors Introduced into Film Thickness Values.

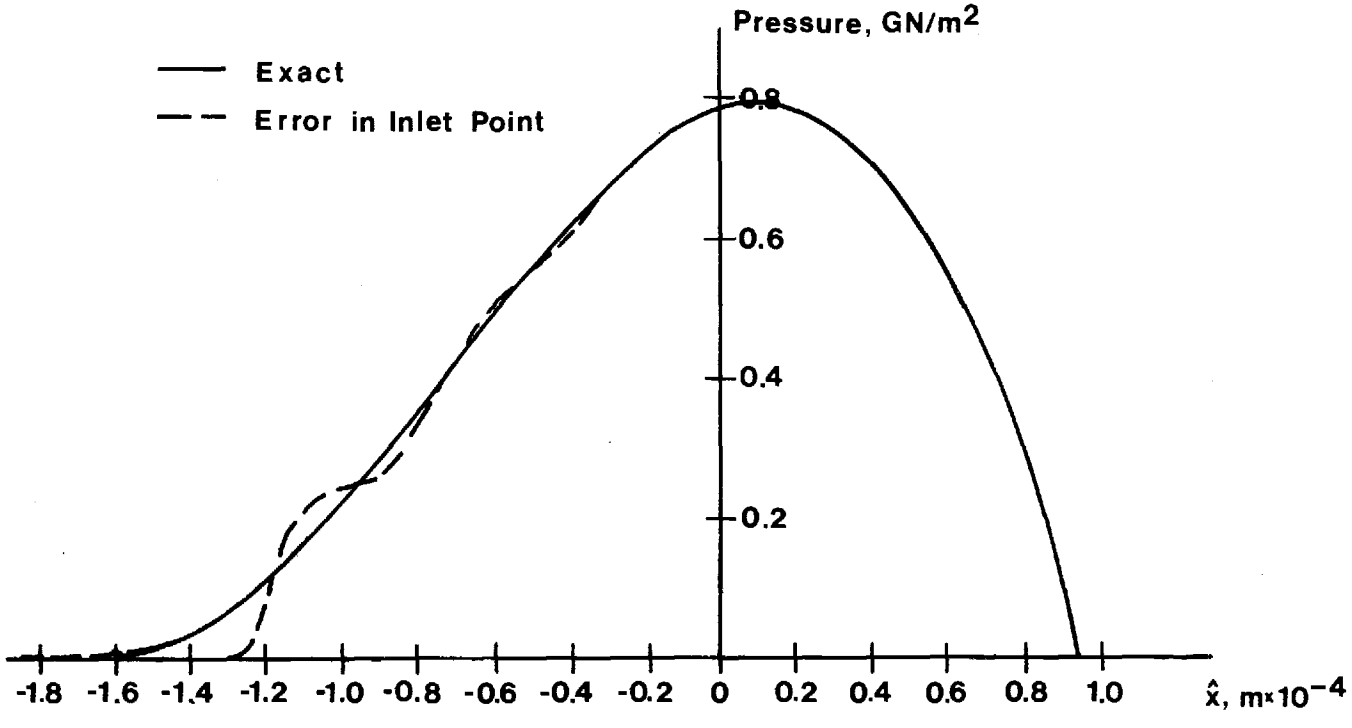

Figure V-10. Test Case 3 - Errors Introduced in Location of Inlet Point.

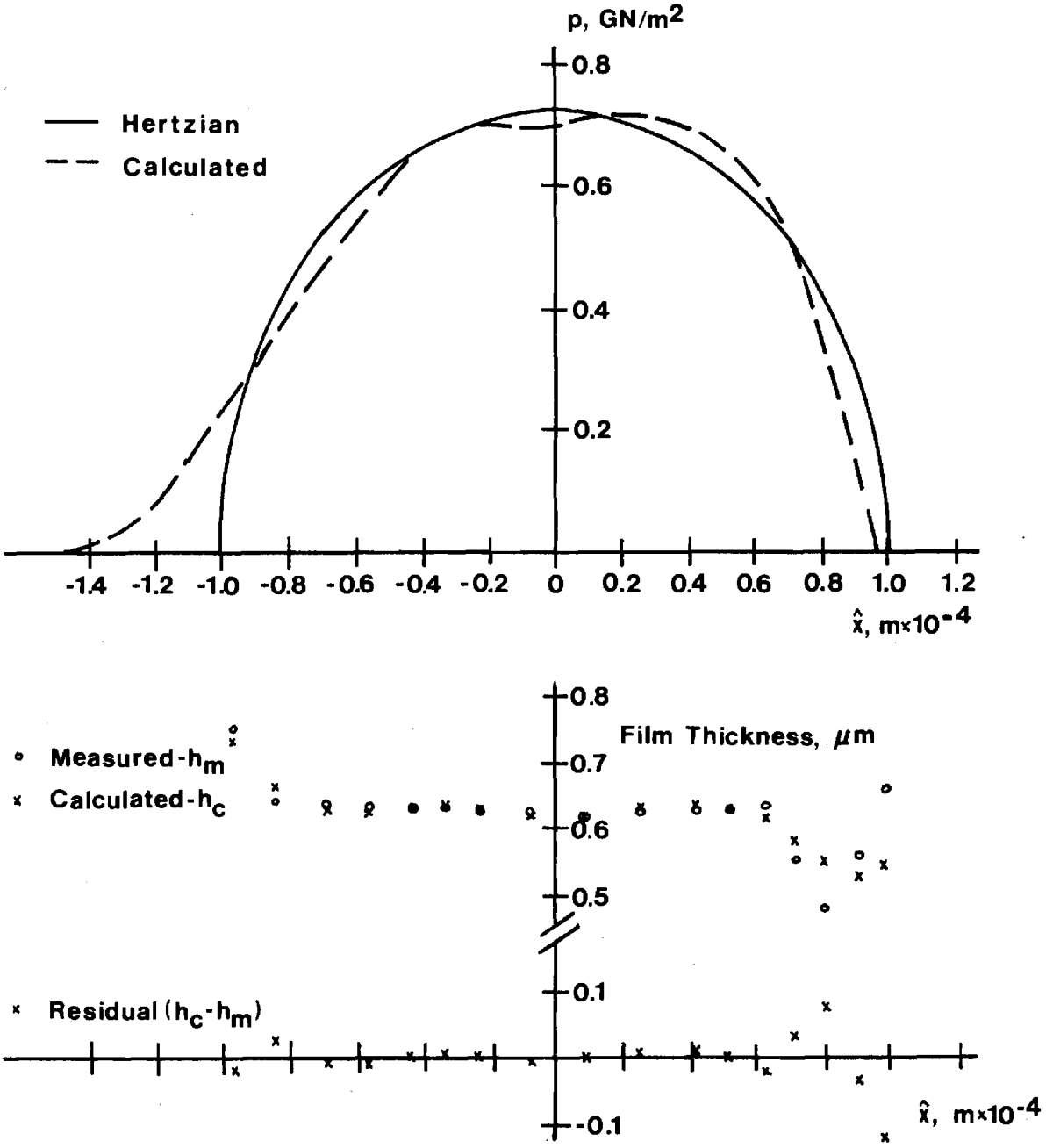

Figure V-11. Calculations Based on Experimental Film Thickness Measurements [71].

APPENDIX A

DESCRIPTION OF EXPERIMENTAL FLUIDS

The following table summarizes the oils investigated in this research and gives characteristic data for each oil.

Experimental Fluids

Symbol	Description
5P4E	Polyphenyl Ether
MCS-1218	Cycloaliphatic Hydrocarbon
MCS-460	Synthetic Hydrocarbon
Santotrac 50	Cycloaliphatic Hydrocarbon Traction Fluid plus additive
N1	Naphthenic Base Oil R-620-15
P1	Paraffinic Base Oil R-620-12
Nap 2	Napthenic Base Oil R-620-16
FN 2961	Super Refined Napthenic Mineral Oil
XRM-177-F4	Synthetic Paraffinic Hydrocarbon plus anti-wear additive
DN-600	Polyalkyl Aromatic
S1	Diester
DC-200-Blend II	Dimethylsiloxane Blend
S3-DC-200-50	Dimethylsiloxane
Advanced Ester	
S2	Polybutene LF-5193

Fluid Characterization

Symbol:	5P4E	
Type:	Five-ring Polyphenyl Ether	
Source:	Monsanto Company	
Properties:	Viscosity at 37.8C, m^2/s	363×10^{-6}
	Viscosity at 98.9C m^2/s	13.1×10^{-6}
	Density at 22.2C, Kg/m^3	1.205×10^{3}
	Density at 37.8C, Kg/m^3	1.19×10^{3}
	Flash Point, C	288
	Pour Point, C	4.4

Symbol:	MCS-1218	
Source:	Monsanto Company	
Type:	Cycloaliphatic Hydrocarbon	
Properties:	It is a combination of two components each have a molecular weight less than 1000.	
	Viscosity at 37.8C, m^2/s	1418×10^{-6}
	Viscosity at 98.9C, m^2/s	18.37×10^{-6}
	Density at 23.9C, Kg/m^3	0.94×10^{3}

Symbol:	MCS-460	
Source:	Monsanto Company	
Type:	Synthetic Hydrocarbon	
Properties:	Viscosity at 37.8C m^2/s	37.2×10^{-6}
	Viscosity at 98.9C m^2/s	4.0×10^{-6}
	Viscosity at 148.9C m^2/s	1.9×10^{-6}
	Pour Point	-29 to -32C
	Density 25C Kg/m^2	$.9327 \times 10^{3}$

Symbol:	Santotrac 50	
Source:	Monsanto Company	
Type:	Synthetic Cycloaliphatic Hydrocarbon Traction Fluid	
Properties:	Viscosity at 37.8C m^2/s	$.34 \times 10^{-4}$
	Viscosity at 98.9C m^2/s	$.056 \times 10^{-4}$
	Pour Point C	-37
	Density at 37.8C	$.889 \times 10^{3}$ Kg/m^3
	Flash Point C	163
	Fire Point C	174
	Specific Heat at 37.8C J/Kg·K	0.51

Additive package includes: Antiwear (zinc dialkyl dithiophosphate), Oxidation inhibitor Antifoam, VI Improver (Polymethacrylate).

Symbol:	N1	
Source:	Sun Oil Company	
Type:	Naphthenic Base Oil R-620-15	
Properties:	Viscosity at 37.8C, m^2/s	24×10^{-6}
	Viscosity at 98.9C, m^2/s	3.728×10^{-6}
	Viscosity Index (ASTM D-2270)	-13
	Flash Point, C	157
	Pour Point	-43
	Density at 20C, gm/cc Kg/m^3	0.9157×10^3
	Average Molecular Weight	305

Symbol:	P1	
Source:	Sun Oil Company	
Type:	Paraffinic Base Oil	
Properties:	Viscosity at 37.8C m^2/s	33.74×10^{-6}
	Viscosity at 98.9C m^2/s	5.402×10^{-6}
	Density at 25C Kg/m^3	$.8602 \times 10^3$
	V.I. (ASTM D-2270)	103
	Pour Point C	-15
	Average molecular weight	404

Symbol:	Nap 2	
Source:	Sun Oil Company	
Type:	Napthenic Base Oil R-620-16	
Properties:	Viscosity at 37.8C m^2/s	114.2×10^{-6}
	Viscosity at 98.9C m^2/s	8.076×10^{-6}
	Viscosity Index (D2270)	< 0
	Density at 20C Kg/m^3	$.9303 \times 10^{3}$
	Average Molecular Weight	357
	Refractive Index	1.5173
	Pour Point C	-23

Symbol:	FN 2961	
Source:	Humble Oil and Refining Company	
Type:	Super Refined Napthenic Mineral Oil	
Properties:	Viscosity at 37.8C m^2/s	78.08×10^{-6}
	Viscosity at 98.9C m^2/s	8.238×10^{-6}
	Viscosity at 148.9C m^2/s	3.3×10^{-6}
	Density at 15.6C Kg/m^3	$.887 \times 10^{3}$
	Pour Point C	-34

Symbol:	XRM-177-F4	
Source:	Mobil	
Type:	Synthetic Paraffinic Hydrocarbon plus antiwear additive	
Properties:	Viscosity at 37.8C Ns/m^2	376×10^{-3}
	Viscosity at 98.9C Ns/m^2	31.6×10^{-3}
	Pour Point C	< -40
	Density 37.8C Kg/m^3	$.8389 \times 10^{-3}$

Symbol:	DN-600	
Source:	Continental Oil Company	
Type:	Polyalkyl Aromatic	
Properties:	Viscosity at 37.8C m^2/s	30×10^{-6}
	Viscosity at 98.9C m^2/s	5.0×10^{-6}
	Viscosity at 148.9C m^2/s	2.3×10^{-6}
	Density at 37.8C Kg/m^3	0.851×10^{3}
	Pour Point C	- 60
	Specific Heat at 37.8C J/Kg C	1624

Symbol:	S1-Diester	
Source:	Rohm and Haas Company	
Type:	Diester-Plexol 201 bis-2-ethyl hexyl sebecate (PL 5159)	
Properties:	Viscosity at -53.9C m^2/s	7988×10^{-6}
	Viscosity at 37.8C m^2/s	12.75×10^{-6}
	Viscosity at 98.9C m^2/s	3.32×10^{-6}
	Cloud Point (ASTM D-2500)	below -54C

Symbol:	DC-200-Blend II	
Source:	Dow Corning Corporation	
Type:	Dimethylsiloxane Blend E1923-49	
Properties:	Viscosity at 25C m^2/s	1060×10^{-6}
	Molecular Weight (GPC)	160,000
	Component Viscosities:	
	50×10^{-6} m^2/s	75%
	$11{,}000 \times 10^{-6}$ m^2/s	12%
	$330{,}000 \times 10^{-6}$ m^2/s	13%

Symbol:	S3-DC-200-Blend II	
Source:	Dow Corning Corporation	
Type:	Dimethylsilixane DC-200	
Properties:	Viscosity at 37.8C m^2/s	82.6×10^{-6}
	Viscosity at 98.9C m^2/s	33.1×10^{-6}
	Density at 25C Kg/m^3	$.968 \times 10^{3}$
	Molecular Weight (Average)	7,000

Symbol:	Advanced Ester	
Source:	Shell Oil Company	
Type:	Based on Pentaerythritol (Aeroshell Turbine Oil 555 Base Oil)	
Properties:	Viscosity at 37.8C m^2/s	25.8×10^{-6}
	Viscosity at 98.9C m^2/s	5.1×10^{-6}
	Viscosity at 148.9C m^2/s	2.3×10^{-6}
	Density at 37.8C Kg/m^3	$.979 \times 10^{3}$

Symbol:	S2	
Source:	American Oil Company	
Type:	Polybutene LF-5193	
Properties:	Viscosity at -17.8C m^2/s	$18{,}836 \times 10^{-6}$
	Viscosity at 37.8C m^2/s	109×10^{-6}
	Viscosity at 98.9C m^2/s	10.6×10^{-6}
	Density at 25C Kg/m^3	0.8443×10^{3}
	V.I. (ASTM D-2270)	87
	Polymer Number Average molecular weight	409

APPENDIX B

PERSONNEL SUPPORTED ON THE GRANT

The following research personnel have been in part supported by this NASA Grant (1971-1976):

1. Principal Investigators:

D. M. Sanborn	W. O. Winer
Associate Professor	Professor
Mechanical Engineering	Mechanical Engineering

2. Research Associates:

S. Bair	G. M. Rentzepis
Research Engineer	Associate Professor
Mechanical Engineering	Engineering Science and Mechanics

3. Doctoral Candidates:

Mohammed A. Alsaad, Ph.D. (1975-76)

"Light-Scattering Study of the Glass Transition and the Glassy State in Lubricating Oils"
(degree granted 8/76)

Stephen L. Carlson (1971-75)

"The General Viscous Lubrication of Rolling and Sliding Elastic Cylinders"

Jørgen Jakobsen, Ph.D. (1971-73)

"Lubricant Rheology at High Shear Stress"
(degree granted 9/73)

Richard K. Kunz (1975-1976)

(Topic: The Mechanics of Glassy Lubricants in EHD)

H. Nagaraj, Ph.D. (1973-76)

"Investigation of Some Temperature-Related Phenomena in Elastohydrodynamic Contacts including Surface Roughness Effects"
(completed 12/76)

4. Master's Thesis Research:

Vernon K. Ausherman, M.S. (1972 - 75)

"Infrared Temperature Mapping in Elastohydrodynamic Lubrication"
(degree granted 3/75)

Richard K. Kunz, M.S. (1974-74)

"Thermal and Traction Behavior in Sliding Elastohydrodynamic Contacts"
(degree granted 11/74)

Manuel A. Molina C., M.S. (1973-74)

"Dynamics of Roller Bearings Considering Elastohydrodynamic Forces"
(degree granted 6/74)

Valentin A. Turchina, M.S. (1972-73)

"Pressure and Temperature Measurement Techniques in Elastohydrodynamic Contacts"
(degree granted 6/73)

David L. Walker, M.S. (1972-73)

"Polymer Degradation in Sliding Elastohydrodynamic Lubrication"
(degree granted 12/73)

APPENDIX C

PUBLICATIONS RESULTING FROM RESEARCH SUPPORTED COMPLETELY OR IN PART BY THE GRANT

I. Student theses completed. Ph.D. theses are published through University Microfilm and abstracted in Dissertation Abstracts.

1. Valentin Alexandru Turchina
"Pressure and Temperature Measurement Techniques in Elastohydrodynamic Contacts", M.S. Thesis, Georgia Institute of Technology, June 1973.

2. Manual A. Molina C.
"Dynamics of Roller Bearings Considering Elastohydrodynamic Forces", M.S. Thesis, Georgia Institute of Technology, June 1974.

3. Jorgen Jakobsen
"Lubricant Rheology at High Shear Stress"
Ph.D. Thesis, Georgia Institute of Technology, September 1973.

4. Mohammed Ahmed Alsaad
"Light-Scattering Study of the Glass Transition and the Glassy State in Lubricating Oils"
Ph. D. Thesis, Georgia Institute of Technology, August, 1976.

5. Vernon K. Ausherman, Jr.
"Infrared Temperature Mapping in Elastohydrodynamic Lubrication", Ph.D. Thesis, Georgia Institute of Technology, March, 1975

6. David L. Walker
"Polymer Degradation in Sliding Elastohydrodynamic Lubrication"
M.S. Thesis, Georgia Institute of Technology, November, 1973.

7. H. Nagaraj
"Investigation of Some Temperature-Related Phenomena in Elastohydrodynamic Contacts Including Surface Roughness Effects", Ph.D. Thesis, Georgia Institute of Technology, December, 1976.

II. Technical Papers

1. Winer, W. O., "A Viscometer for High Pressure Use, and Some Results", Trans. ASME, Vol. 94, No. 3, Series D, The Journal of Basic Engineering, pp. 586-589, 1972.

2. Lee, D., Sanborn, D. M., and Winer, W. O., "Some Observations of the Relationship Between Film Thickness and Load in High Hertz Pressure Elastohydrodynamic Contacts", Trans. ASME, Journal of Lubrication Technology, Vol. 95, pp. 386-390, 1973.

3. Jakobsen, J., Sanborn, D. M., and Winer, W. O., "Simulation of Severe Shear Conditions in Lubrication", Society of Automotive Engineers, SP-382, pp. 59-67, 1973.

4. Turchina, V. A., Sanborn, D. M., and Winer, W. O., "Temperature Measurements in Sliding Elastohydrodynamic Point Contacts", Trans. ASME, Journal of Lubrication Technology, Vol. 96, pp. 410-417, 1974.

5. Winer, W. O., "A Review of Experimental Elastohydrodynamic Lubrication Research", NSF Tribology Workshop Proceedings, 1973.

6. Sanborn, D. M., Jakobsen, J., Carlson, S., and Winer, W. O., "Investigations of Lubricant Rheology as Applied to Elastohydrodynamic Lubrication", NASA CR-121169, NASA Lewis Research Center, June 1972.

7. Sanborn, D. M., Jakobsen, J., Carlson, S., and Winer, W. O., "Investigations of Lubricant Rheology as Applied to Elastohydrodynamic Lubrication", NASA CR-134539, NASA Lewis Research Center, December 1973.

8. Jones, W. R., Johnson, R. L., and Sanborn, D. M., and Winer, W. O., "Viscosity-Pressure Measurements for Several Lubricants to 5.5 x 10^8 N/m^2 (8 x 10^4 psi) and 149 C (300F)", NASA TND-7736, pp. 37, August 1974.

9. Jakobsen, J., and Winer, W. O., "Traction of Elastohydrodynamic Contacts with Thermal Shearing Flow", Trans. ASME, Journal of Lubrication Technology, Vol. 97, No. 3, 424-429, 1975.

10. Jakobsen, J., and Winer, W. O., "Dissipative Heating Effects and EHD Corrections for Viscous Newtonian Flow in High Shear Stress Capillary Viscometry", Trans. ASME, Journal of Lubrication Technology, Vol. 97, No. 3, 472-478, 1975.

11. Jakobsen, J., and Winer, W. O., "High Shear Stress Behavior of Some Representative Lubricants", Trans. ASME, Journal of Lubrication Technology, Vol. 97, No. 3, 479-485, 1975.

12. Jones, W. R., Johnson, R. L., Sanborn, D. M., and Winer, W. O., "Viscosity-Pressure Measurements for Several Lubricants to 5.5×10^8 N/m^2 (8×10^4 psi) and 149 C (300F) (to be published ASLE, Transactions and presented at ASME/ASLE Joint Lubrication Conference, Montreal Canada, October 1974, ASLE Preprint 74LC-4C-1).

13. Carlson, S. F., and Winer, W. O., "The Viscous Lubrication of Rolling and Sliding Rigid Cylinders", ASME Trans., Journal of Lubrication Technology, Vol. 97F, No. 2, 180-186, April 1975.

14. Walker, D., Sanborn, D. M., and Winer, W. O. "Polymer Degradation in Elastohydrodynamic Lubrication", Proceedings of International Colloque on Polymers and Lubrication, C.N.R.S., Brest, France, 1974.

15. Molina-Combita, M. A., Sanborn, D. M., and Winer, W. O., "Dynamics of Roller Bearings Considering Elastohydrodynamic Forces", Proceedings of Japanese Society of Lubrication Engineers/American Society of Lubrication Engineers Joint International Meeting, Tokyo, Japan, June 1975.

16. Winer, W. O., "The Mechanical Properties of Fluids in High Pressure Hydraulic Systems", Proceedings of National Fluid Power Conference, Vol. XXVIII, 412-421, 1974.

17. Walker, D. L., Sanborn, D. M., and Winer, W. O., "Molecular Degradation of Lubricants in Sliding Elastohydrodynamic Contacts", Trans. ASME, Journal of Lubrication Technology, Vol. 97, No. 3, 390-397, 1975.

18. Kunz, R. K., and Winer, W. O., "Prediction of Traction in Sliding EHD Contacts", Trans. ASME, Journal of Lubrication Technology, Vol. 98, Series F, No. 3, 362-365, 1976.

19. Ausherman, V. K., Nagaraj, H. S., Sanborn, D. M., and Winer, W. O., "Infrared Temperature Mapping in Elastohydrodynamic Lubrication", Trans. ASME, Journal of Lubrication Technology, Vol. 98, Series F, No. 2, 236-242, 1976.

20. Sanborn, D. M., and Winer, W. O., "Lubricant Properties in Thin Lubricating Films", presented at ACS Meeting, New York City, 1976.

21. Nagaraj, H. S., Sanborn, D. M., and Winer, W. O., "Effects of Load, Speed and Surface Roughness on Sliding EHD Contact Temperatures", Presented at the Joint ASME-ASLE Lubrication Conference, Boston, Massachusetts, October 1976 and to be published in Trans. ASME, Journal of Lubrication Technology.